Dynamics of the Chemostat

A Bifurcation Theory Approach

Abdelhamid Ajbar
Khalid Alhumaizi

CRC Press
Taylor & Francis Group
A CHAPMAN & HALL BOOK

Dynamics of the Chemostat

A Bifurcation Theory Approach

This page intentionally left blank

Dynamics of the Chemostat

A Bifurcation Theory Approach

Abdelhamid Ajbar
Khalid Alhumaizi

CRC Press
Taylor & Francis Group
Boca Raton London New York

CRC Press is an imprint of the
Taylor & Francis Group an **informa** business
A CHAPMAN & HALL BOOK

CRC Press
Taylor & Francis Group
6000 Broken Sound Parkway NW, Suite 300
Boca Raton, FL 33487-2742

Version Date: 20110613

International Standard Book Number-13: 978-1-4398-6716-7 (eBook - PDF)

We thank God Almighty for the blessings bestowed during the writing of this book. Our thanks also go to our parents and families for their endless support. For Dr. Ajbar: to mother Khadija, wife Saida and kids, Ayman, Sami, and Ziyad. For Dr. Alhumaizi: to mother Sara, wife Muneera and kids, Shatha, Alaa, and Ibrahem.

This page intentionally left blank

Contents

Preface

Since its invention in the late forties of the last century, the chemostat has become a ubiquitous tool for studying microbial physiology and metabolism. Despite its simplicity, the chemostat is known to often present operational problems that manifest themselves in the form of multiple steady states and the occurrence of undesired oscillations for some range of operating parameters of the unit. These instabilities can pose safety hazards and adversely affect the optimization of the bioreactive system. An early detection of difficult operating regions in the bioreactor would allow the removal or at least the reduction of these operational problems in the early stage of process design, and this would ultimately improve the operability of the unit.

The study of the stability of the chemostat for various biological systems has been receiving attention in the literature since the sixties. The models used for these studies varied in complexity and included combinations of (un)structured and (non)segregated models. The tools, on the other hand, used for the stability analysis included linearized stability, continuation techniques, and arguments from the theory of asymptotically autonomous systems as well as the singularity theory. The latter approach found considerable applications in chemical reaction engineering due to the work of Balakotaiah and Luss in the 1980s [42, 43, 44, 45, 46] on the analysis of the multiplicity of the continuous stirred tank reactor. The singularity theory can provide a useful framework for classifying branching phenomena in which different types of multiplicity of the nonlinear model can be delineated. This classification is usually combined with the construction of bifurcation diagrams that can yield substantial information on the prevailing dynamics. These diagrams can also be used to determine if the model supports the steady state and dynamic behavior observed experimentally, and can also guide the design of experiments.

The first application of the singularity theory to study the behavior of the chemostat was carried out by Ajbar and Ibrahim [26] in the late nineties who analyzed the multiplicity of the basic unstructured model of the chemostat with substrate inhibition and constant yield coefficient. This book is based on the work of the author that covered various applications of the use of elementary concepts of bifurcation theory to analyze the static and dynamic behavior of the chemostat. The book's organization includes three introductory chapters: The first chapter includes a survey of the major work carried out in the literature for the study of stability of continuous bioreactors. The second chapter presents the different modeling approaches used for the description

of the bioreactive system, as well as an overview of the different kinetic expressions for growth rates. The third introductory chapter presents a practical introduction to some tools used for the analysis of nonlinear systems. These include concepts of multiplicity, bifurcation as well as an introduction to the singularity theory. The book is afterwards divided into five application parts. The first part (Chapters 4 and 5) studies the static and dynamic behavior of the basic unstructured model of the chemostat for both cases of constant and variable yield coefficients as well as in the presence of wall attachment.

The second part (Chapters 6–10) deals with the dynamics of interacting species, including pure and simple microbial competition, biodegradation of substitutable substrates, dynamics of plasmid-bearing and plasmid-free recombinant cultures, and dynamics of predator–prey interactions. The third part (Chapters 11–13) covers the dynamics of chemostat with product formation for various growth models. The fourth part (Chapters 14–17) provides examples of the use of bifurcation theory to study the operability and dynamics of some models of continuous bioreactors. A final chapter (Chapter 18) is devoted to the application of elementary concepts of bifurcation theory to analyze the dynamics of a periodically forced bioreactor. The book also includes an appendix that provides some theoretical background that supplements the materials covered in the introductory Chapter 3. These include the implicit function theorem, Lyapunov–Schmidt reduction technique, and center manifold theory, as well as some tools used to analyze the dynamics of periodically forced systems.

Chapter 1

INTRODUCTION TO STABILITY OF BIOREACTORS

1.1 Introduction

Nonlinear models of continuous bioreactors are known to exhibit a variety of phenomena ranging from steady-state multiplicity to sustained oscillations. The study of the complex behavior exhibited by these models is not only of theoretical relevance, for these phenomena are rather common in a number of processes. Examples include the multiple steady states exhibited by some cultures [378, 379] and the oscillatory behavior observed during the continuous growth of some populations [87, 151, 274] as well as the unstable behavior found in continuous cultures of recombinant DNA [268]. Large fluctuations or instabilities in bioreactors can pose safety hazards and adversely affect the productivity of the unit.

In this regard, continuous cultures of Hybridoma cells, for instance, are known to exhibit multiple steady states under specific operating conditions. Studies showed that different steady states can be obtained when this mammalian cell culture, grown under the same operating conditions but different initial metabolic states, is switched from fed-batch operation to continuous mode [119, 379]. The existence of this complex behavior is attributed to the existence of multiple metabolic pathways for cell growth, as Hybridoma cells are known to utilize both glucose and glutamine as substitutable substrates serving the needs of the cells [49, 377].

Continuous bioreactors are also known to exhibit complex oscillations. Experimental observations of this behavior are numerous and are associated with several microbial populations such as *Saccharomyces cerevisiae* [75, 177, 252, 270, 301, 343, 362], *Klebsiella pneumoniae* [246], and *Zymomonas mobilis* [66, 87, 175, 243]. *Saccharomyces cerevisiae*, for instance, is an important micro-organism in a number of industries, including, baking, food manufacturing, and genetic engineering. Different types of oscillatory behavior were observed for the baker's yeast. These behaviors, that include sudden appearance and disappearance of oscillations, can occur in both anaerobic [75, 301] and aerobic cultures under glucose-limited environments [290, 343]. The underlying mechanisms behind such oscillatory behavior have been a subject of intensive research in the literature [129, 177, 252, 270, 301, 343, 380]. In

strictly anaerobic conditions, it appears that it is the alternation of conflicting effects of ATP (adenosine triphosphate) molecules on the glycolysis pathway that causes the birth of oscillations [129]. In aerobic cultures, on the other hand, the phenomenon is connected with a periodic change in the metabolic pathway of the cell and a simultaneous synchronization of the budding process [290, 343].

Zymomonas mobilis is another important micro-organism commonly used to perform alcoholic fermentation for both food and energy purposes. Continuous cultures of this micro-organism, using glucose as the main carbon source, are also known to exhibit oscillatory behavior for long periods and for a wide range of operating parameters [175, 243]. This adversely affects ethanol production and reactor operability. The underlying cellular mechanisms causing oscillations are different from those of *S. cerevisiae*, since *Z. mobilis* has special metabolic features, as the micro-organism does not metabolize glucose through the glycolytic pathway and cannot oxidize its carbon source. Various studies [87, 175, 243] provided interpretation and modeling of the oscillatory behavior in the continuous cultures of this micro-organism.

Steady-state multiplicity and oscillatory behavior are also known to occur as a result of competition between various populations. An important example is the problem of plasmid stability and strain reversion in recombinant DNA cultures [150, 158]. In such cultures, the genetic modification usually takes place through the insertion of a plasmid to code for the production of a desired protein. In some cases, the plasmid is not transfered during reproduction introducing therefore a plasmid-free micro-organism into the process. This variant, having a competitive advantage over the plasmid-bearing strain, causes the instability of the bacterium-plasmid system. The study of the stability of such systems is important for the analysis of the outcomes of the competition between plasmid-free and plasmid-bearing organisms.

Oscillatory behavior is also known to occur in predator–prey interactions. Experimental evidence was reported in a number of biological systems [71, 103, 180, 241, 356] such as the predation by the amoebae *Dictyostelium discoideum* on *E. coli* bacteria [356] and the simultaneous continuous cultivation of *Azotobacter vinelandii* and protozoan *T. pyriformis* [180].

Steady-state multiplicity and oscillations also occur in bioreactors used for wastewater treatment. Biological treatment processes are important units for hazardous substance disposal. Static multiplicity was shown, for instance, to occur in continuous nitrification processes [319], as well as in some activated sludge reactors, where protozoa is known to prey on unflocculated bacteria and induces predator–prey dynamics in the reactor [41].

The afromentioned studies recognize that metabolic regulation in the form of control of enzyme synthesis and activity is responsible for nonlinear behavior in bioreactors. However, equally important are the findings that the conditions for the existence of steady-state multiplicity and/or oscillatory behavior are strongly dependent on bioreactor operating conditions such as dilution rate, inlet feed conditions, dissolved oxygen concentration, and agitation

speed. Therefore, while the cellular mechanisms for the occurrence of these complex phenomena may still not be fully understood for a number of microbial systems, what is certain is that the occurrence of such phenomena is caused by the mutual interactions between the microbial adaptation strategies to the environment and the modifications produced in the culture broth by both the cell metabolism and the dilution process [70]. This points to the need to develop appropriate models that can describe the intracellular and operating elements of the bioreactive system, but also to the need to use an appropriate theoretical framework for the mathematical analysis of these models, especially given the large number of operating and kinetic parameters in such systems.

1.2 Stability Studies of Continuous Bioreactors

As noted by Alhumaizi and Aris [33], it seems that one necessary requirement for any chemical or biochemical reacting system to exhibit "exotic" behavior such as multiplicity or oscillatory behavior is that it should have some kind of "feedback mechanism." Some intermediate species or products of the process must be able to affect the rate of earlier steps. This effect may be thermal as in the case of an irreversible exothermic chemical reaction, when the increase in the temperature affects the reaction rate. The feedback may also be chemical as in the case of nonmonotonic (or inhibited) growth or in autocatalytic (e.g., enzymatic) reactions, when a product of reaction increases the reaction rate and thus its own production rate. In this regard, the study of the stability of the continuous stirred tank bioreactor (CSTBR) (the famous chemostat) has been receiving attention in the literature since the sixties. In the following, we present a survey of some major studies that were carried out for the stability analysis of these units.

The existence of multiple steady states in the chemostat with a single substrate-inhibited growth was studied by Andrews [35] and by Chi et al. [78], who showed the existence of two steady states with inhibitory substrates. The authors also found that the region of multiplicity varies with substrate feed concentration, activity of biological material on the reactor wall, and the relative surface area to volume ratio. Aris and Humphrey [37], on the other hand, analyzed the multiplicity problem of the pure and simple competition characterized by substrate inhibition. The authors found that the steady states depend on the relative disposition of the growth curves of each species and identified more than thirty distinct types of situations. The experimental evidence for the existence of multiple steady states and the transition from one state to another were presented, respectively, by Pawlowsky et al. [282] for phenol oxidation and DiBiasio et al. [94] for methanol bioxidation. The experiments included the determination of growth rate, yield, and intermediate

metabolite concentration. This information was used to interpret the stability behavior in terms of biochemistry and bioenergetics of substrate metabolism. A theoretical investigation of dynamic behavior of the chemostat was carried out by Agrawal et al. [7], while Mihail and Straja [247] carried out a theoretical analysis of the multiplicity of the chemostat with cell recycle and substrate inhibition kinetics. The stability and multiplicity phenomena of the activated sludge process were studied by Rozich and Gaudy [304] for a single species system growing on a toxic waste, and by Bertucco et al. [59] for substrate inhibition kinetics and constant solids recycle. Sheintuch [318, 319] also carried out a theoretical study of the stability of activated sludge reactors as well as the continuous nitrification process. The authors found that under the same operating conditions and with different initial conditions, a state of either complete oxidation to nitrate or partial oxidation to nitrite could be reached. Sidhu et al. [322] also studied the stability of the treatment of wastewaters in the activated sludge process. Using a biochemical model consisting of two types of bacteria and two types of ciliated protozoa, the authors studied the performance of a single tank system compared to that of a two-reactor cascade configuration. The authors [259] also carried out a study of the stability and performance of flow reactors compared to membrane reactors, when the kinetics of the biodegradation are described by the Contois growth model [81]. Recently, the same authors [261] carried out a stability analysis of a structured model of activated sludge reactor. The biochemical processes occurring within the reactor were represented by the activated sludge model number 1 (ASM1) [147].

The dynamic features of continuous commensalistic cultures with self and cross inhibition were studied by Sheintuch [317], while a detailed bifurcation analysis was carried out later by Parulekar and Lim [275]. The authors discovered seven steady states in these systems, including a complete washout state, two partial washout states, and four coexistence states.

The dynamics of recombinant cells, on the other hand, were investigated by Chang and Lim [76] for a chemostat containing antibiotic resistant cells. Both the existence of multiple steady states and the occurrence of oscillatory behavior were examined. Sensitivity analysis for several kinetic parameters, such as susceptibility of the plasmid-free cells to an antibiotic, were also carried out. The stability of the chemostat for plasmid-bearing, plasmid-free mixed recombinant cultures was studied, using local stability analysis by Ryder and DiBiasio [311], and later in a more elaborate way by Stephanopoulos and Lapidus [337]. The authors used a general method based on an index theory of singular points to determine the stability portrait of competitive interactions according to mutual dispositions of the growth curves. Recently, Alhumaizi et al. [32] revisited the stability of recombinant DNA using elementary concepts of singularity theory.

Smith and Waltman [329] compiled in their excellent book their extensive work on the dynamics of the chemostat. They included, in particular, the general chemostat, the competition on three trophic levels, the chemostat

with an inhibition, and the variable yield model. The authors showed that global stability results can be obtained in many of the studied systems. Zhang and Henson [378] used the bifurcation theory to study the behavior of three bioreactor models used for the growth of Hybridoma cells, *Zymomonas mobilis* and *Saccharomyces cerevisiae* organisms. The authors illustrated the usefulness of bifurcation tools in analyzing the transient behavior of the chemostat. The multiplicity of the well-known cybernetic model was, on the other hand, analyzed in detail by Namjoshi et al. [254].

Other studies for bioreactor stability include the static multiplicity of a temperature-controlled chemostat [197], where the problem of temperature stabilization in a reactor equipped with a heat exchanger was investigated. The steady-state analysis of polysaccharide production by *Methylomonas mucosa* was carried out in [223]. The authors found two nontrivial steady states for a single continuous stirred tank bioreactor. The dynamic study of a bioreactor subject to product inhibition was carried out by Lenbury et al. [214], who studied the behavior of the process in terms of multiplicity and existence of limit cycles. Edissonov [106], on the other hand, examined the effect of medium viscosity on multiplicity patterns of a chemostat.

The stability analysis of continuous membrane bioreactors was carried out by Lenbury et al. [215]. Bifurcation analysis showed the ability of the studied model to simulate oscillatory and other complex dynamic behavior, which was observed in experimental data. Garhyan and Elnashaie [121] examined the membrane bioreactor for ethanol production. The authors used the model developed by Jöbses et al. [175] to give an exhaustive picture of bifurcations occurring in the dynamical system. The authors also showed theoretically the existence of chaotic behavior. Pinheiro et al. [287] studied the bifurcation analysis of an aerated continuous flow chemostat in which microbial growth was subjected to gaseous substrate limitation. The influence of mass transfer on the system dynamic behavior was studied. Dutta et al. [104], on the other hand, carried out an experimental and theoretical investigation of the multiplicity of the chemostat for microbial reduction of sulfur dioxide.

The dynamics of continuous biofilm reactors were studied by Russo et al. [310] for the conversion of phenol. The study showed that the reciprocal effects of free cells and immobilized biofilm yielded rich bifurcational patterns of the steady-state solutions. Lee and Lim [205], on the other hand, carried out a stability analysis of a model for continuous prefermentation of cheese culture. The authors showed that the proposed model simulated experimental data well and also predicted steady-state multiplicity.

Ho and Li [154] analyzed the occurrence of multiple steady states in a continuous stirred tank bioreactor involving two-substrates, enzyme-catalyzed reactions. The authors also examined the effect of substrate feed concentration, flow rate, and rate of product formation on the existence of bistability. Lapshenkov and Kharitonova [202] studied the dynamics of cultivation of aerobic micro-organisms in a well-stirred reactor using the first Lyapunov method. Vásquez-Bahena et al. [359], on the other hand, carried out experi-

mental work to validate the steady-state multiplicity in a continuous stirred tank reactor during hydrolysis of sucrose by invertase. The authors uncovered two stable steady states and also showed the theoretical existence of a third metastable state. Staniszewski and Koter [333] carried out a theoretical analysis of steady states for ester hydrolysis in an enzymatic membrane reactor with product retention. The effects of product acidity, enzyme properties, and transport properties on the structure of steady states were discussed. Ho and co-workers [80, 152, 153] carried out an extensive study of multiplicity induced by a family of enzymatically catalyzed reaction network in a continuous stirred tank reactor. The system involved esterification of ethanol and oleic acid by lipase [152], oxidation of monophenols by tyrosinase [80], and the production of L-DOPA (L-3,4-dihydroxyphenylalanine) [153]. The authors uncovered a wide range of phenomena including bistability and hysteresis. Xiu et al. [374] studied the effect of metabolic overflow and substrate growth inhibition on the existence of static multiplicity and sustained oscillations in some continuous cultures. Recently, Astudillo and Alzate [40] compiled several experimental and theoretical studies on the stability behavior of fermentation systems for bioethanol production with *S. cerevisiae* and *Z. mobilis*. The authors stressed the importance of these stability studies for the understanding of productivity in industries producing bioethanol.

1.3 Methodologies for Stability Analysis

Concerning the methodologies used in the literature for the stability analysis, one can note that for chemically reacting systems, besides local stability analysis, the following techniques were used: (1) continuation techniques [192]; (2) singularity theory [33, 45, 130]; (3) Lyapunov–Schmidt decomposition [46, 353] (4); Newton polyhedron [229]; (5) method of projections [170]; (6) Carleman linearization [355]; and the reductive perturbation method [169]. These methods differ in their scopes and objectives, and their discussion, except the singularity theory, is beyond the scope of the book. But it should be noted that other than the singularity theory, the other approaches do not, in principle, require that the model equations be reduced (or reducible) to a single steady-state equation. As for the stability of the chemostat, besides local stability analysis [95, 311] and continuation techniques [278], the singularity theory [26, 70] and the arguments from the theory of asymptotically autonomous systems [329] were used for the stability analysis. In the latter approach, the method consists in exploiting the conservation present in the chemostat model, to reduce the study of the behavior of the original high (e.g., three or four) dimensional model to that of a simpler lower order (e.g., two) dimensional system. This allows, in many cases, to obtain global results for the dynamics of the system.

Continuation (or path following) is, on other hand, a set of techniques that are concerned with tracing out paths of solutions of nonlinear problems as a parameter is varied. In general, the nonlinear model of the bioreactor can exhibit a number of multiplicity (or bifurcation) behaviors. Even if a process is not intentionally operated near a singularity, it may pass through it in the course of time due to variations of one or more of its operating parameters. Such a passage would change the process stability behavior. Continuation techniques allow the detection of parameter values at bifurcation points where the number and nature of solutions change. These techniques can lead to more insights about the behavior of the system than time-stepped solutions, as they can locate both stable and unstable solutions. The continuation procedure usually starts with locating a stable steady-state or periodic solution for a given set of parameters. This can be done by dynamic simulation. Then, one of the parameters is varied to allow the continued calculation of solutions, a procedure carried out commonly through predictor-corrector schemes [192].

The results of continuation calculations are typically presented in the form of bifurcation diagrams where the change of state variables is shown as a function of model parameters. Continuation techniques have gained wide acceptance in analyzing nonlinear systems. However, they cannot provide a full picture of the dynamic behavior of the process. An important objective in the study of the stability of nonlinear models is to find a general picture in which the parameter space of the studied model can be divided in a systematic way and samples of different multiplicity behavior can be taken. Because of the generally large number of parameters a nonlinear model can include, the classification of the parameter space is a challenging task. The singularity theory can provide a framework in which different types of multiplicity can be classified according to conditions that depend on the number of vanishing derivatives of the equilibrium points. Basic ideas of singularity theory were known to Thom [350] and were formally developed by Mather [239, 240]. The subject was extended further by Arnold [38, 39]. The two monographs by Golubitsky and Schaeffer [132] and Golubitsky et al. [133] systematized the development of singularity theory and combined it with group theory in treating bifurcation problems with symmetry. The major advantage of the singularity theory is that the investigation of bifurcations of a system around a point, if local and limited to static solutions, can be reduced to a system of algebraic equations. If the system is low dimensional and amenable to a single algebraic equation then the theory usually can provide systematic classification of the model behavior. The singularity theory found considerable applications in the analysis and classification of the multiplicity behavior of chemically reactive systems since Balakotaiah and Luss [42, 43, 44, 45, 46] applied it to the analysis of the continuous stirred tank reactor (CSTR). Other applications of the singularity theory included the work of Alhumaizi and Aris [33], who applied the theory to study the dynamics of a two-compartment tank reactor chemical system. Russo and Bequette [307] used the theory to study the impact of process design on the multiplicity behavior of a continuous stirred tank

reactor. The authors used the same bifurcation tools to study the operability of a polymerization application [309]. Ajbar et al. [24, 25], on the other hand, used the singularity theory to study the stability of gas-phase fluidized bed reactors.

For bioreactive systems, when the chemostat is described by an unstructured and nonsegregated model, the bioreactor model consists generally of a low order lumped parameter system, described by simple ordinary differential equations. These models are generally amenable to analytical manipulations and the singularity theory can be a powerful tool for the analysis. Unlike the approach followed by Smith and Waltman [329], the singularity theory is local in nature. However, the theory provides a useful framework for classifying branching phenomena in which different types of multiplicity of the nonlinear model can be found. This classification is usually combined with the construction of bifurcation diagrams using continuation techniques. These diagrams can yield clear and substantial information on dynamics in terms of different model parameters. However, while quite useful, the singularity theory is not perfect. Beside its local nature, the method may require substantial symbolic and numeric computation, especially when the nonlinear singularities for periodic points are to be determined. The method also gives little information about the bifurcations of periodic orbits as well as global phenomena that occur in dynamical systems [70].

The first application of the singularity theory to study the behavior of the chemostat was carried out by Ajbar and Gamal [26] who analyzed the multiplicity of the basic unstructured model of the chemostat with substrate inhibition and constant yield coefficient. The authors went on to apply the theory to study a variety of bioreactive systems, including cell growth with wall attachment [12], the dynamics of pure and simple microbial competition [23], the biodegradation of substitutable substrates [17, 22], the competition between plasmid-bearing and plasmid-free organisms [18, 32], the dynamics of predator–prey interactions [30, 31], and the stability behavior of large classes of unstructured kinetic models [13, 16]. The authors also used the theory to investigate the operability of some continuous bioreactors [15, 19, 29].

Chapter 2

INTRODUCTION TO BIOREACTORS MODELS

2.1 Introduction

A bioreactor is a vessel in which a biological reaction or change takes place. The biological system may include enzymes, micro-organisms, animal cells, plant cells, and tissues. The bioreactor is a place where an optimum environment is provided to meet the needs of the biological system so that a high productivity of the bioprocess is achieved. Bioreactors are also considered as crude models of natural ecosystems since they are used to study, under controlled laboratory conditions, the different types of interactions that arise between micro-organisms inhabiting the same environment [375]. Bioreactors of various types are used extensively for the manufacture of useful bioproducts and in the biological treatment of wastes. Bioproducts are used directly as drugs or food or are used indirectly as materials in pharmaceutical, food, and chemical industries. Biological treatment processes, on the other hand, when properly designed and operated, have the potential to be a relatively cost-effective method for hazardous substance removal.

The fermentation process typically begins with the addition of a small amount of living cells, i.e., inoculum to the liquid medium, containing the nutrients needed for the growth of the organism. During the growth process of the organism, the number of cells increases and forms the commonly known biomass. Gas is occasionally sparged in the bioreactor to supply required oxygen and to remove carbon dioxide, which is a product of the metabolic cycle of the cell [41, 62, 321].

2.2 Continuous Bioreactors

Bioreactors can be operated in three basic modes: batch, fed-batch, and continuous. The mode of operation depends on type of cells, the desired bioproduct, and the environmental conditions. Moreover, depending on the require-

ment of cells for oxygen, the cultivation can be anaerobic, aerobic, or even microaerobic [112].

The cell growth undergoes typically the following different phases [41, 62, 321]: lag phase, exponential growth, deceleration growth phase, stationary phase, and death phase. In lag phase, cells adapt to their environment after inoculation. Cell mass may increase a little. During the exponential growth phase, the specific growth rate is constant at its maximum value. Cells multiply rapidly increasing the cell mass and in the same time producing primary metabolites. This is the period of balanced growth. The exponential growth phase is followed by the deceleration phase, where the cell mass growth rate decreases either because one of the medium components, oxygen or substrate, becomes limiting or because the growth is inhibited by the formation of a by-product. The growth rate eventually declines and the culture enters the stationary phase where the cell mass growth rate is constant while cells are still active producing secondary metabolites. The last phase is the death phase where cell mass decreases and may contain dead cells as well as cells that cannot induce growth [69].

In a continuous flow bioreactor, fresh nutrient medium is continuously supplied to a well-mixed culture, while products and cells are simultaneously withdrawn. Bioreactors reach after some time steady-state conditions where cell mass growth, product formation, and substrate concentration remain constant. Two types of continuous flow bioreactors are commonly used: the plug flow bioreactor (PFBR) and the continuous stirred tank bioreactor (CSTBR), i.e., the chemostat. In plug flow mode, substrate and cell concentrations vary with the axial position in the reactor. An ideal PFBR resembles a batch reactor in which distance along the fermenter replaces incubation time.

In an ideal chemostat, the continuous feed and withdraw of the cultural broth makes the bioreactor volume constant during the operation. In order to maintain high cell concentration and thus high productivity in the reactor, a fraction of the biomass may be separated from the outlet stream and circulated back to the bioreactor, i.e., bioreactor with cell recycle.

The cellular growth in the bioreactor is typically limited by one essential nutrient while other nutrients are in excess. Most continuous bioreactors require some control elements such as level and pH. Based on type of control, continuous flow bioreactors can be further classified to other groups. Turbidostat, nutristat, or pH-auxostat are some common classifications [8, 73, 360]. In a turbidostat, a constant biomass concentration is maintained by regulating the feed rate through an optical density (turbidity) controller. In a nutristat the substrate concentration is regulated through a feeding strategy. The pH-auxostat is, on the other hand, based on the measurement of pH, a parameter that is easier to measure than substrate or biomass concentrations. This type of bioreactor is suitable when the medium acidity is affected by cell growth.

Compared to batch and fed-batch operation, continuous processes provide constant environmental conditions for growth and product formation. They also yield higher productivity and products of uniform quality. They how-

ever suffer from certain disadvantages such as equipment failure, infection by other micro-organisms, and genetic instability, i.e., spontaneous mutations in cells [268].

2.3 Modeling Bioreactors

The objective of mathematical modeling is the development of sets of mathematical expressions that can capture the essentials aspects of the bioreactor. Mathematical models are valuable tools, since they are abstract equations that can be solved and analyzed using computer calculations. It is therefore safer and cheaper to perform tests on the model using computer simulations than to carry out repetitive experimentations and observations on the real system. Modeling can be used to assist in the design of equipment, to predict behavior, to interpret data, and to control and optimize the bioreactor.

Modeling bioreactive systems is a challenging task. Bioreactors are highly complex systems with reactions occurring both on the macroscopic reactor scale and on the microscopic cellular scale. Each cell is a reactor in its own sense where a complicated series of reactions take place. These reactions occur simultaneously and are regulated by internal cellular controls. Reactions occurring in both macroscopic and microscopic levels influence each other, and are also influenced by the properties of the surrounding environment. Furthermore, cells can be different and can be in various stages of growth. The metabolic activity of cells in each of the phases may also be different.

Bioreactor models can be classified in a number of ways. They can be classified according to how they are derived (i.e., theoretical, empirical, and semiempirical). They can also be classified according to the level of details in the description of cell and population models (i.e., (un)structured, (non)segregated).

2.3.1 Theoretical, Empirical, and Semiempirical Models

Theoretical models are obtained from fundamental principles, such as laws of conservation (balances) along with other biochemical and chemical principles such as growth kinetics, transport phenomena equations, etc. This first-principle model is capable of explaining the underlying physics of the process and is particularly suitable for process design and optimization [235]. The mathematical description may result, however, in a model with a large number of equations with many parameters needed to be estimated. Theoretical models may be further classified to steady-or unsteady-state models. When the physical state of the system remains constant with time, the system is said to be at steady state. Unsteady-state models, on the other hand, represent the situation when the process state variables (dependent variables) change with time. Models that describe unsteady-state situations are also called dynamic

and transient models. Theoretical models can also be classified as lumped or distributed parameter models. Lumped parameter models are those in which state variables and other parameters have or are assumed to have no spatial dependence, i.e., they are considered to be uniform over the entire system. In this case time (for unsteady-state models) is the only independent variable. The ideal chemostat is an example of such systems. Distributed parameter models, on the other hand, are those in which state variables are a function of both time and spatial position. In this case, modeling takes into account the variation of the dependent variables with time and from point to point throughout the entire system (e.g., the plug flow bioreactor). A number of theoretical models were developed in the literature to describe processes ranging from single cell [173] to complex biological systems [368].

Empirical models are, on the other hand, based on experimental process data. These models are developed using data-fitting techniques. Models obtained exclusively from experimental data are also known as black-box models. Such models do not provide a detailed description of the underlying physics of the process. However, they can provide a fair description of the dynamic relationship between inputs and outputs, and are more adequate for control design and implementation [271, 314]. The wide application of these models in investigation is, however, quite limited, since the parameters describing these types of models are restricted to specific data groups and can be rarely used in different experimental conditions.

Semiempirical models are somehow between the two previous models for which uncertain or poorly known process parameters are determined from process data [89].

2.3.2 Unstructured vs. Structured Models

The description of microbial kinetics requires the combination of a cell model with a population model. In the literature, cell models are classified based on the level of details in the description of the cell and its intra cellular processes. Unstructured models represent the simplest philosophies used to model the biological system. These models assume fixed cell composition and do not consider the variations of intracellular properties within the cell. All cellular components are lumped in the total biomass concentration. Typically, unstructured models describe the state of the bioreactor based on a single limiting substrate and consider only substrate uptake, biomass growth, and product formation. Thus, the biological component of the system depends directly on the macroscopic reactor variables. These models are known to provide a fair representation of the biological process when the cell response time to changes in surroundings is negligible [41, 321]. When, on the other hand, the cell composition or the morphology of the cell culture are important variables, different studies showed that these types of models are unable to describe adequately the dynamic experiments [265].

Structured models, on the other hand, take explicitly into consideration the

intra cellular processes. The biomass is no longer assumed of fixed composition but is rather structured into several components or functional groups that are connected with each other, and are also connected with macroscopic reactor conditions through material balances [41, 54, 265, 321]. Structured models include therefore a greater level of details about the biochemical phenomena occurring within the cell. These models have therefore a higher prediction capability than unstructured models, and they can be used to describe growth processes at different operation conditions with the same parameters group. An example of structured models include compartment, cybernetic, and mechanistic models. In compartment models, the biomass is divided into different components while the kinetics for individual reactions are usually described by empirical expressions. Despite the empirical nature of these models, they are often based on well-established cellular mechanisms and can simulate certain characteristics of experiments [92, 265]. Cybernetic models were proposed by Ramkrishna and co-workers [253, 296] for the description of cellular growth on multiple substrates. The cybernetic approach attributes to micro-organisms the ability to adjust to the prevalent conditions such that the available resources are utilized in the most effective manner.

Mechanistic models are, on the other hand, complex types of structured models. They are formulated at the molecular level and can take into consideration key features of individual cells such as cellular geometry [265].

2.3.3 Nonsegregated vs. Segregated Models

Population models are needed, along the cell model, to describe microbial kinetics. These models can be classified to segregated and nonsegregated models. Nonsegregated models consider the entire culture to be homogeneous where cells are uniform and have equal properties. These models consider therefore only one morphological form of the culture. Segregated models, on the other hand, take into account the distribution of population properties such as age, size, morphology, etc. When mass conservation is used to describe the intercellular structure, the model is a mass-structured model. If age is used to differentiate cells in a population, then the model is an age-structured model [146, 331]. Morphologically structured models are variants of segregated models when only a finite number of morphological forms is considered, compared to an infinite number, in other segregated models.

A rigorous model of a biological system should account for all cell complexities and is typically both a structured and a segregated model. In addition to being difficult to formulate and solve, the quantification of the entire biological system needed in these models require the measurement of a large number of variables and rates, which is generally beyond the scope of reasonable measurement techniques. Simplified models can be obtained by neglecting either the intracellular processes (unstructured and segregated models) [54, 100] or by neglecting the cell heterogeneity (structured and nonsegregated models) [74, 177, 297], or by neglecting both aspects (unstructured and nonsegre-

gated). Unstructured and nonsegregated models are the simplest models, and are typically lumped parameter systems consisting of few nonlinear ordinary differential equations that are generally amenable to rigorous analysis.

2.4 Kinetic Models for Cell Growth

Reactions occurring in the bioreactor can be represented, for unstructured and nonsegregated models, roughly as follows [41, 321]:

$$\text{Substrate (S)} + \text{Cells (X)} \rightarrow \text{Product (P)} + \text{Cells (X)} \tag{2.1}$$

The reaction stoichiometry can be defined through yield coefficients, $Y(I/J)$ between species I and J.

$$Y_{I/J} = \frac{I \text{ produced}}{J \text{ consumed}} \text{ where } I \text{ is } (X \text{ or } P) \text{ and } J \text{ is } (S \text{ or } O_2) \tag{2.2}$$

Growth is usually characterized by the specific growth rate μ. It is defined by [321]:

$$\mu = \frac{1}{X}\frac{dX}{dt} \tag{2.3}$$

or equivalently

$$\frac{dX}{dt} = \mu X \tag{2.4}$$

where X is the cell mass. In order to account for the energy required for cell maintenance and cell death, an endogenous decay term $k_d X$ representing the rate of decay in the cell mass is often used to correct the cell growth rate. The net cell growth rate is therefore $r_x = \mu X - k_d X$, where k_d is the endogenous decay coefficient. A number of expressions are often used to describe cell-specific growth rate μ, as summarized in the following.

2.4.1 Substrate-Limited Growth

The dependence of the specific growth rate on the substrate is usually in the form of saturation kinetics, meaning that there exists a maximum growth rate that cannot be exceeded even with the increase in limiting substrate. For cellular systems, these kinetics are described by the Monod equation [249]

$$\mu = \frac{\mu_{max} S}{K_S + S} \tag{2.5}$$

where μ_{max} is the maximum specific growth rate when $S >> K_S$. The Monod equation adequately describes substrate-limited growth only when the growth is slow and the population density is low.

A number of alternatives to the Monod equation are available in the literature [41, 321]:

- Blackman equation

$$\mu = \mu_{max} \text{ if } S \geq 2K_S \tag{2.6}$$

$$\mu = \frac{\mu_{max}}{2K_S} S \text{ if } S < 2K_S \tag{2.7}$$

  This expression often fits data better than the Monod equation but the discontinuity in the equation is problematic.

- Contois equation [81]

$$\mu = \frac{\mu_{max} S}{K_X X + S} \tag{2.8}$$

  The Contois equation is the most commonly used model to account for biomass-dependent growth rate.

2.4.2 Growth Models with Inhibition

The cell growth rate may be inhibited by substrate, product, or other inhibitors [41, 321].

2.4.2.1 Substrate Inhibition

Two forms of substrate inhibition can be found: competitive and noncompetitive inhibition. The mechanisms of these inhibitions are equivalent to those found in the kinetics of enzyme-catalyzed reactions [321]. The growth with noncompetitive substrate inhibition has the following form:

$$\mu = \frac{\mu_{max}}{(1 + \frac{K_S}{S})(1 + \frac{S}{K_I})} \tag{2.9}$$

When $K_I >> K_S$ the growth rate takes the form

$$\mu = \frac{\mu_{max} S}{K_S + S + \frac{S^2}{K_I}} \tag{2.10}$$

which is the well-known Haldane growth model [86].

For competitive substrate inhibition, the growth rate has the following form

$$\mu = \frac{\mu_{max} S}{K_S(1 + \frac{S}{K_I}) + S} \tag{2.11}$$

Substrate inhibition may be in general alleviated by slow and/or intermittent addition of substrate to the medium.

2.4.2.2 Product Inhibition

The secretion of any bioproduct can also be inhibitory to microbial growth. Examples of product inhibition models are [41, 321]:

$$\mu = \frac{\mu_{max} S}{(S + K_S)} (1 - \frac{P}{P_m})^n \tag{2.12}$$

$$\mu = \frac{\mu_{max} S}{(S + K_S)} e^{(\frac{-P}{K_P})} \tag{2.13}$$

where P_m is the product concentration at which the growth stops.

2.4.2.3 Inhibition by Toxic Compounds

The presence of toxic compounds in the growth medium can inhibit the growth of cells or even lead to cell death. Examples of growth models inhibited by a toxic compound (I) are [321]:

$$\text{Competitive inhibition} : \mu = \frac{\mu_{max} S}{K_S(1 + \frac{I}{K_I}) + S} \tag{2.14}$$

$$\text{Noncompetitive inhibition} : \mu = \frac{\mu_{max}}{(1 + \frac{K_S}{S})(1 + \frac{I}{K_I})} \tag{2.15}$$

2.4.2.4 Multiple Substrates

Multiple substrates may limit the growth rate simultaneously. Each limiting substrate may be modeled with equations presented before. One class concerns the simultaneous utilization of two substitutable substrates that are serving the same need for the micro-organism. The two substrates may be involved in an uncompetitive cross-inhibitory interaction with utilization rates, that could be represented as follows [50]:

$$\mu_1 = \frac{\mu_1 S_1}{K_1 + S_1 + S_1^2/K_I + K_3 S_1 S_2} \tag{2.16}$$

and

$$\mu_2 = \frac{\mu_2 S_2}{K_2 + S_2 + K_4 S_1 S_2} \tag{2.17}$$

The culture grows on substrate S_1 following Haldane inhibition kinetics. In the absence of S_1 the culture grows on substrate S_2 following Monod kinetics. When the medium contains both S_1 and S_2 the culture utilizes both of them simultaneously. Other growth models proposed in the literature include [381]:

$$\mu = \mu_{max} (\frac{S_1}{S_1 + K_1})(\frac{S_2}{S_2 + K_2}) \tag{2.18}$$

$$\mu = \frac{\mu_{max} (\frac{\mu_{max1}}{K_1} S_1 + \frac{\mu_{max2}}{K_2} S_2)}{\mu_{max} + \frac{\mu_{max1}}{K_1} S_1 + \frac{\mu_{max2}}{K_2} S_2} \tag{2.19}$$

2.5 Product Formation

When it comes to the formation of metabolic products we can distinguish between three classes [265, 321]:

- Growth associated products: These primary metabolites are synthesized simultaneously to microbial growth. An example is the production of constitutive enzymes.
- Nongrowth associated products: These products are formed when there is no growth, i.e., a stationary phase. A number of secondary metabolites, such as most antibiotics from the *Streptomyces* species and some industrially important enzymes such as proteases from *Bacillus subtilis*, and recombinant proteins are nongrowth associated products.
- Mixed-growth-associated products are, on the other hand, formed during the deceleration and stationary phases. Examples of these products are lactic acid and xanthan gum.

This page intentionally left blank

Chapter 3

INTRODUCTION TO STABILITY AND BIFURCATION THEORY

3.1 Introduction

In this introductory chapter we present some fundamental concepts associated with the stability of nonlinear systems. These issues include static multiplicity, dynamics associated with Hopf points, and the singularity theory as well as some numerical tools used to generate the bifurcation diagrams. The reader should be cautioned that the material in this chapter represents a scratch on the surface of these issues. Nevertheless, the material is presented in a simple and practical manner. The goal is to provide the reader with practical tools to study many of the nonlinear phenomena encountered in unstructured kinetic models of bioreactors. Some concepts and definitions, not directly needed in the materials presented in this chapter, are provided in the Appendix. Details about nonlinear systems and bifurcation theory can be found, for instance, in [136, 198, 237, 303, 315, 354, 366] while the singularity theory and some of its useful applications are available in [33, 39, 42, 43, 44, 45, 46, 70, 132, 133, 227]. Details about continuation techniques can, on the other hand, be found in [98, 134, 183, 192, 199, 315].

We consider in the following a system described by the following set of first-order ordinary differential equations (ODEs), written in a vectorial form

$$\begin{aligned} \frac{dx}{dt} &= f(x, \lambda) \\ x(0) &= x_0 \end{aligned} \tag{3.1}$$

where t represents time, $x = (x_1, x_2, \cdots, x_n)$ is the vector of state variables, $f = (f_1, f_2, \cdots, f_n)$ is a vector of nonlinear functions, $\lambda = (\lambda_1, \lambda_2, \cdots, \lambda_m)$ is the set of model parameters, and x_0 is the vector of initial conditions. We also assume that f does not depend explicitly on the independent variable (t). In this case, the system is said to be autonomous. The system described by the set of first-order ODEs (Equation (3.1)) is also called a lumped parameter system, since the state variables are invariant in all space dimensions and vary only with time. The ideal chemostat is an example of lumped parameter systems. The number (n) of equations, which is also the number of state variables, is refered to as the dimension of the system. The time invariant solutions of the

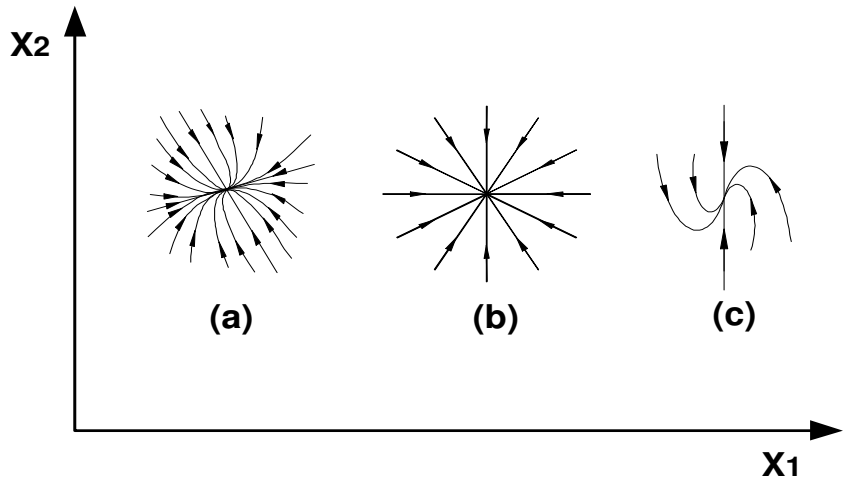

FIGURE 3.1: Types of steady-states nodes. (a) stable node when the eigenvalues are unequal; (b), (c) proper and improper stable nodes when the eigenvalues are equal.

dynamic system (Equation (3.1)) satisfy $\frac{dx}{dt} = 0$, and are called steady states. They are also called stationary points, equilibrium points, or critical points. The steady-state solutions (x_s) satisfy the following set of algebraic equations

$$f(x_s, \lambda) = 0 \tag{3.2}$$

Since $f_i(x)$ are generally nonlinear algebraic equations, Equation (3.2) may have more than one solution x_s. In this case we have a situation of multiple steady states, also called steady-state (static) multiplicity.

3.2 Local Stability of Steady States

The local stability of the steady state (x_s) can be determined by examining the properties of Equation (3.1) when it is linearized around x_s. The Jacobian matrix J of the linearized system of Equation (3.1), at steady state, consists of n^2 first-order partial derivatives

$$J_{ij} = \frac{\partial f_i}{\partial x_j}(x_s), \quad (i, j = 1, 2, \cdots, n) \tag{3.3}$$

According to the result attributed to Lyapunov [315], the real parts of the eigenvalues of the Jacobian matrix J, evaluated at the stationary solution x_s,

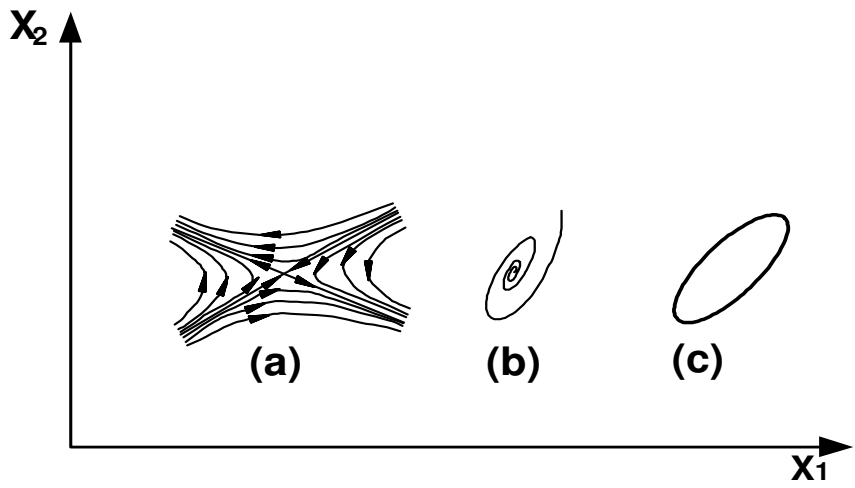

FIGURE 3.2: (a) Saddle steady state; (b) Stable focal steady state; (c) Limit cycle.

determine its stability. The steady state x_s is asymptotically stable if the real parts of all the eigenvalues are negative. If one eigenvalue has a positive real part then the steady state is unstable.

While the stability of x_s depends on the sign of the real parts of the eigenvalues, the nature of the solution $x(t)$ around the steady state depends essentially on the nature of eigenvalues. The different cases pertinent to the nature of the steady state are presented in the following section for a two-dimensional system (i.e., $n = 2$ in Equation (3.1)), for which there are two state variables (x_1, x_2) and two eigenvalues. The reader may consult the references [315, 358] for a detailed discussion of these cases.

- Case 1: Real and unequal eigenvalues of the same sign:
  In this case, the steady state is called a node. When both eigenvalues are negative the steady state is a stable node and the trajectories approach the neighborhood of the node (Figure 3.1a). When, on the other hand, the eigenvalues are positive, the steady state is an unstable node. The directions in Figure 3.1a are reversed, as trajectories leave the neighborhood of the node.

- Case 2: Real and equal eigenvalues:
  In this case, the steady state is either a proper or improper node. For a proper node each trajectory has a different slope (Figure 3.1b) while for an improper node all trajectories approach the node tangentially with the same slope (Figure 3.1c). For an unstable node the direction of trajectories is away from the steady state.

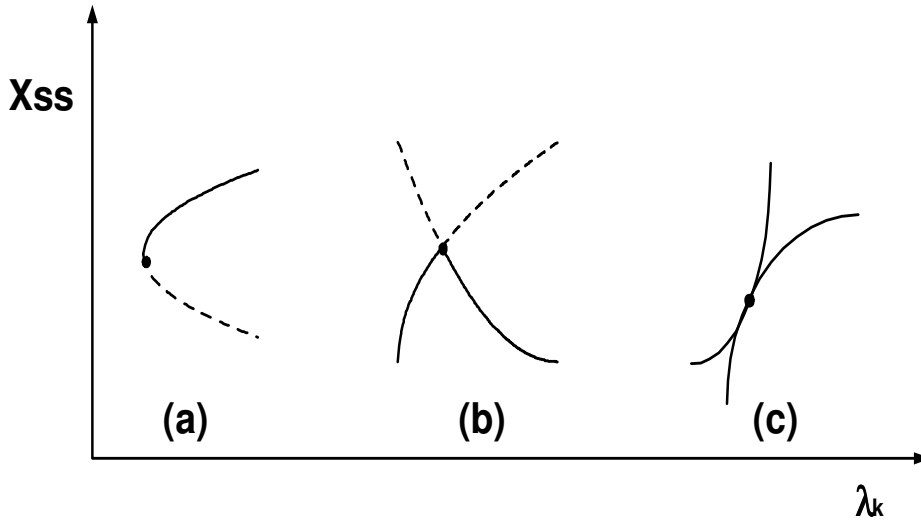

FIGURE 3.3: (a) Static limit point (SLP); (b) Static bifurcation point (SBP); (c) Static cusp point (SCP).

- Case 3: Real and unequal eigenvalues of the opposite sign:
  In this case, the steady state is called a saddle point. Because one of the eigenvalues is positive, the saddle point is inherently unstable, as shown in Figure 3.2a. The two stable manifolds (onset) that enter the saddle point are called separatrices. They divide the phase space into attracting basins.

- Case 4: Complex eigenvalues with a nonzero real part:
  When the eigenvalues are complex conjugates, the steady state is called focal (spiral) (Figure 3.2b). The local stability of the focal steady state is determined by the negativity of the real part of the eigenvalues. For an unstable focal the direction of trajectories is away from the steady state.

- Case 5: Pure imaginary eigenvalues:
  When the eigenvalues are purely imaginary, the trajectory is locally a pure rotation and forms a closed curve called the limit cycle (periodic orbit), as shown in Figure 3.2c.

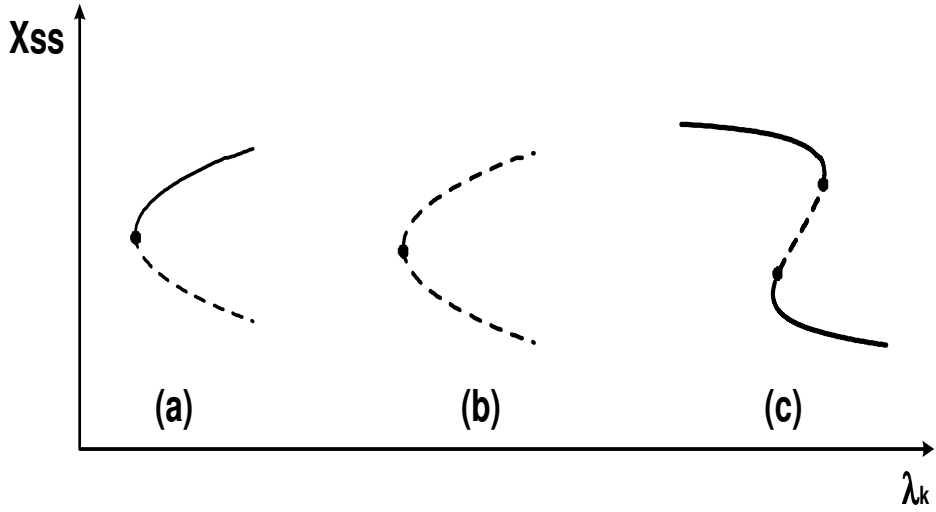

FIGURE 3.4: (a) SLP separating two stable branches; (b) SLP separating unstable branches; (c) Hysteresis.

3.3 Steady-State Multiplicity

The multiplicity of steady states describes the situation when more than one solution of Equation (3.2) occurs for certain values of the free parameter vector λ. Generally, it is of importance to find the variations of the steady-state solution (x_{ss}) with a certain slowly changing variable λ_k. The graph showing the dependence of x_{ss} on λ_k, for fixed values of the other parameters ($\lambda_i, i \neq k$), is called a bifurcation diagram. The variable λ_k is called the bifurcation variable. The objective of bifurcation theory is to characterize the changes in the qualitative dynamic behavior of the nonlinear system as key parameters are varied. The bifurcation diagram consists usually of different branches that often meet at certain points. These points are called steady-state branch points. Commonly encountered points are:

- Static limit point (SLP): The point at which two branches of the steady-state solution have joined limiting tangents is called a static limit point (SLP). At the SLP two branches of the steady states are born or annihilate each other (Figure 3.3a). Another name for the static limit point is the static turning point. Locally there are no solutions on one side of a turning point and two solutions on the other side.

- Static bifurcation point (SBP): At this point two and only two curves possessing distinct tangents cross each other (Figure 3.3b).

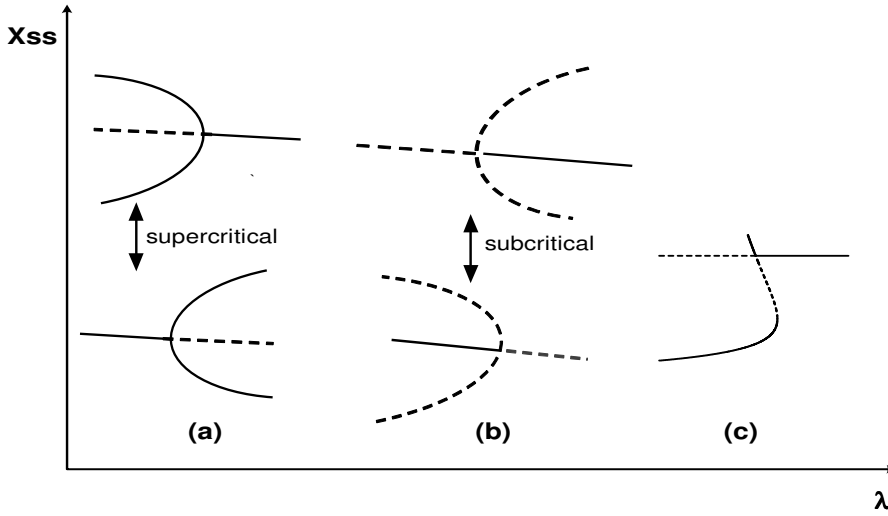

FIGURE 3.5: (a) Supercritical perfect pitchfork; (b) Subcritical perfect pitchfork; (c) Transcritical imperfect pitchfork.

- Static cusp point (SCP): This is the point of contact between two curves of steady states having the same tangent (Figure 3.3c).

These different branch points connect steady state branches and give rise to a variety of bifurcation diagrams. In the following we will review the most common bifurcation diagrams encountered in nonlinear systems.

The simplest bifurcation diagram is the saddle node bifurcation (Figure 3.4a) where a stable branch is separated from an unstable branch by a static limit point. It is a convention to distinguish between stable and unstable branches by using a continuous curve for the former and a dashed curve for the latter. It should be noted that a SLP does not always separate stable steady states from unstable ones. Situations can arise when two unstable branches such as saddle and unstable node meet at a SLP (Figure 3.4b). In some cases, the SLP are born in pairs, resulting in the hysteresis bifurcation phenomenon (Figure 3.4c). The bifurcation diagram for the hysteresis consists of two stable branches connected to a middle unstable branch by two static limit points. It can be seen that for some values of the bifurcation parameter between the two SLPs, three solutions exist (the stable upper branch, the stable lower branch, and the unstable middle branch).

The third qualitatively different bifurcation diagram occurs when a static limit point and a static bifurcation point coincide with each other. This bifurcation point is called a static bifurcation limit point (SBLP). It is also called a perfect pitchfork point (Figure 3.5). The terminology of supercritical and subcritical classification for the perfect pitchfork is widely used. A supercriti-

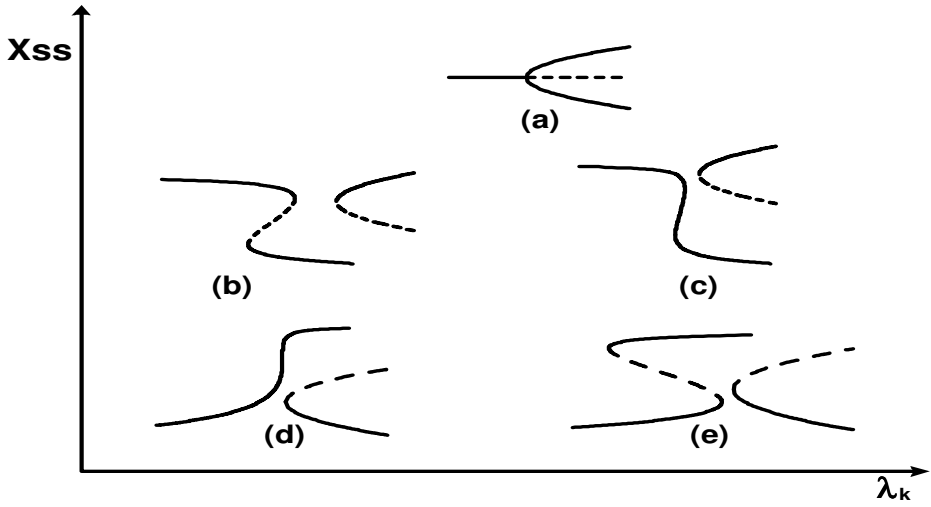

FIGURE 3.6: Perturbed bifurcation diagrams for the pitchfork.

cal perfect pitchfork has stable branches on both sides of the static bifurcation limit point (Figure 3.5a). A subcritical pitchfork, on the other hand, has unstable branches on both sides of the static bifurcation limit point (Figure 3.5b). When the static limit point and the static bifurcation limit point do not coincide with each other, the pitchfork is called a transcritical imperfect pitchfork (Figure 3.5c). It should be noted that perturbations in the perfect pitchfork can yield other bifurcation diagrams, as shown in Figure 3.6.

Besides saddle node, hysteresis and pitchfork, additional bifurcation diagrams can arise in nonlinear systems. These include the formation of an isola and the growth of isola into mushroom bifurcation, as shown in Figures 3.7(a–b). Winged cusp bifurcation (Figure 3.8a) is an other example of additional branching phenomena that may be exhibited by nonlinear systems. Perturbations in the basic winged cusp may yield extra sets of bifurcation diagrams, as shown in Figure 3.8.

3.4 Dynamic Bifurcation

Besides steady-state multiplicity, we present in this section the second important property of nonlinear systems which is the existence of regular periodic oscillations. In contrast to linear systems, it is possible for the autonomous system (Equation (3.1)) to have solutions that form a closed curve in the phase

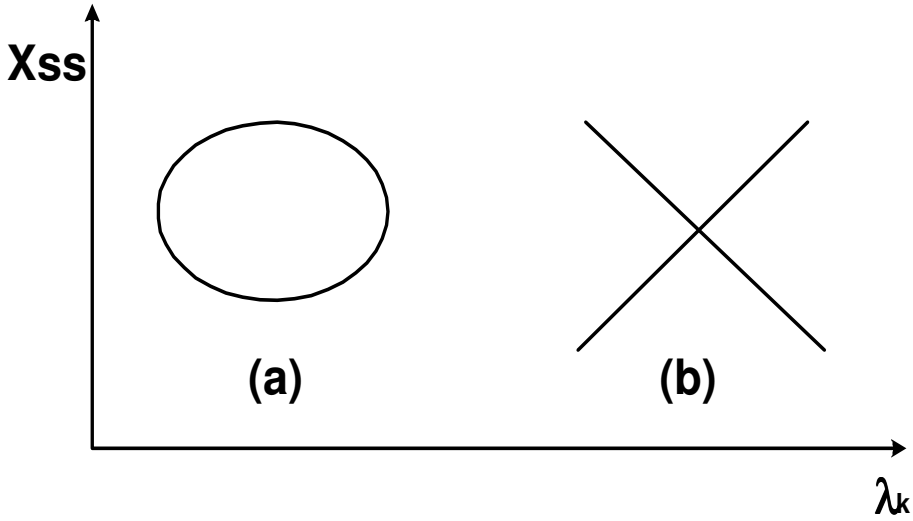

FIGURE 3.7: (a) Isola; (b) Mushroom.

space. The solution is called limit cycle (or periodic attractor). It was already mentioned in Section 3.2 that a limit cycle for a two-dimensional system is associated with pure imaginary eigenvalues. It was Hopf [315] who proved the following theorem for a n-dimensional system that characterizes the bifurcation from equilibria to limit cycles. This bifurcation is commonly known as Hopf bifurcation.

Theorem 1 *Assume that the critical point is located at* (x_0, λ_0). *The eigenvalues* μ *of the Jacobian matrix* J *depend naturally on* λ, *i.e.,* $\mu(\lambda)$. *Assume the following hypotheses:*

- *Hypothesis (H1): At the equilibrium point, the Jacobian matrix* J *has simple eigenvalues* $\pm iw$ *and has no other eigenvalues on the imaginary axis.*

- *Hypothesis (H2) (also called the transversality hypothesis):*

$$\frac{d(Re(\mu(\lambda_0))}{d\lambda)} \neq 0 \tag{3.4}$$

  Where $Re(\mu)$ *is the real part of* μ. *This condition gives a guarantee that the real part of the complex eigenvalue changes its sign when passing through the Hopf bifurcation point.*

- *Hypothesis* (H_3) *(also called the stability hypothesis): The condition for this hypothesis describes the boundary at which the limit cycle changes its stability.*

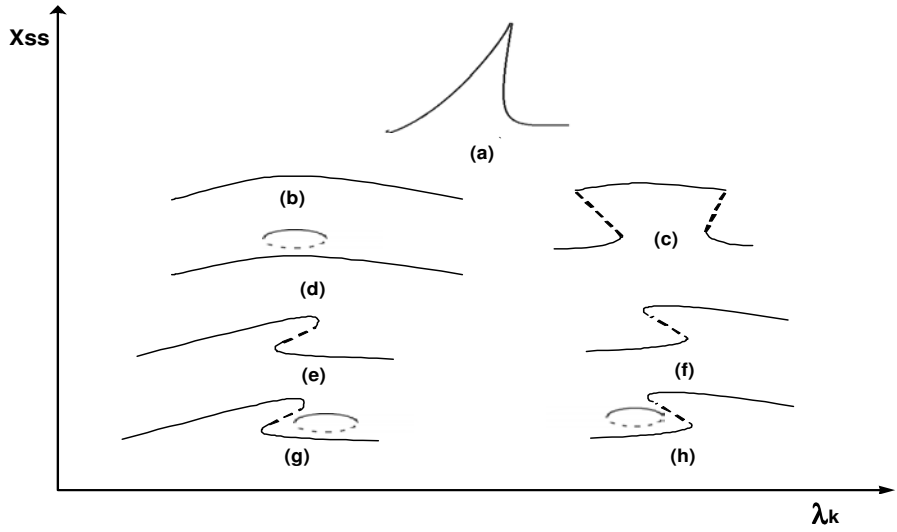

FIGURE 3.8: Perturbed bifurcation diagrams for the winged cusp.

The theorem states that if hypotheses (H1), (H2), and (H3) hold then there exists a unique birth of limit cycles emanating from (x_0, λ_0). □

The different hypotheses in this theorem are reexamined in a later section when Hopf bifurcation degeneracies are discussed.

3.5 Numerical Techniques

The bifurcation diagrams of the autonomous system described by Equation (3.1) can be efficiently obtained using continuation techniques [192, 315]. A number of software including AUTO [98], LOCBIF [183], CONTENT [199], DIVA [137], MATLAB® codes [93], and DIANA [189] have been developed for numerical bifurcation analysis of nonlinear models. The AUTO continuation package is perhaps the most widely used. AUTO can trace out the entire steady-state branches, locate static limit points, and continue these points in two parameters space as well as locating Hopf bifurcation points and continue them. The capabilities of AUTO also include the determination of torus and period-doubling bifurcations among other features. In addition to continuity diagrams, the classical phase plane and time-trace diagrams for the simulation of dynamic behavior can be generated using standard ODE's solvers such as IVPAG [168] and DASSL [65]. Compared to dynamic simulation (i.e., time traces), continuation methods have the advantage of locating both stable and

unstable solutions. Bifurcation diagrams can also be useful in determining if the model can predict the steady-state or dynamic behavior observed in the real process [121, 378]. However, as useful as they are, continuity diagrams are obtained when only one bifurcation parameter is varied at a time. Therefore, they cannot provide the complete picture as far as the effect of other model parameters is concerned. One important objective would be to find a general picture in which the parameter space can be divided into different regions that have different static or dynamic behavior. The classification of the parameter space is a challenging task since the number of parameters in the model can be quite large. The singularity theory, presented in the next section, can provide a general framework for classifying branching phenomena in which different types of multiplicity in the nonlinear model are delineated.

3.6 Singularity Theory

The singularity theory is a useful mathematical tool for studying bifurcation problems. By reducing a singular function to a simple form, the properties of multiple solutions of a bifurcation problem can be determined from a finite number of derivatives of the singular function. The theory of singularity of smooth real-valued scalar functions of vector arguments is also known as elementary catastrophe theory, while its generalization to vector-valued functions of vector arguments is called singularity theory. Basic ideas of singularity theory were known to Thom [350] and were formally developed by Mather [239, 240]. The subject was extended further by Arnold [39]. Golubitsky and Schaeffer [132, 133] developed a special form of the singularity theory (the singularity theory with a distinguished parameter) that can predict all types of local bifurcation diagrams. Here we present a brief overview of the method. Details can be found in [132, 133] while useful summaries are available in [33, 42, 43, 44, 45, 46, 70].

For a large number of models, the set of Equations (3.2) can be reduced, through algebraic manipulations, to a single nonlinear algebraic equation

$$f(x, \theta, \delta_1, \delta_2, \cdots, \delta_p) = 0 \tag{3.5}$$

where θ is the bifurcation parameter and δ_i are other fixed-control parameters. A singularity is defined as being the solution (x_0, θ_0) of Equation (3.5) that satisfies $f_x(x_0, \theta_0) = 0$. Without loss of generality we assume that the singularity under question is located at the origin, i.e., $(x_0, \theta_0) = (0, 0)$. The primary goal is to find an equation, as simple as possible, whose solution has the same qualitative behavior as that of Equation (3.5), and whose bifurcation diagram can easily be obtained by elementary computation. This problem is known as the recognition problem. For a given algebraic equation, such as

Equation (3.5), the recognition problem is therefore to find the simplest polynomial equation for which the solution is in one-to-one correspondence with that of the given equation in a neighborhood of the bifurcation point. This polynomial is called the normal form of the given function, and can be determined solely by the values of a finite number of derivatives of the given function at the bifurcation point.

The first step to achieve this goal is to ignore differences that are not essential. For instance, a change in coordinates should not change the nature of the bifurcation problem. This leads to the following definition:

Definition 1 The functions f and g are said to be contact equivalent when their qualitative features are the same, i.e., there exist smooth functions T and X such that the following holds

$$f(x,\theta) = T(x,\theta)g(X(x,\theta),\Lambda(\theta)) \tag{3.6}$$

with

$$T(0,0) \neq 0, X(0,0) = \Lambda(0) = 0, X_x(0,0) > 0, \Lambda_\theta(0,0) > 0 \tag{3.7}$$

□

For example, the bifurcation problem

$$f(x,\theta) = 1 - \theta - cos(x) = 0 \tag{3.8}$$

is contact equivalent to the following bifurcation problem

$$g(y,\lambda) = y^2 - \lambda = 0 \tag{3.9}$$

since

$$f(x,\theta) = 2g(sin(\frac{x}{2}), \frac{\theta}{2}) \tag{3.10}$$

Thus, the local features of a nonlinear equation can be determined by the analysis of features of a much simpler contact equivalent polynomial equation.

The second step towards a classification of a singularity is to investigate the stability of the bifurcation problem.

Definition 2 $f(x,\theta)$ is said to be structurally stable if the function $f(x,\theta) + g(x,\theta,\epsilon)$ is contact equivalent to $f(x,\theta)$ in the neighborhood of the origin for all sufficiently small smooth functions $g(x,\theta,\epsilon)$. □

As an example, consider the following saddle node bifurcation problem

$$f(x,\theta) = x^2 - \theta = 0 \tag{3.11}$$

This bifurcation problem is structurally stable. For example, if $f(x,\theta)$ is perturbed to the following problem:

$$f_1(x,\theta) = x^2 - \theta - \epsilon x = 0 \tag{3.12}$$

the behavior of both bifurcation problems is qualitatively the same for small values of ϵ. On the other hand, the following bifurcation problem

$$f_2(x, \theta) = x^3 - \theta = 0 \tag{3.13}$$

is unstable since the slightly perturbed new problem

$$f_3(x, \theta) = x^3 - \theta - \epsilon x = 0 \tag{3.14}$$

does not preserve the same qualitative features of the original problem f_2. Figure 3.9 shows examples of bifurcation diagrams that can be obtained for $\epsilon > 0$ and $\epsilon < 0$.

In the following the concept of unfolding is introduced to study specifically the stability of such bifurcation problems.

Definition 3 An unfolding of $f(x, \theta)$ is an m-parameter family

$$U(x, \theta, \alpha_1, \alpha_2, \cdots \alpha_m) \tag{3.15}$$

with

$$U(x, \theta, 0, 0, \cdots, 0) = f(x, \theta) \tag{3.16}$$

Here $\alpha_1, \alpha_2, \cdots, \alpha_m$ are additional parameters. □

As an illustration, the expression f_3 (Equation (3.14)) is an unfolding of f_2 (Equation (3.13)). Attaching an additional term is also an unfolding. Hence, the definition is still too general to be useful for classification. This leads to the following definition.

Definition 4 A universal unfolding is an unfolding with two features:

- It includes all possible small perturbations of $f(x, \theta)$ up to contact equivalence.
- It uses the minimum number of parameters $(\alpha_1, \alpha_2, \cdots, \alpha_m)$.

The number m is called the codimension of $f(x, \theta)$. It is the lowest dimension of the parameter space α, which is necessary to observe a given bifurcation phenomena. □

As an example, the following bifurcation problem

$$f_4(x, \theta) = x^3 + \epsilon^2 x - \theta = 0 \tag{3.17}$$

is an unfolding of f_2 (Equation (3.13)). However, it is not universal since by including the positive term ϵ^2, the bifurcation problem f_4 cannot explain the original diagram (Figure 3.9) for negative values of ϵ. On the other hand, the following bifurcation problem,

$$f_5(x, \theta) = x^3 - \epsilon_1 x^2 - \epsilon_2 x - \theta = 0 \tag{3.18}$$

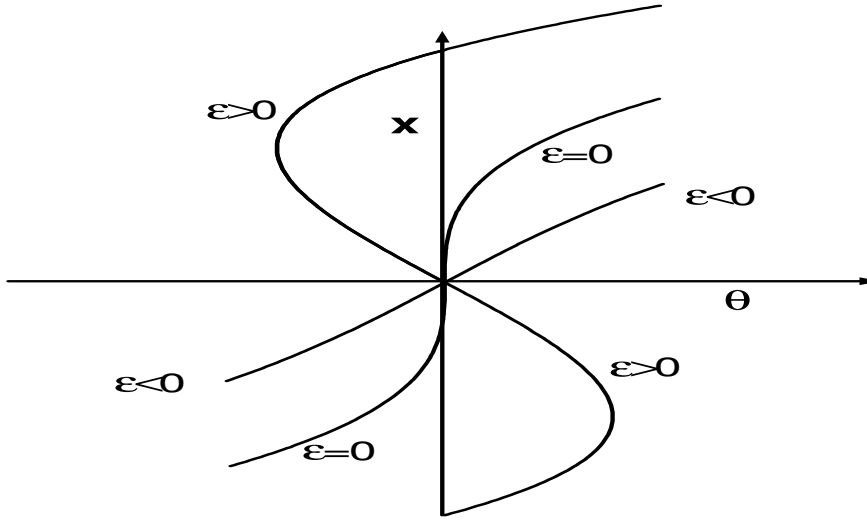

FIGURE 3.9: Perturbed bifurcation diagrams for the bifurcation problem $f_3(x, \theta) = x^3 - \theta - \epsilon x = 0$.

can describe the diagrams of Figure 3.9, but it is not a universal unfolding, since compared to f_3, it requires two parameters ϵ_1 and ϵ_2 instead of one. Therefore, the universal unfolding of f_2 is f_3 since it possesses the minimum number of parameters that are needed to describe all the perturbed bifurcation forms.

The bifurcation problem of Equation (3.5) can be stable for most values of the parameter vector δ. But there exists a set of values of δ at which this function has the most degenerate singularities. Perturbing the system around these points results in forming several qualitatively different stable bifurcation diagrams. These singular points are characterized by the vanishing of a finite number of derivatives of f with respect to x and with respect to the bifurcation parameter θ. In addition, there always exists a normal form that is contact equivalent to f next to these singular points. We present in the following [33] a special case of a more general theorem proved by Golubitsky and Schaeffer [132]. The following theorem provides the universal unfolding for singularities characterized by vanishing the derivatives of f with respect to x only.

Theorem 2 *Suppose that* $f(x,\theta)$ *has a singular point* $(x,\theta) = (0,0)$ *that obeys*

$$f(0,0) = 0, \frac{\partial f^i(0,0)}{\partial x^i} = 0 \quad (i = 1, 2, \cdots j) \tag{3.19}$$

$$\zeta = \frac{\partial^{i+1} f(0,0)}{\partial x^{i+1}} \frac{\partial f(0,0)}{\partial \theta} \neq 0 \tag{3.20}$$

Then locally $f(x,\theta)$ *is contact equivalent to the normal forms*

$$x^{j+1} + \theta, \ \zeta > 0 \tag{3.21}$$

$$x^{j+1} - \theta, \ \zeta < 0 \tag{3.22}$$

The universal unfolding is

$$U(x,\theta,\alpha) = x^{j+1} - \alpha_{j-1}x^{j-1} - \cdots - \alpha_1 x \pm \theta \tag{3.23}$$

□

The theorem states that bifurcation problems can be represented by polynomials that can be seen as normal forms, and that if such singular points exist, the maximum number of solutions of Equation (3.5) next to the singular point is $(j+1)$.

Table 3.1 summarizes the results for systems that have a maximum of three solutions. The normal forms for all singularities of these systems are polynomial functions with cubic or quadratic order in x. Table 3.2 shows the universal unfoldings of the normal forms. In the following section, we present the conditions for the existence of the various singularities shown in Table 3.1.

TABLE 3.1: Codimensions and normal forms, $\epsilon = \pm 1, \delta = \pm 1$

Type	Codimension	Normal form
Saddle node	0	$\epsilon x^2 + \delta\theta$
Isola center	1	$\epsilon(x^2 + \theta^2)$
Mushroom	1	$\epsilon(x^2 - \theta^2)$
Hysteresis	1	$\epsilon x^3 + \delta\theta$
Pitchfork	2	$\epsilon x^3 + \delta\theta x$
Winged cusp	3	$\epsilon x^3 + \delta\theta^2$

TABLE 3.2: Universal unfoldings for some singular functions

Type	Universal unfolding
Saddle node	$\epsilon x^2 + \delta\theta$
Isola	$\epsilon(x^2 + \delta\theta^2 + \alpha)$
Hysteresis	$\epsilon x^3 + \delta\theta + \alpha x$
Pitchfork	$\epsilon x^3 + \delta\theta x + \alpha_1 + \alpha_2 x^2$
Winged cusp	$\epsilon x^3 + \delta\theta^2 + \alpha_1 + \alpha_2 x + \alpha_3 \theta x$

3.6.1 Codimension-0 Singularities

The conditions for the appearance of a saddle node (codimension-0) singularity are that

$$f = f_x = 0 \tag{3.24}$$

with the requirement that $f_{xx} \neq 0$.

3.6.2 Codimension-1 Singularities

3.6.2.1 Hysteresis

The conditions for the appearance/disappearance of a hysteresis bifurcation are that

$$f = f_x = f_{xx} = 0 \tag{3.25}$$

so that the steady-state condition must be satisfied ($f = 0$) and the first two partial derivatives of f with respect to steady-state solutions must vanish. In addition, a number of other derivatives must remain nonzero

$$f_\theta \neq 0, f_{x\theta} \neq 0, f_{xxx} \neq 0 \tag{3.26}$$

3.6.2.2 Isola and Mushroom

The requirements for the appearance of an isola and the growth of an isola into a mushroom are that

$$f = f_x = f_\theta = 0 \tag{3.27}$$

with the additional requirements

$$f_{x\theta} \neq 0, f_{xx} \neq 0, f_{\theta\theta} \neq 0 \tag{3.28}$$

3.6.3 Codimension-2 Singularities

The conditions for the appearance of a pitchfork bifurcation are:

$$f = f_x = f_\theta = f_{xx} = 0 \tag{3.29}$$

and

$$f_{x\theta} \neq 0, \quad f_{xxx} \neq 0 \tag{3.30}$$

3.6.4 Codimension-3 Singularities

The recognition problem for the winged-cusp singularity is solved by the following conditions

$$f = f_x = f_\theta = f_{xx} = f_{x\theta} = 0 \tag{3.31}$$

with

$$f_{xxx} > 0, f_{\theta\theta} > 0 \tag{3.32}$$

3.6.5 Hopf Degeneracies

In this section we present how the singularity theory can also be used to examine Hopf degeneracies. Degenerate Hopf occurs when one or more Hopf hypotheses are violated. We present the results [33] developed by Golubitsky and Langford [131] and Golubitsky and Schaeffer [132] who studied the dynamics near these Hopf degeneracies. There are three types of Hopf degeneracies, I, II, and III, and are associated respectively with the failure of Hopf Hypotheses (H1), (H2), and (H3). In the course of this section, we treat a general n-dimensional dynamical system described by Equation (3.1). Moreover, the analysis is also illustrated by applying the results to a three-dimensional system ($n = 3$ in Equation (3.1)). The eigenvalues μ of the (3×3) Jacobian matrix J are the solutions of the characteristic matrix equation

$$det(J - \mu I) = 0 \tag{3.33}$$

where I is the identity matrix. This equation yields

$$-\lambda^3 + S_1\mu^2 - S_2\mu + S_3 = 0 \tag{3.34}$$

where S_1, S_2, and S_3 are the three invariants of J

$$S_1 = j_{11} + j_{22} + j_{33} \tag{3.35}$$

$$S_2 = det\begin{pmatrix} j_{11} & j_{12} \\ j_{21} & j_{22} \end{pmatrix} + det\begin{pmatrix} j_{22} & j_{23} \\ j_{32} & j_{33} \end{pmatrix} + det\begin{pmatrix} j_{11} & j_{13} \\ j_{31} & j_{33} \end{pmatrix} \tag{3.36}$$

$$S_3 = det(J) \tag{3.37}$$

The j_{11}, j_{12}, $\cdots$ are the elements of J. The conditions of Hopf bifurcation in terms of the coefficients S_1, S_2, and S_3 can be derived by setting $\mu = iw$ into Equation (3.34) to yield the following conditions,

$$F := S_1 S_2 - S_3 = 0 \tag{3.38}$$

$$S_2 > 0 \tag{3.39}$$

3.6.6 Type I Degeneracies

Type I Hopf degeneracies occur when the first hypothesis (H1) of the Hopf bifurcation theorem fails. This occurs when more than one eigenvalue or complex conjugate pair of eigenvalue of the Jacobian matrix have simultaneously zero real parts. When the eigenvalues of the Jacobian matrix evaluated at steady state are on the imaginary axis, the model is structurally unstable. Any variations in the model parameters change the eigenvalues and consequently alters the topology of the local dynamics. When static bifurcation occurs, it involves steady-state bifurcation that leads to multiple steady states. At Hopf bifurcation point, the steady state becomes unstable and periodic branches, which may be stable or unstable, emanate from the Hopf point. To illustrate the methodology for the analysis of type I degeneracies, let's consider the following (n-order) system

$$\frac{dx}{dt} = f(x, \theta, \alpha) \tag{3.40}$$

where x is the vector of n state variables, θ is the bifurcation variable, and α is a vector of constant parameters. The system of Equations (3.40) can always be written using deviation variables $\tilde{x} = x - x_{ss}$ where x_{ss} is the steady-state solution. The obtained model in deviation variables form can be linearized locally to the following form

$$\frac{d\tilde{x}}{dt} = J(x_{ss}, \theta, \alpha)\tilde{x} + g(\tilde{x}, \theta, \alpha) \tag{3.41}$$

where J is the Jacobian matrix and g contains terms that are at least quadratic in $\tilde{x}$. Let's assume that the Jacobian matrix has a N eigenvalues with zero real parts at the point $(x_{ss}, \theta_0, \alpha_0)$, then the next step is to make use of the center manifold theory [33, 136, 366] (presented in the Appendix) to reduce the system (Equation (3.41)) to the following N-dimensional system

$$\frac{dz}{dt} = \Phi z + \Psi(z, \theta, \alpha) \tag{3.42}$$

where the matrix Φ, of order $N \times N$, is in the Jordan form and its eigenvalues have zero real parts at $(x_{ss}, \theta_0, \alpha_0)$. Therefore, it can be seen that the reduced system (Equation (3.42)) preserves the local dynamic features of the original system.

In the following section, we present a description of type I degeneracies. The conditions for the occurrence of these degeneracies are applied to a three-dimensional system ($n = 3$ in Equation (3.1)).

3.6.6.1 F_1 Degeneracy

This degeneracy, called F_1, corresponds to the simplest interactions between a Hopf point and a static limit. In this case, the imaginary part of the complex conjugate eigenvalues pair associated with the Hopf point goes to zero as the Hopf point and the turning point collapse, resulting in a double zero eigenvalue with the following Jordan block of size two:

$$\begin{pmatrix} 0 & 1 \\ 0 & 0 \end{pmatrix}$$

This Jordan block form indicates that there is only one eigenvector corresponding to two zero eigenvalues. The conditions for this degeneracy, for a three-dimensional system, are found by substituting $\mu_1 = 0$ and $\mu_2 = 0$ into the characteristic Equation (3.34), to yield:

$$S_2 = S_3 = 0 \tag{3.43}$$

Close to F_1 degeneracy one can expect steady-state multiplicity and periodic attractors. One might also observe some global bifurcation phenomena such as homoclinic orbits that connect a saddle point to itself by a closed orbit [33, 132, 366].

3.6.6.2 F_2 Degeneracy

In this second class of type I degeneracies, a Hopf point remains a Hopf point as it passes through the limit point so that three eigenvalues are critical. The Jordan block for this degeneracy, called F_2, has the following form

$$\begin{pmatrix} 0 & -w & 0 \\ w & 0 & 0 \\ 0 & 0 & 0 \end{pmatrix}$$

The conditions for this degeneracy for a three-dimensional system are:

$$S_1 = 0 \tag{3.44}$$

$$S_3 = 0 \tag{3.45}$$

$$S_2 > 0 \tag{3.46}$$

Close to F_2 degeneracy, in addition to static multiplicity, periodic solutions and homoclinic orbits, one can anticipate heteroclinic orbits (closed orbits that connect distinct fixed points), and also quasi-periodic oscillations [33, 181, 200, 201].

3.6.6.3 G_1 Degeneracy

For the case of triple-zero eigenvalues, called G_1 singularity, the Jordan block form is

$$\begin{pmatrix} 0 & 1 & 0 \\ 0 & 0 & 1 \\ 0 & 0 & 0 \end{pmatrix}$$

The conditions for this degeneracy in term of the characteristic coefficients are:

$$S_1 = S_2 = S_3 = 0 \tag{3.47}$$

The G_1 degeneracy may produce a variety of phenomena ranging from steady-state multiplicity to chaos [33, 230, 288].

3.6.7 Type II and III Degeneracies

Type II and III degeneracies occur, respectively, when the second (transversality) and the third (stability) hypotheses of the Hopf theorem fail. In order to define these singularities, let's first formalize the (H2) and (H3) hypotheses.

Assume that the system (Equation (3.40)) has conjugate eigenvalues μ and $\bar{\mu}$ around point (x_0, θ_0) that can be written as

$$\mu(\theta) = \nu(\theta) + iw(\theta) \tag{3.48}$$

Let's also assume without loss of generality that the steady-state point under consideration (x_0, θ_0) is transformed to the origin $(0, \theta_0)$. The next step is to make use of the central manifold theory [136, 366] as well as a series of successive coordinates transformations [33, 258, 366] to show that the orbit structure near the point $(0, \theta_0)$ is determined by the following simple two-dimensional normal form,

$$\begin{pmatrix} \dot{x_1} \\ \dot{x_2} \end{pmatrix} = \begin{pmatrix} \nu(\theta) & -w(\theta) \\ w(\theta) & \nu(\theta) \end{pmatrix} \begin{pmatrix} x_1 \\ x_2 \end{pmatrix} + \begin{pmatrix} (a(\theta)x_1 + b(\theta)x_2)(x_1^2 + x_2^2) \\ (b(\theta)x_1 + a(\theta)x_2)(x_1^2 + x_2^2) \end{pmatrix}$$

$$+\text{High order terms} \tag{3.49}$$

where a and b are constant depending on θ. In polar coordinates, the system (Equation (3.49)) is written conveniently as

$$\dot{r} = \nu(\theta)r + a(\theta)r^3 + O(r^5) \tag{3.50}$$

$$\dot{\theta} = w(\theta) + b(\theta)r^2 + O(r^4) \tag{3.51}$$

Expanding the coefficients ν and w in Equations (3.50–3.51) around $\theta = \theta_0$ and neglecting higher order terms yields

$$\dot{r} = \nu'(\theta_0)\theta r + a(\theta_0)r^3 \tag{3.52}$$

$$\dot{\theta} = w(\theta_0) + w'(\theta_0) + b(\theta_0)r^2 \tag{3.53}$$

It can be seen from Equation (3.52) that the second hypothesis of the Hopf theorem, namely the transversality hypothesis, can be written formally as

$$\nu'(\theta_0) \neq 0 \tag{3.54}$$

The stability, on the other hand, of the periodic orbit emanating from the Hopf point is determined by the sign of the coefficient $a := a(\theta_0)$ in Equation (3.52) [33, 366]. The periodic orbit is asymptotically stable when a is negative and unstable for positive values of a. The third Hopf hypothesis can be therefore written formally as

$$a \neq 0 \tag{3.55}$$

The case of $a < 0$ is referred to as supercritical bifurcation where stable limit cycles (commonly shown by dots) emerge from the Hopf point (Figure 3.10). The case of $a > 0$ is known as subcritical bifurcation where unstable periodic solutions (circles) emanate from the Hopf point (Figure 3.10). In the following

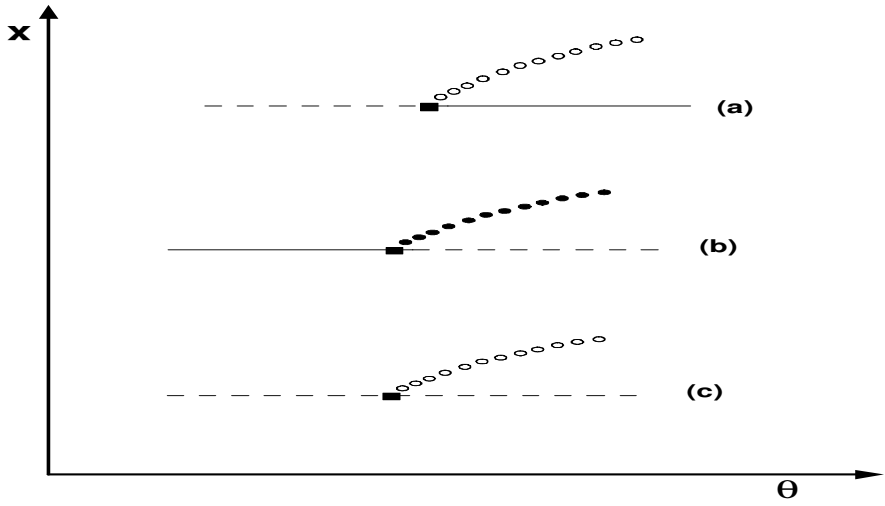

FIGURE 3.10: Examples of (a) Subcritical periodic branch; (b) supercritical; (c) at least one eigenvalue is positive.

section, we discuss the degeneracies associated with the failure of H2 and H3 hypotheses. But first, we introduce the following definition for a general high order degeneracy of these two types.

Definition 5 Introducing a Taylor expansion of the model normal form (Equations (3.50–3.51)) yields

$$\dot{r} = \nu'(\theta_0)\theta r + a_1(\theta_0)r^3 + a_2(\theta_0)r^5 + \cdots \quad (3.56)$$

$$\dot{\theta} = w(\theta_0) + \cdots \quad (3.57)$$

where $a_1 = a$ is the stability coefficient. Suppose that at the Hopf point we have the following conditions:

$$\nu = \nu' = \cdots = \nu^k = 0, \nu^{k+1} \neq 0 \quad (3.58)$$

$$a_1 = a_2 = \cdots = a_m = 0, a_{m+1} \neq 0 \quad (3.59)$$

where ν^j denotes the derivative of order j of ν with respect to the bifurcation parameter θ. A H_{km} Hopf degeneracy is defined as a degeneracy that satisfies conditions of Equations (3.58–3.59). This degeneracy is of codimension $k + m + 1$. □

The singularity theory can be used to analyze the dynamics near these Hopf degeneracies. This makes use of the Lyapunov–Schmidt reduction technique to reduce the bifurcation problem to a single implicitly defined function. Some details of the technique are presented in the Appendix. We present in the following some examples of type II and type III degeneracies.

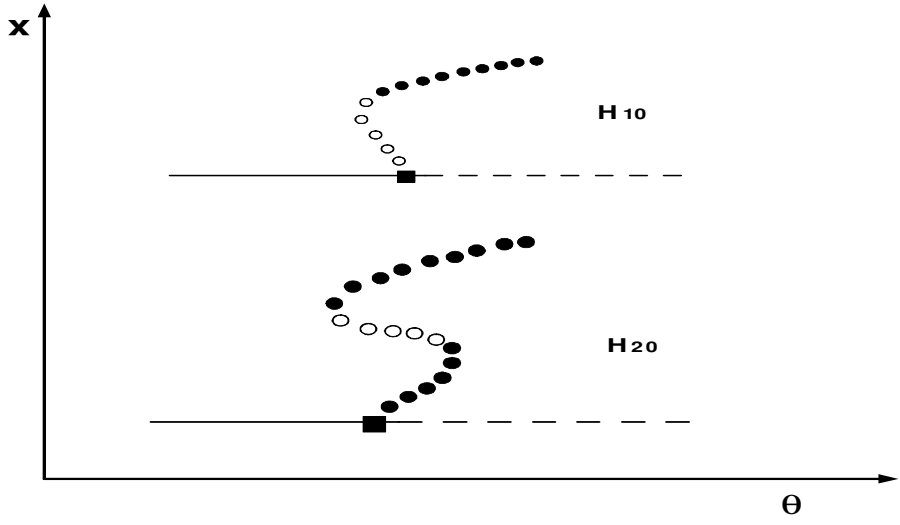

FIGURE 3.11: Examples of bifurcation diagrams resulting from H_{10} and H_{20} singularities.

TABLE 3.3: Normal forms and unfoldings for H_{01} and H_{02} singularities

Type	Normal form	Universal unfolding	Nondegeneracy conditions
H_{01}	$x(\pm x^2 + \theta^2)$	$x(\pm x^2 + \theta^2 + \alpha)$	$a_{10} > 0(\text{or} < 0)$, $a_{02} > 0$
H_{02}	$x(x^2 \pm \theta^3)$	$x(x^2 \pm \theta^3 + \alpha_1 + \alpha_2\theta)$	$a_{10} > 0(\text{or} < 0), a_{03} > 0$

3.6.8 Examples of Type II Degeneracies

A large family of type II degeneracies occur for $k = 0$ in Equations (3.58–3.59). The resulting H_{0m} family of degeneracies is of codimension $m + 1$. The first member of the H_{0m} family corresponds to $m = 1$. The resulting H_{01} degeneracy describes the appearance of two Hopf points while the H_{02} degeneracy involves the interactions between three Hopf points. The H_{0m} family can be described qualitatively as being associated with the appearance of $(m + 1)$ nondegenerate Hopf points.

Instead of using Equations (3.58–3.59), the conditions for the H_{0m} singularity are written more conveniently using the characteristic coefficients

$$F = F_\theta = F_{\theta\theta} = \cdots = \frac{d^m F}{d\theta^m} = 0, \frac{d^{m+1} F}{d\theta^{m+1}} \neq 0 \tag{3.60}$$

with F being defined by Equations (3.38–3.39).

Far from the turning points, the implicit function theorem can be used to define $x_{ss}(\theta)$ as an invertible function, and this is sufficient to write the conditions (Equation (3.60)) in the following more convenient form [111]:

$$F = F_x = F_{xx} = \cdots = \frac{d^m F}{dx^m} = 0, \frac{d^{m+1} F}{dx^{m+1}} \neq 0 \tag{3.61}$$

Using these equations, the conditions for the appearance of the H_{01} singularity are therefore:

$$F = F_x = 0, \quad F_{xx} \neq 0 \tag{3.62}$$

This condition is equivalent to the simplest type of the static bifurcation, i.e., the turning points of the steady-state curve in the bifurcation diagram. H_{01} represents therefore the turning points of the Hopf points curve.

As for the H_{02} singularity, it is defined using the following conditions:

$$F = F_x = F_{xx} = 0, \quad F_{xxx} \neq 0 \tag{3.63}$$

This singularity is analogous to the hysteresis singularity for the static multiplicity. Table 3.3 shows the normal forms associated with H_{01} and H_{02} singularities. The definition of the coefficients a_{10}, a_{02}, a_{03} are given in the appendix.

3.6.9 Examples of Type III Degeneracies

This type of degeneracy occurs when the third hypothesis (H3) of the Hopf theorem is violated. This type may allow for individual Hopf points to produce periodic limit points and therefore multiple periodic orbits. A large family of Type III degeneracy occurs for $m = 0$ in Equations (3.58–3.59). The first member of this family is the H_{10} singularity. It is associated with the transition from subcritical to supercritical Hopf bifurcation. This transition may lead to the formation of a limit point on the periodic branch (Figure 3.11). The second member is the H_{20} singularity. This singularity allows the formation of a hysteresis loop in the periodic branch, and this leads to the formation of multiple periodic orbits (Figure 3.11). Table 3.4 shows the normal forms

TABLE 3.4: Normal forms and unfoldings for H_{10} and H_{20} singularities

Type	Normal form	Universal unfolding	Nondegeneracy conditions
H_{10}	$x(x^4 \pm \theta)$	$x(x^4 \pm \theta + \alpha x^2)$	$a_{01} > 0(\text{or} < 0)$, $a_{20} > 0$
H_{20}	$x(x^6 \pm \theta)$	$x(x^6 + \pm\theta + \alpha_1 x^2 + \alpha_2 x^4)$	$a_{01} > 0(\text{or} < 0), a_{30} > 0$

of H_{10} and H_{20} singularities. The definition of the coefficients describing the degeneracy conditions are also given in the appendix.

This page intentionally left blank

Chapter 4

THE BASIC MODEL OF IDEAL CHEMOSTAT

4.1 Introduction

We start our study with the basic unstructured model of the ideal chemostat. We consider the continuous bioreactor with cell recycle shown in Figure 4.1. The purge fraction W containing the biomass is operated directly from the bioreactor. Ideal conditions are assumed to prevail in the settler. The cell mass is assumed to be formed with a growth rate r_x proportional to biomass concentration X, i.e., $r_x = rX$, where r is the specific growth rate, assumed to depend only on the substrate. The substrate utilization rate r_s is assumed to be a linear function of the cell growth rate r_x, i.e., $r_s = -r_x/Y$ where Y is the yield coefficient, assumed to be independent of the substrate and cell composition. In many cases, it is needed to account for the energy required for cell maintenance and cell death. An endogenous decay term k_dX representing the rate of decay in the cell mass is used to correct the cell growth rate. The net cell growth rate is therefore, $rX - k_dX$, where k_d is the endogenous decay coefficient.

The unstructured model hence established does not recognize any internal structure of the cell nor a diversity between the cell forms. However, it includes the most fundamental observations concerning microbial growth processes: that the rate of cell mass production is proportional to biomass concentration and that there is a decrease in cell mass also proportional to biomass concentration. The quality of the model predictions is variable but it increases whenever the substrate concentration is high enough in the major part of the bioreactor to permit equilibrium of the internal cell composition, the so-called balanced growth condition [263].

As was mentioned in the first chapter, the stability of the basic model of the chemostat was the subject of several investigations in the literature [7, 59, 94]. Useful results on the stability of the chemostat can also be found in the excellent textbooks [41, 265, 321], while a study of the stability of the model using different tools than the singularity theory was carried out in the book of Smith and Waltman [329].

The present chapter has two objectives. One objective is to provide a general framework for the analysis of static multiplicities in the chemostat

model, using the singularity theory. The relative simplicity of the reactor-settler model allows the description of the steady-state behavior of the system in form of a single nonlinear algebraic equation. The singularity theory can therefore provide a useful tool for the classification of the different branching phenomena in the model. The second objective is to study the dynamic bifurcation of the bioreactor model. General conditions for the existence of Hopf points with respect to the selected growth kinetics are derived. The periodic behavior is examined for both constant and variable (substrate dependent) yield coefficient.

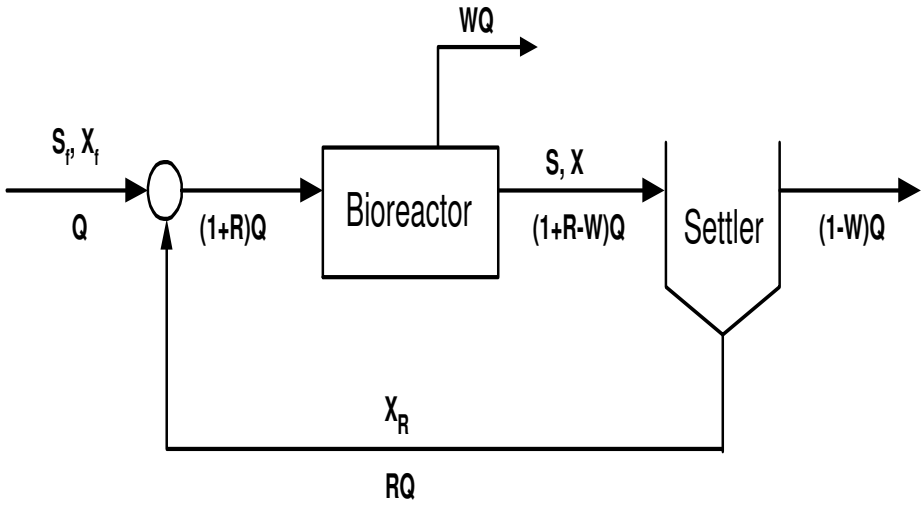

FIGURE 4.1: Schematic diagram of a bioreactor with cell recycle.

4.2 Process Model

The unsteady-state mass balance equation for the substrate S is given by

$$QS_f + QRS - \frac{rXV}{Y} = QWS + Q(1 + R - W)S + V\frac{dS}{dt} \tag{4.1}$$

or equivalently

$$QS_f - QS - \frac{rXV}{Y} = V\frac{dS}{dt} \tag{4.2}$$

Introducing the dilution rate $D = \frac{Q}{V}$, the mass balance is written as

$$D(S_f - S) - \frac{rX}{Y} = \frac{dS}{dt} \tag{4.3}$$

The mass balance equation for the biomass X is

$$QX_f + RQX_R + (r - k_d)X = Q(1 + R)X + V\frac{dX}{dt} \tag{4.4}$$

Ideal conditions in the settler allow the following simple relation between the exit biomass X and the recycle biomass X_R concentrations

$$X_R = X(\frac{1 + R - W}{R}) \tag{4.5}$$

Substituting in Equation (4.4) for the recycle biomass concentration yields

$$QX_f - QWX + (r - k_d)XV = V\frac{dX}{dt} \tag{4.6}$$

or equivalently

$$D(X_f - WX) + (r - k_d)X = \frac{dX}{dt} \tag{4.7}$$

The specific growth rate r is assumed to be described by the Haldane relation [305] with three adjustable parameters

$$r = \frac{\mu_m S}{k_s + S + S^2/k_i} \tag{4.8}$$

where μ_m is the maximum specific growth rate, k_s is the saturation constant, and k_i is the substrate inhibition constant. The mass balances (Equations (4.3, 4.7)) are rendered dimensionless using the following variables

$$\bar{S} = \frac{S}{k_s},\ \bar{X} = \frac{X}{k_s Y},\ K = \frac{k_i}{k_s},\ \bar{t} = \frac{t}{\mu_m},\ \bar{D} = \frac{D}{\mu_m},\ \beta = \frac{k_d}{\mu_m}$$

The dimensionless model is therefore,

$$\bar{D}(\bar{S}_f - \bar{S}) - \bar{r}\bar{X} = \frac{d\bar{S}}{d\bar{t}} \tag{4.9}$$

$$\bar{D}(\bar{X}_f - W\bar{X}) + (\bar{r} - \beta)\bar{X} = \frac{d\bar{X}}{d\bar{t}} \tag{4.10}$$

The growth rate r in dimensionless form is given by

$$\bar{r} = \frac{\bar{S}}{1 + \bar{S} + \frac{\bar{S}^2}{K}} \tag{4.11}$$

Monod growth is obtained as a limiting case of Equation (4.11) when the dimensionless inhibition constant K takes on large values, i.e., $K \to +\infty$.

4.3 Static Analysis

We start by carrying out a steady-state analysis of the bioreactor model. The steady-states equations are obtained by setting the right-hand sides of Equations (4.9, 4.10) to zero. The combination of both of these equations yields

$$\bar{D}(\bar{S}_f - \bar{S}) + \bar{D}\bar{X}_f - \bar{X}(\beta + \bar{D}W) = 0 \tag{4.12}$$

By introducing Equation (4.12) and then Equation (4.11) into Equation (4.9), a third-order polynomial can be obtained for the substrate concentration $\bar{S}$,

$$F(\bar{S}) := a\bar{S}^3 + b\bar{S}^2 + c\bar{S} + d = 0$$

with

$$\begin{array}{ll} a = & \frac{1}{K\bar{S}_f} \\ b = & -\frac{1}{K} + \frac{1}{\bar{S}_f} - \frac{1}{\bar{S}_f(\beta+\bar{D}W)} \\ c = & -1 + \frac{1}{\bar{S}_f} + \frac{1}{\beta+\bar{D}W} + \frac{\bar{X}_f}{\bar{S}_f(\beta+\bar{D}W)} \\ d = & -1 \end{array} \tag{4.13}$$

The steady states of this model are bounded. The substrate concentration $\bar{S}$ is bounded by the feed conditions $\bar{S}_f$, while the maximum concentration of the biomass is obtained by setting $\bar{S} = 0$ in Equation (4.12), to yield

$$\bar{X} = \frac{\bar{D}(\bar{S}_f + \bar{X}_f)}{\beta + \bar{D}W} \tag{4.14}$$

We are interested in the way the steady state $\bar{S}$ depends on the positive system parameters. The dilution rate appearing in Equation (4.13) is selected to be the bifurcation parameter. The steady-state Equation (4.13) is cubic in $\bar{S}$, so for a given value of $\bar{D}$ there will be either one or three real positive roots. In the following, we examine the occurrence of various static singularities for this equation.

4.3.1 Codimension-1 Singularity

Hysteresis

Recasting the results mentioned in Chapter 3, the conditions for the appearance/disappearance of a hysteresis loop are that

$$F = F_{\bar{S}} = F_{\bar{S}\bar{S}} = 0 \tag{4.15}$$

In addition a number of other derivatives must remain nonzero, namely $F_{\bar{D}}$, $F_{\bar{S}\bar{D}}$, and $F_{\bar{S}\bar{S}\bar{S}}$. The hysteresis conditions for the model are then

$$F = a\bar{S}^3 + b\bar{S}^2 + c\bar{S} + d = 0 \tag{4.16}$$

$$F_{\bar{S}} = 3a\bar{S}^2 + 2b\bar{S} + c = 0 \tag{4.17}$$

$$F_{\bar{S}\bar{S}} = 6a\bar{S} + 2b = 0 \tag{4.18}$$

Equation (4.18) has one solution $\bar{S} = -\frac{b}{3a}$. Substituting this solution in Equations (4.16–4.17) yields the following relations for the hysteresis singularity

$$\frac{b^2}{3a} = c \tag{4.19}$$

$$\frac{b^3}{27a^2} = -1 \tag{4.20}$$

These two equations are also equivalent to $b = -3a^{\frac{2}{3}}$ and $c = 3a^{\frac{1}{3}}$. Recasting the expressions of a and b from Equation (4.13) yields the following two relations for the term $\zeta = \frac{1}{\beta + \bar{D}W}$

$$\zeta = 1 - \frac{\bar{S}_f}{K} + \frac{3\bar{S}_f^{\frac{1}{3}}}{K^{\frac{2}{3}}} \tag{4.21}$$

and

$$\zeta = \frac{-1 + \bar{S}_f + \frac{3\bar{S}_f^{\frac{2}{3}}}{K^{\frac{1}{3}}}}{\bar{S}_f + \bar{X}_f} \tag{4.22}$$

Combining these two relations, an expression for the biomass feed concentration $\bar{X}_f$ can be obtained as a function of model parameters $\bar{S}_f$ and K,

$$\bar{X}_f = \frac{-K + 3(K\bar{S}_f)^{\frac{2}{3}} - 3K^{\frac{1}{3}}\bar{S}_f^{\frac{4}{3}} + \bar{S}_f^2}{K + 3(K\bar{S}_f)^{\frac{1}{3}} - \bar{S}_f} \tag{4.23}$$

Equation (4.23) and either Equation (4.21) or Equation (4.22) define the conditions for the hysteresis singularity. Next, we check that the other derivatives at these conditions remain nonzero. It can be noted that $F_{\bar{S}\bar{S}\bar{S}}$ cannot vanish for any values of system parameters, since

$$F_{\bar{S}\bar{S}\bar{S}} = 6a = \frac{6}{K\bar{S}_f} \neq 0 \tag{4.24}$$

The $F_{\bar{D}}$ condition requires, on the other hand, that

$$F_{\bar{D}} = \frac{W\bar{S}(\bar{S} - \bar{S}_f - \bar{X}_f)}{\bar{S}_f(\beta + \bar{D}W)^2} \neq 0 \tag{4.25}$$

$F_{\bar{D}}$ vanishes only at $\bar{S} = 0$ and at $\bar{S} = \bar{S}_f + \bar{X}_f$. Barring the trivial case of $\bar{S} = 0$, the second vanishing point is physically realistic only if $\bar{X}_f = 0$ (i.e., clean feed conditions). This case is to be discussed in a later section, as it gives rise to an other singularity. The other derivative condition is $F_{\bar{D}\bar{S}} \neq 0$. Since

$$F_{\bar{D}\bar{S}} = \frac{W(2\bar{S} - \bar{S}_f - \bar{X}_f)}{\bar{S}_f(\beta + \bar{D}W)^2} \tag{4.26}$$

The condition is equivalent to

$$\bar{S} \neq \frac{\bar{S}_f + \bar{X}_f}{2} \tag{4.27}$$

or equivalently, by recasting the expressions of b and c from Equation (4.13), to

$$\zeta \neq 1 - \frac{5\bar{S}_f}{K} + \frac{\bar{X}_f}{6K} \tag{4.28}$$

Equating this condition with any of conditions (Equation (4.21)) or Equation (4.22) does not yield any real solutions for the model parameters. We conclude therefore that the condition of Equation (4.28) is never violated. Figure 4.2a shows an example of the hysteresis branch set for $\bar{X}_f = 0.05$, $\beta = 0$ and $W = 1$. The hysteresis boundary (H_0) divides the parameter space ($\bar{S}_f, K$) into two regions H_1 and H_2. For any parameter combination in region (H_1) (e.g., $\bar{S}_f = 5.0$ and $K = 4$) the bifurcation diagram, obtained with the Software AUTO [98], has two limit points, as shown in Figure 4.2b. Any abrupt change in the reactor operating parameters can cause the system to jump from a high conversion point to a low conversion operating point. If a sample parameter combination ($\bar{S}_f, K$) is, on the other hand, moved from region H_1 towards the hysteresis boundary (H_0) then the two turning points collapse into one limit point, as shown in Figure 4.2c, for values of $\bar{S}_f = 3.52358$ and $K = 4$. After the boundary is crossed towards region H_2, the hysteresis disappears, as shown by the continuation diagram of Figure 4.2d, for values of $\bar{S}_f = 3$ and $K = 4$.

Isola and Mushroom

The second possible qualitative change that can occur in the steady-state locus is the appearance of an isola and the growth of an isola into a mushroom. The requirements, mentioned in Chapter 3, for these two changes are that

$$F = F_{\bar{S}} = F_{\bar{D}} = 0 \tag{4.29}$$

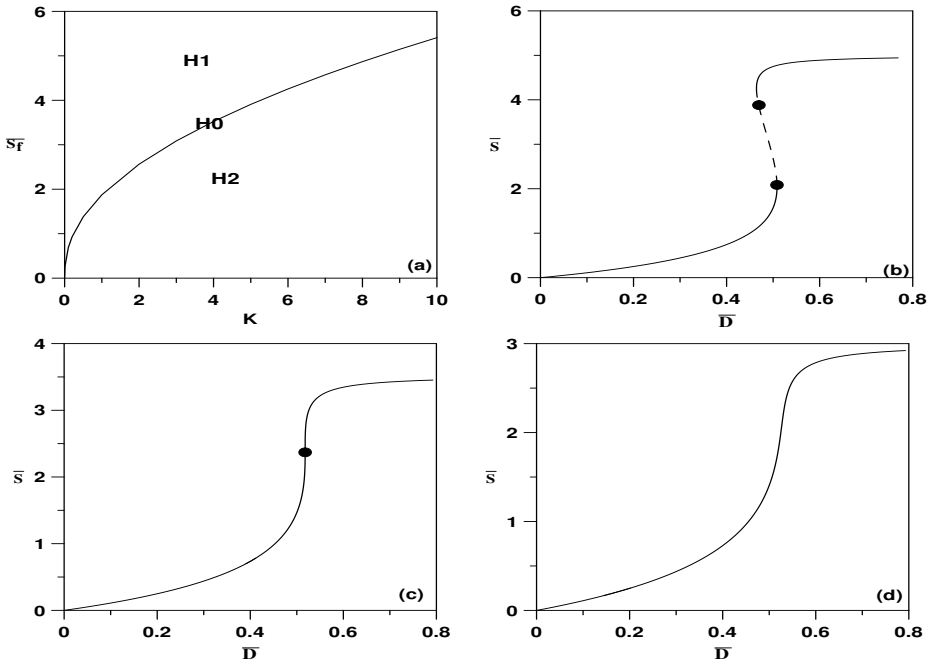

FIGURE 4.2: (a) Branch sets for the hysteresis singularity; (b) Continuity diagram showing hysteresis in region H_1; (c) Continuity diagram for the boundary H_0; (d) Continuity diagram for region H_2; solid line, stable branch; dashed line, unstable; circle, limit point.

with the additional requirements that

$$F_{\bar{S}\bar{D}} \neq 0, F_{\bar{S}\bar{S}} \neq 0, F_{\bar{D}\bar{D}} \neq 0 \tag{4.30}$$

From the expression of $F_{\bar{D}}$ in Equation (4.25), we see that the possible steady-state solutions of $F_{\bar{D}} = 0$ are $\bar{S} = 0$ and $\bar{S} = \bar{S}_f + \bar{X}_f$, but it is straightforward to see that the requirement $F_{\bar{D}\bar{D}} \neq 0$ is not satisfied for any model parameters, since

$$F_{\bar{D}\bar{D}} = \frac{-2W^2\bar{S}(\bar{S} - \bar{S}_f - \bar{X}_f)}{\bar{S}_f(\beta + \bar{D}W)^3} \tag{4.31}$$

vanishes at the considered steady states. The model cannot therefore exhibit an isola or mushroom singularity.

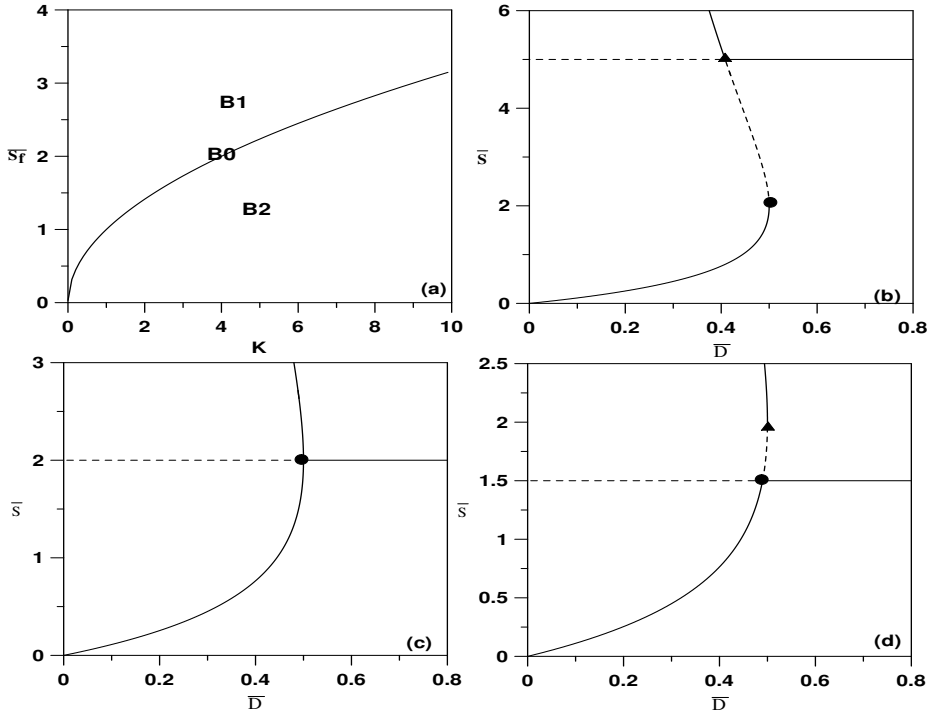

FIGURE 4.3: (a) Branch sets for the pitchfork singularity; (b) Continuity diagram for region B_1; (c) Continuity diagram for the boundary B_0; (c) Continuity diagram for region B_2; solid line, stable; dashed line, unstable; circle, limit point; triangle, bifurcation point.

4.3.2 Codimension-2 Singularity

The conditions for the single scalar function to undergo a pitchfork bifurcation are that

$$F = F_{\bar{S}} = F_{\bar{D}} = F_{\bar{S}\bar{S}} = 0 \tag{4.32}$$

and

$$F_{\bar{S}\bar{D}} \neq 0, F_{\bar{S}\bar{S}\bar{S}} \neq 0 \tag{4.33}$$

The pitchfork conditions for our example are

$$a\bar{S}^3 + b\bar{S}^2 + c\bar{S} + d = 0 \tag{4.34}$$

$$3a\bar{S}^2 + 2b\bar{S} + c = 0 \tag{4.35}$$

$$6a\bar{S} + 2b = 0 \tag{4.36}$$

$$\frac{W\bar{S}(\bar{S} - \bar{S}_f - \bar{X}_f)}{\bar{S}_f(\beta + \bar{D}W)^2} = 0 \tag{4.37}$$

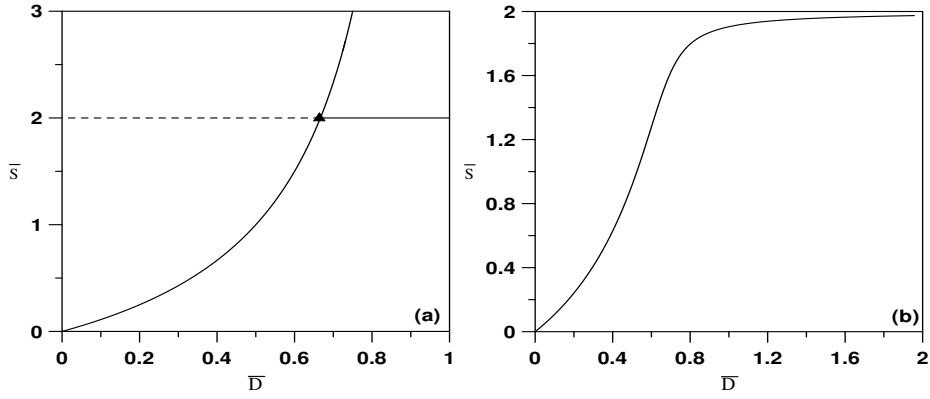

FIGURE 4.4: Bifurcations diagrams for Monod growth; (a) Sterile feed conditions; (b) Case of nonsterile feed with $\bar{X}_f = 0.05$.

Equation (4.37) has one physically realistic solution $\bar{S} = \bar{S}_f + \bar{X}_f$, provided that $\bar{X}_f = 0$, while Equations (4.34–4.36) yield the same steady-state solution $\bar{S} = -\frac{b}{3a}$ and the same conditions of Equations (4.21–4.23), previously obtained for the hysteresis singularity. The steady-state equation $\bar{S} = -\frac{b}{3a}$ should be then equal to $\bar{S} = \bar{S}_f$. Taking Equation (4.19) into consideration, this is equivalent to $-c = b\bar{S}_f$. Recasting the expressions of c and b from Equations (4.13) yields

$$\bar{S}_f = \sqrt{K} \tag{4.38}$$

Substituting in Equation (4.21) or Equation (4.22) yields

$$\zeta = 1 + \frac{2}{\sqrt{K}} \tag{4.39}$$

or equivalently

$$\bar{D} = \frac{1}{W}\left(\frac{1}{1 + \frac{2}{\sqrt{K}}} - \beta\right) \tag{4.40}$$

Washout conditions occur if the dilution rate is larger than the critical value defined by Equation (4.40). The condition $F_{\bar{S}\bar{D}} \neq 0$, on the other hand, is automatically satisfied. Figure 4.3 summarizes the branch set for the pitchfork singularity. Equation (4.38) defines the boundary B_0 for the pitchfork in the $(\bar{S}_f, K)$ plane. This boundary, shown in Figure 4.3a, divides the plane in two regions. For values of parameters $\bar{S}_f$ and K (e.g., $\bar{S}_f = 5$ and $K = 4$) in region B_1, the continuation diagram of Figure 4.3b shows an imperfect pitchfork where a region of instability separates the limit point and the bifurcation point located on the washout line. The system has three steady branches where

the upper one is physically unrealistic. Operating the reactor for dilution rates smaller than the critical value is possible in the lower branch. If the parameters $\bar{S}_f$ and K move on the boundary itself B_0 (e.g., $\bar{S}_f = 2$ and $K = 4$) then the limit point and the bifurcation point collapse in one point yielding a perfect pitchfork, as shown in Figure 4.3c. The same washout conditions exist for this bifurcation as the critical dilution rate is the same. For values of parameters in region B_2 (e.g., $\bar{S}_f = 1.5$ and $K = 4$), the continuity diagram is shown in Figure 4.3d. The limit point in this case moves to the other side of the bifurcation point and occurs on the physically unrealistic branch.

Finally, it should be noted that the pitchfork singularity obtained for $\bar{X}_f = 0$ is the highest singularity the model can exhibit. A codimension-3 singularity, i.e., winged cusp requires that the following conditions be satisfied

$$F = F_{\bar{S}} = F_{\bar{D}} = F_{\bar{S}\bar{S}} = F_{\bar{S}\bar{D}} = 0$$

But it can be seen that conditions $F_{\bar{D}} = 0$ (Equation (4.25)) and $F_{\bar{S}\bar{D}} = 0$ (Equation (4.26)) are incompatible since they would lead to the relation $\bar{S}_f + \bar{X}_f = 0$, which is not physically realistic.

4.3.3 Monod Kinetic Model

The investigation carried out so far with Haldane kinetics can be used to recover the bifurcation behavior for the case of Monod growth. As the dimensionless inhibition constant K takes on large values, i.e., $K \to +\infty$, the steady-state Equation (4.13) becomes quadratic

$$F(\bar{S}) = b\bar{S}^2 + c\bar{S} + d = 0 \tag{4.41}$$

with the coefficient b and c becoming

$$\begin{aligned} b &= \frac{1}{\bar{S}_f} - \frac{\zeta}{\bar{S}_f} \\ c &= -1 + \frac{1}{\bar{S}_f} + \zeta + \frac{\zeta \bar{X}_f}{\bar{S}_f} \\ d &= -1 \end{aligned}$$

For a quadratic equation like Equation (4.41), the singularity theory defines a simple bifurcation (codimension-0), defined by the following conditions

$$F = 0, F_{\bar{S}} = 0, \text{ and } F_{\bar{S}\bar{S}} \neq 0 \tag{4.42}$$

The second condition $F_S = 2b\bar{S} + c = 0$ defines one possible solution $\bar{S} = -\frac{c}{2b}$. Substituting in condition $F = 0$ yields

$$c^2 = -4b \tag{4.43}$$

This condition is satisfied only if $b \leq 0$, which is equivalent to having

$$\zeta = \frac{1}{\beta + \bar{D}W} \geq 1 \tag{4.44}$$

The condition $F_{\bar{S}\bar{S}} \neq 0$, on the other hand, implies that $\zeta \neq 1$. So for $\zeta > 1$, the condition $c^2 = -4b$ is equivalent to

$$(\bar{S}_f + \bar{X}_f)^2\zeta^2 + 2(\bar{X}_f - \bar{S}_f(1 + \bar{S}_f + \bar{X}_f))\zeta + (1 + \bar{S}_f)^2 = 0 \qquad (4.45)$$

The discriminant of this quadratic equation is $\Delta = -16\bar{S}_f\bar{X}_f(1 + \bar{S}_f + \bar{X}_f)$. Therefore, the equation does not have real solutions unless $\bar{X}_f = 0$. For this case, the solution of Equation (4.45) yields

$$\zeta = 1 + \frac{1}{\bar{S}_f} \qquad (4.46)$$

which is obviously greater than 1. The critical dilution rate $\bar{D}_c$ can be defined from Equation (4.46) as follows

$$\bar{D}_c = \frac{1}{W}(\frac{1}{\zeta} - \beta) = \frac{1}{W}(\frac{\bar{S}_f}{1 + \bar{S}_f} - \beta) \qquad (4.47)$$

Washout conditions occur for any dilution rate larger than $\bar{D}_c$. Figure 4.4a shows the continuation diagram for $\bar{X}_f = 0$, $W = 1$, and $\beta = 0$. The system features two stable branches where the upper one is not physically realistic. For the case where the biomass feed exists ($\bar{X}_f \neq 0$), the system features a unique steady-state solution, and the continuity diagram is shown in Figure 4.4b, for the case of $\bar{X}_f = 0.05$, $W = 1$, and $\beta = 0$.

4.4 Dynamic Behavior for Constant Yield Coefficient

In this section we investigate the existence of periodic behavior in the model. As was mentioned in Chapter 1, the existence of oscillatory behavior under suitable operating conditions has long been known in continuous cultures of some micro-organisms such as *S. cerevisiae* [146, 274] and *Z. mobilis* [174]. The two-dimensional system exhibits a Hopf bifurcation point if the Jacobian matrix has pure imaginary eigenvalues. The Jacobian matrix for this model is

$$J = \begin{bmatrix} f_{1\bar{S}} & f_{1\bar{X}} \\ f_{2\bar{S}} & f_{2\bar{X}} \end{bmatrix} \qquad (4.48)$$

where f_1 and f_2 denote the left-hand sides of the mass balances in Equations (4.9–4.10). Substituting the expressions of the gradients yields

$$J = \begin{bmatrix} -\bar{D} - \bar{r}'\bar{X} & -\bar{r} \\ \bar{r}'\bar{X} & -W\bar{D} + \bar{r} - \beta \end{bmatrix} \qquad (4.49)$$

where $\bar{r}'$ is the first derivative of $\bar{r}$. The eigenvalues λ of the Jacobian matrix are the solutions of the characteristic equation

$$\lambda^2 - \lambda(f_{1\bar{S}} + f_{2\bar{X}}) + f_{1\bar{S}}f_{2\bar{X}} - f_{1\bar{X}}f_{2\bar{S}} = 0 \qquad (4.50)$$

The conditions for this equation to have pure nonzeros eigenvalues are that

$$f_{1\bar{S}} + f_{2\bar{X}} = 0 \tag{4.51}$$

$$f_{1\bar{S}} f_{2\bar{X}} - f_{1\bar{X}} f_{2\bar{S}} > 0 \tag{4.52}$$

These relations are equivalent to

$$-\bar{D}(1+W) - \bar{r}'\bar{X} + \bar{r} - \beta = 0 \tag{4.53}$$

$$W\bar{D}^2 - \bar{D}(\bar{r} - \beta) + \bar{r}'\bar{X}(W\bar{D} + \beta) > 0 \tag{4.54}$$

Substituting Equation (4.53) into Equation (4.54) yields,

$$\bar{r}'\bar{X}(\bar{D}(W-1) + \beta) > \bar{D}^2 \tag{4.55}$$

The steady-state form of Equation (4.10) is equivalent to

$$\bar{r} - \beta = -\frac{\bar{D}(\bar{X}_f - W\bar{X})}{\bar{X}} \tag{4.56}$$

Substituting in the first Hopf condition (Equation (4.53)) and expanding yields,

$$\bar{r}'\bar{X} = -\frac{\bar{D}(\bar{X}_f + \bar{X})}{\bar{X}} \tag{4.57}$$

Using, on the other hand, the combination of steady-state Equations (4.9, 4.10) yields

$$\bar{X} = \frac{\bar{D}(\bar{S}_f - \bar{S} + \bar{X}_f)}{\beta + \bar{D}W} \tag{4.58}$$

Finally, substituting for $\bar{r}'\bar{X}$ (Equation (4.57)) and $(\beta + \bar{D}W)$ (Equation (4.58)) in the second Hopf condition (Equation (4.55)) yields

$$-(\bar{X}_f + \bar{X})(\bar{S}_f - \bar{S}) > \bar{X}_f^2 \tag{4.59}$$

The left-hand side of this inequality is always negative, therefore the condition is never satisfied. This analysis was carried out without reference to the explicit expression of the growth model. We conclude therefore that the bioreactor model, cannot predict periodic behavior for any growth rate. This quite interesting result is more general than the one found by Crooke et al. [85] and Ivanitskaya et al. [172], since the studied model takes into consideration cell maintenance and eventual nonsterile feed conditions. This result reflects a fundamental weakness of the basic unstructured kinetic model. Since the metabolic activity is described solely by the specific growth rate and the yield coefficient, it does not recognize any internal structure of the cell nor a diversity between cell forms, and thus fails to describe situations where the cell composition or the morphology of the cell culture are important variables. The inadequacy of the unstructured model manifests itself in its failure to predict transient behavior following sudden changes in operation parameters [265] and, as shown in this analysis, in predicting oscillatory behavior for any growth rate.

4.5 Dynamic Behavior for Variable Yield Coefficient

We consider in this section the case for which the yield coefficient is variable. We relax the previous assumptions by neglecting the endogenous term (i.e., $k_d = 0$), assuming no recycle ($W = 1$) and that the yield coefficient depends solely on the substrate. We will make use of the original equations in dimensional form. The Jacobian matrix for the model in dimensional form (Equations (4.3, 4.7)) is given by

$$J = \begin{bmatrix} -D - (\frac{r}{Y})'X & -\frac{r}{Y} \\ r'X & -D + r \end{bmatrix} \tag{4.60}$$

A similar analysis to the previous section reveals that Hopf conditions are:

$$f_{1S} + f_{2X} = -2D - (\frac{r}{Y})'X + r = 0 \tag{4.61}$$

$$f_{1S}f_{2X} - f_{1X}f_{2S} = D^2 - Dr + D(\frac{r}{Y})'X + \frac{\bar{r}\bar{r}'X}{Y} - (\frac{r}{Y})'rX > 0 \tag{4.62}$$

Substituting Equation (4.61) into Equation (4.62) yields the following condition for the existence of Hopf points,

$$r^2X\frac{Y'}{Y^2} > D^2 \tag{4.63}$$

It can be concluded that, necessarily, the yield should be in such a way that $Y' > 0$. At the steady state (Equation (4.3)), we have that

$$D = \frac{rX}{Y(S_f - S)} \tag{4.64}$$

Combining Equation (4.3) with Equation (4.7) yields

$$X = Y(S_f - S) + X_f \tag{4.65}$$

Substituting these two equations in Equation (4.63) yields the following condition for the existence of Hopf points

$$Y' > \frac{Y}{(S_f - S)} + \frac{X_f}{(S_f - S)^2} \tag{4.66}$$

It is interesting to note that the Hopf condition in this case is independent of the specific growth rate. For the practical case of sterile feed $X_f = 0$, this condition is reduced to

$$\frac{Y'}{Y} > \frac{1}{S_f - S} \tag{4.67}$$

The occurrence of a Hopf bifurcation is therefore conditioned by the inequality $Y'(s) > 0$ and the condition of Equation (4.67). While the condition $Y'(s) > 0$ is satisfied at least in the neighborhood of $S = 0$ for every growth rate, the condition of Equation (4.67) is not always guaranteed. This is particularly the case when the yield is constant. In the following, we consider the case when the yield coefficient is assumed to depend linearly on the substrate:

$$Y = Y_0 + Y_1 S \tag{4.68}$$

The variability of the yield coefficient was shown in the literature to be the case for a number of microbial populations [347]. The linear model for the dependence of the yield coefficient on the substrate was proposed, for instance, by Ivanitskaya et al. [172] to describe the continuous growth of *S. cerevisiae*. The yield for this organism is known to depend on the substrate concentration. This is attributed mainly to the Crabtree effect [290], as the yield for fully oxidative and fully fermentative regimes are known to be significantly different [274]. The variability of the yield coefficient depends therefore on the coexistence of these mechanisms. The relative impact of these pathways on the microbial metabolism is, on the other hand, affected by the inhibitive action that glucose has on the oxidative pathway at high substrate concentration.

The choice of a linear model to describe the variations of the yield is also due to its simplicity. The coefficients of the linear relationship have a meaning of a regression of the experimental values.

For the linear dependence of the yield, the Hopf condition of Equation (4.67) requires that $\frac{Y_1}{Y} > \frac{1}{S_f - S}$, which also necessarily requires that $\frac{Y_1}{Y} > \frac{1}{S_f}$. As was explained in [70], a large dependence of the yield coefficient on the substrate (i.e., large value of Y_1) results in a negative feedback effect caused by the substrate concentration. But high values for this quantity induce quicker growth and a higher biomass yield, which in turn leads to a decrease in substrate concentration. These effects coupled with the autocatalytic nature of the reaction, leads to the occurrence of dynamical bifurcation.

In the following, we describe in detail the dynamic bifurcation induced by the linear dependence of the yield coefficient on the substrate. The Haldane relation is chosen to describe substrate inhibited kinetics,

$$r = \frac{\mu_m S}{k_s + S + \frac{S^2}{k_i}} \tag{4.69}$$

The model is rendered dimensionless using the following variables,

$$\bar{S} = \frac{S}{S_f}, \quad \bar{X} = \frac{X}{Y_0 S_f}, \quad \lambda = \frac{Y_1 S_f}{Y_0}, \quad \bar{D} = \frac{D}{\mu_m}$$

$$\beta = \frac{k_s}{S_f}, \quad \gamma = \frac{S_f}{k_i}, \quad \bar{t} = t\mu_m, \quad \bar{r} = \frac{\bar{r}}{\mu_m}$$

The model in dimensionless form is

$$\frac{d\bar{S}}{d\bar{t}} = \bar{D}(1-\bar{S}) - \frac{\bar{r}\bar{X}}{\lambda\bar{S}+1} \tag{4.70}$$

$$\frac{d\bar{X}}{d\bar{t}} = -\bar{D}\bar{X} + \bar{r}\bar{X} \tag{4.71}$$

The dimensionless specific growth rate is

$$\bar{r} = \frac{\bar{S}}{\beta + \bar{S} + \gamma\bar{S}^2} \tag{4.72}$$

The combination of the steady states of Equations (4.70, 4.71) yields,

$$\bar{X} = (1-\bar{S})(\lambda\bar{S}+1) \tag{4.73}$$

Substituting in the steady state form of Equation (4.70) yields the following algebraic equation,

$$F(\bar{S}) := (1-\bar{S})(-\bar{D}+\bar{r}) \tag{4.74}$$

This equations predicts washout conditions, i.e., $\bar{S}=1$, $\bar{X}=0$ unless

$$\bar{r} = \bar{D} \tag{4.75}$$

With the selected form of the specific growth rate (Equation (4.72)), the steady-state Equation (4.75) is quadratic in $\bar{S}$. The nontrivial solution $\bar{r}=\bar{D}$ exhibits a static limit point when $F_{\bar{S}}=0$ (Equation (4.74)), i.e., $\bar{r}'=0$. The first derivative of the growth rate is given by

$$\bar{r}' = \frac{\beta - \gamma\bar{S}^2}{(\beta + \bar{S} + \gamma\bar{S}^2)^2} \tag{4.76}$$

and vanishes at

$$\bar{S}_{max} = \sqrt{\frac{\beta}{\gamma}} \tag{4.77}$$

The static limit point occurs on the washout line when $\bar{S}=1$. Substituting in Equation (4.77) yields

$$\beta = \gamma \tag{4.78}$$

This relation defines the boundary between two types of static behavior, as it is seen later.

The singularity theory also predicts a number of singularities for the dynamic bifurcation. As mentioned in Chapter 3, the F_1 degeneracy involves

the interaction between a Hopf point and a static limit point. It is defined by solving the static limit point conditions ($F_{\bar{S}} = 0$), i.e., ($\bar{r}' = 0$) (Equation (4.77)) and the equality derived from the Hopf condition (Equation (4.67)), which becomes in dimensionless form

$$\frac{Y'}{Y} = \frac{1}{1-\bar{S}} \tag{4.79}$$

or equivalently

$$\frac{\lambda}{\lambda\bar{S}+1} = \frac{1}{1-\bar{S}} \tag{4.80}$$

Substituting the condition $\bar{r}' = 0$ (Equation (4.77)) into Equation (4.80) yields the following condition for the F_1 singularity,

$$\beta = \frac{\gamma}{4}(1-\frac{1}{\lambda})^2 \tag{4.81}$$

The H_{01} singularity, also discussed in Chapter 3, corresponds to the appearance or coalescence of two Hopf points. The condition for this singularity are:

$$H = H_{\bar{S}} = 0, H_{\bar{S}\bar{S}} \neq 0 \tag{4.82}$$

where

$$H := f_{1\bar{S}} + f_{2\bar{X}} \tag{4.83}$$

with

$$f_{1\bar{S}} f_{2\bar{X}} - f_{1\bar{X}} f_{2\bar{S}} > 0 \tag{4.84}$$

Since there is no simple analytical relation that can be derived from these conditions, the set of Equations (4.82) is solved numerically for (β, γ) to define the boundaries of this singularity. The complete static and dynamic branch set consists of Equation (4.78) defining the static singularity, together with Equations (4.81–4.82) that define, respectively, the F_1 and H_{01} singularities. The branch set is shown in Figure 4.5 in the parameter space (β, γ), for $\lambda = 10$. The branch set is divided in four regions. In region (a), Figure 4.6a shows an example of a continuity diagram for $(\beta, \gamma) = (0.1, 0.8)$. An unstable branch can be seen to separate the static limit point (SLP) and the bifurcation point (BR) corresponding to the crossing with the washout line. The static limit point occurs at dilution rate

$$\bar{D}_{LP} = \bar{r}(\bar{S} = \bar{S}_{max}) = \frac{1}{1+2\sqrt{\beta\gamma}} \tag{4.85}$$

The bifurcation point (BR), on the other hand, occurs at dilution rate $\bar{D}_{BR}$, obtained by setting $\bar{S} = 1$ in Equation (4.75), yielding

$$\bar{D}_{BR} = \frac{1}{\beta+1+\gamma} \tag{4.86}$$

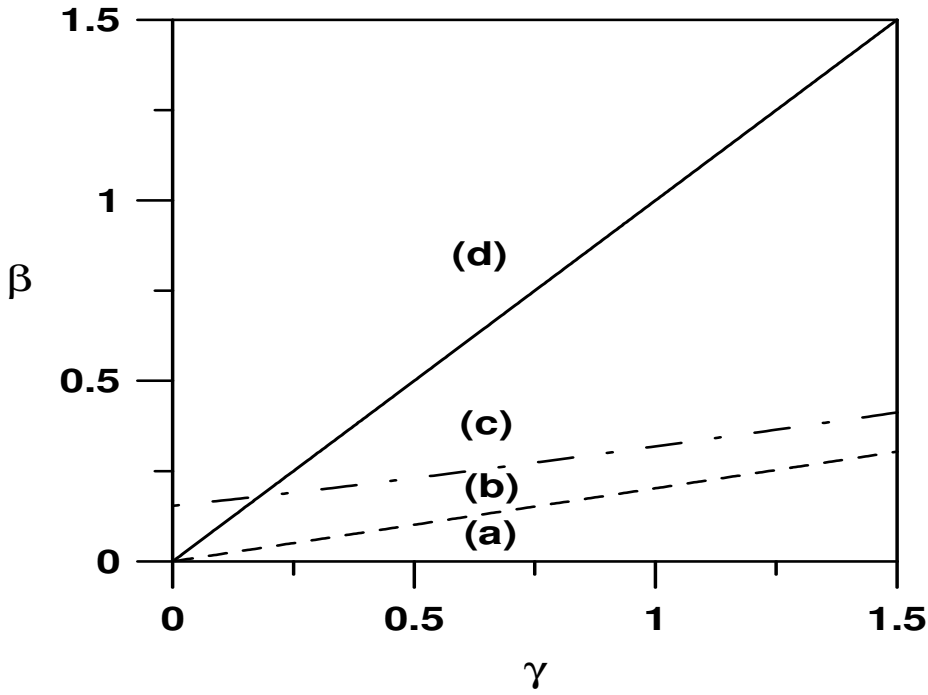

FIGURE 4.5: Complete branch set in the parameter space (β, γ) for variable yield model; solid line, static singularity; dashed line, F_1 singularity; semidashed line, H_{01} singularity.

The continuity diagram is also characterized by the existence of a Hopf point. Stable periodic branches emanate from the HB point and terminate as they collide with the static branch. For conditions between the Hopf point (HB) and the bifurcation point (BR), oscillatory behavior is inevitable. For dilution rates between BR and SLP, there is a situation of bistability where washout and oscillations coexist for any values of the dilution rate. Figure 4.7 shows an example of this situation for $\bar{D} = 0.580$. Small fluctuations of around 3 percent in the dilution rate pushes the process from oscillatory behavior to washout conditions. When crossing the boundary (Figure 4.5) separating regions (a) and (b), a second Hopf point appears as a result of the H_{01} singularity. The continuity diagram, shown in Figures 4.6 (b1–b2) for $(\beta, \gamma) = (0.2, 0.8)$, is characterized by the presence of two Hopf points in addition to the static limit point. A third stable branch also exists between the larger Hopf point and the limit point. Similarly to the previous diagram (Figure 4.6a), oscillations are the only attractors for dilution rates between the HB point and the bifurcation point (BR), while these oscillations coexist

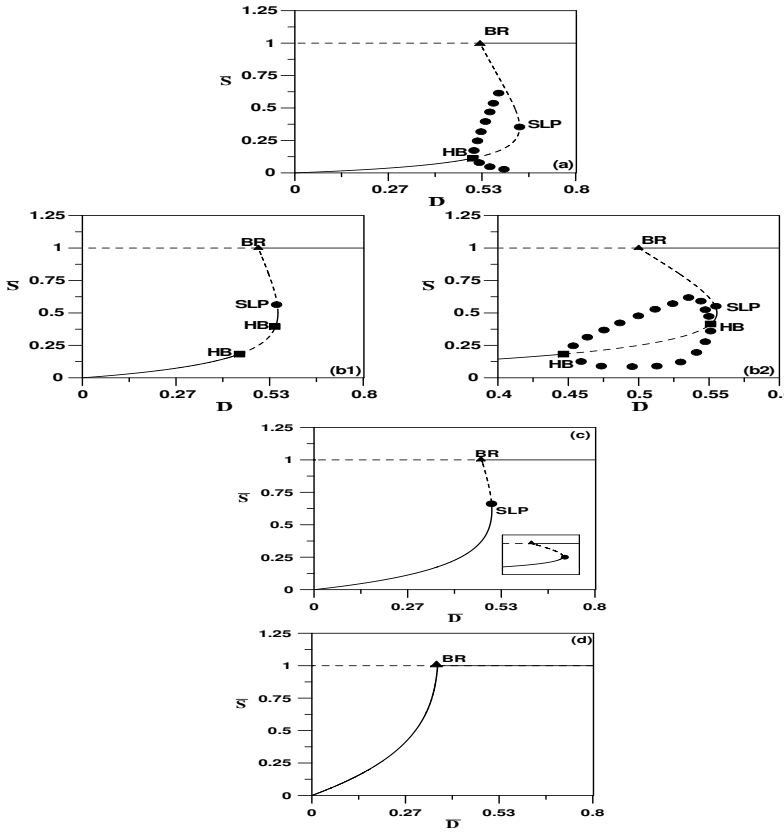

FIGURE 4.6: Continuity diagrams in the different regions of Figure 4.5: (a) Imperfect pitchfork in region (a); (b1) Two Hopf points and a middle stable branch in region (b); (b2) Details of region (b); (c) Imperfect pitchfork in region (c); (d) Monod-like behavior in region (d).

with the washout line for dilution rates between BR and the largest HB point. When crossing to region (c) of Figure 4.5, the two Hopf points disappear. The steady-state portrait (Figure 4.6c), obtained for $(\beta, \gamma) = (0.5, 0.8)$, exhibits a limit point with no HB point. For conditions between BR and SLP, the process exhibits bistability. The operation on the lower static branch may also drift towards washout conditions. Finally, when the parameters (β, γ) cross the static line to region (d) (Figure 4.5), the limit point moves to the other side of the washout line. A Monod-like behavior is expected, as shown in Figure 4.6d, obtained with $(\beta, \gamma) = (1, 0.8)$.

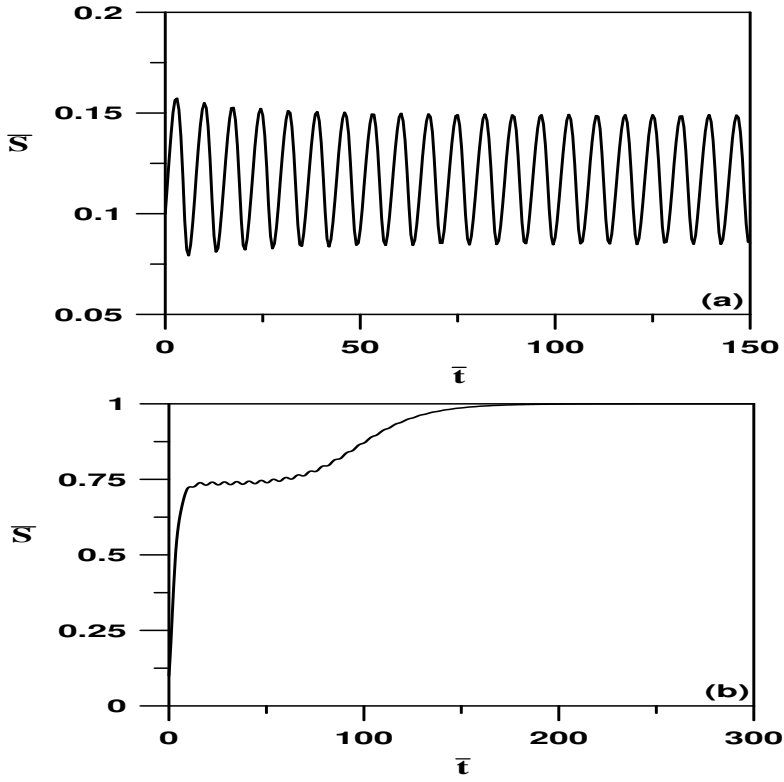

FIGURE 4.7: Time traces showing different behavior in region (a) of Figure 4.6a: (a) Autonomous stable oscillations for $\bar{D} = 0.580$; (b) Small fluctuations in dilution rate move the oscillatory behavior to washout.

4.6 Concluding Remarks

The singularity theory was used to reexamine the bifurcation mechanisms of the basic unstructured model of the chemostat with cell recycle. It was shown that for Haldane substrate inhibition kinetics, the pitchfork singularity that occurs for sterile feed is the highest singularity the model can predict. The investigation of Hopf points has shown that for the case of a constant yield coefficient, neither the presence of a maintenance term nor the assumption of spatial inhomogeneity due to the wall attachment of micro-organisms can produce an oscillatory behavior. It seems therefore that the variability of the yield coefficient with the substrate is a necessary requirement for the two-dimensional model to produce a dynamic bifurcation. This also joins the

results obtained in [286]. For the important case of linear dependence of the yield coefficient on the substrate, the analysis carried out in this chapter has shed some light on some dynamic degeneracies predicted by the model. Recently, this analysis has been extended by Cammarota [70] who uncovered more features regarding Hopf points including the computation of the loci of the H_{10} singularity.

Chapter 5

THE CHEMOSTAT WITH WALL ATTACHMENT

5.1 Introduction

Attachment of microbial cells to the walls of bioreactors is not an uncommon phenomenon. The usual assumption in most applications involving continuous stirred tank bioreactor systems is that the flow rate is fast enough that wall growth can be neglected. However, in many cases, micro-organisms attached to solid surfaces might form a film ranging from a monocellular layer to a thick layer of slime [250]. A biofilm, for instance, consists of microbial cells attached to a solid surface that are usually embedded in a matrix of organic polymers produced by the extracellular polymeric substances (EPS). A good example is the nitrification process where extracellular polymers are excreted and embeded in a slime matrix [99, 138]. The modeling of microbial growth and wall attachment is an important issue. Besides operational problems caused by microbial fouling of the internal surfaces of the bioreactor, a more-or-less loose wall growth leads to the enrichment of cells in the bioreactor and could have important ramifications on the stability characteristics of the unit. It should be noted that the ability of bacteria to attach to surfaces is not only of interest to bioreactors. This issue is of considerable interest to many industries, including medical, food industry, and membrane-based processes. In the latter applications, the development of biofilms on the surface of membrane-based separation systems such as those used in the desalination process is an important issue, since biofouling can lead to the deterioration or even the failure of the separation process.

Attachment of microbial cells is a complex process controlled by diverse characteristics of the growth medium, substratum, and cell surface [102, 269]. In the literature, Topiwala and Hamer [352] were first to propose a model that allows for the growth of a monocellular layer attached to the walls of the chemostat. Among the model assumptions are that the attachment of microbial cells to the solid surface is irreversible and that the population density on the surface is constant. Both of these assumptions were relaxed in the model proposed later by Baltzis and Fredrickson [47] for their study of the competition between microbial populations when one of them exhibits wall attachment. The density of the attached cells was, however, not allowed

to exceed a maximum value, characteristic of the surface and the microbial species. Ratnam et al. [298] also studied the effects of attachment of bacteria to chemostat walls in a microbial predator–prey relationship. Later, Sambanis and Fredrickson [312] investigated the stabilizing effect of cell wall attachment on the feeding-saprotrophy model. Smith and Waltman [329], and Pilyugin and Waltman [285] provided a thorough stability analysis of the chemostat with wall attachment using the basic unstructured model. Abu-Reesh [5], on the other hand, examined the optimal design of chemostats in a series in the presence of microbial wall growth. Dokianakis et al. [99] proposed a general kinetic model based on the modified Topiwala and Hamer model for describing the oxidation of nitrites by autotrophic nitrifiers, when an active biomass is both in suspension and attached to reactor walls. The attached biomass was included in the model as a planar biofilm with uniform properties.

Other approaches were also followed to model microbial wall attachment. Jones et al. [176], for instance, examined the stability of a simple conceptual model of biofilm formation developed by Freter et al. [115] for the implantation of *Escherichia coli* in the intestinal tract. The authors found two steady-state regimes, namely, the complete washout of the microbes from the reactor and the successful colonization of both wall and bulk fluid. Efforts have also been directed towards understanding the complex structural heterogeneity of the formed layers with the goal of shedding light on the mechanisms of the development of biofilms, i.e., the actual placement of daughter cells after cell division. This issue is complicated since it involves the challenging task of understanding the relationships between physical, chemical, and biological processes occurring at very different spatial and temporal scales [96]. In this regard, models of different complexity were proposed to distribute the newly formed biomass. These include models that consider biofilms as layered steady-state films [266] as well as models based on the cellular automaton approach [203, 284, 367]. These models are quite complex and may involve two- or three-dimensional biofilm models [105].

In the previous chapter of this book, we have introduced the effect of wall attachment during the study of the basic unstructured model describing the chemostat. In this chapter, we propose a more complex model for cell wall attachment. The model assumes two morphological variants of the microbial cell: A variant that remains attached to the wall and another one that is sloughed off into the liquid medium. The two forms are connected by metamorphosis reactions. The model, which reduces in the limit to the Topiwala and Hamer model, assumes explicitly the reversibility of wall attachment through the dynamic exchange of material from medium to the wall and vice versa. Models that assume morphological variations between individual cells have been used by a number of authors for the study of the growth of a variety of organisms [61, 127, 265]. Despite their empirical nature, the metamorphosis reactions may have some biological meaning, and can model complex systems where all the mechanisms are not yet known. For the case of wall growth, the assumption of the existence of two morphological forms connected by sim-

ple first-order exchange kinetics provides a simple approach describing the complex phenomena associated with wall attachment. The objective of this chapter is to study, using the proposed model, the effect of wall growth on the stability characteristics of the chemostat, for both the substrate inhibited and Monod kinetics.

5.2 Process Model

We denote by X and X_w both the morphological forms and also their corresponding biomass concentrations. The two morphological forms interact for both the substrate and for a joint exchange of biomass. The exchange of biomass is assumed to be represented by simple first-order kinetics through transfer rate coefficients k_1 (from X to X_w) and k_2 (from X_w to X). The metabolic activity in each morphological form is assumed to be defined in terms of specific growth rate and yield coefficient, assumed identical for both forms.

The unsteady-state mass balance equations, for the case of sterile feed, of the different species are given by

$$\frac{dX}{dt} = rX - k_1X + k_2X_w - DX \tag{5.1}$$

$$\frac{dX_w}{dt} = rX_w + k_1X - k_2X_w \tag{5.2}$$

$$\frac{dS}{dt} = -\frac{r}{Y}(X + X_w) + D(S_f - S) \tag{5.3}$$

S_f is the substrate feed concentration, Y the yield of biomass on substrate (assumed constant) and $D = \frac{Q}{V}$ is the chemostat dilution rate. k_1X and k_2X_w are respectively the rate of the metamorphosis reactions by which X is converted to X_w and X_w is converted to X. It can be noted that, unlike the basic unstructured model with wall attachment, the balance equations for the biomass concentrations in the proposed model also account for the transfer rates, in addition to dilution rate and specific growth rate. The Haldane equation is selected to describe substrate-inhibited growth. The specific growth rate is given by

$$r = \frac{\mu_m S}{k_s + S + S^2/k_i} \tag{5.4}$$

The mass balances (Equations (5.1–5.3)) are rendered dimensionless using the following variables:

$$\bar{S} = \frac{S}{S_f}, \quad \bar{X} = \frac{X}{YS_f}, \quad \bar{X}_w = \frac{X_w}{YS_f}, \quad \beta = \frac{k_s}{S_f}, \quad \gamma = \frac{S_f}{k_i}$$

$$\bar{k}_1 = \frac{k_1}{\mu_m}, \quad \bar{k}_2 = \frac{k_2}{\mu_m}, \quad \bar{D} = \frac{D}{\mu_m}, \quad \bar{t} = \mu_m t$$

The growth rate r in dimensionless form becomes

$$\bar{r} = \frac{\bar{S}}{\beta + \bar{S} + \gamma \bar{S}^2} \tag{5.5}$$

The dimensionless mass balances equations for the different species are:

$$\frac{d\bar{X}}{d\bar{t}} = \bar{r}\bar{X} - \bar{k}_1\bar{X} + \bar{k}_2\bar{X}_w - \bar{D}\bar{X} \tag{5.6}$$

$$\frac{d\bar{X}_w}{d\bar{t}} = \bar{r}\bar{X}_w + \bar{k}_1\bar{X} - \bar{k}_2\bar{X}_w \tag{5.7}$$

$$\frac{d\bar{S}}{d\bar{t}} = -\bar{r}(\bar{X} + \bar{X}_w) + \bar{D}(1 - \bar{S}) \tag{5.8}$$

Combining Equations (5.6–5.7) yields,

$$\frac{d(\bar{X} + \bar{X}_w)}{dt} = -\bar{D}\bar{X} + \bar{r}(\bar{X} + \bar{X}_w) \tag{5.9}$$

From this equation and Equation (5.8), it can be seen that the proposed model is reduced to the model of Topiwala and Hamer, if $\bar{X}_w$ is considered as being the maximum dimensionless concentration, assumed constant, of cells attached to the wall. Moreover, for the limiting case of $\bar{X}_w = 0$, $\bar{k}_1 = 0$, and $\bar{k}_2 = 0$, the proposed model is reduced to the basic homogeneous unstructured model of the chemostat, studied in the previous chapter.

The steady-states equations of the proposed model are obtained by setting the left-hand sides of Equations (5.6–5.8) to zero. At steady state, Equation (5.9) becomes,

$$-\bar{D}\bar{X} + \bar{r}(\bar{X} + \bar{X}_w) = 0 \tag{5.10}$$

Substituting this equation in Equation (5.8) yields the steady-state value of $\bar{X}$,

$$\bar{X} = 1 - \bar{S} \tag{5.11}$$

The steady-state expression for $\bar{X}_w$, on the other hand, is given by

$$\bar{X}_w = \frac{\bar{k}_1}{\bar{k}_2 - \bar{r}}\bar{X} \tag{5.12}$$

The requirement $\bar{k}_2 > \bar{r}$ is necessary for a meaningful existence of $\bar{X}_w$. Moreover, the combination of Equations (5.10–5.12) yields the following expression for the dilution rate,

$$\bar{D} = \frac{\bar{k}_1 + \bar{k}_2 - \bar{r}}{\bar{k}_2 - \bar{r}}\bar{r} \tag{5.13}$$

Since the term $\bar{k}_2 - \bar{r}$ is always positive, it can be concluded from Equation (5.13) that $\bar{D} > \bar{r}$. Finally, substituting Equations (5.11–5.12) into the substrate mass balance, Equation (5.8) yields, a single algebraic equation that depends only on $\bar{S}$ as a state variable,

$$F(S) := (1 - \bar{S})[\bar{r}^2 - \bar{r}(\bar{D} + \bar{k}_1 + \bar{k}_2) + \bar{D}\bar{k}_2] = 0 \tag{5.14}$$

This equation exhibits two solutions: a washout solution, i.e., $\bar{S} = 1, \bar{X} = \bar{X}_w = 0$, and a nontrivial solution when

$$\bar{r}^2 - \bar{r}(\bar{D} + \bar{k}_1 + \bar{k}_2) + \bar{D}\bar{k}_2 = 0 \tag{5.15}$$

With the selected form of the growth rate (Equation (5.5)), the steady-state Equation (5.15) is of a fourth order in $\bar{S}$.

5.3 Static Analysis for Inhibition Kinetics

A rigorous analysis of the static behavior [12] showed that the model can not predict hysteresis or isola-mushroom singularities. The crossing of the nontrivial solution (Equation (5.15)) with the washout line represents the main feature of the static behavior of the model. The nontrivial branch exhibits a static limit point when the condition $\bar{r}'(S) = 0$ is satisfied, i.e., $\bar{S} = \sqrt{\frac{\beta}{\gamma}}$. The static limit point occurs on the washout line for $\bar{S} = 1$. Substituting this condition into $\bar{r}' = 0$ leads to the simple relation,

$$\beta = \gamma \tag{5.16}$$

This condition defines the limit of two types of behavior, as it will be seen later. To the condition of Equation (5.16) should be added the condition $\bar{k}_2 > \bar{r}$ that defines a meaningful existence of X_w. This condition is equivalent to

$$\bar{k}_2\gamma\bar{S}^2 + (\bar{k}_2 - 1)\bar{S} + \bar{k}_2\beta > 0 \tag{5.17}$$

A simple analysis of this quadratic inequality reveals four different cases for the meaningful existence of X_w. Let Δ be the discriminate of the quadratic equation and $\bar{S}_1$, $\bar{S}_2$ its real roots,

$$\bar{S}_1 = \frac{-(k_2 - 1) - \sqrt{\Delta}}{2k_2\gamma} \quad ,\bar{S}_2 = \frac{-(k_2 - 1) + \sqrt{\Delta}}{2k_2\gamma} \tag{5.18}$$

then the following cases are possible:

1. When $\Delta < 0$ or $\Delta > 0$ with $\bar{k}_2 > 1$, the condition $\bar{k}_2 > \bar{r}$ is always satisfied and X_w is meaningful. Note that condition $\bar{k}_2 > 1$ is equivalent to $k_2 > \mu_m$, i.e., the mass transfer rate k_2 from X_w to X is larger than the maximum specific growth rate.

2. When $\Delta > 0$ and $\bar{k}_2 < 1$, three cases can be delineated depending on the relative location of the roots $\bar{S}_i (i = 1, 2)$:
   (a) The first case corresponds to $\bar{S}_2 < 1$. A meaningful existence of X_w is possible for the following range of substrate concentrations, $0 < \bar{S} < \bar{S}_1$ and $\bar{S}_2 < \bar{S} < 1$.
   (b) The second case corresponds to $\bar{S}_1 < 1 < \bar{S}_2$. A meaningful existence is possible for $0 < \bar{S} < \bar{S}_1$.
   (c) The third condition corresponds to $1 < \bar{S}_1$. A meaningful existence of X_w is always satisfied.

The branch set illustrating these different behaviors consist of Equation (5.16) together with $\Delta = 0$ and $\bar{S}_1 = 1$ or $\bar{S}_2 = 1$. The condition $\Delta = 0$ is equivalent to

$$\beta\gamma = \frac{1}{4}(1 - \frac{1}{\bar{k}_2})^2 \tag{5.19}$$

while the conditions $\bar{S}_1 = 1$ or $\bar{S}_2 = 1$ (Equation (5.18)) are equivalent to

$$\beta = \frac{1}{\bar{k}_2} - 1 - \gamma \tag{5.20}$$

Figures 5.1(a–b) show the complete branch set in the parameter space (γ, β) for two cases: $\bar{k}_2 = 0.5 < 1$ and $\bar{k}_2 > 1$. For $\bar{k}_2 < 1$, a total of five qualitatively different regions can be depicted, as shown in Figure 5.1a. Region (a) corresponds to both $\Delta < 0$ and $\beta < \gamma$. The steady-state portrait $(\bar{D}, \bar{S})$ for this region is shown in Figures 5.2(a–c), for example for $(\beta, \gamma) = (1, 5)$. An unstable branch separates the static limit point (SLP) and the bifurcation point (BR) corresponding to the crossing with the washout line. The static limit point corresponds to $F_{\bar{S}} = 0$, i.e., $\bar{r}'(\bar{S}) = 0$, and occurs at the maximum value $\bar{S}_{max}$ defined by

$$\bar{S}_{max} = \sqrt{\frac{\beta}{\gamma}} \tag{5.21}$$

The value of the specific growth rate $\bar{r}$ at the optimum value is given by

$$\bar{r}_{max} = \frac{1}{1 + 2\sqrt{\beta\gamma}} \tag{5.22}$$

At the static limit point, the dilution rate is obtained from Equation (5.13)

$$\bar{D}_{LP} = \frac{(1 + 2\sqrt{\beta\gamma})(\bar{k}_1 + \bar{k}_2) - 1}{(1 + 2\sqrt{\beta\gamma})k_2 - 1} \frac{1}{(1 + 2\sqrt{\beta\gamma})} \tag{5.23}$$

The dilution rate corresponding to the crossing with the washout line is obtained by setting $\bar{S} = 1$ in Equation (5.13), yielding

$$\bar{D}_{BR} = \frac{(1 + \beta + \gamma)(\bar{k}_1 + \bar{k}_2) - 1}{(1 + \beta + \gamma)\bar{k}_2 - 1} \frac{1}{1 + \beta + \gamma} \tag{5.24}$$

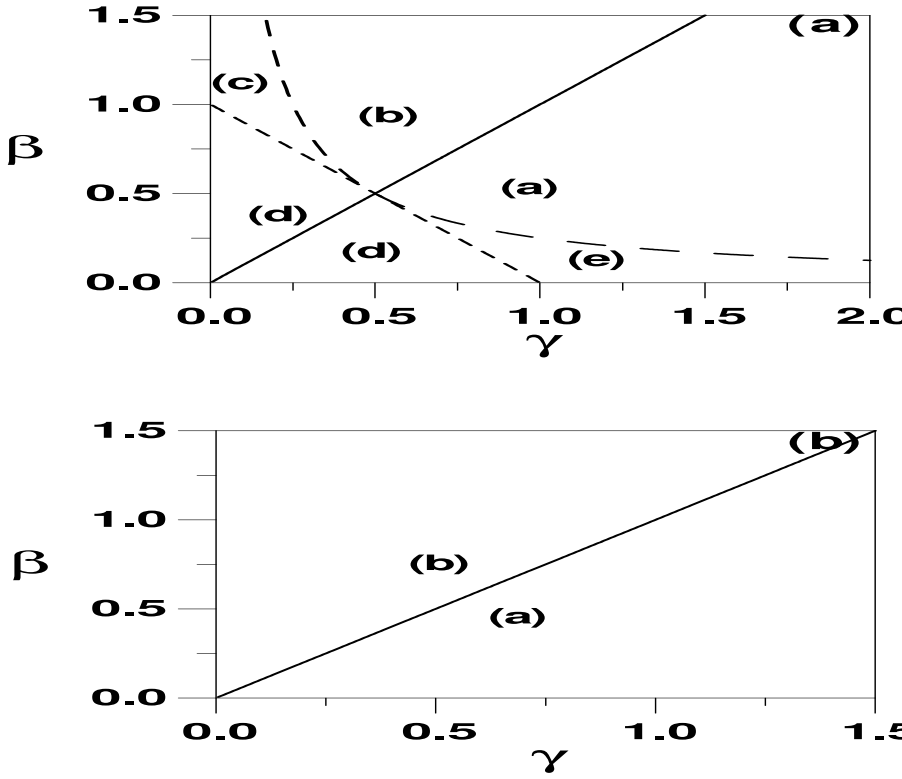

FIGURE 5.1: Branch sets for the model with substrate inhibition: (a) $\bar{k}_2 = 0.5$; (b) $\bar{k}_2 > 1$; solid line corresponds to $\beta = \gamma$; dashed line corresponds to $\Delta = 0$ (Equation (5.19)); semidashed line corresponds to the roots $\bar{S}_1 = 1$ or $\bar{S}_2 = 1$ (Equation (5.20)).

The operation of the bioreactor above $\bar{D}_{LP}$ leads to washout, while a stable operation is possible for dilution rates smaller than $\bar{D}_{BR}$. For conditions between $\bar{D}_{BR}$ and $\bar{D}_{LP}$, the steady-state portrait is characterized by bistability. The concentration $\bar{X}$ (Figure 5.2b) is seen to decrease monotonically from its maximum value of 1. The behavior of the other morphological form X_w is nonmonotonic. The concentration of X_w (Figure 5.2c) can be seen to increase from its initial value and reaches a maximum value before decreasing.

As the pair (β, γ) moves to the boundary separating regions (a) and (b), the unstable region of Figure 5.2a becomes narrower, as the static limit point moves closer to the bifurcation point. On the boundary itself, the two points collapse in one identical point, as it can be seen in the continuity diagram of Figure 5.3, obtained with $(\beta, \gamma) = (1, 1)$. The upper static branch is physically unrealistic. When the parameters (β, γ) move to the other side of the boundary and into region (b) of Figure 5.1a, the static limit point occurs on the

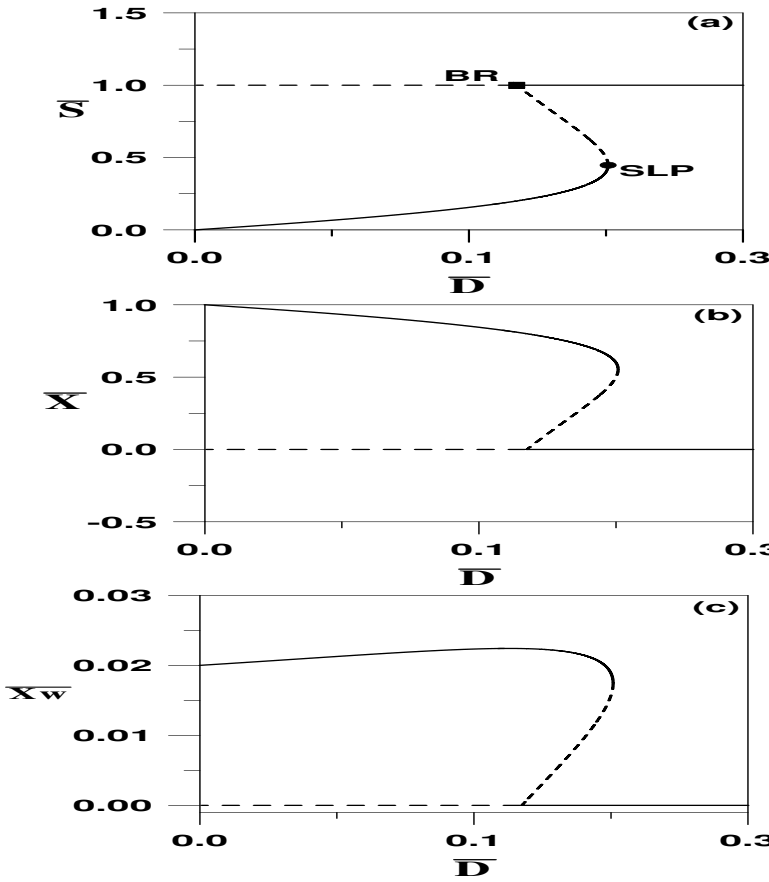

FIGURE 5.2: Continuity diagrams (a)–(c) for region (a) of Figure 5.1a; solid line, stable branch; dashed line, unstable.

physically unrealistic branch. A monotonic and stable behavior is expected in this region, as shown in Figures 5.4(a–c), obtained with $(\beta, \gamma) = (1.5, 0.5)$. The behavior of $\bar{X}$ and $\bar{X}_w$, on the other hand, shows a stable decreasing trend. Moving from region (b) to region (c), the discriminate Δ become positive and a meaningful existence of X_w is also possible for all operating parameters. The steady-state portrait is shown in Figures 5.5(a–c) for $(\beta, \gamma) = (0.75, 0.3)$. In this region, a stable and monotonic increase in the substrate, although different from that of the previous region, can be seen. It can also be seen that while the biomass form $\bar{X}$ decreases monotonically, the profile of $\bar{X}_w$ shows a maximum before decreasing. When crossing to region (d) (Figure 5.1a), the meaningful existence of X_w is satisfied only for substrate concentrations up to the first root $\bar{S}_1$ of the existence Equation (5.18). An example of static behavior in this region (Figures 5.6(a–c)), obtained with $(\beta, \gamma) = (0.25, 0.5)$, shows

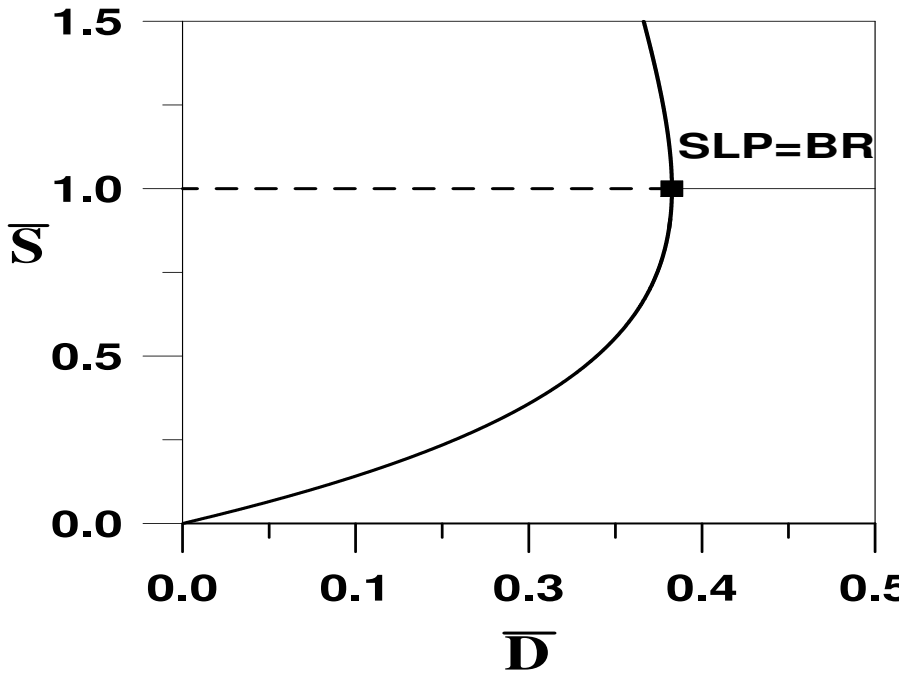

FIGURE 5.3: Continuity diagram on the boundary between region (a) and (b) of Figure 5.1a.

a stable increase in the substrate, until the maximum value $\bar{S}_1$ is reached. The concentration of $\bar{X}$ decreases until it reaches the asymptotic value of $1 - \bar{S}_1$. The behavior of $\bar{X}_w$ with the dilution rate is however unbounded. As both $\bar{S}$ and $\bar{X}$ approach their saturation values, the constant $\bar{k}_2$ approaches the specific growth rate $\bar{r}$, and $\bar{X}_w$ (Equation (5.12)) increases continuously with the dilution rate. Finally, in region (e) the meaningful existence of X_w is satisfied for conditions smaller than $\bar{S}_1$ and larger than $\bar{S}_2$. The continuity diagram is shown in Figures 5.7(a–c), for $(\beta, \gamma) = (0.08, 2.0)$. It can be seen that the substrate concentration continues to increase until the asymptotic value $\bar{S}_1$ is approached. Moreover, an unstable branch can be seen to separate the stable branch and the washout line. The unstable branch corresponds to the other asymptotic value $\bar{S}_2$, and crosses the washout line at the dilution rate $\bar{D}_{BR}$ (Equation (5.24)). Therefore, for any dilution rate larger than $\bar{D}_{BR}$ the process is characterized by bistability. Finally, for the second case of $\bar{k}_2 > 1$, the branch set is characterized by the line $\beta = \gamma$ alone, since a meaningful existence of X_w is always satisfied. The branch set for any value of $\bar{k}_2 > 1$ is shown in Figure 5.1b. Two regions can be delineated: A region similar to

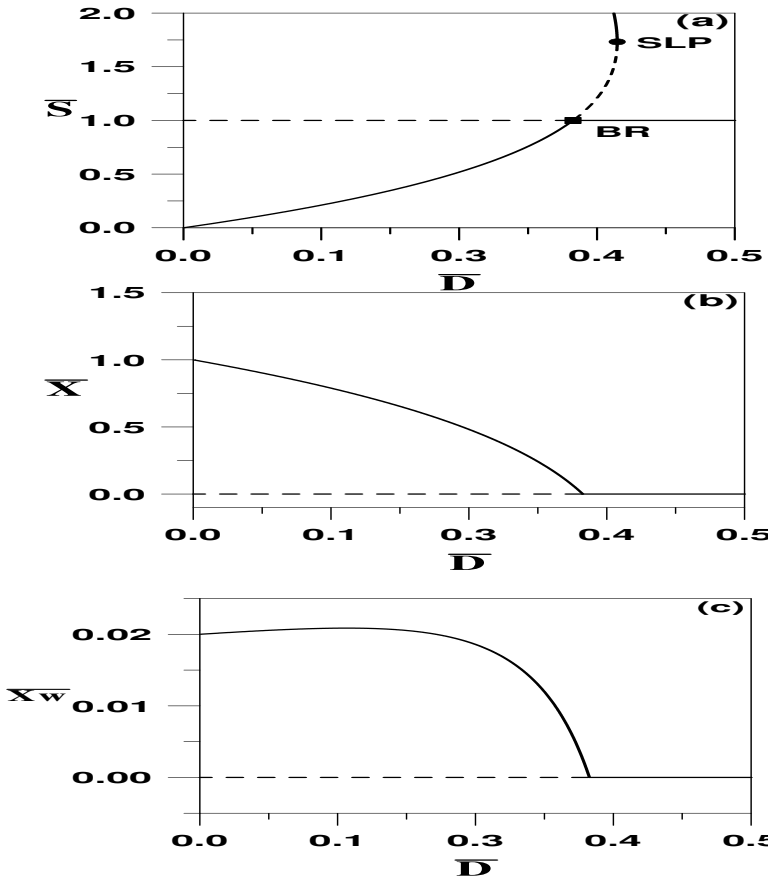

FIGURE 5.4: Continuity diagrams (a)–(c) for region (b) of Figure 5.1a; solid line, stable; dashed line, unstable.

region (a) (Figure 5.2) and a region of monotonic and stable behavior similar to region (b) (Figure 5.4).

5.4 Static Analysis for Monod Growth

The dynamics of the bioreactor for Monod kinetics can be recovered from the analysis carried out in the previous section. As the dimensionless inhibition

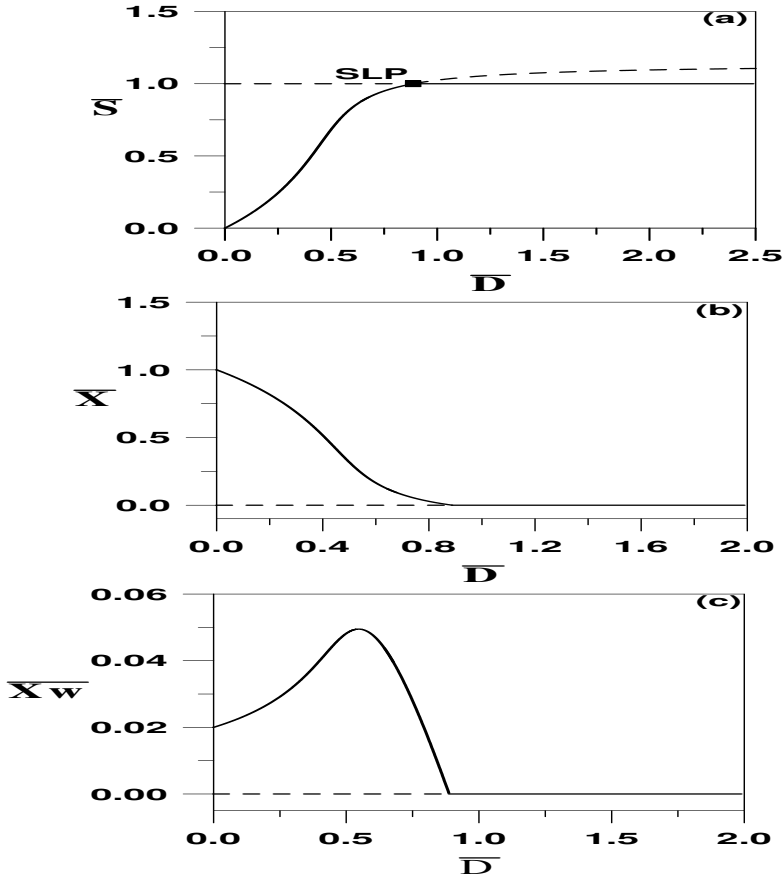

FIGURE 5.5: Continuity diagrams (a)–(c) for region (c) of Figure 5.1a; solid line, stable; dashed line, unstable.

constant goes to zero, the specific growth rate becomes,

$$\bar{r} = \frac{\bar{S}}{\beta + \bar{S}} \tag{5.25}$$

Since $\bar{r}'(\bar{S}) = \frac{\beta}{(\beta+S)^2}$ is always positive, a simple monotonic behavior is expected. The condition $\bar{k}_2 > \bar{r}$ for the meaningful existence of X_w is equivalent to

$$(\bar{k}_2 - 1)\bar{S} + \bar{k}_2\beta > 0 \tag{5.26}$$

and gives birth to two qualitatively different regions:

1. When $\bar{k}_2 > 1$ or $\bar{k}_2 < 1$ with $1 < \frac{\bar{k}_2\beta}{1-\bar{k}_2}$, the condition $\bar{k}_2 > \bar{r}$ is always satisfied and X_w is meaningful.

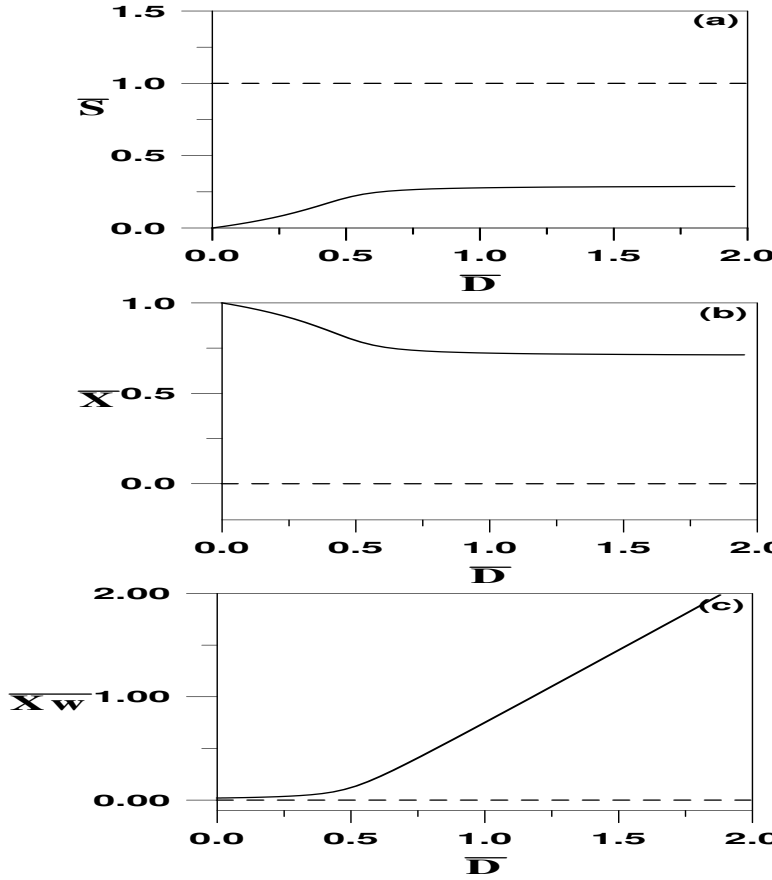

FIGURE 5.6: Continuity diagrams (a)–(c) for region (d) of Figure 5.1a; solid line, stable; dashed line, unstable.

2. When $\bar{k}_2 < 1$ with $\frac{\bar{k}_2\beta}{1-\bar{k}_2} < 1$, a meaningful existence is satisfied for $0 \leq \bar{S} \leq \bar{S}_1 := \frac{\bar{k}_2\beta}{1-\bar{k}_2}$.

The branch set for Monod growth consists therefore in the curve $\bar{S}_1 = 1$, i.e., $\bar{k}_2 = \frac{1}{\beta+1}$ shown in Figure 5.8a. In region (a) of this figure, the continuity diagram (Figure 5.8b), obtained with $(\bar{k}_2, \beta) = (1.5, 0.5)$, shows a monotonic increase in the substrate. A stable and safe behavior is possible for dilution rates below the point of crossing with the washout region (Equation (5.24)), i.e.,

$$\bar{D}_{BR} = \frac{(1+\beta)(\bar{k}_1 + \bar{k}_2) - 1}{(1+\beta)\bar{k}_2 - 1} \frac{1}{1+\beta} \tag{5.27}$$

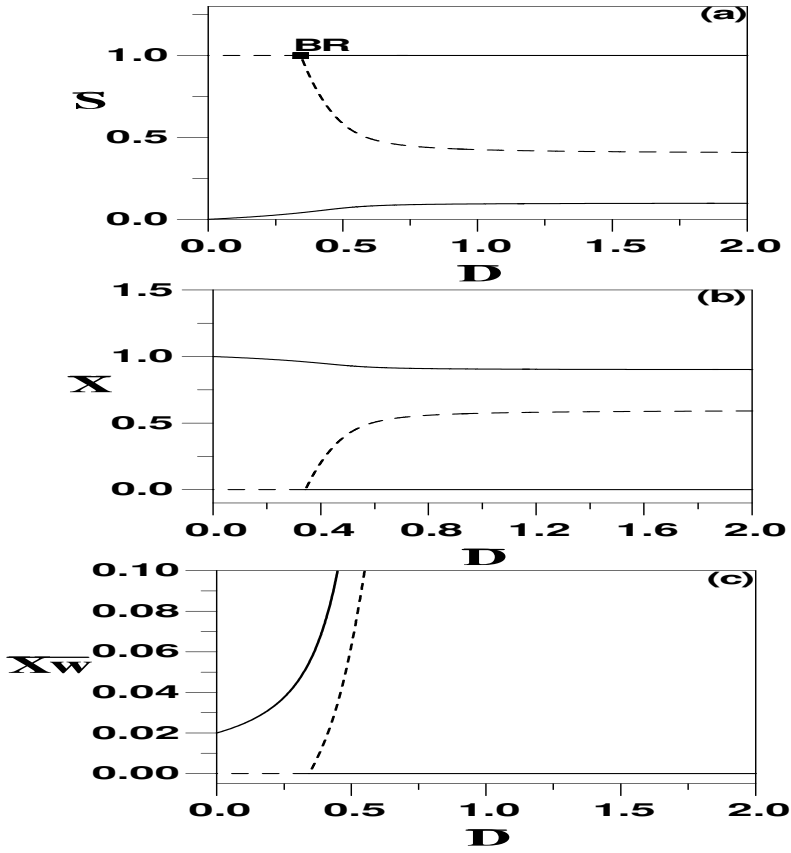

FIGURE 5.7: Continuity diagrams (a)–(c) for region (e) of Figure 5.1a; solid line, stable; dashed line, unstable.

For region (b), the steady-state portrait (Figure 5.8c), obtained with $(\bar{k}_2, \beta) = (0.5, 0.5)$, shows the substrate concentration increasing until the saturation value of $\bar{S} = \bar{S}_1$ is reached, since the meaningful existence of X_w is possible only for substrate values lower than $\bar{S}_1$.

In the next section a quantification of the stabilizing effects of wall attachment is formalized.

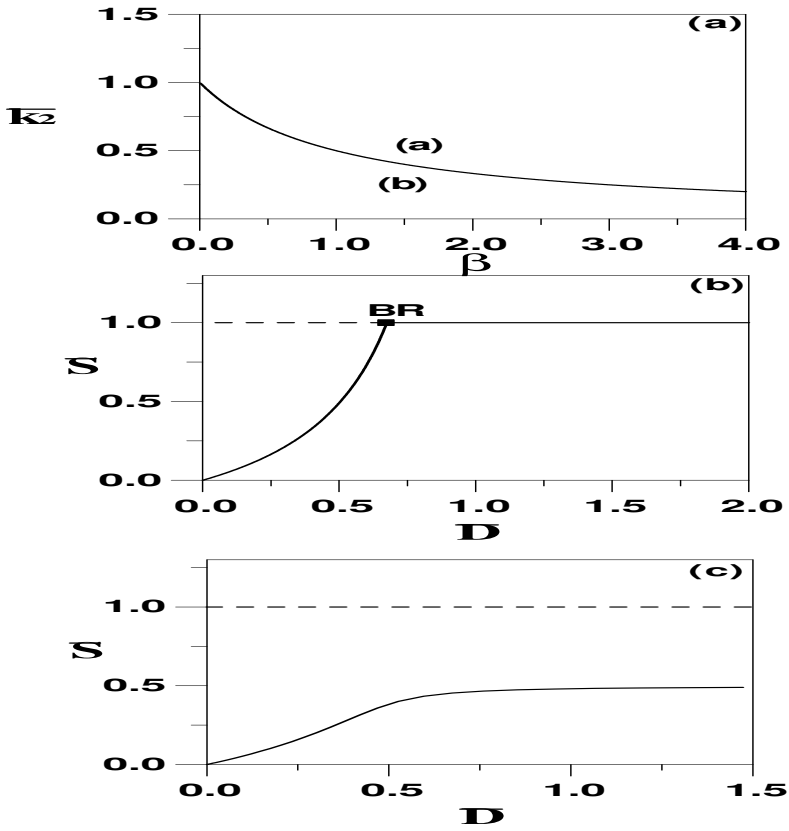

FIGURE 5.8: (a) Branch sets for the static behavior with Monod kinetics; (b) Continuity diagram for region (a); (c) Continuity diagram for region (b); solid line, stable; dashed line, unstable.

5.5 Quantification of the Stabilizing Effect of Walls Attachment

The simple homogeneous unstructured model can be recovered from the proposed model by setting $\bar{k}_1 = \bar{k}_2 = 0$ and $\bar{X}_w = 0$, to yield at steady state,

$$\bar{D}(1 - \bar{S}) - \bar{r}\bar{X} = 0 \tag{5.28}$$

$$-\bar{D}\bar{X} + \bar{r}\bar{X} = 0 \tag{5.29}$$

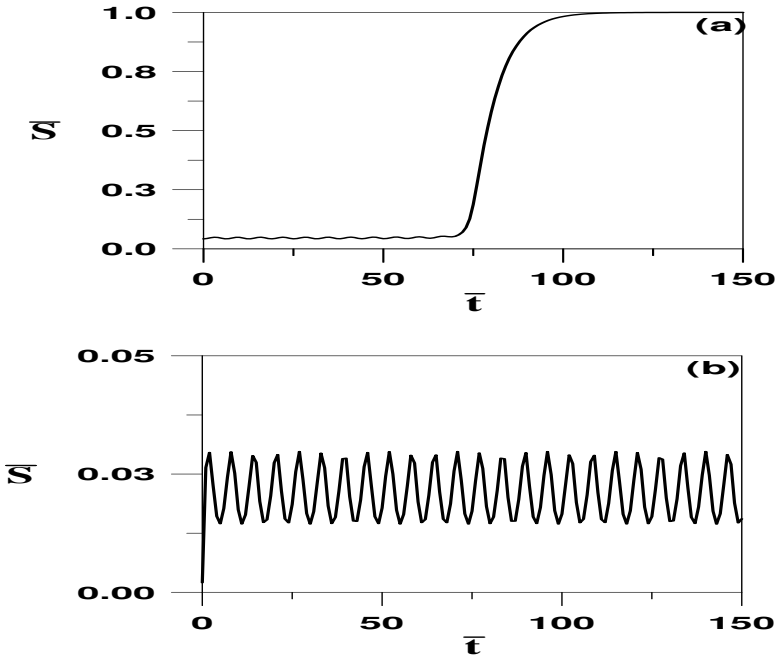

FIGURE 5.9: Stabilization of the steady-state operation by wall attachment. Simulations results for fluctuations in the dilution rate: (a) Homogeneous model; (b) Model with wall attachment.

It can be seen from Equation (5.29) that the model exhibits washout, i.e., $\bar{S} = 1$, $\bar{X} = 0$ unless

$$F(S) := \bar{r} - \bar{D} = 0 \tag{5.30}$$

Similarly to the analysis carried out for the original model, the boundary for the static behavior is defined when the condition $\bar{r}' = 0$ is satisfied at the washout line, i.e., $\bar{S} = 1$. This is also equivalent to the condition $\beta = \gamma$ (Equation (5.16)), already derived. The unstructured model exhibits therefore for $\beta < \gamma$ a behavior similar to Figure 5.2a, where an unstable steady state exists for all $\bar{D} < \bar{r}_{max}$ (Equation (5.22)), together with the stable steady state with $\bar{S} < \bar{S}_{max}$. Washout conditions occur for any dilution rate $\bar{D} > \bar{r}_{max}$. The bioreactor model also exhibits, for $\beta > \gamma$, a Monod-like behavior similar to Figure 5.4a. In this case, washout conditions occur for $\bar{D} > \bar{r}(\bar{S} = 1) = \frac{1}{\beta+1+\gamma}$.

Comparing the steady-state behavior of the proposed model to its counterpart of the homogeneous model, it can be seen that the region of stable and safe behavior extends to $\bar{r}_{max}$ for the homogeneous model, compared to $\bar{D}_{LP}$ (Equation (5.23)) for the proposed model. The difference $\bar{D}_{LP} - \bar{r}_{max}$ represents therefore the enhanced in the range of stability of the reactor as a

result of wall attachment. Recasting the expression of $\bar{D}_{LP}$ (Equation (5.23)) yields,

$$\bar{D}_{LP} - \bar{r}_{max} = \frac{\bar{k}_1 \bar{r}_{max}}{\bar{k}_2 - \bar{r}_{max}} \tag{5.31}$$

From this equation, it can be seen that the range of stability increases with the increase in $\bar{k}_1$ as a result of higher exchange rates from X to X_w. Similarly, a lower exchange rate from X_w to X would also increase the range of stability. To illustrate the improvement in the stability of the bioreactor, we consider the example treated by Villadsen [361], for the treatment of a carbon-lean waste stream consisting of chlorinated toluene. The following parameters are used for the simulations, $k_s = 10$ mg/L, $k_i = 2$ mg/L, $\mu_m = 0.2$ h^{-1}, $Y_{sx} = 0.4$ g/g, and $S_f = 100$ mg/L. The corresponding dimensionless variables are $\beta = 0.1, \gamma = 50, \bar{S}_{max} = 0.04472, \bar{r}_{max} = 0.18274$. Two stable conditions are considered:

$$\text{Condition 1}: \qquad \bar{D} = 0.18250, \bar{S} = 0.04223 \tag{5.32}$$

$$\text{Condition 2}: \qquad \bar{D} = 0.25, \bar{S} = 0.02025, \bar{k}_1 = 1, \bar{k}_2 = 1.5 \tag{5.33}$$

The first case corresponds to conditions just smaller than $\bar{r}_{max}$ while the second case correspond to dilution rate $\bar{D}$ larger than $\bar{r}_{max}$.

Figure 5.9a shows that for the homogeneous model, small fluctuations in the dilution rate $\bar{D}$ leads to washout in the first case, while with wall attachment, stable and small amplitude oscillations in $\bar{S}$ are obtained (Figure 5.9b) for large fluctuations of about 25 percent in $\bar{D}$, and for a space velocity 0.25 h^{-1} much larger than $\bar{r}_{max}$.

Another note is to be made about the stabilizing effect of wall attachment compared to that of cell recycle. A practical configuration [361] for the enrichment of the reactor medium consists in sending the effluent from the reactor to a cell separator, which divides the stream into one stream v that leaves the system with cell concentration $x_e = fx$ and one stream vR with cell concentration $x_R = \beta x$, which is returned to the reactor inlet. A simple mass balance on the reactor settler [361] yields the following steady-state mass balance for the biomass

$$-f\bar{D}\bar{X} + \bar{r}\bar{X} = 0 \tag{5.34}$$

It can be seen that the model with cell recycle exhibits washout conditions unless

$$F := -f\bar{D} + \bar{r} = 0 \tag{5.35}$$

A similar analysis to previous sections shows that the recycle does not change the shape of the steady-state portraits. The model with cell recycle would predict, for the same condition of Equation (5.16), similar static behavior to that shown in Figures (5.2a,5.4a). Washout conditions for cell recycle occur

for $\bar{D} > \frac{\bar{r}_{max}}{f}$. The increase in the stability of the homogeneous reactor due to cell recycle is therefore represented by the difference $\frac{\bar{r}_{max}}{f} - \bar{r}_{max}$. Comparing this relation to Equation (5.31), we can derive an expression for the fraction f that would yield the same enhanced stability as wall attachment,

$$\frac{1}{f} - 1 = \frac{\bar{k}_1}{\bar{k}_2 - \bar{r}_{max}} \tag{5.36}$$

or equivalently

$$f = \frac{\bar{k}_2 - \bar{r}_{max}}{\bar{k}_1 + \bar{k}_2 - \bar{r}_{max}} \tag{5.37}$$

As an example, for the values of $\bar{k}_1$, $\bar{k}_2$, and $\bar{r}_{max}$, presented in the previous section, a cell recycle with $f = 0.570$ would yield the same improved stability as cell wall attachment.

5.6 Concluding Remarks

The work in this chapter has presented a morphological perspective on the modeling and stability behavior of microbial growth and attachment to the wall of the chemostat. The analysis of the static stability has revealed that depending on the values of kinetic parameters, the proposed model can predict a variety of behavior. In summary, regions (a) and (b) of Figure 5.1 offer almost similar behavior. Both predict an increase in substrate concentration with dilution rate until washout occurs. Also both variants of biomass decrease with dilution rate. The only difference is that region (a) predicts a region of bistability with washout for some range of dilution rate. Region (c) offers a similar trend to region (b) except that the variant of biomass attached to the wall shows a maximum with dilution rate. Regions (d) and (e), on the other hand, predict a different behavior. Both regions predict an unbounded increase in the variant of the biomass attached to the wall. This occurs when the mass transfer coefficient of wall to medium approaches the specific growth rate. Both regions predict the substrate concentration to reach an asymptotic value with dilution rate. The only difference is that region (d) does not predict washout while region (e) predicts bistability between nontrivial steady state and washout, for some range of dilution rates. The analysis was also useful in quantifying the stabilizing effects of wall attachment relative to the homogeneous unstructured model with and without cell recycle.

Finally, we should point out two areas where the proposed model may be improved. The assumed first-order exchange kinetics may be substituted by more complex kinetic expressions. Also, because of the high substrate concentration in the boundary layer of the liquid near the surface, the assumption of equal growth rate for the two morphological forms may be relaxed.

This page intentionally left blank

Chapter 6

PURE AND SIMPLE MICROBIAL COMPETITION

6.1 Introduction

In this chapter, we start the study of chemostat dynamics induced by interacting species. Mixed cultures of micro-organisms, inhabiting the same environment, often interact with each other, either in a direct way, i.e., when there is contact between them or indirectly when the interactions occur as a result of an alteration in the abiotic environment. Competition for nutrients and other resources is the most common indirect interaction that occurs between microbial species inhabiting the same environment. The environment may be either a natural ecosystem or an industrial bioprocess. Bioreactors are often used for the study of microbial competition since the number and type of microbial species can be well controlled, and the system can be isolated from other interactions that may occur between the competing micro-organisms [118, 279].

According to the classification provided by Fredrickson and Stephanopoulos [113], the competition is considered to be simple when the interacting species compete for a single resource that is affecting the growth rate of all of them, and is consumed by the interacting populations. The competition is also said to be pure when microbial populations interact in no other way except the competition for a single rate-limiting nutrient. The pure and simple competition is a subject that was studied for decades both theoretically and experimentally [37, 47, 48, 67, 113, 140, 159, 221, 244, 245, 334, 346, 370]. These studies revealed parts of the richness of the dynamics of competition.

For an ideal chemostat with sterile feed and constant operating conditions, that simulates a spatially homogeneous and time-invariant environment, it is established that two competing cultures cannot coexist except at discrete values of dilution rate, when the specific growth curves of the two species cross at a positive value of the substrate concentration. However, at these values of dilution rate the system is structurally unstable [291]. The coexistence of two competing populations in a chemostat is only a theoretical outcome. Operating the bioreactor at the exactly required dilution rates is not possible, since fluctuations are always possible [334] that will eventually cause the dominance of one specie and the extinction of the other. This result is a variation of the competitive exclusion principle [142].

In this chapter, the problem of pure and simple competition in a bioreactor with cell recycle and under time-invariant feed conditions is revisited. Two objectives are sought from this chapter. The first objective is to provide a unified framework, using the singularity theory, for the analysis of static bifurcation induced in the bioreactor by the competing cultures. The second objective is to study the dynamic bifurcation. The combination of results of both static and dynamic analysis helps to draw a useful picture of the different modes of behavior induced in the bioreactor by the competing species.

6.2 Process Model

We consider a bioreactor with cell recycle similar to that of Figure 4.1. Two microbial populations (X_1) and (X_2) are growing on the substrate (S). The unsteady-state mass balances for the different species are established in the following:

Substrate S

The mass balance for substrate S is given by

$$QS_f + QRS - \frac{r_1 X_1 V}{Y_1} - \frac{r_2 X_2 V}{Y_2} = QWS + Q(1+R-W)S + V\frac{dS}{dt} \quad (6.1)$$

where r_1 and r_2 are the specific growth rates associated respectively with X_1 and X_2. Equation (6.1) yields

$$S_f - S - \theta\left(\frac{r_1 X_1}{Y_1} + \frac{r_2 X_2}{Y_2}\right) = \theta\frac{dS}{dt} \quad (6.2)$$

where $\theta = \frac{V}{Q}$ is the reactor residence time (i.e., inverse of dilution rate).

Biomass X_1

The mass balance for X_1 is given by

$$QX_{f_1} + RQX_{R1} + r_1 X_1 V = Q(1+R)X_1 + V\frac{dX_1}{dt} \quad (6.3)$$

Ideal conditions in the settler allow the following simple relation between the exit biomass X_1 and the recycle biomass X_{R1} concentrations,

$$X_{R1} = X_1\left(\frac{1+R-W}{R}\right) \quad (6.4)$$

Substituting in Equation (6.3) for the recycle biomass concentrations yields,

$$X_{f_1} - WX_1 + \theta r_1 X_1 = \theta \frac{dX_1}{dt} \tag{6.5}$$

Biomass X_2

The mass balance for the biomass of X_2 is similar to Equation (6.5)

$$X_{f_2} - WX_2 + \theta r_2 X_2 = \theta \frac{dX_2}{dt} \tag{6.6}$$

The two competing cultures X_1 and X_2 are assumed to grow on substrate S following Haldane inhibition growth rates

$$r_j = \frac{\mu_j S}{K_j + S + S^2/K_{Ij}} \quad \text{j} = 1, 2 \tag{6.7}$$

The mass balances are suitably rendered dimensionless using the variables shown in Table 6.1. The dimensionless model is, therefore,

$$\bar{S}_f - \bar{S} - \bar{\theta}(\bar{r}_1 \bar{X}_1 + \eta \bar{r}_2 \bar{X}_2) = \frac{d\bar{S}}{d\bar{t}} \tag{6.8}$$

$$\bar{X}_{f_1} - W\bar{X}_1 + \bar{\theta}\bar{r}_1 \bar{X}_1 = \frac{d\bar{X}_1}{d\bar{t}} \tag{6.9}$$

$$\bar{X}_{f_2} - W\bar{X}_2 + \bar{\theta}\bar{r}_2 \bar{X}_2 = \frac{d\bar{X}_2}{d\bar{t}} \tag{6.10}$$

The dimensionless expressions of the specific growth rates are given, on the other hand, by

$$\bar{r}_1 = \frac{\bar{S}}{1 + \bar{S} + \gamma_1 \bar{S}^2} \text{ and } \bar{r}_2 = \frac{\phi \bar{S}}{\alpha + \bar{S} + \gamma_2 \bar{S}^2} \tag{6.11}$$

The steady-state equations are obtained by setting the right-hand sides of Equations (6.8–6.10) to zero. Equations (6.9-6.10), in particular, would yield,

$$\bar{X}_1 = \frac{\bar{X}_{f_1}}{W - \bar{r}_1 \bar{\theta}} \quad \text{and} \quad \bar{X}_2 = \frac{\bar{X}_{f_2}}{W - \bar{r}_2 \bar{\theta}} \tag{6.12}$$

By introducing Equations (6.12) into the steady-state form of Equation (6.8), an algebraic equation is obtained for $\bar{S}$,

$$F(\bar{S}) := \bar{S}_f - \bar{S} - \bar{\theta}\left(\frac{\bar{r}_1 \bar{X}_{f_1}}{W - \bar{r}_1 \bar{\theta}} + \eta \frac{\bar{r}_2 \bar{X}_{f_2}}{W - \bar{r}_2 \bar{\theta}}\right) \tag{6.13}$$

TABLE 6.1: Definition of dimensionless variables

Parameter	Definition
θ	$\mu_1\theta$
$\bar{S}$	$\frac{S}{K_1}$
$\bar{t}$	$\frac{t}{\theta}$
$\bar{X}_1$	$\frac{X_1}{Y_1K_1}$
$\bar{X}_2$	$\frac{X_2}{Y_2K_1}$
α	$\frac{K_2}{K_1}$
γ_1	$\frac{K_1}{K_{I1}}$
γ_2	$\frac{K_1}{K_{I2}}$
η	$\frac{Y_1}{Y_2}$
ϕ	$\frac{\mu_2}{\mu_1}$

TABLE 6.2: Coefficients of the polynomial (Equation (6.14))

a_0	$\alpha\bar{S}_f W^2$
a_1	$-\bar{\theta}W\bar{S}_f(\alpha+\phi) - \bar{\theta}W(\alpha\bar{X}_{f_1} + \eta\phi\bar{X}_{f_2}) + W^2(\alpha\bar{S}_f + \bar{S}_f - \alpha)$
a_2	$\phi\bar{S}_f\bar{\theta}^2 + \bar{\theta}W(\alpha+\phi-\bar{S}_f-\phi\bar{S}_f) + W^2(\gamma_2\bar{S}_f + \alpha\gamma_1\bar{S}_f + \bar{S}_f - \alpha - 1)$ $+\phi\bar{\theta}^2(\bar{X}_{f_1} + \eta\bar{X}_{f_2}) - \bar{\theta}W(\bar{X}_{f_1} + \eta\phi\bar{X}_{f_2})$
a_3	$-\phi\bar{\theta}^2 + \bar{\theta}W(1+\phi) - \bar{\theta}W\bar{S}_f(\gamma_2+\phi\gamma_1) - \bar{\theta}W(\gamma_2\bar{X}_{f_1} + \gamma_1\eta\phi\bar{X}_{f_2})$ $+W^2(-\gamma_2 + \gamma_1\bar{S}_f + \gamma_2\bar{S}_f - \alpha\gamma_1 - 1)$
a_4	$\bar{\theta}W(\gamma_2+\phi\gamma_1) - W^2(\gamma_1+\gamma_2) + \gamma_1\gamma_2\bar{S}_f W^2$
a_5	$-\gamma_1\gamma_2 W^2$

Substituting in Equation (6.13) for the expressions of $\bar{r}_1$ and $\bar{r}_2$ (Equation (6.11)), a single fifth-order polynomial is obtained for the substrate concentration $\bar{S}$,

$$F(\bar{S}) := a_5\bar{S}^5 + a_4\bar{S}^4 + a_3\bar{S}^3 + a_2\bar{S}^2 + a_1\bar{S} + a_0 = 0 \tag{6.14}$$

The coefficients a_i are listed in Table 6.2. The residence time appearing explicitly in the coefficients of Equation (6.14) is selected to be the bifurcation parameter. The steady-state Equation (6.14) is of the fifth order in $\bar{S}$, so for a given value of $\bar{\theta}$, a maximum of five steady-state solutions are possible.

6.3 Static Bifurcation for Substrate Inhibition

6.3.1 Hysteresis Singularity

The conditions for the appearance/disappearance of a hysteresis loop are

$$F = F_{\bar{S}} = F_{\bar{S}\bar{S}} = 0 \tag{6.15}$$

In addition, a number of other derivatives must remain nonzero, namely $F_{\bar{\theta}}$, $F_{\bar{S}\bar{\theta}}$, and $F_{\bar{S}\bar{S}\bar{S}}$.

TABLE 6.3: Nominal parameters

Parameter	Value
α	1.063995
γ_1	0.059918
γ_2	0.103665
η	1.137778
ϕ	1.122631
$\bar{S}_f$	6
$\bar{X}_{f\,1}$	0.001
$\bar{X}_{f\,2}$	0.001
W	0.1

Before we establish these boundaries, a simple analysis can be carried out to determine the conditions for the first derivative $F_{\bar{S}}$ to vanish, since it is also a requirement for the existence of a static limit point (SLP). Using the expression of F in Equation (6.13), it can be seen that the first derivative $F_{\bar{S}}$ is such that

$$-F_{\bar{S}} = 1 + \bar{\theta} W \bar{X}_{f\,1} \frac{\bar{r}_1'}{(W - \bar{r}_1\bar{\theta})^2} + \bar{\theta} W \eta \bar{X}_{f\,2} \frac{\bar{r}_2'}{(W - \bar{r}_2\bar{\theta})^2} \tag{6.16}$$

where $\bar{r}_i'(i = 1, 2)$ are the first derivatives of $\bar{r}_i$. It can be seen from Equation (6.16) that for the condition $F_{\bar{S}} = 0$ to be satisfied, it is necessary that either $\bar{r}_1'$ or $\bar{r}_2'$ are negatives. Recalling that

$$\bar{r}_1' = \frac{1 - \gamma_1 \bar{S}^2}{(1 + \bar{S} + \gamma_1 \bar{S}^2)^2} \quad \text{and} \quad \bar{r}_2' = \frac{\phi(\alpha - \gamma_2 \bar{S}^2)}{(\alpha + \bar{S} + \gamma_2 \bar{S}^2)^2} \tag{6.17}$$

Necessary conditions for the occurrence of static limit points are then

$$\frac{1}{\gamma_1} \leq \bar{S}^2 \quad \text{or} \quad \frac{\alpha}{\gamma_2} \leq \bar{S}^2 \tag{6.18}$$

Since $\bar{S}$ is always bounded by the feed condition $\bar{S}_f$, it is necessary then to have

$$\gamma_1 \bar{S}_f^2 \geq 1 \quad \text{or} \quad \frac{\gamma_2}{\alpha} \bar{S}_f^2 \geq 1 \tag{6.19}$$

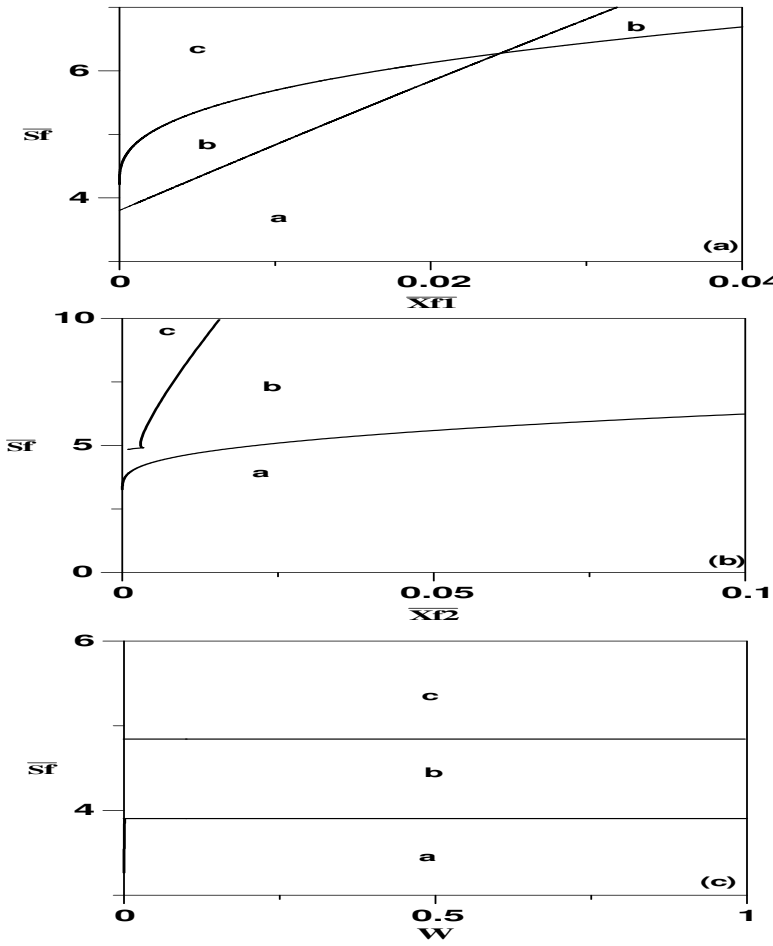

FIGURE 6.1: Branch sets (a)–(c) for the hysteresis singularity.

With these conditions established, the set of nonlinear Equations (6.15) can be solved to determine the limits of the hysteresis region. The simulations are carried out using the kinetic and operating parameters shown in Table 6.3. Figures 6.1(a–c) show the hysteresis boundaries in the parameter spaces $(\bar{S}_f, \bar{X}_{f_1})$ $(\bar{S}_f, \bar{X}_{f_2})$, and $(\bar{S}_f, W)$. The conditions $F_{\bar{\theta}}$, $F_{\bar{S}\theta}$, and $F_{\bar{S}\bar{S}\bar{S}}$ were evaluated numerically along the hysteresis surface and no point was found to violate the conditions. When crossing the boundaries in Figures 6.1(a–c), the number of static limit points in the bifurcation diagrams increase/decrease by two. The boundaries in Figure 6.1a, for instance, divide the parameter space in three regions. Region (a) is characterized, for any combinations of $(\bar{S}_f, \bar{X}_{f_1})$, by the absence of static limit points, i.e., a unique steady-state solution. The expected behavior in this region is shown in the continuity diagram of Figure

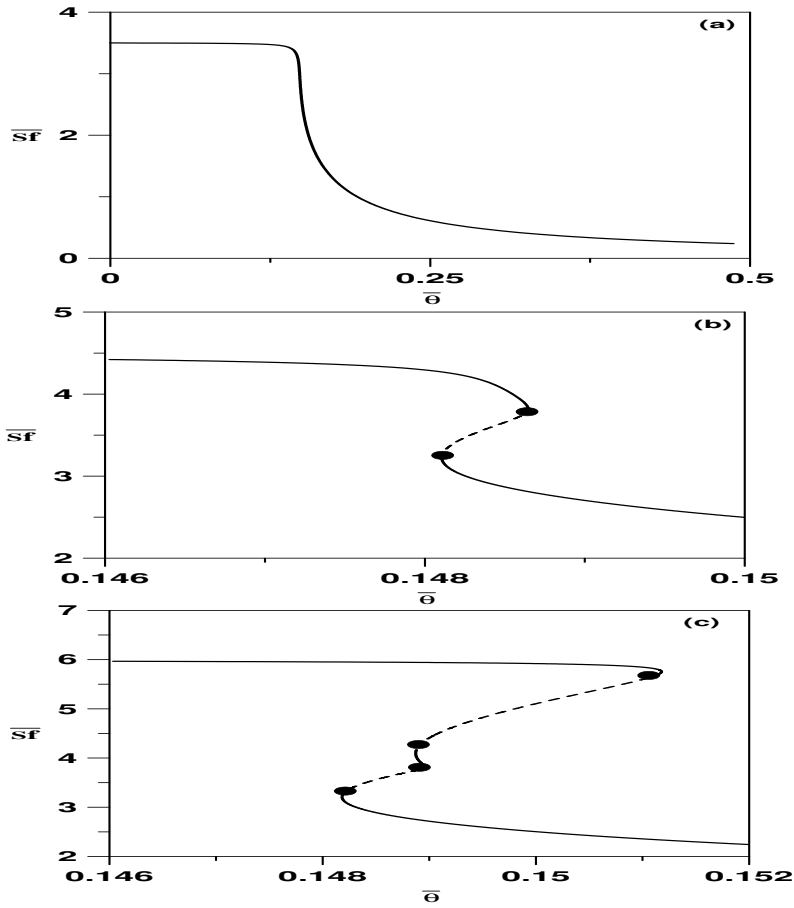

FIGURE 6.2: Continuity diagrams (a)–(c) for the different regions of Figure 6.1; solid line, stable branch; dashed line unstable; circle, static limit point.

6.2a, obtained, for example, with $(\bar{S}_f, \bar{X}_{f_1}) = (3.5, 0.003)$. When crossing the boundary separating regions (a) and (b), two static limit points are born. A hysteresis characterizes the nature of the model in region (b). Figure 6.2b shows an example of the behavior in this region, obtained with $(\bar{S}_f, \bar{X}_{f_1}) = (4.5, 0.003)$. Region (c), on the other hand, is characterized by the presence of four limit points, since two extra SLP are born when crossing the boundary between regions (b) and (c). A maximum of five steady-state solutions are expected in this region, as it can be seen in the continuity diagram of Figure 6.2c obtained with $(\bar{S}_f, \bar{X}_{f_1}) = (5.6, 0.001)$. In addition to stable low and high conversions branches, a third stable branch exists in the middle. The same three modes of behavior are found in the parameter space $(\bar{S}_f, \bar{X}_{f_2})$ (Figure 6.1b). The effect of the purge fraction, on the other hand, can be seen

in Figure 6.1c. It can be seen that when the other operating parameters are invariant, a change in the purge fraction has no effect on the static behavior of the bioreactor.

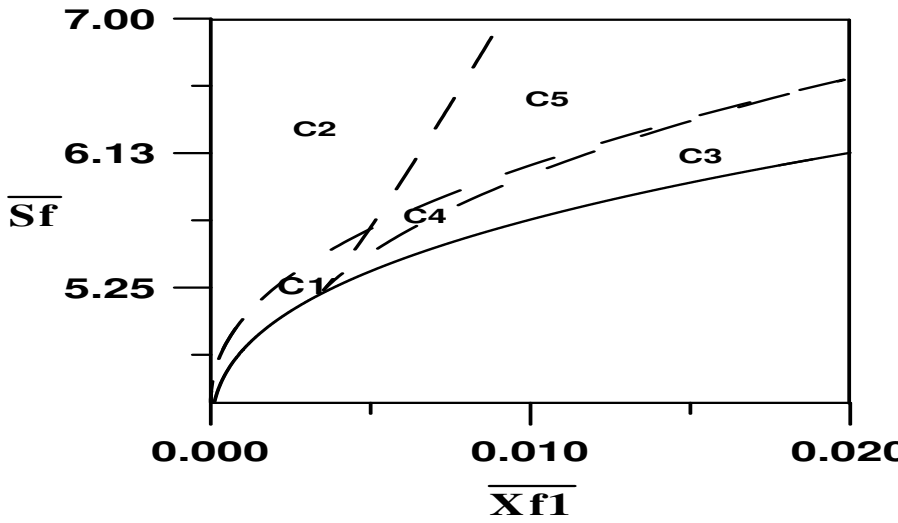

FIGURE 6.3: Branch sets for the double limit singularity; solid line, boundaries for the hysteresis singularity with four static limit points; dashed line, boundaries for the double limit singularity.

6.3.2 Double Limit Singularity

The existence of four static limit points in the model is an indication of potential richness, since the relative location of the limit points can change in the bifurcation diagram. A typical example of this behavior is provided by the double limit singularity when the number of static limit points does not change but their relative positions do. This singularity is defined by the following relations

$$F(\bar{S}_1) = F(\bar{S}_2) = 0 \tag{6.20}$$

and

$$F_{\bar{S}}(\bar{S}_1) = F_{\bar{S}}(\bar{S}_2) = 0 \tag{6.21}$$

with

$$\bar{S}_1 \neq \bar{S}_2 \tag{6.22}$$

These relations require that two distinct points $\bar{S}_1$ and $\bar{S}_2$ satisfy the steady

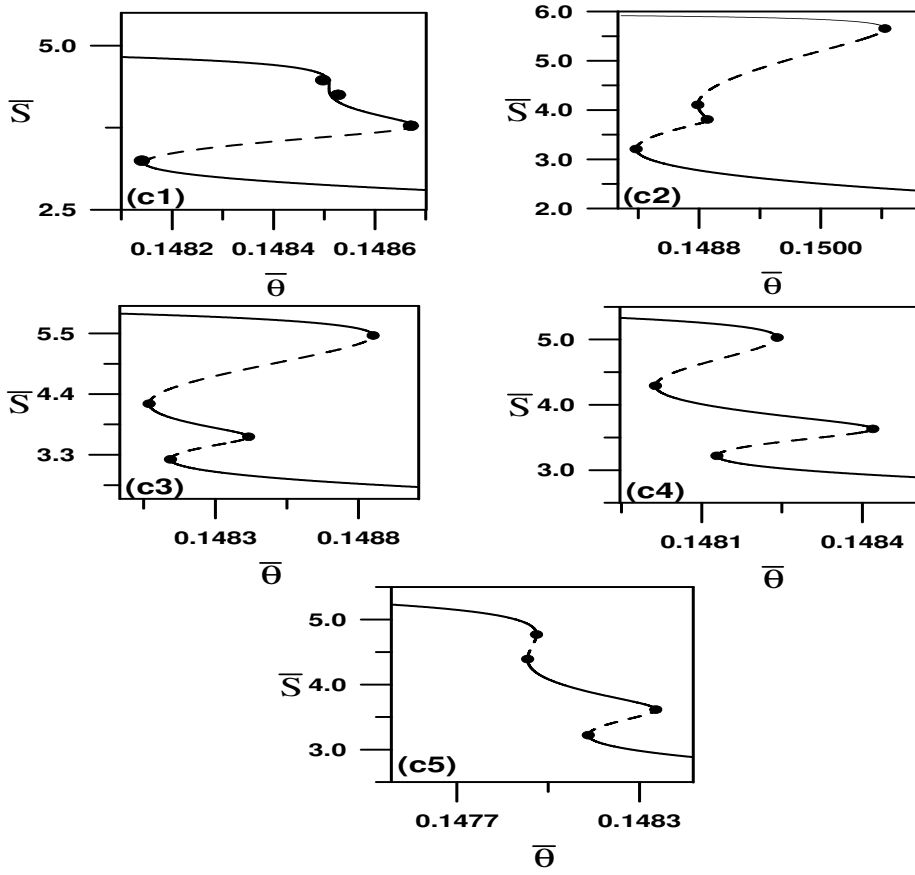

FIGURE 6.4: Continuity diagrams (c_1–c_5) for the different regions of Figure 6.3.

state and also limit point conditions. Figure 6.3 shows the boundaries of the double limit singularity in the parameter space $(\bar{S}_f, \bar{X}_{f_1})$. The region of four static limit points (region (c) in Figure 6.1) can be in fact divided in five different subregions. Figures 6.4(c_1–c_5) show the various expected behaviors. All these regions predict five steady-state solutions in a small or large range of residence time, except region c_5 (Figure 6.4c_5), where the maximum number of steady-state solutions at any residence time is three.

6.3.3 Isola and Mushroom

The requirements for the existence of isola or mushroom are:

$$F = F_{\bar{S}} = F_{\bar{\theta}} = 0 \tag{6.23}$$

with the additional requirements that

$$F_{\bar{S}\bar{\theta}} \neq 0, F_{\bar{S}\bar{S}} \neq 0, F_{\bar{\theta}\bar{\theta}} \neq 0 \tag{6.24}$$

Taking the derivative of F (Equation (6.13)) with respect to $\bar{\theta}$ yields

$$-F_{\bar{\theta}} = \frac{\bar{r}_1 \bar{X}_{f_1} W}{(W - \bar{r}_1\bar{\theta})^2} + \frac{\bar{r}_2 \bar{X}_{f_2} W}{(W - \bar{r}_2\bar{\theta})^2} \tag{6.25}$$

Since all the terms involved in this equation are positive, the requirement that $F_{\bar{\theta}} = 0$ implies necessarily that either one of the following conditions are satisfied,

$$\bar{r}_1 = 0 \quad \text{and} \quad \bar{r}_2 = 0 \tag{6.26}$$

or

$$\bar{X}_{f_1} = 0 \text{ and } \bar{X}_{f_2} = 0 \tag{6.27}$$

The first conditions are satisfied for the case of $\bar{S} = 0$ while the second conditions correspond to clean feed conditions. But both of these conditions would violate the requirement that $F_{\bar{\theta}\bar{\theta}} \neq 0$ since

$$F_{\bar{\theta}\bar{\theta}} = \frac{2\bar{X}_{f_1} \bar{r}_1^2 W}{(W - \bar{r}_1\bar{\theta})^3} + \frac{2\bar{X}_{f_2} \bar{r}_2^2 W}{(W - \bar{r}_1\bar{\theta})^3} \tag{6.28}$$

vanishes exactly at these conditions. The model cannot therefore exhibit an isola or mushroom singularity.

6.3.4 Pitchfork Singularity

The conditions for the pitchfork are

$$F = F_{\bar{S}} = F_{\bar{\theta}} = F_{\bar{S}\bar{S}} = 0 \tag{6.29}$$

and

$$F_{\bar{S}\bar{\theta}} \neq 0, F_{\bar{S}\bar{S}\bar{S}} \neq 0 \tag{6.30}$$

Since the conditions for the existence of a pitchfork include the condition $F_{\bar{\theta}} = 0$ as in the case of isola and mushroom, it is clear that the only possible cases where the system can predict a pitchfork are those of conditions (Equations (6.26–6.27)). For the case $\bar{S} = 0$, the first derivatives of the rates, (Equation (6.17)), are $r_1' = 1$ and $r_2' = \phi$. Since both of these terms are positive, the condition $F_{\bar{S}} = 0$ cannot be satisfied. Moreover, the derivative with respect to $\bar{S}$ of $F_{\bar{\theta}}$ (Equation (6.25)) yields

$$-F_{\bar{S}\bar{\theta}} = W\bar{X}_{f_1}\left[\frac{\bar{r}_1}{(W - \bar{r}_1\bar{\theta})^2}\right]' + W\bar{X}_{f_2}\left[\frac{\bar{r}_2 W}{(W - \bar{r}_2\bar{\theta})^2}\right]' \tag{6.31}$$

It is clear that the condition $F_{\bar{S}\bar{\theta}} \neq 0$ is violated at clean feed conditions. The model cannot therefore exhibit codimension two singularity or a higher one. In the next section we carry out an investigation of the dynamic bifurcation of the model.

6.4 Existence of Periodic Solutions

The conditions for the occurrence of Hopf points are (Equations (3.38–3.39))

$$F_1 := S_1 S_2 - S_3 = 0 \tag{6.32}$$

$$S_2 > 0 \tag{6.33}$$

The elements of the Jacobian matrix are given explicitly by taking the derivatives of Equations (6.8–6.10), yielding

$$j_{11} = -1 - \bar{\theta}(\bar{X}_1 \bar{r}_1' + \eta \bar{X}_2 \bar{r}_2'), \quad j_{12} = -\bar{\theta}\bar{r}_1, \quad j_{13} = -\bar{\theta}\eta\bar{r}_2$$

$$j_{21} = \bar{\theta}\bar{X}_1 \bar{r}_1', \quad j_{22} = -W + \bar{r}_1\bar{\theta}, \quad j_{23} = 0$$

$$j_{31} = \bar{\theta}\bar{X}_2 \bar{r}_2', \quad j_{32} = 0, \quad j_{33} = -W + \bar{r}_2\bar{\theta} \tag{6.34}$$

The first derivatives of $\bar{r}_i$ are given by Equation (6.17). The F_1 degeneracy, is defined by solving the steady-state equation ($F = 0$) (Equation (6.14)), the Hopf condition (Equation (6.32)), and the condition ($S_2 = 0$). Figures 6.5(a–c) show the static and dynamic bifurcation diagrams in the parameter space $(\bar{S}_f, \bar{X}_{f_1})$, $(\bar{S}_f, \bar{X}_{f_2})$, and $(\bar{S}_f, W)$. The boundaries of the double variety singularity are omitted from the analysis since they do not change the nature of the dynamic bifurcation of the model. When crossing the boundaries for the F_1 curve (indicated by a dashed line), the number of Hopf points in the continuity diagrams increases/decreases by one. Moreover, it can be seen that the Hopf boundary and one of the boundaries of the hysteresis surface intersect. This adds interesting features, as five different regions can be depicted in the model. Regions (a),(b), and (c) are unchanged. They are characterized respectively by no static limit point (SLP) or Hopf point (HB), two SLPs and no HB and four SLPs with no HB. Region (d) is characterized, on the other hand, by the presence in this order of a Hopf point and two static limit points. Figure 6.6a shows an example of the continuity diagram for this region, obtained with $(\bar{S}_f, \bar{X}_{f_1}) = (4.4, 0.0002)$. Figure 6.6b shows, on the other hand, an example of the behavior expected in region (e), obtained with $(\bar{S}_f, \bar{X}_{f_1}) = (5.6, 0.001)$. The model is characterized by the presence in this order of two static limit points, one Hopf point and two static limit points. In both regions (d) and (e), periodic branches (enlarged in Figures 6.6(a–b)) emanate from the HB and terminate as they collide with the static branches. Moreover, the location of the periodic branch between static branches introduces bistability where oscillations coexist with the high and low conversion static branches. Figures 6.7(a–c) show time traces for the dilution rate of 6.71077 and three sets of initial conditions.

The same five modes of behavior can be seen in Figure 6.5b showing the effect of the other biomass feed ($\bar{X}_{f_2}$). As for the effect of purge fraction shown

in Figure 6.5c, it can be seen that only four modes of behavior exist. Mode (e) exists but at physically unrealistic values of the purge fraction, i.e., $W > 1$. Moreover, contrary to the static case, the Hopf boundary increases with the purge fraction, and hence a change in the purge fraction has effects on the dynamic behavior of the system. Following changes in the purge fraction, the behavior of the bioreactor can move from region (b) to region (d) characterized by the presence of oscillations. The existence of oscillatory behavior in the model is due to the presence of inhibitory kinetics. In the following section, we show that Monod kinetics can not produce this behavior.

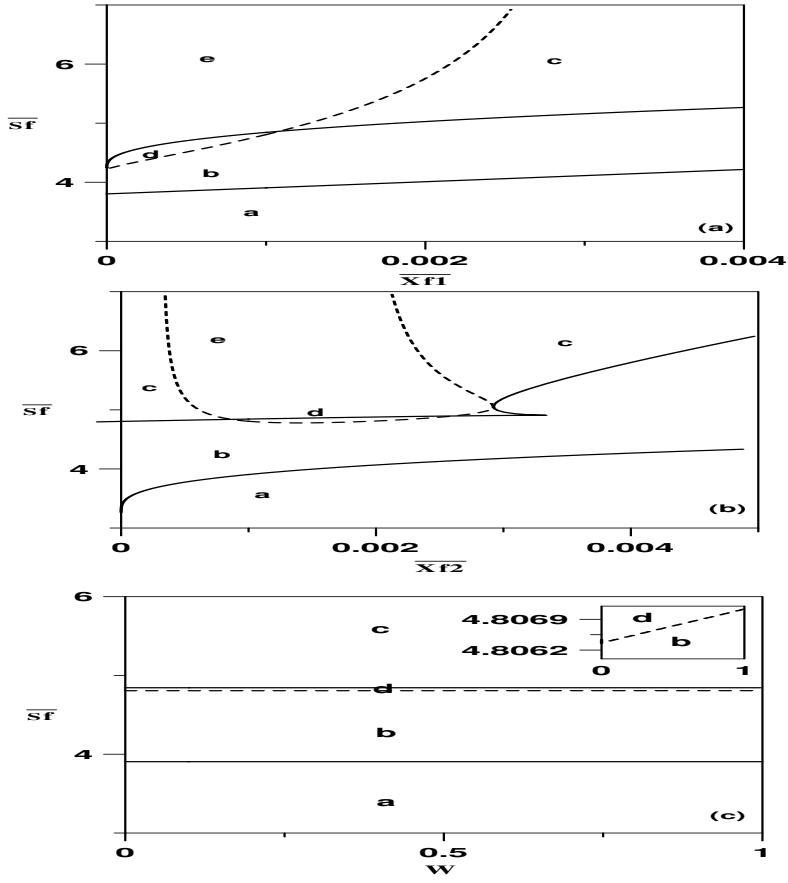

FIGURE 6.5: Static and dynamic branch sets (a)–(c) for the model; solid line, hysteresis curve; dashed line, Hopf bifurcation curve.

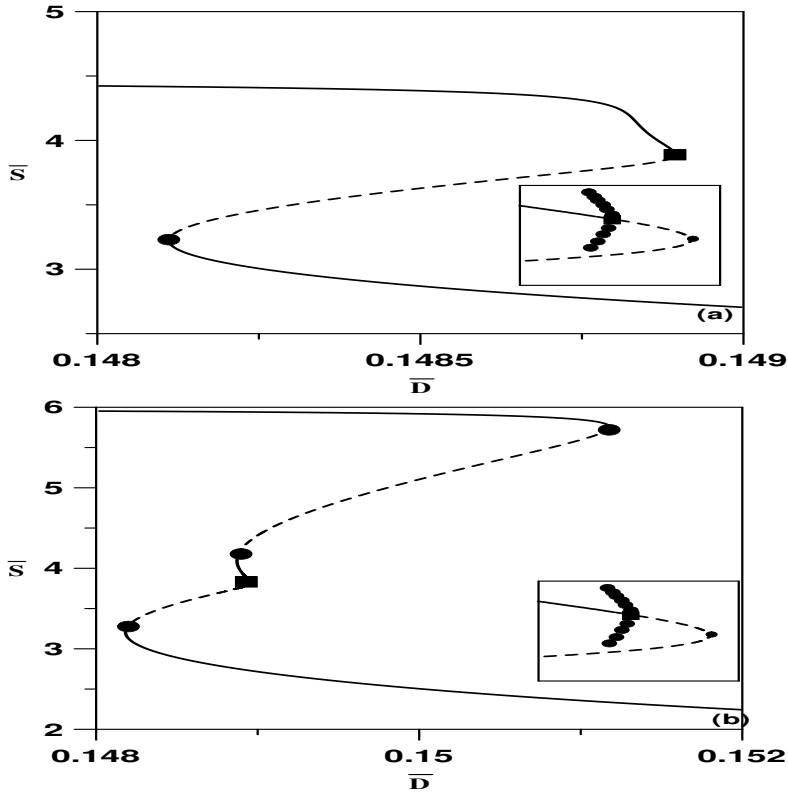

FIGURE 6.6: Continuity diagrams (a)–(b) for regions (d-e) of Figures 6.5; solid line, stable branch; dashed line, unstable; circle, static limit point; square, Hopf point; bold line, periodic branch.

6.5 Monod Kinetics Model

As the dimensionless inhibition constants γ_1 and γ_2 go to zero, the specific growth rates (Equation (6.11)) become

$$\bar{r}_1 = \frac{\bar{S}}{1+\bar{S}} \text{ and } \bar{r}_2 = \frac{\phi\bar{S}}{\alpha+\bar{S}} \tag{6.35}$$

Recasting the expression of $F_{\bar{S}}$ (Equation (6.16)) yields

$$-F_{\bar{S}} = +1 + \bar{\theta}^2\bar{X}_{f\,1}\frac{\bar{r}_1'}{(W-\bar{r}_1\bar{\theta})^2} + \eta\bar{\theta}^2\bar{X}_{f\,2}\frac{\bar{r}_2'}{(W-\bar{r}_2\bar{\theta})^2} \tag{6.36}$$

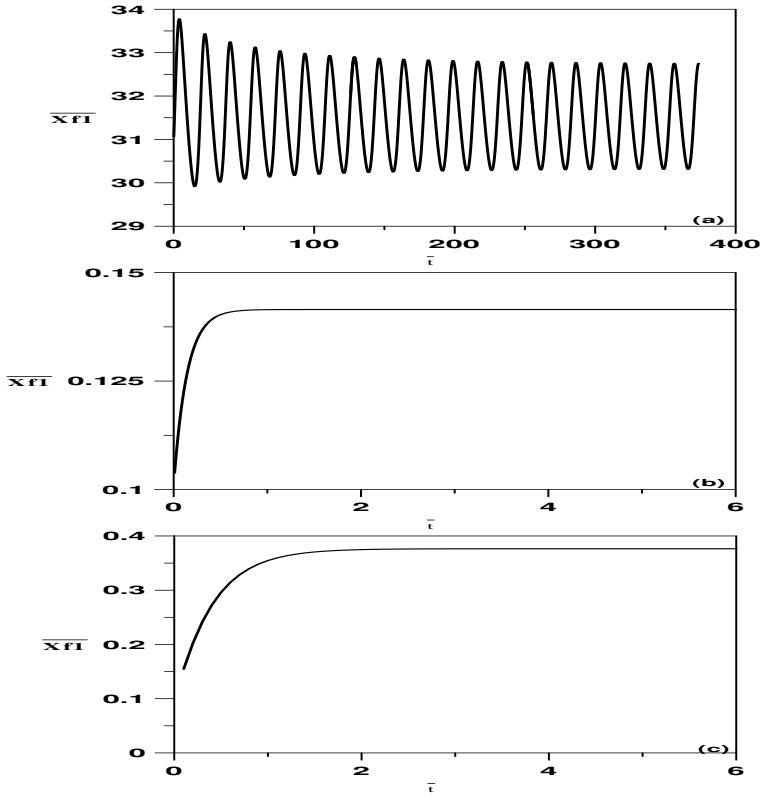

FIGURE 6.7: Time traces showing bistability: (a) Period oscillations obtained with initial conditions $(\bar{S}, \bar{X}_{f_1}, \bar{X}_{f_2}, W) = (3, 31, 9, 0.1)$; (b) Low conversion attractor obtained with initial conditions $(1, 0.1, 0.1, 0.1)$; (c) High conversion attractor obtained with initial conditions $(1, 0.1, 50, 0.1)$.

with

$$\bar{r}'_1 = \frac{1}{(1+\bar{S})^2} \text{ and } \bar{r}'_2 = \frac{\phi\alpha}{(\alpha+\bar{S})^2} \tag{6.37}$$

These two elements are positive, hence all the terms in $F_{\bar{S}}$ are positive. The condition $F_{\bar{S}} = 0$ is thus never satisfied and the model always predicts a unique static solution.

6.5.1 Periodic Solutions for Monod Kinetics

In this section we investigate if Monod kinetics alone are capable of producing an oscillatory behavior in the model. It can be noted that at stationary points,

the two components j_{22} and j_{33} (Equation (6.34)) are equal to

$$j_{22} = -\frac{\bar{X}_{f1}}{\bar{X}_1}, \quad j_{33} = -\frac{\bar{X}_{f1}}{\bar{X}_2} \tag{6.38}$$

with

$$j_{11} = -(j_{22} + w), \quad j_{13} = -\eta(j_{33} + w) \tag{6.39}$$

The term $F_1 := (S_1S_2 - S_3)$ can be obtained analytically,

$$\begin{aligned} -F_1 &= w(j_{21} + \eta j_{31})^2 + (j_{21} + \eta j_{31})(w + \frac{2\bar{X}_{f1}\bar{X}_{f2}}{\bar{X}_1\bar{X}_2}) + (\frac{\bar{X}_{f1}}{\bar{X}_1} + \frac{\bar{X}_{f2}}{\bar{X}_2})^2 \\ &+(w+1)(\frac{\bar{X}_{f1}}{\bar{X}_1}j_{21} + \frac{\bar{X}_{f2}}{\bar{X}_2}j_{31}\eta) + \frac{\bar{X}_{f1}}{\bar{X}_1}(1 + 2j_{31}\eta + j_{31}^2\eta^2 + j_{31}\eta\frac{\bar{X}_{f1}}{\bar{X}_1}) \\ &+\frac{\bar{X}_{f2}}{\bar{X}_2}(1 + 2j_{21} + j_{21}^2 + j_{21}\frac{\bar{X}_{f2}}{\bar{X}_2}) + (j_{21}j_{31}\eta + \frac{\bar{X}_{f1}\bar{X}_{f1}}{\bar{X}_1\bar{X}_2})(\frac{\bar{X}_{f1}}{\bar{X}_1} + \frac{\bar{X}_{f2}}{\bar{X}_2}) \end{aligned} \tag{6.40}$$

It can be seen that $-F_1$ is composed only of positive terms and cannot vanish. The terms j_{21} and j_{31} are, on the other hand, positive since the first derivative of the growth rates $\bar{r}_1$ and $\bar{r}_2$ for Monod kinetics are always positive. As it can be noted from this analysis, the results obtained are more general than the assumption of Monod kinetics. The model can not produce any oscillatory behavior if the first derivatives of both growth rates are positive.

6.6 Case of Sterile Feed

When $\bar{X}_{f1} = \bar{X}_{f2} = 0$ Equation (6.12) predicts two solutions. A trivial one, i.e., $\bar{X}_1 = \bar{X}_2 = 0$ that corresponds to washout conditions $\bar{S} = \bar{S}_f$, and nontrivial solutions if either one of the following conditions are satisfied

$$\bar{r}_1 = \frac{W}{\bar{\theta}} \quad \text{or} \quad \bar{r}_2 = \frac{W}{\bar{\theta}} \tag{6.41}$$

Should the first condition alone be satisfied, this would correspond to $\bar{X}_1 \neq 0$ and similarly for the second condition. Should, on the other hand, the two conditions be simultaneously satisfied then a coexistence of the two cultures is expected. The two species coexist therefore when the growth rates $\bar{r}_1$ and $\bar{r}_2$ cross. The bifurcation diagrams depend on the relative positioning of the two growth rates. The number of configurations resulting from these crossings can be quite large. The static behavior for clean feed conditions will be re-examined in detail in a later chapter for the interesting case of competition between plasmid-bearing, plasmid-free recombinant DNA cultures.

6.6.1 Periodic Solutions for Sterile Feed Conditions

In this section we investigate the existence of periodic solutions for the case of clean feed conditions.

$$(a)(\bar{X}_1 = 0, \bar{X}_2 \neq 0), \quad (b)(\bar{X}_1 \neq 0, \bar{X}_2 = 0), \quad (c)(\bar{X}_1 \neq 0, \bar{X}_2 \neq 0) \tag{6.42}$$

The first case corresponds necessarily to $W - \bar{r}_1\bar{\theta} \neq 0$ and $W - \bar{r}_2\bar{\theta} = 0$. The Jacobian matrix (Equation (6.34)) is reduced to

$$J = \begin{bmatrix} j_{11} & j_{12} & j_{13} \\ 0 & j_{22} & 0 \\ j_{31} & 0 & 0 \end{bmatrix} \tag{6.43}$$

It is easy to check that the eigenvalues λ of the Jacobian matrix satisfies

$$(j_{22} - \lambda)(\lambda^2 - \lambda j_{11} - j_{13}j_{31}) = 0 \tag{6.44}$$

The first egienvalue $\lambda = j_{22}$ is real. For the quadratic equation to have pure imaginary eigenvalues it is necessary to have,

$$j_{11} = 0 \ \text{ and } \ j_{13}j_{31} < 0 \tag{6.45}$$

However, since $\bar{X}_1 = 0$, Equation (6.34) yields $j_{11} = -1 - \eta j_{31}$. Therefore, $j_{31} = \frac{-1}{\eta}$ and the product $j_{13}j_{31}$ is equal to $-\theta\eta r_2 \frac{-1}{\eta} = \theta r_2$, which is always positive. This violates the condition of Equation (6.45). Therefore, no Hopf point can be expected in the model. A similar analysis can be carried out for the case of $(\bar{X}_1 \neq 0, \bar{X}_2 = 0)$.

The third, theoretical, solution corresponds to condition (c) of Equation (6.42), which is also equivalent to

$$-W + \bar{r}_1\bar{\theta} = 0 \ \text{ and } \ -W + \bar{r}_2\bar{\theta} = 0 \tag{6.46}$$

The Jacobian matrix in this case is reduced to

$$J = \begin{bmatrix} j_{11} & j_{12} & j_{13} \\ j_{21} & 0 & 0 \\ j_{31} & 0 & 0 \end{bmatrix} \tag{6.47}$$

The eigenvalues λ satisfy

$$\lambda = 0 \ \text{ or } \ (\lambda^2 - \lambda j_{11} - j_{21}j_{12} - j_{31}j_{13}) = 0 \tag{6.48}$$

For the quadratic equation to have pure nonzero imaginary eigenvalues, it is necessary to have,

$$j_{11} = 0 \ \text{ and } \ j_{21}j_{12} + j_{31}j_{13} < 0 \tag{6.49}$$

But it can be noted using Equations (6.34, 6.46) that $j_{12} = -W$ and

$j_{13} = -\eta W$. The condition of Equation (6.49) is equivalent to $j_{21} + \eta j_{31} > 0$. However, it can be seen from Equation (6.34) that $j_{11} = -1 - j_{21} - \eta j_{31}$. Since $j_{11} = 0$, this results in $j_{21} + \eta j_{31} = -1$, which results in a contradiction.

The analysis in this section was carried out without reference to the explicit expression of the growth expressions. We conclude therefore that the model can not exhibit periodic behavior for the case of clean feed conditions regardless of the selected growth rates.

6.7 Concluding Remarks

The classical problem of pure and simple competition has been revisited using the singularity theory. The investigation has added more information on the previously known dynamics. Specifically, the analysis of static bifurcation for nonsterile feed and substrate inhibition kinetics has shown that the model can exhibit a maximum of five steady-state solutions. The analysis of dynamic bifurcation has revealed that the two competing cultures can coexist in a state of limit cycle for a wide range of parameters. However, these self-sustained oscillations are not orbitally stable and any variations in the feed conditions can annihilate them and bring the system to a stable steady state. The effect of substrate feed, biomass feed, and purge fraction on the relative location of point attractors and limit cycles was studied. While the purge fraction has no effect on the static behavior of the model, it can affect the existence of oscillatory behavior. The general treatment offered by the theory was used to recover the stability characteristics with Monod kinetics. An analysis of the conditions for the existence of oscillations has revealed that inhibitory kinetics are necessary for the occurrence of oscillatory behavior.

Finally, it should be noted that the problem of competition between two microbial species was further investigated in the literature from at least two perspectives. The first approach consists in the study of periodic variations of the bioreactor operating parameters. This mimics the seasonal variations in natural environments. Closely related to the principle of competitive exclusion [142] mentioned in the introduction, is the paradox of the plankton put forward by Hutchinson [162], who observed the coexistence of many species of phytoplankton in a relatively homogeneous environment while competing for a limited number of resources. This paradox was explained by Hutchinson [162] who suggested that seasonable variations of environment conditions provide the competitive advantage to each of the populations for periods of time and allow them to coexist. Studies have also shown that when the feed conditions of the chemostat are periodically varied, the two competing populations can coexist not only in a state of limit cycle [139, 160, 281, 336] but in a chaotic state as well [211, 212]. Experimental evidence of such coexistence was established, for instance, in [88] who showed that periodic variations in pH

managed to achieve stable coexistence of *S. cerevisae* and *E. coli* competing for a glucose rate-limiting nutrient.

The second approach followed in the literature for the dynamics of two competing species is the introduction of spatial heterogeneity in the environment. This can be simulated in the chemostat by imperfect mixing, microbial wall attachment, and/or configuration of two or more interconnected chemostats (i.e., the gradostat) [226]. The dynamics of competition in the gradostat was investigated by a number of authors [196, 213, 328, 335]. Recently Gaki et al. [118] studied the dynamics of competition for the case of nonsterile feed in a gradostat and showed the existence of complex dynamics, including quasi-periodic states and bifurcations of limit cycles via period-doubling sequences.

Chapter 7

STABILITY OF CONTINUOUS RECOMBINANT DNA CULTURES

7.1 Introduction

In the previous chapter, we indicated that bifurcation diagrams for the dynamics of competing microbial populations, for the case of sterile feed conditions, depend essentially on the relative position of cell growth rates. The number of possible configurations can be quite large. In this chapter, we examine the outcomes of competition for the important case of interactions between plasmid-bearing and plasmid-free recombinant DNA cultures.

The ability to manufacture desired bioproducts through genetically altered organisms represents one of the major developments in biotechnology. Genetic modification commonly takes place through the insertion of a plasmid to code for the production of the desired protein. The stability of bacterium-plasmid system during prolonged continuous cultivation is however limited, since the formation of large amounts of foreign protein is always detrimental to the host cell that tends to lose plasmid and return to its unaltered form. Moreover, cells that lose the capacity to make the target protein have often growth advantage over the more productive strains, leading to genetic instability [321]. The instability of continuous cultures of recombinant plasmid DNA was studied both experimentally and theoretically since the late 1970s [9, 18, 31, 108, 150, 156, 158, 167, 184, 208, 209, 220, 228, 232, 268, 311, 313, 337]. This instability is known to be caused by at least the following factors: (1) segregational instability that occurs when a portion of cells in the population lose their plasmids during reproduction; (2) instability when some cells retain plasmids but alter their forms to reduce the harmful effects on the cell; (3) mutations in host cells that alter cellular regulation and result in reduced target protein synthesis; (4) growth disadvantage of plasmid-bearing strains, compared with plasmid-free strain variants, and the variants containing plasmids with altered structure.

Among the various models proposed in the literature for modeling genetic instability, the model proposed in the 1980s by Cooper et al. [82] and Stephanopoulos and Lapidus [337] has probably been the most widely studied. The model describes the segregational instability of the recombinant strains by considering only two types of cells: plasmid-bearing and plasmid-free. The

model describes the dynamics of the competing populations by taking into consideration the probability of spontaneous plasmid loss in cell division and plasmid conjugal transfer between cells. Despite its simple unstructured nature, the model was shown [311, 337] to provide a fair quantification of general dominance trends and coexistence characteristics in recombinant cultures. The stability analysis of the model was carried out in a number of studies. Ryder and DiBiasio [311], for instance, carried out a local stability analysis for general growth kinetics. Since the coexistence was found to be unstable, the authors suggested an operational strategy involving feedback control to ensure stability. Stephanopoulos and Lapidus [337] were probably the first to study in detail the different static behavior the model can predict. Using arguments from index theory, the authors determined steady-state portraits of the competitive interactions, based on the shape and mutual disposition of the specific growth rates. The analysis was carried out assuming the growth of both strains to follow Monod and/or Haldane substrate-inhibition kinetics. The authors also reached the widely accepted conclusion that a stable partial washout steady state with only parental cell growth is not possible, and that the coexistence of the two species is the best outcome that can be hoped for. However, the study left unanswered the possibility of the model to predict periodic behavior. Hsu et al. [158], on the other hand, carried out a global stability analysis of the model for the case when the growth rates of both strains are substrate-uninhibited. The authors showed that the model cannot predict any nontrivial periodic solutions. Later, Luo and Hsu [228] extended the global asymptotic analysis of the model to the case when the growth rates of the competing cells are substrate-inhibited. Using a reduction approach [348] similar to their previous work [158], the authors examined the global stability characteristics of the reduced system for both static and periodic conditions.

In this chapter, we reexamine the stability of the recombinant system using the singularity theory. The first part of this chapter analyzes the model for arbitrary growth kinetics. The analysis of dynamic bifurcation allows the derivation of necessary conditions for the existence of Hopf points, for arbitrary growth kinetics. The conditions derived in this work are very simple: the model can predict a Hopf point only if the first derivatives of the growth rate of plasmid-bearing cells is positive and that of plasmid-free cells is negative. The importance of this result is that it can help to readily screen, beforehand, the growth rates that do not have the ability to produce an oscillatory behavior in the model. The singularity theory also allows the study of a number of Hopf degeneracies, which identifies regions in the model parameter space where one, two, or more Hopf points can occur.

In the second part, the different analytical conditions for static and dynamic behavior of the model are applied explicitly to specific forms of growth rates. In this regard, Monod growth rate is selected to be the uninhibited form while Haldane growth is selected as the substrate-inhibited form. For the static behavior, it is shown that simple analytical conditions (quadratic for the most part) are derived in terms of model parameters, which allows the systematic

classification of the parameter space into regions of different features. For the periodic behavior, it is shown that the conditions for the existence of Hopf points are reduced to a polynomial that may lend itself to mathematical manipulations. The combination of results of both static and dynamic analysis helps to construct a picture composed of 45 different regions. Unlike the approach followed by of Hsu et al. [158] and Luo and Hsu [228], the singularity theory is local in nature. However, the theory provides a useful framework for classifying the branching phenomena predicted by the model. This classification is combined with the construction of bifurcation diagrams using continuation techniques. These diagrams can yield clear and substantial information on the outcomes of the competition in terms of different model parameters. The practical implication of the resulting dynamics on the yield/selectivity of the chemostat are also investigated.

7.2 Process Model

The following is the unstructured model [337] describing the interactions between substrate S, plasmid-bearing X_1, and plasmid-free X_2 species:

$$\frac{dS}{dt} = D(S_f - S) - \frac{r_1 X_1}{Y_1} - \frac{r_2 X_2}{Y_2} \tag{7.1}$$

$$\frac{dX_1}{dt} = -DX_1 + (1-p)r_1 X_1 \tag{7.2}$$

$$\frac{dX_2}{dt} = -DX_2 + r_2 X_2 + p r_1 X_1 \tag{7.3}$$

D is the dilution rate, r_1 and r_2 are the specific growth rates for plasmid-bearing and plasmid-free cell populations, respectively, p the probability (assumed constant) that upon division a plasmid is lost or becomes modified and Y_i $(i = 1, 2)$ are the corresponding yields (also assumed constants). The model is rendered dimensionless using the following variables:

$$\bar{S} = \frac{S}{S_{ref}}, \quad \bar{S}_f = \frac{S_f}{S_{ref}}, \quad \bar{X}_1 = \frac{X_1}{Y_1 S_{ref}}, \quad \bar{X}_2 = \frac{X_2}{Y_2 S_{ref}} \tag{7.4}$$

$$\bar{r}_1 = \frac{r_1}{r_{ref}}, \quad \bar{r}_2 = \frac{r_2}{r_{ref}}, \quad \bar{D} = \frac{D}{r_{ref}}, \quad \bar{t} = r_{ref} t, \quad \eta = \frac{Y_1}{Y_2} \tag{7.5}$$

S_{ref} and r_{ref} are reference quantifies for S and r_1, respectively. The dimensionless model equations are:

$$\frac{d\bar{S}}{d\bar{t}} = \bar{D}(\bar{S}_f - \bar{S}) - (\bar{r}_1 \bar{X}_1 + \bar{r}_2 \bar{X}_2) \tag{7.6}$$

$$\frac{d\bar{X}_1}{d\bar{t}} = -\bar{D}\bar{X}_1 + (1-p)\bar{r}_1\bar{X}_1 \tag{7.7}$$

$$\frac{d\bar{X}_2}{d\bar{t}} = -\bar{X}_2(\bar{D} - \bar{r}_2) + \eta p\bar{r}_1\bar{X}_1 \tag{7.8}$$

The steady-state equations are obtained by setting the left-hand sides of Equations (7.6–7.8) to zero. Equations (7.7-7.8), in particular, would yield,

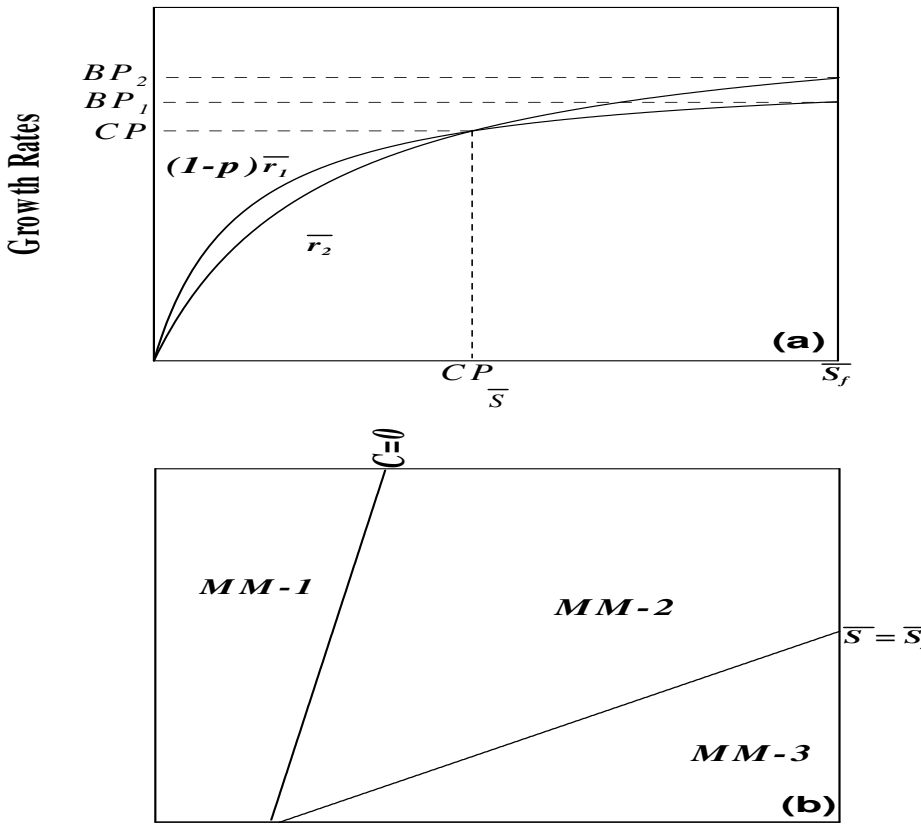

FIGURE 7.1: (a) Example of mutual disposition of growth rates for Monod-Monod case; (b) Branch set for Monod-Monod case.

$$\bar{X}_1(-\bar{D} + (1-p)\bar{r}_1) = 0 \tag{7.9}$$

and

$$\bar{X}_2 = \frac{\eta p\bar{r}_1\bar{X}_1}{\bar{D} - \bar{r}_2} \tag{7.10}$$

Equation (7.9) implies that $\bar{X}_1 = 0$ or $\bar{D} = (1-p)\bar{r}_1$. Substituting successively these conditions in the steady-state forms of Equations (7.6,7.8) yields the following three possible steady states:

- $\bar{X}_1 = 0$, $\bar{X}_2 = 0$ and $\bar{S} = \bar{S}_f$. This corresponds to total washout conditions.
- $\bar{X}_1 = 0$, $\bar{X}_2 = \bar{S}_f - \bar{S}$ and $\bar{D} = \bar{r}_2$, which corresponds to washout of plasmid-bearing cell populations.
- $\bar{X}_1 > 0$, $\bar{X}_2 > 0$ and $\bar{D} = (1-p)\bar{r}_1$ which corresponds to the coexistence of the two populations. The concentrations $\bar{X}_1$ and $\bar{X}_2$ in this case are given by

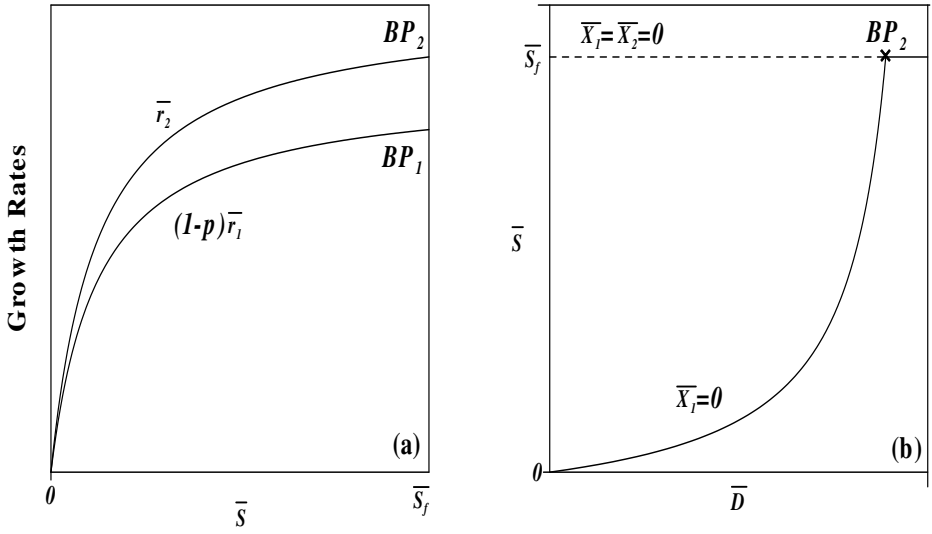

FIGURE 7.2: Details of region MM1 of Figure 7.1b: (a) Growth rates; (b) Continuity diagram; solid line, stable; dashed line, unstable.

$$\bar{X}_1 = \frac{(1-p)((1-p)\bar{r}_1 - \bar{r}_2)(\bar{S}_f - \bar{S})}{(1-p)\bar{r}_1 - (1-\eta p)\bar{r}_2} \tag{7.11}$$

$$\bar{X}_2 = \frac{\eta p(1-p)\bar{r}_1(\bar{S}_f - \bar{S})}{(1-p)\bar{r}_1 - (1-\eta p)\bar{r}_2} \tag{7.12}$$

The combination of Equations (7.11–7.12) yields the following useful relation between the species concentrations $\bar{X}_1$, $\bar{X}_2$, and $\bar{S}$,

$$\frac{1-\eta p}{1-p}\bar{X}_1 + \bar{X}_2 + \bar{S} = \bar{S}_f \tag{7.13}$$

The productivity (P) and the selectivity (Y) are defined respectively by

$$P := \bar{D}\bar{X}_1 \text{ and } Y := \frac{X_1}{X_2} = \frac{(1-p)\bar{r}_1 - \bar{r}_2}{\eta p \bar{r}_1} \tag{7.14}$$

It can be noted that a washout of plasmid-free cells is not possible. As noted in [337], given that $p > 0$, there is a continuous seed of X_2 cells from the plasmid-bearing population so that the derivative in Equation (7.8) cannot vanish.

In the course of this analysis, the dilution rate $\bar{D}$ is selected as the main bifurcation parameter. The bifurcation diagram in the parameter space $(\bar{S}, \bar{D})$ has always, as a solution, the total washout line ($\bar{S} = \bar{S}_f$), in addition to the solutions corresponding to the plasmid-bearing washout and/or that corresponding to the coexistence of the two cell populations.

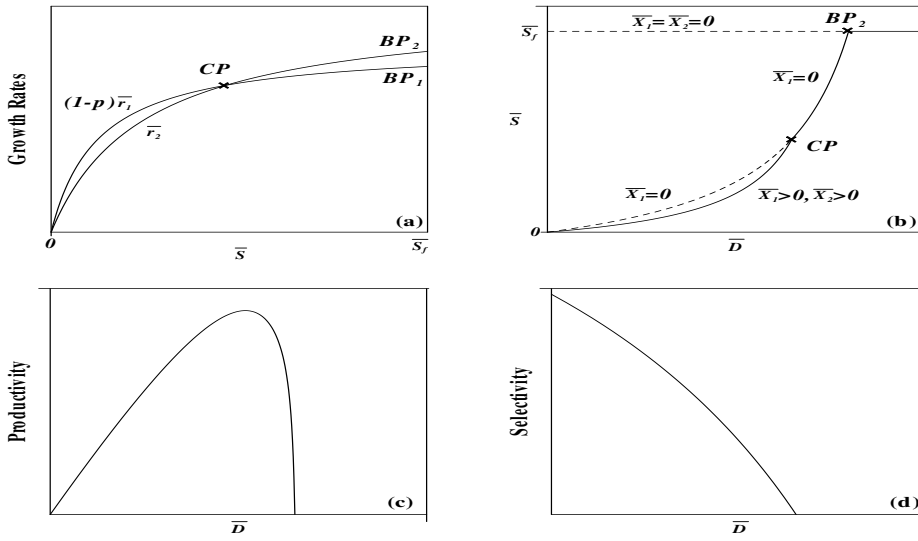

FIGURE 7.3: Details of region MM2 of Figure 7.1b: (a) Growth rates; (b) Continuity diagram; (c) Productivity; (d) Selectivity; solid line, stable; dashed line, unstable.

7.3 Dynamic Bifurcation

The elements of the Jacobian matrix are given explicitly by taking the derivatives of Equations (7.6–7.8), yielding

$$j_{11} = -\bar{D} - (\bar{r}_{1\bar{S}}\bar{X}_1 + \bar{r}_{2\bar{S}}\bar{X}_2), \quad j_{12} = -\bar{r}_1, \quad j_{13} = -\bar{r}_2 \tag{7.15}$$

$$j_{21} = (1-p)\bar{r}_{1\bar{S}}\bar{X}_1, \quad j_{22} = -\bar{D} + (1-p)\bar{r}_1, \quad j_{23} = 0 \tag{7.16}$$

$$j_{31} = \bar{r}_{2\bar{S}}\bar{X}_2 + \eta p\bar{r}_{1\bar{S}}\bar{X}_1, \quad j_{32} = p\eta\bar{r}_1 \quad j_{33} = -\bar{D} + \bar{r}_2 \tag{7.17}$$

The Hopf conditions are given by Equations (3.38–3.39). Simplified expres-

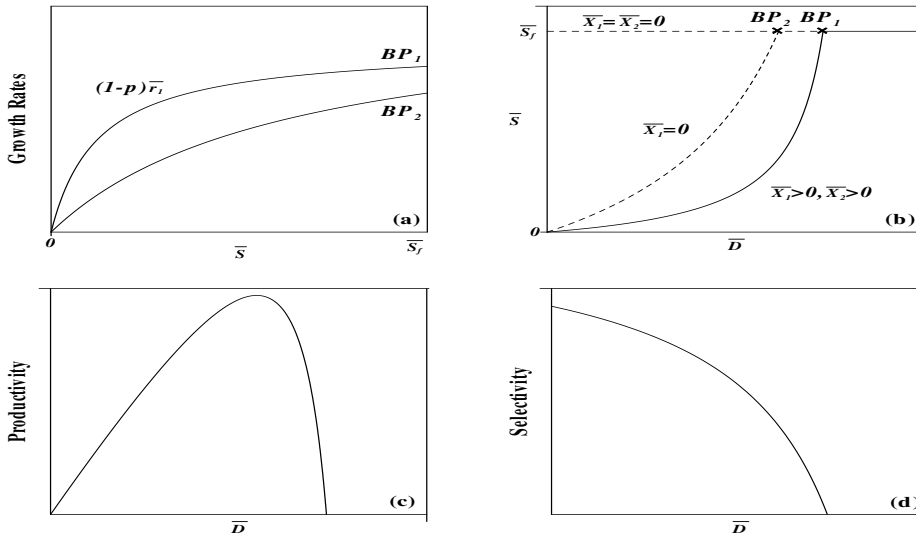

FIGURE 7.4: Details of region MM3 of Figure 7.1b: (a) Growth rates; (b) Continuity diagram; (c) Productivity; (d) Selectivity; solid line, stable; dashed line, unstable.

sions for the terms S_i $(i = 1, 3)$ (Equations (3.35–3.37)) are obtained using the software MATHEMATICA [238], for the important case of the coexistence of cells (i.e., $\bar{D} = (1-p)\bar{r}_1$)

$$S_1 = -2(1-p)\bar{r}_1 + \bar{r}_2 - (\bar{r}_{1\bar{S}}\bar{X}_1 + \bar{r}_{2\bar{S}}\bar{X}_2) \tag{7.18}$$

$$\begin{aligned} S_2 \quad = \quad & (1-p)^2\bar{r}_1^2 + (p-1)\bar{r}_1\bar{r}_2 + (1-p)\bar{r}_1(\bar{r}_{1\bar{S}}\bar{X}_1 + \bar{r}_{2\bar{S}}\bar{X}_2) + \\ & \bar{r}_{1\bar{S}}\bar{X}_1((1-p)\bar{r}_1 - (1-\eta p)\bar{r}_2) \end{aligned} \tag{7.19}$$

$$S_3 = -(1-p)\bar{r}_1\bar{r}_{1\bar{S}}[(1-p)\bar{r}_1 - (1-\eta p)\bar{r}_2]\bar{X}_1 \tag{7.20}$$

Algebraic manipulations yield the following useful relations,

$$\bar{D}S_2 + S_3 = -D^2(S_1 + \bar{D}) \tag{7.21}$$

Substituting in the first Hopf condition $F_1 := S_1S_2 - S_3$ yields

$$F_1 := (S_1 + \bar{D})(S_2 + \bar{D}^2) = 0 \text{ and } S_2 > 0 \tag{7.22}$$

Since S_2 is required to be positive, these Hopf conditions are reduced to

$$(S_1 + \bar{D}) = 0 \text{ and } S_2 > 0 \tag{7.23}$$

From Equation (7.18), the condition $S_1 + \bar{D} = 0$ is equivalent to

$$[(1-p)\bar{r}_1 - \bar{r}_2] + (\bar{r}_{1\bar{S}}\bar{X}_1 + \bar{r}_{2\bar{S}}\bar{X}_2) = 0 \tag{7.24}$$

The first term of this equation is positive (to ensure the meaningful coexistence of cells), therefore this equation requires necessarily that

$$\bar{r}_{1\bar{S}} < 0 \text{ or } \bar{r}_{2\bar{S}} < 0 \tag{7.25}$$

Using Equation (7.19), the second Hopf condition $S_2 > 0$ is equivalent after some manipulations to

$$S_2 = \bar{r}_{1\bar{S}}[(1-p)\bar{r}_1 - (1-\eta p)\bar{r}_2]\bar{X}_1 > 0 \tag{7.26}$$

Since from Equation (7.12), the term $((1-p)\bar{r}_1 - (1-\eta p)\bar{r}_2)$ is positive, then the condition of Equation (7.26) is equivalent to

$$\bar{r}_{1\bar{S}} > 0 \tag{7.27}$$

Combining Equation (7.25) and Equation (7.27), we conclude that the necessary conditions for the occurrence of Hopf points are

$$\bar{r}_{1\bar{S}} > 0 \text{ and } \bar{r}_{2\bar{S}} < 0 \tag{7.28}$$

These Hopf conditions are simple and are given explicitly in term of first derivatives of the growth rates. This result can help to readily screen growth kinetics that do not have the ability to produce an oscillatory behavior in the model. In the following we examine the occurrence of some Hopf degeneracies.

7.3.1 F_1 Degeneracy

The F_1 degeneracy is determined by solving the steady-state equations, the condition $S_2 = 0$ (Equation (7.19)), and the static limit point condition, $S_3 = 0$ (Equation (7.20)). Since from Equation (7.12) the term $((1-p)\bar{r}_1 - (1-\eta p)\bar{r}_2)$ is strictly positive and barring the trivial cases of $p = 1$, $\bar{r}_1 = 0$, the condition $S_3 = 0$ (Equation (7.20)) yields $\bar{r}_{1\bar{S}} = 0$. Substituting in S_2 (Equation (7.19)) yields

$$S_2 = (1-p)\bar{r}_1((1-p)\bar{r}_1 - \bar{r}_2 + \bar{r}_{2\bar{S}}\bar{X}_2) \tag{7.29}$$

At the F_1 singularity this term vanishes, which yields,

$$\bar{X}_2 = \frac{\bar{r}_2 - (1-p)\bar{r}_1}{\bar{r}_{2\bar{S}}} \tag{7.30}$$

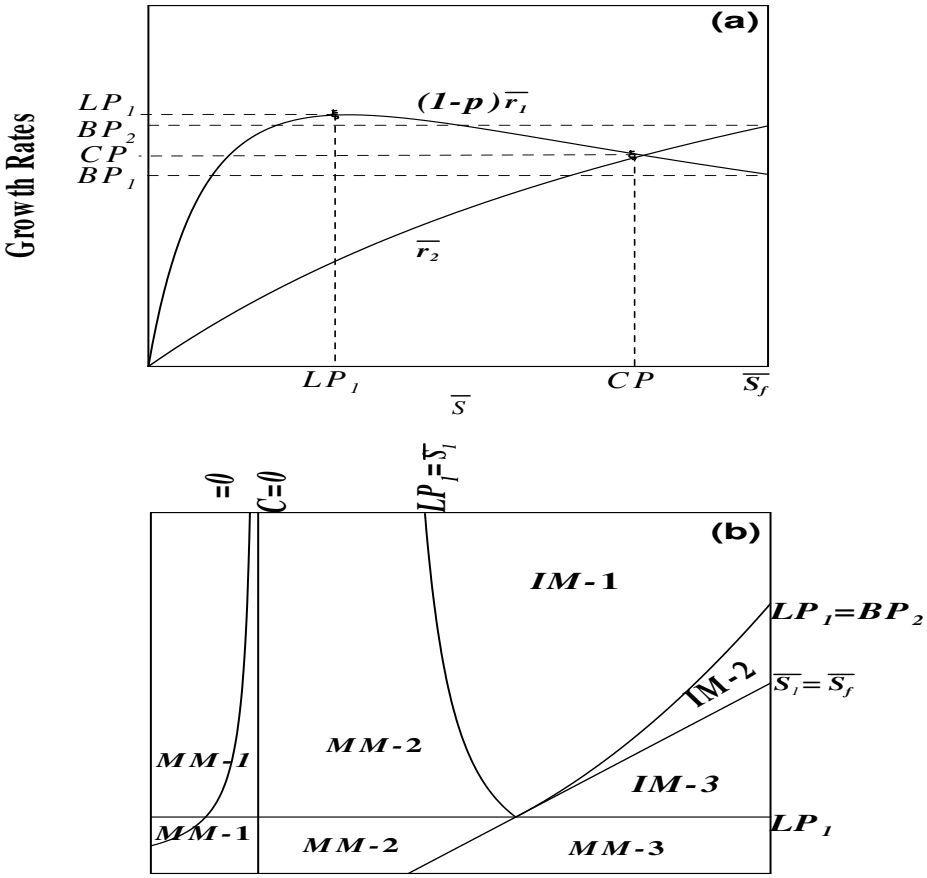

FIGURE 7.5: (a) Example of mutual disposition of growth rates for inhibition-Monod case; (b) Branch set for inhibition-Monod case.

Substituting for $\bar{X}_2$ (Equation (7.30)), the steady-state value of $\bar{X}_1$ (Equation (7.10)) and $\bar{D} = (1-p)\bar{r}_1$ in the steady-state Equation (7.6) yields the following condition for the occurrence of the F_1 singularity

$$\bar{S}_f - \bar{S}_H + \frac{[(1-p)\bar{r}_1 - \bar{r}_2][(1-p)\bar{r}_1 - (1-\eta p)\bar{r}_2]}{\eta p(1-p)\bar{r}_1\bar{r}_2'} = 0 \qquad (7.31)$$

with $\bar{S}_H$ satisfying the condition $\bar{r}_1'(\bar{S}_H) = 0$. Equation (7.31) represents, therefore, general conditions with respect to any growth rates for the occurrence of the F_1 singularity. When crossing the curve(s) defining this singularity, the number of Hopf points in the continuity diagram increases/decreases by one.

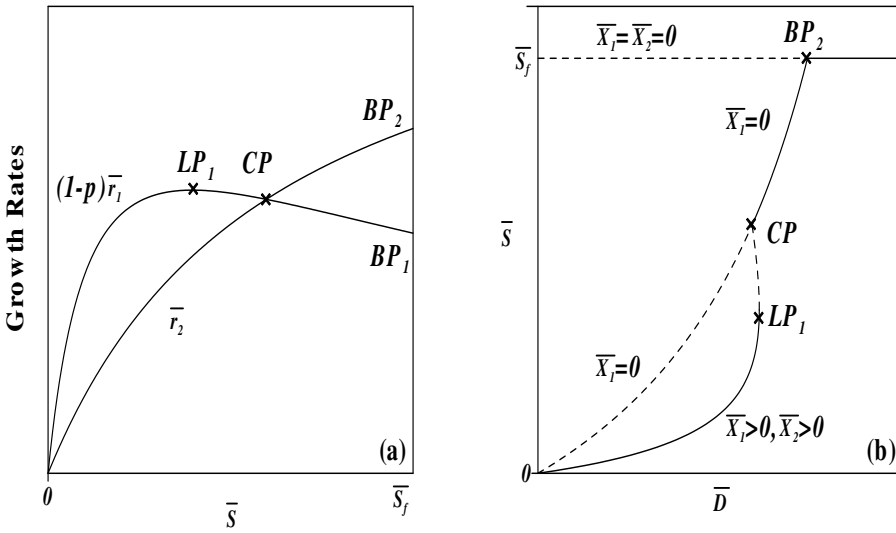

FIGURE 7.6: Details of region IM1 of Figure 7.5b: (a) Growth rates; (b) Continuity diagram; solid line, stable; dashed line, unstable.

7.3.2 H_{01} Singularity

The H_{01} singularity corresponds to the appearance or coalescence of two Hopf points in the bifurcation diagram. The conditions for this singularity are:

$$F_1 = F_{1\bar{S}} = 0, F_{1\bar{S}\bar{S}} \neq 0 \quad S_2 > 0 \tag{7.32}$$

with $F_1 = S_1 S - 2 - S_3$. Using Equation (7.22), the conditions of Equation (7.32) are equivalent to

$$S_1 + \bar{D} = 0, (S_1 + D)_{\bar{S}} = 0, (S_1 + D)_{\bar{S}\bar{S}} \neq 0 \text{ and } S_2 > 0 \tag{7.33}$$

Since no simple analytical conditions can be derived for this singularity, the conditions of Equations (7.33) are solved numerically to delineate the boundaries for this singularity.

In the next section, we provide a detailed analysis of these singularities for the case when the growth rates r_1 or r_2 follow Monod and/or Haldane substrate-inhibited kinetics.

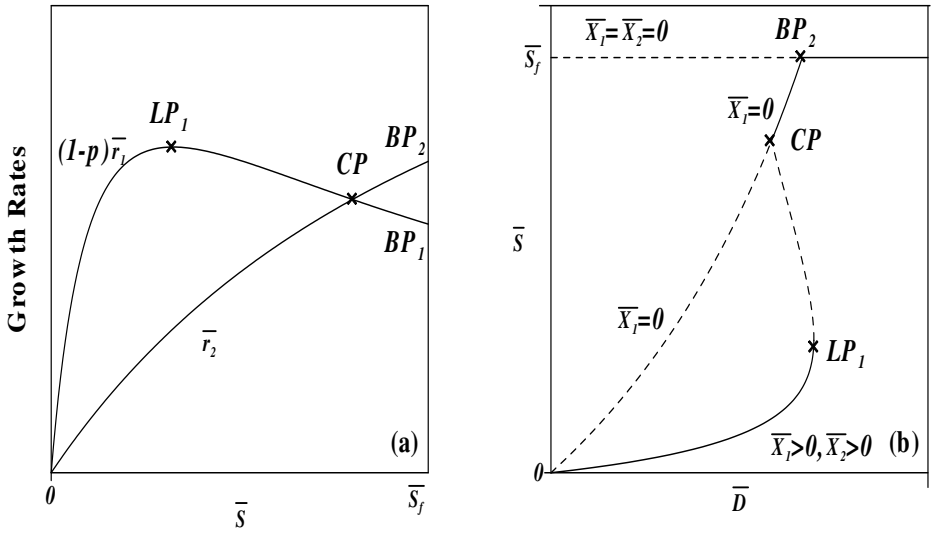

FIGURE 7.7: Details of region IM2 of Figure 7.5b: (a) Growth rates; (b) Continuity diagram; solid line, stable; dashed line, unstable.

7.4 Applications to Monod/Haldane Substrate-Inhibited Kinetics

The expressions for r_j take the form,

$$r_j = \frac{\mu_j S}{K_j + S + S^2/K_{Ij}}, \quad (j = 1, 2) \tag{7.34}$$

where the $K_{Ij} (j = 1, 2)$ are the inhibition constants. Using the following reference quantities in Equations (7.4–7.5),

$$S_{ref} = K_1 \text{ and } r_{ref} = \mu_1 \tag{7.35}$$

the dimensionless expressions for the specific growth rates are

$$\bar{r}_1 = \frac{\bar{S}}{1 + \bar{S} + \gamma_1 \bar{S}^2} \text{ and } \bar{r}_2 = \frac{\phi \bar{S}}{\alpha + \bar{S} + \gamma_2 \bar{S}^2} \tag{7.36}$$

with the following definitions

$$\alpha = \frac{K_2}{K_1}, \gamma_1 = \frac{K_1}{K_{I1}}, \gamma_2 = \frac{K_1}{K_{I2}}, \phi = \frac{\mu_2}{\mu_1} \tag{7.37}$$

The model contains eight independent parameters $\bar{D}$, $\bar{S}_f$, γ_1, γ_2, ϕ, α, p, and η. Monod growth rates are obtained as a limiting case of Equation (7.36) as the

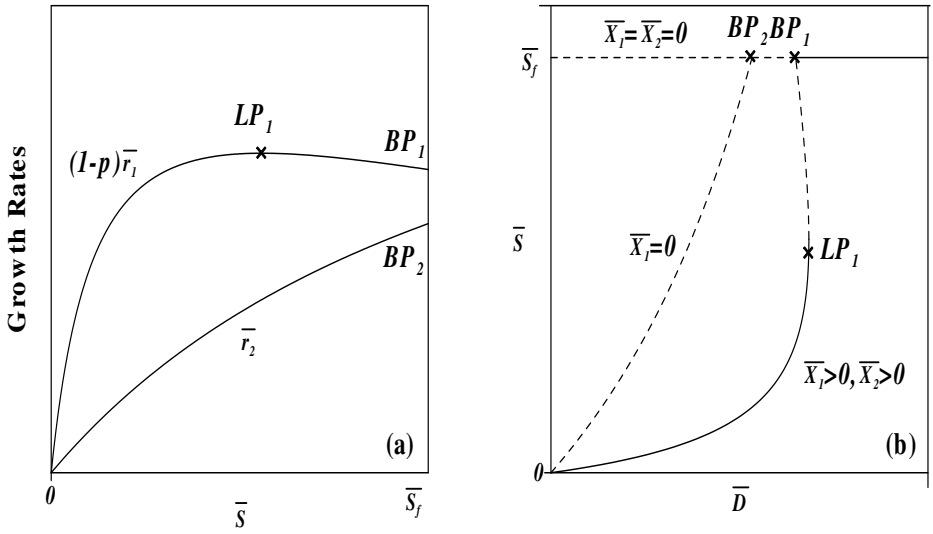

FIGURE 7.8: Details of region IM3 of Figure 7.5b: (a) Growth rates; (b) Continuity diagram; solid line, stable; dashed line, unstable.

dimensionless inhibition constants γ_1 and γ_2 take on small values, i.e., $\gamma_j \to 0$, $(j = 1, 2)$. For the sake of simplicity we will assume equal yields for the two cells, i.e. $\eta = 1$. Moreover, since in practice the maximum specific growth of plasmid-free cells is greater than that of plasmid-bearing cells, the quantity ϕ (Equation (7.37)) is assumed to be larger than unity. In the following, we treat systematically both the static and dynamic bifurcation for the following four cases: (1) Both cells grow following Monod kinetics (Monod-Monod) (2) the growth of plasmid-bearing cells is substrate inhibited while that of plasmid-free cells is of the Monod form (inhibition-Monod) (3) the Monod-inhibition case, and (4) the inhibition-inhibition case. The objective of the analysis is to construct practical branch sets that delineate the various bifurcation behavior. But first we derive some useful relations from the general discussion carried out in previous sections. For $\eta = 1$, the steady-state condition of Equation (7.13) is reduced to

$$\bar{X}_1 + \bar{X}_2 + \bar{S} = \bar{S}_f \tag{7.38}$$

The condition $(1 - p)\bar{r}_1 = \bar{r}_2$ for the crossing of growth rates is equivalent to the quadratic equation,

$$a\bar{S}^2 + b\bar{S} + c = 0 \tag{7.39}$$

with

$$a = (1 - p)\gamma_2 - \phi\gamma_1, \quad b = (1 - p) - \phi, \quad c = \alpha(1 - p) - \phi \tag{7.40}$$

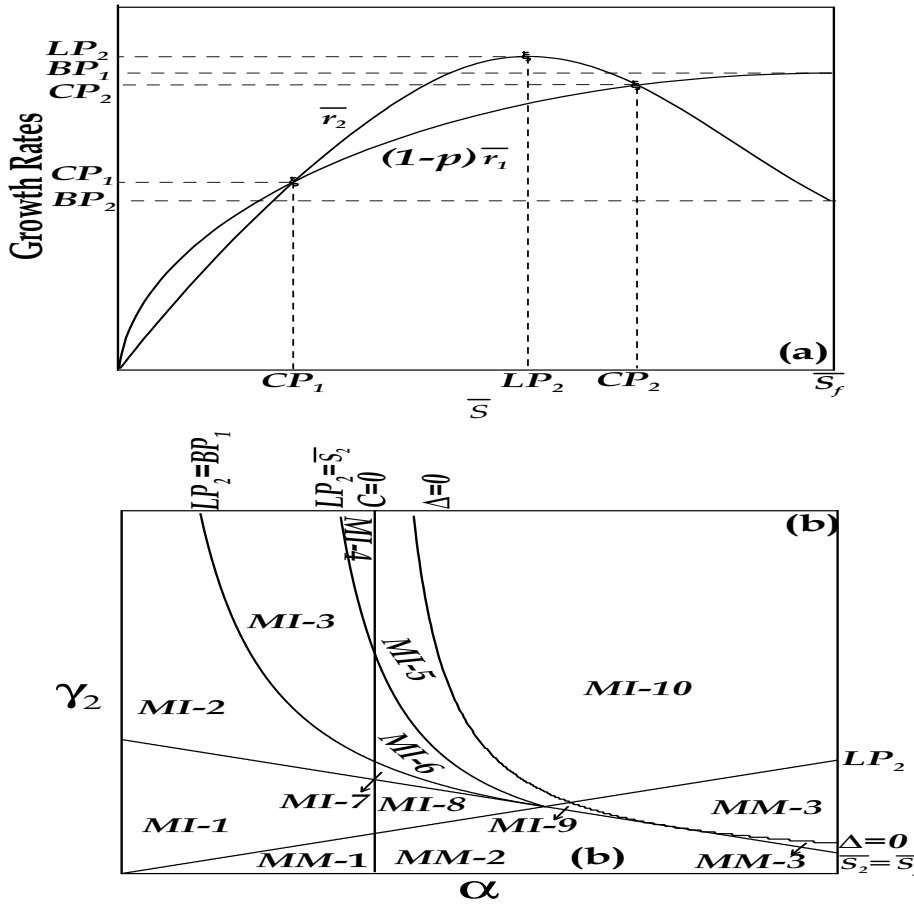

FIGURE 7.9: (a) Example of mutual disposition of growth rates for Monod-inhibition case; (b) Branch set for Monod-inhibition case.

It can be noted that since ϕ is always greater than unity and since the probability p is restricted between 0 and 1, then the term (b) is always negative. The crossing points of the two growth rates, if they exist, are solutions of Equation (7.39)

$$\bar{S}_1 = \frac{-b - \sqrt{\Delta}}{2a} \text{ and } \bar{S}_2 = \frac{-b + \sqrt{\Delta}}{2a} \tag{7.41}$$

In the chosen parameter space $(\bar{D}, \bar{S})$, the crossing of the plasmid-bearing washout curve with the total washout line occurs at the dilution rate obtained by substituting $\bar{S}_f$ in $(\bar{D} = \bar{r}_2)$, to yield

$$\bar{D} = \frac{\phi \bar{S}_f}{\alpha + \bar{S}_f + \gamma_2 \bar{S}_f^2} \tag{7.42}$$

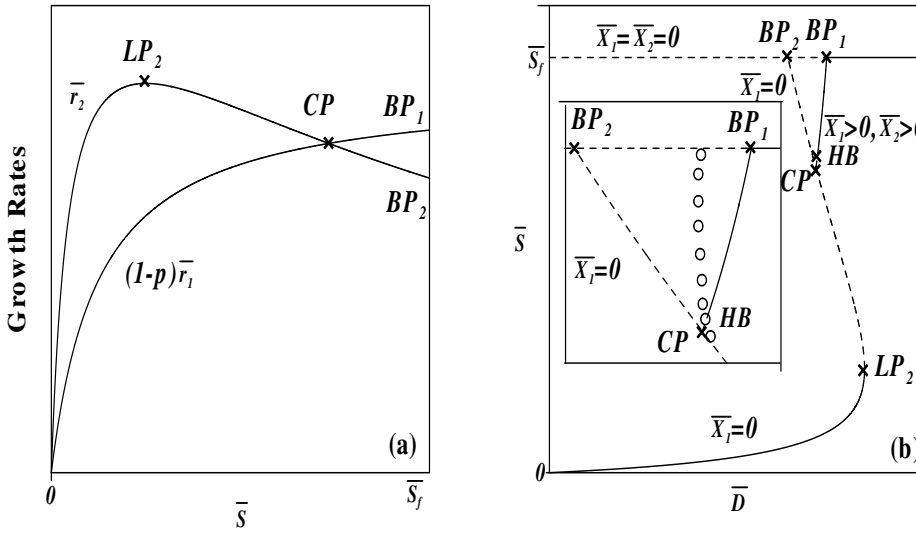

FIGURE 7.10: Details of region MI2 of Figure 7.9b: (a) Growth rates; (b) Continuity diagram; solid line, stable; dashed line, unstable; circles, unstable periodic branches.

The crossing, on the other hand, of the coexistence curve with the total washout line is obtained by substituting $\bar{S}_f$ in $(\bar{D} = (1-p)\bar{r}_1)$, to yield

$$\bar{D} = \frac{(1-p)\bar{S}_f}{1 + \bar{S}_f + \gamma_1 \bar{S}_f^2} \tag{7.43}$$

The first derivatives of $\bar{r}_1$ and $\bar{r}_2$ are given by

$$\bar{r}_{1\bar{S}} = \frac{1 - \gamma_1 \bar{S}^2}{(1 + \bar{S} + \gamma_1 \bar{S}^2)^2} \quad \text{and} \quad \bar{r}_{2\bar{S}} = \frac{\phi(\alpha - \gamma_2 \bar{S}^2)}{(\alpha + \bar{S} + \gamma_2 \bar{S}^2)^2} \tag{7.44}$$

In the $(\bar{D}, \bar{S})$ space, the curve of the coexistence of two cells may have a static limit point if $(1-p)\bar{r}_{1\bar{S}} = 0$. This occurs at

$$\bar{S} = \frac{1}{\sqrt{\gamma_1}} \tag{7.45}$$

Since $\bar{S}$ is constrained by $\bar{S}_f$, a necessary condition for the existence of static limit points is that

$$\gamma_1 \geq \frac{1}{\bar{S}_f^2} \tag{7.46}$$

Similarly, the existence of a static limit point on the plasmid-bearing washout curve is conditioned by $\bar{r}_{2\bar{S}} = 0$, and occurs at

$$\bar{S} = \sqrt{\frac{\alpha}{\gamma_2}} \tag{7.47}$$

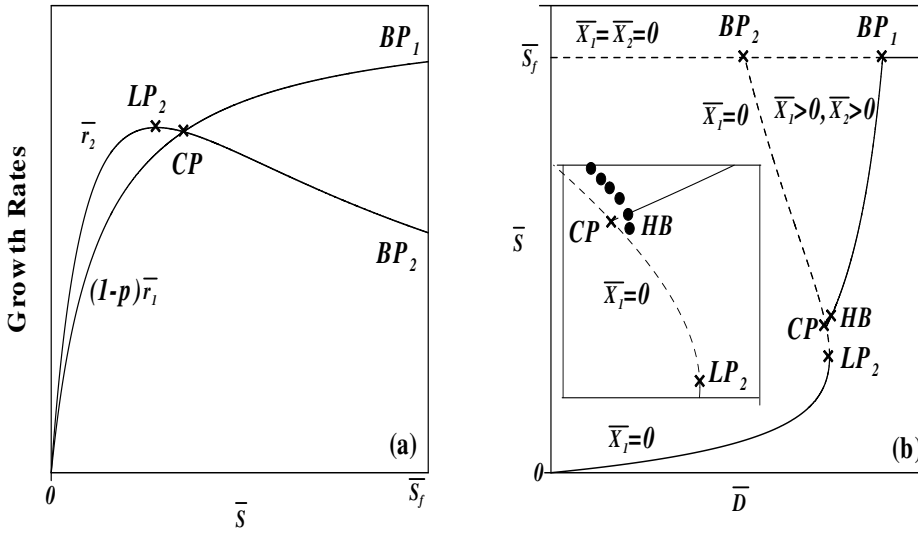

FIGURE 7.11: Details of region MI3 of Figure 7.9b for ($\bar{S}_f = 8, \alpha = 1, \gamma_1 = 0, \gamma_2 = 0.2, \phi = 1.4, p = 0.01$): (a) Growth rates; (b) Continuity diagram; solid line, stable; dashed line, unstable; dots, stable periodic branches.

For the same arguments, a necessary condition for the existence of static limit points is that

$$\gamma_2 \geq \frac{\alpha}{\bar{S}_f^2} \tag{7.48}$$

As for the occurrence of Hopf points in the model, besides the necessary conditions of Equation (7.28), the original conditions of Hopf points (Equation (7.22)) can be explicitly detailed. Substituting for $\bar{X}_1$ (Equation (7.11)) and $\bar{X}_2$ (Equation (7.12)), the Hopf condition (Equation (7.22)) is reduced to a polynomial of seventh-order in $\bar{S}$. This results indicates that the model can predict up to seven Hopf points.

7.4.1 Monod-Monod Case

For the Monod-Monod case, the specific growth rates (Equation (7.36)) are reduced to the following forms

$$\bar{r}_1 = \frac{\bar{S}}{1 + \bar{S}} \text{ and } \bar{r}_2 = \frac{\phi \bar{S}}{\alpha + \bar{S}} \tag{7.49}$$

Before the analysis is carried out any further, it can be noted that for this case (Monod-Monod) the first derivative $\bar{r}_{2\bar{S}}$ is always positive. Therefore, the model cannot predict any periodic behavior, since the necessary Hopf

conditions of Equation (7.28) are never satisfied. For the static behavior we will show how a systematic approach can be used to construct a branch set where all the different possible behaviors can be expected. The approach followed for the Monod-Monod case will serve as an example for the other cases to be discussed in later sections. To construct the branch set, we start by showing in Figure 7.1a, one scenario of the mutual disposition of the two growth rates, $(1-p)\bar{r}_1$ and $\bar{r}_2$. The point of crossing is obtained from Equation (7.39), which is reduced to

$$b\bar{S} + c = 0 \tag{7.50}$$

Since b is always negative, the existence of a positive solution to this equation

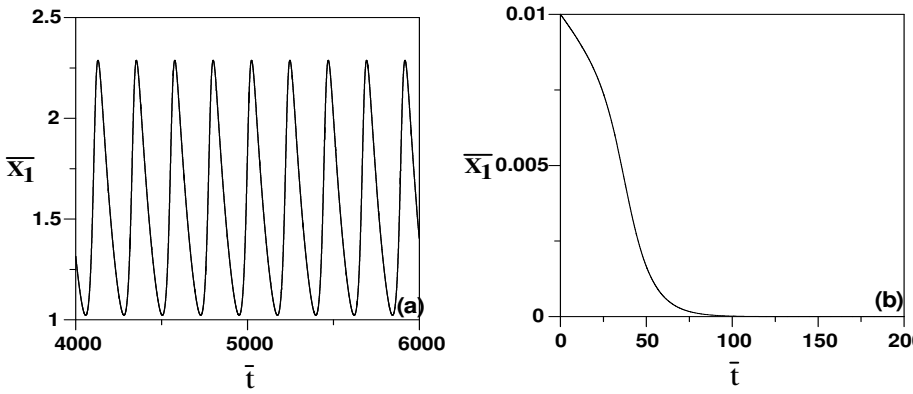

FIGURE 7.12: Dynamics showing bistability in region MI3, for $\bar{D} = 0.7321$: (a) Initial conditions $(\bar{S}, \bar{X}_1, \bar{X}_2) = (2.83, 1.4678, 3.6969)$ lead to oscillations; (b) $(\bar{S}, \bar{X}_1, \bar{X}_2) = (2.73, 0.01, 5.27)$ lead to plasmid-bearing washout.

depends on the sign of c. The equation $(c = 0)$ represents therefore one condition forming the branch set. Should a real and positive solution to Equation (7.50) exist, then it should also satisfy the natural constraint $\bar{S} < \bar{S}_f$. The condition $\bar{S} = \bar{S}_f$ is therefore another element of the branch set. The branch set can be represented in any model parameters space. We select (ϕ, α) as the parameter space. The condition $c = 0$ yields the following line

$$\phi = (1-p)\alpha \tag{7.51}$$

while equation $\bar{S} = \bar{S}_f$ yields another line

$$\phi = \alpha\frac{1-p}{1+\bar{S}_f} + \frac{(1-p)\bar{S}_f}{1+\bar{S}_f} \tag{7.52}$$

Equations (7.51–7.52) are therefore lines that form the branch set, shown in Figure 7.1b. The branch set exists only for $\phi > 1$ as indicated in earlier

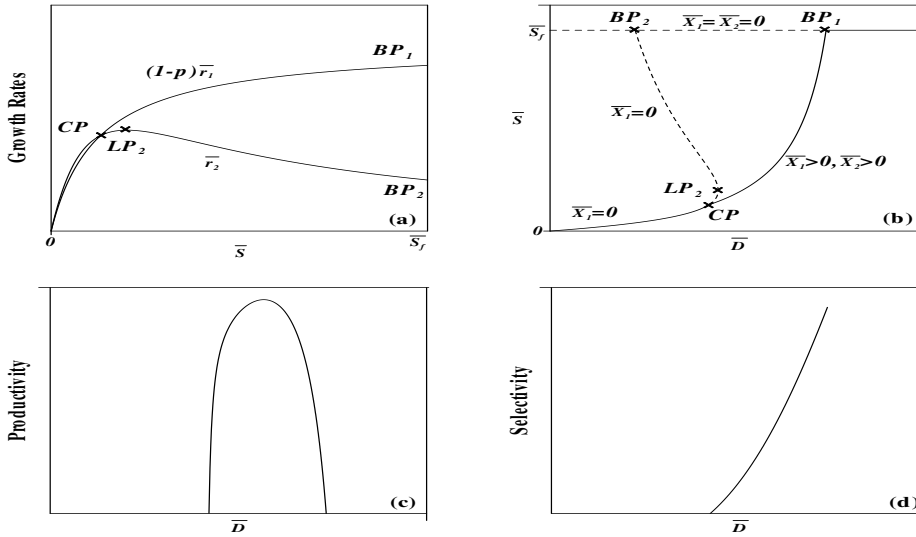

FIGURE 7.13: Details of region MI4 of Figure 7.9b: (a) Growth rates; (b) Continuity diagram; (c) Productivity; (d) Selectivity; solid line, stable; dashed line, unstable.

sections. There are only three behaviors that can be found for arbitrary values of model parameters. We start with region MM1 of Figure 7.1b. It can be seen (Figure 7.2a) that plasmid-free cells always outgrow their counterparts, i.e., $\bar{r}_2 > (1-p)\bar{r}_1$, and therefore no coexistence of cells is possible. The corresponding steady-state portrait (Figure 7.2b) shows two curves: a stable curve that corresponds to washout of plasmid-bearing cells, and the horizontal total washout line. The crossing of the two curves occurs at the dilution rate corresponding to the bifurcation point BP_2, solution of (Equation (7.42)) with $\gamma_2 = 0$. (The subscript 2 in BP_2 is associated with the growth rate r_2). Operating conditions smaller than BP_2 lead to plasmid-bearing washout while larger values lead to the total washout. The second region (MM2) of the branch set of Figure 7.1b arises when the line $c = 0$ is crossed. This leads to the existence of a positive and meaningful (i.e., $< \bar{S}_f$) solution to the coexistence equation. The two growth rates can be seen to cross in Figure 7.3a. The associated continuity diagram is shown in Figure 7.3b. Besides the plasmid-bearing washout curve and the total washout line, Figure 7.3b also has the coexistence curve. The crossing (CP) of the plasmid-bearing washout curve and the coexistence curve occurs at the substrate concentration, solution of Equation (7.50). For dilution rates smaller than CP, the operation of the bioreactor leads to the stable coexistence of the two cells. Values larger than CP and smaller than BP_2 lead to plasmid-bearing washout, while larger values than BP_2 lead, as in the MM1 case, to a total washout. For the MM2 region, and since the coexistence of the two cells is possible, Figures 7.3(c-d) show

the variations of productivity and selectivity with the dilution rate. It can be seen that the productivity reaches a maximum while the selectivity is a decreasing function. In the rest of the analysis and for the sake of space, the plots of productivity and selectivity are omitted for most regions, except for those that are deemed necessary. The third region MM3 of the branch set (Figure 7.1b) arises when the line of $\bar{S} = \bar{S}_f$ is crossed. The crossing point CP of the two growth rates is not meaningful anymore, i.e., $\bar{S} > \bar{S}_f$. Figure 7.4a shows that plasmid-bearing cells always outgrow their counterparts. The corresponding steady-state portrait is shown in Figure 7.4b. The coexistence curve is stable and extends until its crossing with the total washout line at BP_1, the solution of Equation (7.43) with $\gamma_1 = 0$. Values of dilution rates smaller than BP_1 lead to the stable coexistence since the plasmid-bearing washout curve is always unstable. Larger values than BP_1 lead, on the other hand, to total washout.

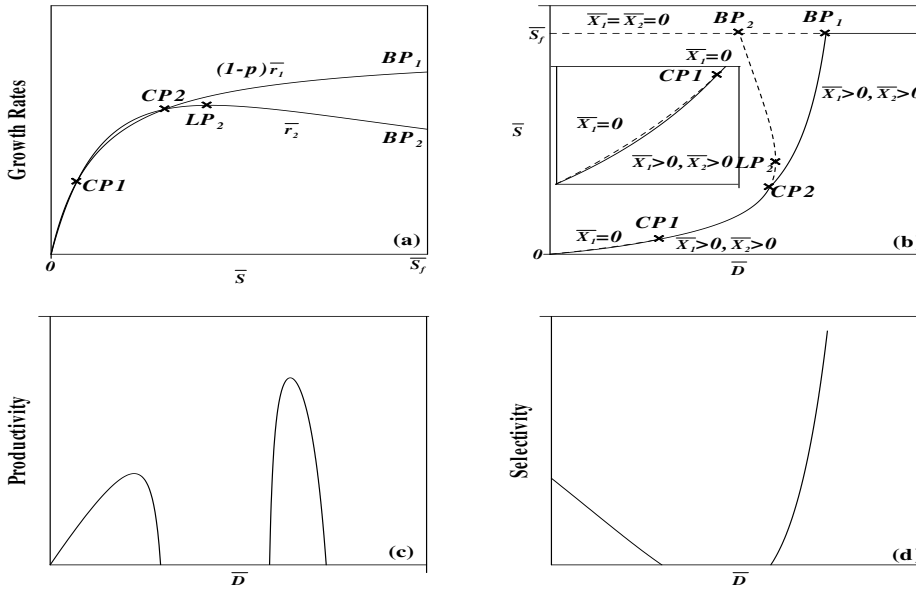

FIGURE 7.14: Details of region MI5 of Figure 7.9b: (a) Growth rates; (b) Continuity diagram; (c) Productivity; (d) Selectivity; solid line, stable; dashed line, unstable.

7.4.2 Inhibition-Monod Case

For the inhibition-Monod case, the specific growth rates are given by Equation (7.36) with $\gamma_2 = 0$. Similarly to the Monod-Monod case, since the growth rate $\bar{r}_{2\bar{S}}$ is always positive, the model cannot predict any oscillatory behavior. The crossing of the growth rates is still given by the quadratic Equation (7.39–

7.40) with $\gamma_2 = 0$. Note that for this case both terms b and $a = -\phi\gamma_1$ are negative. Therefore, it can be seen from Equation (7.41) that the root $\bar{S}_2$ is always negative and the two growth rates $(1-p)\bar{r}_1$ and $\bar{r}_2$ can cross only at one point $\bar{S}_1$. To construct branch sets for this example we proceed following the same approach used for the Monod-Monod case. We choose to represent the branch set in the parameter space (α, γ_1). Figure 7.5a shows an example of the disposition of the growth rates. The crossing of the growth rates is conditional on the discriminant Δ of Equation (7.39) being positive. $\Delta = 0$ is therefore one element of the branch set. It corresponds to the curve

$$\gamma_1 = \frac{-(1-p-\phi)^2}{4\phi(\alpha(1-p)-\phi)} \tag{7.53}$$

Should the root exist then it should satisfy $0 \leq \bar{S} \leq \bar{S}_f$. The conditions $\bar{S} = 0$ and $\bar{S} = \bar{S}_f$ are two other elements of the branch set. They correspond respectively to the vertical line

$$\alpha = \frac{\phi}{1-p} \tag{7.54}$$

and to the line

$$\gamma_1 = \frac{\alpha(1-p)}{\phi\bar{S}_f^2} + \frac{(1-p)\bar{S}_f - \phi(1+\bar{S}_f)}{\phi\bar{S}_f^2} \tag{7.55}$$

The inhibition nature of the growth root $\bar{r}_1$ introduces other elements in the branch sets. First, the occurrence of the static limit points is conditioned by Equation (7.46). Therefore, $\gamma_1 = \frac{1}{\bar{S}_f^2}$ is another element of the branch set. It separates regions of occurrence of the static limit from regions of Monod-like behavior. Should the limit point exist then, from Figure 7.5a, it can be seen that another element of the branch set is the position of the limit point relative to the root. The condition $LP_1 = CP$ is therefore another element of the branch set. It is equivalent to

$$\gamma_1 = \frac{(\phi - 1 + p)^2}{(2\phi - (1-p)\alpha)^2} \tag{7.56}$$

Finally, as can be seen from Figure 7.5a, the location of the y-values of limit point LP_1 relative to that of BP_2 constitutes another, and the last element of the branch set. This condition is equivalent to

$$(1-p)\bar{r}_1(LP_1) = \bar{r}_2(\bar{S}_f) \tag{7.57}$$

and yields

$$\gamma_1 = \frac{1}{4}\left(\frac{(\alpha + \bar{S}_f)(1-p)}{\phi\bar{S}_f} - 1\right))^2 \tag{7.58}$$

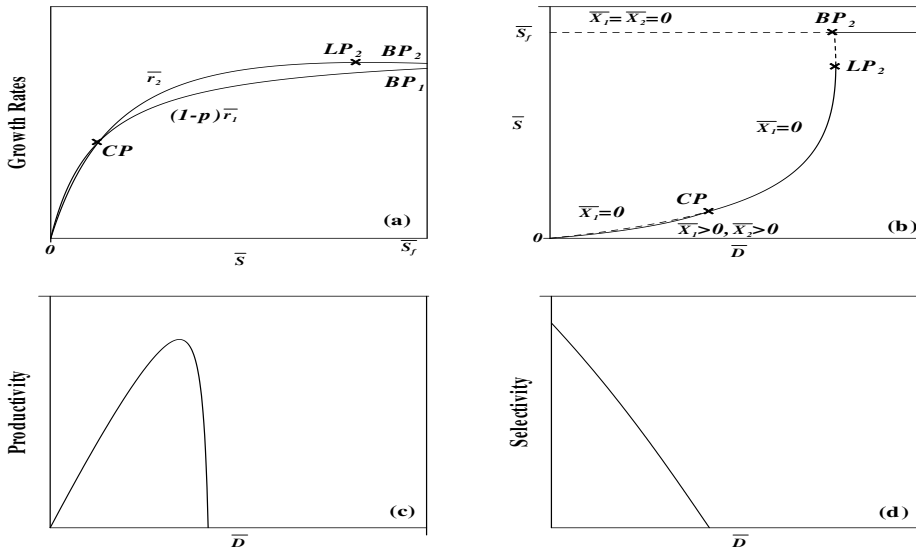

FIGURE 7.15: Details of region MI8 of Figure 7.9b: (a) Growth rates; (b) Continuity diagram; (c) Productivity; (d) Selectivity; solid line, stable; dashed line, unstable.

Figure 7.5b shows the general form of the branch set. It can be noted that not all the regions are new. In fact only three new regions (IM1, IM2, IM3) are found in the branch set. Below the horizontal line, no limit point exists and the growth rate $\bar{r}_1$ exhibits a Monod-like behavior. Therefore, all the regions below this line have been discussed earlier in the branch set of the Monod-Monod case. The new IM1 region of the branch set is shown in Figure 7.6a. There is a limit point (LP_1), and the crossing CP of the growth rates occurs after the limit point. The corresponding steady-state portrait is shown in Figure 7.6b. The presence of the limit point introduces a saddle-node bifurcation. For dilution rates smaller than that of crossing CP, the operation of the bioreactor leads to a stable coexistence. For values of dilution rates between CP and LP_1, the steady-state portrait is characterized by bistability, i.e., coexistence of two stable branches: the branch of cell coexistence and that of plasmid-bearing washout. Different start-up conditions or fluctuations in operating parameters ($\bar{S}_f$ or $\bar{D}$) can cause the operation of the bioreactor to jump from one branch to the other. Values of dilution rates larger than LP_1 and smaller than BP_2 lead to plasmid-bearing washout, while larger values than BP_2 lead to total washout. The IM2 region is obtained from Figure 7.5b, after crossing the $LP_1 = BP_2$ line. Figure 7.7a shows that the maximum y-value of LP_1 is larger than that of BP_2. This is reflected in the steady-state portrait (Figure 7.7b), as the dilution rate for LP_1 is larger than that of BP_2. This introduces new changes in the static behavior as the region of bistability between the

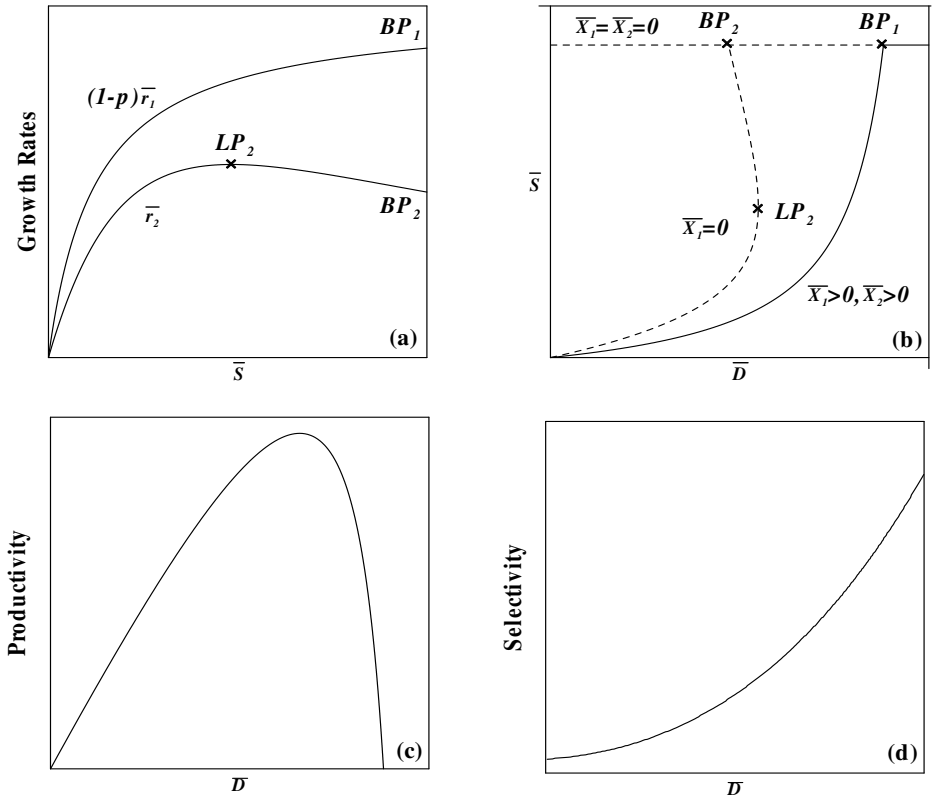

FIGURE 7.16: Details of region MI10 of Figure 7.9b: (a) Growth rates; (b) Continuity diagram; (c) Productivity; (d) Selectivity; solid line, stable; dashed line, unstable.

curve of plasmid-bearing washout and that of the coexistence extends from CP to BP_2. Moreover, another region of bistability exists between BP_2 and LP_1, and involves the coexistence branch and the total washout line. The last new region (IM3) of Figure 7.5b, is obtained after crossing the $\bar{S}_1 = \bar{S}_f$ line, so the crossing root $\bar{S}_1$ becomes larger than $\bar{S}_f$. Figure 7.8a shows that plasmid-bearing cells always outgrow their counterparts. The corresponding continuity diagram (Figure 7.8b) shows that for all dilution rates smaller than BP_1, a stable coexistence is the only outcome of the competition. For dilution rates between BP_1 and LP_1, the operation of the bioreactor may also lead to total washout while for dilution rates larger than LP_1, total washout occurs.

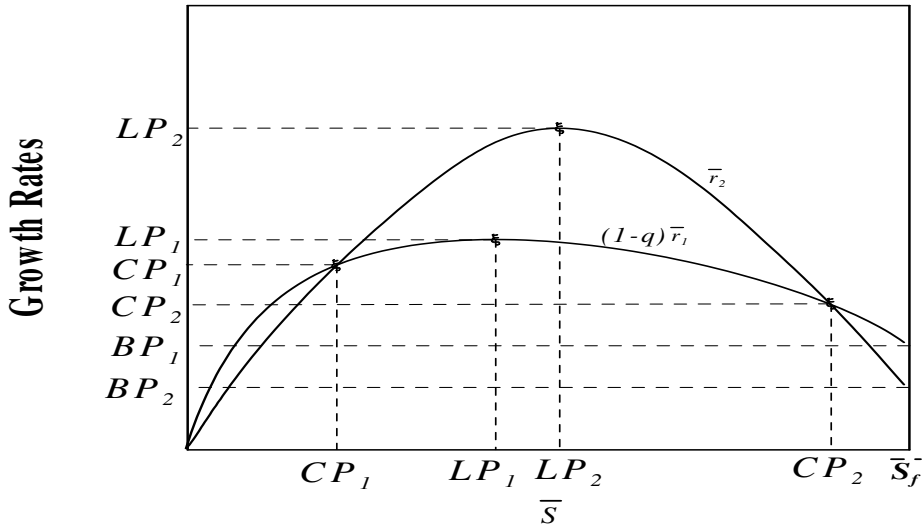

FIGURE 7.17: Example of mutual disposition of growth rates for inhibition-inhibition case.

7.4.3 Monod-Inhibition Case

For the Monod-inhibition case, the specific growth rates are given by Equation (7.36) with $\gamma_1 = 0$. We first start with the dynamic behavior. Unlike the previous cases and since $r_{2\bar{S}}$ may take negative values, the Hopf conditions (Equation (7.28)) may be satisfied for this case, and an oscillatory behavior cannot be ruled out. Moreover, the condition $\bar{r}_{2\bar{S}} < 0$ implies that Hopf points have to occur in the region of existence of static limit points. As for the static branch set, it is constructed in a similar way to the previous cases, for example in the parameter space (α, γ_2). Note that for this case the term $(a = (1-p)\gamma_2)$ of Equation (7.40) is always positive and since b is negative then the second root $\bar{S}_2$ (Equation (7.41)) is always positive. Therefore, unlike the inhibition-Monod case there is the possibility of two crossings of the growth rates, with $\bar{S}_1$ being always smaller than $\bar{S}_2$. Figure 7.9a shows an example of the mutual disposition of the two growth rates. The branch set consists of the following elements. Similarly to the previous case, the conditions $\Delta = 0$, $c = 0$, and $\bar{S}_1 = \bar{S}_f$ are the first three elements of the branch set. They separate regions of real, positive, and meaningful $(\leq \bar{S}_f)$ crossings to regions of no crossings. Also because of the inhibition nature of $\bar{r}_2$, the occurrence of static limit points is conditioned by $\gamma_2 = \frac{\alpha}{\bar{S}_f^2}$, which is another element of the branch set. It separates regions of occurrence of static limit points from regions of Monod-like behavior. The relative position of the limit point LP_2 and the root $\bar{S}_2$ introduces another element in the branch set. Finally, the relative position on the y-axis of LP_2 and BP_1 is the last element of the branch set.

Figure 7.9b shows the branch set for this case. Similarly to the previous case, there are a number of regions that are similar to the Monod-Monod case. The branch set introduces a total of ten new different regions. The discussion of all these regions would be a lengthy exercise. Instead, we prefer to examine

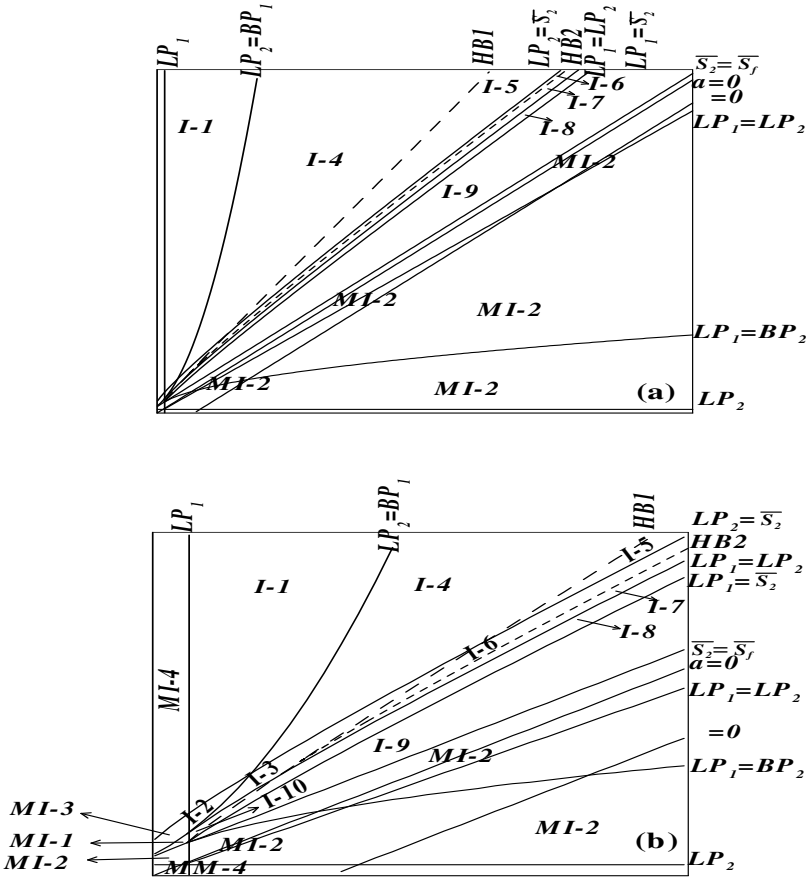

FIGURE 7.18: (a) Branch set for inhibition-inhibition case for $c < 0$; (b) Enlargement of (a).

features of key emerging regions. Region MI2 (Figure 7.10a) corresponds to the existence of one crossing and a limit point that occurs before the crossing and above BP_1. The corresponding continuity diagram (Figure 7.10b) shows the existence of a Hopf point as a result of dynamic bifurcation. The periodic branches are, however, unstable. Region MI3 (Figure 7.11a) is similar to region MI2 except that the y-value of LP_2 is smaller than that of BP_1. The continuity diagram (Figure 7.11b) shows the existence of a Hopf point and stable periodic branches emanating from it. Around the Hopf point, a

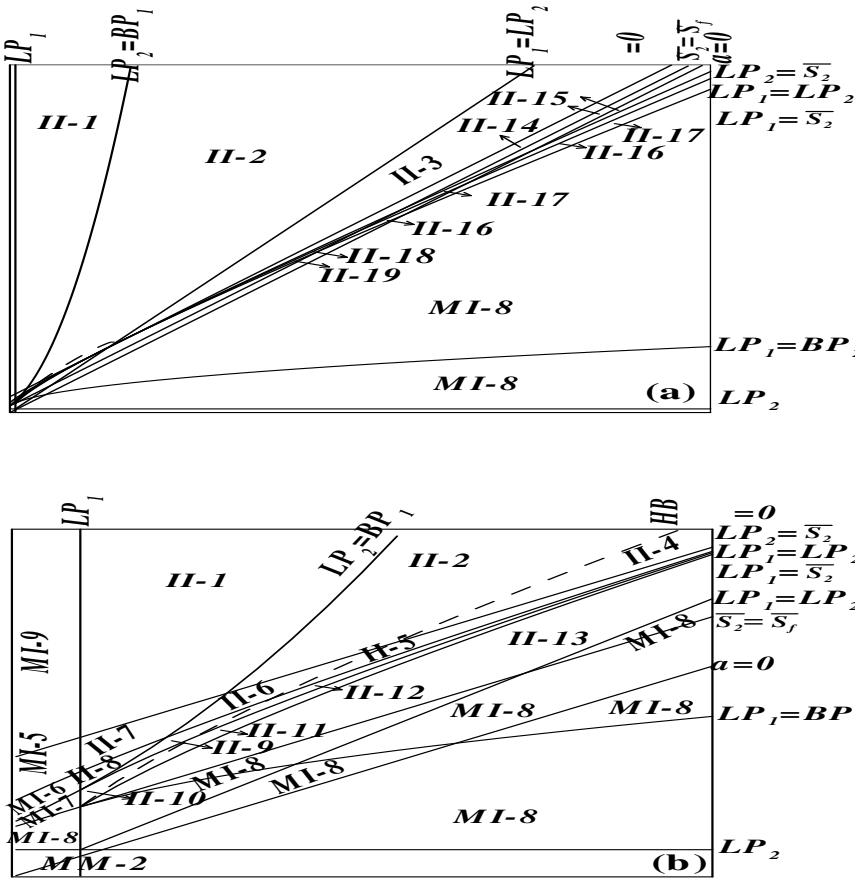

FIGURE 7.19: (a) Branch set for inhibition-inhibition case for $c > 0$; (b) Enlargement of (a).

stable periodic behavior exists. However, this periodic behavior also coexists with the static branch corresponding to plasmid-bearing washout. Therefore, different initial conditions can lead to either oscillations or to plasmid-bearing washout, as shown in Figures 7.12(a-b). Regions MI4 (Figure 7.13), MI5 (Figure 7.14), MI8 (Figure 7.15), and MI10 (Figure 7.16) do not predict any Hopf point but they exhibit interesting features for the profiles of productivity and selectivity. These features are discussed in a later section.

7.4.4 Inhibition-Inhibition Case

For the case of inhibition-inhibition, the growth rates are given by Equation (7.36). Figure 7.17 shows an example of mutual disposition of growth rates.

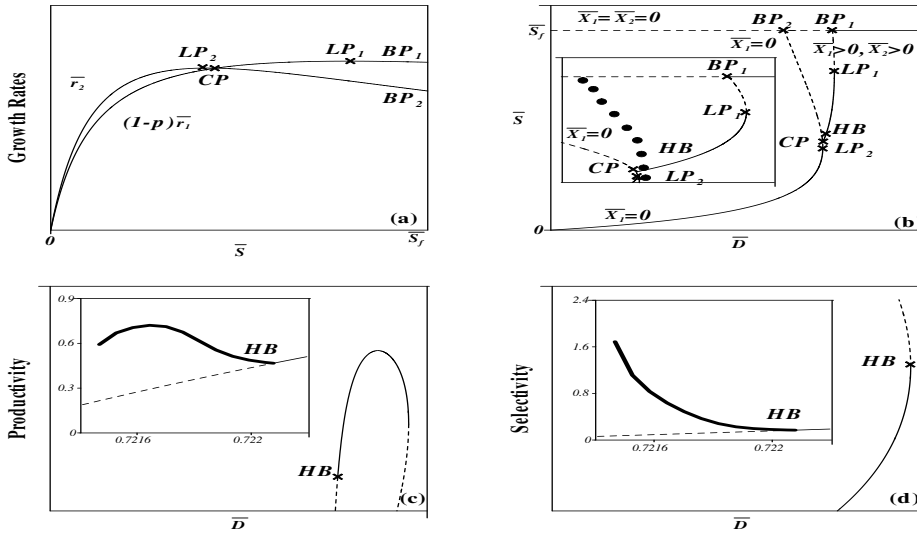

FIGURE 7.20: Details of region I2 of Figure 7.18b for ($\bar{S}_f = 8, \alpha = 1.1, \gamma_1 = 0.020, \gamma_2 = 0.1, \phi = 1.2, p = 0.01$): (a) Growth rates; (b) Continuity diagram; (c) Productivity; (d) Selectivity; solid line, stable; dashed line, unstable; dots, stable periodic branch; thick solid lines, average values.

Two limit points, as well as two crossings, are possible. We choose to represent the branch set in the parameter space (γ_1, γ_2). To construct the static branch set, the following conditions are considered. First, $\Delta = 0$ defines the region of the existence/absence of crossings between the growth rates. $\bar{S} = \bar{S}_f$ defines the region of meaningful/unmeaningful crossings. Since the terms a and c of the crossing Equation (7.39–7.40) can have arbitrary signs then both $a = 0$ and $c = 0$ are elements of the branch set. However, since c does not depend on γ_1 or γ_2, two separate branch sets are possible: one for $c < 0$ and another one for $c > 0$. The case of $c = 0$ (Equations (7.39–7.40)) introduces only one nontrivial crossing and does not produce any new regions. In addition to these conditions, the following other elements constitute the branch set. First, Equations (7.45, 7.48) define regions of existence/absence of static limit points. The condition $LP_1 = LP_2$ defines the relative position of static limit points while the condition $(1-p)\bar{r}_1(LP_1) = \bar{r}_2(LP_2)$ defines the relative position of the y-values (dilution rates) of LP_1 and LP_2. The two conditions $LP_1 = \bar{S}_1$ and $LP_2 = \bar{S}_2$ define, on the other hand, the relative position of the static limit points vis-à-vis the roots. Finally, the conditions $(1-p)\bar{r}_1(LP_1) = BP_2$ and $\bar{r}_2(LP_2) = BP_1$ define the relative position of the dilution rates associated with each limit point to those associated with $\bar{S}_f$. The analytical expressions of all these conditions are quite simple and can be derived in a similar manner to previous cases.

For the dynamic bifurcation, both the F_1 and the H_{01} singularity are de-

fined for the inhibition-inhibition case and are shown in the branch sets along with static branches. Figures 7.18(a–b) and Figure 7.19(a–b) show the branch sets respectively for $c < 0$ and $c > 0$. The combination of static and dynamic branches gives birth to a total of 10 new regions for the case of $c < 0$ and 19 new regions for $c > 0$. The rest of emerging regions are either Monod-inhibition (MI) or inhibition-Monod (IM) branches, and were discussed earlier. Once again we limit the discussion to key new regions. Regions I2 (Figure 7.20) and I3 (Figure 7.21) feature one Hopf point with stable periodic branches emanating from them. Region I6 (Figure 7.22), on the other hand, features two Hopf points with only one exhibiting stable periodic branches. Of all these regions, regions I2 (Figure 7.20) and I3 (Figure 7.21) feature new and interesting behavior. It can be seen in the enlargement of the continuity diagrams (Figure 20b and even clearer in Figure 7.21b) that stable periodic branches are the only attractors between LP_2 and HB. Unlike other regions for which stable periodic behavior coexists with static branches, all start up conditions for the region between LP_2 and HB lead to an oscillatory behavior. Regions II6 (Figure 7.23) and II13 (Figure 7.24) do not involve any Hopf points but they offer some new features as far as the selectivity is concerned. These regions are discussed in a later section.

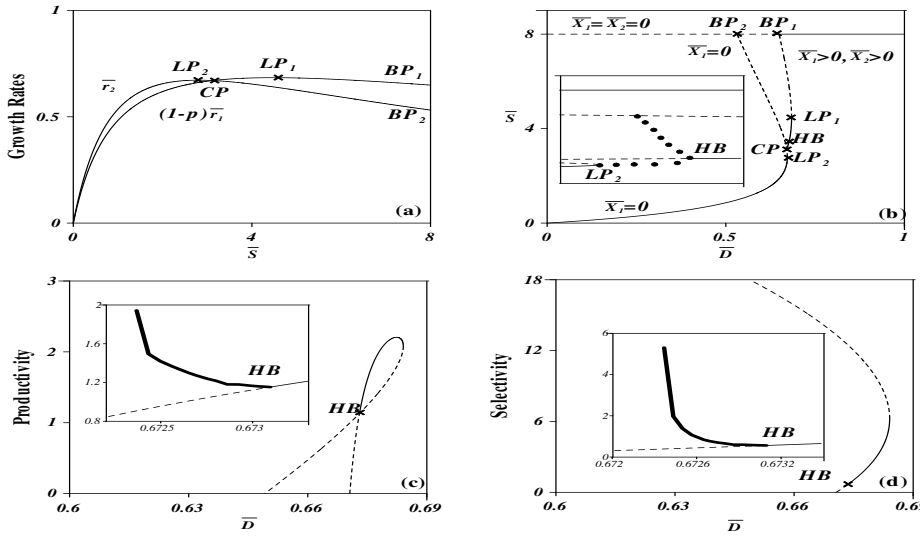

FIGURE 7.21: Details of region I3 of Figure 7.18b for ($\bar{S}_f = 8, \alpha = 1.1, \gamma_1 = 0.05, \gamma_2 = 0.14, \phi = 1.2, p = 0.01$): (a) Growth rates; (b) Continuity diagram; (c) Productivity; (d) Selectivity; solid line, stable; dashed line, unstable; dots, stable periodic branch; thick solid lines, average values.

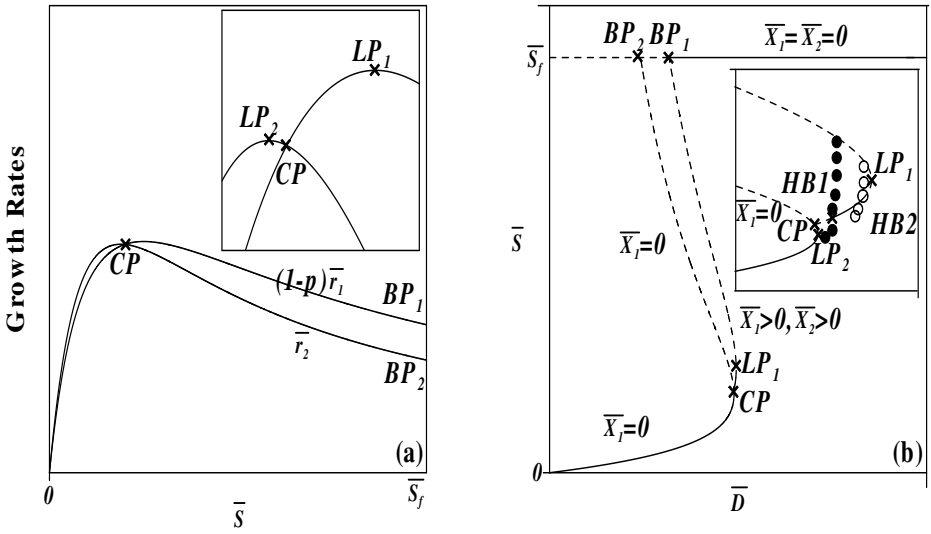

FIGURE 7.22: Details of region I6 of Figure 7.18b: (a) Growth rates; (b) Continuity diagram; solid line, stable; dashed line, unstable; dots, stable periodic branches; circles, unstable periodic branch.

7.5 Implication of Resulting Dynamics

The number (forty-five) of different regions found in this analysis is quite large. In order to carry out some kind of comparison between these regions, some of their key features are summarized in Table 7.1. This table can enable some insights about the possible effects that various limiting substrates can have on recombinant culture stability, and about the desired rate properties to be looked for in screening media formulations. Five criteria for comparison are selected: The first criteria is the number of regions of dilution rate where coexistence is possible. There are regions that do not predict a coexistence of cells, regions where the coexistence is limited to one range of dilution rates, and regions where coexistence is possible at small as well as at large dilution rates. The second characteristic concerns the existence/absence of bistability in the diagram. This includes bistability between cell coexistence and plasmid-bearing washout, bistability between coexistence and total washout as well as bistability between periodic branch and plasmid-bearing washout and/or total washout. The third feature is whether a Hopf point exists and whether stable or unstable periodic branches emanate from the point.

These three criteria concern the general aspects of the continuity diagram $(\bar{D}, \bar{S})$. We add to these criteria, some aspects associated with profiles of productivity and selectivity. The fourth feature, therefore, concerns the stability

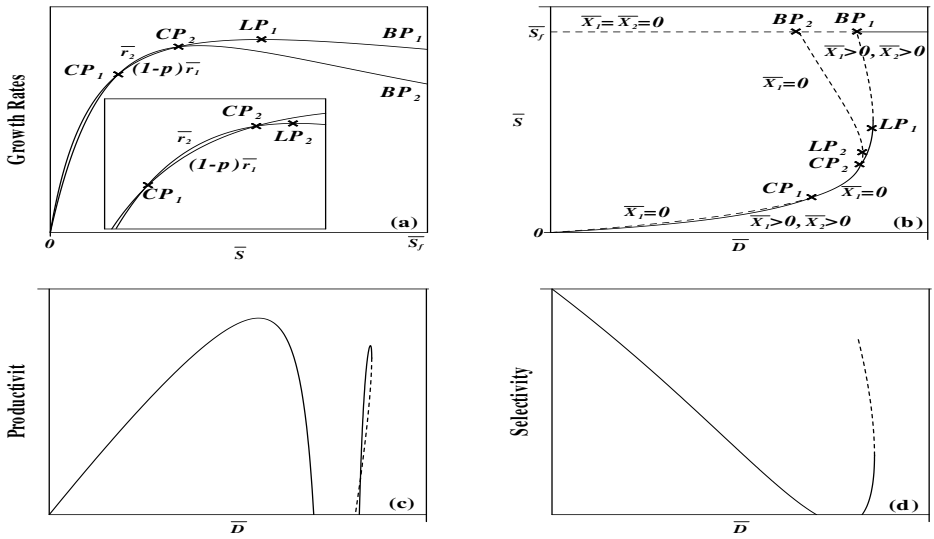

FIGURE 7.23: Details of region II6 of Figure 7.19b: (a) Growth rates; (b) Continuity diagram;(c) Productivity; (d) Selectivity; solid line, stable; dashed line, nstable.

nature of point of maximum productivity, i.e., stable/unstable, while the fifth feature concerns whether the maximum point occurs in a region of bistability. It is understood that if it is desired to operate the bioreactor at an unstable point or in a bistability region then a stabilizing effect (for example through feedback control) is needed. Table 7.1 summarizes the regions and their five features. Out of the total of forty-five regions, nine regions offer some interesting behavior. We will discuss these regions as well as the needed plasmid modifications that could achieve the desired mutual disposition of the growth rates. Region MM3 (Figure 7.4) certainly offers a desired scenario since it guarantees the outgrowth of plasmid-bearing cells over their counterparts over the whole range of substrate concentrations. However this cannot be achieved unless external change is applied, such as coding for antibiotic resistance [156, 330].

Region MI10 (Figure 7.16) offers a variation on MM3 where the plasmid-free cell is inhibited at high substrate concentrations while the plasmid-bearing cell is of the Monod form. Substrate inhibition was observed, for instance, in methanol utilizing organisms. Region MI10 may also offer an advantage over region MM3 in term of selectivity, since the selectivity is expected to be large when the difference between the growth rates is wide (Equation (7.14)). The scenario of MI10 could be achieved by further incorporation of a plasmid that deregulates growth inhibition of plasmid-bearing cells. In the MM2 case (Figure 7.3), both growths are of the Monod form with plasmid-bearing cells growing faster at smaller substrate concentrations. This could be achieved by

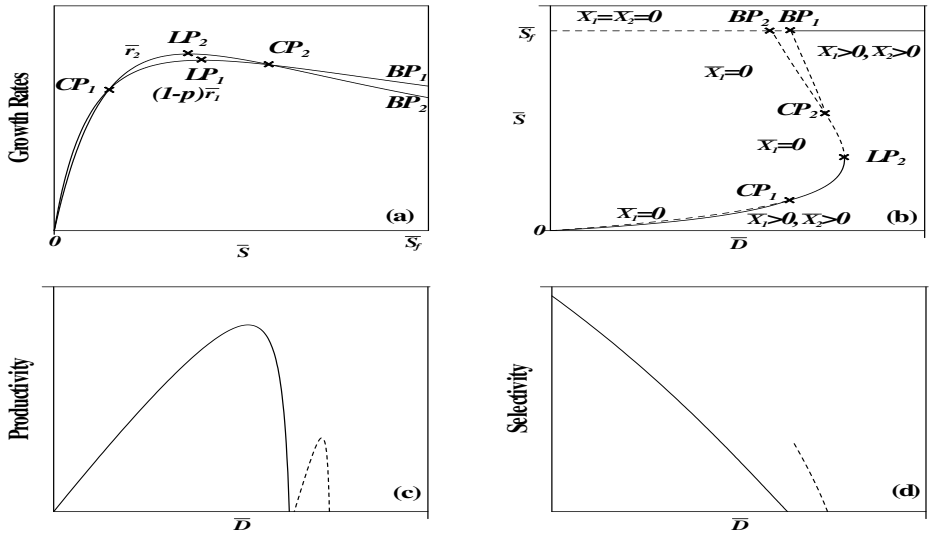

FIGURE 7.24: Details of region II13 of Figure19b: (a) Growth rates; (b) Continuity diagram;(c) Productivity; (d) Selectivity; solid line, stable; dashed line, unstable.

cloning the gene for the enzyme responsible for growth limitation in the recombinant plasmid. MI8 (Figure 7.15) presents a variation of MM2 where the plasmid-free cells are inhibited at larger substrate concentrations. Again this scenario can be achieved through the same approach applied to the MI10 region. Region MI4 (Figure 7.13), besides its obvious features (Table 7.1), offers another advantage in terms of selectivity, since the plasmid-free cells are inhibited at larger substrate concentrations while the growth of plasmid-bearing cells is of the Monod form. The maximum productivity can also be seen to occur after LP_2. Moreover, since the selectivity increases with the dilution rate, it could be beneficial to operate at values of dilution rates slightly larger than that of maximum productivity. The productivity will decrease slightly at the benefit of a larger selectivity. Again for the scenario of MI4 to be possible, further incorporation of a plasmid that deregulates growth inhibition of plasmid-bearing cells is required. MI5 region (Figure 7.14) offers the advantage of coexistence in two regions of the dilution rate with the maximum productivity occurring at a larger dilution rate. Similarly to region MI4, region MI5 also offers an advantage in terms of selectivity. The increasing profile of selectivity in the larger dilution rates region also suggests that a small sacrifice in productivity can be compensated for by a larger selectivity. The mutual disposition of growth rates in region MI5 is however quite distorted. It is an open question whether it is possible to achieve this type of growth rates disposition. Region II13 (Figure 7.24) is a variation of MI5 where the plasmid-bearing cell outgrows its counterpart in two different regions but plasmid-bearing cells are

inhibited. It can be seen that the maximum productivity occurs in regions of small dilution rates, while the selectivity is decreasing. In terms of selectivity this region is not attractive. Region II6 (Figure 7.23) represents the case when plasmid-bearing cells outgrow their counterparts in two regions, while both cells are inhibited at large substrate concentrations. Two regions of coexistence are therefore possible with the maximum productivity occurring in the region of smaller dilution rates. It can also be seen that the selectivity increases in the region of larger dilution rates. Therefore, it may be beneficial to operate in this region. However, the point of operation may be unstable and a feedback control is needed.

It can be noted that all the discussed regions do not exhibit a Hopf point. The issue to be investigated is whether there is any benefit from operating the bioreactor at a periodic regime. Our simulations for all regions that have Hopf(s) point(s), with the exception of region I3 (Figure 7.21), showed that the selectivity is smaller than if the chemostat is operated at static branches. Region I3 (Figure 7.21) offers, however, a different perspective on this subject. It should be recalled that in region I3 periodic behavior is the only attractor between LP_2 and the Hopf point. Shown in the small boxes of Figures 7.21(c–d) are respectively the average productivity and average selectivity of the periodic branches emanating from the Hopf point. Away from the Hopf point, the selectivity increases and exceeds even the value associated with the point of maximum productivity. Therefore, it may be beneficial to operate the bioreactor at this stable limit cycle.

7.6 Concluding Remarks

The stability behavior of the classical unstructured model for the competition between plasmid-bearing and plasmid-free cells was revisited using a combination of bifurcation and continuation techniques. The analysis of the model stability has offered a clear, yet simple picture of the dynamics of competitive growth which, at the end, has the most profound effect on the plasmid stability. Simple necessary conditions in terms of growth rates were also derived for the existence of Hopf points in the model. These general conditions were applied to Monod/Haldane substrate-inhibited growth models. Practical branch sets in terms of model parameters were readily constructed for Monod-Monod, Monod-inhibition, inhibition-Monod and inhibition-inhibition cases. The richness of the model was demonstrated by the large number of different behaviors found in it. But there is still room for further investigation. The analysis has revealed that the model can predict a maximum of seven Hopf points, but our numerical investigation revealed only two Hopf points. The existence of more than two Hopf points is certainly not ruled out. Would this be the case then this will give rise to a number of new singularities that connect

TABLE 7.1: Summary of the regions and their characteristics

Region	Criteria I	II	III	IV	V
MM1	0	No		No	No
MM2	1	No		Yes	No
MM3	1	No		Yes	No
IM1	1	Yes		Yes	No
IM2	1	Yes		Yes	Yes
IM3	1	Yes		Yes	No
MI1	0	No	Hopf-unstable	No	No
MI2	1	Yes		Yes	Yes
MI3	1	Yes	Hopf-stable	Yes	No
MI4	1	No		Yes	No
MI5	2	No		Yes	No
MI6	2	Yes	Hopf-stable	Yes	No
MI7	2	Yes	Hopf-unstable	Yes	No
MI8	1	No		Yes	No
MI9	2	No		Yes	No
MI10	1	No		Yes	No
I1	1	Yes		Yes	No
I2	1	Yes	Hopf-stable	Yes	No
I3	1	Yes	Hopf-stable	Yes	Yes
I4	1	Yes		Yes	Yes
I5	1	Yes	Hopf-unstable	Yes	Yes
I6	1	Yes	2 Hopfs-one stable	No	No
I7	1	No		No	No
I8	1	No		No	No
I9	1	No		No	No
I10	1	Yes	Hopf-stable	Yes	Yes
II1	1	Yes		Yes	Yes
II2	1	Yes		Yes	Yes
II3	1	Yes		Yes	Yes
II4	1	Yes	Hopf-stable	Yes	No
II5	2	Yes		Yes	No
II6	2	Yes		Yes	No
II7	2	Yes		Yes	No
II8	2	Yes		Yes	No
II9	2	Yes		Yes	No
II10	2	Yes		Yes	No
II11	1	No		No	No
II12	2	No		Yes	No
II13	2	No		Yes	No
II14	2	Yes		Yes	Yes
II15	1	Yes		Yes	Yes
II16	1	Yes		Yes	Yes
II17	2	Yes		Yes	Yes
II18	2	Yes		Yes	Yes
II19	2	Yes		Yes	Yes

the different Hopf points, and this would certainly add more richness to the model. From a practical point of view, the study of Hopf points is useful from two perspectives. On one hand, it helps to investigate whether the operation of the chemostat in a periodic region can be beneficial in terms of productivity and selectivity. On the other hand, it helps to study if strange chaotic or nonchaotic behavior can emerge from the bifurcation of periodic attractors. Our investigation did not encounter any such behavior but given the richness of the model, this cannot be ruled out and it deserves further investigation.

Finally, it should be noted that a number of studies investigated ways to improve the stability of these systems. These include introducing changes in feeding strategy, the alteration of the medium in such a way as to favor the plasmid-bearing organism and the operation of the bioreactor under cycling conditions [77, 195, 204, 276, 277, 330, 338, 339, 345, 372].

Chapter 8

BIODEGRADATION OF MIXED SUBSTRATES

8.1 Introduction

The simultaneous biodegradation of mixed wastes is an important class of biological processes. In a number of applications, the growth of the biomass in a microbial system is not limited by one nutrient, but rather by two or more nutrients that are serving the needs of the micro-organism simultaneously. In wastewater applications, for instance, it is known that the availability of multiple carbon/energy sources often enhances the biodegradation of recalcitrant compounds. Mixed-substrate growth is also important in ecology, since microbial growth in a natural mixed-substrate environment plays a fundamental role in maintaining global environmental balance. The growing interest in in-situ microbial degradation of groundwater sources, contaminated by different pollutants, is another example of the need for better understanding of the mixed-substrate growth.

Nutrients generally can be grouped according to their physiological function [381]. Homologous nutrients, also called perfectly substitutable substrates [294] or mixed substrates [257] are nutrients that accomplish the same physiological function during growth. Examples of such mixtures include pairs of carbon and energy sources (e.g., glucose, fructose), nitrogen sources (e.g., ammonia, nitrate) or electron acceptors (e.g., oxygen, nitrate) [107, 255]. Heterologous nutrients, also called noninteractive or complementary nutrients, are on the other hand, nutrients that satisfy different physiological requirements of the cell. For example, nitrogen (e.g., ammonium) and a carbon source (e.g., glucose) are heterologous substrates since one cannot be replaced by the other, at least when they contain no C or N, respectively. A classification of nutrients to other subgroups is also available in the literature [381].

One important goal in modeling microbial growth under dual nutrients is the development of adequate growth kinetics. Zinn et al. [381] provided an excellent review of modeling approaches and some resulting models. Some of the commonly used models include simple extension of Monod growth (Equation (2.18)) [245], and the sum of growth rates on individual nutrients (Equation (2.19)) [216, 217, 218], as well as cybernetic models [342]. But as was mentioned in [381], some of these models suffer from lack of experimental valida-

tion while others such as cybernetic models require a detailed quantification of the microbial system, which is sometimes beyond reasonable measurement techniques.

In this chapter, we study the stability of the biodegradation of mixed wastes in a continuous bioreactor modeled by an unstructured model. The objective is to delineate the different static behaviors the model can predict and study its implications on the outcome of the biodegradation [17, 22]. The selected growth rates are based on the experimental work of Baltzis el al. [50, 210, 364] who showed that cross-inhibitory expressions are the most adequate kinetic models for predicting the growth of a pure culture of *Pseudomonas putida* in a media containing phenol and glucose. These growth models were successfully used in stability and optimization studies in cyclically operated bioreactors [50, 210, 364].

8.2 Bioreactor Model

We consider a bioreactor with cell recycle similar to the one in Figure 4.1. A microbial culture (X) is capable of utilizing two dissimilar substrates (S_1) and (S_2). The balance equations around the reactor for the different species are:

$$S_{f_1} - S_1 - \theta \frac{r_1 X}{Y_1} = \theta \frac{dS_1}{dt} \tag{8.1}$$

$$S_{f_2} - S_2 - \theta \frac{r_2 X}{Y_2} = \theta \frac{dS_2}{dt} \tag{8.2}$$

$$X_f - WX + \theta(r_1 + r_2)X = \theta \frac{dX}{dt} \tag{8.3}$$

where $\theta = \frac{V}{Q}$ is the reactor residence time (inverse of dilution rate), r_1, r_2 are respectively the specific growth rates associated with utilization of S_1 and S_2, and W is the purge fraction. The two substrates are involved in an uncompetitive cross inhibitory interaction with utilization rates, given by

$$r_1 = \frac{\mu_1 S_1}{K_1 + S_1 + S_1^2/K_I + K_3 S_1 S_2} \tag{8.4}$$

and

$$r_2 = \frac{\mu_2 S_2}{K_2 + S_2 + K_4 S_1 S_2} \tag{8.5}$$

In the absence of S_2, the culture grows on substrate S_1 following Haldane inhibition kinetics. In the absence of S_1, the culture grows on substrate S_2 following Monod kinetics. When the medium contains both S_1 and S_2, the culture utilizes both of them simultaneously with the modified growth rates. The mass balances are suitably rendered dimensionless using the variables

TABLE 8.1:
Dimensionless variables

Parameter	Definition
θ	$\theta\mu_1$
$\bar{S}_1$	$\frac{S_1}{K_1}$
$\bar{S}_2$	$\frac{S_2}{K_2}$
$\bar{t}$	$\frac{t}{\theta}$
$\bar{X}$	$\frac{X}{Y_1K_1}$
α	$\frac{K_1}{K_I}$
γ	$\frac{Y_1K_1}{Y_2K_2}$
μ	$\mu_2\mu_1$
λ_1	K_2K_3
λ_2	K_1K_4

shown in Table 8.1. The dimensionless model equations are:

$$\bar{S_{f}}_1 - \bar{S}_1 - \bar{\theta}\bar{r}_1\bar{X} = \frac{d\bar{S}_1}{d\bar{t}} \tag{8.6}$$

$$\bar{S_{f}}_2 - \bar{S}_2 - \bar{\theta}\gamma\mu\bar{r}_2\bar{X} = \frac{d\bar{S}_2}{d\bar{t}} \tag{8.7}$$

$$\bar{X}_f - W\bar{X} + \bar{\theta}(\bar{r}_1 + \mu\bar{r}_2)\bar{X} = \frac{d\bar{X}}{d\bar{t}} \tag{8.8}$$

The dimensionless growth rates are given by

$$\bar{r}_1 = \frac{\bar{S}_1}{1 + \bar{S}_1 + \alpha\bar{S}_1^2 + \lambda_1\bar{S}_1\bar{S}_2} \tag{8.9}$$

and

$$\bar{r}_2 = \frac{\bar{S}_2}{1 + \bar{S}_2 + \lambda_2\bar{S}_1\bar{S}_2} \tag{8.10}$$

TABLE 8.2: Nominal values of parameters

Parameter	Nominal Value
α	0.0599
λ_1	1.1936
λ_2	0.244
γ	0.7136
μ	0.9365
$\bar{S}_{f_1}$	4.
$\bar{S}_{f_2}$	2
$\bar{X}_f$	0.1

8.3 Static Analysis

A simple relation involving the three species can be obtained by multiplying the steady-state forms of Equation (8.6) and Equation (8.8) by γ and summing up Equations (8.6–8.8). This yields

$$\bar{X} = \frac{\bar{S}_{f_1} - \bar{S}_1}{w} + \frac{\bar{S}_{f_2} - \bar{S}_2}{\gamma w} + \frac{\bar{X}_f}{w} \tag{8.11}$$

Substituting for $\bar{X}$ in the steady-state form of Equation (8.6) yields,

$$\bar{S}_{f_1} - \bar{S}_1 = \frac{\bar{\theta}\bar{S}_1}{1 + \bar{S}_1 + \bar{\alpha}\bar{S}_1^2 + \lambda_1\bar{S}_1\bar{S}_2}\left(\frac{\bar{S}_{f_1} - \bar{S}_1}{w} + \frac{\bar{S}_{f_2} - \bar{S}_2}{\gamma w} + \frac{\bar{X}_f}{w}\right) \tag{8.12}$$

By expanding this relation, the substrate concentration $\bar{S}_2$ can be obtained explicitly as a function of $\bar{S}_1$ and the other model parameters,

$$\bar{S}_2 = \frac{f_1(\bar{S}_1)}{f_2(\bar{S}_1)} \tag{8.13}$$

where

$$f_1(\bar{S}_1) \quad := \quad -(\bar{S}_{f_1} - \bar{S}_1)(1 + \bar{S}_1 + \alpha\bar{S}_1^2) + \frac{\bar{S}_1\theta}{w}(\bar{S}_{f_1} - \bar{S}_1) + \frac{\bar{S}_1\bar{\theta}}{w}(\bar{X}_f + \frac{\bar{S}_{f_2}}{\gamma}) \tag{8.14}$$

$$f_2(\bar{S}_1) := \frac{\bar{\theta}\bar{S}_1}{\gamma w} + \lambda_1\bar{S}_1(\bar{S}_{f_1} - \bar{S}_1) \tag{8.15}$$

Another relation is obtained by dividing the steady-state form of Equation (8.6) by Equation (8.7), yielding a relation between $\bar{S}_1$ and $\bar{S}_2$ that does not involve the residence time $\bar{\theta}$,

$$\frac{\bar{S}_{f\,1} - \bar{S}_1}{\bar{S}_{f\,2} - \bar{S}_2} = \frac{\bar{r}_1}{\mu\gamma\bar{r}_2} \tag{8.16}$$

Substituting for the expressions of the growth rates (Equations (8.9–8.10)) and expanding Equation (8.16) yields,

$$\mu\gamma(\bar{S}_2\bar{S}_{f\,1} - \bar{S}_1)(1 + \bar{S}_1 + \alpha\bar{S}_1^2 + \lambda_1\bar{S}_1\bar{S}_2) \quad = \quad \bar{S}_1(\bar{S}_{f\,2} - \bar{S}_2)(1 + \bar{S}_2 + \lambda\bar{S}_1\bar{S}_2) \tag{8.17}$$

Finally, substituting Equation (8.13) into Equation (8.17) yields a single seven-order polynomial in $\bar{S}_1$.

The steady states of the model are bounded. The substrate concentrations $\bar{S}_1$ and $\bar{S}_2$ are bounded by the feed conditions $\bar{S}_{f1}$ and $\bar{S}_{f2}$, while the maximum concentration $\bar{X}_{max}$ of the biomass is obtained by setting $\bar{S}_1 = \bar{S}_2 = 0$ in Equation (8.11) to yield

$$\bar{X}_{max} = \frac{\bar{S}_{f\,1}}{w} + \frac{\bar{S}_{f\,2}}{\gamma w} + \frac{\bar{X}_f}{w} \tag{8.18}$$

In the following, we study the occurrence of static singularities in the model.

8.3.1 Hysteresis

The conditions for the appearance/disappearance of a hysteresis loop are that

$$F = F_{\bar{S}_1} = F_{\bar{S}_1\bar{S}_1} = 0 \tag{8.19}$$

In addition to $F_{\bar{\theta}}$, $F_{\bar{S}_1\bar{\theta}}$, and $F_{\bar{S}_1\bar{S}_1\bar{S}_1}$ being non-nil.

The set of nonlinear Equations (8.19) is solved to determine the limits of the hysteresis regions using the nominal values of the model kinetic and operating parameters, shown in Table 8.2. Figures 8.1–8.2 show the hysteresis boundaries in the parameter space of the different model parameters. The boundary lines divide each of the parameter space in two regions. Region (I) is characterized by the presence of two static limit points. Figure 8.3a shows an example of the behavior in this region for $(\bar{S}_{f\,1}, \bar{S}_{f\,2}) = (3.5, 3)$. If the parameters of the model move on the boundary itself then the two static limit points collapse in one point, as shown in the continuity diagram of Figure 8.3b, obtained with $(\bar{S}_{f\,1}, \bar{S}_{f\,2}) = (2.141, 3)$. When crossing the boundary to region (II), the two static limit points disappear and a unique steady-state solution is found, as shown in the continuity diagram of Figure 8.3c, obtained with $(\bar{S}_{f\,1}, \bar{S}_{f\,2}) = (1, 3)$. It should be noted that although the general model

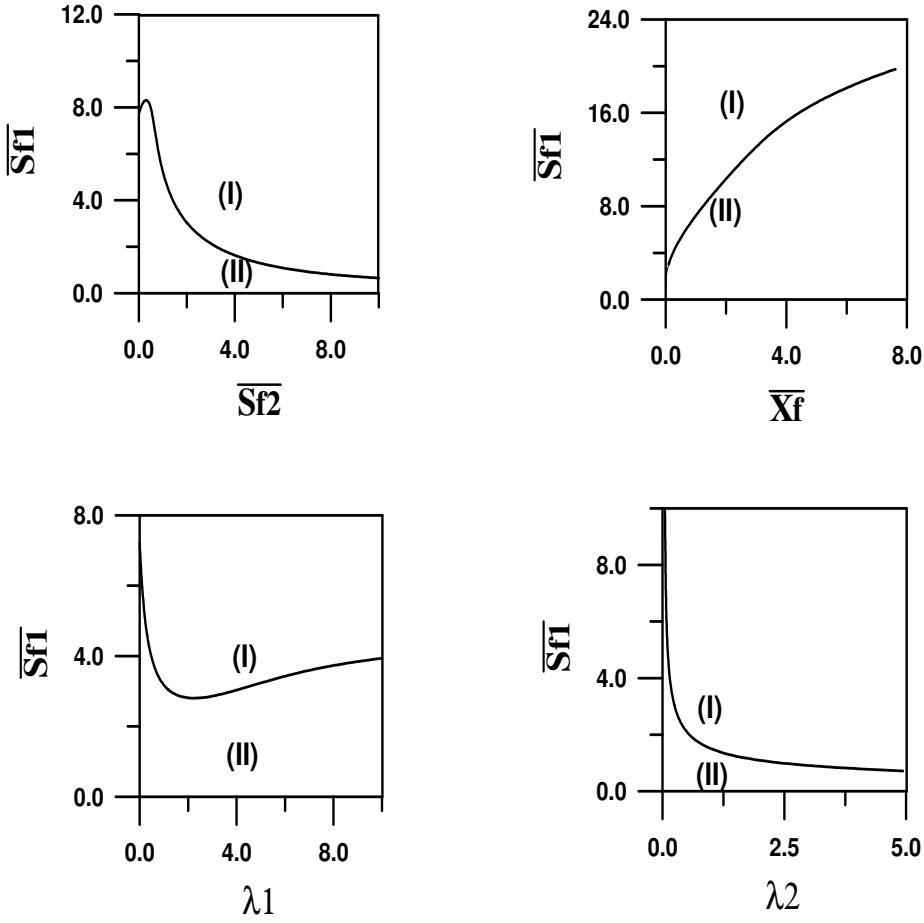

FIGURE 8.1: Branch sets for hysteresis singularity.

Equation (8.17) predicts a maximum of seven steady-state solutions, the studied model with the values of kinetic parameters was unable to predict more than three steady-state solutions. The other four solutions are either complex or physically unrealistic.

Figures 8.1–8.2 also allow the analysis of the effect of the model parameters on the stability of the bioreactor. It can be seen in the domain $(\bar{S_f}_2, \bar{S_f}_1)$ that an increase in the feed concentration $\bar{S_f}_2$ enlarges the domain of hysteresis (region I), since multiplicity can occur for smaller values of $\bar{S_f}_1$. An increase in cell feed concentration $\bar{X}_f$ reduces the region of instability and allows to operate at larger values of $\bar{S_f}_1$ without the occurrence of hysteresis. Small values of the cross-substrate inhibition constant λ_1, stabilize the process (re-

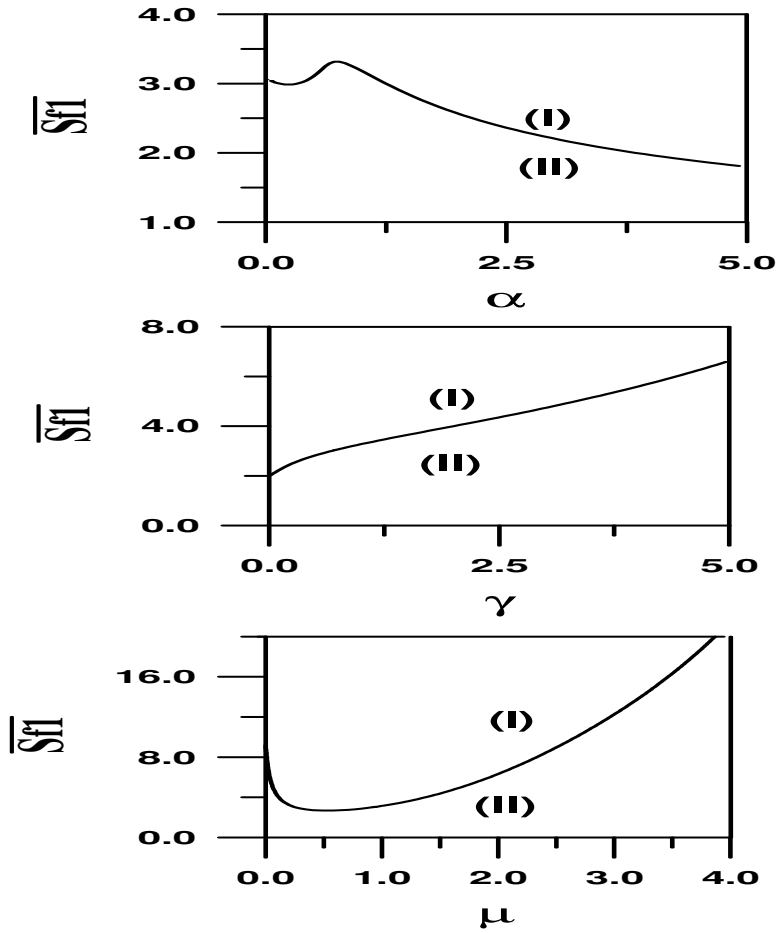

FIGURE 8.2: Branch sets for hysteresis singularity.

gion II is larger) while larger values of λ_1 also increase the stability, although mildly.

In contrast to λ_1, the increase in the other cross-substrate inhibition constant λ_2, enlarges the instability of the process. The increase in the self-substrate inhibition constant (α) also increases region I of hysteresis. The effect of an increase in γ can be seen to enlarge the region of Monod-like behavior. It can be recalled that γ incorporates the ratio of the yield coefficients and the dimensional saturation constants. Finally, increasing the product (μ) of the maximum specific growth rates also increases the stability of the process.

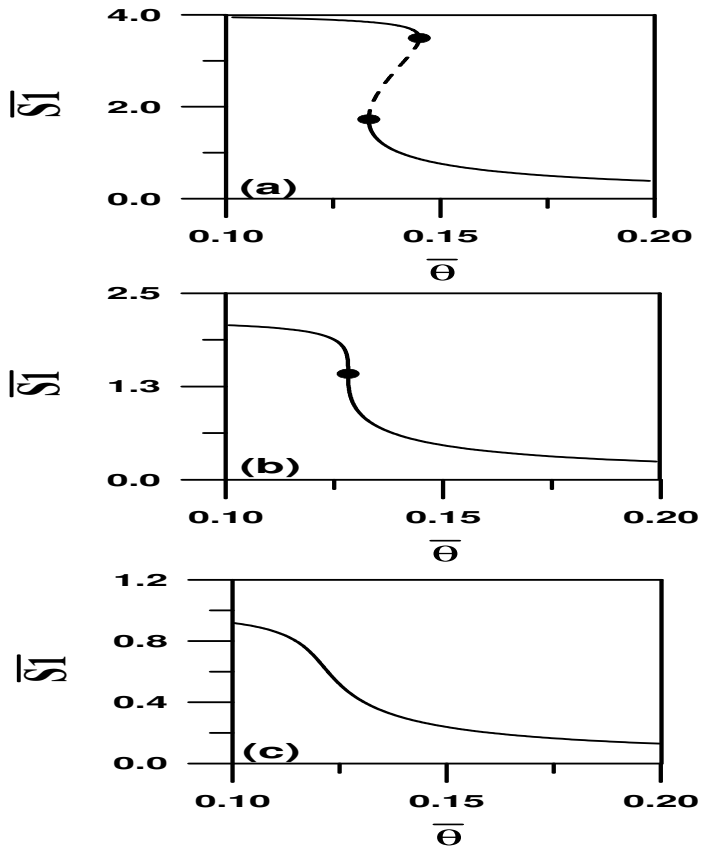

FIGURE 8.3: Continuity diagrams for the different regions of Figure 8.1: (a) Three solution in region (I); (b) The two static limit point collapse in on point on the boundary; (c) Unique solution in region (II); solid line, stable branch; dashed line, unstable.

8.3.2 Isola and Mushroom

The conditions for these two changes are:

$$F = F_{\bar{S}_1} = F_{\bar{\theta}} = 0 \tag{8.20}$$

with the additional requirements that

$$F_{\bar{S}_1\bar{\theta}} \neq 0, F_{\bar{S}_1\bar{S}_1} \neq 0, F_{\bar{\theta}\bar{\theta}} \neq 0 \tag{8.21}$$

To establish the conditions for the existence of isola, we start with the steady-state form of Equation (8.6) that gives an implicit relation for $\bar{S}_1$,

$$F(\bar{S}_1) := \bar{S}_{f_1} - \bar{S}_1 - \bar{\theta}\bar{r}_1\bar{X} = 0 \tag{8.22}$$

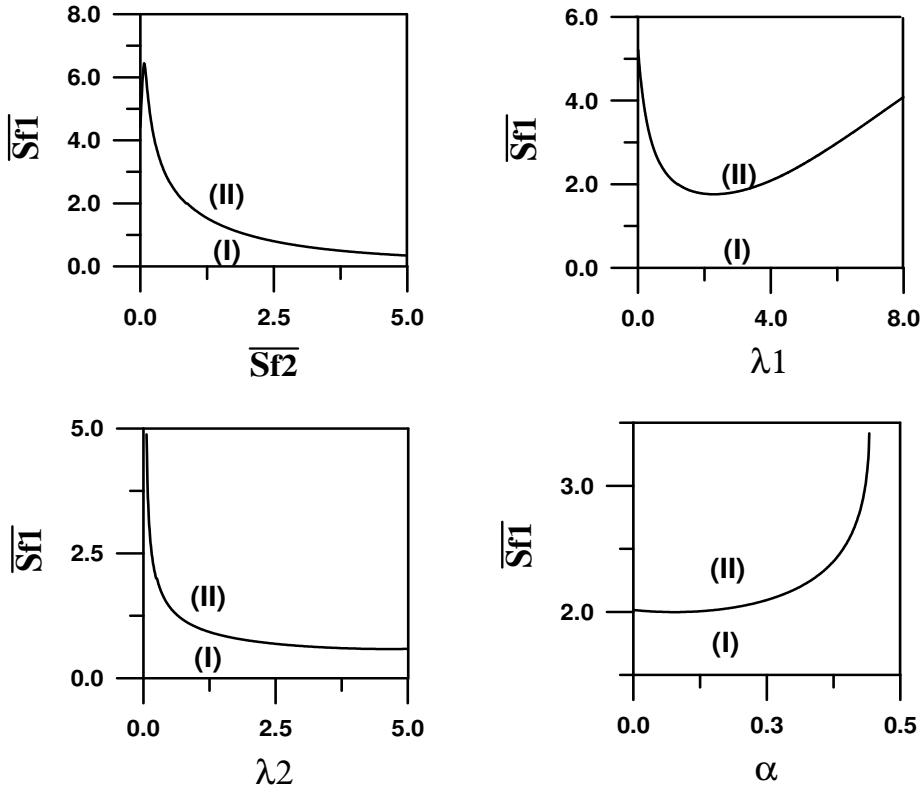

FIGURE 8.4: Branch sets for the pitchfork singularity.

Substituting for the expression of $\bar{X}$ from Equation (8.11) yields,

$$F(\bar{S}_1) := \bar{S}_{f_1} - \bar{S}_1 - \bar{\theta}\bar{r}_1\left(\frac{\bar{S}_{f_1} - \bar{S}_1}{w} + \frac{\bar{S}_{f_2} - \bar{S}_2}{\gamma w} + \frac{\bar{X}_f}{w}\right) \tag{8.23}$$

This relation is linear in $\bar{\theta}$, since the explicit relation between $\bar{S}_2$ and $\bar{S}_1$ (Equation (8.13)) does not involve $\bar{\theta}$. Taking the derivative of F with respect to $\bar{\theta}$ yields then

$$F_{\bar{\theta}} = -\bar{r}_1\left(\frac{\bar{S}_{f_1} - \bar{S}_1}{w} + \frac{\bar{S}_{f_2} - \bar{S}_2}{\gamma w} + \frac{\bar{X}_f}{w}\right) \tag{8.24}$$

The condition $F_{\bar{\theta}} = 0$ for the existence of the isola, requires that one of the two terms of Equation (8.24) vanishes. Condition $\bar{r}_1 = 0$ implies necessarily that $\bar{S}_1 = 0$. The second term is, on the other hand, always positive, since $\bar{S}_{f_1} \geq \bar{S}_1, \bar{S}_{f_2} \geq \bar{S}_2$, and $\bar{X}_f \geq 0$. This term vanishes only if

$$\bar{S}_1 = \bar{S}_{f_1}, \quad \bar{\mathrm{S}}_2 = \bar{\mathrm{S}}_{\mathrm{f}2}, \quad \bar{\mathrm{X}}_{\mathrm{f}} = 0 \tag{8.25}$$

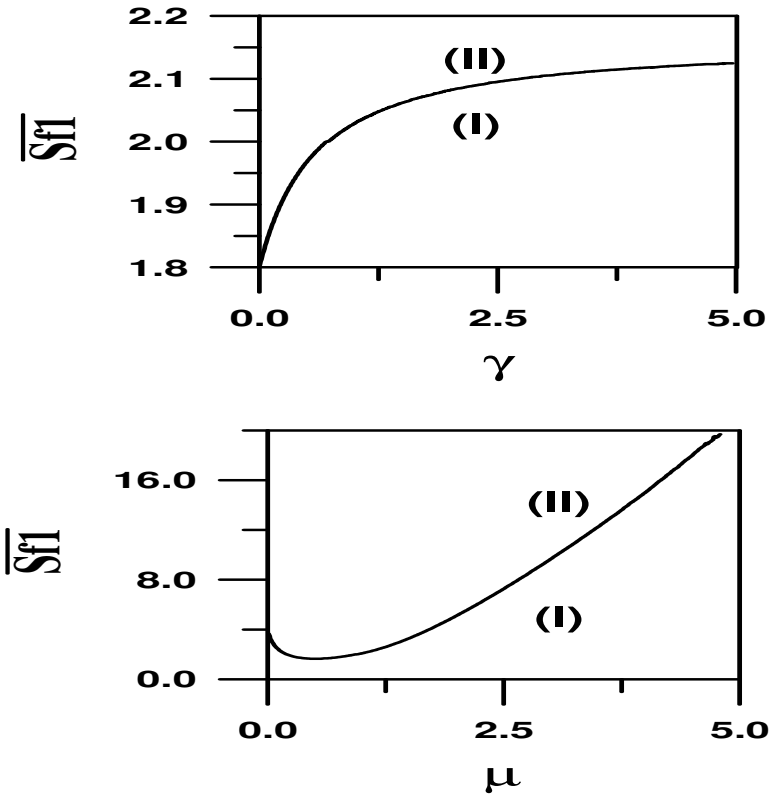

FIGURE 8.5: Branch sets for the pitchfork singularity.

This corresponds to washout conditions. However, since F is linear in $\bar{\theta}$, the term $F_{\bar{\theta}\bar{\theta}}$ is always equal to zero, thus violating the condition (Equation (8.21)) of the existence of isola. We conclude therefore that the model cannot exhibit an isola or mushroom singularity.

8.3.3 Pitchfork Singularity

The requirements for pitchfork singularity are

$$F = F_{\bar{S}_1} = F_{\bar{\theta}} = F_{\bar{S}_1\bar{S}_1} = 0 \tag{8.26}$$

and

$$F_{\bar{S}_1\bar{\theta}} \neq 0, F_{\bar{S}_1\bar{S}_1\bar{S}_1} \neq 0 \tag{8.27}$$

Since the condition of the existence of a pitchfork includes the condition $F_{\bar{\theta}} = 0$, as in the case before of the isola and mushroom, it is clear that the only

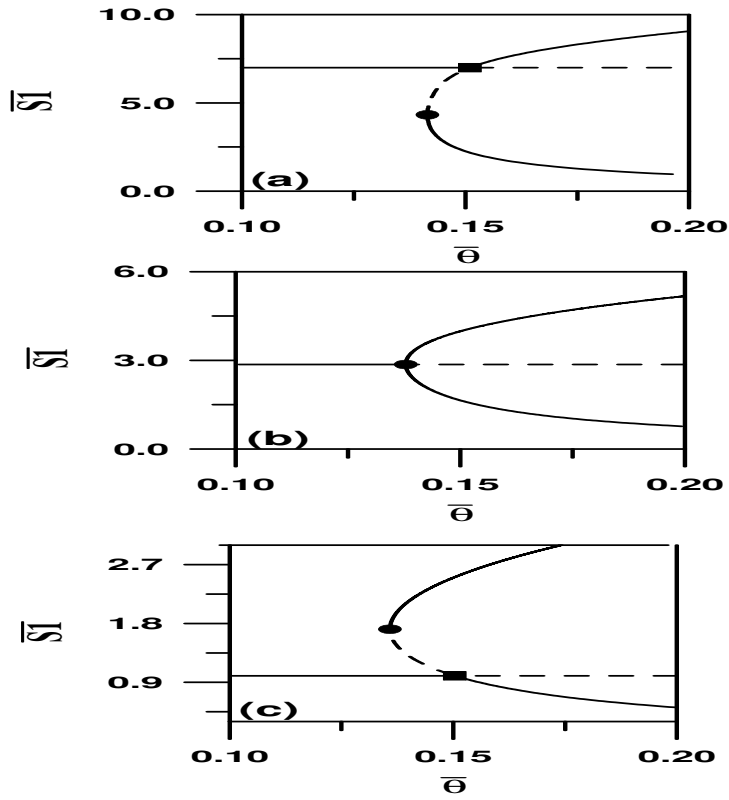

FIGURE 8.6: Continuity diagrams for the different regions of Figure 8.4: (a) Imperfect pitchfork in region (I); (b) Perfect pitchfork on the boundary; (c) The limit point is located on the upper physically realistic branch in region (II); solid line, stable branch; dashed line, unstable; circle, static limit point; square, bifurcation point.

possible cases when the system can predict a pitchfork are either when $\bar{S}_1 = 0$ or at the washout conditions.

For the case $\bar{S}_1 = 0$ the model (Equations (8.6, 8.8)) is reduced to

$$\bar{S}_{f_2} - \bar{S}_2 - \mu\gamma\bar{r}_2\bar{X}\bar{\theta} = 0 \tag{8.28}$$

$$\bar{X}_f - w\bar{X} + \mu\bar{r}_2\bar{X}\bar{\theta} = 0 \tag{8.29}$$

The specific growth rate $\bar{r}_2$ (Equation (8.10)) becomes,

$$\bar{r}_2 = \frac{\bar{S}_2}{1 + \bar{S}_2} \tag{8.30}$$

Eliminating the rate $\bar{r}_2$ (Equations (8.28–8.29)) yields a simple relation be-

tween $\bar{X}$ and $\bar{S}_2$,

$$\bar{X} = \frac{\bar{S}_{f\,2} - \bar{S}_2}{\gamma w} + \frac{\bar{X}_f}{w} \tag{8.31}$$

Substituting back in Equation (8.28) results in a second-order polynomial in $\bar{S}_2$,

$$F(\bar{S}_2) := a_2 \bar{S}_2^2 + a_1 \bar{S}_2 + a_0 = 0 \tag{8.32}$$

where

$$a_0 = -\bar{S}_{f\,2} w, \quad \mathrm{a_1} = -\mu \bar{\mathrm{S}}_{\mathrm{f\,2}} \bar{\theta} - \mathrm{w} + \bar{\mathrm{S}}_{\mathrm{f\,2}} \mathrm{w} - \mu\gamma\bar{\theta}\bar{\mathrm{X}}_{\mathrm{f}}, \quad \mathrm{a_2} = \mu\bar{\theta} + \mathrm{w} \tag{8.33}$$

A quadratic equation such as Equation (8.33) cannot predict a pitchfork singularity since the third-order derivative $F_{\bar{S}_2 \bar{S}_2 \bar{S}_2}$ is always zero. The only remaining case for which a pitchfork singularity can exist is at washout conditions (Equation (8.25)). However, at clean feed conditions of $\bar{X}_f = 0$, Equation (8.8)

$$\bar{X} = \frac{\bar{X}_f}{w - (\bar{r}_1 + \mu \bar{r}_2)\bar{\theta}} \tag{8.34}$$

predicts washout conditions, i.e., $\bar{X} = 0$, unless the rate expressions satisfy the following relation

$$w - (\bar{r}_1 + \mu \bar{r}_2)\bar{\theta} = 0 \tag{8.35}$$

It follows that the pitchfork singularity occurs when the washout line (Equation (8.25)) crosses the curve defined by Equation (8.35). The system of Equations (8.26) can be solved numerically at this crossing point to define the boundaries of the pitchfork singularity. These boundaries are shown in Figures 8.4–8.5. For any combinations of model parameters in region (I), an imperfect pitchfork is expected, as shown in the continuity diagram of Figure 8.6a, obtained for example, with $(\bar{S}_{f\,1}, \bar{S}_{f\,2}) = (7, 0.5)$. It can be seen that an unstable region separates the static limit point and the bifurcation point that occurs at the crossing of the curve with the washout line. The model exhibits three steady states where the upper one is not realistic. If the model parameters move on the boundary itself then the limit point and the bifurcation point collapse in one point, yielding a perfect pitchfork, as shown in the continuity diagram of Figure 8.6b, obtained with $(\bar{S}_{f\,1}, \bar{S}_{f\,2}) = (2.86, 0.5)$. For values of the parameters in region (II), the continuity diagram obtained with $(\bar{S}_{f\,1}, \bar{S}_{f\,2}) = (1, 0.5)$ is shown in Figure 8.6c. The static limit point in this case moves to the other side of the washout line, and occurs on the physically unrealistic branch.

Similarly to the hysteresis, the branch sets of Figures 8.4–8.5 allow the delineation of the effect of parameters on the stability of the process. For the case of pitchfork singularity, it is region (II) that provides a stable regime for all dilution rates.

8.3.4 Winged-Cusp Singularity

The requirements for a winged-cusp singularity are:

$$F = F_{\bar{S}_1} = F_{\bar{\theta}} = F_{\bar{S}_1\bar{S}_2} = F_{\bar{S}_1\bar{\theta}} = 0$$

Since this set of conditions includes the condition $F_{\bar{\theta}} = 0$, it follows that the winged-cusp singularity may exist for washout condition only. Next, we will show that the condition $F_{\bar{\theta}} = 0$ and $F_{\bar{S}_1\bar{\theta}} = 0$ are incompatible. Taking the derivative of $F_{\bar{\theta}}$ (Equation (8.24)) with respect to $\bar{S}_1$ yields

$$-wF_{\bar{\theta}\bar{S}_1} = \frac{\partial r_1}{\partial S_1}(\bar{S}_{f_1} - \bar{S}_1 + \frac{\bar{S}_{f_2} - \bar{S}_2}{\gamma} + \bar{X}_f) - \bar{r}_1(1 + \frac{1}{\gamma}\frac{\partial \bar{S}_2}{\partial \bar{S}_1}) \tag{8.36}$$

At washout conditions, Equation (8.36) yields,

$$F_{\theta S_1} = \frac{\bar{r}_1}{w}(1 + \frac{1}{\gamma}\frac{\partial \bar{S}_2}{\partial \bar{S}_1}) \tag{8.37}$$

Excluding the condition $\bar{r}_1 = 0$, i.e., $\bar{S}_1 = 0$, it can be seen that for the term $F_{\bar{\theta}\bar{S}_1}$ to vanish, it is necessary that $1 + \frac{1}{\gamma}\frac{\partial \bar{S}_2}{\partial \bar{S}_1}$ is zero.

Recasting the steady-state form of Equation (8.7) and substituting for the expression of $\bar{X}$ (Equation (8.11)) and the rate $\bar{r}_2$ (Equation (8.10)) yields,

$$w(\bar{S}_{f_2} - \bar{S}_2)(1 + \bar{S}_2 + \lambda_2\bar{S}_1\bar{S}_2) = \mu\gamma\bar{\theta}\bar{S}_2(\bar{S}_{f_1} - \bar{S}_1 + \frac{\bar{S}_{f_2} - \bar{S}_2}{\gamma} + \bar{X}_f) \tag{8.38}$$

Differentiating each side of the equation yields,

$$\frac{\partial \bar{S}_2}{\partial \bar{S}_1} = \frac{g_1}{g_2} \tag{8.39}$$

where:

$$g_1 := \lambda_2\bar{S}_{f_2}\bar{S}_2 - \lambda_2\bar{S}_2^2 + \mu\gamma\bar{\theta}\bar{S}_2/w \tag{8.40}$$

$$\begin{aligned} g_2 \quad := \quad & \frac{\mu\gamma\bar{\theta}}{w}(\bar{S}_{f_1} - \bar{S}_1 + (\bar{S}_{f_2} - 2\bar{S}_2)/\gamma + \bar{X}_f) - \lambda_2\bar{S}_{f_2}\bar{S}_1 + 1 \\ & +2\lambda_2\bar{S}_1\bar{S}_2 + 2\bar{S}_2 - \bar{S}_{f_2} \end{aligned} \tag{8.41}$$

Substituting for washout conditions (Equation (8.25)) yields,

$$\frac{\partial \bar{S}_2}{\partial \bar{S}_1} = \frac{\gamma\mu\bar{S}_{f_2}\bar{\theta}}{w + w\lambda_2\bar{S}_{f_1}\bar{S}_{f_2} - \mu\bar{S}_{f_2}\bar{\theta}} \tag{8.42}$$

The term $\frac{1}{\gamma}\frac{\partial \bar{S}_2}{\partial \bar{S}_1} + 1$ is equal then to

$$\frac{1 + \lambda_1\bar{S}_{f_1}\bar{S}_{f_2} + \bar{S}_{f_2}}{1 + \lambda_2 S_{f_1}S_{f_2} - \frac{\mu S_{f_2}\theta}{w}} \tag{8.43}$$

This term vanishes only if

$$1 + \lambda_2 \bar{S}_{f1} \bar{S}_{f2} + \bar{S}_{f2} = 0 \tag{8.44}$$

which is impossible given that all the terms involved are positive. We conclude therefore that the model cannot exhibit winged-cusp singularity, and that the highest singularity the model can predict is the pitchfork singularity.

8.4 Concluding Remarks

The analysis of the basic unstructured model describing the biodegradation of mixed wastes has shown that pitchfork is the highest singularity the model can predict. The model, which was based on experimentally validated kinetics, showed in particular that for sterile feed conditions, the model predicts two critical residence times. For the operations below the smaller value (i.e., the larger dilution rate), washout is the only outcome of the biodegradation. Between the two critical residence times, the operation of the bioreactor can lead to either washout or to the survival state. For operations above the larger critical value (i.e., the smaller dilution rate), the operation leads to the survival state. The lumped nature of the model, like similar unstructured models of mixed substrates [144, 349] does not allow it to predict any richer dynamic behavior. Examples of experimental findings in the chemostat with mixed substrates include the existence of more than one stable survival state [363] and the preferential utilization of one of the available substrates [107]. These rich behaviors can only be predicted by structured models. A number of such models were proposed in the literature [186, 255, 257, 293]. Some proposed models [186, 293] made use of the well-known cybernetic approach that allows for the regulatory mechanisms to be described by optimality principles that are assumed to be followed by microbes. Narang et al. [257], on the other hand, developed a model based on the well-known idea that the growth patterns in mixed substrate environments are dictated by the enzymes that catalyze the transport of substrates into the cell. The author [255] went on to carry out a study of static multiplicity and showed that the model can capture the sequential and simultaneous substrate utilization patterns observed experimentally [107]. These include the occurrence of regions of dilution rates where one of the substrates is preferentially utilized as well as a region where both substrates are utilized simultaneously. In another study, the same authors [300] used the model developed in [257] to construct practical operating diagrams and also to carry out a comparative study with other models of gene regulation in mixed-substrate microbial growth [256]. Other modeling approaches were also proposed by Brandt et al. [63, 64] who formulated a model for slow microbial adaptation involving the synthesis of new enzymes in response to changes in the availability of substitutable substrates.

Chapter 9

PREDATOR–PREY INTERACTIONS

9.1 Introduction

Predator–prey interactions are quite common in many natural ecosystems as well as in waste treatment bioreactors. The study of predation is therefore important for understanding the dynamics of ecosystems and is also important for the optimization of the biological treatment of wastes. In activated sludge reactors, for instance, protozoa is known to play a valuable role by preying on unflocculated bacteria and thereby clarifying the reactor effluent [41].

Describing the consumption process in predator–prey interactions has been a research topic in population dynamics since the early work of Lotka and Volterra in the 1920s. For continuous cultures, a number of unstructured kinetic models with a variety of growth rate expressions were proposed to model predator–prey–substrate interactions [71, 103, 180, 241, 356]. In this regard, Tsuchiya et al. [356] proposed a saturation model for both growth of predator on prey and prey on a limiting substrate for the modeling of interactions between the amoeba *Dictyostelium discoideum* and *E. coli* bacteria. The authors showed that their proposed model managed to reproduce the experimental characteristics of the oscillations and also to predict the operating conditions at which oscillations occur. Moreover, the saturation model was able to predict oscillations that are independent on start-up conditions, i.e., hard oscillations that are more reminiscent of actual predator–prey behavior in real life. This saturation model was however unable to predict the type of oscillatory behavior found by Jost et al. [180] during the simultaneous continuous cultivation of *Azotobacter vinelandii* and protozoan *T. pyriformis*. These oscillations were found to occur only in a range of dilution rates. The authors proposed a "multiple saturation" model for the predator growth rate in order to predict this type of oscillatory behavior.

This chapter reexamines the dynamics of predator–prey interactions in continuous cultures but for a general class of unstructured kinetic models. Using arbitrary expressions for growth rates of prey on substrate and predator on prey, it is shown that closed analytical conditions can be derived that identify the regions of oscillatory behavior in these models. These analytical conditions can be used to construct practical diagrams, in terms of kinetic

and operating parameters, that delineate the regions where different behaviors are predicted by the model. Examples of behavior found in predator–prey–substrate interactions include the coexistence of species in a nontrivial steady state, in a state of sustained oscillations, or eventually one specie or all of them washout from the chemostat.

9.2 Bioreactor Model

A general unstructured kinetic model for substrate S, prey X, and predator Y is described by the following equations:

$$\frac{dS}{dt} = D(S_f - S) - \frac{1}{Y_S}\mu(S)X \tag{9.1}$$

$$\frac{dX}{dt} = -DX + \mu(S)X - \frac{1}{Y_P}p(X)Y \tag{9.2}$$

$$\frac{dY}{dt} = -DY + p(X)Y \tag{9.3}$$

S, X, and Y are the concentrations of substrate, prey, and predator, respectively, S_f is the substrate feed concentration, D is the dilution rate and Y_S and Y_P the yields (assumed constant) for prey growth on substrate and predator growth on prey, respectively. $\mu(S)$ and $p(X)$ are general expressions for the specific growth rates for prey and predator, respectively. The model equations are rendered dimensionless using the following variables,

$$\bar{S} = \frac{S}{S_{ref}}, \quad \bar{\mu} = \frac{\mu}{\mu_{ref}}, \quad \bar{X} = \frac{X}{Y_S S_{ref}}, \quad \bar{Y} = \frac{Y}{S_{ref} Y_S Y_P} \tag{9.4}$$

$$\bar{p} = \frac{p}{\mu_{ref}}, \quad \bar{D} = \frac{D}{\mu_{ref}}, \quad \bar{t} = t\mu_{ref} \tag{9.5}$$

S_{ref} and μ_{ref} are reference quantities for S and μ, respectively. The model in dimensionless form is

$$\frac{d\bar{S}}{d\bar{t}} = \bar{D}(\bar{S}_f - \bar{S}) - \bar{\mu}(\bar{S})\bar{X} \tag{9.6}$$

$$\frac{d\bar{X}}{dt} = -\bar{D}\bar{X} + \bar{\mu}(\bar{S})\bar{X} - \bar{p}(\bar{X})\bar{Y} \tag{9.7}$$

$$\frac{d\bar{Y}}{d\bar{t}} = -\bar{D}\bar{Y} + \bar{p}(\bar{X})\bar{Y} \tag{9.8}$$

The following relations can be derived for the model steady-state points. Equations (9.6–9.8) yield implicit expressions of $\bar{X}$ and $\bar{Y}$ as function of $\bar{S}$,

$$\frac{\bar{X}}{\bar{p}} = \frac{(\bar{S}_f - \bar{S})}{\bar{\mu}(\bar{S})} \tag{9.9}$$

$$\bar{Y} = \frac{(\bar{S}_f - \bar{S})(\bar{\mu}(\bar{S}) - \bar{p}(\bar{X}))}{\bar{\mu}(\bar{S})} \tag{9.10}$$

Adding Equations (9.9) and (9.10) yields the following expected steady-state relation between the three species,

$$\bar{X} + \bar{Y} + \bar{S} = \bar{S}_f \tag{9.11}$$

9.3 Existence of Oscillatory Behavior

The different elements j_{ik} of the Jacobian matrix are given by

$$j_{11} = -\bar{D} - \bar{\mu}_{\bar{S}}\bar{X}, \quad j_{12} = -\bar{\mu}, \quad j_{13} = 0 \tag{9.12}$$

$$j_{21} = \bar{\mu}_{\bar{S}}\bar{X}, \quad j_{22} = -\bar{D} + \bar{\mu} - \bar{p}_{\bar{X}}\bar{Y}, \quad j_{23} = -\bar{p}, \tag{9.13}$$

$$j_{31} = 0, \quad j_{32} = \bar{p}_{\bar{X}}, \quad j_{33} = -\bar{D} + \bar{p} \tag{9.14}$$

$\bar{\mu}_{\bar{S}}$ and $\bar{p}_{\bar{X}}$ represent respectively the first derivative of $\bar{\mu}$ and $\bar{p}$ with respect to $\bar{S}$ and $\bar{X}$. The coefficients S_i (Equations (3.35–3.37)) of Hopf condition $F_1 := S_1S_2 - S_3 = 0$ are given by

$$S_1 = -2\bar{p} - \bar{p}_{\bar{X}}\bar{Y} + \bar{\mu} - \bar{\mu}_{\bar{S}}\bar{X} \tag{9.15}$$

$$S_2 = \bar{p}^2 + 2\bar{p}\bar{p}_{\bar{X}}\bar{Y} - \bar{p}\bar{\mu} + \bar{p}\bar{\mu}_{\bar{S}}\bar{X} + \bar{p}_{\bar{X}}\bar{\mu}_{\bar{S}}\bar{X}\bar{Y} \tag{9.16}$$

$$S_3 = -\bar{p}^2\bar{p}_{\bar{X}}\bar{Y} - \bar{p}\bar{p}_{\bar{X}}\bar{\mu}_{\bar{S}}\bar{X}\bar{Y} \tag{9.17}$$

Algebraic manipulations reduce the first Hopf condition to the following expression:

$$F_1 := (S_1 + \bar{p})(S_2 + \bar{p}^2) = 0 \tag{9.18}$$

Since the second Hopf condition requires S_2 to be positive, the first Hopf condition of Equation (9.18) is equivalent to

$$S_1 + \bar{p} = 0 \tag{9.19}$$

or equivalently by substituting the expression of S_1 (Equation (9.15))

$$\bar{\mu} - \bar{p} - \bar{p}_{\bar{X}}\bar{Y} - \bar{\mu}_{\bar{S}}\bar{X} = 0 \tag{9.20}$$

The following useful relation also holds between S_1 and S_2,

$$(S_1 + \bar{p})\bar{p} + S_2 = \bar{p}_{\bar{X}}\bar{Y}(\bar{p} + \bar{\mu}_{\bar{S}}\bar{X}) \tag{9.21}$$

Taking into consideration Equation (9.19), the second Hopf condition is therefore reduced to

$$S_2 = \bar{p}_{\bar{X}}\bar{Y}(\bar{p} + \bar{\mu}_{\bar{S}}\bar{X}) > 0 \tag{9.22}$$

The conditions of Equations (9.20, 9.22) along with the steady-state Equations (9.9–9.10) represent the conditions, in terms of arbitrary growth rates $\bar{\mu}(\bar{S})$ and $\bar{p}(\bar{X})$, for the existence of a Hopf point in the model. Before the analysis is carried out any further, it can be noted that if both growth rates $\bar{\mu}$ and $\bar{p}$ are monotonic, i.e., $\bar{\mu}_{\bar{S}} > 0$ and $\bar{p}_{\bar{X}} > 0$, then the second Hopf condition $S_2 > 0$ (Equation (9.22)) is always satisfied. If, on the other hand, $\bar{\mu}_{\bar{S}}$ is positive while the growth rate $\bar{p}(\bar{X})$ of the predator is inhibited by the prey, i.e., $\bar{p}_{\bar{X}} < 0$ for all values of $\bar{X}$, then the condition $S_2 > 0$ is never satisfied and the model cannot predict any oscillatory behavior.

9.4 Construction of Operating Diagrams

In this section, we show how a systematic construction of operating diagrams $(\bar{S}_f, \bar{D})$ can be carried out for arbitrary specific growth rates $\bar{\mu}(\bar{S})$ and $\bar{p}(\bar{X})$. The construction of such diagrams is useful in delineating regions with different modes of interactions between prey and predator populations. The line(s) showing the loci of Hopf points can be constructed by solving Equations (9.20, 9.22) defining the Hopf points for each values of $\bar{S}_f$ and $\bar{D}$. The line(s) representing the predator washout $\bar{Y} = 0$, i.e., $\bar{X} = \bar{S}_f - \bar{S}$ are obtained by substituting $\bar{X} = \bar{S}_f - \bar{S}$ into Equation (9.10), to yield

$$\bar{\mu}(\bar{S}) = \bar{p}(\bar{X} = \bar{S}_f - \bar{S}) \tag{9.23}$$

The real solution $\bar{S}$ of this equation is then substituted into the dilution rate expression

$$\bar{D} = \bar{p}(\bar{X} = \bar{S}_f - \bar{S}) \tag{9.24}$$

to yield an explicit relation between $\bar{D}$ and $\bar{S}_f$. The line defining the complete washout $\bar{S} = \bar{S}_f$, $\bar{X} = 0$, and $\bar{Y} = 0$ is defined, on the other hand, explicitly by

$$\bar{D} = \bar{\mu}(\bar{S}_f) \tag{9.25}$$

In the following, we apply these general results to the study of dynamics of two popular growth models that were investigated experimentally in the literature, namely the saturation [356] and multiple saturation models [180].

9.5 Application to the Saturation Model

For the saturation model, both specific growth rates $\bar{\mu}$ and $\bar{p}$ follow Monod kinetics,

$$\mu = \frac{\mu_m S}{K_S + S} \text{ and } p = \frac{\mu_p X}{K_X + X} \tag{9.26}$$

This model was shown [356] to predict the hard oscillations that occur in predation by the amoebae *Dictyostelium discoideum* on *E. coli* bacteria in a chemostat where glucose was the limiting substrate. We will show that the analytical conditions derived in the previous section can provide a deep insight into the problem of oscillatory coexistence, including the determination of the exact location of Hopf points. The model equations are rendered dimensionless using the variables defined in Equations (9.4–9.5), with

$$S_{ref} = K_S, \quad \mu_{ref} = \mu_m, \quad \lambda = \frac{\mu_p}{\mu_m}, \quad \bar{K} = \frac{K_X}{Y_S K_S} \tag{9.27}$$

The dimensionless expressions of the specific growth rates are

$$\bar{\mu} = \frac{\bar{S}}{1 + \bar{S}}, \quad \bar{p} = \frac{\lambda \bar{X}}{\bar{K} + \bar{X}} \tag{9.28}$$

In the first step of the analysis, we will delineate the domains where a meaningful existence of species is possible. Substituting for the expressions of $\bar{\mu}(\bar{S})$ and $\bar{p}(\bar{X})$ in Equations (9.9–9.10) yields the following nontrivial steady-state expressions for $\bar{S}$, $\bar{X}$, and $\bar{Y}$,

$$(\lambda - \bar{D})\bar{S}^2 + (\bar{D}(\bar{S}_f - 1) - \lambda(\bar{S}_f - 1) + \bar{K})\bar{S} + (\bar{D} - \lambda)\bar{S}_f = 0 \tag{9.29}$$

$$\bar{X} = \frac{\lambda(\bar{S}_f - \bar{S})(1 + \bar{S})}{\bar{S}} - \bar{K} \tag{9.30}$$

and

$$\bar{Y} = \bar{S}_f - \bar{S} - \bar{X} \tag{9.31}$$

Substituting for the expression of $\bar{X}$ (Equation (9.30)) into Equation (9.31) yields the following quadratic condition for a meaningful existence of $\bar{Y}$, i.e., $\bar{Y} > 0$,

$$\bar{S}^2(1 - \lambda) + \bar{S}(\bar{S}_f - \lambda\bar{S}_f + \lambda + \bar{K}) - \lambda\bar{S}_f > 0 \tag{9.32}$$

together with the natural constraints

$$0 < \bar{S} < \bar{S}_f \tag{9.33}$$

These simple quadratic Equations (9.29, 9.32) can be solved for given values of model parameters $\bar{S}_f$, λ, and $\bar{K}$ to determine the domains where the predator is not washed out. The location of Hopf points, on the other hand, is determined by the two Hopf conditions of Equations (9.20, 9.22). It can be noted that since both specific growth rates $\bar{\mu}$ and $\bar{p}$ are monotonic, their first derivatives $\bar{\mu}_{\bar{S}}$ and $\bar{p}_{\bar{X}}$ are positive. The second Hopf condition $S_2 > 0$ of Equation (9.22) is therefore always satisfied. Recasting the expression of the first Hopf condition (Equation (9.20)) and using the steady-state Equation (9.10) yields the following equation for Hopf points

$$\frac{\bar{p}(\bar{X})\bar{Y}}{\bar{S}_f - \bar{S}} = \bar{p}_{\bar{X}}\bar{Y} + \bar{\mu}_{\bar{S}}\bar{X} \tag{9.34}$$

Substituting the expression of $\bar{Y}$ from Equation (9.31) yields,

$$\bar{p} - \frac{\bar{p}\bar{X}}{\bar{S}_f - \bar{S}} = \bar{p}_{\bar{X}}(\bar{S}_f - \bar{S}) - \bar{X}\bar{p}_{\bar{X}} + \bar{\mu}_{\bar{S}}\bar{X} \tag{9.35}$$

Substituting into this equation the expression for the first derivatives $\bar{\mu}_{\bar{S}} = \frac{1}{(1+\bar{S})^2}$ and $\bar{p}_{\bar{X}} = \frac{\lambda\bar{K}}{(\bar{K}+\bar{X})^2}$, and then the explicit expression of $\bar{X}$ (Equation (9.30)), yields the following cubic equation defining the loci of Hopf points in terms of the model parameters,

$$\frac{(1-\lambda)}{\lambda\bar{S}_f^2}\bar{S}^3 + \frac{(-\bar{K} - \bar{S}_f + \lambda\bar{S}_f)}{\lambda\bar{S}_f^2}\bar{S}^2 - \frac{\bar{S}}{\bar{S}_f} + 1 = 0 \tag{9.36}$$

The real root(s) of this equation determines the value of the substrate at which the Hopf point(s) occur. The corresponding values of $\bar{X}$ and $\bar{Y}$ can be obtained explicitly from Equations (9.30–9.31), while the value of the dilution rate is obtained through the relation $\bar{D} = \bar{p}(\bar{X})$. A deeper analysis of this cubic equation shows that the equation has always one and only one positive and meaningful (smaller than $\bar{S}_f$) root for any values of the model parameters $\bar{S}_f$, $\bar{K}$, and λ. This result implies that the saturation model can *always* predict oscillatory behavior for any values of the model kinetic ($\lambda, \bar{K}$) or operating parameters ($\bar{S}_f$). The results also indicates that two Hopf points are not possible with this model.

An example of dynamics that can be expected with the saturation model is provided in the bifurcation diagram of Figures 9.1(a–b) for the following parameters $\bar{S}_f = 1000$, $\lambda = 0.96$, $\bar{K} = 264.0$. The following solutions can be identified in the diagram: (1) the complete washout solution seen on the top of the diagram (branch (ABC)); (2) a region where only the predator is washed out ($\bar{Y} = 0$) (branch (BED)). This line is derived from the model equations by setting $\bar{Y} = 0$ to yield

$$\bar{D} = \bar{\mu}(\bar{S}) = \frac{\bar{S}}{\bar{S} + 1} \tag{9.37}$$

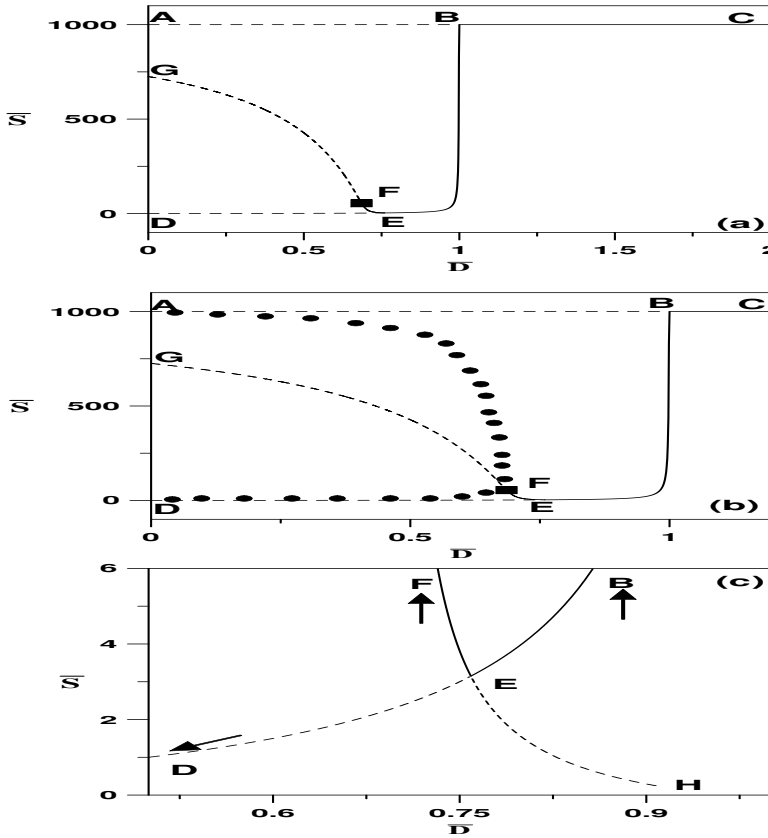

FIGURE 9.1: (a) Continuity diagram for the saturation model; (b) Enlargement of Figure 9.4a; (c) Enlargement of behavior around point E; solid line, stable branch; dashed line, unstable; square, Hopf point; dots, stable periodic branch.

The model also predicts a stable nontrivial static coexistence of species (branch (EFG)) that corresponds to Equations (9.29–9.31). The continuity diagram is also characterized by the presence of a Hopf point, solution of Equation (9.36), at $\bar{S}_{HB} = 54.831$, $\bar{X}_{HB} = 659.910$, $\bar{Y}_{HB} = 285.258$, and at the dilution rate $\bar{D}_{HB} = 0.685$. Stable periodic branches enlarged in Figure 9.1b can be seen to emanate from the Hopf point. The continuity diagram of Figure 9.1b predicts therefore three different behaviors. For dilution rates smaller than the Hopf point (F), periodic branches are the only stable attractors, since the total washout line is unstable. In this region the species coexist in a stable oscillatory mode regardless of initial populations values. An example of the stable limit cycle is shown in Figure 9.2 for $\bar{D} = 0.5$. For dilution rates between E and F (Figure 9.1b), the species coexist on a static

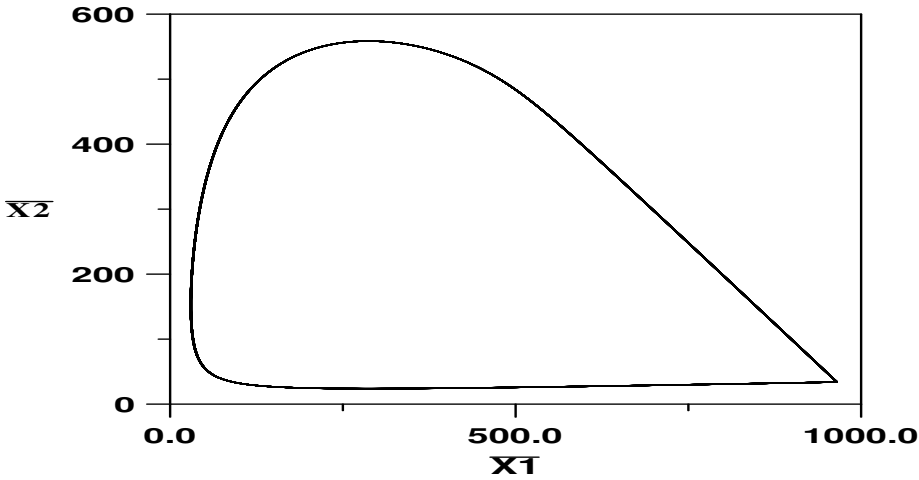

FIGURE 9.2: Phase plane showing limit cycle in Figure 9.1b, for $\bar{D} = 0.5$.

nontrivial branch, again for any initial conditions since the total washout line is unstable. The region of dilution rates extending from the origin and up to point E is therefore characterized by the coexistence of species either in a state of limit cycle or in a static mode regardless of initial population values. For dilution rates between point E and B (Figure 9.1b), the operation of the chemostat leads to predator washout for any initial conditions. Finally, values of dilution rates larger than B lead to a total washout. Moreover, it can be seen that another unstable branch (EH) emanates from point E (Figure 9.1c). This branch was not shown in the original diagrams (Figures 9.1(a–b)) since it corresponds to negative values of predator concentrations (Y) and hence is not physically realistic.

The general analytical conditions of Equations (9.23–9.25) can be used to construct branch sets delineating the different dynamic regions that result from species interactions. The line of predator washout is obtained using Equations (9.23–9.24), yielding

$$\bar{D} = \frac{\lambda(\bar{S}_f - \bar{S}_1)}{\bar{K} + \bar{S}_f - \bar{S}_1} \tag{9.38}$$

where $\bar{S}_1$ is the solution of the predator washout condition (Equation (9.32)), i.e.,

$$\bar{S}_1 = \frac{-(\bar{S}_f(1-\lambda) + \lambda + \bar{K}) + \sqrt{(\bar{S}_f(1-\lambda) + \lambda + \bar{K})^2 + 4\lambda(1-\lambda)\bar{S}_f}}{2(1-\lambda)} \tag{9.39}$$

The complete washout line is, on the other hand, defined by Equation (9.25),

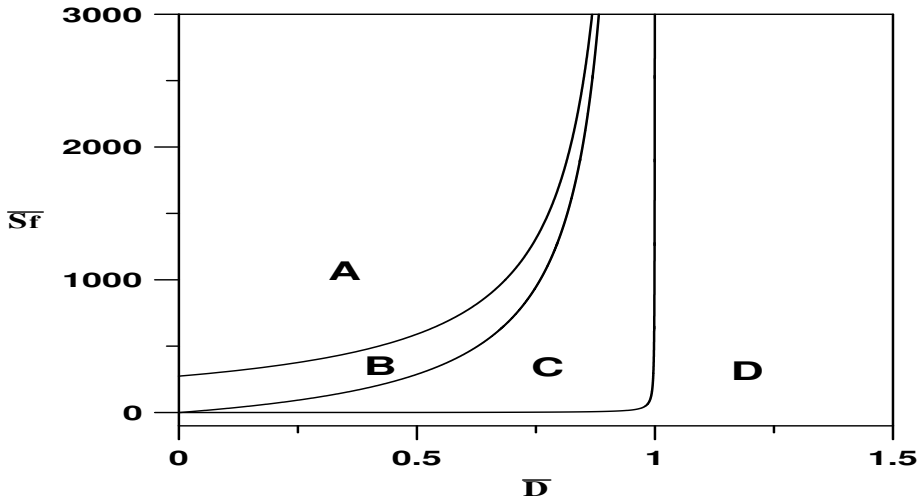

FIGURE 9.3: Bifurcation diagram showing the different outcomes of predator–prey–substrate interactions; (A) region of oscillations; (B) region of static coexistence; (C) region of predator washout; (D) region of total washout.

to yield

$$\bar{D} = \frac{\bar{S}_f}{1 + \bar{S}_f} \tag{9.40}$$

Figure 9.3 shows the four possible scenarios in the operating parameter space $(\bar{S}_f, \bar{D})$. Region (A) is the region where hard oscillations are expected, (B) is the region where static coexistence of the two species is possible. As the substrate feed concentration increases, this region can be seen to narrow at the benefit of region (C) of predator washout. At larger dilution rates, the complete washout (region D) is the only outcome of interactions between the species.

9.6 Application to the Multiple Saturation Model

The second example for a prey dependent model corresponds to the following specific growth rate for the predator

$$p(X) = \frac{\mu_p X^2}{(K_{1X} + X)(K_{2X} + X)} \tag{9.41}$$

This "multiple saturation model" was proposed in [180] to model oscillations found in the simultaneous cultivation of *Azotobacter vinelandii* and protozoan *T. pyriformis*. As was observed by the authors, the oscillatory behavior was confined to a range of dilution rates. Our analysis in the previous section of the simple saturation model has shown its inability to predict this type of behavior. The model is rendered dimensionless using Equations (9.4–9.5). The specific growth rate $\bar{p}(\bar{X})$ takes the form

$$\bar{p}(\bar{X}) = \frac{\lambda \bar{X}^2}{(\bar{K}_1 + \bar{X})(\bar{K}_2 + \bar{X})} \tag{9.42}$$

An example of the behavior of this model is shown in Figures 9.4(a–b)

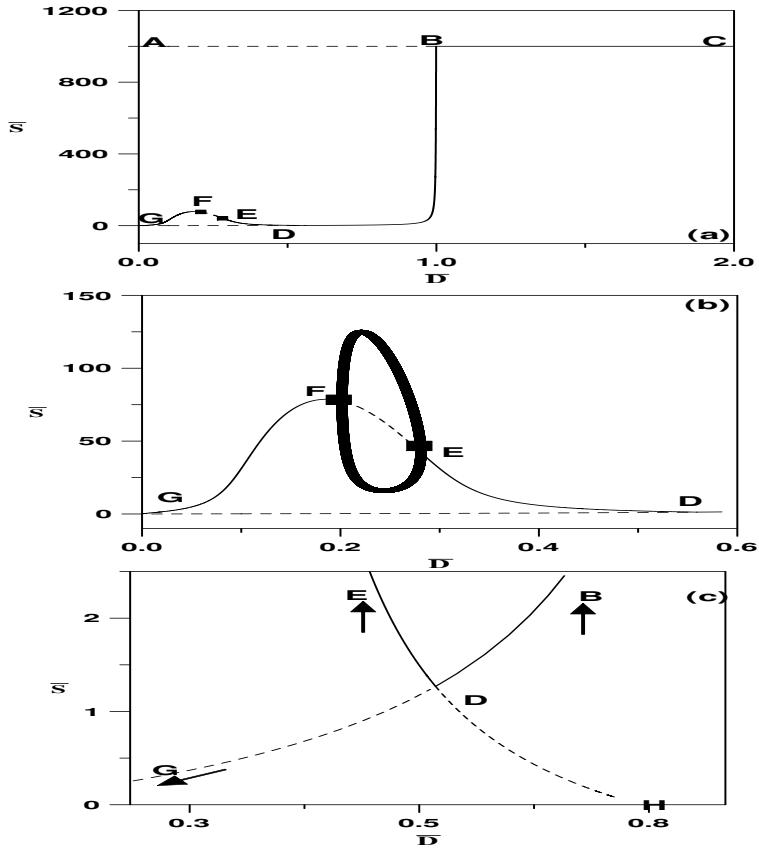

FIGURE 9.4: (a) Continuity diagram for the multiple saturation model; (b) Enlargement of Figure 9.1a; (c) Enlargement of the behavior around point D; solid line, stable branch; dashed line, unstable branch; square, Hopf point; dots, stable periodic branch.

for the following values of model parameters, $\bar{S}_f = 1000$, $\lambda = 0.8$, $\bar{K}_1 = 300$, $\bar{K}_2 = 100$. It can be seen that two Hopf points instead of one characterize the behavior of the model. The two Hopf points occur respectively at dilution rates $\bar{D}_{1HB} = 0.201$ and $\bar{D}_{2HB} = 0.281$. Stable periodic branches, enlarged in Figure 9.4b, can be seen to connect the two points. The bifurcation diagram is also characterized, as in the previous example, by the existence of the washout line (ABC), the line of predator washout (GDB), and the line of static coexistence of species (lines DE and FG). The "multiple saturation"

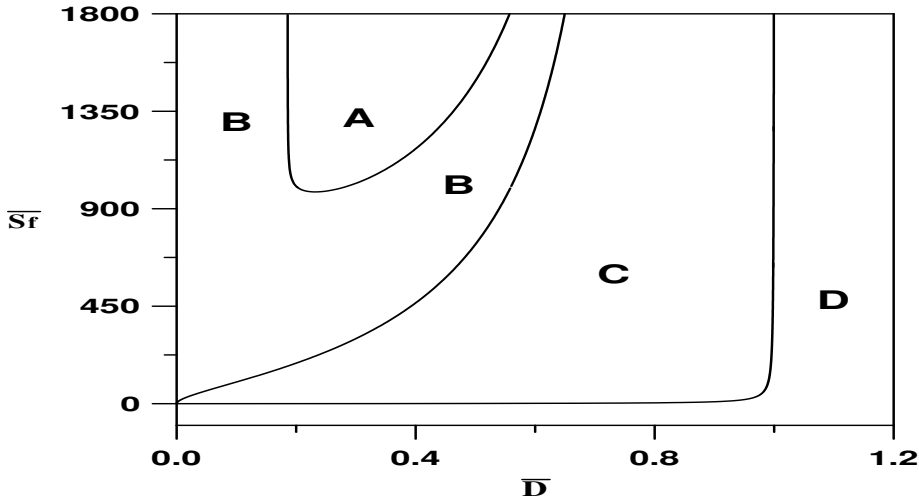

FIGURE 9.5: Operating diagram showing the different outcomes of predator–prey–substrate interactions for multiple saturation model; (A) region of oscillations; (B) region of static coexistence; (C) region of predator washout; (D) region of total washout.

model predicts therefore similar regions to the simple saturation model. The only new feature of the model is its ability to predict oscillations that are confined within a specific range of dilution rates. It can also be noted that an unstable branch (DH), not shown in the original diagrams of Figures 9.4(a–b), is seen to bifurcate from point D. This unstable branch corresponds to negative values of predator concentrations and hence is not physically realistic. The operating diagram $(\bar{S}_f, \bar{D})$ (Figure 9.5) showing the different behaviors is constructed in a similar way to the previous example. The line defining the complete washout is unchanged from Equation (9.40), since it depends solely on $\bar{\mu}(\bar{S})$. The line defining the predator washout is, on the other hand, obtained by first solving Equation (9.24), yielding the following cubic equation for $\bar{S}$,

$$a_0\bar{S}^3 + a_1\bar{S}^2 + a_2\bar{S} + a_3 = 0 \tag{9.43}$$

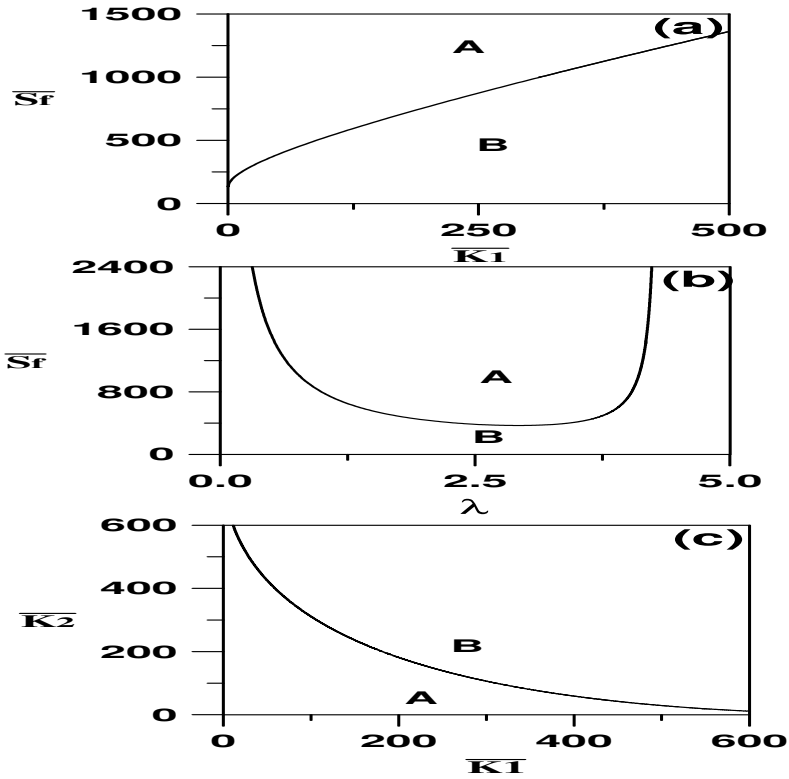

FIGURE 9.6: Branch sets showing the regions of period behavior in the parameter spaces: (a) $(\bar{S}_f, \bar{K}_1)$; (b) $(\bar{S}_f, \lambda)$; (c) $(\bar{K}_1, \bar{K}_2)$.

with

$$a_0 = (1-\lambda), \quad a_1 = (-\bar{K}_1 - \bar{K}_2 - 2\bar{S}_f - \lambda + 2\lambda\bar{S}_f)$$

$$a_2 = (\bar{K}_1\bar{K}_2 + \bar{K}_1\bar{S}_f + \bar{K}_2\bar{S}_f + \bar{S}_f^2 + 2\lambda\bar{S}_f - \lambda\bar{S}_f^2), \quad a_3 = -\lambda\bar{S}_f^2$$

The line of predator washout is defined by $\bar{D} = \bar{p}(\bar{S}_f - \bar{S})$, yielding

$$\bar{D} = \frac{\lambda(\bar{S}_f - \bar{S})^2}{(\bar{K}_1 + \bar{S}_f - \bar{S})(\bar{K}_2 + \bar{S}_f - \bar{S})} \tag{9.44}$$

where $\bar{S}$ is the real solution of Equation (9.43). Figure 9.5 shows that region (A) of stable oscillations exists only for values of $\bar{S}_f$ larger than a certain value. Moreover, region (A) can also be seen to increase, in terms of the dilution rate, as $\bar{S}_f$ increases. Smaller values of $\bar{S}_f$ yield region (B) of static coexistence while larger values of dilution rates yield either region (C) of predator washout or region (D) of total washout.

Figures 9.6(a–c) show the domains of oscillatory behavior in the other

parameter spaces $(\bar{S}_f, \bar{K}_1)$, $(\bar{S}_f, \lambda)$, and $(\bar{K}_2, \bar{K}_1)$. Figure 9.6a shows that the oscillatory behavior (region A) is possible only for $\bar{S}_f$ larger than a certain value. For constant $\bar{K}_1$, the range of periodic behavior can be seen to increase with $\bar{S}_f$. The effect, on the other hand, of λ is shown in Figure 9.6b. It can also be seen that for each value of $\bar{S}_f$, the periodic behavior is confined to a specific range of λ. Figure 9.6c shows, on the other hand, that the region of periodic behavior narrows with increasing values of either $\bar{K}_1$ or $\bar{K}_2$.

9.7 Concluding Remarks

The dynamics of interactions between predator, prey, and a limiting substrate in a continuous bioreactor were reinvestigated with the help of elementary concepts of bifurcation theory. Using an unstructured kinetic model, general analytical conditions with respect to arbitrary specific growth rates of prey on substrate and predator on prey were established that describe the conditions for the occurrence of an oscillatory behavior. Moreover, these analytical conditions have permitted the systematic construction of bifurcation diagrams in any parameters space and in particular in the operating parameters space (substrate feed concentration vs. dilution rate). These general results were applied to two experimentally validated models. In this regard, it was shown that the model with Monod growth for both prey and predator always predicts oscillatory behavior, for any values of its parameters.

The analysis of the multiple saturation model has revealed its ability to predict two Hopf points. Hard oscillations are expected within the dilution rates corresponding to the two Hopf points. For both models, practical diagrams in different parameter spaces were constructed. This allowed the delineation of regions of hard oscillations, regions of static coexistence, regions of predator washout and regions of total washout. In the next chapter, the issue of predator–prey interaction is reexamined for another class of unstructured models, namely ratio-dependent models.

This page intentionally left blank

Chapter 10

RATIO-DEPENDENT MODELS

10.1 Introduction

The previous chapter covered a general class of models for predator–prey interactions for which the predator growth rate was assumed to depend solely on prey density, while the effects of predator population were ignored. These are called strictly prey-dependent models and constitute the classical class of predator–prey models. Despite their rich dynamics and their ability to duplicate real-life behavior of many biological systems, the strictly prey-dependent models were shown to be unable to predict a number of experimental observations. These models cannot predict, for instance, the situation in which both populations can either coexist or become extinct depending on their initial values. This type of mutual extinction was, for instance, observed in the protozoan, *Paramecium* and its predator *Didinium* [3, 124].

Attempts to remedy the shortcomings of prey-dependent models started by recognizing that predator density could have a direct effect on its growth rate. A number of such predator-dependent models were proposed in the literature [91]. Arditi and Ginzburg [36] suggested that the essential properties of predator-dependence could be implemented by a simpler form in which the predator growth rate is assumed to depend on the ratio of prey to predator abundance, thus the name of "ratio-dependent model." This model has since been studied extensively in the literature [28, 51, 53, 56, 97, 114, 157, 185, 187, 371, 373]. These theoretical studies have shown that ratio-dependent models can provide much richer dynamics. Unlike strictly prey-dependent models, ratio-dependent models predict that even if there is a positive steady state, both prey and predator can still go extinct [191]. Mathematically, much of the rich dynamics provided by ratio-dependent models occur on the boundary and close to the origin. The reason is that the origin, being a complicated singular point, provides interesting dynamics of its own.

In this chapter, we extend the study of the dynamics of ratio-dependent models to a chemostat involving interactions between one predator, one prey, and a limiting substrate. It is shown that closed analytical conditions can be derived even for arbitrary growth rates for the occurrence of stable oscillatory behavior in the model. The different static behaviors are also delineated, including the coexistence of predator and prey populations or their mutual

washout depending on their initial values. The analysis carried out in this chapter sheds some light on the conditions for the existence of this unique feature and its implications on the behavior of predator–prey interactions.

10.2 Process Model

The following general unstructured kinetic model is written for substrate S, prey X, and predator Y populations, using the same notation as in the previous chapter,

$$\frac{dS}{dt} = D(S_f - S) - \frac{1}{Y_S}\mu(S)X \tag{10.1}$$

$$\frac{dX}{dt} = -DX + \mu(S)X - \frac{1}{Y_P}p(X,Y)Y \tag{10.2}$$

$$\frac{dY}{dt} = -DY + p(X,Y)Y \tag{10.3}$$

When the specific growth rate $p(X,Y)$ of predator on prey depends on prey X alone, i.e., $p(X,Y) = p(X)$, the model is the classical strictly prey-dependent model. When $p(X,Y)$ depends on the ratio $\frac{X}{Y}$, i.e., $p(X,Y) = p(\frac{X}{Y})$, the model is called ratio-dependent. In the following, we examine in detail the dynamics when the following expressions are selected for both specific growth rates,

$$\mu = \frac{\mu_m S}{K_S + S} \quad \text{and} \quad p = \frac{\mu_p \frac{X}{Y}}{K + \frac{X}{Y}} \tag{10.4}$$

The prey grows following Monod kinetics while the predator growth rate (p) has a Monod-like form in ($\frac{X}{Y}$). The model is rendered dimensionless using the following variables:

$$\bar{S} = \frac{S}{K_S}, \quad \bar{S}_f = \frac{S_f}{K_S}, \quad \bar{\mu} = \frac{\mu}{\mu_m}, \quad \bar{X} = \frac{X}{Y_S K_S}, \quad \bar{Y} = \frac{Y}{K_S Y_S Y_P} \tag{10.5}$$

$$\bar{t} = t\mu_m, \quad \bar{p} = \frac{p}{\mu_m}, \quad \bar{D} = \frac{D}{\mu_m}, \quad \lambda = \frac{\mu_P}{\mu_m}, \quad \bar{K} = KY_P \tag{10.6}$$

The model equations in the dimensionless form are

$$\frac{d\bar{S}}{d\bar{t}} = \bar{D}(\bar{S}_f - \bar{S}) - \bar{\mu}(\bar{S})\bar{X} \tag{10.7}$$

$$\frac{d\bar{X}}{d\bar{t}} = -\bar{D}\bar{X} + \bar{\mu}(\bar{S})\bar{X} - \bar{p}(\bar{X},\bar{Y})\bar{Y} \tag{10.8}$$

$$\frac{d\bar{Y}}{d\bar{t}} = -\bar{D}\bar{Y} + \bar{p}(\bar{X},\bar{Y})\bar{Y} \tag{10.9}$$

The dimensionless growth rates are given by

$$\bar{\mu} = \frac{\bar{S}}{1+\bar{S}} \text{ and } \bar{p} = \frac{\lambda \frac{\bar{X}}{\bar{Y}}}{\bar{K} + \frac{\bar{X}}{\bar{Y}}} \tag{10.10}$$

The parameter λ and $\bar{K}$ have the following physical interpretation. For large prey concentrations ($\bar{X}$), the term $\bar{p}\bar{Y}$ becomes $\lambda\bar{Y}$. Substituting in the predator balance (Equation (10.9)), it can be seen that λ represents the asymptotic predator growth rate for an "infinite" prey concentration. The parameter λ is therefore called "predator growing ability". When, on the other hand, the predator concentration ($\bar{Y}$) is large, then the term $\bar{p}\bar{Y}$ becomes $(\frac{\lambda}{\bar{K}})\bar{X}$. Substituting in the prey balance (Equation (10.8)), it can be seen that the term $(\frac{\lambda}{\bar{K}})$ represents the asymptotic prey death rate due to predation, for an "infinite" predator concentration. It is refereed to as the "consumption ability".

The analysis of the model (Equations (10.7–10.9)) reveals the following equilibrium points:

- Total washout, i.e., $(\bar{S} = \bar{S}_f, \bar{X} = 0, \bar{Y} = 0)$.
- Predator washout defined by $(\bar{\mu}(\bar{S}) = \bar{D}, \bar{X} = \bar{S}_f - \bar{S}, \bar{Y} = 0)$. The dependence of $\bar{S}$ on the dilution rate $\bar{D}$ is given explicitly by solving $\bar{\mu}(\bar{S}) = \bar{D}$ to yield

$$\bar{S} = \frac{\bar{D}}{1-\bar{D}} \tag{10.11}$$

- A nontrivial static coexistence of species defined by solving Equations (10.7–10.9) to yield,

$$\bar{X} = \frac{(\bar{S}_f - \bar{S})(\frac{\lambda}{\bar{\mu}} - \bar{K})}{1-\bar{K}} \tag{10.12}$$

$$\bar{Y} = \bar{S}_f - \bar{S} - \bar{X} = \frac{(\bar{S}_f - \bar{S})(1 - \frac{\lambda}{\bar{\mu}})}{1-\bar{K}} \tag{10.13}$$

Substituting the expression of $\bar{X}$ into the steady-state form of Equation (10.7) yields the explicit dependence of $\bar{S}$ on $\bar{D}$, for the case of static coexistence,

$$\bar{S} = \frac{\frac{\lambda}{\bar{K}} - \bar{D}(\frac{1}{\bar{K}} - 1)}{1 - (\frac{\lambda}{\bar{K}} - \bar{D}(\frac{1}{\bar{K}} - 1))} \tag{10.14}$$

In the first step of the analysis, we construct the branch set for the meaningful existence of the interacting species. A simple mathematical analysis of Equations (10.12–10.13) for the meaningful existence of X, Y, and $\bar{S}$, i.e., $\bar{X} > 0$, $\bar{Y} > 0$, and $0 < \bar{S} < \bar{S}_f$, leads to the following cases, depicted in the branch set of Figure 10.1a.

- Region (A) of Figure 10.1a is defined by $\lambda < \frac{\bar{S}_f}{1+\bar{S}_f}$ and $\frac{\lambda(1+\bar{S}_f)}{\bar{S}_f} < \bar{K} < 1$. In this region X is meaningful for $0 < \bar{S} < \frac{\lambda}{\bar{K}-\lambda}$, while Y is meaningful for $\frac{\lambda}{1-\lambda} < \bar{S} < \bar{S}_f$
- Region (B) of Figure 10.1a is defined by $\lambda < \frac{\bar{S}_f}{1+\bar{S}_f}$ and $\bar{K} < \frac{\lambda(1+\bar{S}_f)}{\bar{S}_f}$. In this region X is meaningful for all values $0 < \bar{S} < \bar{S}_f$, while Y is meaningful for $\frac{\lambda}{1-\lambda} < \bar{S} < \bar{S}_f$
- Region (A´) of Figure 10.1a is defined by $\lambda < \frac{\bar{S}_f}{1+\bar{S}_f}$ and $\bar{K} > 1$. In this region X is meaningful for $\frac{\lambda}{\bar{K}-\lambda} < \bar{S} < \bar{S}_f$, while Y is meaningful for $0 < \bar{S} < \frac{\lambda}{1-\lambda}$
- Region (B´) of Figure 10.1a is defined by $\lambda > \frac{\bar{S}_f}{1+\bar{S}_f}$ and $\bar{K} > \frac{\lambda(1+\bar{S}_f)}{\bar{S}_f}$. In this region X is meaningful for $\frac{\lambda}{\bar{K}-\lambda} < \bar{S} < \bar{S}_f$, while Y is meaningful for all values $0 < \bar{S} < \bar{S}_f$.
- Region (C) of Figure 10.1a. This region includes any region other than A, B, A´, and B´. In this region either the prey or predator is not meaningful for all values $0 < \bar{S} < \bar{S}_f$.

10.3 Existence of Periodic Solutions

The elements of the Jacobian matrix are

$$j_{11} = -\bar{D} - \bar{\mu}_{\bar{S}}\bar{X}, \quad j_{12} = -\bar{\mu}, \quad j_{13} = 0 \tag{10.15}$$

$$j_{21} = \bar{\mu}_{\bar{S}}\bar{X}, \quad j_{22} = -\bar{D} + \bar{\mu} - \bar{p}_{\frac{\bar{X}}{\bar{Y}}}, \quad j_{23} = \frac{\bar{X}}{\bar{Y}}\bar{p}_{\frac{\bar{X}}{\bar{Y}}} - \bar{p} \tag{10.16}$$

$$j_{31} = 0, \quad j_{32} = \bar{p}_{\frac{\bar{X}}{\bar{Y}}}, \quad j_{33} = -\bar{D} + \bar{p} - \frac{\bar{X}}{\bar{Y}}\bar{p}_{\frac{\bar{X}}{\bar{Y}}} \tag{10.17}$$

$\bar{\mu}_{\bar{S}}$ is the first derivative of $\bar{\mu}$ with respect to $\bar{S}$ and $\bar{p}_{\frac{\bar{X}}{\bar{Y}}}$ is the derivative of $\bar{p}$ with respect to $v = \frac{\bar{X}}{\bar{Y}}$. The terms S_i $(i = 1, 3)$ (Equations (3.35–3.37)) of the first Hopf condition $F_1 = S_1S_2 - S_3 = 0$ are given by

$$S_1 = -2\bar{p} + \bar{\mu} - \bar{\mu}_{\bar{S}}\bar{X} - \bar{p}_{\frac{\bar{X}}{\bar{Y}}}(1 + \frac{\bar{X}}{\bar{Y}}) \tag{10.18}$$

$$S_2 = \bar{p}^2 + 2\bar{p}\bar{p}_{\frac{\bar{X}}{\bar{Y}}} - \bar{p}\bar{\mu} + \bar{p}\bar{\mu}_{\bar{S}}\bar{X} + \bar{p}_{\frac{\bar{X}}{\bar{Y}}}\bar{\mu}_{\bar{S}}\bar{X} + 2\bar{p}\bar{p}_{\frac{\bar{X}}{\bar{Y}}}\frac{\bar{X}}{\bar{Y}} - \bar{p}_{\frac{\bar{X}}{\bar{Y}}}\bar{\mu}\frac{\bar{X}}{\bar{Y}} + \bar{p}_{\frac{\bar{X}}{\bar{Y}}}\bar{\mu}_{\bar{S}}\frac{\bar{X}^2}{\bar{Y}} \tag{10.19}$$

$$S_3 = -\bar{p}^2\bar{p}_{\frac{\bar{X}}{\bar{Y}}} - \bar{p}\bar{p}_{\frac{\bar{X}}{\bar{Y}}}\bar{\mu}_{\bar{S}}\bar{X} - \bar{p}^2\bar{p}_{\frac{\bar{X}}{\bar{Y}}}\frac{\bar{X}}{\bar{Y}} + \bar{p}\bar{p}_{\frac{\bar{X}}{\bar{Y}}}\bar{\mu}\frac{\bar{X}}{\bar{Y}} - \bar{p}\bar{p}_{\frac{\bar{X}}{\bar{Y}}}\bar{\mu}_{\bar{S}}\frac{\bar{X}^2}{\bar{Y}} \tag{10.20}$$

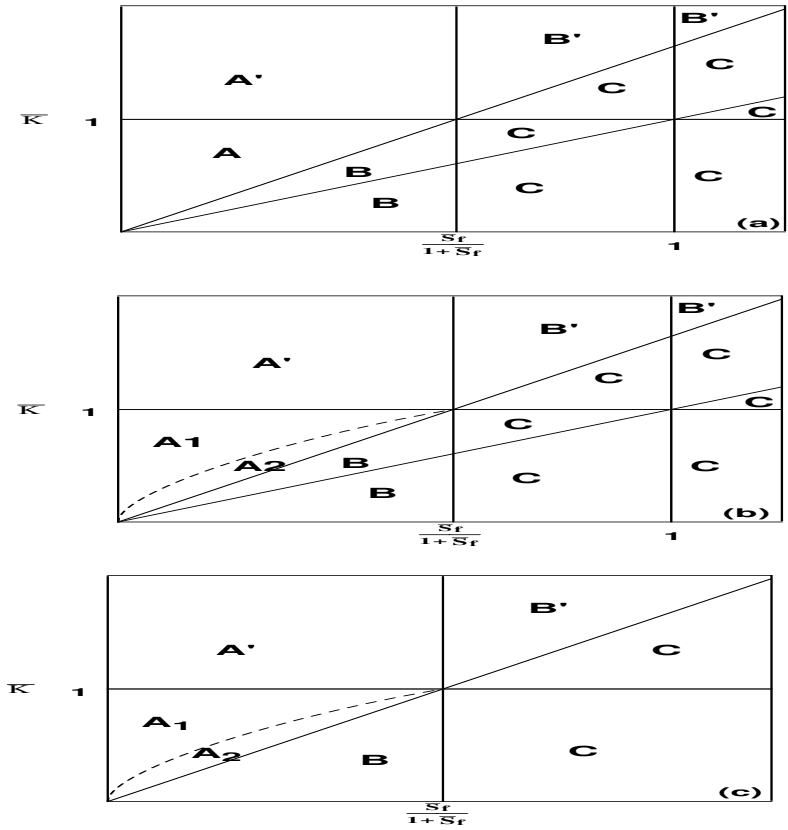

FIGURE 10.1: (a) Branch sets for the ratio-dependent model; (b) Changes in the branch set as result of dynamic bifurcation. The dashed line is the line of Hopf points; (c) Simplified branch set showing the six qualitatively different regions.

The following useful relations can be obtained between the terms S_i, $(i = 1, 3)$,

$$\frac{S_2}{\bar{p}} + \frac{S_3}{\bar{p}^2} + S_1 = -\bar{p} \tag{10.21}$$

$$(S_1 + \bar{p})\bar{p} + S_2 = (\bar{p} + \bar{\mu}_{\bar{S}}\bar{X})(1 + \frac{\bar{X}}{\bar{Y}})\bar{p}_{\frac{\bar{X}}{\bar{Y}}} - \bar{p}_{\frac{\bar{X}}{\bar{Y}}}\bar{\mu}\frac{\bar{X}}{\bar{Y}} \tag{10.22}$$

Using Equation (10.21), the first Hopf condition $F_1 = S_1 S_2 - S_3 = 0$ is reduced to the simpler and more convenient form

$$F_1 = (S_1 + \bar{p})(S_2 + \bar{p}^2) = 0 \tag{10.23}$$

Since S_2 is required to be positive, the first Hopf condition is reduced to

$$S_1 + \bar{p} = 0 \tag{10.24}$$

or equivalently by using the expression of S_1 (Equation (10.18)), to

$$\bar{\mu} - \bar{p} - \bar{\mu}_{\bar{S}}\bar{X} - \bar{p}_{\frac{\bar{X}}{\bar{Y}}}(1 + \frac{\bar{X}}{\bar{Y}}) = 0 \tag{10.25}$$

Substituting, on the other hand, Equation (10.24) into Equation (10.22) yields the following expression for S_2

$$S_2 = (\bar{p} + \bar{\mu}_{\bar{S}}\bar{X})(1 + \frac{\bar{X}}{\bar{Y}})\bar{p}_{\frac{\bar{X}}{\bar{Y}}} - \bar{p}_{\frac{\bar{X}}{\bar{Y}}}\bar{\mu}\frac{\bar{X}}{\bar{Y}} \tag{10.26}$$

Equation (10.25) also implies that

$$\bar{p} + \bar{\mu}_{\bar{S}}\bar{X} = \bar{\mu} - \bar{p}_{\frac{\bar{X}}{\bar{Y}}}(1 + \frac{\bar{X}}{\bar{Y}}) \tag{10.27}$$

Substituting this equation into Equation (10.26), yields the following simpler form for the second Hopf condition $S_2 > 0$

$$S_2 = \bar{p}_{\frac{\bar{X}}{\bar{Y}}}[\bar{\mu} - \bar{p}_{\frac{\bar{X}}{\bar{Y}}}(1 + \frac{\bar{X}}{\bar{Y}})^2] > 0 \tag{10.28}$$

Note that the Hopf conditions (Equations (10.25, 10.28)) were derived for arbitrary expressions of growth rates $\bar{\mu}$ and $\bar{p}$. For the selected growth rate (p) (Equation (10.10)), substituting for $\bar{X}$ (Equation (10.12)), $\bar{Y}$ (Equation (10.13)) and the first derivative $\bar{p}_{\frac{\bar{X}}{\bar{Y}}} = \frac{\lambda\bar{K}}{(\bar{K}+\frac{\bar{X}}{\bar{Y}})^2}$ into Equation (10.25) yields the following expression for the first Hopf condition,

$$(\lambda - \bar{K}\bar{\mu})(-\bar{\mu}^2 + \bar{\mu}\lambda + \lambda\bar{\mu}_{\bar{S}}(\bar{S}_f - \bar{S})) = 0 \tag{10.29}$$

Since $\bar{p}_{\frac{\bar{X}}{\bar{Y}}}$ is positive, Equation (10.28) requires that

$$\bar{\mu} > \frac{\bar{p}_{\frac{\bar{X}}{\bar{Y}}}(\bar{X} + \bar{Y})^2}{\bar{Y}^2} \tag{10.30}$$

Substituting the equation $\bar{X} + \bar{Y} = \bar{S}_f - \bar{S}$ and the expression of $\bar{Y}$ (Equation (10.13)) into Equation (10.30) yields the following simple condition,

$$\bar{\mu} > \frac{\bar{K}\bar{\mu}^2}{\lambda} \tag{10.31}$$

or equivalently

$$\frac{\bar{K}\bar{\mu}}{\lambda} < 1 \tag{10.32}$$

It can be seen from Equation (10.29) that Hopf points should satisfy one of the two conditions,

$$\bar{\mu} = \frac{\lambda}{\bar{K}} \tag{10.33}$$

$$-\bar{\mu}^2 + \lambda\bar{\mu} + \lambda\bar{\mu}_{\bar{S}}(\bar{S}_f - \bar{S}) = 0 \tag{10.34}$$

However, Equation (10.33) violates the second Hopf condition (Equation (10.32)). This leaves the two conditions (Equations (10.32, 10.34)) as the Hopf conditions. Note also that these equations were derived for the general expression for $\mu(\bar{S})$ but not for that of $\bar{p}(\frac{\bar{X}}{\bar{Y}})$. For the explicit form $\bar{\mu}(\bar{S}) = \frac{\bar{S}}{1+\bar{S}}$, the Hopf conditions (Equations (10.32, 10.34)) are reduced to

$$\bar{S}^2(\lambda - 1) + \lambda\bar{S}_f = 0 \tag{10.35}$$

and

$$\frac{\bar{K}\bar{S}}{1+\bar{S}} < \lambda \tag{10.36}$$

It can be concluded from Equation (10.35) that the Hopf point necessarily occurs for predator growing ability λ smaller than unity, and exactly at

$$\bar{S} = \sqrt{\frac{\lambda\bar{S}_f}{1-\lambda}} \tag{10.37}$$

The Hopf point is meaningful, i.e., $\bar{S} < \bar{S}_f$, provided that $\lambda < \frac{\bar{S}_f}{1+\bar{S}_f}$. The Hopf point should satisfy the condition of $S_2 > 0$ (Equation (10.36)). Substituting Equation (10.37) in Equation (10.36) yields

$$\bar{K} < \lambda + \sqrt{\frac{\lambda(1-\lambda)}{\bar{S}_f}} \tag{10.38}$$

This condition is added to the parameter space $(\bar{K}, \lambda)$ along with other lines in Figure 10.1b. This line (dashed) divides region A of Figure 10.1a, into two subregions A_1 and A_2. The Hopf point is absent from region A_1 while it is always expected in regions A_2 and B. The different regions of the branch set in Figure 10.1b can be lumped into six regions of qualitatively different behavior, shown in Figure 10.1c.

10.4 Dynamics Near the Washout Line

Before the behavior in each region of Figure 10.1c is analyzed, it should be noted that parts of the richness of the ratio-dependent model depend on the

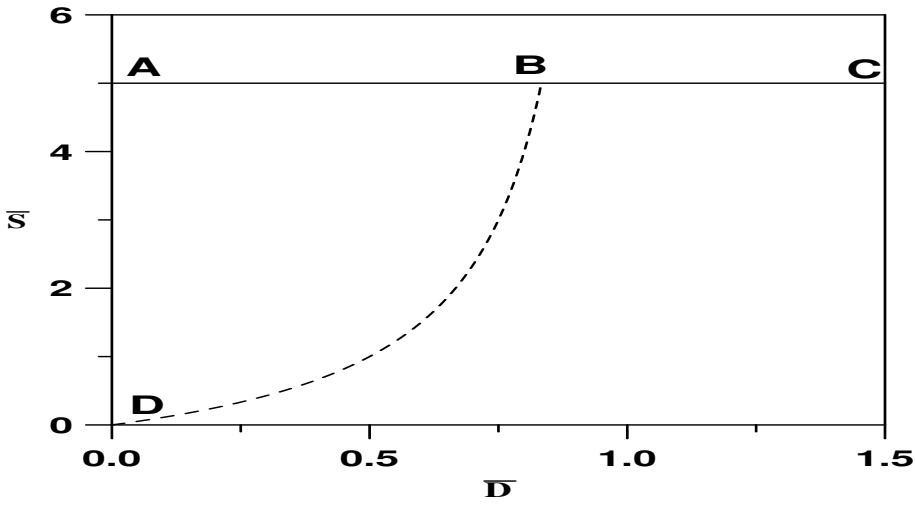

FIGURE 10.2: Continuity diagram for region (C) of Figure 10.1c; (ABC), total washout line; (DB), predator washout line; solid line, stable branch; dashed line, unstable branch.

stability characteristics of the washout line, since the behavior of the model near the total washout line $O : (\bar{S} = \bar{S}_f, \bar{X} = 0, \bar{Y} = 0)$ is rather complicated. On one hand, the growth rate $\bar{p} = \frac{\lambda \bar{X}}{K\bar{Y}+\bar{X}}$ is not defined at the washout line. On the other hand, by introducing the following change for the independent variable, $d\bar{t}^{\star} = (\bar{K}\bar{Y} + \bar{X})d\bar{t}$, the model Equations (10.7–10.9) become

$$\frac{d\bar{S}}{d\bar{t}^{\star}} = \bar{D}(\bar{S}_f - \bar{S})(\bar{K}\bar{Y} + \bar{X}) - \frac{\bar{S}}{1+\bar{S}}\bar{X}(\bar{K}\bar{Y} + \bar{X}) \tag{10.39}$$

$$\frac{d\bar{X}}{d\bar{t}^{\star}} = -\bar{D}\bar{X}(\bar{K}\bar{Y} + \bar{X}) + \frac{\bar{S}}{1+\bar{S}}\bar{X}(\bar{K}\bar{Y} + \bar{X}) - \lambda\bar{X}\bar{Y} \tag{10.40}$$

$$\frac{d\bar{Y}}{d\bar{t}^{\star}} = -\bar{D}\bar{Y}(\bar{K}\bar{Y} + \bar{X}) + \lambda\bar{X}\bar{Y} \tag{10.41}$$

It can be seen from the new equations that the origin (O) is an equilibrium point for which all the eigenvalues are equal to zero. Such points are qualified in the literature [179] as being a *nonanalytical vector field*. In order to study the stability near the washout line (O), we make use of the procedure previously adopted by a number of authors [57, 58, 179]. The first step consists in making the following change of variables, $\bar{S} = \bar{S}$, $\bar{X} = \bar{X}$, $\bar{U} = \frac{\bar{Y}}{\bar{X}}$. This transforms in a nondegenerate way the first quadrant of the $(\bar{X}, \bar{Y})$-plane, except $\bar{X} = 0$, into the first quadrant of the $(\bar{X}, \bar{U})$-plane, and "blows-up" point (O) into the

$\bar{U}$-axis. The transformed model equations with $\bar{S}$, $\bar{X}$, and $\bar{U} = \frac{\bar{Y}}{\bar{X}}$ are

$$\frac{d\bar{S}}{d\bar{t}} = \bar{D}(\bar{S}_f - \bar{S}) - \frac{\bar{S}}{1+\bar{S}}\bar{X} \tag{10.42}$$

$$\frac{d\bar{X}}{d\bar{t}} = -\bar{D}\bar{X} + \frac{\bar{S}}{1+\bar{S}}\bar{X} - \frac{\lambda\bar{X}}{\bar{K}\bar{U}+1}\bar{U} \tag{10.43}$$

$$\frac{d\bar{U}}{d\bar{t}} = \frac{\lambda U}{\bar{K}\bar{U}+1} - \frac{\bar{S}}{\bar{S}+1}\bar{U} + \frac{\lambda\bar{U}^2}{K\bar{U}+1} \tag{10.44}$$

The elements of the Jacobian matrix J are

$$j_{11} = -\bar{D} - \tfrac{1}{(1+\bar{S})^2}\bar{X}, \quad j_{12} = -\tfrac{\bar{S}}{1+\bar{S}}, \quad j_{13} = 0 \tag{10.45}$$

$$j_{21} = \tfrac{1}{(1+\bar{S})^2}\bar{X}, \quad j_{22} = -\bar{D} + \tfrac{\bar{S}}{1+\bar{S}} - \lambda\tfrac{\bar{U}}{K\bar{U}+1}, \quad j_{23} = \tfrac{-\lambda\bar{X}}{(K\bar{U}+1)^2} \tag{10.46}$$

$$j_{31} = -\tfrac{\bar{U}}{(1+\bar{S})^2}, \quad j_{32} = 0, \quad j_{33} = \tfrac{-\bar{S}}{1+\bar{S}} + \tfrac{\lambda(1+\bar{K}\bar{U}^2+2\bar{U})}{(\bar{K}\bar{U}+1)^2} \tag{10.47}$$

It can be shown that $O_1 := (\bar{S} = \bar{S}_f, \bar{X} = 0, \bar{U} = 0)$ is an equilibrium point for the modified model for which the eigenvalues are:

$$-\bar{D}, -\bar{D} + \frac{\bar{S}_f}{1+\bar{S}_f}, \lambda - \frac{\bar{S}_f}{1+\bar{S}_f} \tag{10.48}$$

The second step is to make the following change of variables, $\bar{S} = \bar{S}$, $\bar{Y} = \bar{Y}$, $\bar{W} = \frac{\bar{X}}{\bar{Y}}$. Similarly to the previous case, this procedure transforms in a nondegenerate way the first quadrant of the $(\bar{X}, \bar{Y})$-plane, except $\bar{Y} = 0$, into the first quadrant of the $(\bar{Y}, \bar{W})$-plane and "blows-up" point O into the $\bar{W}$-axis. The transformed model equations with $\bar{S}$, $\bar{Y}$ and $\bar{W} = \frac{\bar{X}}{\bar{Y}}$ are

$$\frac{d\bar{S}}{d\bar{t}} = \bar{D}(\bar{S}_f - \bar{S}) - \frac{\bar{S}\bar{W}\bar{Y}}{1+\bar{S}} \tag{10.49}$$

$$\frac{d\bar{Y}}{d\bar{t}} = -\bar{D}\bar{Y} + \frac{\lambda\bar{W}\bar{Y}}{\bar{K}+\bar{W}} \tag{10.50}$$

$$\frac{d\bar{W}}{d\bar{t}} = \frac{\bar{S}\bar{W}}{1+\bar{S}} - \frac{\lambda(\bar{W}+\bar{W}^2)}{\bar{K}+\bar{W}} \tag{10.51}$$

The elements of the Jacobian matrix J are

$$j_{11} = -\bar{D} - \tfrac{1}{(1+\bar{S})^2}\bar{W}\bar{Y}, \quad j_{12} = -\tfrac{\bar{S}\bar{W}}{1+\bar{S}}, \quad j_{13} = -\tfrac{\bar{S}\bar{Y}}{1+\bar{S}} \tag{10.52}$$

$$j_{21} = 0, \quad j_{22} = -\bar{D} + \tfrac{\lambda\bar{W}}{\bar{K}+\bar{W}}, \quad j_{23} = \tfrac{\lambda\bar{K}\bar{Y}}{(\bar{K}+\bar{W})^2} \tag{10.53}$$

$$j_{31} = \tfrac{\bar{W}}{(1+\bar{S})^2}, \quad j_{32} = 0, \quad j_{33} = \tfrac{\bar{S}}{1+\bar{S}} - \tfrac{\lambda(\bar{K}+2\bar{K}\bar{W}+\bar{W}^2)}{(\bar{K}+\bar{W})^2} \tag{10.54}$$

Similarly to the previous case, it can be seen that $O_2 := (\bar{S} = \bar{S}_f, \bar{Y} = 0, \bar{W} = 0)$ is an equilibrium point for which the eigenvalues are:

$$-\bar{D}, -\bar{D}, \frac{\bar{S}_f}{1+\bar{S}_f} - \frac{\lambda}{\bar{K}} \tag{10.55}$$

These results can be combined to provide the behavior of the original model near the total washout line (point O). It can be seen that for $\lambda < \frac{\bar{S}_f}{1+\bar{S}_f}$ and $\frac{\lambda}{K} > \frac{\bar{S}_f}{1+\bar{S}_f}$ (which corresponds to region B of Figure 10.1c), point O_1 (Equation (10.48)) is a stable node for $\bar{D} > \frac{\bar{S}_f}{1+\bar{S}_f}$ and a saddle for $\bar{D} < \frac{\bar{S}_f}{1+\bar{S}_f}$, while point O_2 (Equation (10.55)) is a stable node for all dilution rates $\bar{D}$. Therefore, in region B, the topological structure in the neighborhood of the washout line, for $\bar{D} < \frac{\bar{S}_f}{1+\bar{S}_f}$, consists of two sectors: a saddle sector and an attracting node sector. Therefore, unlike the strictly prey-dependent models, the washout line for the ratio-dependent model, can have its *own* basin of attraction, for some values of model parameters. This has important implications on the types of behaviors the model can predict, as it will be seen in the following discussion of the different regions of Figure 10.1c.

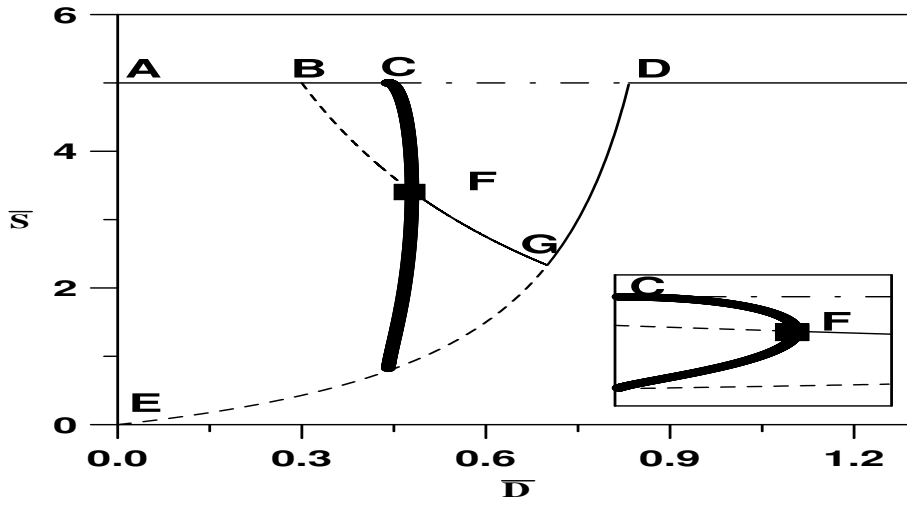

FIGURE 10.3: Continuity diagrams for region (B) of Figure 10.1c; (ABCD) total washout line; (EGD) predator washout line; (BFG) static coexistence line; solid line, stable branch; dashed line, unstable branch; semidashed line, region with saddle sector and attracting node sector; square, Hopf point; bold line, stable periodic branch.

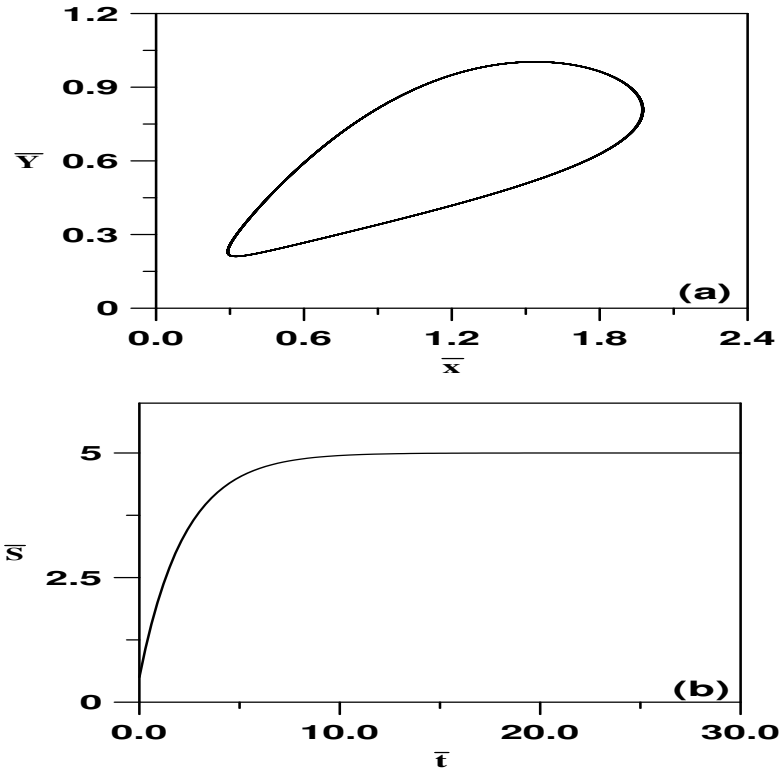

FIGURE 10.4: Dynamics for $\bar{D} = 0.47$ in region (B) of Figure 10.3; (a) The start-up conditions $(\bar{S}, \bar{X}, \bar{Y}) = (3, 0.7, 0.8)$ lead to stable limit cycle; (b) The initial conditions $(\bar{S}, \bar{X}, \bar{Y}) = (3, 0.002, 0.8)$ lead to total washout.

10.5 Bifurcation Diagrams

The branch set of Figure 10.1c provides a classification of the behavior of the model in terms of its parameters λ, $\bar{K}$, and $\bar{S}_f$. The effect of the dilution rate $\bar{D}$ is included by constructing continuity diagrams where $\bar{D}$ is the bifurcation parameter. Each continuity diagram consists of three static branches: the total washout line, the curve of predator washout (Equation (10.11)), and the branch of static coexistence (Equation (10.14)). These equations are explicit in $\bar{D}$ and can be readily solved for the remaining values of model parameters. A number of results can be obtained for the relative position of these curves in the continuity diagrams. First, the curves of static coexistence and predator

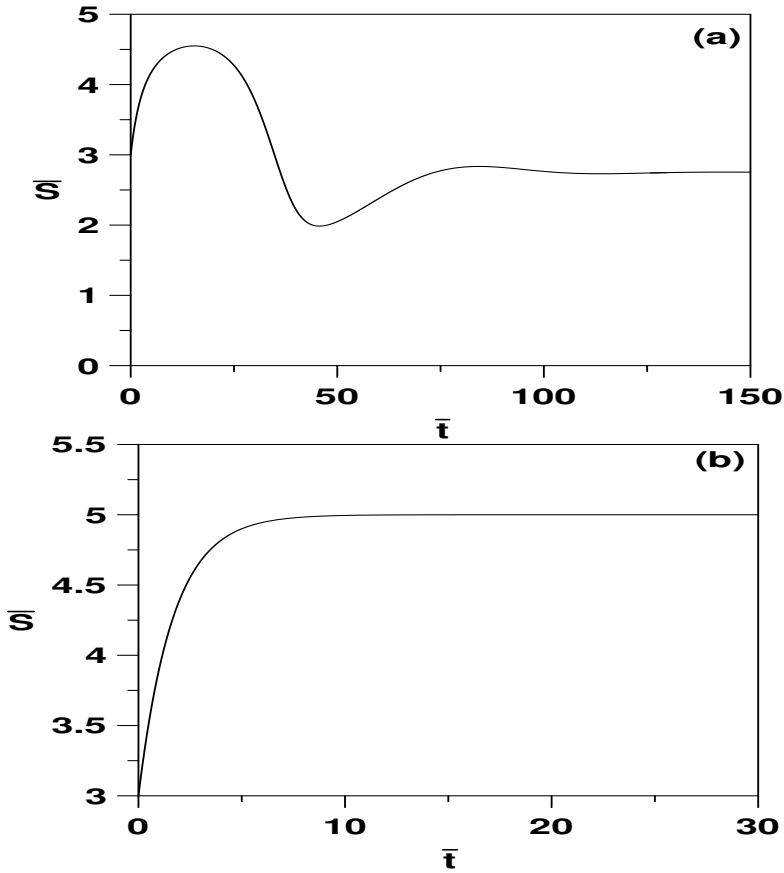

FIGURE 10.5: Dynamics for $\bar{D} = 0.60$ in region (B) of Figure 10.3; (a) Start-up conditions $(\bar{S}, \bar{X}, \bar{Y}) = (3, 0.9, 0.6)$ lead to nontrivial coexistence; (b) $(\bar{S}, \bar{X}, \bar{Y}) = (3, 0.002, 0.8)$ lead to total washout.

washout (Equations (10.11–10.14)) cross at

$$\bar{D} = \lambda, \quad \bar{S} = \frac{\lambda}{1 - \lambda} \tag{10.56}$$

Therefore, provided that the crossing is meaningful, i.e., $\bar{S} < \bar{S}_f$, the predator is washed out when the dilution rate $\bar{D}$ is larger than its growing ability λ. The curve of static coexistence, on the other hand, crosses the total washout line at the dilution rate, solution of Equation (10.14), with $\bar{S} = \bar{S}_f$,

$$\bar{D} = \frac{\bar{S}_f(\bar{K} - \lambda) - \lambda}{(\bar{S}_f + 1)(\bar{K} - 1)} \tag{10.57}$$

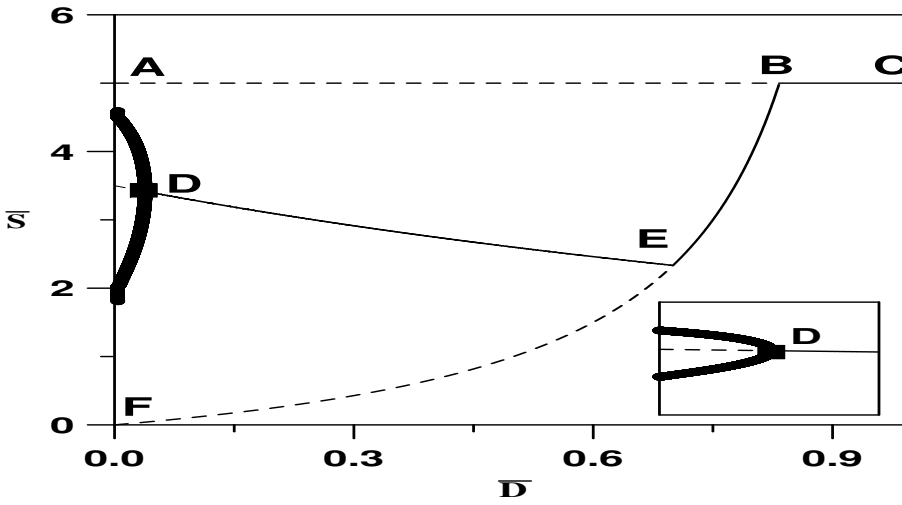

FIGURE 10.6: Continuity diagrams for region (A_2) of Figure 10.1c; (ABC), total washout line; (BEF), predator washout line; (DE), static coexistence line.

Finally, the curve of predator washout crosses the total washout line at dilution rate $\bar{D} = \frac{\bar{S}_f}{1+\bar{S}_f}$. Therefore, when the dilution rate exceeds this critical value total washout occurs. In the following section we examine the bifurcation diagrams for each region of Figure 10.1c.

10.5.1 Coextinction of Species

Figure 10.2 shows an example of continuity diagram for region C, for the following parameters: $\bar{S}_f = 5$, $\bar{K} = 0.7$, and $\lambda = 0.9$. In this case, the operation of the reactor leads to total washout (line ABC), since the only other branch that exists is the predator washout line (DB), which is unstable. A total washout or "coextinction" of species in this region can be interpreted in the following way. Due to its high growing ability $\lambda > \frac{\bar{S}_f}{1+\bar{S}_f}$ and high consumption ability $\frac{\lambda}{\bar{K}} > \frac{\bar{S}_f}{1+\bar{S}_f}$, the predator population is "overefficient." It grows so quickly that all preys are consumed, which also leads to the extinction of predators.

10.5.2 Conditional Coexistence

Region B of Figure 10.1c corresponds to $\frac{\lambda}{\bar{K}} > \frac{\bar{S}_f}{1+\bar{S}_f}$ and $\lambda < \frac{\bar{S}_f}{1+\bar{S}_f}$. It is characterized by a relatively smaller predator growing ability λ. The consump-

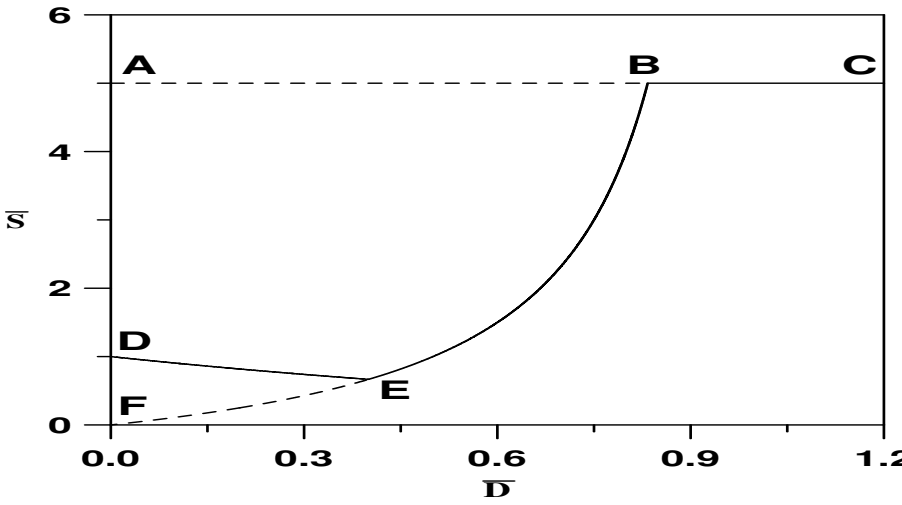

FIGURE 10.7: Continuity diagrams for region (A_1) of Figure 10.1c; (ABC), total washout line; (BEF), predator washout line; (DE), static coexistence line.

tion and growing ability generate balanced dynamics that allow the mutual coexistence of the species. Figure 10.3 shows an example of continuity diagram for the following set of parameters: $\bar{S}_f = 5$, $\bar{K} = 0.75$, and $\lambda = 0.7$. Three branches can be seen in the diagram: the total washout line (ABCD), the predator washout line (EGD), and the nontrivial coexistence of species (BFG). The diagram is also characterized by the presence of a Hopf point, as in the solution of Equation (10.37). The diagram is therefore characterized for some range of dilution rates by the coexistence of species either in a static or periodic mode. The peculiarities of the ratio-dependent model are illustrated when Figure 10.3 is analyzed in more detail. Note that point D of Figure 10.3 corresponds to $\bar{D} = \frac{\bar{S}_f}{1+\bar{S}_f}$. For values of $\bar{D} < \frac{S_f}{1+S_f}$ (smaller than point D), the analysis carried out in previous sections has shown that the topological structure near the washout line consists of a saddle sector and an attracting node sector, providing the washout line with its own basin of attraction. Consequently, for region between C and F (enlarged in the smaller diagram of Figure 10.3), the model predicts the coexistence of species in an oscillatory mode. However, unlike prey-dependent models, the species can also reach total washout depending on their initial conditions. Figures 10.4(a–b) show an example of this situation for $\bar{D} = 0.47$ and two sets of initial conditions. For initial conditions $(\bar{S}, \bar{X}, \bar{Y}) = (3, 0.7, 0.8)$, the system eventually reaches a stable limit cycle. When, on the other hand, initial conditions are selected

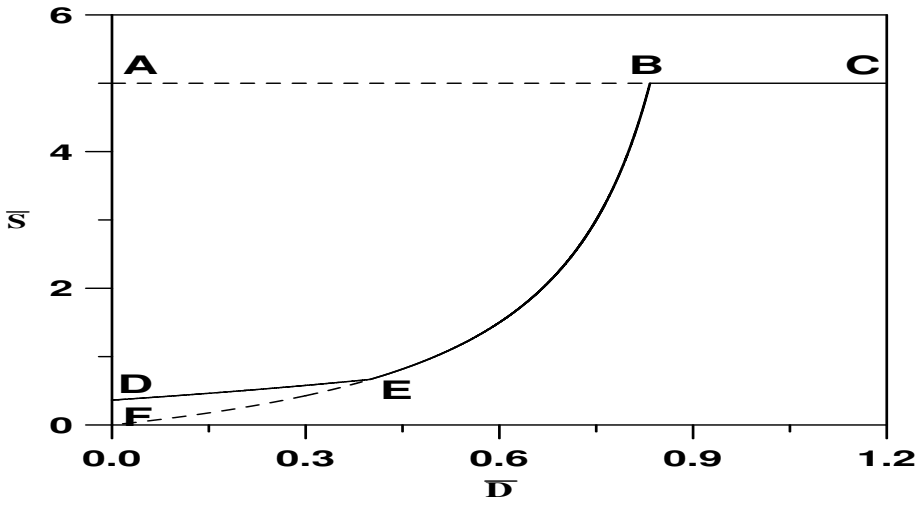

FIGURE 10.8: Continuity diagrams for region (A´) of Figure 10.1c; (ABC), total washout line; (BEF), predator washout line; (DE), static coexistence line.

such that the ratio of prey to predator is small $(\bar{S}, \bar{X}, \bar{Y}) = (3, 0.002, 0.8)$, the system is attracted towards the origin and total washout occurs.

For dilution rates between F and G (Figure 10.3), the species coexist in a nontrivial steady-state mode, but again the species can also reach washout depending on initial conditions. Figures 10.5(a–b) show an example of this behavior for $\bar{D} = 0.60$ and two sets of initial conditions. Start-up conditions $(\bar{S}, \bar{X}, \bar{Y}) = (3, 0.9, 0.6)$ lead the system into a nontrivial steady state while identical initial conditions to the previous example $(\bar{S}, \bar{X}, \bar{Y}) = (3, 0.002, 0.8)$ lead to total washout. The ratio-dependent model exhibits therefore a unique behavior that distinguishes it from strictly prey-dependent models. The model foresees, for the same parameters, the coexistence of regions of total washout ("coextinction") and regions of species coexistence. These regions can be therefore qualified as regions of conditional coexistence of species.

10.5.3 Unconditional Coexistence

Going back to Figure 10.1c, it can be seen that region A_2 is characterized by an even smaller predator growing ability λ and also by a much smaller consumption ability, i.e., $\frac{\lambda}{K} \leq \frac{\bar{S}_f}{1+\bar{S}_f}$. Figure 10.6 shows the continuity diagram for this region, obtained with $(\bar{S}_f, \bar{K}, \lambda) = (5, 0.9, 0.7)$. From the origin (not included) and up to the Hopf point (D) (enlarged in the smaller diagram), the species coexist in a state of stable limit cycle for any initial conditions.

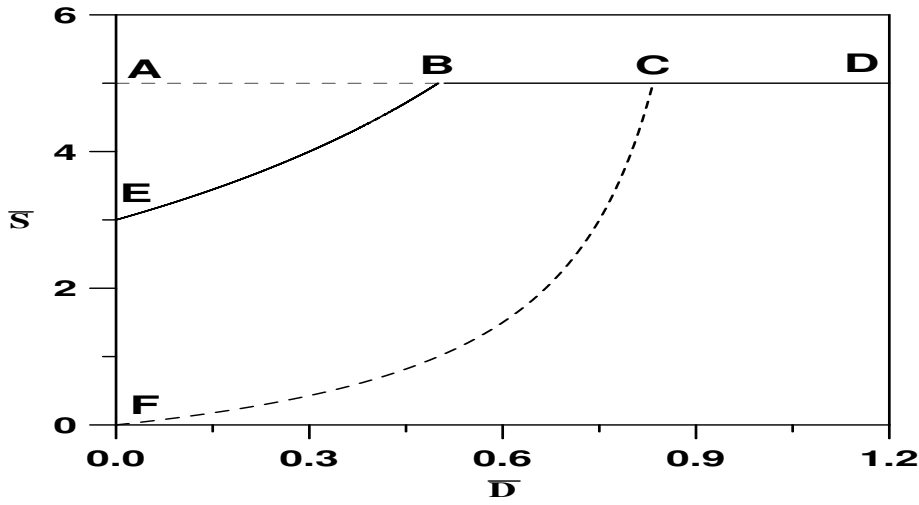

FIGURE 10.9: Continuity diagrams for region (B´) of Figure 10.1c; (ABCD), total washout line; (FC), predator washout line; (EB), static coexistence line.

For dilution rates between points D and E, the species coexist in a state of nontrivial equilibrium, again for any initial conditions. For dilution rates between E and B, the predator is washed out while for dilution rates larger than point B, total washout occurs. Region A_2 imparts to the system a behavior similar to the one found in prey-dependent models. The coexistence of species either in a state of limit cycle or in a static mode is independent of initial conditions. This region is therefore qualified as an area of "unconditional coexistence of species." When crossing the line of Hopf points and into region A_1 of Figure 10.1c, the Hopf point disappears but the topological structure near the washout line for $\bar{D} < \frac{\bar{S}_f}{1+\bar{S}_f}$ is unchanged from region A_2. The continuity diagram for this region is shown in Figure 10.7, for $(\bar{S}_f, \bar{K}, \lambda) = (5, 0.8, 0.40)$. Region A_1 also imparts to the model an "unconditional coexistence" behavior.

10.5.4 Predator Growing Ability Larger Than Its Consumption Ability

The behavior of the model up to this point was analyzed for values of $\bar{K} < 1$, which corresponds to the case when predator growing ability (λ) is smaller than its consumption ability ($\frac{\lambda}{\bar{K}}$). This is the usual assumption made in the study of predator–prey interactions, for it is assumed that the prey is the only food available to the predator. The other case is when $\bar{K} > 1$ can also be of interest as well. This can be the case when the predator feeds on other

resources in such a way that the prey is the limiting factor. Regions A´ and B´ in the branch set of Figure 10.1c correspond to this situation. Figure 10.8 shows an example of a bifurcation diagram for region A´, for $(\bar{S}_f, \bar{K}, \lambda) = (5, 1.5, 0.40)$. The diagram is similar to region A_1, except that the substrate concentration is seen to increase with the dilution rate on the coexistence branch.

The other region (B´) offers an interesting feature of the ratio-dependent model. An example of the behavior in this region is shown in the diagram of Figure 10.9, obtained with $(\bar{S}_f, \bar{K}, \lambda) = (5, 1.2, 0.9)$. Three branches can be seen in the diagram: the total washout line (ABCD), the nontrivial steady-state coexistence (EB), and the predator washout branch (FC). For dilution rates smaller than point B, all initial conditions lead to a stable coexistence of species. For dilution rates larger than B, the operation of the bioreactor leads to a total washout for all initial conditions. Region (B´) offers therefore the unique feature of a direct transition from coexistence to total washout without going through predator washout. The reason for this behavior is that the crossing between the coexistence and the predator washout curves occurs at the value of $\frac{\lambda}{1-\lambda}$ (Equation (10.56)), which is in this case larger than $\bar{S}_f$.

10.6 Concluding Remarks

The dynamic characteristics of a ratio-dependent model when applied to a continuous bioreactor were investigated in this chapter. General analytical conditions with respect to arbitrary growth rates of prey on substrate and predator on prey were established that describe the conditions for the occurrence of an oscillatory behavior in the model. The analysis of an example for which both prey and predator grow following a Monod-like behavior, has revealed the exact location of the one single Hopf point predicted by the model. Branch sets were also constructed that revealed some of the peculiarities of the model.

In summary, the studied ratio-dependent model can predict essentially four scenarios: (1) coextinction of species for all initial conditions, (2) predator washout and survival of prey for all initial conditions, (3) coexistence (either static or oscillatory) of species, for all initial conditions, and (4) coexistence or coextinction depending on initial conditions. As was mentioned in the introduction, all these behaviors were observed in real life but the strictly prey-dependent models are not able to produce the fourth scenario.

Looking back at the branch set of Figure 10.1c, it can be seen that the line $\lambda = \frac{\bar{S}_f}{1+\bar{S}_f}$ represents a hard boundary for the system, since crossing this line from region (B) to (C) leads to the coextinction of the species for any dilution rate. This mode of extinction results from high predator efficiency in

dealing with the prey, which results in the extinction of the predator itself. For given predator–prey growth parameters λ and $\bar{K}$, increasing the substrate feed concentration narrows the domain C of coextinction at the expense of region B of conditional coexistence. Moreover, within regions of coexistence B, A_1, and A_2, it is possible to alter the dynamics of the chemostat through the manipulation of the dilution rate. The curve $\bar{D} = \frac{\bar{S}_f}{1+\bar{S}_f}$ can also be considered as a hard boundary, since operating the chemostat at larger dilution rates leads to total washout. Within regions B, A_1, and A_2, the predator is washed out when the dilution rate $\bar{D}$ exceeds its growing ability λ. Predators under these conditions are unable to grow fast enough to compensate for their death rates. The line $\frac{\lambda}{\bar{K}} = \frac{\bar{S}_f}{1+\bar{S}_f}$ is another boundary for the system. It separates regions of unconditional coexistence from regions where the coexistence is dependent on initial conditions. The mode of extinction that occurs in region B is different from that of region C, and occurs when the initial prey/predator ratio is very low. This means that altering the ratio of prey to predator may lead to the collapse of the whole system and the extinction of both species. When the predator growing ability is larger than its consumption ability, the line $\frac{\lambda}{\bar{K}} = \frac{\bar{S}_f}{1+\bar{S}_f}$ can be considered as a hard boundary for the system, since crossing it from the region of coexistence B´ leads to coextinction. Moreover, in this case it is possible to force a direct transition from coexistence to coextinction without going through a region of predator washout. This is possible by selecting the substrate feed concentration $\bar{S}_f$ smaller than $\frac{\lambda}{1-\lambda}$.

Chapter 11

MODELS WITH PRODUCT FORMATION

11.1 Introduction

In this part of the book, we revisit the unstructured model, already studied in Chapter 4, by including the dynamics associated with the formation of a metabolic product. The continuous bioreactor is described by the following unstructured model for the biomass X, a limiting substrate S, and a desired nonbiomass product P,

$$\frac{dX}{dt} = \mu X - DX \tag{11.1}$$

$$\frac{dS}{dt} = D(S_f - S) - \sigma X \tag{11.2}$$

$$\frac{dP}{dt} = \epsilon X - DP \tag{11.3}$$

μ is the specific cell growth rate, σ is the cell mass specific net utilization rate of limiting substrate, and ϵ is the cell mass specific net production rate. We also assume clean feed conditions, i.e., no cells or product enter the bioreactor through the feed. In its most general form defined by Equations (11.1–11.3), the rates μ, σ, and ϵ may, theoretically, depend on the process state variables X, S, and P, and may not be related. However, as pointed out by Parulekar [272], the general unstructured model described by Equations (11.1–11.3) can be classified in a practical way based on eventual relations among the specific growth rates μ, ϵ, and σ. In this part of the book, we examine the stability behavior of three large classes of models derived from the general Equations (11.1-11.3). The classification is inspired, but different from the one proposed in [272].

- Type I models: For this class of models, both the substrate utilization rate σ and the product formation rate ϵ are linear functions of cell growth rate μ,

$$\sigma = Y_{xs}\mu + m_s \tag{11.4}$$

$$\epsilon = Y_{xp}\mu + m_p \tag{11.5}$$

where Y_{xs} and Y_{xp} are the yield coefficients, assumed constant, and m_s and m_p are the maintenance coefficients, also assumed constants. Moreover, no restriction is imposed on the explicit form of cell growth rate μ (on which both σ and ϵ depend) as it is allowed to depend arbitrarily on X, S and P. For type I models, strictly growth associated products are characterized by the following direct relationship

$$\epsilon = Y_{xp}\mu \tag{11.6}$$

while for nongrowth associated products, the specific rate of product formation is constant, i.e.,

$$\epsilon = m_p \tag{11.7}$$

Mixed-growth-associated products are, on the other hand, described by Equation (11.5). This class of models, based on a variety of kinetic expressions, was used in several investigations to model a number of important bioprocesses, including the alcohol fermentation [52, 155, 206, 207, 219, 248, 320], the ammonium lactate fermentation [341], propionic acid production from *Propionibacterium shermanii* [145], and the production of a number of secondary metabolites [6, 194, 306].

- Type II models: For this class, the specific rate σ of substrate utilization and the specific rate ϵ of product formation are related directly by

$$\sigma = a\epsilon \tag{11.8}$$

For this type of model, the kinetics of the bioprocess are described by both cell growth rate μ and product formation rate ϵ. Both these rates can have independent kinetic expressions. This class of models was used in the literature to model a number of bioprocesses, including ethanol fermentation of cellulose-hydrolystate [126, 272, 357].

- Type III models: For these models, the utilization rate of the limiting substrate is linearly proportional to cell growth rate but not to the formation of the desired product

$$\sigma = a\mu \tag{11.9}$$

Similarly to type II models, the kinetics of the bioprocess can be described by both the cell growth rate μ and the product formation rate ϵ. This type of model was, for instance, used by Aiba and Shoda [10] and Aiba et al. [11] for ethanol production from glucose by *Saccharomyces cerevisiae*.

11.2 Type I Models

We start with the class of models for which the specific rate ϵ of product formation and the substrate utilization rate σ are given as a linear function of the cell growth rate μ. In the first part of this work, general analytical conditions are derived for the occurrence of Hopf points in these models. This allows the classification of cases where an oscillatory behavior is possible.

The model (Equations (11.1–11.3)) can be suitably rendered dimensionless by introducing the following variables,

$$\bar{S} = \frac{S}{S_r}, \quad \bar{X} = \frac{Y_{xs}X}{S_r}, \quad \bar{P} = \frac{P}{P_r}, \quad \alpha = \frac{Y_{xp}S_r}{Y_{xs}P_r}, \quad \beta_s = \frac{m_s}{Y_{xs}\mu_r}, \quad \beta_p = \frac{m_p S_r}{a\mu_r P_r}$$

$$\bar{D} = \frac{D}{\mu_r}, \quad \bar{t} = t\mu_r, \quad \bar{\mu} = \frac{\mu}{\mu_r} \tag{11.10}$$

where S_r and P_r and μ_r are reference terms for S and P and μ, respectively. The model in a dimensionless form is given by

$$\frac{d\bar{X}}{d\bar{t}} = -\bar{D}\bar{X} + \bar{\mu}\bar{X} \tag{11.11}$$

$$\frac{d\bar{S}}{d\bar{t}} = \bar{D}(\bar{S}_f - \bar{S}) - (\bar{\mu} + \beta_s)\bar{X} \tag{11.12}$$

$$\frac{d\bar{P}}{d\bar{t}} = (\alpha\bar{\mu} + \beta_p)\bar{X} - \bar{D}\bar{P} \tag{11.13}$$

The steady-state value of $\bar{X}$ is related to $\bar{S}$ by the simple relation,

$$\bar{X} = \frac{\bar{S}_f - \bar{S}}{1 + \frac{\beta_s}{\bar{\mu}}} \tag{11.14}$$

An implicit relation for $\bar{P}$ is obtained by,

$$\bar{P} = \frac{(\alpha\bar{\mu} + \beta_p)}{\bar{\mu}} \frac{(\bar{S}_f - \bar{S})}{1 + \frac{\beta_s}{\bar{\mu}}} \tag{11.15}$$

11.2.1 Existence of Periodic Solutions

The elements of the Jacobian matrix are given by

$$j_{11} = \bar{\mu}_{\bar{X}}\bar{X} + \bar{\mu} - \bar{D}, \quad j_{12} = \bar{\mu}_{\bar{S}}\bar{X}, \quad j_{13} = \bar{\mu}_{\bar{P}}\bar{X} \tag{11.16}$$

$$j_{21} = -(\bar{\mu}_{\bar{X}}\bar{X} + \bar{\mu} + \beta_s), \quad j_{22} = -\bar{D} - \bar{\mu}_{\bar{S}}\bar{X}, \quad j_{23} = -\bar{\mu}_{\bar{P}}\bar{X} \tag{11.17}$$

$$j_{31} = \alpha\bar{\mu}_{\bar{X}}\bar{X} + (\alpha\bar{\mu} + \beta_p), \quad j_{32} = \alpha\bar{\mu}_{\bar{S}}\bar{X}, \quad j_{33} = \alpha\bar{\mu}_{\bar{P}}\bar{X} - \bar{D} \tag{11.18}$$

The Hopf conditions are given by:

$$F_1 := S_1 S_2 - S_3 = 0 \tag{11.19}$$

$$S_2 > 0 \tag{11.20}$$

where S_i $(i = 1, 3)$ were defined in Chapter 3. The following expressions for these terms are:

$$S_1 = -2\bar{\mu} + (\alpha\bar{\mu}_{\bar{P}} + \bar{\mu}_{\bar{X}} - \bar{\mu}_{\bar{S}})\bar{X} \tag{11.21}$$

$$S_2 = 2\bar{\mu}\bar{X}(\bar{\mu}_{\bar{S}} - \bar{\mu}_{\bar{X}} - \alpha\bar{\mu}_{\bar{P}}) + \bar{X}(\beta_s\bar{\mu}_{\bar{S}} - \beta_p\bar{\mu}_{\bar{P}}) + \bar{\mu}^2 \tag{11.22}$$

$$S_3 = \bar{\mu}^2\bar{X}(\alpha\bar{\mu}_{\bar{P}} + \bar{\mu}_{\bar{X}} - \bar{\mu}_{\bar{S}}) + \bar{\mu}\bar{X}(\beta_p\bar{\mu}_{\bar{P}} - \beta_s\bar{\mu}_{\bar{S}}) \tag{11.23}$$

Using the steady-state condition ($\bar{\mu} = \bar{D}$), algebraic manipulations allow the derivation of the following useful relation for the first Hopf condition (Equation (11.19)),

$$F_1 = (S_1 + \bar{\mu})(S_2 + \bar{\mu}^2) \tag{11.24}$$

Since S_2 is required to be strictly positive (Equation (11.20)), the first Hopf condition $F_1 = 0$ is equivalent to:

$$S_1 + \bar{\mu} = 0 \tag{11.25}$$

Recasting the expression of S_1 from Equation (11.21) yields,

$$\bar{\mu} = (\alpha\bar{\mu}_{\bar{P}} + \bar{\mu}_{\bar{X}} - \bar{\mu}_{\bar{S}})\bar{X} \tag{11.26}$$

This relation along with $S_2 > 0$ form the conditions for the occurrence of Hopf points in the model. In the following section, these two Hopf conditions are used to analyze the behavior of some important cases of the studied models.

The first case pertains to bioprocesses for which the rate μ depends exclusively on S. This basic unstructured model was used extensively in the literature. Examples of growth rate expressions include both monotonic and non-monotonic growth kinetics [41], as was mentioned in the introductory Chapter 2. For this type of models, the conditions $\bar{\mu}_{\bar{X}} = \bar{\mu}_{\bar{P}} = 0$ hold. Substituting in the Hopf condition (Equation (11.26)) yields the simple relation

$$\bar{\mu} = -\bar{\mu}_{\bar{S}}\bar{X} \tag{11.27}$$

The condition $S_2 > 0$ (Equation (11.22)) becomes,

$$S_2 = \bar{X}\bar{\mu}_{\bar{S}}(\beta_s + 2\bar{\mu}) + \bar{\mu}^2 > 0 \tag{11.28}$$

Substituting Equation (11.27) into Equation (11.28) yields,

$$S_2 = -\beta_s \bar{\mu} - \bar{\mu}^2 \tag{11.29}$$

The second Hopf condition $S_2 > 0$ is therefore never satisfied. This result joins the conclusion reached in Chapter 4, and shows that the basic unstructured model cannot predict periodic behavior for any form of cell growth rate even if product dynamics are included, as long as the cell growth rate depends solely on the substrate and the yield is assumed to be constant.

The second example of models corresponds to the case for which the product is strictly growth associated ($\alpha \neq 0$ and $\beta_p = 0$), and for which the rate μ depends on both S and P with the condition $\mu_P < 0$ being satisfied. Case studies of these bioprocesses include a number of models for alcohol formations processes [52, 155, 206, 219, 320] and production of ethanol by *Z. mobilis* [207, 248]. Examples of kinetic expressions reported in the literature include the following expressions,

$$\mu(S, P) = \mu_1(S)\mu_2(P) \tag{11.30}$$

where $\mu_2(P)$ can have one of the following forms,

$$\mu_2(P) = \frac{K_P}{K_P + P} \tag{11.31}$$

$$\mu_2(P) = (1 - \frac{P}{P_m})^n \tag{11.32}$$

$$\mu_2(P) = exp(-\alpha P) \tag{11.33}$$

It can be noted that the condition $\mu_P < 0$ is satisfied in all these examples. For these types of models, the condition $\bar{\mu}_{\bar{X}} = 0$ holds. The two Hopf conditions $S_2 > 0$ (Equation (11.22)) and $F_1 = 0$ (Equation (11.26)) are reduced in this case to

$$2\bar{\mu}\bar{X}(\bar{\mu}_S - \alpha\bar{\mu}_P) + \bar{X}\beta_s\bar{\mu}_{\bar{S}} + \bar{\mu}^2 > 0 \tag{11.34}$$

and

$$\bar{\mu} = (\alpha\bar{\mu}_{\bar{P}} - \bar{\mu}_{\bar{S}})\bar{X} \tag{11.35}$$

Substituting Equation (11.35) into Equation (11.34) yields

$$\bar{X}\beta_s\bar{\mu}_{\bar{S}} > \bar{\mu}^2 \tag{11.36}$$

This condition requires $\bar{\mu}_{\bar{S}}$ to be positive. However, since $\bar{\mu}_{\bar{P}}$ was assumed to be negative, Equation (11.35) requires $\bar{\mu}$ to be negative, which is impossible. Again this simple analysis was carried out without the explicit expressions of

$\bar{\mu}(\bar{S}, \bar{P})$. The only requirement is for $\bar{\mu}_{\bar{P}}$ to be negative, which is the most likely effect expected from the product. We conclude therefore that these types of models cannot predict oscillatory behavior regardless of the form of the kinetic expressions.

For the general case of $\alpha \neq 0$ and $\beta_p \neq 0$, the two Hopf conditions $S_2 > 0$ (Equation (11.22)) and $F_1 = 0$ (Equation (11.26)) are not incompatible and do not exclude the existence of Hopf points. These conditions can be used to construct, in terms of model parameters, the domains for which an oscillatory behavior is possible. In the next section, a case model belonging to this class is analyzed in detail. The kinetic rate $\mu(S, P)$ is assumed to have the following form

$$\mu(S, P) = \mu_1(S)\mu_2(P) \tag{11.37}$$

with

$$\mu_1(S) = \frac{\mu_m S}{K_S + S + \frac{S^2}{K_I}} \tag{11.38}$$

and

$$\mu_2(P) = (1 - \frac{P}{P_m})^n \tag{11.39}$$

The model is based on Haldane substrate inhibition with the product inhibiting the maximum specific growth rate through $\mu_2(P)$. This model was used in a number of case studies [6, 145, 194, 341].

Neglecting the maintenance term β_s, the model is rendered dimensionless in the form of Equations (11.11–11.13) with $S_r = K_S$, $P_r = P_m$, and $\mu_r = \mu_m$. The dimensionless specific growth rate is given by

$$\bar{\mu} = \frac{\bar{S}}{1 + \bar{S} + \gamma \bar{S}^2}(1 - \bar{P})^n := \bar{\mu}_1(\bar{S})\bar{\mu}_2(\bar{P}) \tag{11.40}$$

First, the model equations at steady state are reduced to one algebraic equation by substituting Equation (11.13) in the steady-state form of Equation (11.11) to yield a single algebraic equation that depends only on $\bar{S}$ as a state variable.

$$F(\bar{S}) := (\bar{S}_f - \bar{S})(-\bar{D} + \bar{\mu}) \tag{11.41}$$

The state variable $\bar{P}$ that appears in $\bar{\mu}$ is implicitly related to $\bar{S}$ by Equation (11.15). Equation (11.41) predicts washout conditions, i.e., $\bar{S} = \bar{S}_f$, $\bar{X} = 0$, and a nontrivial solution

$$\bar{\mu} = \bar{D} \tag{11.42}$$

The number of solutions this equation may have depends on the coefficient n

in Equation (11.39), and therefore a large number of static behaviors can be expected. Here the analysis is limited to the static feature that occurs when the limit point of Equation (11.42) crosses the washout line. The nontrivial solution (Equation (11.42)) exhibits a static limit point $F_{\bar{S}} = 0$ when $\frac{d\bar{\mu}}{d\bar{S}} = 0$. Taking the first derivative of the growth rate (Equation (11.40)) yields

$$\frac{d\bar{\mu}}{d\bar{S}} = \bar{\mu}_{1S}(1-\bar{P})^n - n\bar{\mu}_1(1-\bar{P})^{n-1}\frac{d\bar{P}}{d\bar{S}} = 0 \tag{11.43}$$

The derivative $\frac{d\bar{P}}{d\bar{S}}$ can be obtained analytically using the implicit relation of Equation (11.15). The crossing of the nontrivial solution with the washout line occurs for $\bar{S} = \bar{S}_f$. Using this condition and noting that $\bar{P} = 0$ (Equation (11.15)), the derivative $\frac{d\bar{P}}{d\bar{S}}$ is reduced to

$$\frac{d\bar{P}}{d\bar{S}} = -\alpha - \frac{\beta_p}{\bar{\mu}_1(\bar{S}_f)} \tag{11.44}$$

Substituting back into Equation (11.43) yields the condition for the occurrence of the static limit point on the washout line

$$\bar{\mu}_{1S}(\bar{S}_f) + n(\alpha\bar{\mu}_1(\bar{S}_f) + \beta_p) = 0 \tag{11.45}$$

With the expression chosen for $\bar{\mu}_1(\bar{S})$ (Equation (11.40)), the derivative $\bar{\mu}_{1\bar{S}}$ is given by

$$\bar{\mu}_{1S} = \frac{1-\gamma\bar{S}^2}{(1+\bar{S}+\gamma\bar{S}^2)^2} \tag{11.46}$$

The condition of Equation (11.45) is equivalent then to

$$\frac{1-\gamma\bar{S}_f{}^2}{(1+\bar{S}_f+\gamma\bar{S}_f{}^2)^2} + n\left(\frac{\alpha\bar{S}_f}{1+\bar{S}_f+\gamma\bar{S}_f{}^2} + \beta_p\right) = 0 \tag{11.47}$$

This condition separates two types of behavior. The static behavior for the case when the product is strictly growth associated can also be described by the above relation, by setting $\beta_p = 0$, to yield

$$\frac{1-\gamma\bar{S}_f{}^2}{(1+\bar{S}_f+\gamma\bar{S}_f{}^2)} + n\alpha\bar{S}_f = 0 \tag{11.48}$$

11.2.2 Hopf Singularities

The H_{01} singularity that corresponds to the appearance or coalescence of two Hopf points is given by the following conditions,

$$F_1 = F_{1\bar{S}} = 0, F_{1\bar{S}\bar{S}} \neq 0, S_2 > 0 \tag{11.49}$$

where F_1 is defined by Equation (11.19). It can be seen from Equation (11.19) that since $S_2 > 0$, the condition $F_1 = 0$ is equivalent to $S_1 + \bar{\mu} = 0$. The condition $F_{1\bar{S}} = 0$ implies therefore that

$$S_{1S} + \bar{\mu}_{\bar{S}} = 0 \tag{11.50}$$

which can be obtained analytically by taking the derivative of Equation (11.21). The two analytical conditions of Equations (11.26, 11.50) along with the steady-state equations can be used to determine the boundaries of the H_{01} singularity.

The complete branch set for the studied model consists therefore of (Equation (11.47)) together with that of the H_{01} singularity (Equations (11.24, 11.50)).

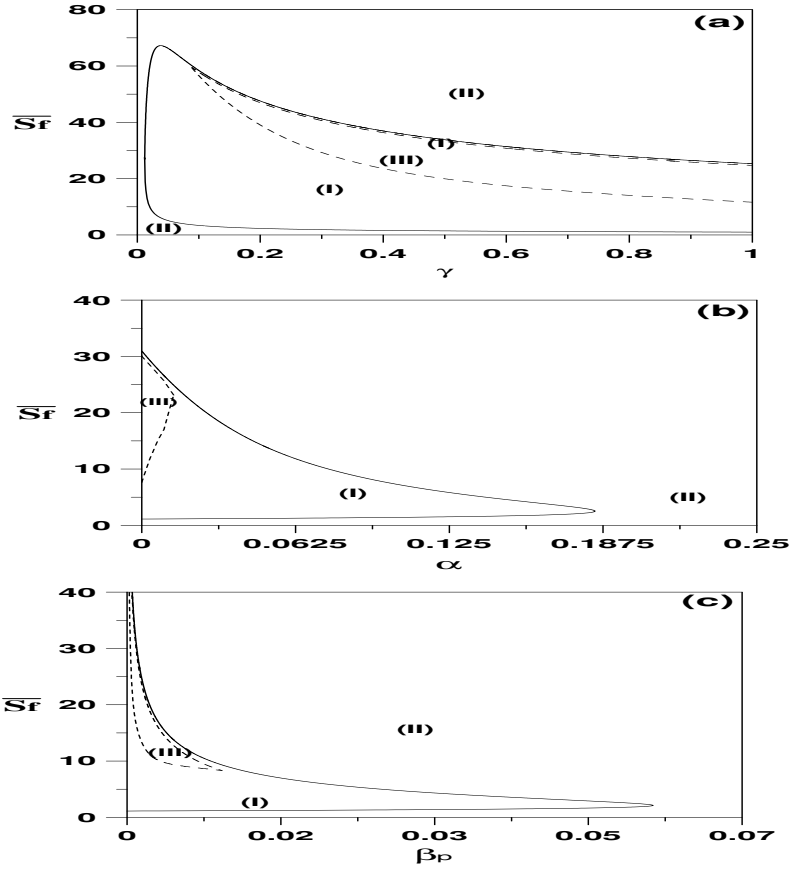

FIGURE 11.1: (a)–(c) Branch sets in different parameter spaces; solid line, static singularity; dashed line, H_{01} singularity.

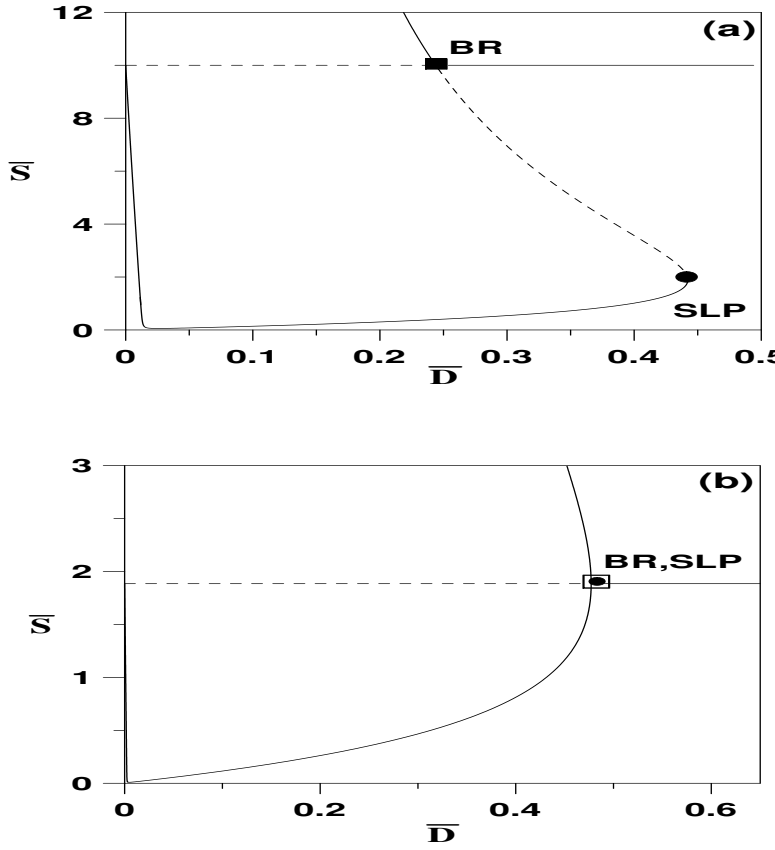

FIGURE 11.2: Bifurcation diagrams of Figure 11.1: (a) regions (I); (b) boundary between (I) and (II); solid line, stable branch; dashed line, unstable branch; SLP, static limit point; BR, bifurcation point.

Figures 11.1(a–c) show the complete branch sets in the different parameter space $(\bar{S}_f, \gamma)$, $(\bar{S}_f, \alpha)$, and $(\bar{S}_f, \beta_p)$. The nominal values used for the simulations are:

$$\alpha = 6.310^{-3}, \quad \beta_p = 1.210^{-3}, \quad \gamma = 0.8, \quad n = 1 \tag{11.51}$$

Each of the branch sets is divided into three regions. In region (I), Figure 11.2a shows an example of the bifurcation diagram for $(\bar{S}_f, \gamma) = (1, 0.3)$. It can be seen that an unstable region separates the static limit point (SLP) and the bifurcation point (BR) that occurs on the crossing of the curve with the washout line (the upper branch being physically unrealistic). A safe operation of the bioreactor is possible only for values of dilution rate smaller than that corresponding to the static limit point, defined by $\bar{D}_{LP} = \bar{\mu}(\bar{S}_{max})$, where $\bar{S}_{max}$ is the root of $\frac{d\bar{\mu}}{d\bar{S}} = 0$ (Equation (11.43)). For dilution rates smaller than

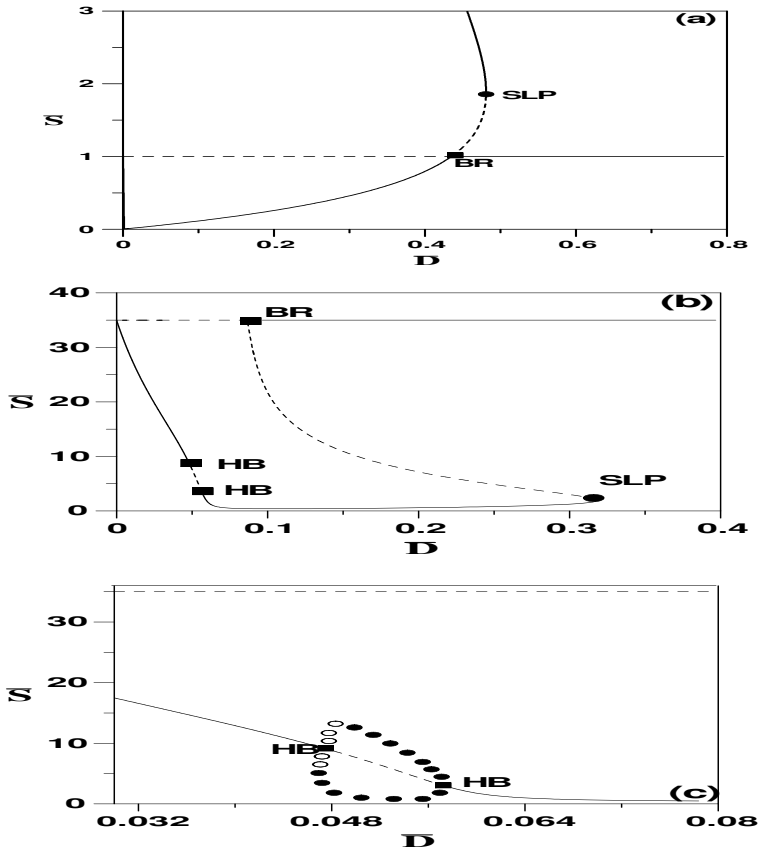

FIGURE 11.3: Bifurcation diagram in regions (II) and (III) of Figure 11.1: (a) The static limit point moves to the upper physically unrealistic branch in region (II); (b) Two Hopfs exist in region (III); (c) Enlargement of region (b) showing stable periodic branch connecting the two Hopf points.

$\bar{D}_{BR}$, a unique steady state exists. $\bar{D}_{BR}$ is obtained by setting $\bar{S} = \bar{S}_f$ into Equation (11.42) with $\bar{P} = 0$. This yields

$$\bar{D}_{BR} = \frac{\bar{S}_f}{1 + \bar{S}_f + \gamma \bar{S}_f} \tag{11.52}$$

For conditions between $\bar{D}_{BR}$ and $\bar{D}_{LP}$, the steady-state portrait is characterized by bistability. If the parameters of the model move on the boundary separating regions (I) and (II), then the static limit point (SLP) and the bifurcation point (BR) collapse in one point, as shown in Figure 11.2b, obtained with $(\bar{S}_f, \gamma) = (1.885, 0.3)$.

When the parameters move to region (II), the static limit point is located

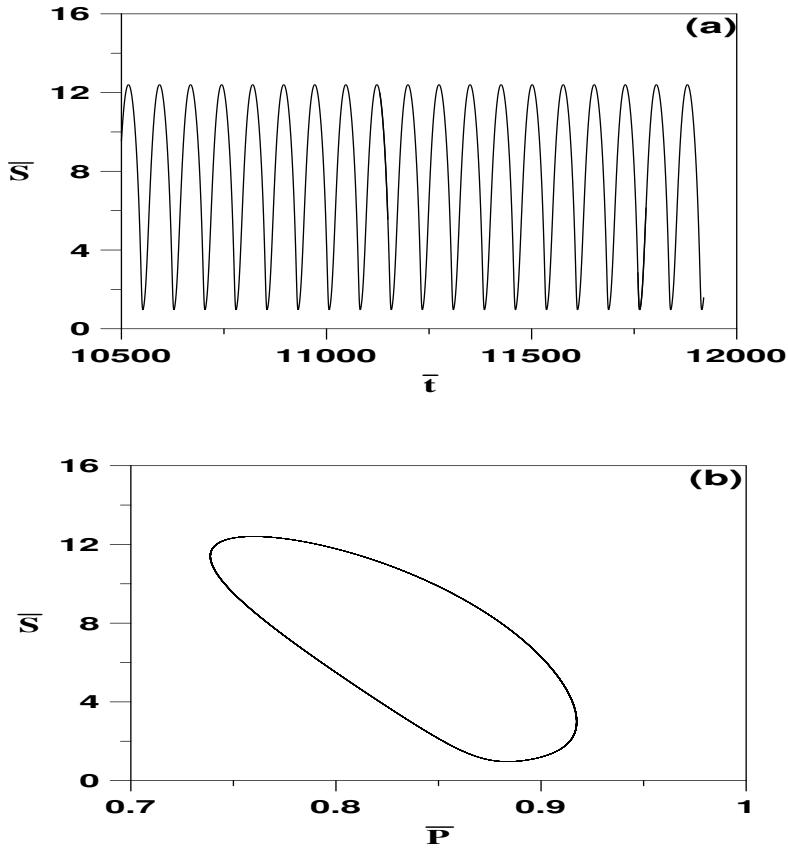

FIGURE 11.4: Simulations showing periodic oscillations for $\bar{D} = 0.05$: (a) Time domain; (b) Phase space.

on the other side of the washout line and occurs on the physically unrealistic branch. An example of behavior in this region is shown in Figure 11.3a, obtained with $(\bar{S}_f, \gamma) = (10.0, 0.3)$. In this case, the model exhibits a unique solution, and the safe operation of the reactor is possible for the dilution rate smaller than $\bar{D}_{BR}$. When moving from region (I) to region (III), the H_{01} boundary is crossed giving rise to two Hopf points. The continuity diagram, (Figure 11.3b), obtained for example for $(\bar{S}_f, \gamma) = (35.0, 0.3)$, is characterized by the presence of two Hopf points at dilution rates $\bar{D}_1 = 0.0468$ and $\bar{D}_2 = 0.0575$, respectively, in addition to the presence of a static limit point at $\bar{D}_{LP} = 0.318$. The same phenomenon of bistability found in region (I) exists for any conditions between the static limit point (SLP) and the bifurcation point (BR). However, the interesting feature in this region is that sustained oscillations do exist for any dilution rate between the two Hopf points. The dynamic bifurcation, enlarged in Figure 11.3c, shows a periodic branch con-

necting the two Hopf points. Figures 11.4(a–b) show an example of this limit cycle for $\bar{D} = 0.05$.

The branch sets of Figure 11.1(a–c) also allow a useful study of the effect of the model parameters. It can be seen from Figure 11.1a that the region of static multiplicity (region I) exists only for values of an inhibition constant larger than a certain value. As a consequence, the bioreactor would not exhibit any multiplicity for Monod-like behavior, i.e., $\gamma = 0$. Similarly, the existence of oscillatory behavior (region II) is confined to values of an inhibition constant γ larger than a certain value. It can also be seen that as the substrate inhibition increases, the region of oscillatory behavior widens at the expense of region (I) of static bistability. The branch set $(\bar{S}_f, \alpha)$ (Figure 11.1b) shows that both regions of static multiplicity and periodic behavior are confined to values of α smaller than certain values. The range of oscillatory behavior can be seen to decrease with increasing α. Finally, the branch set $(\bar{S}_f, \beta_p)$ of Figure 11.1c shows that static multiplicity (region I) is possible only for values of β_p smaller than a critical value. However, contrary to the effect of α, static multiplicity exists for the asymptotic value of $\beta_p = 0$, for any value of $\bar{S}_f$. The region of oscillatory behavior (region III), on the other hand, is confined to certain values of $\bar{S}_f$, and becomes narrower with increasing $\bar{S}_f$.

Chapter 12

MODELS WITH PRODUCT FORMATION: TYPE II MODELS

12.1 Process Model

For type II models, the specific rate σ of substrate utilization is directly proportional to the specific rate ϵ of product formation,

$$\sigma = a\epsilon \tag{12.1}$$

where a is a positive stoichiometric constant while μ and ϵ are allowed to have general dependence on S and P. It can be noted that when both the maintenance terms m_s and m_p of the previous type I model (Equations (11.4–11.5)) are negligible then type I model becomes a special case of type II model, since in this case the rates σ and ϵ are related by

$$\sigma = \frac{Yxs}{Y_{xp}}\epsilon \tag{12.2}$$

Type II models are, therefore, more general since independent expressions can be assumed for μ and ϵ. The model Equations (11.1–11.3) can be suitably rendered dimensionless by introducing the following variables,

$$\bar{S} = \frac{S}{S_{ref}}, \quad \bar{X} = \frac{aX}{S_{ref}}, \quad \bar{P} = \frac{P}{P_{ref}}, \quad \bar{D} = \frac{D}{\mu_{ref}} \tag{12.3}$$

$$\bar{t} = t\mu_{ref}, \quad \mu = \mu_{ref}\bar{\mu}, \quad \epsilon = \epsilon_{ref}\bar{\epsilon}, \quad \lambda_1 = \frac{\epsilon_{ref}}{\mu_{ref}} \quad \lambda_2 = \frac{\epsilon_{ref}S_{ref}}{a\mu_{ref}P_{ref}} \tag{12.4}$$

where P_{ref}, S_{ref}, ϵ_{ref}, and μ_{ref} are reference terms for P, S, ϵ, and μ, respectively. The model in dimensionless form is given by

$$\frac{d\bar{X}}{d\bar{t}} = \bar{\mu}\bar{X} - \bar{D}\bar{X} \tag{12.5}$$

$$\frac{d\bar{S}}{d\bar{t}} = \bar{D}(\bar{S}_f - \bar{S}) - \lambda_1\bar{\epsilon}\bar{X} \tag{12.6}$$

$$\frac{d\bar{P}}{d\bar{t}} = \lambda_2 \bar{\epsilon} \bar{X} - \bar{D}\bar{P} \tag{12.7}$$

We assume that the rates $\bar{\mu}$ and $\bar{\epsilon}$ are given by the following forms:

$$\bar{\mu}(\bar{S}, \bar{P}) = \bar{\mu}_1(\bar{S})\bar{\mu}_2(\bar{P}) \tag{12.8}$$

$$\bar{\epsilon}(\bar{S}, \bar{P}) = \bar{\epsilon}_1(\bar{S})\bar{\epsilon}_2(\bar{P}) \tag{12.9}$$

As was mentioned in the previous chapter, this class of models was used in the literature to model a number of bioprocesses such as ethanol fermentation of cellulose-hydrolystate [126, 272, 357].

12.2 Static Analysis

The steady-state values of $\bar{X}$ and $\bar{P}$ are related to $\bar{S}$ by the simple relations,

$$\bar{X} = \frac{\bar{\mu}(\bar{S}_f - \bar{S})}{\lambda_1 \bar{\epsilon}} \tag{12.10}$$

and

$$\bar{P} = \frac{\lambda_2 \bar{\epsilon} \bar{X}}{\bar{\mu}} = \frac{\lambda_2}{\lambda_1}(\bar{S}_f - \bar{S}) \tag{12.11}$$

The model equations at steady state are reduced to one algebraic equation by substituting Equation (12.10) into the steady-state form of Equation (12.6), to yield a single algebraic equation that depends on $\bar{S}$ as a state variable.

$$F(\bar{S}) := (\bar{S}_f - \bar{S})(\bar{D} - \bar{\mu}) \tag{12.12}$$

The state variable $\bar{P}$ that appears in $\bar{\mu}$ is explicitly related to $\bar{S}$ by Equation (12.11). In the following we study the static singularities the model can exhibit.

12.2.1 Hysteresis Singularity

The conditions for the appearance/disappearance of a hysteresis loop are

$$F = F_{\bar{S}} = F_{\bar{S}\bar{S}} = 0 \tag{12.13}$$

In addition, the following other derivatives must remain nonzero, namely $F_{\bar{D}}$, $F_{\bar{S}\bar{D}}$, and $F_{\bar{S}\bar{S}\bar{S}}$. Excluding the trivial washout condition $\bar{S} = \bar{S}_f$, the condition $F = 0$ (Equation (12.12)) yields

$$\bar{\mu} = \bar{D} \tag{12.14}$$

Taking into consideration this equation, the conditions $F_{\bar{S}} = 0$ and $F_{\bar{S}\bar{S}} = 0$ are equivalent to

$$\bar{\mu}_{\bar{S}} = 0 \quad \text{and} \quad \bar{\mu}_{\bar{S}\bar{S}} = 0 \tag{12.15}$$

or equivalently, by taking into consideration the general form of $\bar{\mu}$ (Equation (12.8))

$$0 = \frac{d\bar{\mu}}{d\bar{S}} = \bar{\mu}_{1\bar{S}}(\bar{S})\bar{\mu}_2(\bar{P}) + \bar{\mu}_1(\bar{S})\bar{\mu}_{2\bar{P}}(\bar{P})\frac{d\bar{P}}{d\bar{S}} \tag{12.16}$$

$$0 = \frac{d^2\bar{\mu}}{d\bar{S}^2} = \bar{\mu}_{1\bar{S}\bar{S}}(\bar{S})\bar{\mu}_2(\bar{P}) + 2\bar{\mu}_{1\bar{S}}(\bar{S})\bar{\mu}_{2\bar{P}}(\bar{P})\frac{d\bar{P}}{d\bar{S}} + \bar{\mu}_1(\bar{S})\bar{\mu}_{2\bar{P}\bar{P}}(\bar{P})(\frac{d\bar{P}}{d\bar{S}})^2 + \bar{\mu}_1(\bar{S})\bar{\mu}_{2\bar{P}}(\bar{P})\frac{d^2\bar{P}}{d\bar{S}^2} \tag{12.17}$$

The first derivative $\frac{d\bar{P}}{d\bar{S}}$ is obtained analytically by taking the derivative of Equation (12.11) to yield,

$$\frac{d\bar{P}}{d\bar{S}} = -\frac{\bar{\lambda}_2}{\lambda_1} \tag{12.18}$$

The second derivative $\frac{d^2\bar{P}}{d\bar{S}^2}$ is zero. Substituting in Equations (12.16–12.17) yields the following simplified equations for the hysteresis singularity,

$$\bar{\mu}_{1\bar{S}}(\bar{S})\bar{\mu}_2(\bar{P}) - \frac{\lambda_2}{\lambda_1}\bar{\mu}_1(\bar{S})\bar{\mu}_{2\bar{P}}(\bar{P}) = 0 \tag{12.19}$$

$$\bar{\mu}_{1\bar{S}\bar{S}}(\bar{S})\bar{\mu}_2(\bar{P}) - \frac{2\lambda_2}{\lambda_1}\bar{\mu}_{1\bar{S}}(\bar{S})\bar{\mu}_{2\bar{P}}(\bar{P}) + (\frac{\lambda_2}{\lambda_1})^2\bar{\mu}_1(\bar{S})\bar{\mu}_{2\bar{P}\bar{P}}(\bar{P}) = 0 \tag{12.20}$$

The other hysteresis condition $F_{\bar{D}} = \bar{S}_f - \bar{S}$ vanishes only at the trivial washout condition while $F_{\bar{D}\bar{S}} = -1 \neq 0$ is always satisfied. The condition $F_{\bar{S}\bar{S}\bar{S}} \neq 0$, on the other hand, will be evaluated numerically along the hysteresis boundaries.

12.2.2 Isola and Mushroom Singularities

The requirements for these two changes in the steady-state behavior are that

$$F = F_{\bar{S}} = F_{\bar{D}} = 0 \tag{12.21}$$

with the additional requirements that

$$F_{\bar{S}\bar{D}} \neq 0, F_{\bar{S}\bar{S}} \neq 0, F_{\bar{D}\bar{D}} \neq 0 \tag{12.22}$$

It can be seen by taking the derivative of F (Equation (12.12)) with respect to $\bar{D}$ that $F_{\bar{D}\bar{D}}$ is always zero, implying that the model cannot exhibit a mushroom or isola singularity.

12.2.3 Pitchfork Singularity

The pitchfork conditions are

$$F = F_{\bar{S}} = F_{\bar{D}} = F_{\bar{S}\bar{S}} = 0 \tag{12.23}$$

and

$$F_{\bar{S}\bar{D}} \neq 0, F_{\bar{S}\bar{S}\bar{S}} \neq 0 \tag{12.24}$$

Excluding the washout solution, the conditions $F_{\bar{S}} = 0$ and $F_{\bar{S}\bar{S}} = 0$ are equivalent to Equations (12.15). The condition $F_{\bar{D}} = 0$ (Equation (12.12)), on the other hand, requires that $\bar{S} = \bar{S}_f$, i.e., $\bar{X} = 0$ and $\bar{P} = 0$. Substituting the conditions $\bar{S} = \bar{S}_f$ and $\bar{P} = 0$ into Equations (12.15), yields the conditions for the pitchfork singularity

$$\frac{d\bar{\mu}}{d\bar{S}}(\bar{S} = \bar{S}_f, \bar{P} = 0) = 0 \quad \text{and} \quad \frac{d^2\bar{\mu}}{d\bar{S}^2}(\bar{S} = \bar{S}_f, \bar{P} = 0) = 0 \tag{12.25}$$

or equivalently,

$$\bar{\mu}_{1\bar{S}}(\bar{S}_f)\bar{\mu}_2(0) - \frac{\lambda_2}{\lambda_1}\bar{\mu}_1(\bar{S}_f)\bar{\mu}_{2\bar{P}}(0) = 0 \tag{12.26}$$

$$\bar{\mu}_{1\bar{S}\bar{S}}(\bar{S}_f)\bar{\mu}_2(0) - \frac{2\lambda_2}{\lambda_1}\bar{\mu}_{1\bar{S}}(\bar{S}_f)\bar{\mu}_{2\bar{P}}(0) + (\frac{\lambda_2}{\lambda_1})^2\bar{\mu}_1(\bar{S}_f)\bar{\mu}_{2\bar{P}\bar{P}}(0) = 0 \tag{12.27}$$

The other pitchfork condition $F_{\bar{S}\bar{D}} = -1 \neq 0$ is always satisfied while the condition $F_{\bar{S}\bar{S}\bar{S}} \neq 0$ will be evaluated numerically along the pitchfork boundaries.

In the following section, we provide explicit examples of this static analysis for some case models used in the literature.

12.3 Case Model 1

We start the examples with models based on the well-known Haldane substrate inhibition kinetics with the product inhibiting the maximum specific growth rate. The growth rate $\mu(S, P)$ is assumed to have the following form:

$$\mu(S, P) = \mu_1(S)\mu_2(P) \tag{12.28}$$

with

$$\mu_1(S) = \frac{\mu_{1m}S}{K_{1S} + S + \frac{S^2}{K_{1I}}} \tag{12.29}$$

and

$$\mu_2(P) = 1 - \frac{P}{P_{1m}} \tag{12.30}$$

A similar relation is assumed for ϵ

$$\epsilon(S,P) = \epsilon_1(S)\epsilon_2(P) \tag{12.31}$$

with

$$\epsilon_1(S) = \frac{\mu_{2m}S}{K_{2S} + S + \frac{S^2}{K_{2I}}} \tag{12.32}$$

and

$$\epsilon_2(P) = 1 - \frac{P}{P_{2m}} \tag{12.33}$$

The model is rendered dimensionless in the form of Equations (12.5–12.7), using the following variables

$$S_{ref} = S_f, \quad P_{ref} = P_{1m}, \quad \mu_{ref} = \mu_{1m} \text{ and } \epsilon_{ref} = \mu_{2m} \tag{12.34}$$

The dimensionless model parameters are

$$\bar{S}_f = 1, \quad \lambda_1 = \frac{\mu_{2m}}{\mu_{1m}} \text{ and } \lambda_2 = \frac{\mu_{2m}S_f}{a\mu_{1m}P_{1m}} \tag{12.35}$$

while the dimensionless kinetic rates are

$$\bar{\mu} = \frac{\bar{S}}{\beta_1 + \bar{S} + \gamma_1\bar{S}^2}(1 - \bar{P}) := \bar{\mu}_1(\bar{S})\bar{\mu}_2(\bar{P}) \tag{12.36}$$

and

$$\bar{\epsilon} = \frac{\bar{S}}{\beta_2 + \bar{S} + \gamma_2\bar{S}^2}(1 - \lambda_3\bar{P}) := \bar{\epsilon}_1(\bar{S})\bar{\epsilon}_2(\bar{P}) \tag{12.37}$$

with

$$\beta_i = \frac{K_{iS}}{S_f} \quad (\mathrm{i} = 1,2), \quad \gamma_i = \frac{S_f}{K_{iI}} \quad (\mathrm{i} = 1,2) \text{ and } \lambda_3 = \frac{P_{1m}}{P_{2m}} \tag{12.38}$$

The first and second derivatives of $\bar{\mu}_1$ are given by

$$\bar{\mu}_{1\bar{S}} = \frac{\beta_1 - \gamma_1\bar{S}^2}{(\beta_1 + \bar{S} + \gamma_1\bar{S}^2)^2} \tag{12.39}$$

$$\bar{\mu}_{1\bar{S}\bar{S}} = \frac{-2\gamma_1\bar{S}}{(\beta_1 + \bar{S} + \gamma_1\bar{S}^2)^2} - \frac{2(1 + 2\gamma_1\bar{S})(\beta_1 - \gamma_1\bar{S}^2)}{(\beta_1 + \bar{S} + \gamma_1\bar{S}^2)^3} \tag{12.40}$$

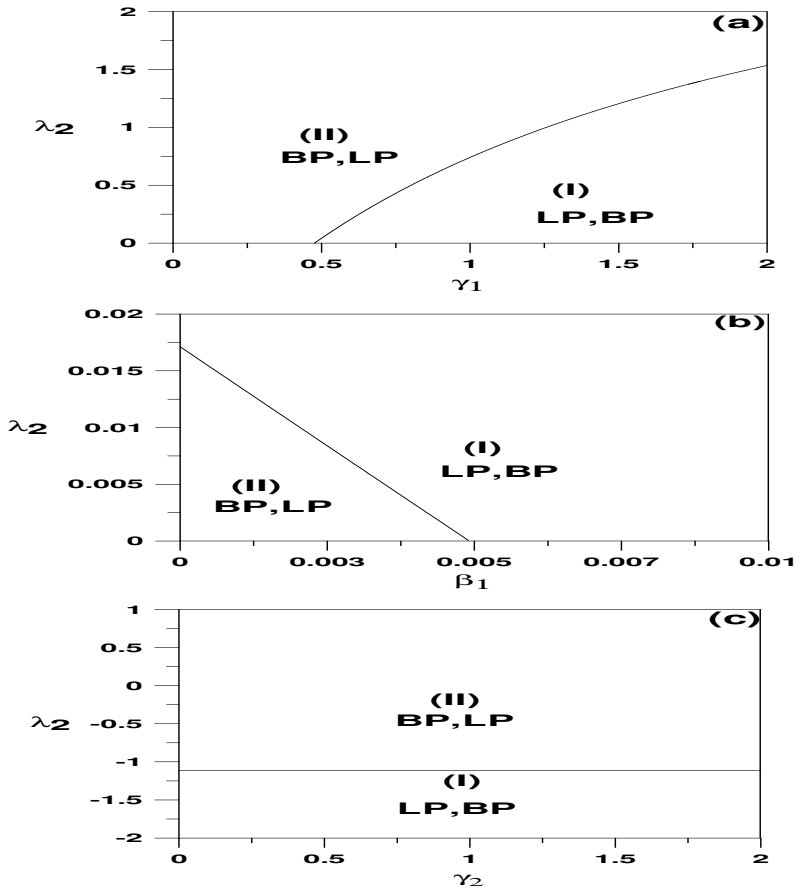

FIGURE 12.1: (a)–(c) Branch sets for the first case model.

Similar relations hold for $\bar{\epsilon}_{1\bar{S}}$ and $\bar{\epsilon}_{1\bar{S}\bar{S}}$ with β_2 and γ_2 replacing β_1 and γ_1. The derivatives for $\bar{\mu}_2(\bar{P})$ and $\bar{\epsilon}_2(\bar{P})$ are given by

$$\bar{\mu}_{2\bar{P}} = -1 \text{ and } \bar{\epsilon}_{2\bar{P}} = -\lambda_3 \tag{12.41}$$

while the second derivatives $\bar{\mu}_{2\bar{P}\bar{P}}$ and $\bar{\epsilon}_{2\bar{P}\bar{P}}$ are zero. Using these derivatives and applying the pitchfork conditions of Equations (12.25–12.27) at $\bar{S} = \bar{S}_f = 1$ and $\bar{P} = 0$ yields

$$\frac{\beta_1 - \gamma_1}{(\beta_1 + 1 + \gamma_1)} + \frac{\lambda_2}{\lambda_1} = 0 \tag{12.42}$$

$$\frac{-3\beta_1\gamma_1 + \gamma_1^2 - \beta_1}{(\beta_1 + 1 + \gamma_1)} + \frac{\lambda_2}{\lambda_1}(\beta_1 - \gamma_1) = 0 \tag{12.43}$$

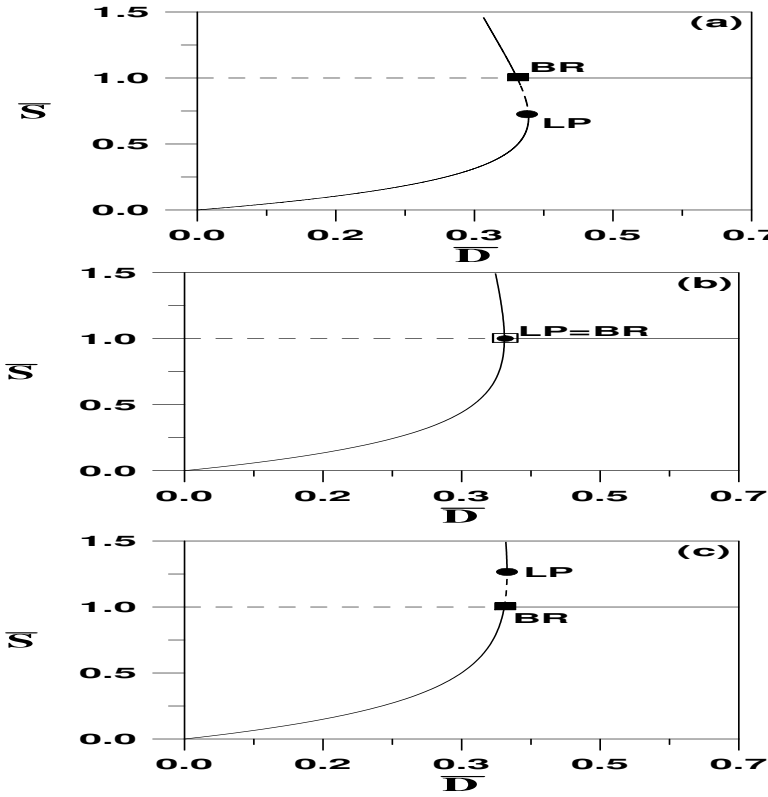

FIGURE 12.2: Continuity diagram in the different regions of Figure 12.1: (a) Imperfect pitchfork in region (I); (b) Perfect pitchfork on the boundary of (I) and (II); (c) The static limit point moves to the upper physically unrealistic branch in region (II); solid line, stable branch; dashed line, unstable. LP, static limit point; BR, bifurcation point.

These useful analytical relations represent the boundaries for the pitchfork singularity, in terms of the model kinetic and operating parameters.

As for the hysteresis singularity, it can be noted that since $\bar{\mu}_{2\bar{P}\bar{P}} = 0$, Equations (12.19, 12.20) for the hysteresis boundaries are reduced to,

$$\bar{\mu}_{1\bar{S}}\bar{\mu}_2 = \frac{\lambda_2}{\lambda_1}\bar{\mu}_1\bar{\mu}_{2\bar{P}} \tag{12.44}$$

$$\bar{\mu}_{1\bar{S}S}\bar{\mu}_2 = \frac{2\lambda_2}{\lambda_1}\bar{\mu}_{1\bar{S}}\bar{\mu}_{2\bar{P}} \tag{12.45}$$

Combining these relations yields,

$$2\bar{\mu}_{1\bar{S}}^2 = \bar{\mu}_1\bar{\mu}_{1\bar{S}\bar{S}} \tag{12.46}$$

Substituting the expressions of $\bar{\mu}_1$ (Equation (12.36)), $\bar{\mu}_{1\bar{S}}$ (Equation (12.39)) and $\bar{\mu}_{1\bar{S}\bar{S}}$ (Equation (12.40)) into Equation (12.46) reduces it to the following relation,

$$\gamma_1 \bar{S}^2 + \bar{S} + \beta_1 = 0 \tag{12.47}$$

This relation cannot hold since all the terms involved are positive. We conclude therefore that the model cannot exhibit a hysteresis singularity.

Figures 12.1(a–c) show examples of the branch set in the parameter spaces (λ_2, γ_1), (λ_2, β_1) and (λ_2, γ_2), for the following nominal values:

$$\beta_1 = 0.476, \gamma_1 = 4.91510^{-3}, \beta_2 = 0.6667, \gamma_2 = 3.33410^{-3}$$

$$\lambda_1 = 3.5, \lambda_2 = 1.89110^{-2}, \lambda_3 = 0.763 \tag{12.48}$$

Each of the branch sets is divided into two regions. For any combinations of model parameters in region (I), an imperfect pitchfork is expected, as shown in the continuity diagram of Figure 12.2a, obtained with $(\lambda_2, \gamma_1) = (0.05, 1)$. A safe operation of the bioreactor is possible for values of dilution rates smaller than that corresponding to the static limit point defined by

$$\bar{D}_{LP} = \bar{\mu}(\bar{S}_{max}) \tag{12.49}$$

where $\bar{S}_{max}$ is the root of $\frac{d\bar{\mu}}{d\bar{S}} = 0$ (Equation (12.16)). Substituting in Equation (12.49) for the partial derivatives of $\bar{\mu}_{1\bar{S}}$ (Equation (12.39)) and $\bar{\mu}_{2\bar{P}}$ (Equation (12.41)) yields the following quadratic equation for $\bar{S}_{max}$

$$\beta_1(1 - \frac{\lambda_2}{\lambda_1}) + \frac{2\beta_1\lambda_2}{\lambda_1}\bar{S}_{max} + (-\gamma_1 + \frac{\lambda_2}{\lambda_1} + \frac{\gamma_1\lambda_2}{\lambda_1})\bar{S}^2_{max} = 0 \tag{12.50}$$

For the set of chosen parameters, the static limit point occurs at $\bar{S}_{max} = 0.70201$ and at dilution rate $\bar{D} = \bar{\mu}(\bar{S} = \bar{S}_{max}) = 0.41836$.

Moreover, for dilution rates in Figure 12.2a smaller than $\bar{D}_{BR}$, a unique steady state exists. $\bar{D}_{BR}$ is obtained by setting $\bar{S} = \bar{S}_f = 1$, i.e., $\bar{P} = 0$ into Equation (12.14) to yield

$$\bar{D}_{BR} = \frac{1}{\beta_1 + 1 + \gamma_1} \tag{12.51}$$

For dilution rates between $\bar{D}_{BR}$ and $\bar{D}_{LP}$, the steady-state portrait is characterized by bistability. The operation of the process on the lower static branch may drift to washout conditions as a result of fluctuations in process operating conditions. If the parameters of the model move on the boundary separating regions (I) and (II), then the static limit point (LP) and the bifurcation point (BR) collapse in one point yielding a perfect pitchfork, as shown in Figure 12.2b, obtained with $(\lambda_2, \gamma_1) = (0.7407, 1)$. When the parameters move to region (II), the static limit point is located on the other side of washout

conditions and occurs on the physically unrealistic branch. An example of the steady-state portrait in this region is shown in Figure 12.2c, obtained with $(\lambda_2, \gamma_1) = (1, 1)$. In this case, the model exhibits a unique solution, and the safe operation of the reactor is possible for dilution rate smaller than $\bar{D}_{BR}$.

The branch sets of Figures 12.1(a–c) also allow a useful analysis of the effect of model parameters. It can be seen from Figure 12.1a that bistability (region I) exists only for values of the dimensionless inhibition constant γ_1 larger than β_1 ($= 0.476$, for the chosen nominal values of Equation (12.48)). This region also widens, as expected, with increasing γ_1. Figure 12.1b shows, on the other hand, that the region of bistability exists for a large range of the dimensionless substrate saturation constant β_1.

A final note should be made about the effect of kinetic parameters $\beta_2, \gamma_2, \lambda_3$, pertinent to the product synthesis rate $\bar{\epsilon}$ (Equation (12.37)). It can be seen from the general Equations (12.26-12.27) and Equations (12.42–12.43) that the pitchfork boundaries are independent of $\bar{\epsilon}$. Consequently, these boundaries are insensitive to variations of any of the parameters β_2, γ_2, or λ_3, as can be seen in Figure 12.1c. For the chosen nominal values (Equation (12.48)), this boundary is negative and physically unrealistic. Consequently the behavior of the process for any value of γ_2 is characterized by region (II) where a Monod-like behavior, similar to Figure 12.2c, prevails.

12.4 Case Model 2

The second example pertains to the following form of $\mu_2(P)$ and $\epsilon_2(P)$,

$$\mu_2(P) = \frac{K_{1P}}{K_{1P} + P} \tag{12.52}$$

$$\epsilon_2(P) = \frac{K_{2P}}{K_{2P} + P} \tag{12.53}$$

The model is rendered dimensionless using the definitions of Equation (12.34) with

$$P_{ref} = K_{1P} \quad \text{and} \quad \lambda_2 = \frac{\mu_{2m} S_f}{a \mu_{1m} K_{1p}} \tag{12.54}$$

The dimensionless cell growth rate becomes

$$\bar{\mu} = \bar{\mu}_1(\bar{S}) \bar{\mu}_2(\bar{P}) \tag{12.55}$$

with $\bar{\mu}_1(\bar{S})$ given by Equation (12.36) and

$$\bar{\mu}_2(\bar{P}) = \frac{1}{1 + \bar{P}} \tag{12.56}$$

The dimensionless rate of product synthesis becomes

$$\bar{\epsilon} = \bar{\epsilon}_1(\bar{S})\bar{\epsilon}_2(\bar{P}) \tag{12.57}$$

with $\bar{\epsilon}_1(\bar{S})$ given by Equation (12.32) and

$$\bar{\epsilon}_2(\bar{P}) = \frac{1}{1+\lambda_3\bar{P}} \tag{12.58}$$

with $\lambda_3 = \frac{K_{1P}}{K_{2P}}$.
The first and second derivatives of the growth rates are given by

$$\bar{\mu}_{2\bar{P}}(\bar{P}) = \frac{-1}{(1+\bar{P})^2}, \quad \bar{\mu}_{2\bar{P}\bar{P}}(\bar{P}) = \frac{2}{(1+\bar{P})^3} \tag{12.59}$$

$$\bar{\epsilon}_{2\bar{P}}(\bar{P}) = \frac{-\lambda_3}{(1+\lambda_3\bar{P})^2}, \quad \bar{\epsilon}_{2\bar{P}\bar{P}}(\bar{P}) = \frac{2\lambda_3^2}{(1+\lambda_3\bar{P})^3} \tag{12.60}$$

The branch sets for hysteresis and pitchfork singularities for this example are shown (Figures 12.3(a–c)) in the parameter spaces (λ_2, γ_1), (λ_2, β_1), and (λ_2, γ_2), for the nominal values

$$\beta_1 = 4.710^{-2}, \gamma_1 = 1.65, \beta_2 = 0.1, \gamma_2 = 1, \lambda_1 = 0.5, \lambda_2 = 0.7, \lambda_3 = 1 \tag{12.61}$$

The relative position of the boundaries of the hysteresis (dashed line) and the pitchfork (solid line) singularities divides the branch set of Figure 12.3a into three different regions. For parameters in region (I) the continuity diagram, as shown in Figure 12.4a for $(\lambda_2, \gamma_1) = (0.1, 1.2)$, is characterized by the presence of two static limit points located on the opposite side of the washout line. Since the upper branch is physically unrealistic, the operation of the bioreactor in this region is similar to region (I) of the previous model (Figure 12.2a). The operation of the reactor, in this region, is characterized by bistability for dilution rates between the bifurcation point BR (defined by Equation (12.51)) and the static limit point LP_1, defined by Equation (12.49). Substituting for the expressions of $\bar{\mu}_1$ (Equation (12.36)), $\bar{\mu}_{1\bar{S}}$ (Equation (12.39)), and $\bar{\mu}_{2\bar{P}}$ (Equation (12.59)) into Equation (12.49) yields the positions of the static limit points,

$$\beta_1(1+\frac{\lambda_2}{\lambda_1}) + (-\gamma_1 + \frac{\lambda_2}{\lambda_1} - \frac{\gamma_1\lambda_2}{\lambda_1})\bar{S}_{max}^2 + \frac{2\gamma_1\lambda_2}{\lambda_1}\bar{S}_{max}^3 = 0 \tag{12.62}$$

When the pair of parameters crosses the boundary of the pitchfork singularity and moves to region (II), the second static limit point LP_2 moves to the physically realistic branch, as shown in the continuity diagram of Figure 12.4b, obtained with $(\lambda_2, \gamma_1) = (0.35, 1.2)$. The operation of the bioreactor in this case is quite complex as can be seen in the enlargement of the continuity diagram (Figure 12.4c). For dilution rates smaller than that of LP_2 ($\bar{D}_{LP2} =$

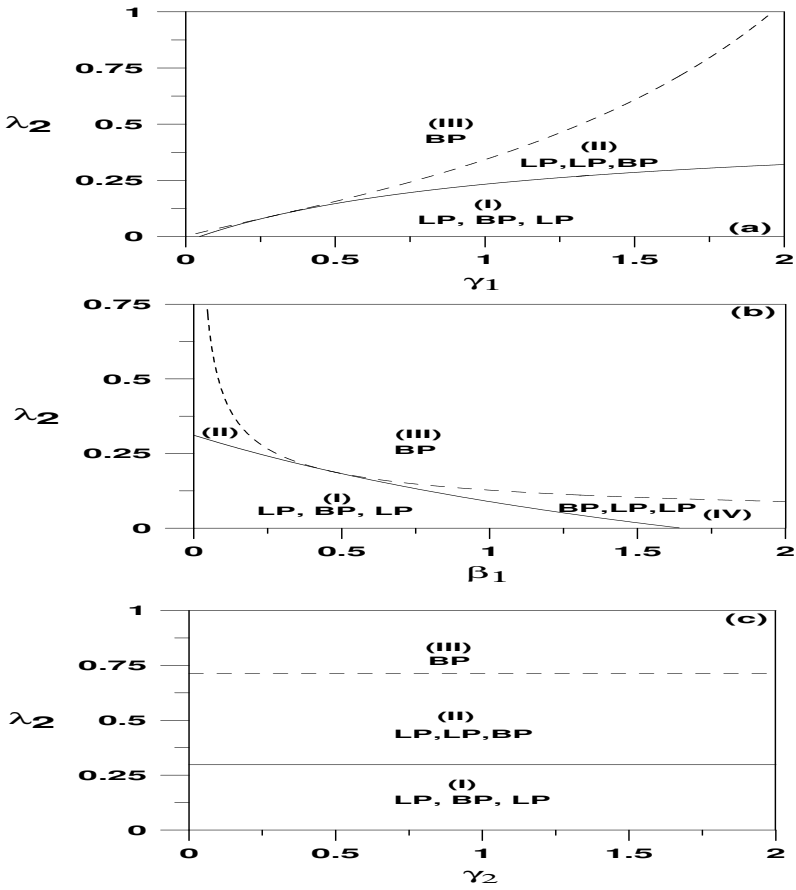

FIGURE 12.3: (a)–(c) Branch sets for the second case model.

0.433), the process settles on the lower nontrivial steady state for any start-up conditions. For dilution rates between LP_2 and LP_1 ($\bar{D}_{LP1} = 0.4425$), two stable nontrivial branches coexist. For the narrow conditions between LP_1 and BR ($\bar{D}_{BR} = 0.4450$), the lower stable branch coexists with washout conditions.

When the parameters move to region (III), the hysteresis line is crossed and therefore the two static limit point disappear. An example of the steady-state portrait is shown in Figure 12.5a, for $(\lambda_2, \gamma_1) = (0.45, 1.2)$. Similarly to region (II) of the previous model (Figure 12.2c), the process does not exhibit any bistability and the safe operation of the bioreactor is possible for dilution rates smaller than $\bar{D}_{BR}$. However, the evolution trend of the substrate with the dilution rate is qualitatively different from Figure 12.2c.

The branch set is also shown in the parameter space (λ_2, β_1) (Figure 12.4b).

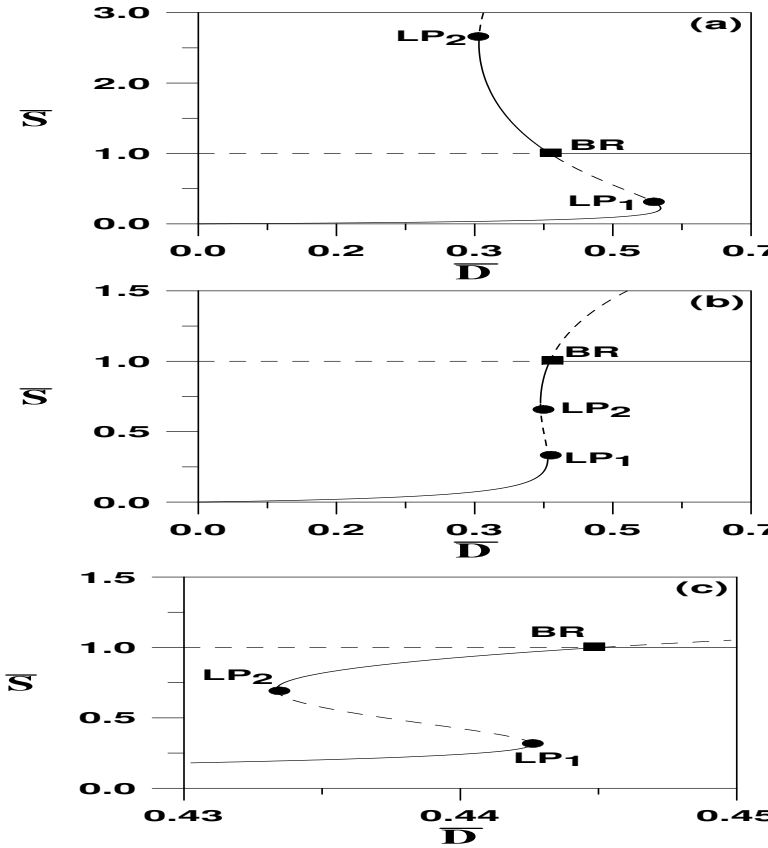

FIGURE 12.4: Continuity diagram in the different regions of Figures 12.3(a–b): (a) region (I); (b) region II; (c) Enlargement of region (b); solid line, stable branch; dashed line, unstable; LP, static limit point; BR, bifurcation point.

It can be seen that a fourth region (IV) appears in the diagram that is characterized by the presence of two static limit points in the physically unrealistic region. The evolutionary trend of the substrate with the dilution rate is similar to region (II) of the previous model (Figure 12.2c), as can be shown in the continuity diagram of Figure 12.5b, obtained with $(\lambda_2, \beta_1) = (0.07, 2)$.

The branch sets of Figure 12.3(a–c) also allow a useful analysis of the effect of model parameters. It can be seen from Figure 12.3a that as the substrate inhibition constant γ_1 increases, the region (II) characterized by the two physically realistic limit points widens at the expense of both regions (I) of one static limit point and region (III) of stable behavior. Moreover, for small values of γ_1, the behavior of the process is dominated by the pitchfork singularity where the process is either stable (region III) or exhibits bistability with washout conditions (region I).

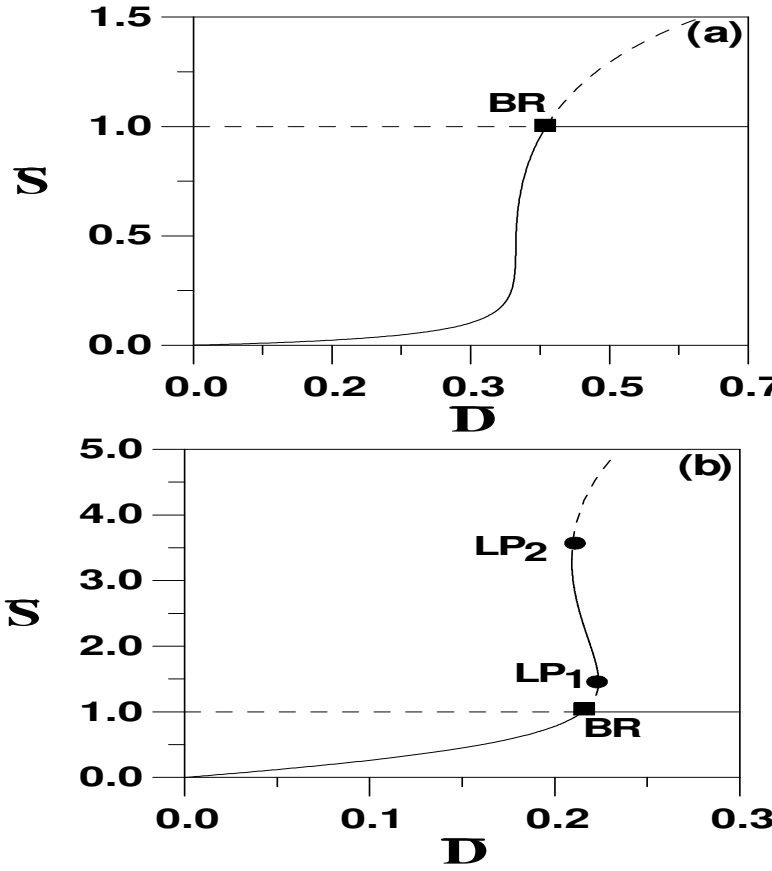

FIGURE 12.5: Continuity diagram in the different regions of Figures 12.3(a–b) (a) region (III); (b) region (IV); solid line, stable branch; dashed line, unstable; LP, static limit point; BR, bifurcation point.

The effect of the substrate saturation constant β_1 (Figure 12.3b) shows that region (II) of coexistence of two nontrivial stable branches is confined only to a smaller region ($\beta_1 < 0.45$) and ($\lambda_2 > 0.195$). As β_1 increases, region (I) narrows and the process is dominated by a stable behavior, either in region (III) or in region (IV). The effect of the other substrate-inhibition constant γ_2 is shown in Figure 12.3c. Similarly to the observations made in the previous section, both the hysteresis (dashed line) and pitchfork (solid line) are insensitive to changes in γ_2. The region (I) of bistability is confined to values of λ_2 smaller than 0.2972. The region (II) of coexistence of two stable branches extend to $\lambda_2 = .7135$. For higher values, the region (III) of stable behavior dominates.

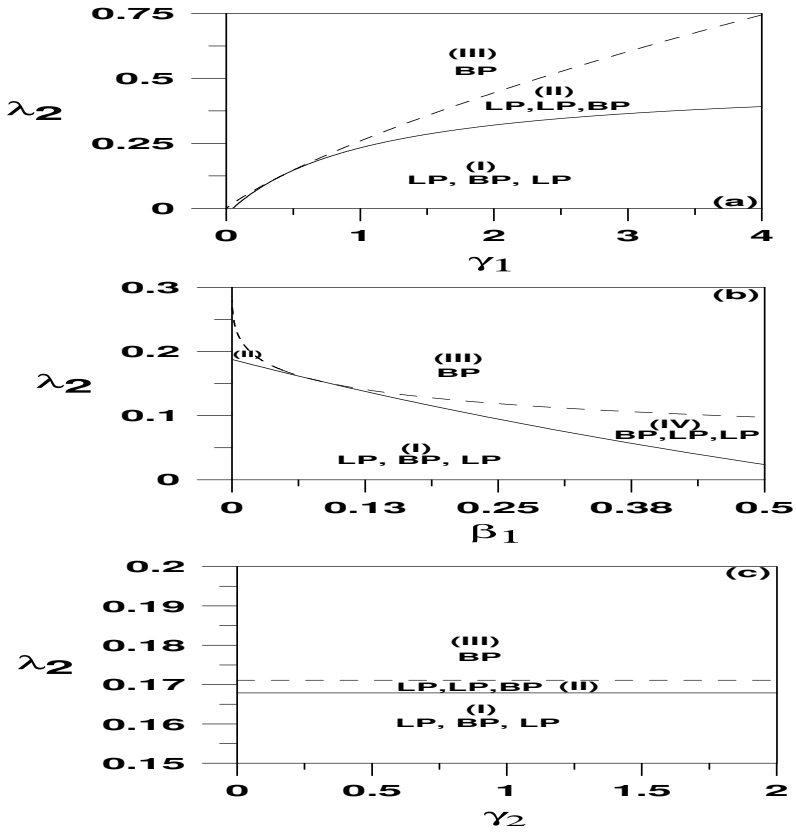

FIGURE 12.6: (a)–(c) Branch sets for the third case model.

12.5 Case Model 3

The third and last example consists of the following form of $\mu_2(P)$

$$\mu_2(P) = e^{-\alpha P} \tag{12.63}$$

The model is rendered dimensionless using the following variables

$$\bar{S}_{ref} = S_f, \quad P_{ref} = \frac{1}{\alpha} \text{ and } \lambda_3 = \frac{\mu_{2m} S_f \alpha}{a \mu_{1m}} \tag{12.64}$$

yielding,

$$\bar{\mu}_2(\bar{P}) = e^{-\bar{P}} \tag{12.65}$$

while $\bar{\mu}_1(\bar{S})$ is still given by Equation (12.36).

The complete branch set for this case is shown in Figures 12.6(a–c). The branch sets are qualitatively similar to the previous example. Three different regions can be seen in the parameter space (λ_2, γ_1), i.e., a region of stable behavior (region III), a region of bistability between the nontrivial steady state and washout conditions (region I), and a region (II) of coexistence of two stable nontrivial steady states. Moreover, a fourth region, similar to the previous case can be found in the parameter space (λ_2, β_1) (Figure 12.6b). Finally, the boundaries of the hysteresis and pitchfork singularities can be seen to be insensitive to variations in γ_2 (Figure 12.6c), with region (II) being confined to a narrow domain between $\lambda_2 = 0.1679$ and 0.1711.

This page intentionally left blank

Chapter 13

MODELS WITH PRODUCT FORMATION: TYPE III MODELS

13.1 Bioreactor Model

For type III models, the specific rates of cell growth and substrate utilization are related by the linear equation

$$\sigma = a\mu \tag{13.1}$$

where a is a positive stoichiometric constant. The model Equations (11.1–11.3) can be suitably rendered dimensionless by introducing the following variables,

$$\bar{S} = \frac{S}{S_{ref}}, \quad \bar{X} = \frac{aX}{S_{ref}}, \quad \bar{P} = \frac{P}{P_{ref}}, \quad \bar{D} = \frac{D}{\mu_{ref}} \tag{13.2}$$

$$\bar{t} = t\mu_{ref}, \quad \mu = \mu_{ref}\bar{\mu}, \quad \epsilon = \epsilon_{ref}\bar{\epsilon}, \quad \alpha = \frac{\epsilon_{ref}S_{ref}}{a\mu_{ref}P_{ref}} \tag{13.3}$$

where P_{ref}, S_{ref}, ϵ_{ref}, and μ_{ref} are reference quantities for P, S, ϵ, and μ, respectively. The model in dimensionless form is given by

$$\frac{d\bar{X}}{d\bar{t}} = -\bar{D}\bar{X} + \bar{\mu}\bar{X} \tag{13.4}$$

$$\frac{d\bar{S}}{d\bar{t}} = \bar{D}(\bar{S}_f - \bar{S}) - \bar{\mu}\bar{X} \tag{13.5}$$

$$\frac{d\bar{P}}{d\bar{t}} = \alpha\bar{\epsilon}\bar{X} - \bar{D}\bar{P} \tag{13.6}$$

We assume that the rates $\bar{\mu}$ and $\bar{\epsilon}$ are given by the following forms,

$$\bar{\mu}(\bar{S}, \bar{P}) = \bar{\mu}_1(\bar{S})\bar{\mu}_2(\bar{P}) \tag{13.7}$$

$$\bar{\epsilon}(\bar{S}, \bar{P}) = \bar{\epsilon}_1(\bar{S})\bar{\epsilon}_2(\bar{P}) \tag{13.8}$$

As was mentioned in Chapter 11, this class of model was, for instance, used by Aiba and Shoda [10] and Aiba et al. [11] for ethanol production from glucose by *Saccharomyces cerevisiae*.

13.2 Static Singularities

The steady-state values of $\bar{X}$ and $\bar{P}$ are related to $\bar{S}$ by the simple relations,

$$\bar{X} = (\bar{S}_f - \bar{S}) \tag{13.9}$$

and

$$\bar{P} = \frac{\alpha\bar{\epsilon}\bar{X}}{\bar{\mu}} \tag{13.10}$$

or equivalently

$$\bar{P}\frac{\bar{\mu}_2(\bar{P})}{\bar{\epsilon}_2(\bar{P})} = \frac{\alpha\bar{\epsilon}_1(\bar{S})(\bar{S}_f - \bar{S})}{\bar{\mu}_1(\bar{S})} \tag{13.11}$$

Similarly to the previous models, the following single variable algebraic equation can be obtained from the steady-state equation,

$$F(\bar{S}) := (\bar{S}_f - \bar{S})(\bar{D} - \bar{\mu}) \tag{13.12}$$

The state variable $\bar{P}$ that appears in $\bar{\mu}$ is implicitly related to $\bar{S}$ by Equation (13.11).

13.2.1 Hysteresis Singularity

Excluding the trivial washout condition $\bar{S} = \bar{S}_f$, the condition $F = 0$ (Equation (13.12)) yields

$$\bar{\mu} = \bar{D} \tag{13.13}$$

Taking into consideration this equation, the conditions $F_{\bar{S}} = 0$ and $F_{\bar{S}\bar{S}} = 0$ are equivalent to

$$\bar{\mu}_{\bar{S}} = 0 \quad \text{and} \quad \bar{\mu}_{\bar{S}\bar{S}} = 0 \tag{13.14}$$

or equivalently, by taking into consideration the general form of $\bar{\mu}$ (Equation (13.7))

$$\begin{aligned} 0 = \frac{d\bar{\mu}}{d\bar{S}} &= \bar{\mu}_{1\bar{S}}(\bar{S})\bar{\mu}_2(\bar{P}) + \bar{\mu}_1(\bar{S})\bar{\mu}_{2\bar{P}}(\bar{P})\frac{d\bar{P}}{d\bar{S}} \\ 0 = \frac{d^2\bar{\mu}}{d\bar{S}^2} &= \bar{\mu}_{1\bar{S}\bar{S}}(\bar{S})\bar{\mu}_2(\bar{P}) + 2\bar{\mu}_{1\bar{S}}(\bar{S})\bar{\mu}_{2\bar{P}}(\bar{P})\frac{d\bar{P}}{d\bar{S}} + \bar{\mu}_1(\bar{S})\bar{\mu}_{2\bar{P}\bar{P}}(\bar{P})(\frac{d\bar{P}}{d\bar{S}})^2 \\ &\quad +\bar{\mu}_1(\bar{S})\bar{\mu}_{2\bar{P}}(\bar{P})\frac{d^2\bar{P}}{d\bar{S}^2} \end{aligned} \tag{13.15}$$

The first derivative $\frac{d\bar{P}}{d\bar{S}}$ is obtained analytically by taking the derivatives of both sides of Equation (13.11) to yield,

$$\frac{d\bar{P}}{d\bar{S}} f(\bar{P}) = \alpha g(\bar{S}) \tag{13.16}$$

where

$$f(\bar{P}) := \frac{\bar{\mu}_2}{\bar{\epsilon}_2} + \frac{\bar{P}\bar{\mu}_{2\bar{P}}}{\bar{\epsilon}_2} - \frac{\bar{P}\bar{\mu}_2\bar{\epsilon}_{2\bar{P}}}{\bar{\epsilon}_2^2} \tag{13.17}$$

and

$$g(\bar{S}) := \frac{-\bar{\epsilon}_1}{\bar{\mu}_1} + \frac{(\bar{S}_f - \bar{S})\bar{\epsilon}_{1\bar{S}}}{\bar{\mu}_1} - \frac{(\bar{S}_f - \bar{S})\bar{\mu}_{1\bar{S}}\bar{\epsilon}_1}{\bar{\mu}_1^2} \tag{13.18}$$

The second derivative $\frac{d^2\bar{P}}{d\bar{S}^2}$ is obtained by taking the derivative of Equation (13.16) to yield,

$$\frac{d^2\bar{P}}{d\bar{S}^2} f(\bar{P}) + (\frac{d\bar{P}}{d\bar{S}})^2 f_{\bar{P}}(\bar{P}) = \alpha g_{\bar{S}}(\bar{S}) \tag{13.19}$$

with

$$\begin{aligned} g_{\bar{S}}(\bar{S}) \quad = \quad & \frac{-(\bar{\mu}_{1\bar{S}}\bar{\epsilon}_1 - \bar{\mu}_1\bar{\epsilon}_{1\bar{S}})}{\bar{\mu}_1^2} - \frac{\bar{\epsilon}_{1\bar{S}}}{\bar{\mu}_1} + \frac{(\bar{S}_f - \bar{S})\bar{\epsilon}_{1\bar{S}\bar{S}}}{\bar{\mu}_1} \\ & - \frac{(\bar{S}_f - \bar{S})\bar{\epsilon}_{1\bar{S}}\bar{\mu}_{1\bar{S}}}{\bar{\mu}_1^2} + \frac{\bar{\epsilon}_1\bar{\mu}_{1\bar{S}}}{\bar{\mu}_1^2} - \frac{(\bar{S}_f - \bar{S})\bar{\epsilon}_{1\bar{S}}\bar{\mu}_{1\bar{S}}}{\bar{\mu}_1^2} \\ & - \frac{(\bar{S}_f - \bar{S})\bar{\epsilon}_1\bar{\mu}_{1\bar{S}\bar{S}}}{\bar{\mu}_1^2} + 2(\bar{S}_f - \bar{S})\bar{\mu}_1\bar{\mu}_{1\bar{S}}^2\bar{\epsilon}_1 \end{aligned} \tag{13.20}$$

and

$$\begin{aligned} f_{\bar{P}}(\bar{P}): \quad = \quad & \frac{(\bar{\epsilon}_2\bar{\mu}_{2\bar{P}} - \bar{\epsilon}_{2\bar{P}}\bar{\mu}_2)}{\bar{\epsilon}_2^2} + \frac{\bar{\mu}_{2\bar{P}}}{\bar{\epsilon}_2} + \frac{\bar{P}\bar{\mu}_{2\bar{P}\bar{P}}}{\bar{\epsilon}_2} - \frac{\bar{P}\bar{\mu}_{2\bar{P}}\bar{\epsilon}_{2\bar{P}}}{\bar{\epsilon}_2^2} \\ & - \frac{\bar{\mu}_2\bar{\epsilon}_{2\bar{P}}}{\bar{\epsilon}_2^2} - \frac{\bar{P}\bar{\epsilon}_{2\bar{P}}}{\bar{\epsilon}_2^2} - \frac{\bar{P}\bar{\mu}_2\bar{\epsilon}_{2\bar{P}\bar{P}}}{\bar{\epsilon}_2^2} + 2\bar{P}\bar{\mu}_2\bar{\epsilon}_{2\bar{P}}^2\bar{\epsilon}_2^3 \end{aligned} \tag{13.21}$$

13.2.2 Pitchfork Singularity

Similarly to the previous model, the conditions for the pitchfork singularity are

$$\frac{d\bar{\mu}}{d\bar{S}}(\bar{S} = \bar{S}_f, \bar{P} = 0) = 0 \text{ and } \frac{d^2\bar{\mu}}{d\bar{S}^2}(\bar{S} = \bar{S}_f, \bar{P} = 0) = 0 \tag{13.22}$$

or equivalently,

$$\begin{aligned} 0 &= \frac{d\bar{\mu}}{d\bar{S}} = \bar{\mu}_{1\bar{S}}\bar{\mu}_2 + \bar{\mu}_1\bar{\mu}_{2\bar{P}}\frac{d\bar{P}}{d\bar{S}} \\ 0 &= \frac{d^2\bar{\mu}}{d\bar{S}^2} = \bar{\mu}_{1\bar{S}\bar{S}}\bar{\mu}_2 + 2\bar{\mu}_{1\bar{S}}\bar{\mu}_{2\bar{P}}\frac{d\bar{P}}{d\bar{S}} \\ &\quad +\bar{\mu}_1 + \bar{\mu}_{2\bar{P}\bar{P}}(\frac{d\bar{P}}{d\bar{S}})^2 + \bar{\mu}_1\bar{\mu}_{2\bar{P}}\frac{d^2\bar{P}}{d\bar{S}^2} \end{aligned} \tag{13.23}$$

In the next section, we provide explicit examples of this static analysis for some case models used in the literature.

13.3 Case Model 1

The growth rate $\mu(S, P)$ is assumed to have the following form

$$\mu(S, P) = \mu_1(S)\mu_2(P) \tag{13.24}$$

with

$$\mu_1(S) = \frac{\mu_{1m}S}{K_{1S} + S + \frac{S^2}{K_{1I}}} \tag{13.25}$$

and

$$\mu_2(P) = (1 - \frac{P}{P_{1m}})^{n1} \tag{13.26}$$

A similar relation is assumed for ϵ

$$\epsilon(S, P) = \epsilon_1(S)\epsilon_2(P) \tag{13.27}$$

with

$$\epsilon_1(S) = \frac{\mu_{2m}S}{K_{2S} + S + \frac{S^2}{K_{2I}}} \tag{13.28}$$

and

$$\epsilon_2(P) = (1 - \frac{P}{P_{2m}})^{n2} \tag{13.29}$$

The model is rendered dimensionless in the form of Equations (13.4–13.6) using the following variables,

$$S_{ref} = S_f, \quad P_{ref} = P_{1m}, \quad \mu_{ref} = \mu_{1m} \text{ and } \epsilon_{ref} = \mu_{2m} \tag{13.30}$$

The dimensionless model parameters are

$$\bar{S}_f = 1 \text{ and } \alpha = \frac{\mu_{2m} S_f}{a\mu_{1m} P_{1m}} \tag{13.31}$$

The dimensionless growth rates are

$$\bar{\mu} = \frac{\bar{S}}{\beta_1 + \bar{S} + \gamma_1 \bar{S}^2}(1-\bar{P})^{n1} := \bar{\mu}_1(\bar{S})\bar{\mu}_2(\bar{P}) \tag{13.32}$$

and

$$\bar{\epsilon} = \frac{\bar{S}}{\beta_2 + \bar{S} + \gamma_2 \bar{S}^2}(1-\lambda\bar{P})^{n2} := \bar{\epsilon}_1(\bar{S})\bar{\epsilon}_2(\bar{P}) \tag{13.33}$$

with

$$\beta_i = \frac{K_{iS}}{S_f} \quad (\mathrm{i} = 1,2), \quad \gamma_i = \frac{S_f}{K_{iI}} \quad (\mathrm{i} = 1,2) \text{ and } \lambda = \frac{P_{1m}}{P_{2m}} \tag{13.34}$$

The first and second derivatives of $\bar{\mu}_1$ are given by

$$\begin{aligned} \bar{\mu}_{1\bar{S}} &= \frac{\beta_1 - \gamma_1 \bar{S}^2}{(\beta_1 + \bar{S} + \gamma_1 \bar{S}^2)^2} \\ \bar{\mu}_{1\bar{S}\bar{S}} &= \frac{-2\gamma_1 \bar{S}}{(\beta_1 + \bar{S} + \gamma_1 \bar{S}^2)^2} - \frac{2(1+2\gamma_1\bar{S})(\beta_1 - \gamma_1\bar{S}^2)}{(\beta_1 + \bar{S} + \gamma_1 \bar{S}^2)^3} \end{aligned} \tag{13.35}$$

Similar relations hold for $\bar{\epsilon}_{1\bar{S}}$ and $\bar{\epsilon}_{1\bar{S}\bar{S}}$ with β_2 and γ_2 replacing β_1 and γ_1. The derivatives for $\bar{\mu}_2(\bar{P})$ and $\bar{\epsilon}_2(\bar{P})$ are given by

$$\bar{\mu}_{2\bar{P}} = -n_1(1-\bar{P})^{n_1-1}, \quad \bar{\mu}_{2\bar{P}\bar{P}} = n_1(n_1-1)(1-\bar{P})^{n_1-2} \tag{13.36}$$

$$\bar{\epsilon}_{2\bar{P}} = -n_2\lambda(1-\lambda\bar{P})^{n_2-1}, \quad \bar{\epsilon}_{2\bar{P}\bar{P}} = n_2(n_2-1)\lambda^2(1-\lambda\bar{P})^{n_2-2} \tag{13.37}$$

Using these derivatives and applying the pitchfork conditions of Equation (13.23) yields

$$\frac{\beta_1 - \gamma_1}{(\beta_1 + 1 + \gamma_1)^2} + \frac{n_1\alpha}{(\beta_2 + 1 + \gamma_2)} = 0 \tag{13.38}$$

$$a\alpha^2 + b\alpha + c = 0 \tag{13.39}$$

with

$$\begin{aligned} a &= \frac{n_1(-1-n_1+2\lambda n_2)(1+\beta_1+\gamma_1)}{(1+\beta_2+\gamma_2)^2} \\ b &= \frac{2n_1(\beta_2-\gamma_2)}{(1+\beta_2+\gamma_2)^2} \\ c &= \frac{2(-\beta_1 - 3\beta_1\gamma_1 + \gamma_1^2)}{(1+\beta_1+\gamma_1)^3} \end{aligned} \tag{13.40}$$

It should also be noted that these general equations for pitchfork singularity can be used to recover the static behavior for Monod growth kinetics $\gamma_1 = 0$ and/or $\gamma_2 = 0$, as well as to recover the important case when the product synthesis rate ϵ is proportional to the specific cell growth rate μ. In this case, the dimensionless rates $\bar{\mu}$ and $\bar{\epsilon}$ are equal. Therefore, by setting $\beta_1 = \beta_2$, $\gamma_1 = \gamma_2$, $\lambda = 1$, and $n_1 = n_2$ into Equations (13.40), the pitchfork conditions are reduced to,

$$\frac{\beta_1 - \gamma_1}{\beta_1 + 1 + \gamma_1} + n_1\alpha = 0 \quad (13.41)$$

$$n_1(n_1 - 1)\alpha^2 + \frac{2n_1\alpha(\beta_1 - \gamma_1)}{(\beta_1 + 1 + \gamma_1)} + \frac{2(\gamma_1^2 - 3\gamma_1\beta_1 - \beta_1)}{(\beta_1 + 1 + \gamma_1)^2} = 0 \quad (13.42)$$

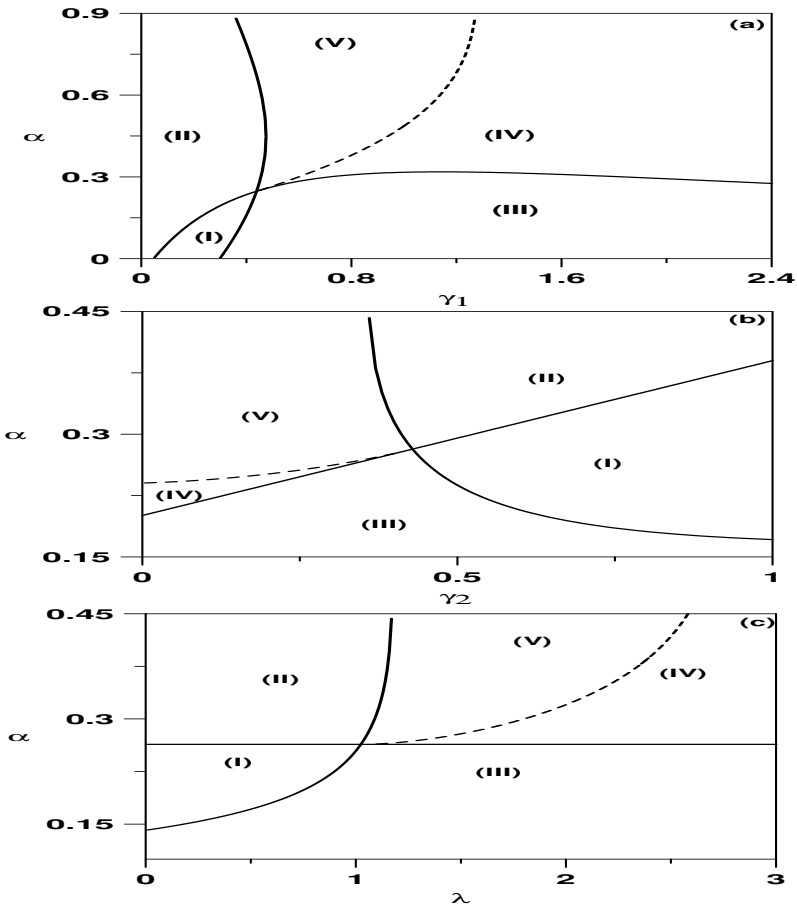

FIGURE 13.1: (a)–(c) Branch sets for the first case model.

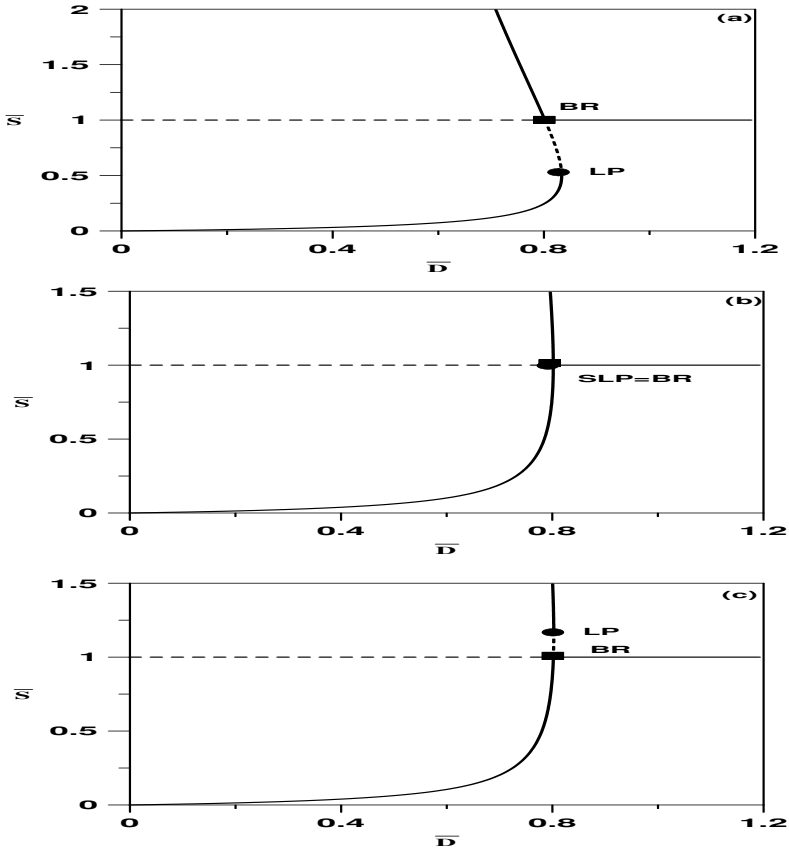

FIGURE 13.2: Continuity diagrams (a)–(c) in the different regions of Figure 13.2; solid line, stable branch; dashed line, unstable branch; SLP, static limit point; BR, bifurcation point.

The complete branch set for this model consists therefore in the hysteresis singularity along with the pitchfork singularities (Equations (13.38–13.39)). Figures 13.1(a–c) show examples of branch sets in the parameter spaces (α, γ_1), (α, γ_2), and (α, λ), for the following nominal values:

$$\beta_1 = 0.047, \gamma_1 = 0.50, \beta_2 = 0.06, \gamma_2 = 0.3333, \lambda = 1.2, n_1 = 1, n_2 = 1 \quad (13.43)$$

The crossing of the boundaries of the hysteresis (dashed line) and the pitchfork (solid line) singularities divides each of the branch sets (Figures 13.1(a–c)) into five different regions. For any combinations of model parameters in region (I) of Figure 13.1a, an imperfect pitchfork is expected, as shown in the steady-state portrait of Figure 13.2a, obtained for example with $(\alpha, \gamma_1) = (0.01, 0.2)$. A safe operation of the bioreactor is possible only for values of a dilution rate

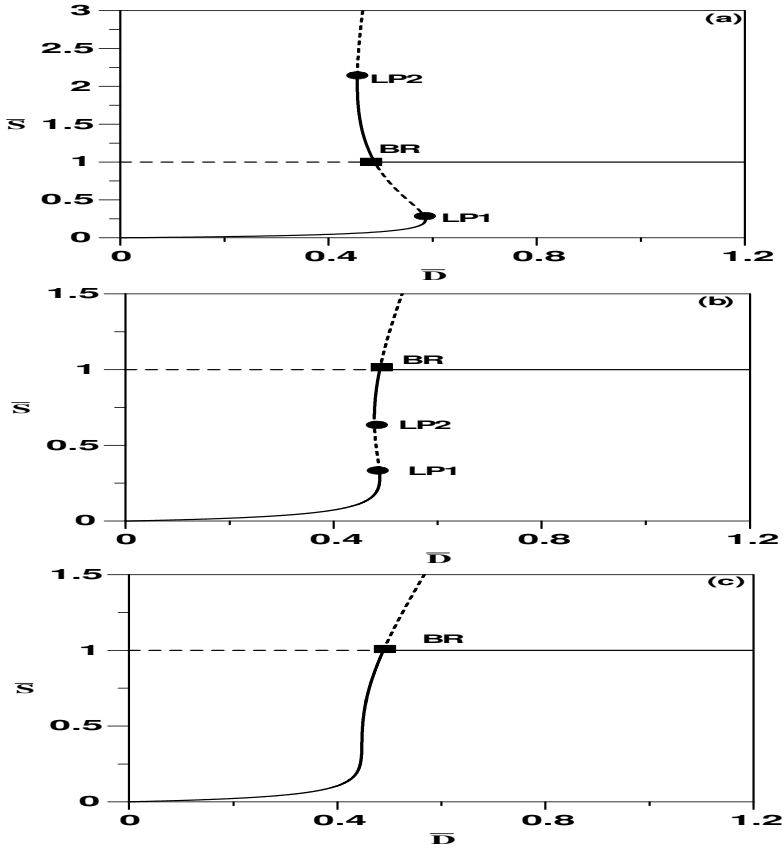

FIGURE 13.3: Continuity diagrams (a)–(c) in the different regions of Figure 13.2; solid line, stable branch; dashed line, unstable branch; SLP, static limit point; BR, bifurcation point.

smaller than that corresponding to the static limit point, defined by

$$\bar{D}_{LP} = \bar{\mu}(\bar{S}_{max}) \tag{13.44}$$

where $\bar{S}_{max}$ is the root of $\frac{d\bar{\mu}}{d\bar{S}} = 0$. For dilution rates smaller than $\bar{D}_{BR}$, a unique steady state exists. $\bar{D}_{BR}$ is obtained by setting $\bar{S} = \bar{S}_f = 1$, i.e., $\bar{P} = 0$ into Equation (13.13) to yield

$$\bar{D}_{BR} = \frac{1}{\beta_1 + 1 + \gamma_1} \tag{13.45}$$

For dilution rates between $\bar{D}_{BR}(= 0.802)$ and $\bar{D}_{LP}(= 0.834)$, the steady-state portrait is characterized by bistability where more than one attractor exists for any value of the dilution rate.

If the parameters of the model move on the boundary separating regions (I) and (II) (Figure 13.1a), then the static limit point (SLP) and the bifurcation point (BR) collapse in one point yielding a perfect pitchfork, as shown in the steady-state portrait of Figure 13.2b, obtained with $(\alpha, \gamma_1) = (0.13709, 0.2)$.

When the parameters move to region (II), the static limit point is located on the other side of washout conditions and occurs on the physically unrealistic branch. An example of a steady-state portrait in this region is shown in Figure 13.2c, obtained with $(\alpha, \gamma_1) = (0.15, 0.2)$.

For parameters in region (III), the continuity diagram, as shown in Figure 13.3a for $(\alpha, \gamma_1) = (0.2, 1.0)$, is characterized by the presence of two static limit points located on the opposite side of the washout line. Since the upper branch is physically unrealistic, the operation of the bioreactor in this region is similar to region (I) (Figure 13.2a). When the pair of parameters move to region (IV), the second static limit point (SLP_2) moves to the physically realistic branch, as shown in the continuity diagram of Figure 13.3b, obtained with $(\alpha, \gamma_1) = (0.4, 1.0)$. For dilution rates smaller than that of SLP_2 ($\bar{D}_{LP2} = 0.4781$), the process settles on the lower nontrivial steady state for any start-up conditions. For dilution rates between SLP_2 and BR ($\bar{D}_{BR} = 0.48852$) two stable branches coexist. For the narrow conditions between BR and SLP_1 ($\bar{D}_{LP1} = 0.48865$), the lower stable branch coexists with washout conditions. Finally, when the parameters move to region (V) the hysteresis line is crossed and therefore the two static limit points disappear. An example of a steady-state portrait is shown in Figure 13.3c for $(\alpha, \gamma_1) = (0.5, 1.0)$. The evolutionary trend for the substrate with the dilution rate is qualitatively different from region (II) (Figure 13.2c).

The branch sets of Figures 13.1(a–c) also allow a useful analysis of the effect of model parameters. It can be seen from Figure 13.1a that the hysteresis line exists only for values of γ_1 larger than a certain value ($\gamma_1 = 0.43$, for the chosen nominal values). The process therefore cannot exhibit multiplicity when the cell growth rate $\bar{\mu}$ exhibits Monod kinetics, i.e., $\gamma_1 = 0$, even if the other substrate-inhibition constant γ_2 is nonzero. Moreover, for smaller values of γ_1 the behavior of the process is dominated by the pitchfork singularity where the process is either stable (region II) or exhibits bistability with washout conditions (region I). As the substrate inhibition constant γ_1 increases, both regions (IV) and (V) of multiplicity widen at the expense of region (III). In fact, for all values of γ_1 larger than 1.5 and α larger than 0.40, the operation of the process settles on region (IV) where the model predicts the coexistence of two stable solutions, for some range of dilution rates, and the coexistence of a stable solution with washout conditions for a smaller range of dilution rates.

The effect of the other substrate-inhibition constant γ_2, pertinent to the product formation rate ϵ, is shown in Figure 13.1b. It can be seen that unlike γ_1, the behavior of the process, for larger values of γ_2, is dominated by the pitchfork singularity. The hysteresis boundaries exist only for values of γ_2 smaller than a certain value ($\gamma_2 = 0.40$ for the chosen nominal parameters).

Moreover, the region of hysteresis (region IV) widens for decreasing values of γ_2. Unlike Figure 13.1a, the branch set predicts hysteresis even when the product formation rate ϵ exhibits Monod growth kinetics, i.e., $\gamma_2 = 0$.

Figure 13.1c shows the effect of λ on the static behavior of the process. The same five regions are found in this branch set. It can be noted that one of the pitchfork boundaries consists of a horizontal line. This corresponds to Equation (13.38), which does not depend on λ. It can also be seen that region (IV) of multiplicity increases with increasing λ. For smaller values of λ ($\lambda \leq 1.024$ and $\alpha \leq 0.263$) the operation of the process (region I) is dominated by the coexistence of a stable branch with washout conditions.

13.4 Case Model 2

The second example pertains to the following form of $\mu_2(P)$ and $\epsilon_2(P)$

$$\mu_2(P) = \frac{K_{1P}}{K_{1P} + P} \tag{13.46}$$

$$\epsilon_2(P) = \frac{K_{2P}}{K_{2P} + P} \tag{13.47}$$

The model is rendered dimensionless using the definitions of Equations (13.4–13.6) with

$$P_{ref} = K_{1P} \quad \text{and} \quad \alpha = \frac{\mu_{2m} S_f}{a \mu_{1m} K_{1p}} \tag{13.48}$$

The dimensionless cell growth rate becomes

$$\bar{\mu} = \bar{\mu}_1(\bar{S}) \bar{\mu}_2(\bar{P}) \tag{13.49}$$

with $\bar{\mu}_1(\bar{S})$ given by Equation (13.32) and

$$\bar{\mu}_2(\bar{P}) = \frac{1}{1 + \bar{P}} \tag{13.50}$$

The dimensionless rate of product synthesis becomes

$$\bar{\epsilon} = \bar{\epsilon}_1(\bar{S}) \bar{\epsilon}_2(\bar{P}) \tag{13.51}$$

with $\bar{\epsilon}_1(\bar{S})$ given by Equation (13.33) and

$$\bar{\epsilon}_2(\bar{P}) = \frac{1}{1 + \lambda \bar{P}} \tag{13.52}$$

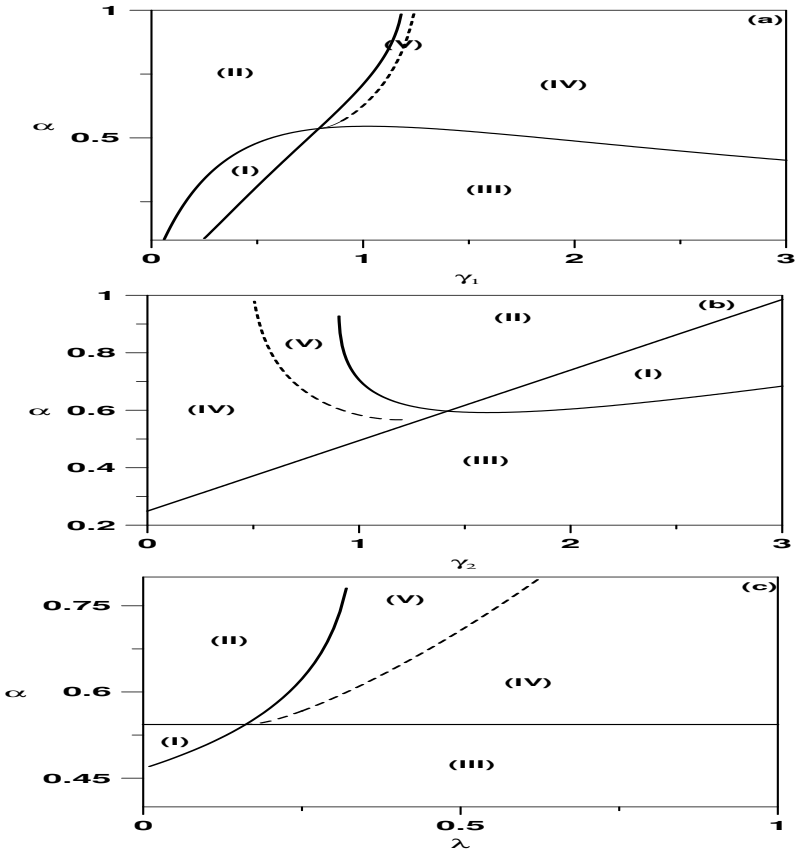

FIGURE 13.4: (a)–(c) Branch sets for the second case model.

with $\lambda = \frac{K_{1P}}{K_{2P}}$. The first and second derivatives of the growth rates are given by

$$\bar{\mu}_{2\bar{P}}(\bar{P}) = \frac{-1}{(1+\bar{P})^2}, \quad \bar{\mu}_{2\bar{P}\bar{P}}(\bar{P}) = \frac{2}{(1+\bar{P})^3} \tag{13.53}$$

$$\bar{\epsilon}_{2\bar{P}}(\bar{P}) = \frac{-\lambda}{(1+\bar{P})^2}, \quad \bar{\epsilon}_{2\bar{P}\bar{P}}(\bar{P}) = \frac{2\lambda^2}{(1+\bar{P})^3} \tag{13.54}$$

Applying the general pitchfork conditions of Equation (13.23) yields the following relations

$$\begin{aligned} \frac{\beta_1 - \gamma_1}{(\beta_1 + 1 + \gamma_1)^2} + \frac{\alpha}{(\beta_2 + 1 + \gamma_2)} &= 0 \\ a\alpha^2 + b\alpha + c &= 0 \end{aligned} \tag{13.55}$$

with

$$\begin{aligned} a &= 2\lambda(1+\beta_1+\gamma_1) \\ b &= 2(\beta_2-\gamma_2) \\ c &= \frac{2(-\beta_1-3\beta_1\gamma_1+\gamma_1^2)}{(1+\beta_1+\gamma_1)} \end{aligned} \tag{13.56}$$

For the asymptotic case of $\bar{\mu} = \bar{\epsilon}$, the pitchfork conditions (Equations (13.55–13.56)) become,

$$\begin{aligned} \frac{\beta_1-\gamma_1}{\beta_1+1+\gamma_1}+\alpha &= 0 \\ 2\alpha^2+\frac{2\alpha(\beta_1-\gamma_1)}{(\beta_1+1+\gamma_1)}+\frac{2(\gamma_1^2-3\gamma_1\beta_1-\beta_1)}{(\beta_1+1+\gamma_1)^2} &= 0 \end{aligned} \tag{13.57}$$

The branch sets for the hysteresis and pitchfork singularities for this example are shown (Figures 13.4(a–c)) in the parameter spaces (α, γ_1), (α, γ_2), and (α, λ), for the nominal values

$$\beta_1 = 0.00733, \gamma_1 = 0.9, \beta_2 = 0.01466, \gamma_2 = 1.2, \lambda = 0.25$$

Similarly to the previous example, five different regions are found in each of the branch sets. It can be seen from Figure 13.4a that an increase in γ_1 reduces the region of pitchfork. However, unlike the previous example, the region (V) of monotonic and stable behavior is confined to a narrower domain.

Figure 13.4b shows the effect of the other substrate-inhibition constant γ_2. It can be seen that region (IV) of coexistence of two stable branches widens with decreasing γ_2. Furthermore, and unlike the previous example, this model does not predict any hysteresis behavior for Monod-like kinetics, i.e., $\gamma_2 = 0$. Region (III) of stable behavior can also be seen to widen with increasing γ_2 at the expense of region (I) of bistability.

Finally, the effect of the ratio λ of product saturation constants is shown in Figure 13.4c. The same five behaviors can be found in the diagram.

13.5 Concluding Remarks

This part of the book (Chapters 11, 12, 13) investigated the stability of three large classes of unstructured models of continuous bioreactors with product formation. The class of models was classified according to the relationships between the substrate utilization rate, the cell growth rate, and the product formation rate. The kinetic expressions were allowed to depend arbitrarily on substrate, cell, and product. The three classes of models, based on a variety of kinetic expressions, were used in several investigations to model a number

of important industrial bioprocesses. Models belonging to type I are those for which both the substrate utilization rate and the product formation rate are linear functions of cell growth rate. A number of interesting results were obtained for this class of models. It was shown that the unstructured kinetic model for which the cell growth rate depends exclusively on the substrate, with the yield coefficient being constant, cannot produce oscillatory behavior even if the product dynamics are included. The same result was shown to hold for many cases for which the product is strictly growth associated. It was also shown that for a number of important cases, the occurrence of oscillatory behavior is conditioned mainly by the kinetics of product formation. Analytical results were derived that allowed the classification of the parameter space into regions of unique solutions, regions of coexistence between nontrivial steady states and washout conditions as well as regions of periodic behavior.

Models belonging to type II, are those for which the nonbiomass product formation rate is proportional to the utilization rate of limiting substrate. Models belonging to type III, on the other hand, are those for which the rate of utilization of limiting substrate is proportional to cell growth rate. The stability analysis of type II and type III models was limited to steady-state multiplicity. Analytical results were derived that allowed the systematic classification of the multidimensional parameter space into regions of unique solutions and regions of multiplicity resulting from pitchfork and hysteresis phenomena. These general results were illustrated for some case models. Practical pictures in terms of kinetic and operating parameters were constructed for each of these models. These pictures allowed the delineation of regions of unique stable behavior, regions of coexistence of two stable nontrivial branches as well as regions of coexistence of a stable nontrivial branch with washout conditions. It is hoped that this classification can be useful in the understanding of the bioreactor operational features and can help in the control and optimization tasks.

This page intentionally left blank

Chapter 14

OPERABILITY OF NONIDEAL BIOREACTORS

14.1 Introduction

As we have seen in previous chapters of this book, bioreactors models can predict operational problems that manifest themselves essentially in the form of input and output multiplicities, and the occurrence of oscillatory behavior. Input multiplicities arise when different values of a manipulated input variable produce the same value of a desired controlled output variable. The occurrence of such behavior is known to affect the closed-loop performance, regardless of the selected control scheme [308]. Output multiplicities arise when the same value of an input variable produces different values of the output variable. The hysteresis phenomenon is the most common form of output multiplicity and is associated with the existence of a region of open-loop unstable behavior. Output multiplicities are also known to adversely affect the control performance of the bioreactor [292]. The study of the operability (interactions between design and control) is a useful task. An early detection of difficult operating regions in bioreactors would allow the removal or at least the reduction of these operational problems in the early stage of process design, and this would ultimately improve the operability of the bioreactor. The detection of operational problems in bioreactors is best carried out through the study of the behavior of the open-loop process. This task requires two elements: a good model and adequate tools for the analysis. The singularity theory was proved to be a useful tool for this task. The theory, which was successfully used to study the operability of chemical reactors [109, 120, 308, 309, 325], can help to delineate how the design and operating parameters influence the operating characteristics of the bioreactor.

In this chapter, we analyze the operability of a large class of unstructured models of bioreactors with cell recycle, while in the next chapter the operability of a special case pertinent to the prefermentation of cheese culture is investigated. There are a number of aspects that make the analysis in this chapter quite general. First a nonideal bioreactor is considered. The nonideal mixing follows the Lo–Chollette model [224, 225]. The nonideal behavior is described by the fraction of the total volume, which is perfectly mixed and by the fraction of the feed entering the perfectly mixed zone. This model was

used to study the effect of nonideal mixing on input and output multiplicities of a proportional-integral (PI)-controlled nonideal, continuous stirred tank reactor (CSTR) [283], and was also used to investigate the complex dynamics of a bioreactor model under a PI controller [163]. The second aspect concerns the selection of growth kinetics. The analysis is carried out for arbitrary substrate-dependent growth rate expressions. The third generality aspect concerns the variations of the yield coefficient. Both constant and substrate-dependent yield coefficients are considered. As was shown in Chapter 4, variable yield models can predict the existence of oscillatory behavior in bioreactors. After the general conditions for the existence of the different static and dynamic bifurcations are derived, for arbitrary growth rate and yield coefficients, a specific example is provided to illustrate the analysis.

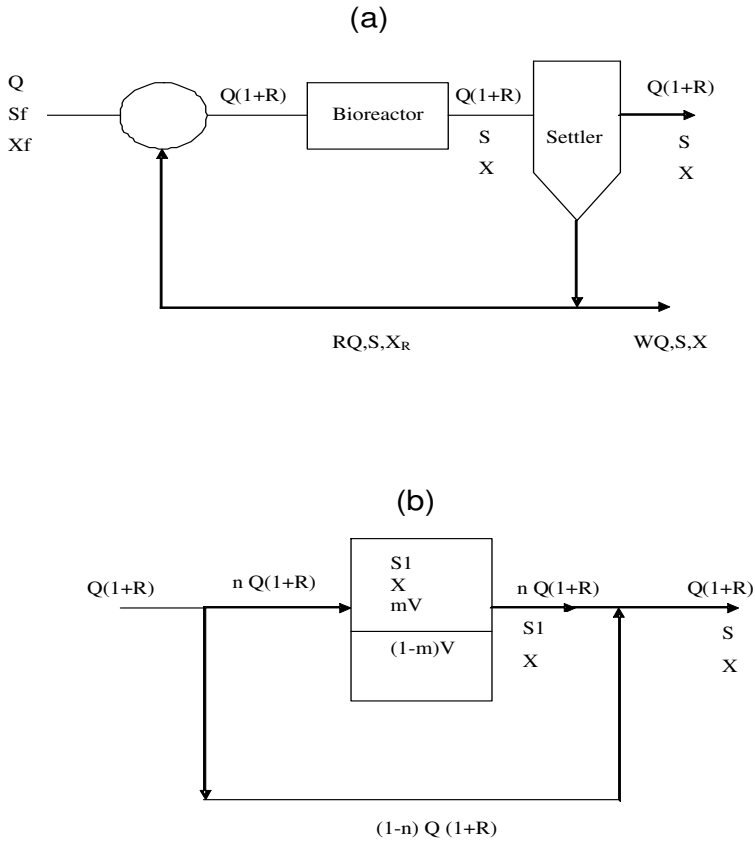

FIGURE 14.1: (a) Schematic diagram of the bioreactor-settler system; (b) Schematic diagram of the bioreactor with nonideality features.

14.2 Process Model

We consider the continuous bioprocess shown in Figure 14.1. The process consists of a bioreactor and a settler. Nonideal behavior is assumed to prevail in the bioreactor. The nonideality follows the Lo-Cholette model [224, 225]. The parameter m represents the fraction of the reactor volume, which is perfectly mixed. The parameter n represents, on the other hand, the fraction of the reactant feed that enters the zone of perfect mixing. The substrate concentration in the mixed part of the bioreactor is denoted by S_1. The feed conditions consist of the feed flow rate Q, and the substrate and biomass feed concentrations S_f and X_f. The recycle conditions are described by the recycle ratio R and the recycle biomass concentration X_R. The settling unit is described by the fraction w of the sludge wasted after passing through the settling unit. The growth rate of the biomass is denoted by r, which depends arbitrarily on the substrate S_1, i.e., $r = r(S_1)$. The yield coefficient is denoted by Y and is an arbitrary positive function of the substrate, i.e., $Y = Y(S_1) > 0$. The mass balances of both substrate and biomass are described by the following equations:

- Substrate mass balance:

$$n(QS_f + RQS) - \frac{r(S_1)XmV}{Y(S_1)} = nQ(1+R)S_1 + mV\frac{dS_1}{dt} \tag{14.1}$$

- Biomass mass balance:

$$n(QX_f + RQX_R) + r(S_1)XmV = nQ(1+R)X + mV\frac{dX}{dt} \tag{14.2}$$

- Balance around the bioreactor:

$$nQ(1+R)S_1 + (1-n)(QS_f + RQS) = Q(1+R)S \tag{14.3}$$

- Balance around the settler:

$$Q(1+R)X = RQX_R + wQX_R \tag{14.4}$$

Equation (14.3) yields the following relation between the concentrations S_1 and S,

$$S_1 = \frac{S(1+Rn) + S_f(n-1)}{n(1+R)} \tag{14.5}$$

Taking the derivatives yields

$$\frac{dS_1}{dt} = \frac{(1+Rn)}{n(1+R)}\frac{dS}{dt} \tag{14.6}$$

Substituting for the expression of S_1 and $\frac{dS_1}{dt}$ (Equations (14.5–14.6)) in the substrate mass balance (Equation (14.1)), and rearranging yields

$$QS_f - QS - \frac{r(S_1)XmV}{Y(S_1)} = \frac{mV(1+Rn)}{n(1+R)}\frac{dS}{dt} \tag{14.7}$$

The settler balance (Equation (14.4)) yields,

$$X_R = \frac{(1+R)X}{(R+w)} \tag{14.8}$$

Substituting this equation in Equation (14.2) and rearranging yields

$$nQX_f - \frac{nw(1+R)}{R+w}QX + r(S_1)mVX = mV\frac{dX}{dt} \tag{14.9}$$

Introducing the dilution rate $D = \frac{Q}{V}$, the mass balances (Equations (14.7, 14.9)) are equivalent to

$$D(S_f - S) - \frac{r(S_1)Xm}{Y(S_1)} = \frac{m(1+nR)}{n(1+R)}\frac{dS}{dt} \tag{14.10}$$

and

$$nDX_f - \frac{n(1+R)w}{R+w}DX + r(S_1)mX = m\frac{dX}{dt} \tag{14.11}$$

For the asymptotic case of $n = m = 1$, Equation (14.5) yields $S_1 = S$ and we recover the model for the ideal bioreactor with cell recycle

$$D(S_f - S) - \frac{r(S)}{Y(S)X} = \frac{dS}{dt} \tag{14.12}$$

$$DX_f - \frac{(1+R)w}{R+w}DX + r(S)X = \frac{dX}{dt} \tag{14.13}$$

14.3 Static Singularities

The nonlinear model (Equations (14.10, 14.11)) can exhibit a number of static multiplicities that can influence the control of the process. The study of these multiplicities and the associated control ramifications can be suitably carried out within the framework of the singularity theory. The starting point of the analysis is to see whether the steady-state equations of the model can be reduced to a single variable algebraic equation. This is fortunately the case. The model (Equations (14.10, 14.11)) is written in the following form

$$D(S_f - S) - \frac{r(S_1)Xm}{Y(S_1)} = \lambda\frac{dS}{dt} \tag{14.14}$$

$$nDX_f - n\alpha DX + r(S_1)mX = m\frac{dX}{dt} \tag{14.15}$$

with

$$\lambda = \frac{m(1+nR)}{n(1+R)} \quad \text{and } \alpha = \frac{(1+R)w}{R+w)} \tag{14.16}$$

Combining the steady-state forms of Equation (14.14) and Equation (14.15) yields the following equation for X

$$Y(S_1)D(S_f - S) + nDX_f - nXD\alpha = 0 \tag{14.17}$$

or equivalently

$$X = \frac{Y(S_1)(S_f - S) + nX_f}{n\alpha} \tag{14.18}$$

Substituting Equation (14.18) into Equation (14.14), at the steady state, yields the following single variable equation in $\bar{S}$,

$$D(S_f - S) - m\frac{r(S_1)}{Y(S_1)}\frac{(Y(S_1)(S_f - S) + nX_f)}{n\alpha} = 0 \tag{14.19}$$

or by recasting the value of α (Equation (14.16)),

$$D(S_f - S) - \frac{r(S_1)}{Y(S_1)}\frac{m(R+w)}{nw(1+R)}(Y(S_1)(S_f - S) + nX_f) \quad = \quad 0 \tag{14.20}$$

Denote by $F(S,u)$ the left-hand side of Equation (14.20)

$$F(S,u): \quad = \quad D(S_f - S) - \frac{r(S_1)}{Y(S_1)}\frac{m(R+w)}{nw(1+R)}(Y(S_1)(S_f - S) + nX_f) \tag{14.21}$$

where S is the output (controlled variable) and u is the selected input or manipulated variable, which is a distinguished parameter in the singularity theory. It can be seen that the single algebraic Equation (14.21) includes a number of potentially variable parameters. These include the dilution rate D, the substrate feed concentration S_f, the biomass feed concentration X_f, the recycle ratio R, and the fraction w of sludge wasted. The parameters m and n can be considered as "design" parameters since they depend on mixing conditions. The selection of the controlled variable for the bioreactor is obviously an important issue. In a number of applications, pH or temperature are used as regulation variables for optimizing the microbial growth [360]. These variables are easier to measure and control and have negligible perturbations. However, variables subject to large fluctuations such as substrate concentration, selected

in this work, can be just as important for growth optimization [101]. Large levels of substrate can be toxic for the microbial growth while too little can force an early stationary or decay phase. For these reasons, the control of bioreactors based on substrate concentration has become an important issue in many applications such as the production of bioproducts of high added value, alcoholic fermentation, and wastewater biotreatment, where strict environmental regulations require limits on organic matter released in effluents [234, 295]. The use of substrate as a controlled variable is not however without practical implementation problems. The lack of reliable on line sensors for the substrate may require the use of observers to estimate the unmeasured states [234].

In the following section, we examine which of the mentioned model parameters, if chosen as manipulated variables, can lead to multiplicity in the nonlinear model. From a control point of view, both input and output multiplicities should be considered. The necessary conditions for the existence of input multiplicity for the variable u are that

$$F = \frac{\partial F}{\partial u} = 0 \tag{14.22}$$

while the necessary conditions for output multiplicity are that

$$F = \frac{\partial F}{\partial S} = 0 \tag{14.23}$$

Input or output multiplicities, when they occur, manifest themselves in the form of specific behavior, as the selected manipulated variable is varied. The simplest static bifurcation is the saddle-node bifurcation (Figure 3.4a), which is one form of output multiplicity. The necessary conditions for the existence of this singularity are given by Equation (14.23), in addition to:

$$\frac{\partial F}{\partial u} \neq 0 \text{ and } \frac{\partial^2 F}{\partial S^2} \neq 0 \tag{14.24}$$

The second static multiplicity is the formation of an isola and the development of an isola into a mushroom, as shown in Figures 3.7(a–b). These singularities can involve both input and output multiplicities. They arise when the following conditions are satisfied

$$F = F_S = F_u = 0 \tag{14.25}$$

$$F_{Su} \neq 0, F_{SS} \neq 0, F_{uu} \neq 0 \tag{14.26}$$

The third qualitative change is the appearance of hysteresis singularity that produces output multiplicity. The conditions for the hysteresis singularity are that

$$F = F_S = F_{SS} = 0 \tag{14.27}$$

$$F_u \neq 0, F_{Su} \neq 0, F_{SSS} \neq 0 \tag{14.28}$$

The last singularity to be considered is the pitchfork singularity (Figure 3.6a). Pitchfork singularity is an example of both input and output multiplicities, as can be seen in Figure 3.6 showing the perturbed forms of the pitchfork. The conditions of the existence of pitchfork are

$$F = F_S = F_u = F_{SS} = 0 \tag{14.29}$$

and

$$F_{Su} \neq 0, F_{SSS} \neq 0 \tag{14.30}$$

By characterizing the type of static singularity the model can predict, one can understand how to minimize or even eliminate the associated multiplicity. In particular, if the multiplicity between the output variable S and any of the operating parameters is eliminated then the bioreactor will be generally easier to control and safer to operate, since the process gain would remain with the same sign over the operating region of interest. However, this does not guarantee that the bioreactor is asymptotically stable, since limit cycles can also occur. Periodic behavior is examined in a later section. The derivatives of F (Equation (14.21)) with respect to the different parameters are given by:

$$\frac{\partial F}{\partial D} = S_f - S, \quad \frac{\partial F}{\partial R} = \frac{mr(S_1)(w-1)(Y(S_1)(S_f - S) + nX_f)}{n(1+R)^2 w Y(S_1)} \tag{14.31}$$

$$\frac{\partial F}{\partial w} = \frac{mr(S_1)R(Y(S_1)(S_f - S) + nX_f)}{n(1+R)w^2 Y(S_1)}, \quad \frac{\partial F}{\partial S_f} = D - \frac{mr(S_1)(R+w)}{n(1+R)w} \tag{14.32}$$

$$\frac{\partial F}{\partial X_f} = \frac{-mr(S_1)(R+w)}{(1+R)wY(S_1)}, \quad \frac{\partial F}{\partial m} = \frac{-r(S_1)(R+w)(S_f - S) + nX_f)}{n(1+R)wY(S_1)} \tag{14.33}$$

$$\frac{\partial F}{\partial n} = \frac{-mr(S_1)(S - S_f)(R+w)}{n^2(1+R)w} \tag{14.34}$$

Using the steady-state Equation (14.21) and substituting in the Equations (14.31–14.34) yields,

$$\frac{\partial F}{\partial R} = \frac{D(S_f - S)(w-1)}{(1+R)(R+w)}, \quad \frac{\partial F}{\partial w} = \frac{DR(S_f - S)}{w(R+w)} \tag{14.35}$$

$$\frac{\partial F}{\partial S_f} = \frac{nDX_f}{Y(S_1)(S_f - S) + nX_f}, \quad \frac{\partial F}{\partial X_f} = \frac{-nD(S_f - S)}{Y(S_1)(S_f - S) + nX_f} \tag{14.36}$$

$$\frac{\partial F}{\partial m} = \frac{-D(S_f - S)}{m}, \quad \frac{\partial F}{\partial n} = \frac{D(S_f - S)^2 Y(S_1)}{n(Y(S_1)(S_f - S) + nX_f)} \tag{14.37}$$

In examining these equations, we can conclude that the following conditions should be satisfied for the system to exhibit input multiplicities ($F_u = 0$) for the selected variables:

- For $u = D$, input multiplicity implies necessarily that $S = S_f$.
- For $u = R$, this implies that $D = 0$, $w = 1$, or $S = S_f$.
- For $u = w$, this implies that $D = 0$, $R = 0$, or $S = S_f$.
- For $u = S_f$, this implies that $D = 0$, $n = 0$, or $X_f = 0$.
- For $u = X_f$, this implies that $D = 0$, $n = 0$, or $S = S_f$.
- For $u = m$, this implies that $D = 0$ or $S = S_f$.
- For $u = n$, this implies that $D = 0$ or $S = S_f$.

Barring the trivial cases of $D = 0$ and $n = 0$, $S = S_f$, $w = 1$, and $R = 0$, it can be seen that input multiplicity is possible only for $X_f = 0$, i.e., sterile feed. If input multiplicity is ruled out then we can rule out the existence of isola and mushroom singularities as well as the occurrence of pitchfork singularities, since all of these singularities require that $F_u = 0$. The case of sterile feed ($X_f = 0$) is examined in more detail in a later section.

As for output multiplicities, the existence of the hysteresis singularity is defined by the conditions of Equations (14.27–14.28). It can be noted that since input multiplicity $F_u = 0$ is not satisfied except for the cases $w = 1$, $R = 0$, i.e., no recycle and $X_f = 0$, we therefore anticipate that output multiplicity may exist for other parameters. However, the condition $F_{Su} \neq 0$ should be satisfied. Taking the derivatives F_S and F_{SS} of Equation (14.21) yields

$$F_S = -D - \frac{m(R + w)}{nw(1 + R)}(r_{S_1}(S_f - S) - r(S_1) + nX_f(\frac{r}{Y})_S) \tag{14.38}$$

$$F_{SS} = -\frac{m(R + w)}{nw(1 + R)}(r_{S_1 S_1}(S_f - S) - 2r_S + nX_f(\frac{r}{Y})_{SS}) \tag{14.39}$$

Taking the derivative F_{uS} (with u being one of the model parameters) yields:

$$F_{DS} = -1, \quad F_{S_f S} = -\frac{m(R + w)}{nw(1 + R)} r_S, \quad F_{X_f S} = -\frac{m(R + w)}{w(1 + R)}(\frac{r}{Y})_S \tag{14.40}$$

$$F_{mS} = -\frac{(R+w)}{nw(1+R)}(r_S(S_f - S) - r(S_1) + nX_f(\frac{r}{Y})_S) \tag{14.41}$$

$$F_{nS} = \frac{-m(R+w)}{n^2w(1+R)}(r_S(S_f - S) - r(S_1) + nX_f(\frac{r}{Y})_S) \tag{14.42}$$

$$F_{RS} = -\frac{m(1-w)}{nw(1+R)^2}(r_S(S_f - S) - r(S_1) + nX_f(\frac{r}{Y})_S) \tag{14.43}$$

$$F_{wS} = \frac{-mR}{n(1+R)w^2}(r_S(S_f - S) - r(S_1) + nX_f(\frac{r}{Y})_S) \tag{14.44}$$

Using the condition $F_S = 0$ (Equation (14.38)), these derivatives are reduced to

$$F_{mS} = \frac{D}{m}, \quad F_{nS} = \frac{Dm}{n} \tag{14.45}$$

$$F_{RS} = \frac{D(1-w)}{(1+R)(R+w)}, \quad F_{wS} = \frac{DR}{w(R+w)} \tag{14.46}$$

It can be seen therefore that barring the trivial cases of $D = 0$, $m = 0$, $w = 1$, and $R = 0$, the conditions $F_{mS} \neq 0$, $F_{nS} \neq 0$, $F_{RS} \neq 0$, $F_{wS} \neq 0$ are always satisfied. The conditions $F_{X_f S}$ and $F_{S_f S}$ are, on the other hand, non-nil when r_{S_1} and $(\frac{r}{Y})_{S_1}$ are non-nil. We conclude therefore that output multiplicity in the form of hysteresis is possible in the bioreactor for nonsterile feed conditions.

14.3.1 Case of Sterile Feed

The case of $X_f = 0$ warrants more discussion, since it arises in the conditions pertinent to input multiplicity. The steady-state value of X is given by Equation (14.18)

$$X = \frac{Y(S_1)(S_f - S)}{n\alpha} \tag{14.47}$$

Substituting this equation in Equation (14.21) yields the following algebraic equation that depends solely on S,

$$F(S,u) := (S_f - S)(D - \frac{m(R+w)}{nw(1+R)}r(S_1)) = 0 \tag{14.48}$$

The washout solution $S = S_f$ always exists for the sterile feed case. The other solution satisfies the following condition,

$$F(S,u) = D - \frac{m(R+w)}{nw(1+R)}r(S_1) = 0 \tag{14.49}$$

For this equation, the hysteresis conditions yield

$$F = 0, \quad r_S = 0, \quad \text{and} \quad r_{SS} = 0 \tag{14.50}$$

Let us examine the non-nil conditions

$$F_u \neq 0, F_{Su} \neq 0 \ \text{ and } \ F_{SSS} \neq 0 \tag{14.51}$$

When $u = D$, it can be seen that $F_D = 1$, therefore $F_{SD} = 0$, and no hysteresis can be found for D. This also holds for all other variables, n, w, and R. We conclude therefore that hysteresis singularity cannot exist for the sterile feed case. With $F_{DD} = 0$, we also rule out the existence of isola and mushroom singularities for D, and the same holds for the other parameters. As for pitchfork singularity, the requirements are that

$$F_S = F_u = 0 \ \text{ and } F_{uS} \neq 0 \tag{14.52}$$

When $u = D$, we have that $F_D = 1 \neq 0$. Therefore, pitchfork singularity cannot exist. For the other parameters the condition $F_S = 0$ requires that $r_S = 0$ but as it was shown previously, this violates the condition $F_{uS} \neq 0$. Therefore, the only singularity that may exist for sterile feed is the simple saddle-node bifurcation defined by

$$F = 0 \ \text{ and } \ F_S = 0 \tag{14.53}$$

TABLE 14.1:
Nominal values of parameters

Parameter	Value
β	0.1
γ	2
R	1.5
w	0.1
n	0.1
m	0.1
δ	5
$\bar{X}_f$	0.1

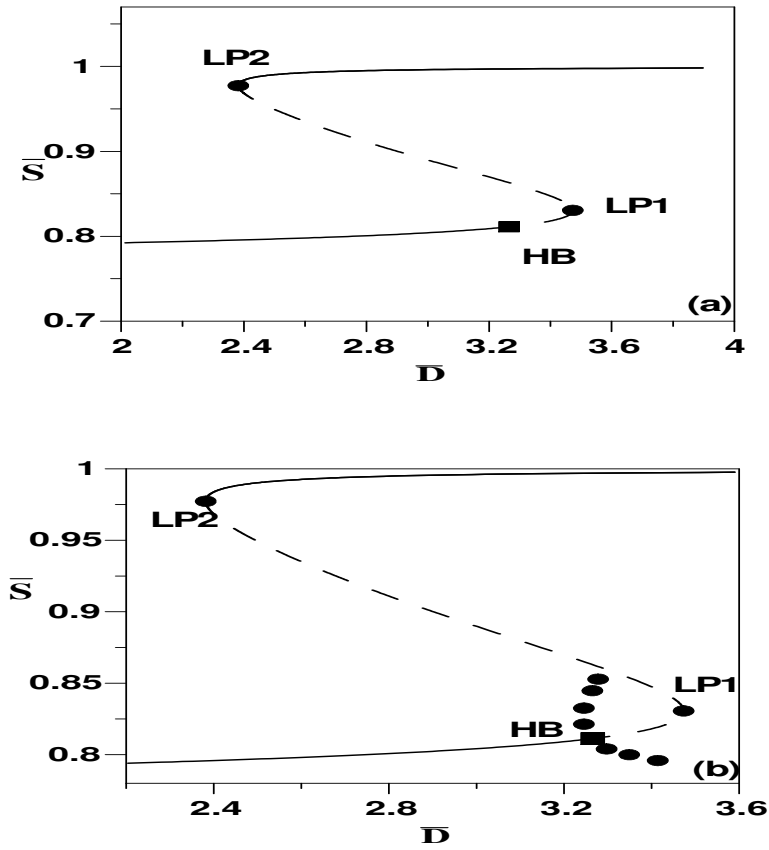

FIGURE 14.2: (a)–(c) Continuity diagrams showing periodic behavior emanating from Hopf point; solid line, stable branch; dashed line, unstable branch; $LP_1$and LP_2, static limit points; HB, Hopf point.

14.4 Dynamic Bifurcation

In this section we investigate the existence of Hopf points in the studied model. The conditions for the occurrence of Hopf points are:

$$f_{1S} + f_{2X} = 0 \tag{14.54}$$

$$f_{1S} f_{2X} - f_{1X} f_{2S} > 0 \tag{14.55}$$

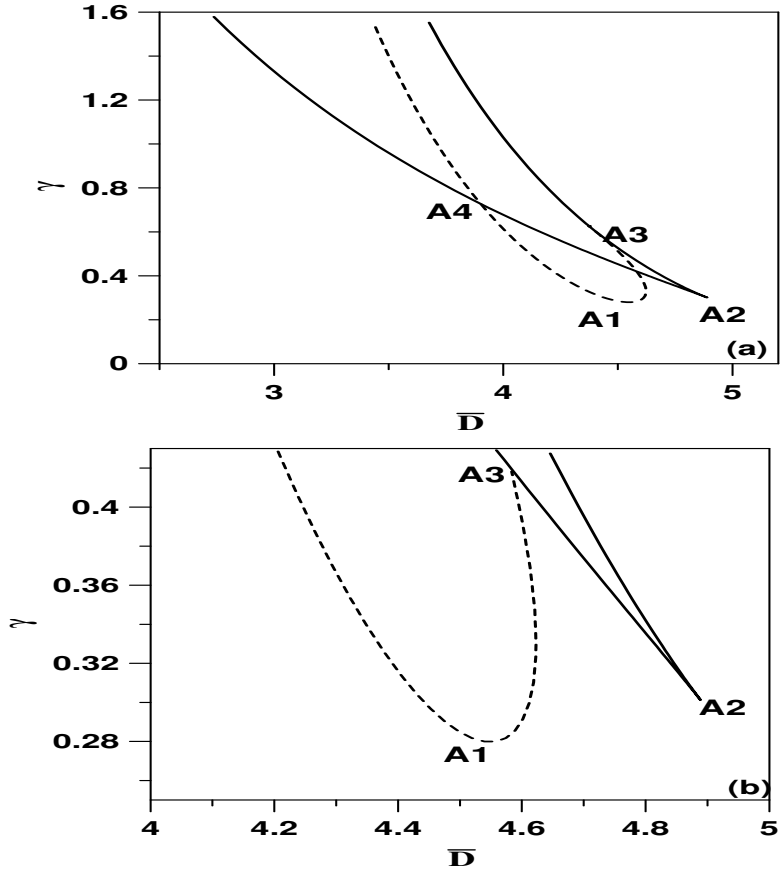

FIGURE 14.3: Diagram showing the domain of hysteresis (solid line) and Hopf points (dashed line) in parameter space: (a) $(\bar{D}, \gamma)$; (b) Enlargement of (a).

where f_1 and f_2 denote the left-hand sides of Equations (14.10–14.11). Substituting for these expressions yields

$$f_{1S} = \frac{(-D - mX(\frac{r}{Y})_S)}{\lambda}, \quad f_{1X} = \frac{-mr}{Y(S)\lambda} \tag{14.56}$$

$$f_{2S} = Xr_S, \quad f_{2X} = \frac{(-n\alpha D + mr)}{m} \tag{14.57}$$

The condition $f_{1S} + f_{2X} = 0$ is equivalent to

$$\frac{-D}{\lambda} - \frac{mX}{\lambda}(\frac{r}{Y})_S - \frac{n\alpha D}{m} + r = 0 \tag{14.58}$$

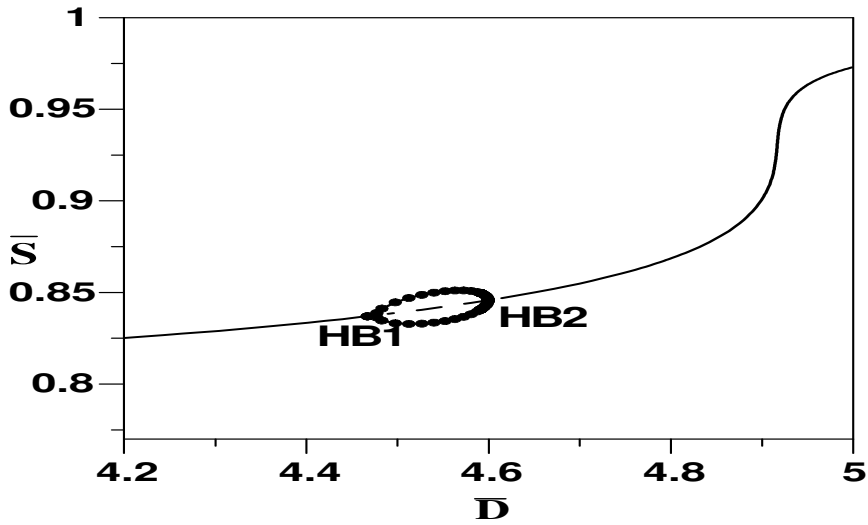

FIGURE 14.4: Continuity diagrams for the case of $\gamma = 0.286$ in Figure 14.3b, showing periodic behavior emanating from the two Hopf points; solid line, stable branch; dashed line, unstable branch; HB_1 and HB_2, Hopf points.

while the condition $f_{1S}f_{2X} - f_{1X}f_{2S} > 0$ is equivalent to

$$n\alpha D^2 - mrD + n\alpha DmX(\frac{r}{Y})_S - rm^2X(\frac{r}{Y})_S + \frac{rm^2X}{Y}r_S \quad > \quad 0 \tag{14.59}$$

Before the analysis is carried out any further we examine the important case of the constant yield coefficient. For this case, the second Hopf condition (Equation (14.59)) is equivalent to

$$n\alpha D^2 - mrD + n\alpha DmX\frac{r_S}{Y} > 0 \tag{14.60}$$

which is also equivalent to

$$n\alpha D - mr + n\alpha mX\frac{r_S}{Y} > 0 \tag{14.61}$$

The first Hopf condition (Equation (14.58)), on the other hand, is equivalent to

$$\frac{mXr_S}{\lambda Y} = \frac{-D}{\lambda} - \frac{n\alpha D}{m} + r \tag{14.62}$$

Substituting Equation (14.62) into Equation (14.60) yields

$$n\alpha D - mr + n\alpha\lambda(r - \frac{D}{\lambda} - \frac{n\alpha D}{m}) > 0 \tag{14.63}$$

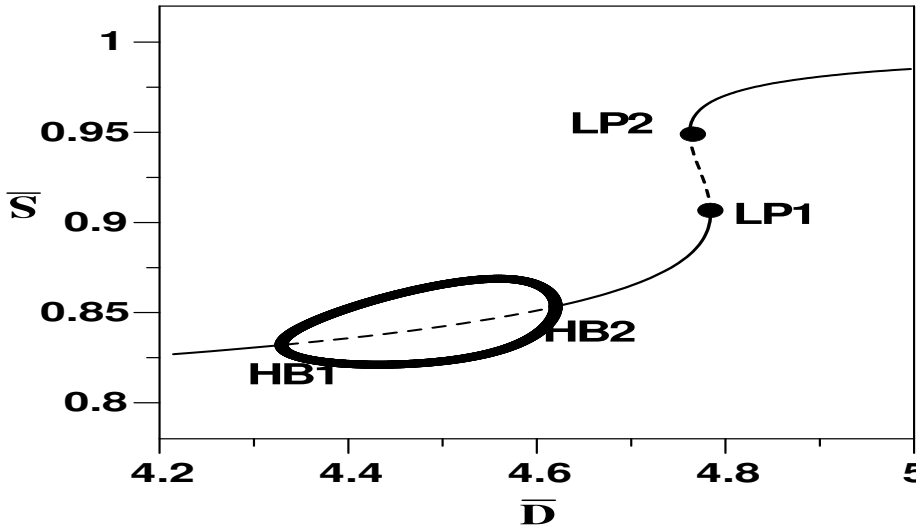

FIGURE 14.5: Continuity diagrams for the case of $\gamma = 0.35$ in Figure 14.3b; solid line, stable branch; dashed line, unstable branch; LP_1 and LP_2, static limit points; HB_1 and HB_2, Hopf points.

which is equivalent to

$$r(n\alpha\lambda - m) > \frac{n^2\alpha^2\lambda D}{m} \tag{14.64}$$

Recasting the expression of α and λ from Equation (14.16), it can be shown that $(n\alpha\lambda - m) = \frac{(wn-1)R}{R+w}$, which is always negative (since the product wn is smaller than 1). The condition of Equation (14.64) is therefore never satisfied. We reach therefore the important conclusion that *the unstructured model even with nonideality cannot exhibit oscillatory behavior for constant yield, regardless of the expression of the substrate-dependent growth rate.* This result joins the conclusion reached in Chapter 4 that showed that neither the presence of a maintenance term nor the assumption of spatial inhomogeneity due to the adhesion of micro-organisms to the reactor wall can cause the appearance of limit cycles in the model. It seems therefore that a dependence of the yield coefficient on the substrate is a necessary condition for the existence of limit cycles in the two-dimensional model, a result that was proved before for the case of the basic model of the ideal chemostat by Ajbar [14] and Pilyugin and Waltman [286].

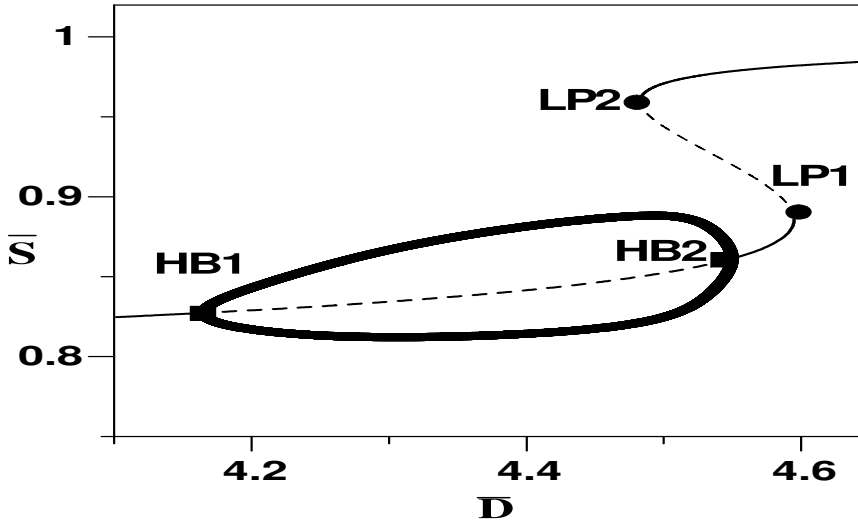

FIGURE 14.6: Continuity diagrams for the case of $\gamma = 0.46$ in Figure 14.3a; solid line, stable branch; dashed line, unstable branch; LP_1 and LP_2, static limit points; HB_1 and HB_2, Hopf points.

14.5 Application to a Case Model

In this section we consider a model with Haldane growth rate [305] and linear dependence of the yield on the substrate.

$$r(S) = \frac{\mu_m S}{K_S + S + S^2/K_I} \tag{14.65}$$

$$Y(S) = a + bS \tag{14.66}$$

As was shown in Chapter 4, variable yield models were used successfully to predict oscillatory behavior in bioreactors. The original model (Equations (14.10, 14.11)) with growth rate (Equation (14.65)) and yield expression (Equation (14.66)) is rendered dimensionless using the following variables

$$\bar{S} = \frac{S}{S_f}, \quad \bar{S}_1 = \frac{S_1}{S_f}, \quad \bar{X} = \frac{X}{aS_f}, \quad \bar{D} = \frac{D}{\mu_m}, \quad \bar{t} = t\mu_m \tag{14.67}$$

$$\beta = \frac{K_s}{S_f}, \quad \gamma = \frac{S_f}{K_I}, \quad \delta = \frac{bS_f}{a} \tag{14.68}$$

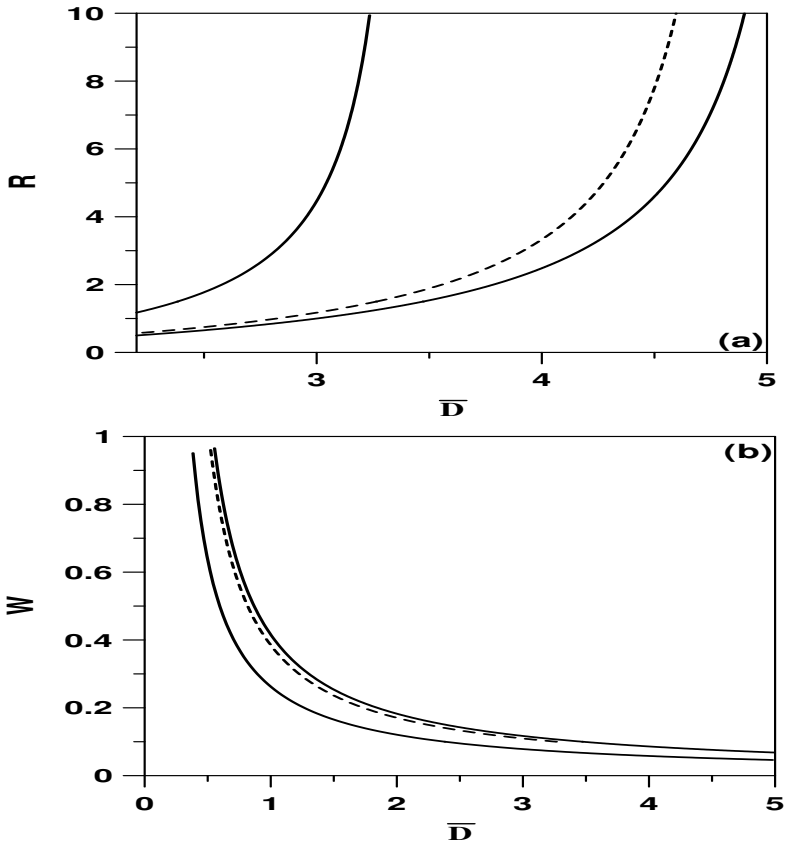

FIGURE 14.7: Diagram showing the domain of hysteresis (solid line) and Hopf points (dashed line) in parameter spaces: (a) $(\bar{D}, R)$; (b) $(\bar{D}, w)$.

The model (Equations (14.10–14.11)) in dimensionless form is given by

$$\bar{D}(1-\bar{S}) - \bar{r}(\bar{S}_1)\bar{X}m = \lambda\frac{d\bar{S}}{d\bar{t}} \tag{14.69}$$

$$n\bar{D}\bar{X}_f - n\alpha\bar{D}\bar{X} + \bar{r}\bar{X}m = m\frac{d\bar{X}}{d\bar{t}} \tag{14.70}$$

with

$$\bar{r}(\bar{S}_1) = \frac{\bar{S}_1}{\beta + 1 + \gamma\bar{S}_1^2} \tag{14.71}$$

$$\bar{S}_1 = \frac{\bar{S}(1+Rn) + (n-1)}{n(1+R)} \tag{14.72}$$

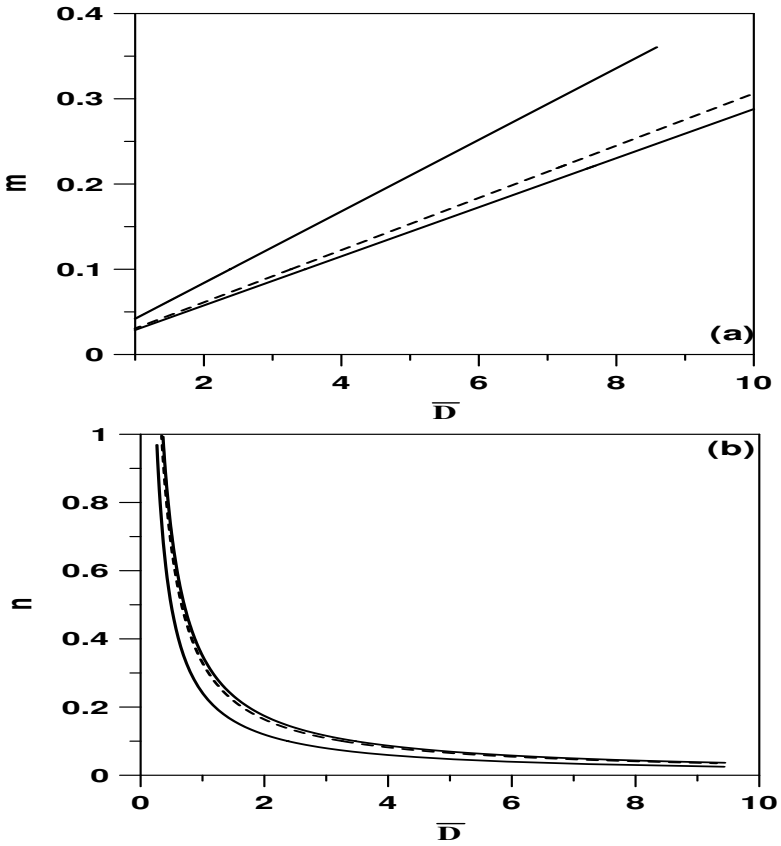

FIGURE 14.8: Diagram showing the domain of hysteresis (solid line) and Hopf points (dashed line) in parameter spaces: (a) $(\bar{D}, m)$; (b) $(\bar{D}, n)$.

$$\lambda = \frac{m(1+nR)}{n(1+R)}, \alpha = \frac{(1+R)w}{R+w)} \tag{14.73}$$

For this specific model, the algebraic steady-state equation ($F(\bar{S}) = 0$) (Equation (14.21)) consists of a polynomial of fourth order. In the following, the simulations are carried out using the nominal values of the parameters shown in Table 14.1. Figure 14.2 shows the bifurcation diagram. The figure is characterized by the existence of two stable branches separated by an unstable region. There is also the appearance of a Hopf point as a result of dynamic bifurcation. Therefore, for dilution rates smaller than LP_2, the operation of the bioreactor leads to high conversion. Between the Hopf point HB and LP_1, the operation of the bioreactor may lead either to oscillatory behavior or to the low conversion branch.

Two-parameter diagrams are useful to delineate the effect of model param-

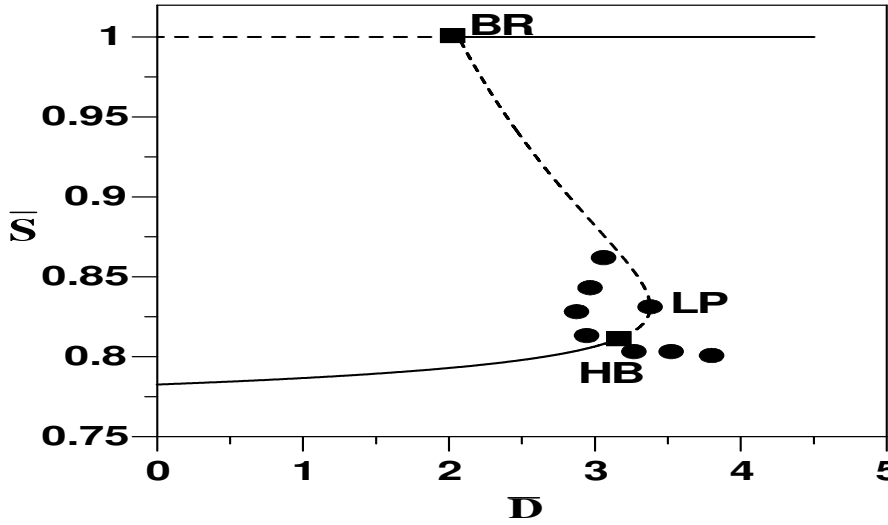

FIGURE 14.9: Continuity diagrams for the case of sterile feed; solid line, stable branch; dashed line, unstable branch; LP, static limit point; HB, Hopf point; BR, bifurcation point.

eters. Figure 14.3 shows the effect of the inhibition constant γ. The dashed line of the Hopf point exhibits a minimum (sign of H_{01} degeneracy) and terminates along another static branch. A number of behaviors can be delineated in the diagram. We start with the point of minimum of Hopf points (dashed line). It can be seen in the enlargement of Figure 14.3a (shown in Figure 14.3b) that the minimum A_1 of Hopf points is lower than that of the static branch A_2. Therefore, for region extending between A_1 and A_2 only Hopf points are expected. An example of this behavior is shown in Figure 14.4, for $\gamma = 0.286$. For dilution rates between the two Hopf points, oscillatory behavior alone is to be expected. This is an interesting result, since it shows that oscillatory behavior alone can exist for some range of dilution rates without the occurrence of any static multiplicity. Going back to Figure 14.3b, it can be seen that above point A_2 and until the first crossing A_3, the behavior of the system is characterized by the existence in this order of a HB, HB, LP, and LP. An example of this behavior is shown in Figure 14.5 for $\gamma = 0.35$. Again oscillatory behavior alone is expected for dilution rates between the two Hopf points. However, hysteresis is also expected between the two limit points. Going back to Figure 14.3a, another behavior is expected between the first crossing A_3 and the second one A_4. Here the system is characterized by the occurrence in this order of a HB, LP, HB, and LP. Figure 14.6 shows an example of this behavior for $\gamma = 0.46$. For this case and because of the relative location of Hopf and static limit points, it can be seen that between HB_1 and LP_2 only oscillatory behavior exists. For dilution rates between LP_2

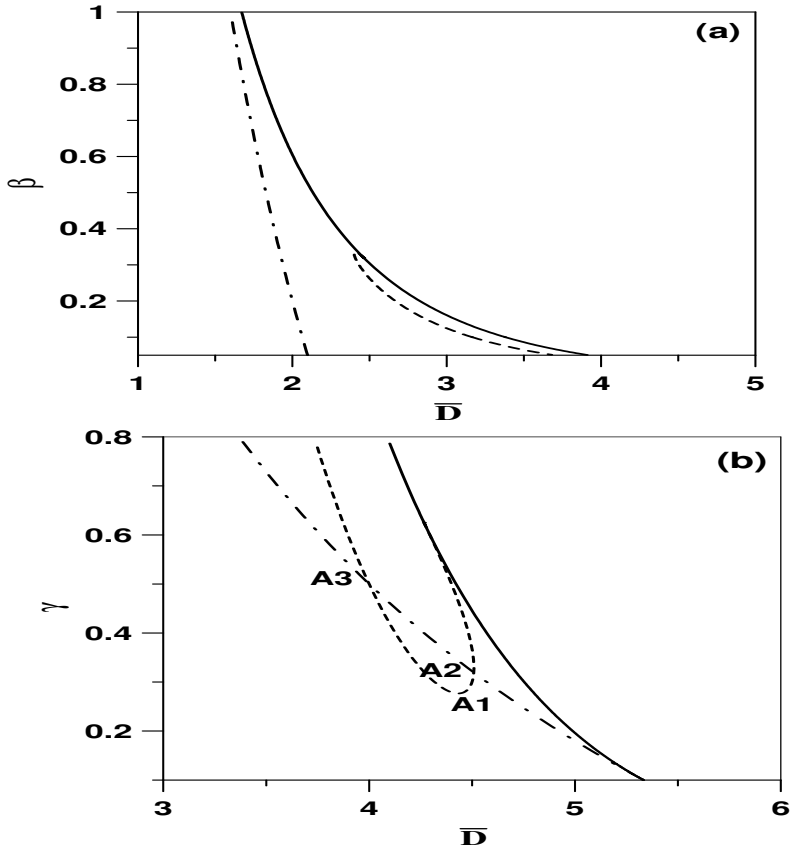

FIGURE 14.10: Diagram showing the domain of limit point (solid line), Hopf point (dashed line) and washout critical point (semidashed line) of Figure 14.9: (a) $(\bar{D}, \beta)$; (b) $(\bar{D}, \gamma)$.

and HB_2, oscillations coexist with the upper stable branch, while for values between LP_2 and LP_1 simple hysteresis occurs. Figure 14.7a shows the effect of the recycle ratio and the purge fraction. For each value of the recycle ratio, a Hopf point (dashed line) is expected between two static limit points. It can also be seen that both hysteresis and Hopf regions increase with increasing values of the recycle ratio. Figure 14.7b shows that the Hopf line also exists for each value of the purge fraction w, although the region of periodic behavior, in terms of dilution rate, is quite narrow. The effect of nonideality of the bioreactor is shown in Figures 14.8(a–b). We recall that the nonideality is described by the fraction m of the reactor volume, which is perfectly mixed and the fraction n of the reactant feed that enters the zone of perfect mixing. It can be seen that for each value of m (Figure 14.8a) or that of n (Figure 14.8b), a Hopf point is expected between two static limit points. It can also

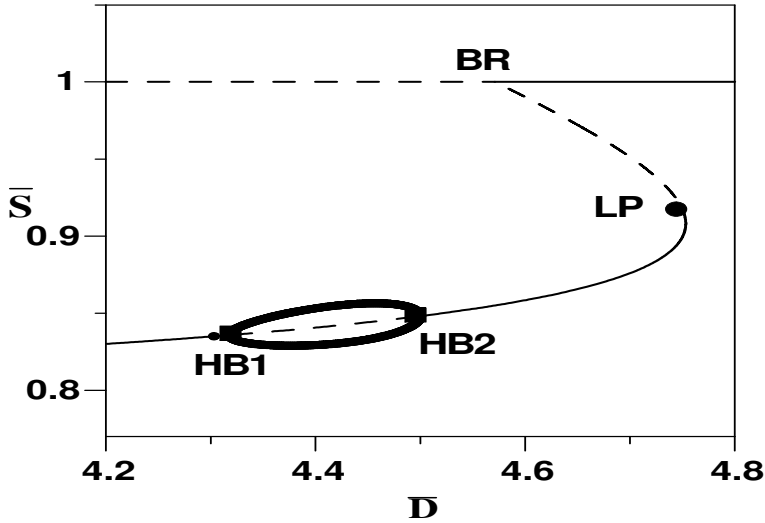

FIGURE 14.11: Continuity diagrams for $\gamma = 0.3$ of Figure 14.10b; solid line, stable branch; dashed line, unstable branch; LP, static limit point; HB_1 and HB_2, Hopf points; BR, bifurcation point.

be noted that increasing the mixing in the reactor (by increasing the value of m) widens the region of hysteresis (the two solid lines) and also widens the region between the Hopf point and the limit point. This shows that increasing the mixing widens (in terms of the dilution rate) the region of instability (either hysteresis or periodic behavior). The effect of the other parameter n is shown in Figure 14.8b. It can be seen that for all values of n the region of periodic behavior is narrow (in terms of dilution rates). Moreover, for n near the asymptotic values of $n = 1$ (perfect case) or $n = 0$ (imperfect case), the hysteresis region is narrow. The domain of instability (i.e., hysteresis) is larger for values of n in the middle (in this case for values between 0.1 and 0.4).

As was mentioned in the analysis carried out in previous sections, the sterile feed case can give rise to saddle-node bifurcation. Figure 14.9 shows the continuity diagram for this case. The diagram is characterized by the presence of single Hopf and limit points. The point BR is the bifurcation point resulting from the crossing of the total washout line with the nontrivial steady state. The effects of saturation constant β and inhibition coefficient γ are shown in Figures 14.10(a–b). For this case, the Hopf line forms a minimum (degeneracy) and collides with the static limit point (another degeneracy). For values of γ smaller than the minimum point A_1, the bifurcation diagram exhibits no Hopf point. For values of γ between A_1 and A_2 (the crossing with the washout line), the bifurcation diagram is characterized by the occurrence in this order of HB, HB, BR, and LP. An example of this behavior is shown in Figure 14.11 for $\gamma = 0.3$. For dilution rates between the two Hopf points,

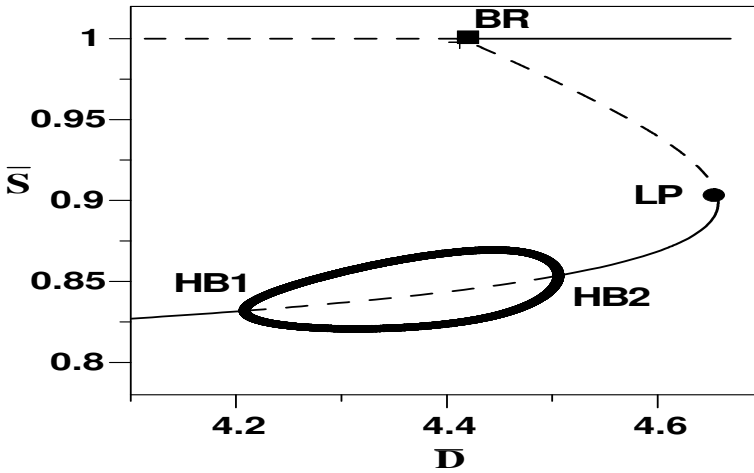

FIGURE 14.12: Continuity diagrams for $\gamma = 0.35$ of Figure 14.10b; solid line, stable branch; dashed line, unstable branch; LP, static limit point; HB_1 and HB_2, Hopf points; BR, bifurcation point.

stable oscillatory behavior is inevitable. For dilution rates between HB_2 and BR, the lower static branch is the only outcome of the dynamics. Between BR and LP, there is bistability between the static branch and the total washout line, while for dilution rates larger than LP, total washout occurs. Going back to Figure 14.10b, it can be seen that for values of γ between A_2 and A_3, the bifurcation diagram is characterized by the occurrence of HB, BR (washout), HB, and LP. An example of this behavior is shown in Figure 14.12 for $\gamma = 0.35$. It can be seen that for dilution rates between the HB and BR points, stable oscillatory behavior is inevitable. For dilution rates between BR and HB_2, the oscillatory behavior coexists with the washout line. Between HB_2 and LP, the lower static branch coexists with the total washout line, while for values larger than LP, total washout occurs.

The effect of some bioreactor parameters are shown in Figure 14.13. In the same diagram are plotted the loci of the limit point (LP), the Hopf point (HB), and the bifurcation point (BR) for the washout line. The plots for $(\bar{D}, m)$ and $(\bar{D}, n)$ show that for each value of the parameters m or n, the bifurcation diagram is characterized by the occurrence of BR, HB and LP points. Similarly to the case of nonsterile feed, it can be seen that an increase in mixing (Figure 14.13a) substantially widens the region of bistability between the limit point and the BR (washout line). The region between LP and HB also increases, but modestly with the increase in m. The effect of the other nonideality parameter n is shown in Figure 14.13b. It can be seen that close to the asymptotic cases of $n = 1$ or $n = 0$, the domain of bistability decreases but the unsafe range of operation is larger for values of n in the middle.

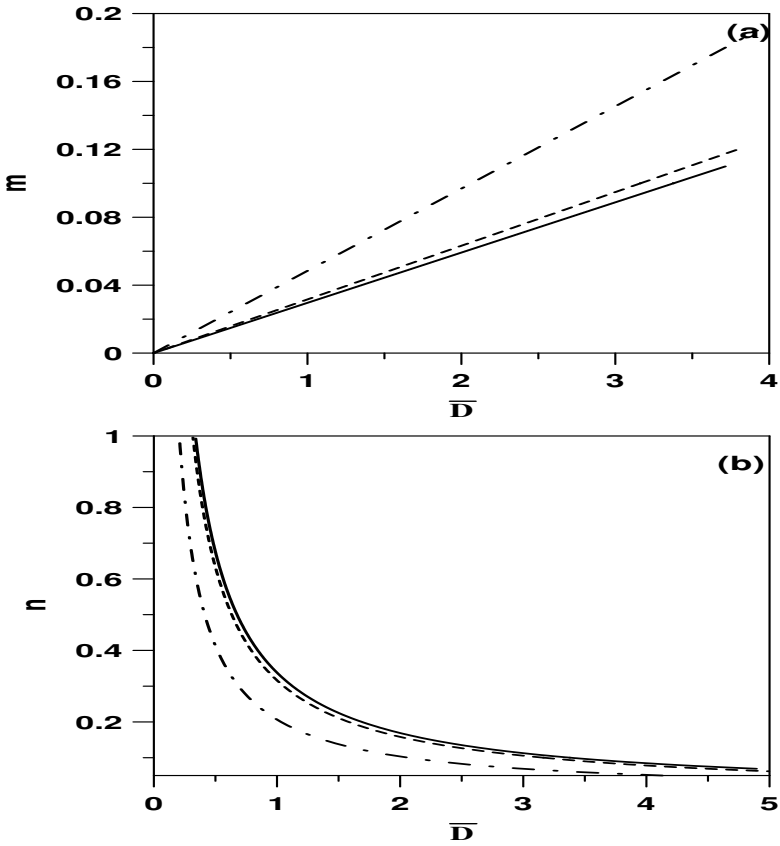

FIGURE 14.13: Diagram showing the domain of limit point (solid line), Hopf point (dashed line) and critical washout point (semidashed line) of Figure 14.10: (a) $(\bar{D}, m)$; (b) $(\bar{D}, n)$.

14.6 Concluding Remarks

This chapter has investigated in some detail the operability of a large class of unstructured kinetic models of a bioreactor-recycle system. A number of features has made the analysis quite general. The model of the bioreactor assumes nonideal behavior by dividing the bioreactor into a well-mixed region and an unreacted region. The analysis was made for a general growth rate expression and for general dependence of the yield coefficient on the substrate. The analysis of the model static and dynamic singularities has shed some light on the operability of the bioreactor. The analysis has shown that input multiplicity cannot occur in the studied model. However, output multiplicity

in the form of hysteresis in the case of nonsterile feed and saddle node in the case of sterile feed are possible. The study has also shown that when the yield coefficient is independent of the substrate, the model even with nonideality cannot predict periodic behavior regardless of the expression of the growth rate. These general results were illustrated for the case of substrate-inhibition growth rate with linear dependence of the yield on the substrate, for both cases of sterile and nonsterile feed conditions. The study of this example has allowed the delineation of the different interactions between the static and Hopf points. For the case of nonsterile feed conditions, it was found that an increase in the substrate-inhibition constant increases the instability of the process in the form of hysteresis and/or the appearance of stable limit cycles. However, depending on the values of this kinetic parameter a variety of behaviors can be found. For cultures with weak substrate-inhibition effects, it is interesting to note that the model predicts that the only operational problem in the bioreactor is the occurrence of spontaneous stable periodic behavior for some range of dilution rates with no appearance of any static multiplicity. If the substrate-inhibition effect is stronger, then the model predicts, in addition to stable oscillations, the existence of a different region of static multiplicity at larger dilution rates. For even stronger inhibition effects, the model predicts the existence of distinct regions of dilution rates, where periodic behavior and hysteresis are expected. But the model also predicts a region of dilution rates where oscillations can exist or die out, depending on the start-up and/or feed conditions. For cultures subject to very strong substrate-inhibition effects, the operational problems in the chemostat manifest themselves in the presence of hysteresis for some range of dilution rates while periodic behavior is also expected in a smaller range of dilution rates. However, all the oscillations are dependent on start-up and/or feed conditions. For the practical case of sterile feed conditions, the same patterns are also observed, except that the static multiplicity consists of a saddle node bifurcation instead of a hysteresis, and the oscillations for some cases coexist with the unsafe washout region. For the effect of operating parameters, it was found that the region of unsafe behavior (bistability or periodic behavior) increases with the increase in the recycle ratio but decreases with the increase in the purge fraction. The increase in the mixing widens, in terms of the dilution rates, the region of unsafe behavior. The increase, on the other hand, in the fraction of the reactant feed that enters the zone of perfect mixing tends to decrease the unsafe behavior but only past certain values.

This page intentionally left blank

Chapter 15

OPERABILITY OF PREFERMENTATION OF CHEESE CULTURE

15.1 Introduction

This chapter addresses the issue of bioreactor operability when applied to a continuous prefermentation of cheese culture. Cheese production is traditionally a batch process, but with an-ever increasing cheese consumption, the mass production of cheese is of great interest to the dairy industry. For this reason, the study of a potential continuous process for cheese production would help to achieve two goals: The first is to study the improvement in the bioreactor productivity while the second objective is to analyze the potential operating problems that may be inherent in the continuous bioprocess. A number of models were developed in the literature for cell growth and lactic acid production [90, 178, 267, 332, 376]. These models were, however, limited to either constant or optimal controlled pH values. These models may present some shortcomings since the cheese prefermentation process is known to be a hydrogen ion dependent process, as the pH of milk changes with cell growth and lactic acid production. Funahashi et al. [116] proposed a kinetic model that can predict both growth and lactic acid production in prefermentation without external pH control. The proposed model was shown to simulate uncontrolled pH experiments. The same authors, in another study [117, 205], carried out a local stability analysis for the model and showed that for given values of kinetic parameters, the model can predict static multiplicity. The authors also studied the case when a seed tank was added to the bioreactor. Their analysis showed that the addition of the seed tank provided a stabilizing effect on the bioreactor dynamics.

This chapter studies the operability of the same bioreactor model. The static analysis enables the derivation of analytical results that determine the exact type of multiplicity predicted by the model. Saddle-node, hysteresis, and pitchfork singularities are shown to occur in the bioreactor model. The effect of bioreactor parameters on the occurrence/removal of these instabilities is also discussed.

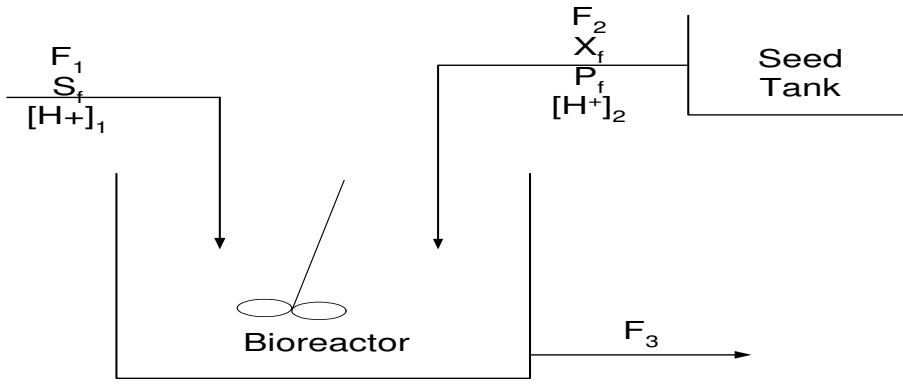

FIGURE 15.1: Schematic diagram of the bioreactor-seed tank system.

15.2 Process Model

The balance equations for the concentrations of cells (X), lactose (S), and lactic acid (P) in the bioreactor, shown in Figure 15.1, are given by the following:

$$\frac{dX}{dt} = \frac{F_2 X_f - F_3 X}{V} + \mu X \tag{15.1}$$

$$\frac{dS}{dt} = \frac{F_1 S_f - F_3 S}{V} - \sigma X \tag{15.2}$$

$$\frac{dP}{dt} = \frac{F_2 P_f - F_3 P}{V} + \pi X \tag{15.3}$$

$$\frac{d[H^+]}{dt} = \frac{F_1[H^+]_1 + F_2[H^+]_2 - F_3[H^+]}{V} + \nu X \tag{15.4}$$

$$\frac{dV}{dt} = F_1 + F_2 - F_3 \tag{15.5}$$

X_f, S_f, and P_f are the feed concentrations. $[H^+]$,$[H^+]_1$, and $[H^+]_2$ are respectively hydrogen ion concentrations in the bioreactor, in the feed, and in the seed tank. F_1, F_2, F_3 are respectively the lactose, the seed, and the exit feed rates. μ is the specific growth rate of cells, σ the lactose consumption

rate, π the lactic acid production rate, and ν the hydrogen ion production rate. These kinetic rates have the following expressions:

$$\mu = \frac{\mu_0[H^+]}{K_1 + [H^+] + [H^+]^2/K_2} \tag{15.6}$$

$$\sigma = \frac{\sigma_0[H^+]}{K_3 + [H^+] + [H^+]^2/K_4} \tag{15.7}$$

$$\pi = \frac{\pi_0[H^+]}{K_5 + [H^+] + [H^+]^2/K_6} \tag{15.8}$$

$$\nu = \frac{\nu_0[H^+]}{K_5 + [H^+] + [H^+]^2/K_6} \tag{15.9}$$

The model rational and assumptions were given in [116, 205]. It can be noted that the specific kinetic rates (Equations (15.6–15.9)) are assumed to depend solely on hydrogen ion concentration. The authors [116, 205] showed that this assumption is appropriate when the system involves high lactose and low lactic acid concentrations.

Introducing the dilution rate $D = \frac{F_3}{V}$, the ratio of seed to substrate feed rate $\alpha = \frac{F_2}{F_1}$, and using the fact that $F_3 = F_1 + F_2$, the steady-state model can be written as follows

$$D(\frac{\alpha X_f}{1+\alpha} - X) + \mu([H^+])X = 0 \tag{15.10}$$

$$D(\frac{S_f}{1+\alpha} - S) - \sigma([H^+])X = 0 \tag{15.11}$$

$$D(\frac{\alpha P_f}{1+\alpha} - P) + \pi([H^+])X = 0 \tag{15.12}$$

$$D(\frac{[H^+]_1}{1+\alpha} + \frac{\alpha[H^+]_2}{1+\alpha} - [H^+]) + \nu([H^+])X = 0 \tag{15.13}$$

It can be noted that since the specific growth rates depend only on $[H^+]$, the mass balance equations for cells and $[H^+]$ concentrations (Equations (15.10, 15.13)) do not include lactose or lactic acid concentrations. These two equations can be, therefore, considered as a two independent variables system. Equation (15.10), in particular, would yield,

$$X = \frac{\alpha D X_f}{(1+\alpha)(D - \mu([H^+])} \tag{15.14}$$

Substituting in Equation (15.13) yields the following algebraic equation for $[H^+]$,

$$\frac{[H^+]_1}{1+\alpha} + \frac{\alpha[H^+]_2}{1+\alpha} - [H^+] + \frac{\alpha X_f}{(1+\alpha)} \frac{\nu([H^+])}{(D - \mu([H^+]))} = 0 \tag{15.15}$$

Substituting for X (Equation (15.14)) in Equations (15.11–15.12) yields the expressions for S and P, respectively

$$S = \frac{S_f}{1+\alpha} - \frac{\sigma([H^+])}{D}X \tag{15.16}$$

$$P = \frac{\alpha P_f}{1+\alpha} + \frac{\pi([H^+])}{D}X \tag{15.17}$$

Examining Equation (15.15), it can be seen that the model equations have collapsed into a single algebraic equation. Equation (15.15) is written in the following compact form,

$$F([H^+], u) = 0 \tag{15.18}$$

where $[H^+]$ is the output (controlled variable) and u is the selected input (manipulated variable). Excluding the kinetic parameters, assumed constant, it can be seen that Equation (15.18) includes a number of variable parameters. These include the dilution rate D, the ratio α of seed to substrate feed rates, the feed pHs ($[H^+]_1$ and $[H^+]_2$) and cell feed concentration X_f. The two other operating parameters S_f and P_f that exist in the original model are not present in this Equation (15.15). This is due, as mentioned before, to the decoupling between Equations (15.10, 15.13), on one hand, and Equations (15.11, 15.12), on the other hand. Consequently, for this model, these two parameters do not have an effect on the model multiplicity. However, they have an effect on setting boundaries for the meaningful existence of steady-state solutions of the model, since the natural constraints $X > 0$ and $0 < S < S_f$ should always be satisfied.

15.3 Static Multiplicity

In the following section, we examine which of the mentioned parameters, if chosen as the manipulated variable, can lead to multiplicity in the nonlinear model. The necessary conditions for the existence of input multiplicity for the variable u are:

$$F = \frac{\partial F}{\partial u} = 0 \tag{15.19}$$

while the necessary conditions for output multiplicity are:

$$F = \frac{\partial F}{\partial [H^+]} = 0 \tag{15.20}$$

We turn now our attention to examine the conditions for input or output multiplicity in the model. In a later section, the different singularities are studied. The derivatives of F (Equation (15.15)) with respect to $[H^+]_1$, $[H^+]_2$, D, α, and X_f yield, respectively

$$\frac{\partial F}{\partial [H^+]_1} = \frac{1}{1+\alpha} \tag{15.21}$$

$$\frac{\partial F}{\partial [H^+]_2} = \frac{\alpha}{1+\alpha} \tag{15.22}$$

$$\frac{\partial F}{\partial X_f} = \frac{\alpha}{(1+\alpha)} \frac{\nu}{(D-\mu)} \tag{15.23}$$

$$\frac{\partial F}{\partial D} = -\frac{\alpha X_f}{(1+\alpha)} \frac{\nu}{(D-\mu)^2} \tag{15.24}$$

$$\frac{\partial F}{\partial \alpha} = -\frac{[H^+]_1}{(1+\alpha)^2} + \frac{[H^+]_2}{(1+\alpha)^2} + \frac{X_f \nu}{(D-\mu)(1+\alpha)^2} \tag{15.25}$$

TABLE 15.1: Model parameters

Parameter	Value
K_1(g/l)	4×10^{-7}
K_2(g/l)	6.85×10^{-6}
K_3(g/l)	4.88×10^{-8}
K_4(g/l)	4.2×10^{-6}
K_5(g/l)	1.5×10^{-6}
K_6(g/l)	3.91×10^{-6}
$\mu_0(h^{-1})$	0.51
$\nu_0(h^{-1})$	3.35×10^{-7}
$\pi_0(h^{-1})$	3.35
$\sigma_0(h^{-1})$	1.02
S_f(g/l)	80
X_f(g/l)	5.5
P_f(g/l)	5.9
pH_1	6.7
pH_2	5.5
$D(h^{-1})$	0.35
α	0.03

A number of conclusions can be reached from these equations. First, since $\frac{\partial F}{\partial [H^+]_1}$ (Equation (15.21)) is always non-nil, the model cannot predict input multiplicity with respect to feed pH ($[H^+]_1$). From Equations (15.22–15.23), we see that the existence of input multiplicity with respect to $[H^+]_2$ or X_f is only possible when $\alpha = 0$, i.e., the case when no seed tank is present. This particular case is treated in a later section. From Equation (15.24), it can also be seen that input multiplicity with respect to the dilution rate can only occur when $\alpha = 0$ or $X_f = 0$. Again, these special cases are treated independently in a later section. The derivative of F with respect to α (Equation (15.25)) provides, on the other hand, explicit conditions for the existence of input multiplicity. We conclude therefore that for the general case of $\alpha \neq 0$ and $X_f \neq 0$, the model can predict input multiplicity only when α is varied. Moreover, with the absence of input multiplicity for $[H^+]_1$, $[H^+]_2$, and D, we anticipate that isola, mushroom and pitchfork singularities cannot occur with any of these parameters, and can only occur when α is allowed to vary. Therefore, we see that α is an important variable that warrants some type of control such as a feedforward ratio control. In the following, we examine in more detail the occurrence of static singularities for α, i.e., $(u = \alpha)$. It can be noted from Equation (15.25) that if F_α is zero then $F_{\alpha\alpha}$ also vanishes. We conclude therefore that an isola-mushroom singularity cannot occur for α. As for the occurrence of a pitchfork singularity, it can be noted that the condition $F_\alpha = 0$ leads, from Equation (15.25), to

$$-[H^+]_1 + [H^+]_2 + \frac{X_f \nu([H^+])}{D - \mu([H^+])} = 0 \tag{15.26}$$

Combining this equation with that of $F = 0$ (Equation (15.15)) leads to the simple condition

$$[H] = [H^+]_1 \tag{15.27}$$

Therefore, the pitchfork conditions are equivalent to the following algebraic equations, evaluated at $[H^+] = [H^+]_1$,

$$F_\alpha = 0, F_{[H^+]} = 0, F_{[H^+][H^+]} = 0 \tag{15.28}$$

This leads to the following system of algebraic equations, again evaluated at $[H^+] = [H^+]_1$,

$$-[H^+]_1 + [H^+]_2 + \frac{\nu X_f}{D - \mu} = 0 \tag{15.29}$$

$$-1 + \frac{\alpha X_f}{(1+\alpha)} \frac{d(\frac{\nu}{D-\mu})}{d[H^+]} = 0 \tag{15.30}$$

$$\frac{d^2(\frac{\nu}{D-\mu})}{d[H^+]^2} = 0 \tag{15.31}$$

This system can be solved to construct branch sets that delineate the do-

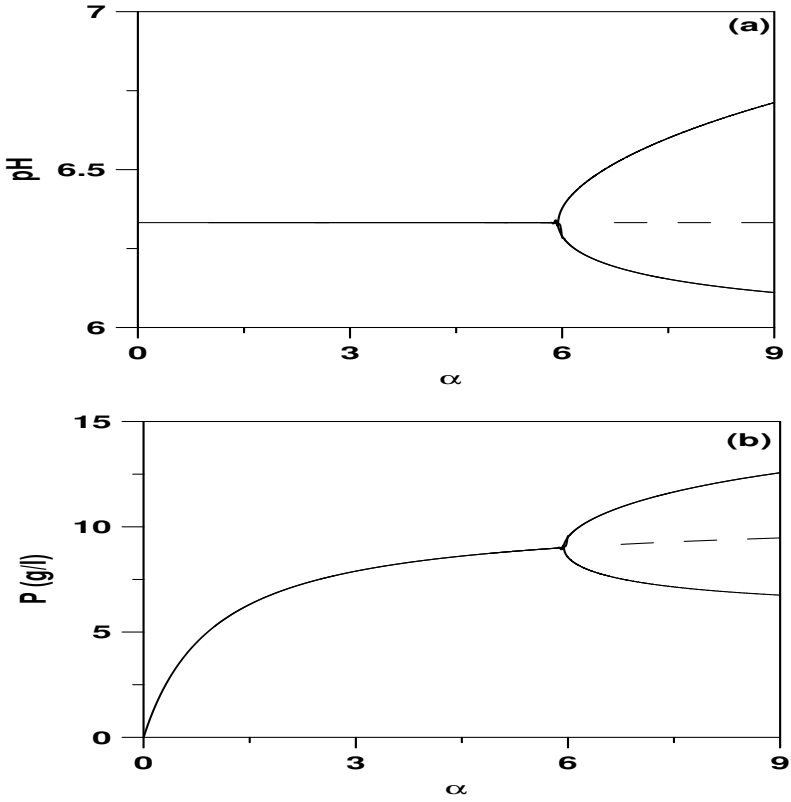

FIGURE 15.2: Continuity diagram showing pitchfork singularity in parameter spaces: (a) (α, pH); (b) (α, P); solid line, stable branch; dashed line, unstable branch.

mains where a pitchfork can occur. But first, we show an example of pitchfork behavior obtained with values of model parameters, shown in Table 15.1, with $X_f = 1.41$ g/l, pH_1=6.33, pH_2=8.49, and D=0.5 h^{-1}. The continuity diagram is shown in Figure 15.2. It can be seen that for values of α smaller than 5.95 a single stable branch is possible, while for larger values, the system is characterized by three branches. The value of occurrence of multiplicity ($\alpha = 5.95$) is rather large, but with possible variations in model kinetic parameters, it is not ruled out that the qualitative behavior of Figure 15.2 can occur within more realistic values of α. However, this investigation is limited to the effects of operating parameters. Next, we study the effect of these parameters on the boundaries of the pitchfork. Figure 15.3a shows the effect of a slight increase in the pH of the feed, from 6.33 to 6.4. It can be seen that the structure of the basic pitchfork has completely changed. This is expected, since as was seen in Figure 3.6, perturbations around the basic pitchfork can lead in some

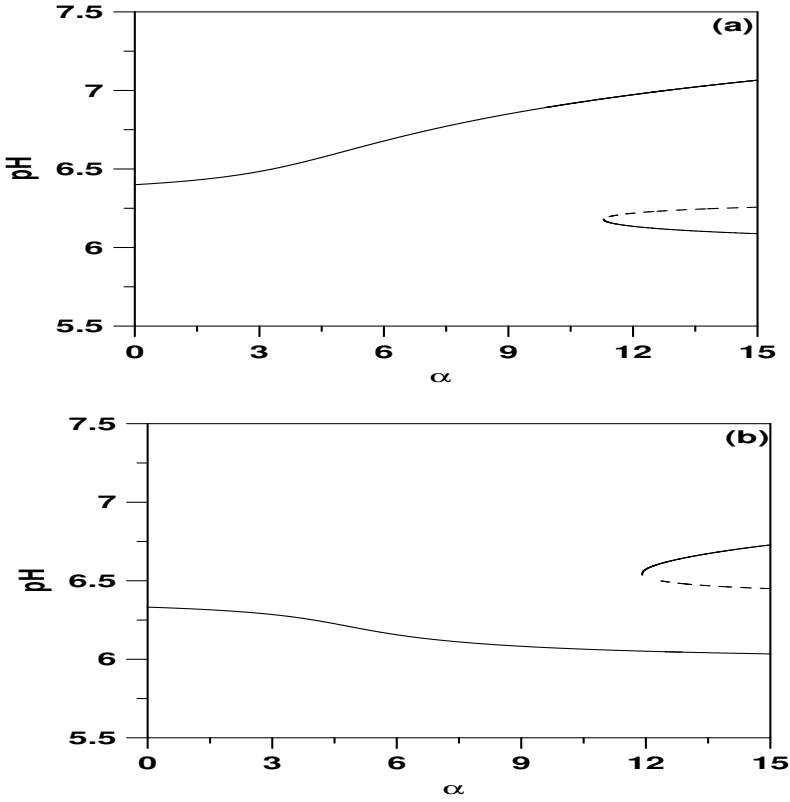

FIGURE 15.3: Continuity diagrams showing the effect on the pitchfork singularity (Figure 15.2) of: (a) an increase in pH of feed; (b) a decrease in pH of seed tank; solid line, stable branch; dashed line, unstable branch.

cases to other multiplicity behaviors. Compared to Figure 15.2a, where the multiplicity is born at $\alpha = 5.95$, it can be seen in Figure 15.3a that an increase in the feed pH increases the range to around $\alpha = 12$. Therefore, an increase in feed pH has a stabilizing effect on the bioreactor. Figure 15.3b shows, on the other hand, the effect of a decrease in the pH of the seed tank. Again, the pitchfork singularity has changed, and the range of multiplicity is pushed to larger values of α. Figure 15.4a shows the effect of an increase in cell feed concentration, from 1.41 to 1.45 (g/l). It can be seen that the increase in X_f also stabilizes the bioreactor. Finally, Figure 15.4b shows the effect of a decrease in the dilution rate, from 0.50 to 0.49 h^{-1}. It can be seen that a decrease in D also has a stabilizing effect on the bioreactor, since the range in terms of α of the stable steady-state uniqueness is increased.

Having examined input multiplicities, we turn our attention to the study of possible output multiplicities. Taking the derivatives $F_{[H^+]}, F_{[H^+][H^+]}$ yields

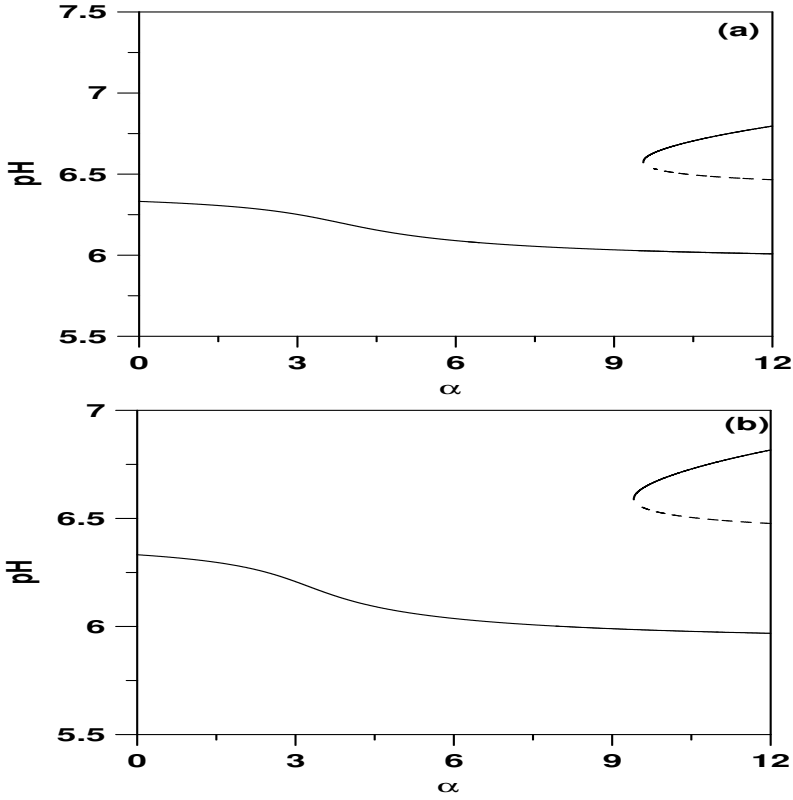

FIGURE 15.4: Continuity diagrams showing the effect on the pitchfork (Figure 15.2) of: (a) an increase in cell feed concentration X_f; (b) decrease in dilution rate D; solid line, stable branch; dashed line, unstable branch.

the following conditions for hysteresis, together with the condition $F = 0$,

$$-1 + \frac{\alpha X_f}{(1+\alpha)} \frac{d(\frac{\nu}{D-\mu})}{d[H^+]} = 0 \tag{15.32}$$

$$\frac{d^2(\frac{\nu}{D-\mu})}{d[H^+]^2} = 0 \tag{15.33}$$

Using the expression of $F_{[H^+]}$ (Equation (15.32)), it can be seen that its does not involve $[H^+]_1$ or $[H^+]_2$. Therefore $F_{[H^+],[H^+]_1} = F_{[H^+][H^+]_2} = 0$, and the hysteresis cannot exist if either $[H^+]_1$ or $[H^+]_2$ is varied. For X_f, we can see that $F_{[H^+]X_f}$ is non-nil except for the particular case of $\alpha = 0$. When, on the other hand, α or D are chosen as input variables then the conditions $F_{\alpha[H^+]}$ and $F_{D[H^+]}$ can be shown to be non-nil except when X_f or $\alpha = 0$. We conclude therefore that the model cannot predict hysteresis except when α or D are varied. Figure 15.5 shows an example of hysteresis behavior as

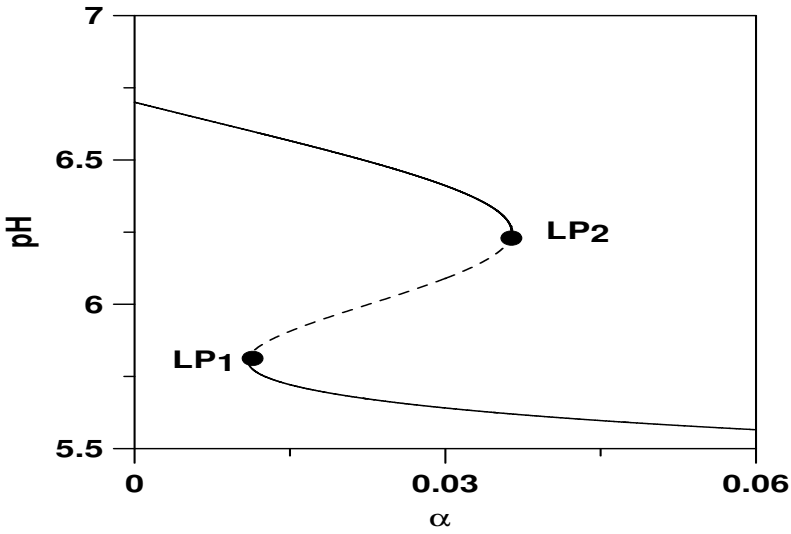

FIGURE 15.5: Continuity diagrams showing hysteresis due to α; solid line, stable branch; dashed line, unstable branch. LP_1 and LP_2, static limit points.

a function of α. The multiplicity in the hysteresis loop exists for values of α extending from 0.011 to 0.037. Hysteresis boundaries are, on the other hand, shown in Figures 15.6(a–c). Hysteresis behavior is confined between the two curves. Figure 15.6a shows that hysteresis exists only for pH_1 values larger than 6.05. Moreover, as the values of pH_1 increase, the hysteresis domain (in terms of α) also increases. Figure 15.6b shows the hysteresis boundary in the (α, X_f) space. Again, the hysteresis is possible only for values of X_f larger than a certain value, i.e., 0.12 g/l. The hysteresis domain is seen to increase with increasing values of X_f. The effect of the dilution rate is, on the other hand, shown in Figure 15.6c. It can be seen that the hysteresis is confined to values of α smaller than 0.052.

Hysteresis can also occur when the dilution rate is selected as the manipulated variable. Figure 15.7 shows an example of hysteresis for model parameters given in Table 15.1. This output multiplicity occurs for dilution rates in the range of 0.33 h^{-1} to 0.36 h^{-1}. Similar branch sets to Figures 15.6(a–c) can be constructed that show the effect of the operating parameters. However, we choose to show this effect directly on the continuity diagrams. Figure 15.8a shows that hysteresis is attenuated with a decrease in pH_1 values. When the value of pH_1 is reduced to 6.0, a stable behavior is found for all values of dilution rates. Similarly, Figure 15.8b shows that a decrease in values of pH_2 also stabilizes the behavior of the bioreactor. Figure 15.9a shows, on the other hand, that an increase in cell feed concentration X_f reduces the multiplicity region. For values of $X_f = 12$ g/l, the hysteresis disappears. Finally, Figure 15.9b shows that an increase in α also attenuates the hysteresis multiplicity.

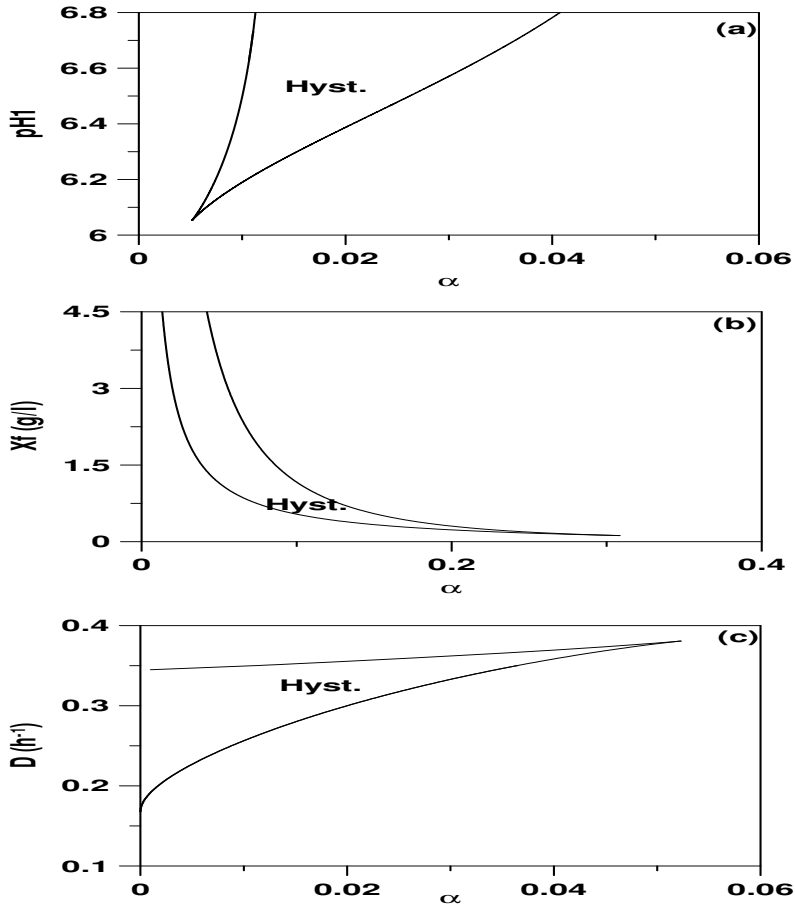

FIGURE 15.6: Diagram showing the domain of hysteresis in parameter spaces: (a) (pH_1, α); (b) (X_f, α); (c) (D, α).

15.3.1 Case of Absence of Additional Seed Tank

The results of the previous section have shown that the case when the bioreactor is not equipped with a seed tank ($\alpha = 0$) is an important case that should be treated separately. For this case, the model steady-state Equations (15.10–15.13) become

$$-DX + \mu([H^+])X = 0 \tag{15.34}$$

$$D(S_f - S) - \sigma([H^+])X = 0 \tag{15.35}$$

$$-DP + \pi([H^+])X = 0 \tag{15.36}$$

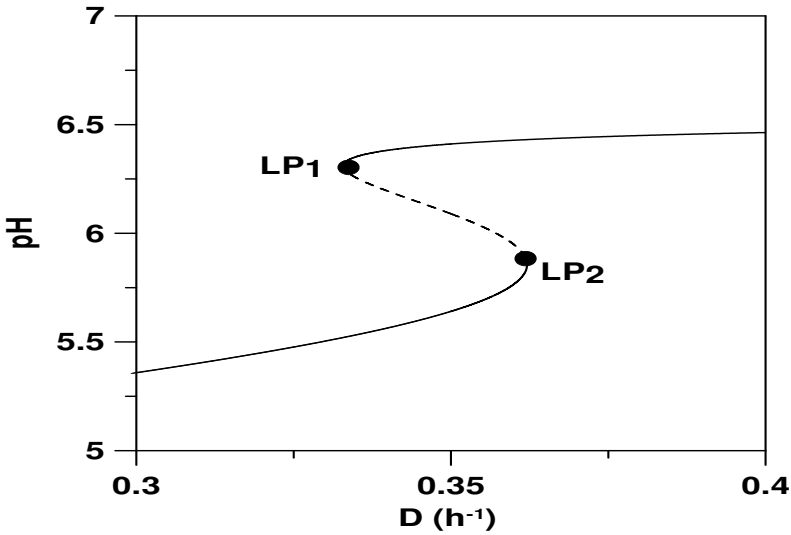

FIGURE 15.7: Continuity diagrams showing hysteresis due to dilution rate D; solid line, stable branch; dashed line, unstable branch; LP_1 and LP_2, static limit points.

$$D([H^+]_1 - [H^+]) + \nu([H^+])X = 0 \tag{15.37}$$

The primary difference is that the model predicts, for the case of $\alpha = 0$, the existence of total washout, $(X = 0, S = S_f, P = 0, H = H_1)$, as a trivial steady-state solution. The additional nontrivial steady state occurs when

$$F := \mu([H^+]) - D = 0 \tag{15.38}$$

Substituting for the expression of $\mu([H^+])$ yields the following equation

$$\frac{D}{K_2}[H^+]^2 + [H^+](D - \mu_0) + DK_1 = 0 \tag{15.39}$$

This equation provides steady-state values of $[H^+]$ as a function of D, while the species concentrations are given by

$$X = \frac{-D([H^+]_1 - [H])}{\nu([H^+])} \tag{15.40}$$

$$S = S_f - \frac{\sigma([H^+])X}{D} \tag{15.41}$$

$$P = \frac{\pi([H^+])X}{D} \tag{15.42}$$

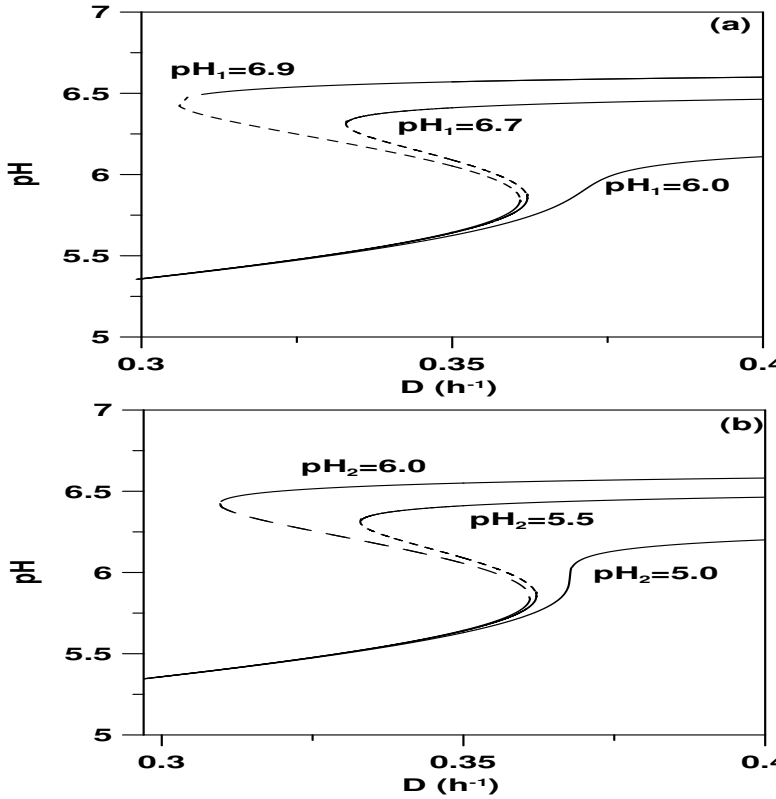

FIGURE 15.8: Continuity diagrams showing the effect on the hysteresis (Figure 15.7) of: (a) changes in pH_1; (b) changes in pH_2; solid line, stable branch; dashed line, unstable branch.

The only operating parameters that may produce multiplicity are $[H^+]_1$ and D. However, it is straightforward to check that the model cannot predict any multiplicity as $[H^+]_1$ is varied. As for the dilution rate, Equation (15.38) predicts a simple saddle-node bifurcation, defined by $F = 0$, $F_{[H^+]} = 0$, and $F_{[H^+][H^+]} \neq 0$. The condition $F_{[H^+]} = 0$ requires, from Equation (15.38), that $\mu'([H^+]) = 0$. This occurs at the limit point (LP) defined by

$$[H^+] = \sqrt{K_1 K_2}, \quad D_{LP} = \frac{\mu_0 \sqrt{K_2}}{2\sqrt{K_1} + \sqrt{K_2}} \tag{15.43}$$

The washout line crosses the nontrivial steady state at the bifurcation point (BR) defined by substituting $[H^+] = [H^+]_1$ in Equation (15.38), to yield

$$D_{BR} = \frac{\mu_0 [H^+]_1}{K_1 + [H^+]_1 + \frac{{[H^+]_1}^2}{K_2}} \tag{15.44}$$

Depending on the relative position of the limit point (LP) (Equation (15.43)) and the bifurcation point (BR), different behaviors in the model are obtained. The condition $D_{BR} = D_{LP}$ represents therefore a boundary for the model. This condition is equivalent to

$$[H^+]_1 = \sqrt{K_1 K_2} \tag{15.45}$$

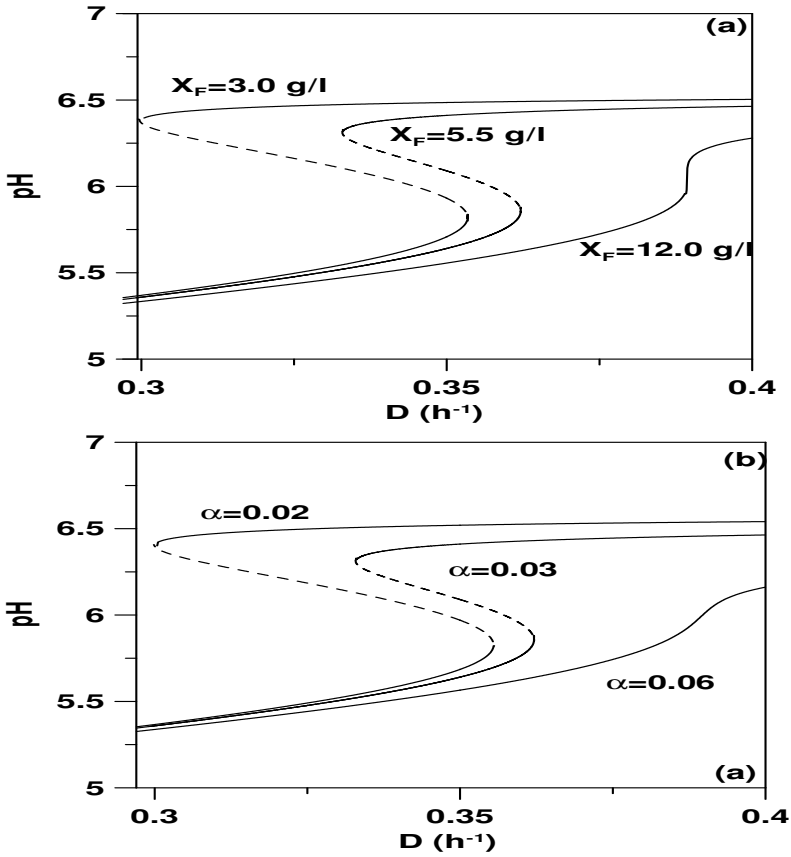

FIGURE 15.9: Continuity diagrams showing the effect on the hysteresis of: (a) changes in X_f; (b) changes in α; solid line, stable branch; dashed line, unstable branch.

For $[H^+]_1 = \sqrt{K_1 K_2}$, the bifurcation diagram, (Figure 15.10a), shows a perfect pitchfork. However, since the meaningful existence of cell (i.e., $X > 0$) requires, from Equation (15.40), that $[H^+] > [H^+]_1$, then the unstable upper branch is physically unrealistic. For dilution rates smaller than D_{LP}, the operation of the bioreactor leads to the nontrivial lower steady state while

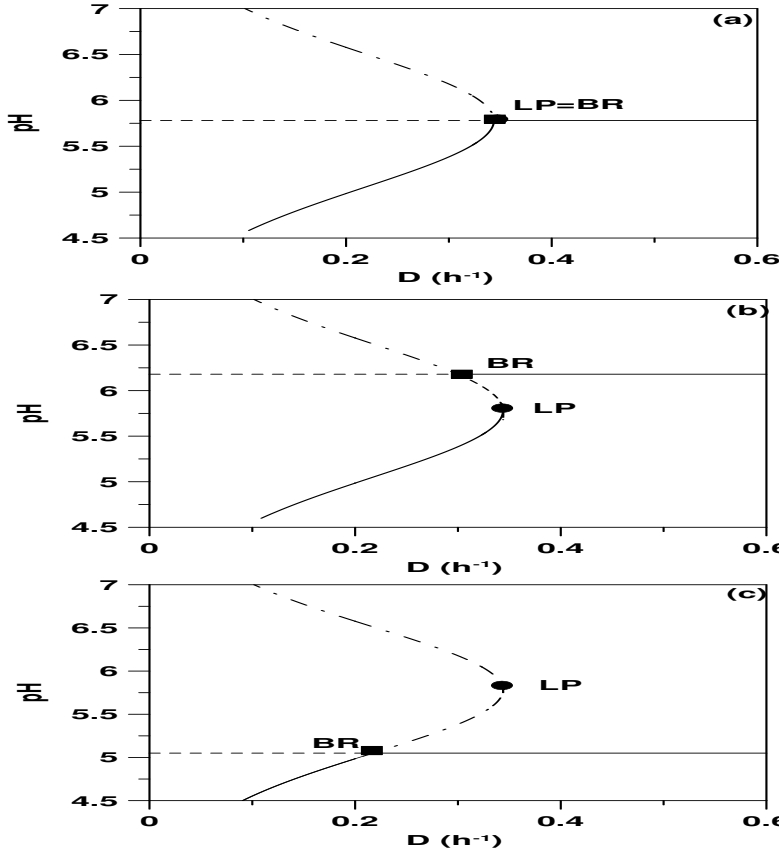

FIGURE 15.10: Continuity diagrams for the case of $\alpha = 0$: (a) $[H^+]_1 = \sqrt{K_1 K_2}$; (b) $[H^+]_1 < \sqrt{K_1 K_2}$; (c) $[H^+]_1 > \sqrt{K_1 K_2}$; solid line, stable branch; dashed line, unstable branch; semidashed line, unstable and physically unrealistic branch; BR, bifurcation point, LP limit point.

for dilution rates larger than D_{LP}, total washout occurs. The case $[H^+]_1 < \sqrt{K_1 K_2}$ is shown in Figure 15.10b. In this case the bifurcation point BR is smaller than the limit point. The upper unstable branch is still physically unrealistic. Between BR and LP points, there is multiplicity in the form of bistability between the lower nontrivial steady state and the total washout. The case of $[H^+]_1 > \sqrt{K_1 K_2}$ is shown in Figure 15.10c. The position of points BR and LP has changed. However, since the whole upper branch is physically unrealistic then this case is similar to the case of a perfect pitchfork (Figure 15.10a).

The final case to be analyzed is when the seed tank is cell-free, (i.e., $\alpha \neq 0$ and $X_f = 0$) and contains only product P_f and hydrogen ion $[H^+]_2$ feeds. The original model Equations (15.11–15.13) are unchanged with the exception of

Equation (15.10) that becomes,

$$-DX + \mu X = 0 \tag{15.46}$$

For this case, the model always has as a steady-state solution, the following "modified" washout solution,

$$X = 0, \quad S = \frac{S_f}{1+\alpha}, \quad P = \frac{\alpha P_f}{1+\alpha}, \quad [H^+] = \frac{[H^+]_1}{1+\alpha} + \frac{\alpha[H^+]_2}{1+\alpha} \tag{15.47}$$

The nontrivial steady-state solution corresponds to

$$\mu = D \tag{15.48}$$

and

$$X = -\frac{D(\frac{[H^+]_1}{1+\alpha} + \frac{\alpha[H^+]_2}{1+\alpha} - [H^+])}{\nu([H^+])} \tag{15.49}$$

The expressions for S and P are identical to Equations (15.16–15.17). Since the equation defining the pH (Equation (15.48)) is the same as in the previous case ($\alpha = 0, X_f \neq 0$), therefore when D is selected as the manipulated variable, the same previously discussed pitchfork behavior of Figures 15.10(a–c) occurs. The only difference is that the pitchfork boundary is defined by

$$\frac{[H^+]_1}{1+\alpha} + \frac{\alpha[H^+]_2}{1+\alpha} = \sqrt{K_1 K_2} \tag{15.50}$$

This equation is reduced to Equation (15.45) when $\alpha = 0$.

15.4 Concluding Remarks

In this chapter, the effects of operating parameters on the steady-state behavior of a bioreactor for cheese prefermentation were analyzed. The singularity theory was used to classify the different multiplicities the model can predict. For the case when the bioreactor is equipped with a seed tank, the analysis has shown that the two important manipulated variables that can lead to input and output multiplicities are the dilution rate and the ratio of seed to lactose feed rates. The analysis also allowed the study of the effect of the other operating parameters, such as hydrogen ion and cell feed concentrations. In this regard, a pitchfork singularity can only occur with variations in the ratio of feeds while hysteresis is possible with variations of any of the two parameters. When pitchfork singularity occurs, the improvement of the stability of the bioreactor can be achieved by a reduction in the dilution rate, an increase

in the feed pH, a decrease in seed tank pH, or an increase in cell feed concentration. When hysteresis occurs, as the ratio of feeds is manipulated, the instability of the bioreactor can be reduced by a decrease in feed pH or a decrease in cell feed concentration. When, on the other hand, hysteresis occurs with variations in the dilution rate, then the stability can be improved through reducing the feed pH, increasing the ratio of feed rates, or increasing the cell feed concentration. The analysis also covered the case when the bioreactor is operated without any seed tank. In this case it was shown that when the dilution rate is chosen as the manipulated variable, the behavior of the bioreactor is reduced to a pitchfork. A simple algebraic equation was derived between the feed pH and the kinetic parameters associated with cell growth rate. The algebraic equation can be used to select values for feed pH that reduces the multiplicity in the bioreactor.

The results of this chapter have provided practical guidelines on the selection of operating parameters that can eliminate difficult operating regions associated with steady-state multiplicity, and that can consequently improve the operability of the bioreactor.

This page intentionally left blank

Chapter 16

BIODEGRADATION OF WASTEWATER

16.1 Introduction

Bioreactors of different configurations are used for the biodegradation of municipal and industrial wastes. These include flow bioreactors with or without recycle, suspended batch reactors (SBR), and plug flow reactors (PFR), among other configurations. Among all types of bioreactors, flow reactors have been used extensively in the treatment of industrial wastewaters. One advantage they offer over other types of bioreactors is that they produce a greater operational stability in response to shock loads. In this chapter, we investigate the performance of a continuous stirred tank bioreactor with the following features: (1) the bioreactor is considered for the case of a gaseous limiting substrate. This situation occurs in aerobic growth subjected to oxygen limitation and accounts for the mass transfer of oxygen; (2) the growth rate is assumed to follow the Contois model [81]. This biomass growth-dependent model is qualitatively different from substrate-dependent growth models studied in previous chapters and also studied by Pinheiro et al. [287]. The Contois growth model was used in a number of biodegradation studies of different food and industrial wastes [55, 60, 125, 161, 171, 190, 260]. The methodology in this chapter consists of the analysis of an unstructured model for the aerated bioreactor. Unlike structured models [147], simpler unstructured models are better suited for rigorous analysis and may provide useful insights in the complex dynamics of the process. The complexity of the real microbial system is accounted for by allowing the kinetic rates in the model to take on a wide but reasonable range. This allows a general analysis of the effect of operating and kinetic parameters [21].

16.2 Bioreactor Model

We consider a continuous bioreactor where the feed conditions consist of feed flow rate Q and substrate concentration S_f. V is the volume of the bioreactor, X and S are, respectively, the cell and substrate concentrations in the output stream, and ϵ is the volumetric fraction of bubbles. The growth rate of the biomass is denoted by r, which depends on substrate S and biomass X, i.e., $r = r(S, X)$. The yield coefficient is denoted by Y and is a function of the substrate, i.e., $Y = Y(S)$. The oxygen transfer from the gas bubbles to cells is assumed to be limited by oxygen transfer through the liquid film surrounding the gas bubbles. The oxygen transfer rate (OTR) from the gas to liquid phase is given by

$$OTR = k_L a(S^\star - S) \tag{16.1}$$

where k_L is the oxygen transfer coefficient, a the gas-liquid interfacial area, and $S^\star$ is the saturation concentration. The mass balances of both biomass and substrate are described by the following equations:

- Biomass mass balance:

$$(1-\epsilon)V\frac{dX}{dt} = -QX + (1-\epsilon)Vr(S,X)X \tag{16.2}$$

- Substrate mass balance:

$$(1-\epsilon)V\frac{dS}{dt} = Q(S_f - S) + k_L aV(S^\star - S) - (1-\epsilon)V\frac{r(s,X)}{Y(S)}X \tag{16.3}$$

These equations are rendered dimensionless using the following variables

$$\bar{S} = \frac{S}{S^\star}, \quad \bar{X} = \frac{X}{Y(S^\star)S^\star}, \quad \bar{r} = \frac{r}{r_{ref}}, \quad \bar{t} = tr_{ref} \tag{16.4}$$

where r_{ref} is a reference quantity for the growth rate r. The dimensionless dilution rate is given by

$$\bar{D} = \frac{D}{r_{ref}} \quad \text{with } D = \frac{Q}{(1-\epsilon)V} \tag{16.5}$$

The model in dimensionless form becomes

$$\frac{d\bar{X}}{d\bar{t}} = -\bar{D}\bar{X} + \bar{r}(\bar{S},\bar{X})\bar{X} \tag{16.6}$$

$$\frac{d\bar{S}}{d\bar{t}} = \bar{D}(\bar{S}_f - \bar{S}) + \delta(1-\bar{S}) - \frac{\bar{r}(\bar{S},\bar{X})}{\bar{Y}(\bar{S})}\bar{X} \tag{16.7}$$

with

$$\delta = \frac{k_L a}{r_{ref}(1-\epsilon)} \text{ and } \bar{Y}(\bar{S}) = \frac{Y(S)}{Y(S^\star)} \tag{16.8}$$

Using the specific case of the Contois growth model,

$$r(S,X) = \frac{\mu_m S}{KX + S} \tag{16.9}$$

and a linear model for the yield coefficient,

$$Y(S) = a + bS \tag{16.10}$$

the dimensionless model is obtained by setting in Equations (16.4–16.5)

$$r_{ref} = \mu_m \text{ and } \bar{K} = KY(S^\star) \tag{16.11}$$

The dimensionless growth rates and the dimensionless yield coefficient are given by

$$\bar{r} = \frac{\bar{S}}{\bar{K}\bar{X} + \bar{S}}, \quad \bar{Y}(\bar{S}) = \frac{1 + \lambda\bar{S}}{1+\lambda} \quad \text{with} \quad \lambda = \frac{bS^\star}{a} \tag{16.12}$$

The dimensionless model (Equations (16.6–16.7)) is therefore,

$$\frac{d\bar{X}}{d\bar{t}} = -\bar{D}\bar{X} + \frac{\bar{S}\bar{X}}{\bar{K}\bar{X} + \bar{S}} \tag{16.13}$$

$$\frac{d\bar{S}}{d\bar{t}} = \bar{D}(\bar{S}_f - \bar{S}) + \delta(1-\bar{S}) - \frac{\bar{S}\bar{X}(1+\lambda)}{(\bar{K}\bar{X} + \bar{S})(1+\lambda\bar{S})} \tag{16.14}$$

It can be seen that the model includes the following operating parameters: S_f, $\bar{D}$, and δ. The parameters λ and $\bar{K}$ are, on the other hand, kinetic parameters. In particular, δ is associated with oxygen rate transfer while λ is associated with the yield coefficient.

16.3 Steady-State Analysis

The analysis of steady-state solutions (Equations (16.13–16.14)) shows that the model has the following steady states:

- Washout solution, i.e., $\bar{X} = 0$. Substituting in Equation (16.14) yields the value of the substrate at the washout condition

$$\bar{S} = \frac{\bar{D}\bar{S}_f + \delta}{\bar{D} + \delta} \tag{16.15}$$

- A nontrivial steady state that can be obtained by solving Equation (16.13) for $\bar{X}$ to yield

$$\bar{X} = \frac{\bar{S}(1-\bar{D})}{\bar{D}\bar{K}} \tag{16.16}$$

Substituting in Equation (16.14) yields the following quadratic equation for $\bar{S}$,

$$a_2\bar{S}^2 + a_1\bar{S} + a_0 = 0 \tag{16.17}$$

with

$$a_2 = -(\bar{D}+\delta)\bar{K}\lambda \tag{16.18}$$

$$a_1 = -1 + \delta\bar{K}(-1+\lambda) - \lambda + \bar{D}(1+\lambda+\bar{K}(-1+\bar{S}_f\lambda)) \tag{16.19}$$

$$a_0 = \bar{K}(\delta + \bar{D}\bar{S}_f) \tag{16.20}$$

The discriminant of the quadratic equation $\Delta = a_1^2 - 4a_2a_0$ is equal to

$$\begin{aligned} \Delta &= (-1+\delta\bar{K}(-1+\lambda) - \lambda + \bar{D}(1+\lambda+\bar{K}(-1+\bar{S}_f\lambda)))^2 \\ &+ 4(\bar{D}+\delta)\bar{K}^2(\delta+\bar{D}\bar{S}_f)\lambda \end{aligned} \tag{16.21}$$

The discriminant is always positive and it can be shown that the equation has only one positive solution.

Next we examine the stability of steady-state solutions. The Jacobian matrix for this model is

$$J = \begin{bmatrix} f_{1S} & f_{1X} \\ f_{2S} & f_{2X} \end{bmatrix} \tag{16.22}$$

where f_1 and f_2 denote the right-hand sides of the mass balances in Equations (16.13–16.14). The eigenvalues λ of the Jacobian matrix are the solutions of the characteristic equation

$$\lambda^2 - \lambda(f_{1S} + f_{2X}) + f_{1S}f_{2X} - f_{1X}f_{2S} = 0 \tag{16.23}$$

Taking the derivatives yields,

$$f_{1\bar{X}} = -\bar{D} + \frac{\bar{S}^2}{(\bar{S}+\bar{K}\bar{X})^2} \tag{16.24}$$

$$f_{1\bar{S}} = \frac{\bar{K}\bar{X}^2}{\bar{S}+\bar{K}\bar{X})^2} \tag{16.25}$$

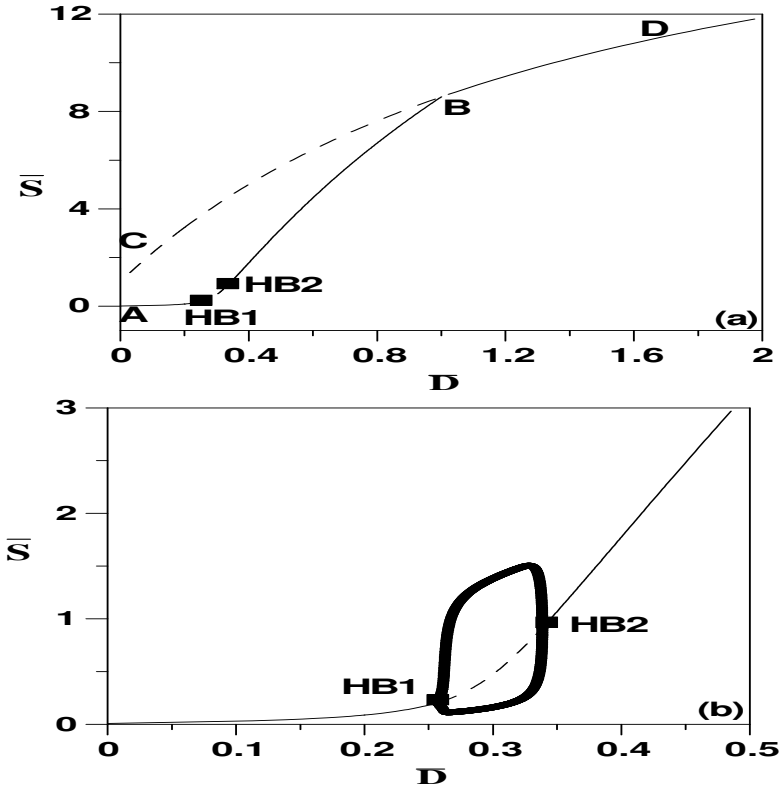

FIGURE 16.1: (a) Diagram showing the behavior of the bioreactor model; (b) Enlargement of (a) showing periodic branches connecting the two Hopf points; solid line, stable branch; dashed line, unstable branch; square, Hopf point; dots, stable periodic branch.

$$f_{2\bar{X}} = -\frac{\bar{S}^2(1+\lambda)}{(\bar{S}+\bar{K}\bar{X})^2(1+\bar{S}\lambda)} \tag{16.26}$$

$$f_{2\bar{S}} = -\bar{D} + \frac{-(\delta(\bar{S}+\bar{K}\bar{X})^2(1+\bar{S}\lambda)^2) + \bar{X}(1+\lambda)(-\bar{K}\bar{X}+\bar{S}^2\lambda)}{(\bar{S}+\bar{K}\bar{X})^2(1+\bar{S}\lambda)^2} \tag{16.27}$$

For the washout solution ($\bar{X} = 0$), substituting in Equations (16.24–16.27) yields the eigenvalues,

$$\lambda_1 = 1 - \bar{D}, \quad \lambda_2 = -\bar{D} - \delta \tag{16.28}$$

The washout solution is therefore stable provided that $\bar{D} > 1$. The value $\bar{D}_w = 1$ represents the dilution rate at which the washout solution crosses the nontrivial steady-state solution.

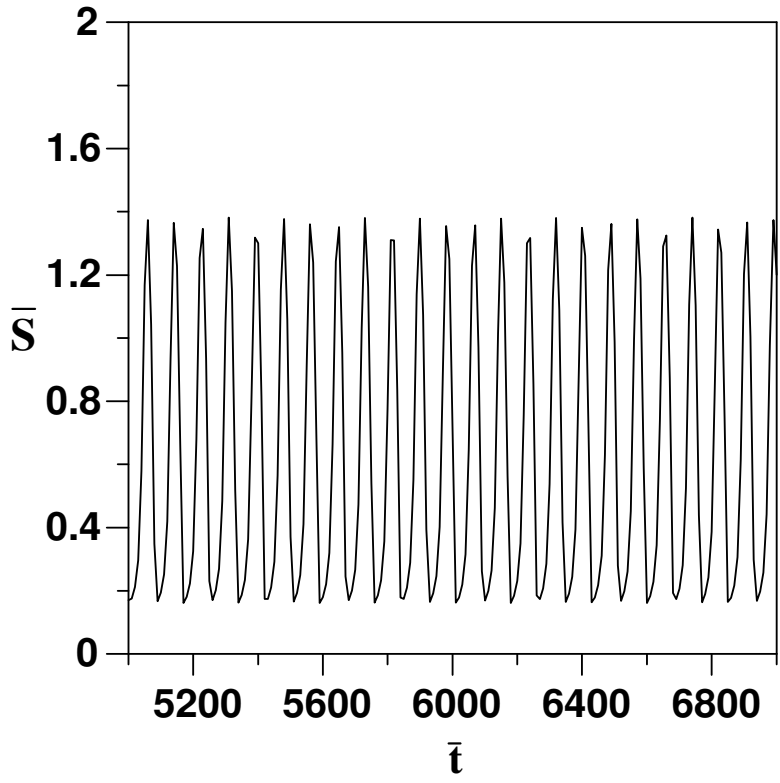

FIGURE 16.2: Examples of oscillations in Figure 16.1, for $\bar{D} = 0.3$.

16.4 Dynamic Behavior of the Model

It was seen from the last section that, besides the washout solution, the model can predict only one nontrivial steady-state solution. However, this does not exclude the existence of periodic solutions predicted by the model. The conditions for Hopf points are

$$f_{1S} + f_{2X} = 0 \tag{16.29}$$

$$f_{1\bar{S}} f_{2\bar{X}} - f_{1\bar{X}} f_{2\bar{S}} > 0 \tag{16.30}$$

These conditions are not easily amenable to analytical manipulations. Therefore, by recasting the expression of the gradients (Equations (16.24–16.27)), the conditions for Hopf points are solving numerically.

Before numerical simulations are shown, it is worth to carry out at this point a comparison between the dynamics of the bioreactor with the biomass

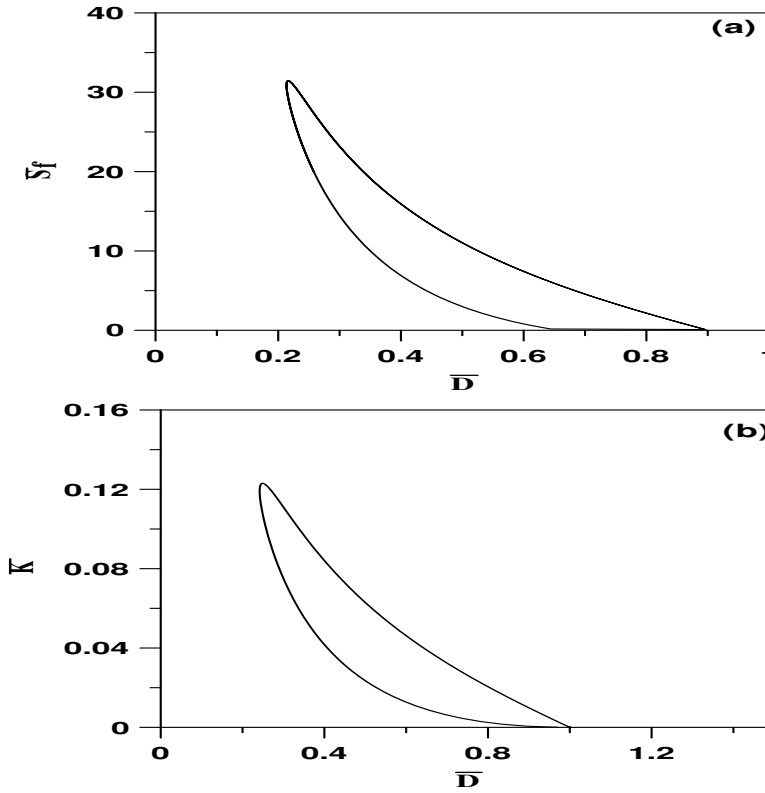

FIGURE 16.3: Diagrams showing the domain of Hopf points in parameter spaces: (a) $(\bar{D}, \bar{S}_f)$; (b) $(\bar{D}, \bar{K})$.

dependent growth rate against the case when the growth rate depends solely on substrate [287, 305]. A similar model to Equations (16.6–16.7) can be written for the case when the growth rate depends solely on the substrate (i.e., $\bar{r} = \bar{r}(\bar{S})$):

$$\frac{d\bar{X}}{d\bar{t}} = -\bar{D}\bar{X} + \bar{r}(\bar{S})\bar{X} \tag{16.31}$$

$$\frac{d\bar{S}}{d\bar{t}} = \bar{D}(\bar{S}_f - \bar{S}) + \delta(1 - \bar{S}) - \frac{\bar{r}(\bar{S})}{\bar{Y}(\bar{S})}\bar{X} \tag{16.32}$$

The washout solution ($\bar{X} = 0$) yields the same value for the substrate as Equation (16.15)

$$\bar{S}_w = \frac{\bar{D}\bar{S}_f + \delta}{\bar{D} + \delta} \tag{16.33}$$

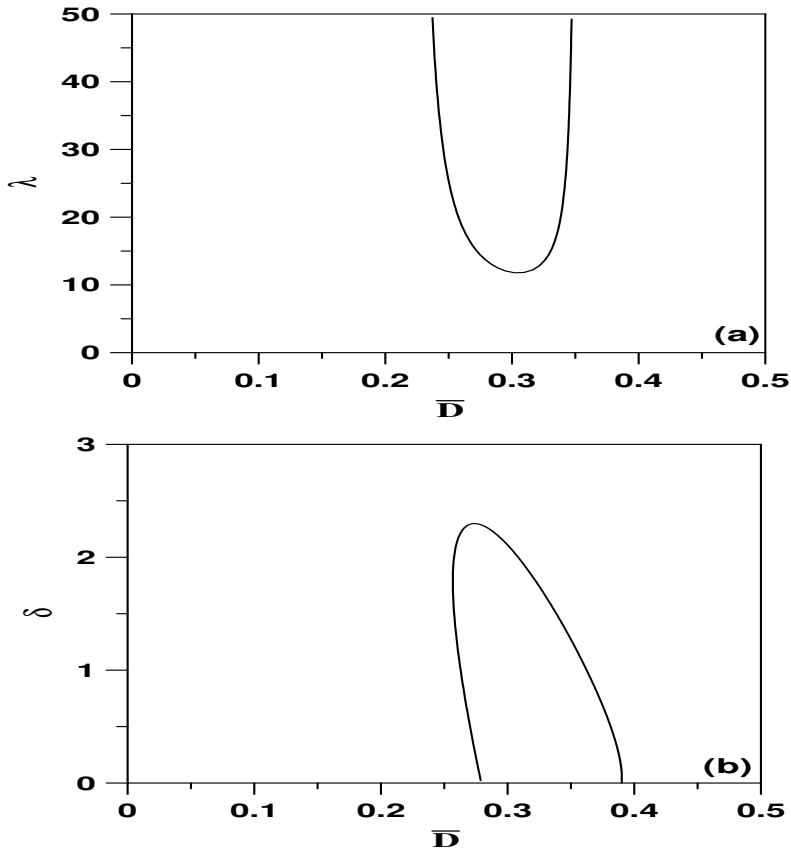

FIGURE 16.4: Diagrams showing the domain of Hopf points in parameter spaces: (a) $(\bar{D}, \bar{\lambda})$; (b) $(\bar{D}, \bar{\delta})$.

Substituting in Equation (16.31) yields the critical value of the dilution rate at which the washout solution crosses the nontrivial steady state,

$$\bar{D}_w = \bar{r}(\bar{S} = \bar{S}_w) \tag{16.34}$$

The interesting remark to be made is that for the Contois growth model, the critical value of the dilution rate $\bar{D}_w$ is constant (= 1) and especially, it does not depend on the feed concentration. This is not the case for Equation (16.34) when the growth rate depends on the substrate. Therefore, with the Contois growth model, it is possible to feed the bioreactor with wastewater containing dilute concentrations. For the case when the growth rate depends solely on the substrate, washout may occur if the substrate feed concentration is low [260].

An other aspect of comparison concerns the occurrence of Hopf points on both models, for the important case of constant yield coefficient, i.e., $\bar{Y} =$

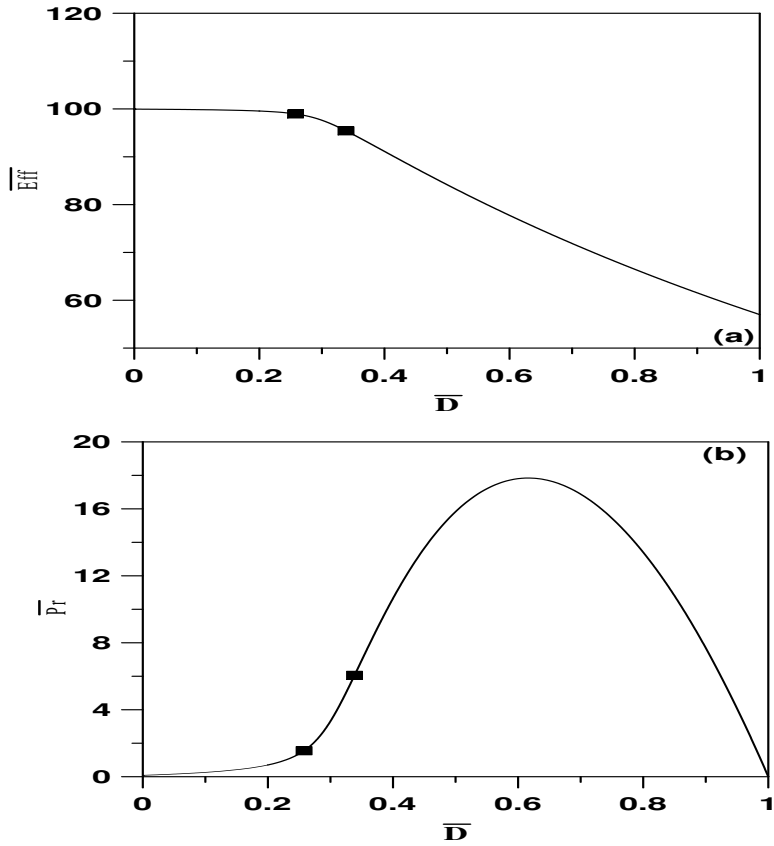

FIGURE 16.5: Performance of the bioreactor: (a) Efficiency; (b) productivity; square, Hopf point.

1 in Equation (16.3). The Hopf conditions of Equations (16.29, 16.30) are equivalent under these conditions to the following simpler forms:

$$f_{1\bar{S}} + f_{2\bar{X}} = -\bar{r} + \bar{r}_{\bar{S}}\bar{X} - \bar{r}_{\bar{X}}\bar{X} = 0 \quad (16.35)$$

$$f_{1\bar{S}} f_{2\bar{X}} - f_{1\bar{X}} f_{2\bar{S}} = -\bar{r}(\bar{r}_{\bar{S}}\bar{X} - \bar{r}_{\bar{X}}\bar{X}) + \delta\bar{r}_{\bar{X}}\bar{X} > 0 \quad (16.36)$$

The following simpler relation can be obtained between the two equations,

$$f_{1\bar{S}} f_{2\bar{X}} - f_{1\bar{X}} f_{2\bar{S}} = -\bar{r}(f_{1\bar{S}} + f_{2\bar{X}} + \bar{r}) + \delta\bar{r}_{\bar{X}}\bar{X} \quad (16.37)$$

Substituting for the first Hopf condition (Equation (16.35)) in Equation (16.37) yields,

$$f_{1\bar{S}} f_{2\bar{X}} - f_{1\bar{X}} f_{2\bar{S}} = -\bar{r}^2 + \delta\bar{r}_{\bar{X}}\bar{X} > 0 \quad (16.38)$$

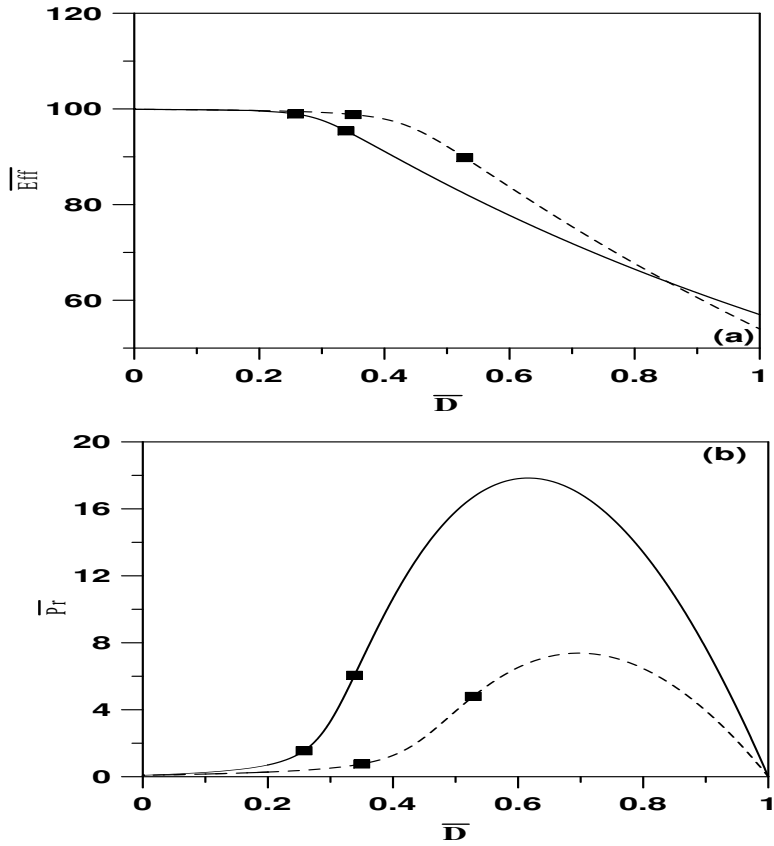

FIGURE 16.6: Effect of $\bar{S}_f$ on the performance of the bioreactor: (a) Efficiency; (b) productivity; solid line, $\bar{S}_f = 20$; dashed line, $\bar{S}_f = 10$; square, Hopf point.

This condition requires therefore that

$$\delta \bar{r}_{\bar{X}} \bar{X} > \bar{r}^2 \tag{16.39}$$

It can be seen from this condition that if $\bar{r}_{\bar{X}}$ is negative then the condition of Equation (16.39) is never satisfied for any growth rate, and the model can not predict Hopf points. This is particularly the case for the Contois growth model where $\bar{r}_{\bar{X}}$ is negative for all values of $\bar{X}$. This is also true when the rate depends only on the substrate, i.e., $\bar{r}_{\bar{X}} = 0$. These results show that even with oxygen limitation, the existence of periodic behavior for the two dimensional model is conditioned mainly by the variability of the yield coefficient. When this coefficient is constant, the model can not predict periodic solutions for any growth rate that depends solely on the substrate. The same results hold when the specific growth rate is inhibited by the biomass. These results join

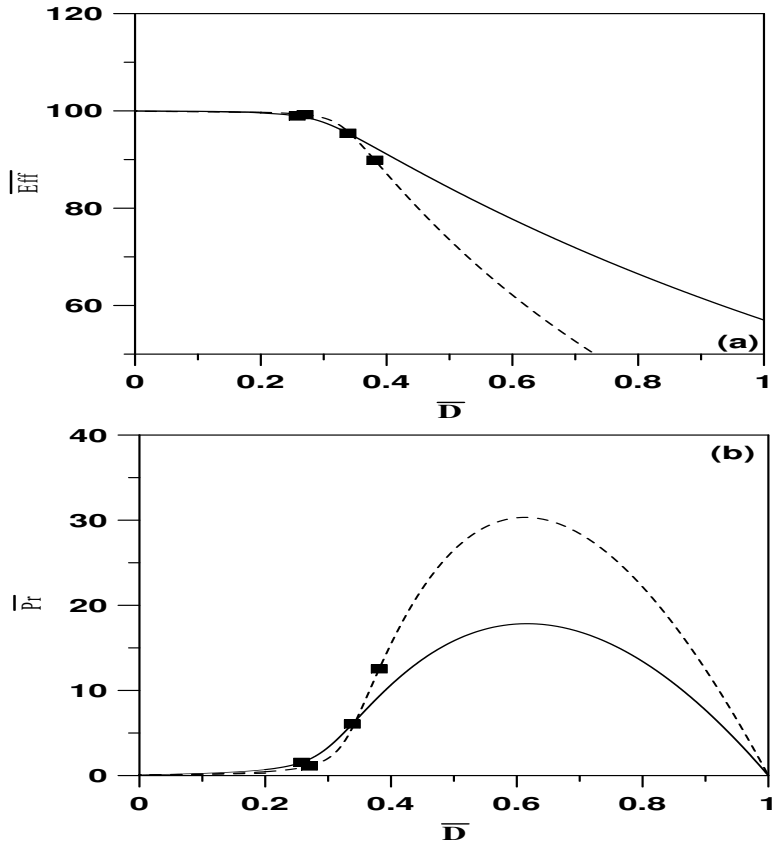

FIGURE 16.7: Effect of δ on the performance of the bioreactor: (a) Efficiency; (b) productivity; solid line, $\delta = 1.5$; dashed line, $\delta = 0.5$; square, Hopf point.

the ones found in Chapter 4 where it was shown that neither the presence of a maintenance term nor the assumption of spatial inhomogeneity due to wall attachment of microorganisms can produce an oscillatory behavior. It seems therefore that the variability of the yield coefficient with substrate is a necessary requirement for the two dimensional model to produce a dynamic bifurcation.

In the following section, we provide explicit examples of the results that were derived in the previous section using the following nominal values $\bar{S}_f = 20, \delta = 1.5, \bar{K} = 0.1, \lambda = 20$. We start with showing the steady-state behavior. Figure 16.a shows the continuity diagram. The curve (AB) in the figure corresponds to the nontrivial steady state while the curve (CD) corresponds to the washout solution ($\bar{X} = 0$). The two curves cross at $\bar{D} = 1$. In addition to these two branches, the appearance of a region of instability between the

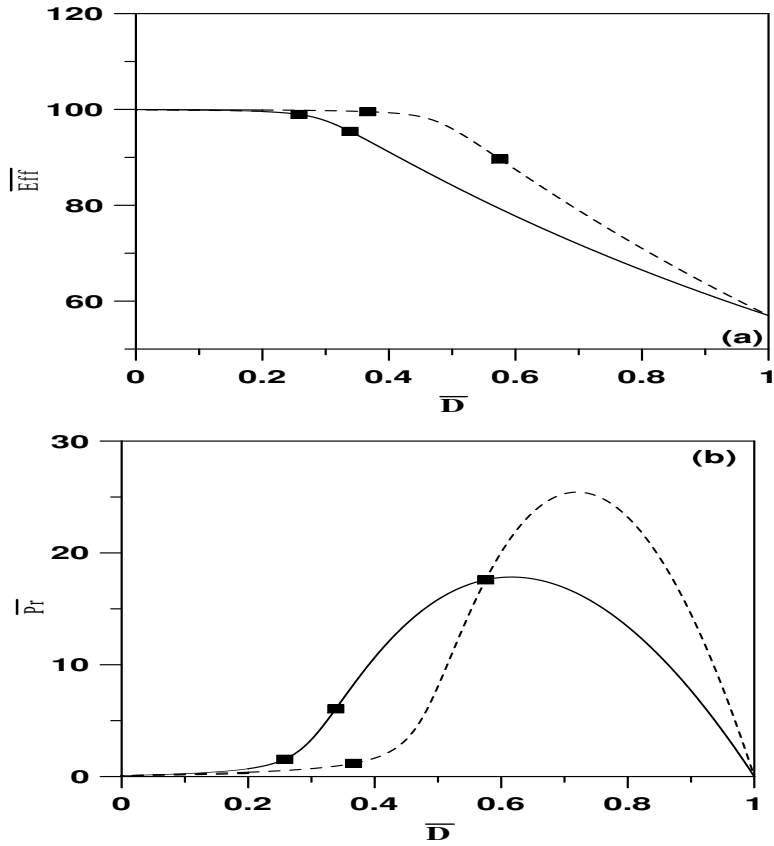

FIGURE 16.8: Effect of $\bar{K}$ on the performance of the bioreactor. (a) Efficiency; (b) productivity; solid line, $\bar{K} = 0.1$; dashed line, $\bar{K} = 0.05$; square, Hopf point.

two Hopf points (HB_1 and HB_2) can also be seen. Figure 16.1b shows periodic branches connecting the two HB points. For dilution rates smaller than HB_1 ($\bar{D} < \bar{D} = 0.258$), the process settles on the lower nontrivial steady state. For dilution rates between the two Hopf points ($0.258 < \bar{D} < 0.338$), the process settles on stable periodic oscillations, regardless of start-up conditions. An example of the oscillatory behavior is shown in Figure 16.2 for $\bar{D} = 0.3$. For dilution rates larger than HB_2 ($\bar{D} > 0.384$) and up to point (B) ($\bar{D} = 1$), the process settles on the nontrivial steady state, while for dilution rates larger than ($\bar{D} = 1$), washout occurs.

At this point, it is useful to show the effect of the different operating and kinetic parameters on the existence of periodic behavior in the model. Figure 16.3a shows the effect of the substrate feed concentration. The loop shows the loci of the two Hopf points HB_1 and HB_2. So it can be seen that for

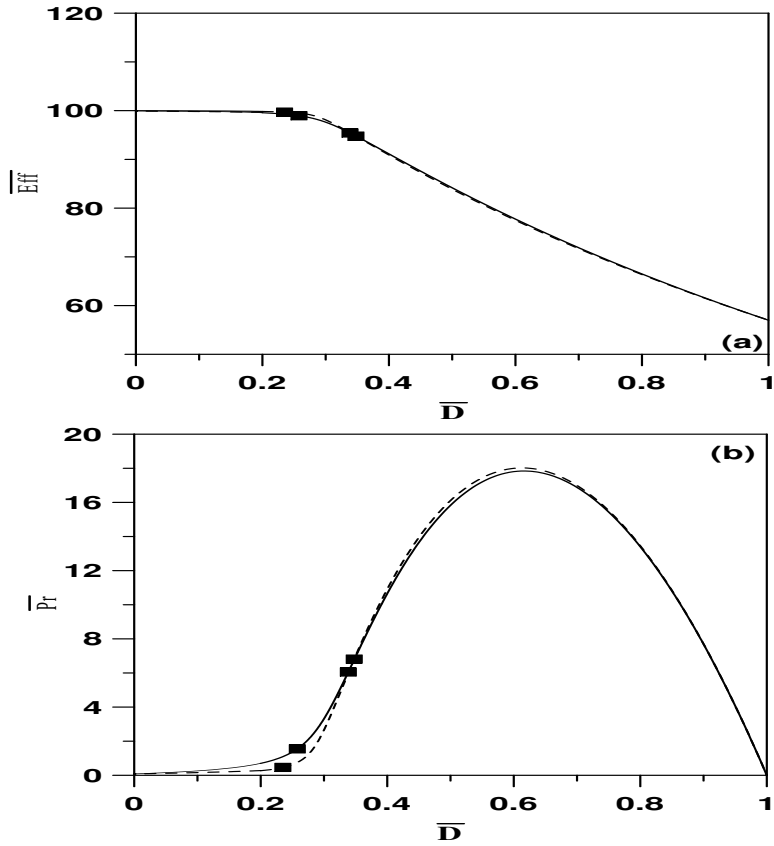

FIGURE 16.9: Effect of λ on the performance of the bioreactor: (a) Efficiency; (b) productivity; solid line, $\lambda = 20$; dashed line, $\lambda = 60$; square, Hopf point.

each value of feed concentration below the value of $\bar{S}_f = 32$ (the cusp), the model exhibits two Hopf points. Keeping in mind that the critical dilution rate for washout conditions is $\bar{D} = 1$, it can be seen that the values at which the points (HB_1, HB_2) occur are below the washout point and are therefore meaningful. For values of $\bar{S}_f$ larger than the cusp, the model does not exhibit any periodic solutions and the behavior is similar to Figure 16.1a but without the occurrence of regions of oscillations.

Figure 16.3b shows the effect of the kinetic constant ($\bar{K}$). Again, for values of $\bar{K}$ smaller than the cusp ($\bar{K} < 0.13$), two Hopf points (HB_1 & HB_2) are expected in the diagram. The effect of λ is shown in Figure 16.4a. It can be recalled that λ (Equation (16.12)) incorporates both the yield coefficient and the saturation concentration. Small values of λ are associated with weak dependence of the yield on the substrate. It can be seen from Figure 16.4a,

that the two Hopf points are expected only for values of λ larger than a certain critical value ($\lambda > 13$). This also shows that for the case of constant yield coefficient ($\lambda = 0$), the model cannot predict oscillatory behavior.

As for the effect of δ, it is shown in Figure 16.4b. The dimensionless variable δ essentially incorporates the effect of oxygen transfer. It can be seen that a periodic behavior is possible for all values of δ smaller than the cusp ($\delta < 2.4$). It can also be concluded that even with the absence of oxygen limitations (very small values of δ), the model can exhibit a periodic behavior.

16.5 Performance Analysis

Having investigated in some detail the different static and dynamic behaviors of the bioreactor, we turn our attention in this section to investigate the performance of the unit. The performance of the bioreactor can be expressed in a number of ways, depending on the goal of the biodegradation. We present in the following the definition of two of these performance criteria. Let (S) denotes the exit substrate concentration (i.e., the solution of the quadratic Equation (16.17)),

- The process efficiency is defined by

$$E_{ff} = 100(1 - \frac{S}{S_f}) \tag{16.40}$$

- The reactor productivity is defined by

$$P_r = QX \tag{16.41}$$

In the dimensionless form, the efficiency and the productivity are defined by

$$\bar{E}_{ff} = 100(1 - \frac{\bar{S}}{\bar{S}_f}) \tag{16.42}$$

and

$$\bar{P}_r = \bar{D}\bar{X} \tag{16.43}$$

It should be noted that explicit expressions for the efficiency and productivity can be obtained by directly substituting the solution $\bar{S}$ of Equation (16.17) into Equations (16.42–16.43). Figures 16.5(a–b) show an example of variations of the efficiency and the productivity with the dilution rate. Figure 16.5a shows that the productivity is relatively constant for small dilution rates ($\bar{D} < 0.25$), and then decreases continuously. The two square points

represent the two Hopf points HB_1 and HB_2. Between these two points the static branch is unstable and stable periodic branches exist. So the efficiency or the productivity between these two points should be calculated as the time average of the periodic oscillations. The productivity, on the other hand, exhibits an interesting behavior in Figure 16.5b. It reaches a maximum around the dilution rate of $\bar{D} = 0.6$ before decreasing. As mentioned in a number of studies [256–257], the average efficiency or productivity within the periodic regimes are never larger than that of the static branch. The operation of the bioreactor between these points should be therefore avoided.

Next, the effect of the different operating and kinetic parameters on the efficiency and the productivity are examined. Figures 16.6(a–b) show the effect of decreasing the feed concentration $\bar{S}_f$ from 20 to 10. It can be seen that for small dilution rates ($\bar{D} < 0.3$) the efficiency is unchanged. It is larger between dilution rates 0.3 and 0.8 and then decreases slightly. As to the productivity, a clear effect can be seen in Figure 16.6b, since the productivity for $\bar{S}_f = 10$ is much smaller. Moreover, the maximum value is reached at a larger dilution rate. Taking into consideration the solution of Equation (16.17), we can explicitly obtain the asymptotic values of the efficiency and productivity as the feed concentration takes on large values:

$$\bar{E}_{ff}(\bar{S}_f \to \infty) = 100(1 - \frac{\bar{D}}{(\bar{D} + \delta)\bar{S}_f}) \tag{16.44}$$

and

$$\bar{P}_r(\bar{S}_f \to \infty) = \frac{\bar{D}(1 - \bar{D})}{(\bar{D} + \delta)\bar{K}} \tag{16.45}$$

This asymptotic expression (Equation (16.45)) can yield explicit relations for the dilution rate $\bar{D}_{max}$ at which the maximum productivity $\bar{P}_{rmax}$ is obtained.

$$\bar{D}_{max} = -\delta + (\delta + \delta^2)^{\frac{1}{2}} \tag{16.46}$$

$$\bar{P}_{rmax} = \frac{1}{\bar{K} + 2\delta\bar{K} + 2\bar{K}(\delta + \delta^2)^{\frac{1}{2}}} \tag{16.47}$$

Figures 16.7(a–b) show, on the other hand, the effect of δ on the performance. It can be recalled that δ is associated with oxygen mass transfer. It can be seen that a decrease in δ from 1.5 to 0.5, substantially deteriorates the efficiency when the dilution rate is larger than 0.4. As to the productivity, the decrease in δ increases it, but the dilution rate at which the productivity reaches a maximum is practically unchanged. The asymptotic values of the performances are:

$$\bar{E}_{ff}(\delta \to \infty) = 100\% \tag{16.48}$$

and

$$\bar{P}_r(\delta \to \infty) = \frac{1-\bar{D}}{\bar{K}} \tag{16.49}$$

Figures 16.8(a–b) show the effect of the kinetic constant $\bar{K}$. It can be seen that a decrease of $\bar{K}$ from 0.1 to 0.05 has a large effect on the efficiency, which increases at larger dilution rates. The decrease in $\bar{K}$ also increases the productivity at larger dilution rates. Following the same analysis for $\bar{S}_f$ and δ, we can obtain the asymptotic values for efficiency and productivity,

$$\bar{E}_{ff}(\bar{K} \to \infty) = 100\frac{\delta(-1+\bar{S}_f)}{(\bar{D}+\delta)\bar{S}_f} \tag{16.50}$$

and

$$\bar{P}_r(\bar{K} \to \infty) = \frac{(1-\bar{D})(\delta+\bar{D}\bar{S}_f)}{(\bar{D}+\delta)\bar{S}_f} \tag{16.51}$$

The effect of λ is shown in Figures 16.9(a–b). It can be recalled that λ is associated with the yield coefficient. The value of λ was increased from $\lambda = 20$ to $\lambda = 60$. It can be seen that the effect of λ on both the efficiency and the productivity is negligible. The asymptotic values of the efficiency and the productivity for large values of λ are:

$$\bar{E}_{ff}(\lambda \to \infty) = 100\frac{(1-\bar{D})+\delta\bar{K}(-1+\bar{S}_f)}{(\bar{D}+\delta)\bar{K}\bar{S}_f} \tag{16.52}$$

and

$$\bar{P}_r(\lambda \to \infty) = \frac{(1-\bar{D})(-1+\bar{D}+\delta\bar{K}+\bar{D}\bar{K}\bar{S}_f)}{(\bar{D}+\delta)\bar{K}^2} \tag{16.53}$$

Finally, it should be noted that similar expressions to Equations (16.46–16.47) can be readily derived for the other cases.

16.6 Concluding Remarks

This chapter investigated the static and dynamic behavior of a continuous flow bioreactor for the aerobic biodegradation of municipal and industrial wastes. The unstructured kinetic model for the bioreactor accounted for oxygen limitation. The growth rate was assumed to follow the Contois model while the yield coefficient was assumed to depend linearly on the substrate. The analysis showed the ability of the model to predict oscillations for some range of kinetic and operating parameters. The analysis of the loci of periodic points allowed

the determination of the effects of substrate feed concentration and oxygen mass transfer on the existence of dynamic bifurcation. It was also found that the more dependent the yield on the substrate is, the larger is the range of dilution rates for which oscillations are expected. The analysis of the performance of the bioreactor was carried out by plotting both the process efficiency and productivity. It was found that the efficiency has a decreasing trend with the dilution rate while the productivity reaches a maximum. The effect of the different model parameters on the performance was studied. Because of the relative simplicity of the model, the analysis allowed the derivation of explicit analytic expressions for both the efficiency and the productivity. Thus, a decrease in the feed concentration was found to increase the efficiency for a relatively wide range of dilution rates, but it has the effect of decreasing the productivity. Decreasing the oxygen transfer was found to decrease the efficiency at larger dilution rates while the productivity is increased over a wide range of dilution rates. The increase in the dependence of the yield coefficient on the substrate was found not have much effect on the performance of the bioreactor. The results in this chapter, therefore, yielded information about the behavior of the bioreactor that may help in the definition of its working operational conditions and in the development of control and optimization policies.

This page intentionally left blank

Chapter 17

DYNAMICS OF ACTIVATED SLUDGE REACTORS

17.1 Introduction

The heterogeneity and the complexity of activated sludge processes pose a continuous challenge to developing models that can incorporate all the necessary levels of information concerning the process, and be accurate enough for the adequate control and safe operation of the bioreactor. The complete quantification of the microbial system requires the understanding of the complex biological and physico-chemical interactions in the process, and the measurement of a large number of reaction rates, which is often beyond the scope of reasonable measurement techniques. This task is particularly complicated when dynamic modeling is sought. Simple and unstructured steady-state models are generally sufficient for the purpose of plant design. However, these models are generally inadequate for dynamic analysis. Because of the generally low levels of substrate in the chemostat, a transient experiment, such as change in flow rate, can result in drastic changes in the cell environment, and the unstructured model may break down [110, 264]. Moreover, as was shown in Chapter 4, the basic unstructured model fails to predict periodic behavior for any growth rates.

Structured models, on the other hand, with different degrees of complexity can supplement the inadequacies of unstructured models. Structured models take into account the inevitable changes in cell population composition, since the model microbial kinetics are constructed on the basis of at least some of the knowledge accumulated in the vast repository of fundamental biochemistry and microbiology. Structured models, however, may sometimes suffer from over detailed information that cannot be verified, making them inappropriate for practical use. A good structured model should have a reasonable number of parameters to provide it with some levels of flexibility [141, 164, 316].

In this chapter, the dynamic characteristics of a flexible model of activated sludge process with solids recycle are studied. The proposed model, also studied by Ajbar and Ibrahim [27], is a simplified version of a structured model used by Andrews [35], and Busby and Andrews [68] for the dynamic simulation and control of activated sludge processes. The model is structured upon substrate and intermediate component growth-depending processes. The model

kinetics are based, on the other hand, on substrate and intermediate product inhibitory effects.

17.2 Process Model

The proposed model

$$\text{Substrate (S)} \rightarrow \text{ Particulate product } (X_s) \rightarrow \text{ Biomass } (X_a)$$

is structured upon two processes: (1) the formation of an intermediate particulate product (X_s) depending on the substrate; and (2) an active biomass (X_a) synthesis. The model is a simplified version of the original Andrew's model [35, 68] for the activated sludge process where the decay rate is assumed negligible. This assumption is acceptable when operating at low cell residence time.

The substrate S is converted to a slowly biodegradable particulate product following a substrate-inhibition growth rate

$$\mu_1 = \frac{\mu_m S}{(S + K_s + \alpha S^2)} \tag{17.1}$$

Substrate-inhibition models are fundamental in predicting stability characteristics of activated sludge reactors such as the occurrence of hysteresis [128, 305].

TABLE 17.1: Values of Model Parameters

Parameter	Value	Reference
K_i (mg/l)	10	[86]
K_s (mg/l)	10	[148]
K_x (mg/l)	700	[92]
S_f (mg/l)	500	
W	0.1	
X_{af} (mg/l)	80	
X_{sf} (mg/l)	20	
$Y_{x/s}$	0.50	[148]
α (l/mg)	0.02	[86]
$\bar{\mu}_m$ (hr^{-1})	3.0	[148]

Besides the direct inhibitory effects due to the substrate, a delayed inhibitory effect caused by the intermediate product is also assumed. The growth

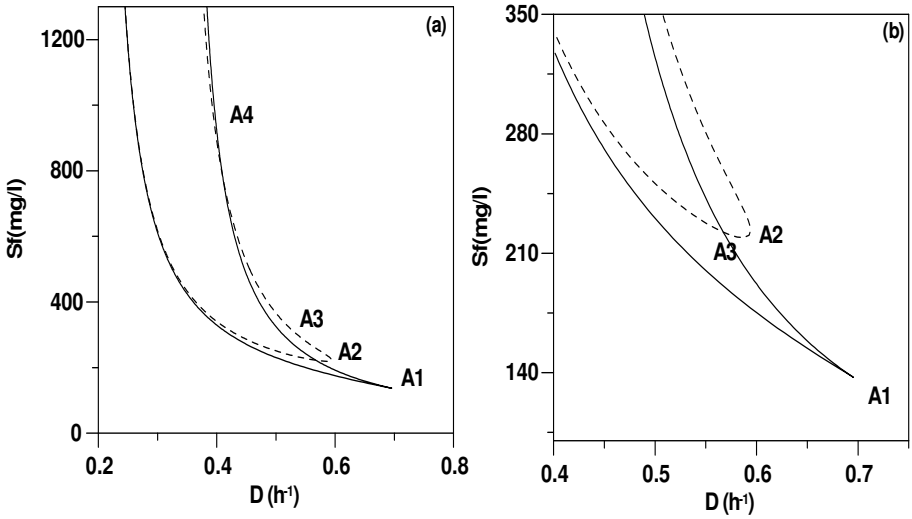

FIGURE 17.1: (a) Two-parameter continuation diagram showing the loci of the static limit points (SLP) and the Hopf (HB) points; (b) Enlargement of (a) showing the details of the intersection of the SLP and HB curves; solid line, static limit point; dashed line, Hopf point.

of the intermediate product is assumed to affect the maximum growth rate μ_m negatively

$$\mu_m = \frac{\bar{\mu}_m K_i}{K_i + X_s} \tag{17.2}$$

where K_i is the inhibition constant. The biomass growth rate, on the other hand, depends on the intermediate product following the common Monod model

$$\mu_2 = \frac{\mu_m X_s}{K_x + X_s} \tag{17.3}$$

where μ_2 is the specific growth rate and K_x is the saturation constant for biomass synthesis. The intermediate product inhibition affects therefore both the substrate uptake rate and the biomass growth rate through the term μ_m. This is in agreement with observations made in [302] on the influence of particulate intermediate products on the performances of microbial cultures.

Equations (17.1-17.3) form the model kinetics. In the following section, the unsteady-state balance equations around a reactor settler, similar to Figure 4.1, are written for the different species.

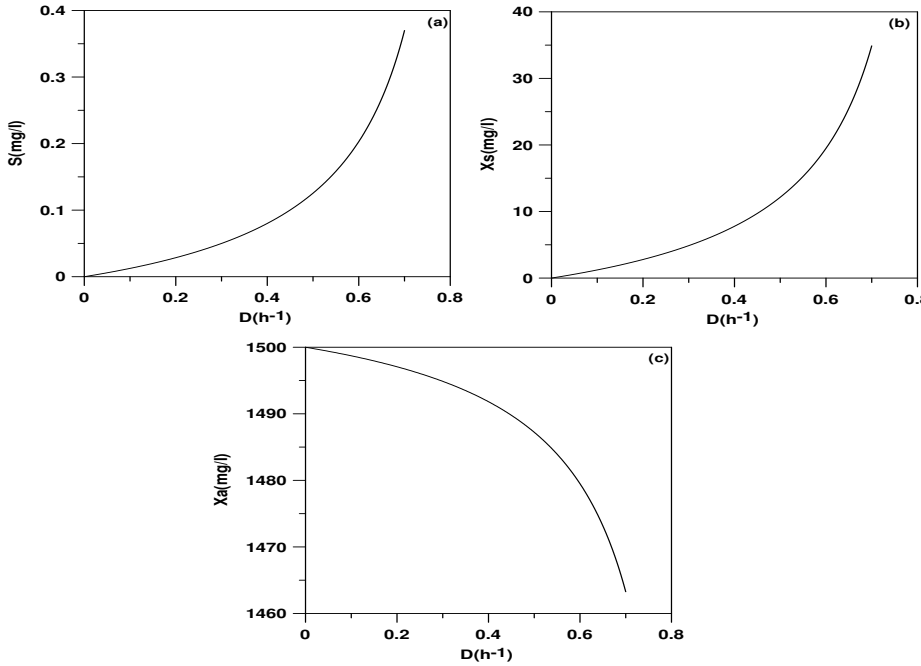

FIGURE 17.2: (a)–(c) Continuity diagrams for feed conditions $S_f = 100\frac{mg}{l}$. The system exhibits the classical Monod behavior.

Substrate S

The substrate is consumed to produce the intermediate particulate product X_s. The unsteady-state component balance yields

$$QS_f + QRS - V\frac{\mu_1}{Y_{x/s}}X_a = QWS + Q(1 + R - W)S + V\frac{dS}{dt} \qquad (17.4)$$

with $Y_{x/s}$ as the yield coefficient, assumed constant. Equation (17.4) is also equivalent to

$$D(S_f - S) - \frac{\mu_1}{Y_{x/s}}X_a = \frac{dS}{dt} \qquad (17.5)$$

where D is the dilution rate.

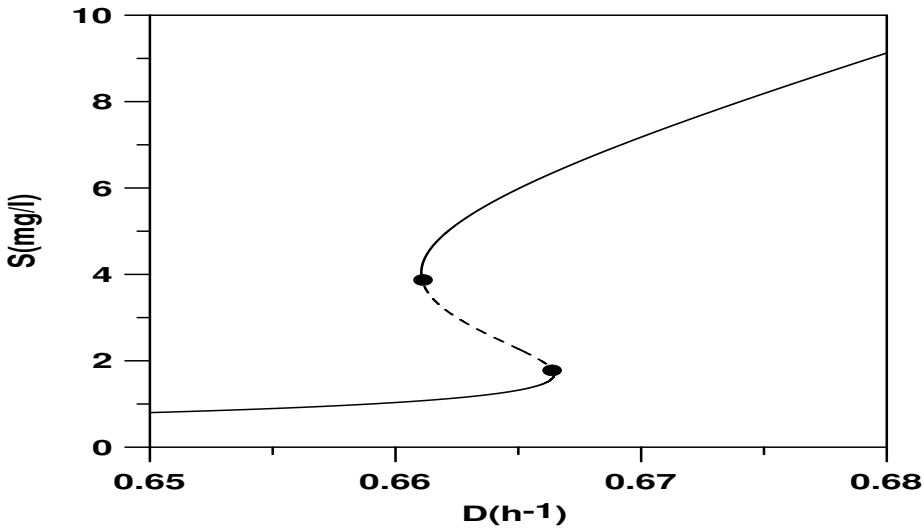

FIGURE 17.3: Continuity diagram for feed condition $S_f = 150\frac{mg}{l}$ showing hysteresis.

Particulate intermediate product X_s

The particulate product X_s is consumed to produce the biomass. A component balance yields

$$QX_{sf} + QRX_{sR} + V(\mu_2 - \mu_1)X_a = QWX_s + Q(1 + R - W)X_s + V\frac{dX_s}{dt} \tag{17.6}$$

The assumed ideal conditions in the settler allows the following simple relation between the recycle X_{sR} and the effluent X_s concentrations

$$X_{sR} = X_s\frac{(1 + R - W)}{R} \tag{17.7}$$

Equation (17.6) is then equivalent to

$$D(X_{sf} - WX_s) + (\mu_2 - \mu_1)X_a = \frac{dX_s}{dt} \tag{17.8}$$

Active biomass X_a

The component balance equation for the biomass is

$$QX_{af} + QRX_{aR} + V\mu_2 X_a = QWX_a + Q(1 + R - W)X_a + V\frac{dX_a}{dt} \tag{17.9}$$

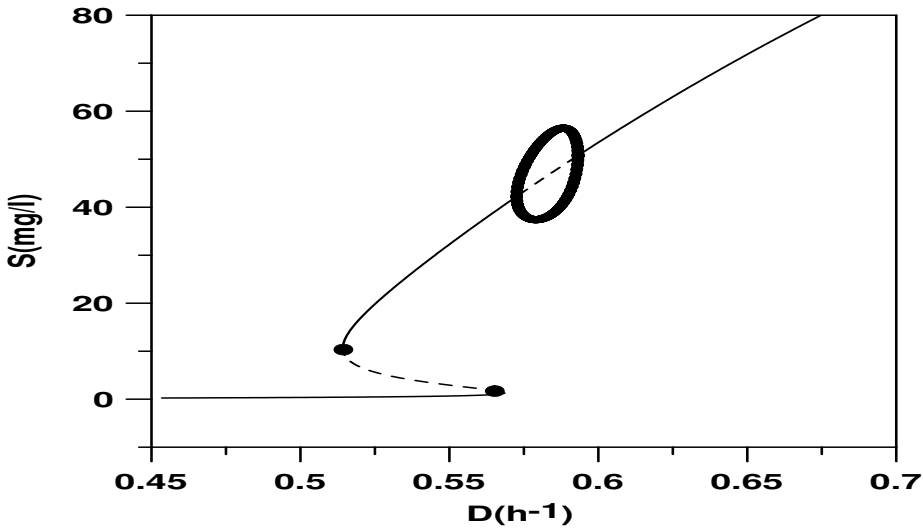

FIGURE 17.4: (a) Continuity diagram for feed conditions $S_f = 221\frac{mg}{l}$. The two Hopf points are connected by stable periodic branches; solid line, stable branch; dashed line, unstable branch.

Similar to the intermediate product (Equation (17.7)), a simple relation links the recycle $X_{a\,R}$ and the effluent X_a biomass concentrations

$$X_{a\,R} = X_a \frac{(1 + R - W)}{R} \tag{17.10}$$

Equation (17.9) is equivalent then to

$$D(X_{a\,f} - W X_a) + \mu_2 X_a = \frac{dX_a}{dt} \tag{17.11}$$

Equations (17.5, 17.8, 17.11) form the model of the bioreactor. Besides the reactor operating parameters, i.e., feed conditions and purge fraction, the nominal values of the other model parameters are given in Table 17.1. These nominal values, as shown in the table, are taken from realistic ranges given in the literature.

17.3 Results and Discussion

In the beginning of this analysis, it is helpful to build an overall picture of the possible bifurcation mechanisms that the model may exhibit. This task is

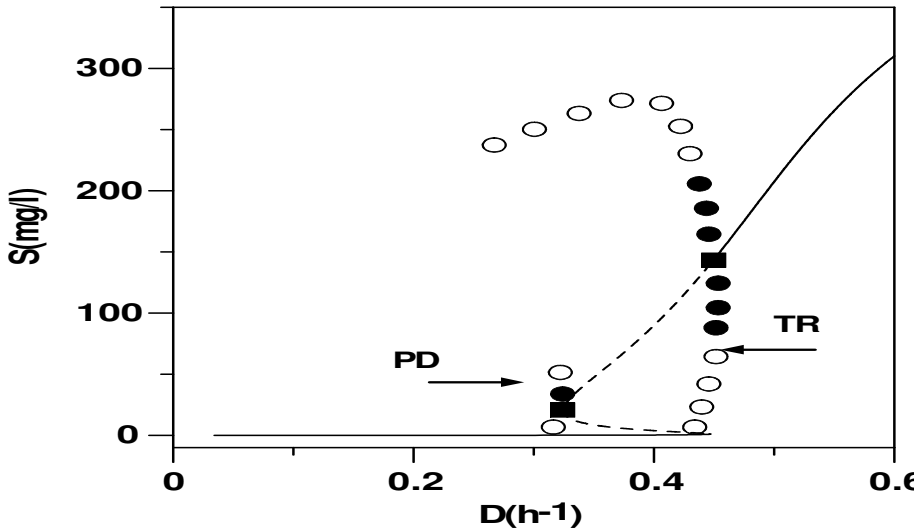

FIGURE 17.5: Continuity diagram for feed conditions $S_f = 500\frac{mg}{l}$; PD, period-doubling; TR, torus bifurcation; solid line, stable branch; dashed line, unstable branch.

best achieved by showing both the loci of the static limit points and the Hopf points in a two-parameter continuation diagram. Figures 17.1(a–b) show the SLP curve and the HB curve, for instance, in the parameter space $(D,\bar{S}_f)$. It can be seen from this figure that the loci of the HB points (dashed lines) consists of two lines that form a minimum at point A_2, i.e., a sign of H_{01} singularity. An oscillatory behavior is expected in the model for any value of the substrate feed concentration larger than A_2 ($S_f = 221.20\frac{mg}{l}$). It can also be seen from the shape of the HB curve that the range of oscillatory behavior increases with the values of substrate feed concentration.

Similar to the HB curve, the loci of the static limit points, shown by solid lines, consist of two lines that form a cusp at point A_1. Static limit points are expected in the model for any values of feed concentrations larger than A_1 ($S_f = 108.45\frac{mg}{l}$). The diagrams of Figures 17.1(a–b) also show that the HB curve crosses the SLP curve respectively at points A_3 and A_4 (enlarged in Figure 17.1b). These points are degenerate, since they give rise to type F_1 degeneracy. The two curves can also be seen to collapse in one line along the left branch of the diagram. This gives birth to another type of degeneracy, i.e., the F_2 degeneracy. It should be noted that, as mentioned in Chapter 3, an interesting dynamic behavior can be found in the vicinity of degenerate points A_2, A_3, and A_4.

In order to have a better understanding of the different bifurcation mechanisms in the system, the diagram of Figure 17.1a is divided into different

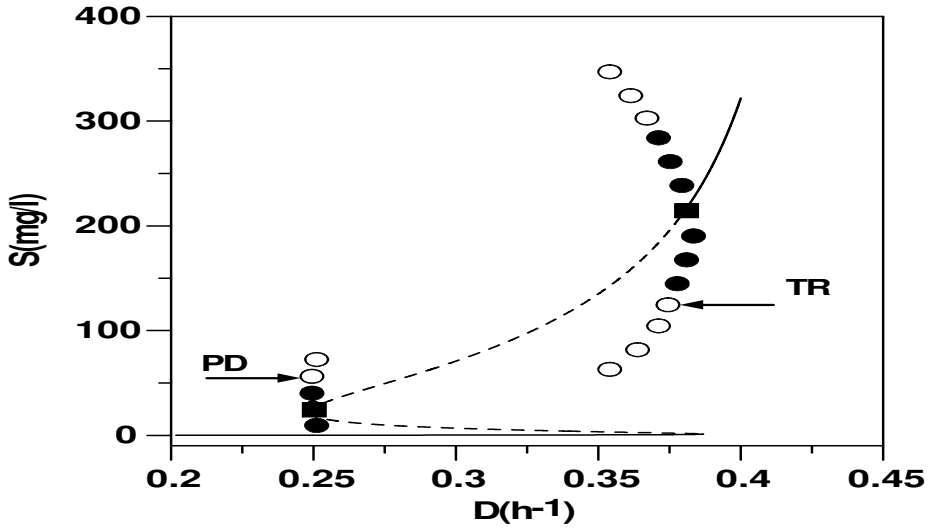

FIGURE 17.6: Continuity diagram for feed conditions $S_f = 1200\frac{mg}{l}$; PD, period-doubling; TR, torus bifurcation; solid line, stable branch; dashed line, unstable; dots, stable periodic branch; circles, unstable periodic branch.

regions, and the static and dynamic bifurcation for each region are studied in some detail.

17.3.1 Monod-Like Behavior

This region extends below the value of S_f that corresponds to the cusp formed by the SLP curves, at $S_f = 137.2\frac{mg}{l}$ (point A_1 in Figure 17.1a). This region is characterized by the absence of any limit or Hopf point. A simple behavior is then expected in this region. Figures 17.2(a–c) show the continuity diagram, for example, for $S_f = 100\frac{mg}{l}$. This behavior is similar to the behavior that can be encountered in unstructured models with Monod growth kinetics. The behavior of the assumed particulate intermediate species X_s follows a similar behavior to the substrate S while the active biomass concentration X_a is seen to decrease with the dilution rate.

17.3.2 Hysteresis Behavior

This region extends from the cusp formed by the SLP curves (point A_1 on Figure 17.1) to the value of $S_f = 219.2\frac{mg}{l}$ (point A_2) that corresponds to the minimum formed by the loci of the HB points. This region is characterized by the presence of two limit points but no Hopf points. Figure 17.3 shows an example of this behavior, which is characteristic of substrate-inhibition

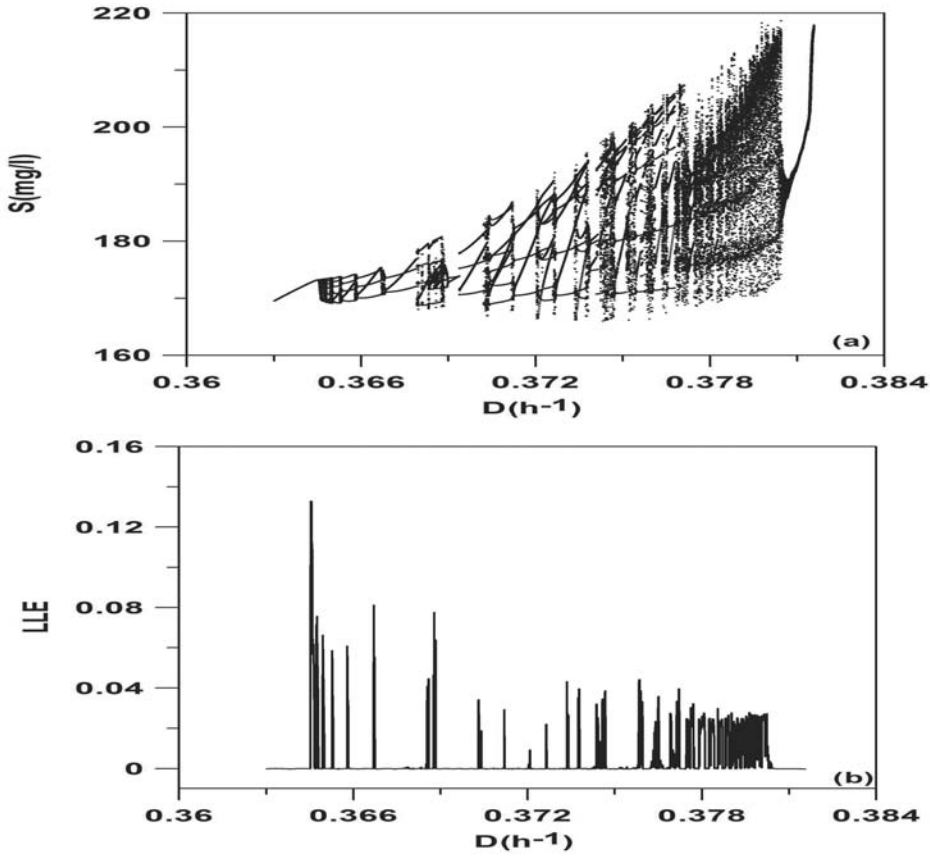

FIGURE 17.7: (a) Poincaré bifurcation diagram for the largest Hopf point in Figure 17.6; (b) Corresponding largest Lyapunov exponent.

kinetics. Hysteresis behavior was reported experimentally in activated sludge reactors [59, 282].

17.3.3 Periodic Behavior

This region corresponds to values of S_f extending above the point where the HB curves form a minimum, i.e., (point A_2 in Figure 17.1b) to just below the point where the HB curves cross the SLP curves, i.e., $S_f = 222.6\frac{mg}{l}$) (point A_3 in Figure 17.1b). This region is characterized by the presence respectively, in this order, of a static limit point, static limit point, Hopf point, and Hopf point. The static and dynamic bifurcation are shown in Figure 17.4 for the value of $S_f = 221\frac{mg}{l}$. A stable periodic branch can be seen to connect the two

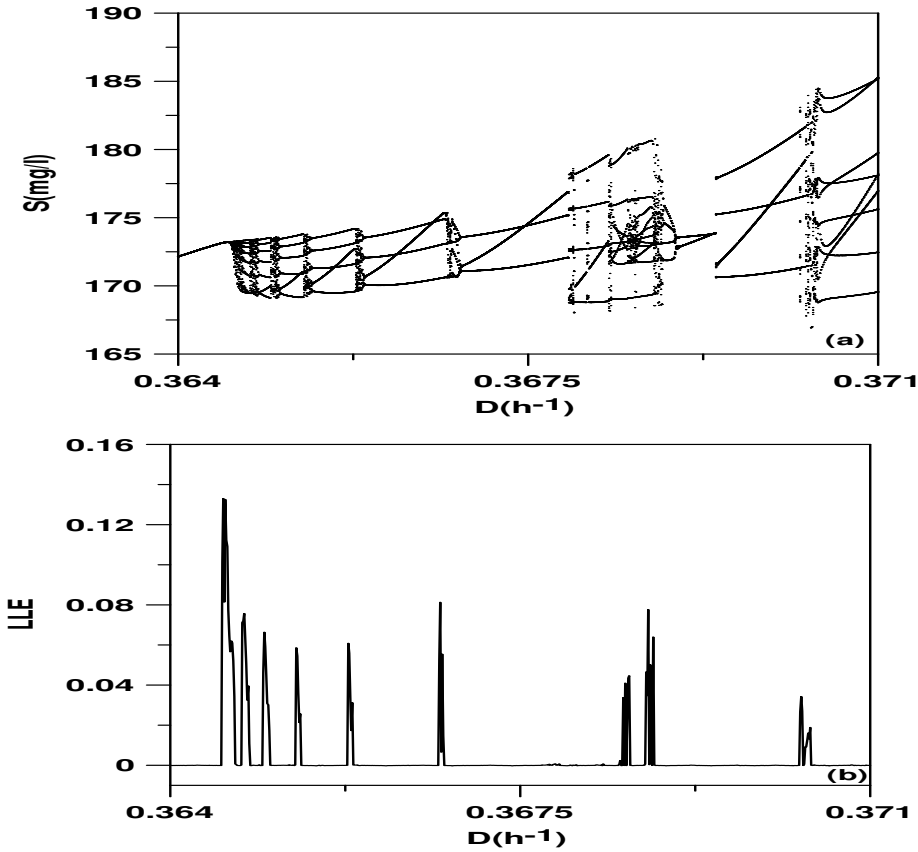

FIGURE 17.8: (a) Enlargement of Figure 17.7a; (b) Enlargement of Figure 17.7b.

Hopf points. Stable oscillations are the only attractors for any dilution rates between the two Hopf points.

17.3.4 Complex Behavior

The next region to be studied extends from the first crossing of the SLP and the HB curves (point A_3 of Figure 17.1a) until the second crossing (point A_4). Here the system is characterized by the presence, in this order, of a static limit point, Hopf point, static limit point, and Hopf point. An example of behavior in this region is shown in Figure 17.5, for $S_f = 500\frac{mg}{l}$. Dynamics around the smallest Hopf point indicate that the stable periodic branches that emanate from the Hopf point lose their stability through the period-doubling (PD) sequence. Period-doubling bifurcation occurs when one of the Floquet multipliers crosses the unit circle at -1 on the real axis, while the other

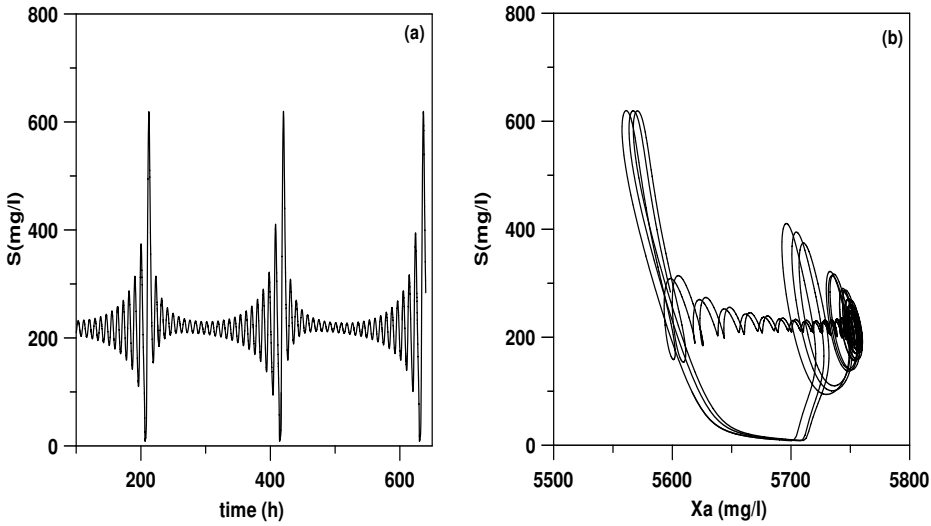

FIGURE 17.9: Dynamics for $D = 0.380$ of Figure 17.8: (a) Time trace; (a) Phase plane.

multipliers remain inside the unit circle. In this phenomenon, one starts with a system with a periodic motion, then as the bifurcation parameter is varied, the system undergoes a secondary bifurcation to a periodic motion twice the period of the original solution. A brief review of the stability of limit cycles is given in the appendix. Bifurcation around the largest Hopf point shows that stable periodic branches emanate from the Hopf point and then lose their stability through a torus bifurcation. Bifurcation to a torus occurs when the Floquet multipliers leave the unit circle transversally. The motion of the system near the torus bifurcation is characterized by a quasi-periodic behavior.

The last region to be discussed extends from the second crossing of the SLP and the HB curves (point A_4 in Figure 17.1a) to larger values of the feed condition S_f. This region is the subject of F_2 degeneracy, mentioned in previous sections. The two-parameter continuation diagram is characterized by the occurrence, in this order, of a static limit point, Hopf point, Hopf point, and a static limit point. The continuity diagram, for example, for the value of $S_f = 1200\frac{mg}{l}$, is shown in Figure 17.6. Again in this region, a period-doubling sequence and torus bifurcation characterize the behavior emanating from the two Hopf points.

The complex dynamics predicted by the model in the last two regions can be conveniently visualized using a Poincaré bifurcation diagram. This technique consists in plotting discrete points (also called return points) of crossing between the trajectories and a hypersurface of dimension $(n-1)$, where n is the dimension of the model. The return points are taken such

that the trajectories intersect the hypersurface transversally and in the same direction.

Since period-doubling bifurcations (Figures 17.5–17.6) occur at a very small range of the dilution rate, we focus on the bifurcations around the largest Hopf points. Figure 17.7a shows the Poincaré bifurcation diagram for the largest Hopf point of Figure 17.6. On the scale of this figure, the diagram looks like an alternation of periodic regimes interrupted by chaotic-like strips via period-adding bifurcation. As the dilution rate increases further and beyond $D = 0.378$, the periodic windows decrease in width and a chaos-like regime persists. The characteristics of chaos-like strips are confirmed by computing the largest Lyapunov exponents (LLE). A chaotic attractor has at least one positive Lyapunov exponent. These exponents can be computed efficiently using the technique and algorithm of Wolf et al. [369]. An overview of Lyapunov exponents and their computations is provided in the appendix. Figure 17.7b, plotted on the same scale as Figure 17.7a, shows the chaos-like strips are effectively chaotic regimes, as seen from the positive values of LLE. The details of the bifurcation mechanisms are illustrated in the enlargement of Figure 17.8. It can be seen that starting from a period-1 attractor, a high periodicity attractor emerges from a chaotic strip.

The period attractor culminates into a chaotic strip and a period-7 attractor regime emerges. From there, it can be seen that the bifurcation mechanism is that of reverse period-adding, where the periodicity of the periodic attractor decreases after emerging from a chaotic regime. However, starting from the emerging period-3 attractor, the bifurcation goes through a period-adding mechanism leading to a period-4 attractor that itself goes into a complicated period-adding and reverse period-adding bifurcation, and emerges as a period-2 attractor. The period-2 attractor starts again a sequence of period-adding bifurcation that continues until chaotic regimes dominate (Figure 17.8a). Figure 17.9 shows an example of chaotic behavior for $D = 0.380$. The oscillations are clearly not periodic as confirmed by the positive value of the largest Lyapunov exponent.

17.4 Concluding Remarks

The behavior of unstructured models investigated in previous chapters was limited, in its complexity, to the existence of simple oscillatory behavior. Numerical simulations were not successful in predicting any nonperiodic behavior such as the one found in the analysis carried in this chapter for the structured, yet simple model of an activated sludge reactor. Even within the limited range of values of operating parameters, the current model was able to predict a variety of complex behavior ranging from simple Monod and hysteresis to periodic, quasi-periodic, and period-doubling sequences culminating into chaotic

regimes. The model in question was lately reinvestigated in [165], and more complex behavior was uncovered, including the occurrence of four static limit points. The complex (i.e., chaotic) behavior predicted by the current model as well as similar models for activated sludge reactors [165, 166] are still to be confirmed experimentally. However, the application of bifurcation theory to predict real-life complex nonperiodic behavior in continuous bioreactors is an issue that was investigated by a number of authors. Zhang and Henson [378], for instance, studied the structured cybernetic models proposed by Guardia et al. [135] for Hybridoma cells as well as the model of Jones and Kompala [177] for growth of *Saccharomyces cerevisiae*. The authors applied bifurcation theory to these models in order to predict complex periodic behavior exhibited by these continuous cultures, including the sudden appearance and disappearance of sustained oscillations. Garhyan et al. [123, 233], and Garhyan and Elnashaie [121, 122], on the other hand, developed structured models for ethanol fermentation, carried out necessary experimental validation and investigated the complex bifurcation behavior of the bioreactor, including period-doubling sequences leading to different types of periodic and chaotic attractors.

This page intentionally left blank

Chapter 18

COMPLEX DYNAMICS IN FORCED BIOREACTORS

18.1 Introduction

The rich dynamics exhibited by the different models studied in previous chapters were all uncovered when the chemostat was operated under time-invariant conditions. In this chapter, we investigate the dynamic charcteristics of an unstructed model of the chemostat when it is periodically forced. The dynamics of continuous bioreactors subject to periodic forcing of one or more bioreactor feed conditions were studied both theoretically and experimentally by a number of authors [4, 194, 272, 273, 281, 306, 339]. These studies showed that suitable periodic variations in one of the bioreactor inputs, e.g., dilution rate and feed concentration can, in a number of cases, improve the time-average performance of the continuous bioprocess vis-á-vis its operation at a stable nontrivial steady state. In the aforementioned studies, the periodic forcing was carried out around a stable steady state, i.e., a point attractor for which the periodic operation of the bioreactor can only yield periodic behavior. In this chapter a different situation is examined for which the chosen center of forcing is itself a stable limit cycle. The bioreactor model selected for this investigation consists of the classical unstructured model for which the yield coefficient is linearly proportional to the substrate. This model was studied in Chapter 4 and was shown to predict oscillatory behavior for a wide range of model kinetic and operating parameters. The objectives of this chapter are twofold. The first objective is to examine the different nonlinear patterns that arise in the bioreactor when the substrate feed concentration is periodically varied around a limit cycle. The results of the investigation illustrate the interactions between the feed inputs, i.e., substrate feed concentration and the nonlinearities of the bioreactor. These results also show the impredictibility of the behavior of the bioreactor resulting from these parametric perturbations. Dramatic changes can be expected in the nature of the emerging dynamic behavior of the forced process [20].

The second objective of this chapter is to investigate the effect of forcing on the performance of the bioreactor. It is shown that for constant forcing frequency, the time-average substrate consumption can be substantially improved by a suitable choice of the forcing amplitude.

A final note is to be made about the methodology used in this investigation and the novelty of the present work. Unlike the periodic forcing of point attractors for which a number of analytical techniques, such as the π criterion [272, 273, 327, 340, 365] are available to provide theoretical guidance for the optimization task, it is not the case for forcing limit cycles. The analysis of the periodically forced model, in this case, is best achieved through numerical investigation. Moreover, while the study of periodically forced chemically and biochemically reactive systems was carried out for a number of cases in the literature [83, 182, 242, 280, 326], the effect of forcing a limit cycle on the performance of the bioreactor was investigated in a limited number of studies [2].

18.2 Process Model and Presentations Techniques

The classical unstructured model of the continuous bioreactor, previously discussed in Chapter 4, is revisited

$$\frac{dS}{dt} = D(S_f - S) - \frac{rX}{Y} \tag{18.1}$$

$$\frac{dX}{dt} = -DX + rX \tag{18.2}$$

Both sterile feed and negligible maintenance needs are assumed. The yield is assumed to depend linearly on the substrate,

$$Y = Y_0 + Y_1 S \tag{18.3}$$

The Monod equation is chosen to describe the growth kinetics,

$$r = \frac{\mu_m S}{k_s + S} \tag{18.4}$$

The model is rendered dimensionless using the following variables,

$$\bar{S} = \frac{S}{k_s}, \quad \bar{X} = \frac{X}{Y_0 k_s}, \quad \lambda = \frac{Y_1 k_s}{Y_0}, \quad \bar{D} = \frac{D}{\mu_m} \quad \bar{t} = t\mu_m, \quad \bar{r} = \frac{r}{\mu_m}$$

The model in the dimensionless form is given by

$$\frac{d\bar{S}}{d\bar{t}} = \bar{D}(\bar{S}_f - \bar{S}) - \frac{\bar{r}\bar{X}}{\lambda\bar{S} + 1} \tag{18.5}$$

$$\frac{d\bar{X}}{d\bar{t}} = -\bar{D}\bar{X} + \bar{r}\bar{X} \tag{18.6}$$

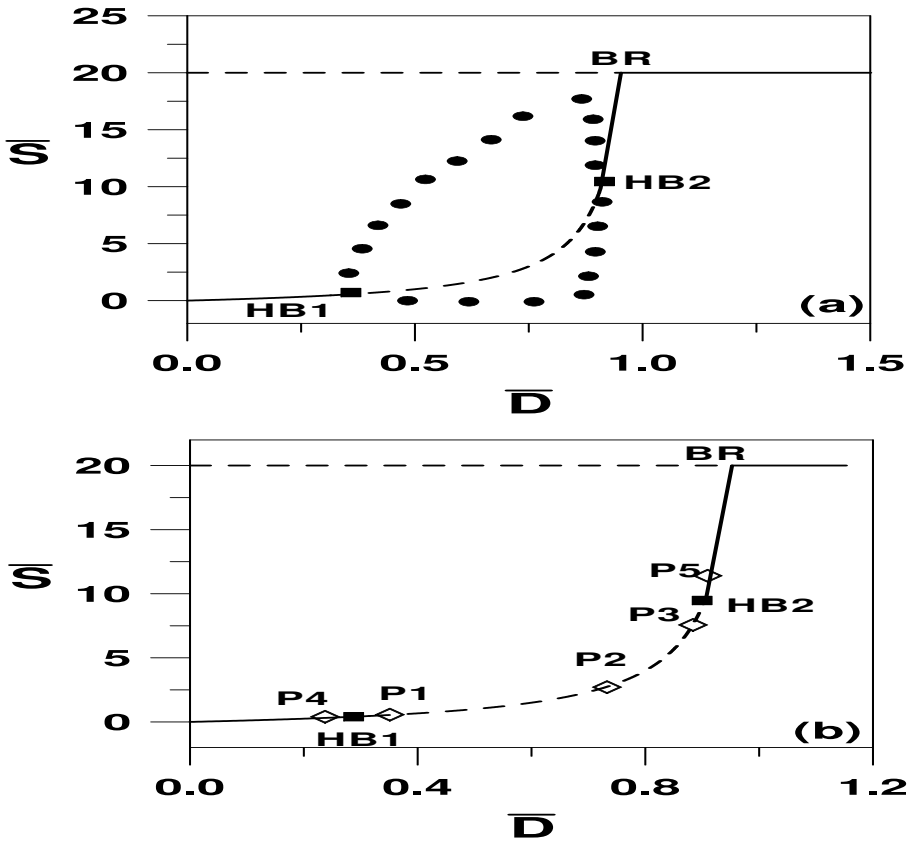

FIGURE 18.1: (a) Continuity diagram of the unforced system; (b) location of the centers of forcing (P_i, $i = 1, 5$) used in the numerical investigation; solid line, stable branch; dashed line, unstable.

with the dimensionless specific growth rate given by

$$\bar{r} = \frac{\bar{S}}{1 + \bar{S}} \tag{18.7}$$

In the first part of this investigation, the behavior of the autonomous, i.e., unforced model is examined. The following values of the model parameters are used:

$$\mu_m = 0.3 \ \ hr^{-1}, \quad Y_0 = 0.01, \quad Y_1 = 0.03, \quad k_s = 1.75 \text{ g/l} , \quad S_f = 35 \text{ g/l} \tag{18.8}$$

The corresponding values of the model dimensionless parameters are $\lambda = 5.25$ and $\bar{S}_f = 20$. Figure 18.1a shows the corresponding continuty diagram in the

parameter space $(\bar{S}, \bar{D})$. The diagram is characterized by two stable branches connected to an unstable branch in the middle by two Hopf points occurring respectively at $\bar{D}_{HB1} = 0.3157$ and $\bar{D}_{HB2} = 0.9037$. The operation of the bioreactor for any dilution rates between the two Hopf points will lead to stable oscillations for any start-up conditions. Moreover, for dilution rates larger than the crossing of the static branch with the washout line at $\bar{D}_{BR} := \frac{\bar{S}_f}{1+\bar{S}_f} = 0.9523$, the operation of the bioreactor leads to washout.

Next, we examine the dynamics of the process when the substrate feed concentration is periodically varied. The centers of forcing chosen in this investigation occur at conditions between the two Hopf points and correspond therefore to stable limit cycles. The substrate feed concentration $\bar{S}_f$, chosen to be the forcing variable, takes the following form

$$\bar{S}_f = \bar{S}_{f0} + A_m sin(2\pi f_f t) \tag{18.9}$$

where $\bar{S}_{f0} = 20$ is the nominal value, and A_m and f_f are respectively the forcing amplitude and frequency.

In the course of this investigation, three different points (P_1, P_2, P_3) are forced. They correspond, respectively, (Figure 18.1b) to $\bar{D}_{P_1} = 0.33$, $\bar{D}_{P_2} = 0.75$, and $\bar{D}_{P_3} = 0.85$. All of these points correspond to limit cycles and to different locations between the two Hopf points. One objective of the investigation is to study the effects of the position of the center of forcing on the dynamics of the forced system. For each case, the ratio $\frac{f_f}{f_0}$ of the forcing frequency to the system natural frequency is taken to be equal to 3. The investigation of the periodically forced system is suitably carried out using a Poincaré map. The phase projection of the trajectories are inspected at specific times t_s which are multiples of the forcing period, i.e., $t_s = m2\pi f_f$. The resulting Poincaré diagram is also called the stroboscopic map and the points are known as stroboscopic points. Transient or chaotic motions appear as scattered dots on the map while the emergence of a periodic attractor of order m would be seen as jumps between m fixed points. The forcing period is chosen to strobe the system because it is always present in the response of the forced system, be it periodic, quasi-periodic, or chaotic.

It is clear that the simplicity of presentation is lost when the strobing period is not accurately determined. A shooting method [192], explained in the appendix, was used for the accurate determination of these natural frequencies.

18.3 Results and Discussion

The effect of variations in the forcing amplitudes at constant frequency are shown in the stroboscopic diagram of Figure 18.2a, when the center of forcing

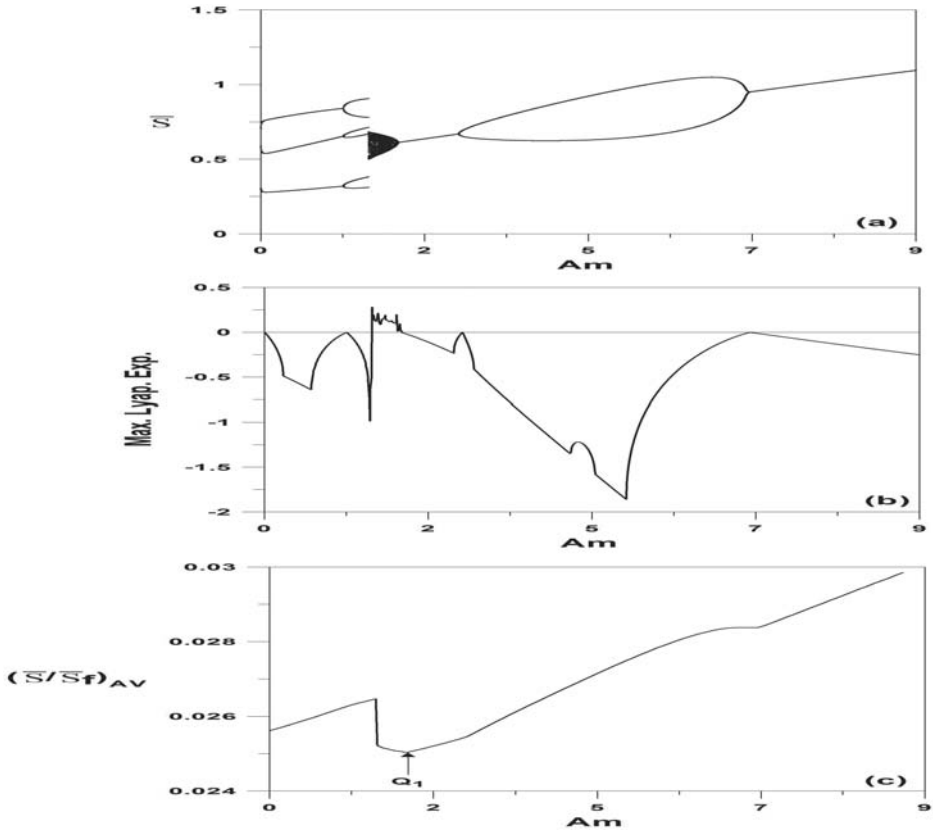

FIGURE 18.2: (a) One-parameter stroboscopic diagram for the forcing of point P_1 of Figure 18.1b; (b) Variations of the maximum Lyapunov exponent; (c) Variations of ratio of cycle-average substrate concentration in the reactor to cycle-average concentration in the reactor feed.

is point (P_1). The limiting case of this region is the autonomous oscillatory system ($A_m = 0.00$). It can be seen that even at small forcing amplitudes, three branches emerge on the stroboscopic diagram of Figure 18.2a. This corresponds to frequency locking as three subharmonic saddles and three nodes are born on the surface of a three-dimensional torus, and the system is entrained by the forcing frequency. Each of the three branches undergoes a period-doubling bifurcation at $A_m = 1.152$ that abruptly terminates at $A_m = 1.495$ to give birth to a chaotic-like regime. This regime persists until $A_m = 1.891$ where a period-1 attractor emerges. The period-1 attractor, itself, undergoes a period-doubling bifurcation that terminates at $A_m = 6.765$. Beyond this value, the system is fully entrained as the forcing term dominates the dynamics of the process, and the only response of the forced system is a stable limit

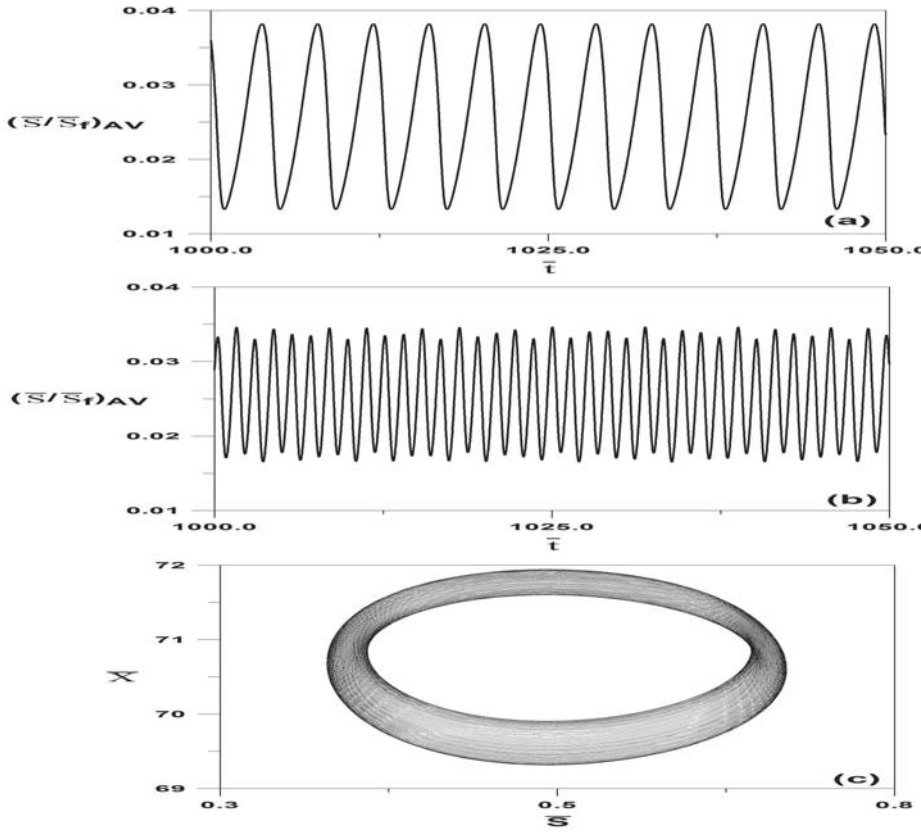

FIGURE 18.3: (a) Time trace for the unforced system ($A_m = 0$) of Figure 18.2a; (b) time trace for the point of maximum substrate consumption (point Q_1, Figure 18.2c); (c) Phase plane for dynamics of point (Q_1).

cycle. The accurate characterization of the emerging attractors of Figure 18.2a can be best achieved by computing the largest Lyapunov exponent [369]. The Lyapunov spectrum is shown in Figure 18.2b where a negative value indicates a periodic regime while a chaotic attractor is characterized by a positive value of the spectrum. Expect then for a narrow regime of chaotic behavior, the behavior of the forced system of Figure 18.2a is dominated by periodic regimes of various periodicities.

The effect of amplitude forcing on the performance of the bioreactor can be seen in Figure 18.2c, showing the variations of ratio of cycle-average substrate concentration in the reactor to cycle-average concentration in the reactor feed. Starting with a value of $\frac{\bar{S}}{S_f} = 0.02561$, corresponding to the autonomous system ($A_m = 0.0$), it can be seen that the average substrate concentration increases throughout the period-3 attractor. However, a sudden drop to a value

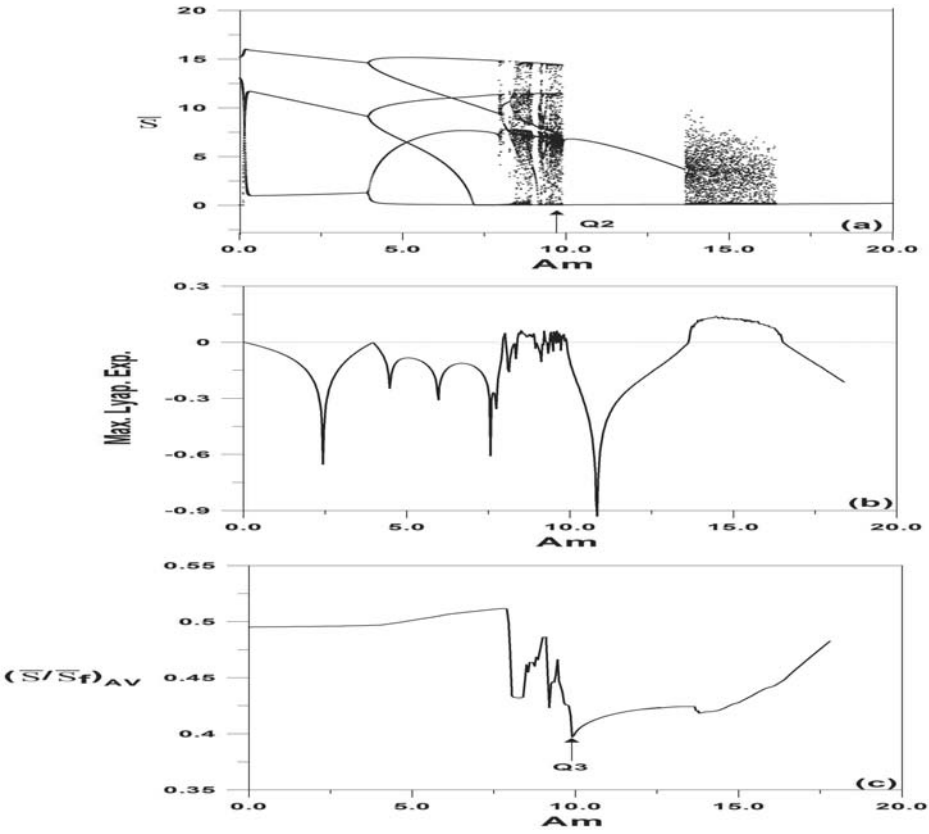

FIGURE 18.4: (a) One-parameter stroboscopic diagram for forcing point P_2 of Figure 18.1b; (b) Variations of the maximum Lyapunov exponent; (c) Variations of ratio of cycle-average substrate concentration in the reactor to cycle-average concentration in the reactor feed.

of $\frac{\bar{S}}{S_f} = 0.02501$ is observed within the chaotic regime at $A_m = 1.881$ (point Q_1, Figure 18.2c). Beyond this point, the substrate concentration increases steadily throughout the periodic regimes of Figure 18.2a. The time traces for the unforced periodic attractor ($A_m = 0$) and the maximum substrate consumption (point Q_1, Figure 18.2c) are shown in Figures 18.3(a–b). The two figures, shown in the same scale, indicate clearly that the fluctuations of the chaotic oscillations around the mean (Figure 18.3b) are smaller than those of the unforced system (Figure 18.3a). Moreover, the phase plane of Figure 18.3c illustrates the aperiodic nature of the point of maximum substrate consumption.

The analysis carried out for point P_1 is repeated for the two other points P_2 and P_3 of Figure 18.1b. For each point, the corresponding stroboscopic

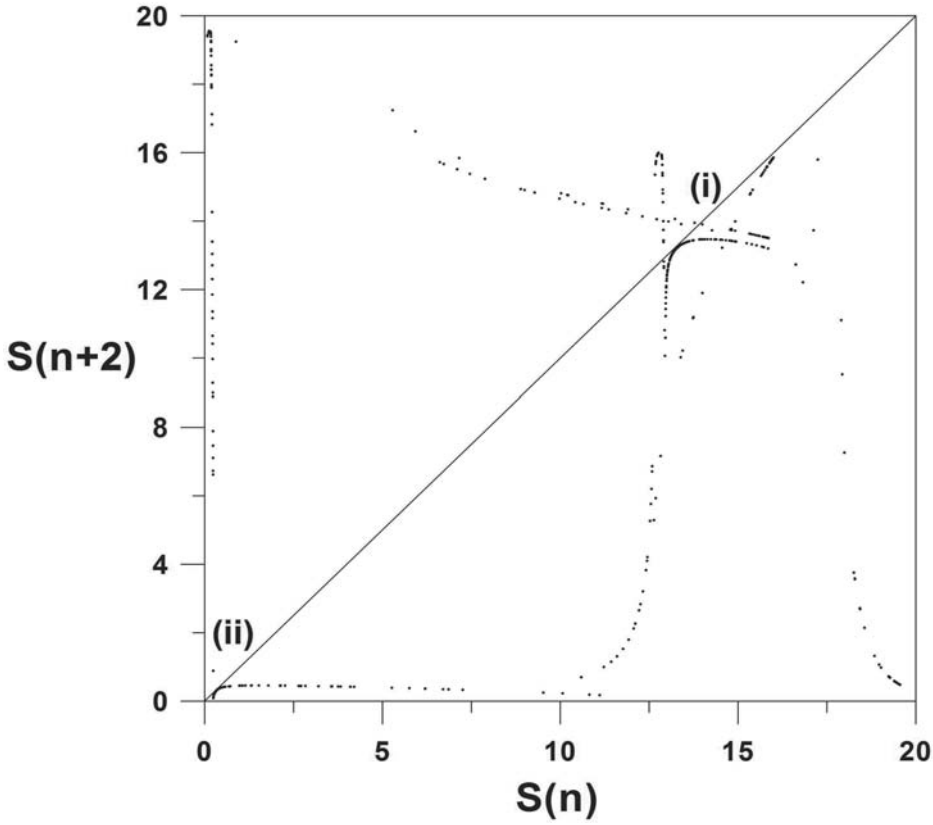

FIGURE 18.5: Characteristics of the intermittent chaos at point Q_2 ($A_m = 9.945$) of Figure 18.4a; Second-iterate map; The trajectory is tangent at the diagonal in two points (i) and (ii).

diagram, Lyapunov spectrum, and the variations of the time-average substrate concentration are plotted against the forcing amplitude.

As can be seen in the stroboscopic diagram of Figure 18.4a, the move of the center of forcing from point P_1 to P_2 has dramatic effects on the emerging dynamic patterns of the forced bioreactor. Similarly to point P_1, three branches emerge at low forcing amplitudes. However, each of the three emerging branches undergoes a period-doubling bifurcation yielding a period-6 attractor that persists until $A_m = 7.952$. The period-6 attractor culminates into a chaotic strip. It can be seen from Figure 18.4a that this chaotic strip is itself interrupted by small periodic windows. The chaotic strip abruptly terminates at $A_m = 9.952$ and a period-2 attractor emerges. The period-2 attractor bifurcates again to chaos and gives rise to a period-1 attractor, as the system becomes fully entrained. Compared to the process dynamics obtained

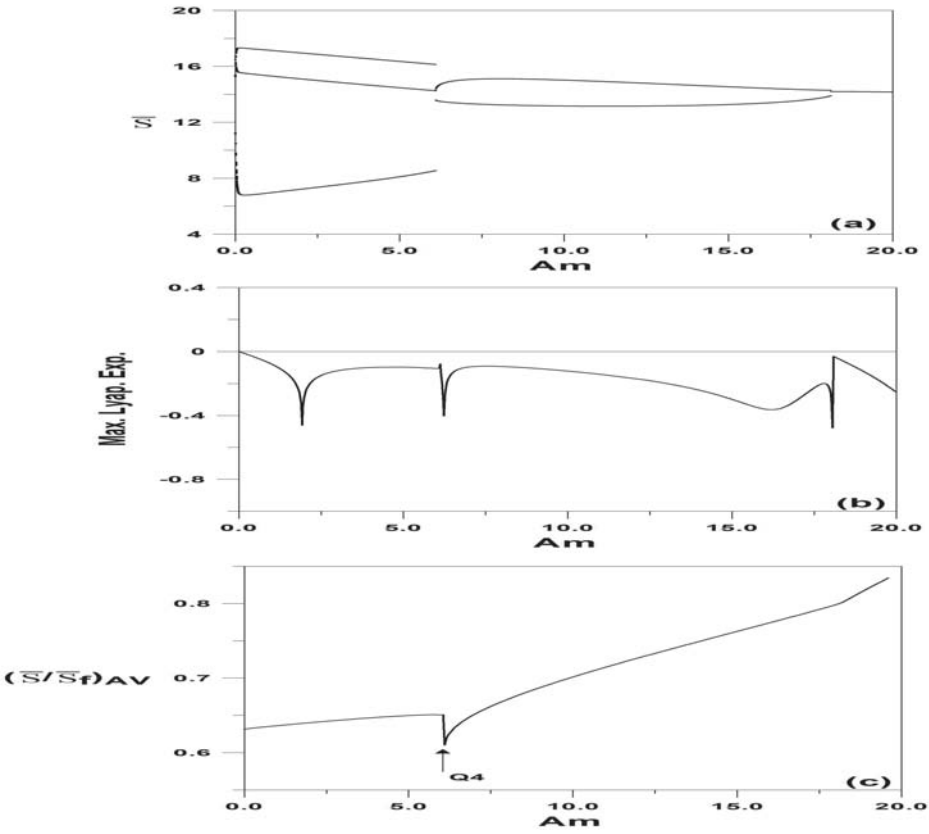

FIGURE 18.6: (a) One-parameter stroboscopic diagram for the forcing of point P_3 of Figure 18.1b; (b) Variations of the maximum Lyapunov exponent; (c) Variations of ratio of cycle-average substrate concentration in the reactor to cycle-average concentration in the reactor feed.

for point P_1 (Figure 18.2a), the emerging patterns (Figure 18.4a) for point P_2 are dominated by larger regimes of chaos, as confirmed by the Lyapunov spectrum of Figure 18.4b.

The exact mechanism of bifurcation from the chaotic behavior to a periodic regime is investigated by considering, for example, point Q_2 (Figure 18.4a) corresponding to $A_m = 9.945$. This point is located just before the emergence of a period-2 attractor from the chaotic regime. Figure 18.5 shows the plot of the second iterate of the substrate $\bar{S}(n+2)$ against $\bar{S}(n)$. It can be seen that the curve approaches the diagonal and almost becomes tangent at two points (i) and (ii) (Figure 18.5). The chaotic attractor is thus destroyed by the mechanism of intermittency [289]. The term intermittency refers to

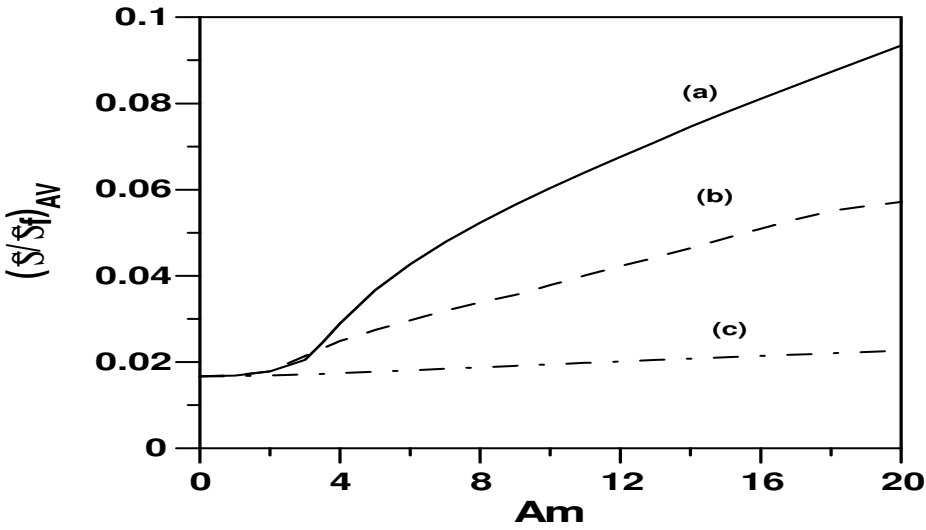

FIGURE 18.7: Results of forcing point attractor P_4 at $\bar{D} = 0.25$ of Figure 18.1b; Variations of ratio of cycle-average substrate concentration in the reactor to cycle-average concentration in the reactor feed for different forcing frequencies; (a) solid line, $f_1 = 0.14$; (b) dashed line, $f_2 = 0.22$; (c) semidashed line, $f_3 = 0.72$.

oscillations that are periodic for certain intervals (laminar phase) interrupted by intermittent erratic bursts of periodic oscillations of finite duration.

The effect of amplitude forcing on the substrate consumption is shown in Figure 18.4c. It can be seen that a substantial increase in the substrate consumption occurs at the chaotic regime (point Q_3, Figure 18.4c). The substrate concentration decreases from $\frac{\bar{S}}{S_f} = 0.4950$ for the unforced process, i.e., $A_m = 0$ to $\frac{\bar{S}}{S_f} = 0.3971$ for $A_m = 9.950$, i.e., an improvement of about 20%.

Closer to the other Hopf point (HB_2) of Figure 18.1b, the process dynamics are shown in Figures 18.6(a–b) when the center of forcing is point P_3 (Figure 18.1b). The three emerging periodic branches abruptly terminate at $A_m = 6.103$ to give rise to a period-2 regime. The period-2 attractor undergoes a reverse period-doubling sequence that terminates at $A_m = 18.127$ to yield a period-1 attractor, as the process becomes fully entrained. Unlike the dynamics induced by points P_1 and P_2 (Figure 18.2a and Figure 18.4a), the behavior of the forced process for point P_3 (Figure 18.6a) is characterized by the presence of periodic attractors alone with no chaotic regimes. This is further confirmed by the negative values seen in the Lyapunov spectrum of Figure 18.6b.

The effect of forcing on the substrate consumption are, on the other hand, shown in Figure 18.6c. Starting from an initial value of $\frac{\bar{S}}{S_f} = 0.6316$

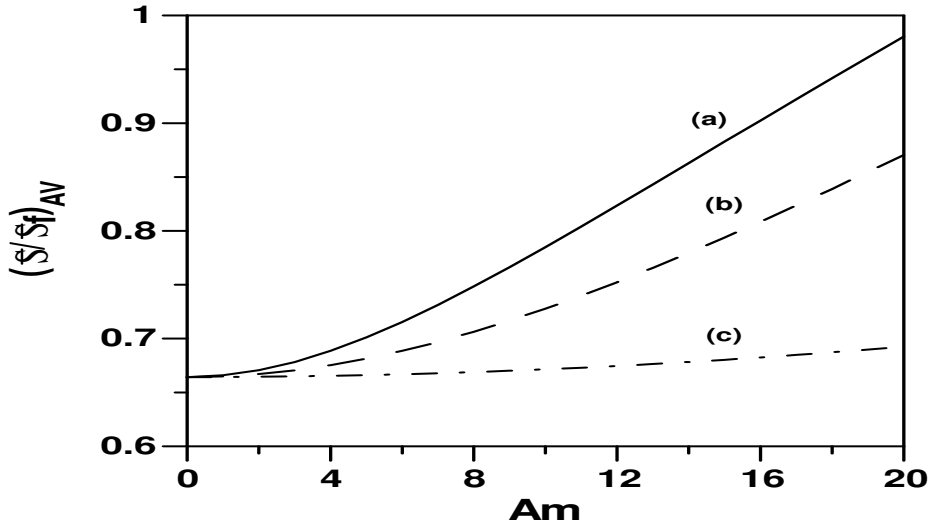

FIGURE 18.8: Results of forcing point attractor P_5 at $\bar{D} = 0.93$ of Figure 18.1b; Variations of ratio of cycle-average substrate concentration in the reactor to cycle-average concentration in the reactor feed for different forcing frequencies; (a) solid line, $f_1 = 0.14$; (b) dashed line, $f_2 = 0.22$; (c) semidashed line, $f_3 = 0.72$.

corresponding to the unforced process $A_m = 0$, the substrate concentration increases throughout the period-3 regime but reaches a clear minimum $\frac{\bar{S}}{S_f} = 0.6106$ at $A_m = 6.101$ (point Q_4, Figure 18.6c), that occurs close to the boundary between the period-3 and period-2 regimes of Figure 18.6a.

Having examined the effect of forcing a stable limit cycle, it is interesting to compare these results to the conventional approach of forcing a stable steady state (i.e., point attractor). From a dynamical point of view, the periodic forcing of a point attractor leads only to limit cycles, compared to the variety of dynamic behavior (e.g., period-doubling and chaos) that were found when a limit cycle was forced. As to the effect of forcing on the performance of the biodegradation, extensive numerical simulations were carried out for this purpose. In the following we show a sample of results on forcing two point attractors that occur at dilution rates $\bar{D} = 0.25$ and $\bar{D} = 0.93$, respectively. These two points P_4 and P_5, shown in Figure 18.1b, correspond to stable steady states located on both sides of the periodic points. Point P_4 corresponds to high steady-state conversion (low substrate concentration) while point P_5 is closer to the washout branch. The simulations were carried out for a wide range of forcing amplitudes A_m (i.e., from 0 to 20) and using three distinct values of forcing frequencies i.e., $f_1 = 0.14$, $f_2 = 0.22$, and $f_3 = 0.72$. Figure 18.7 shows the results of forcing point P_4 ($\bar{D} = 0.25$). Starting with a value of

$\frac{\bar{S}}{S_f} = 0.01667$ corresponding to the unforced system ($A_m = 0.0$), it can be seen that for all the three forcing frequencies, the ratio $\frac{\bar{S}}{S_f}$ increases monotonically with the forcing amplitude. Consequently, compared to the unforced system, the performance of the biodegradation deteriorates with the increase in the forcing amplitude for all the studied frequencies. This is unlike forcing a stable limit cycle, when we have found that the efficiency of the biodegradation can increase in some regions of the forced system. A number of other remarks can be made about forcing a point attractor. It can be seen in Figure 18.7 that for low forcing amplitudes (i.e., A_m smaller than 2) the effect of forcing frequency is negligible while this effect is quite pronounced for larger forcing amplitudes. For instance, for a forcing amplitude of $A_m = 10$, the increase in the frequency from f_1 to f_3 increases the substrate consumption substantially, as the ratio $\frac{\bar{S}}{S_f}$ decreases from 0.0603 to 0.0195. However, even for large values of forcing amplitudes and frequencies, extensive simulations showed that the value of $\frac{\bar{S}}{S_f}$ is always higher than the one corresponding to the unforced system. Another remark concerns the effect of forcing frequency. When the process is forced with a large frequency such as f_3, the increase in the forcing amplitude does not have a substantial effect on the biodegradation efficiency. In fact, for the forcing frequency (f_3), the increase in forcing amplitude A_m from 0 to 20 changes the substrate consumption $\frac{\bar{S}}{S_f}$ from 0.01667 to only 0.0226, while this change is more pronounced for the smaller forcing frequencies f_1 and f_2, as shown in Figure 18.7.

A similar trend to Figure 18.7 can be found in Figure 18.8 showing the effect of forcing the other point attractor (P_5 at $\bar{D} = 0.93$). The only peculiarity of this situation is that since point P_5 is close to the washout branch, the forcing may actually lead to washout conditions for large values of forcing amplitude, as the ratio $\frac{\bar{S}}{S_f}$ approaches unity (Figure 18.8).

18.4 Concluding Remarks

This chapter has shed some light on the effects of forcing on the dynamics as well as on the time-average performance of an unstructured model of the chemostat. The investigation focused on utilizing the substrate feed concentration to periodically force different points in a region of stable limit cycles of the unforced system. The numerical investigation has revealed the complex dynamics resulting from interactions between the nonlinearities of the bioreactor and its feed input. Chaotic as well as nonchaotic regimes emerge from the periodic system even for small forcing amplitudes. Different mechanisms for the transition between chaotic and periodic regions, including period-doubling and period-adding bifurcation have been analyzed. The investigation has also

shown the dominance of chaotic regimes in the forced process as the center of forcing is moved away from either Hopf points. Extensive numerical simulations were carried out to study the effect of the forcing on the performance of the bioreactor. It was found that the time-average performance always deteriorates in a region of periodic behavior. However, a substantial improvement in the substrate consumption can be observed for certain values of forcing amplitudes. These values seem to occur close to boundaries of transition from chaotic behavior to a periodic regime, as well as in boundaries of transitions from a periodic regime to another periodic regime.

It should be noted that the same ideas in this chapter were applied recently [2] to study the dynamics and chaotic behavior of a validated model of bioethanol fermenter, subject to periodic perturbations in the feed concentration. The investigation revealed that the center of forcing has a significant effect on the dynamic response of the periodically forced bioreactor. Chaotic behavior is developed when the center of forcing is relatively close to a homoclinic infinite period orbit, while quasi-periodicity is, on the other hand, developed when the center of forcing is in the neighborhood of a Hopf point. The authors [2] concluded that the best policy for the production of bioethanol is to operate the forced fermenter in frequency-locking regions at small forcing amplitudes.

This page intentionally left blank

Appendix A

In this appendix, we provide a set of definitions and theorems, as well as an overview of some numerical techniques connected with nonlinear theory. These issues were not covered in Chapter 3 and are deemed essential for understanding some fundamentals aspects of bifurcation problems as well as some numerical techniques that were used throughout the book.

A.1 Implicit Function Theorem

The implicit function theorem is of fundamental importance in bifurcation theory. It allows to convert relations to functions by representing the relation as a graph of the function. The following definitions are adapted from the excellent references [188, 193, 231, 315].

Consider the following bifurcation problem

$$f(x, \lambda) = 0 \tag{A.1}$$

where x and λ are scalars, and f is a scalar-valued function defined in a neighborhood of a point (x_0, λ_0) that satisfies

$$f(x_0, \lambda_0) = 0 \tag{A.2}$$

We wish to solve $f(x, \lambda) = 0$ for x in terms of λ when λ is small. The theorem asserts that if f_x is continuous near (x_0, λ_0) and $f_x(x_0, \lambda_0) \neq 0$, then there exists a unique solution $x = \phi(\lambda)$ for λ sufficiently small. The functions ϕ are generally defined implicitly. Some simple situations arise when the functions are derived explicitly. A simple example is the following bifurcation problem [315],

$$x^2 + \lambda^2 = r^2 \tag{A.3}$$

which defines the equation of a circle of radius r. For this problem we can explicitly obtain x as function of λ

$$x = \phi(\lambda) = \pm(r^2 - \lambda^2)^{\frac{1}{2}} \tag{A.4}$$

which is defined for $-r \leq \lambda \leq r$. The following theorem provides a generalization to the case when both x and f are vectors of dimension n.

Theorem 1 Assume f to be k-th order differentiable ($k \geq 1$) and satisfy (Equation (A.2)). Assume that $f_x(x_0, \lambda_0)$ is nonsingular. Then the following are true:

- There exists a neighborhood of λ such that Equation (A.1) has a unique solution $x = \phi(\lambda)$, i.e., satisfying $f(\phi(\lambda), \lambda) = 0$
- The function ϕ is k-th differentiable
- $f_\lambda(x, \lambda) + f_x(x, \lambda)\frac{dx}{d\lambda} = 0$

The theorem asserts the existence and uniqueness of an implicitly defined function $\phi(\lambda)$ that can be continued in the neighborhood of λ until f_x becomes singular.

A.2 Lyapunov–Schmidt Reduction Technique

The Lyapunov–Schmidt reduction, mentioned in Chapter 3 in connection with Hopf degeneracies, is an important technique in bifurcation theory. The technique allows the reduction of the dimensionality of the problem to be solved, so that the study of local solutions can be carried out in a much lower dimensional system (sometimes even a single variable equation). The following summary is adapted from the excellent sources [132, 222, 231, 323]:

Consider the following linearized system,

$$-\lambda x + Jx + H(x, \lambda) = 0 \tag{A.5}$$

where J can be thought of as being the Jacobian matrix and $H(x, \lambda)$ is a column matrix that satisfies

$$H(x, \lambda) = O(||x|| + |\lambda|) \tag{A.6}$$

$||.||$ denotes some norm in a finite dimensional space and $O(z)$ refers to terms of order smaller than z, i.e., $\frac{O(z)}{z} \to 0$ when $z \to 0$. Equation (A.5) can also be written as

$$(J - \lambda I)x + H(x, \lambda) = 0 \tag{A.7}$$

where I is the identity matrix. Assume that the matrix J has a real eigenvalue λ_0 with multiplicity ($m \geq 1$). We would like to examine the local behavior of the system around λ_0. The space $X = \Re^n$ can be decomposed into the direct sum of two invariant subspaces of the operator as follows:

$$X = X_1 \bigoplus X_2 \tag{A.8}$$

where X_1 is defined as

$$X_1 = \bigcup_{n \in \aleph} \{x \in X, (J - \lambda_0 I)^n x\} = 0 \tag{A.9}$$

The dimension of X_1 is m. The matrix J can also be decomposed as:

$$J = J_0 + J_1 \tag{A.10}$$

where

$$J_0 = J|X_1 : X_1 \to X_1, \quad J_1 = J|X_2 : X_2 \to X_2$$

Next, let's $P : X \to X_1$ and $Q = I - P : X \to X_2$ be the canonical projections. Let's write any element $x \in X$ as

$$x = u + v \tag{A.11}$$

where $u \in X_1$ and $v \in X_2$. Applying the projections P and Q, the original problem of Equation (A.7) becomes

$$-\lambda u + J_0 u + PH(u + v, \lambda) = 0 \tag{A.12}$$

$$-\lambda v + J_1 v + QH(u + v, \lambda) = 0 \tag{A.13}$$

Noting that $-\lambda I + J_1 : X_2 \to X_2$ is invertible, then by the implicit function theorem, Equation (A.13) can be solved in the neighborhood of $u = 0$ and $v = 0$

$$v = v(u, \lambda) \text{ with } v(u, \lambda) = O(||u||) \tag{A.14}$$

Substituting Equation (A.14) into Equation (A.12) yields the following reduced m-dimensional equation

$$-\lambda u + J_0 u + PH(u + v(u, \lambda), \lambda) = 0 \tag{A.15}$$

This equation is called the bifurcation (or branching) equation.

A.3 Center Manifold

The center manifold reduction is another important technique in bifurcation theory, also mentioned in Chapter 3 in connection with type II and III Hopf degeneracies. The technique also allows the reduction of the dimension of an arbitrary high order system by observing that the interesting dynamics near a bifurcation occurs on a low dimension subset of the phase space called the center manifold. The dimension of this space determines the dimension of

the corresponding normal form. The connection between the center manifold reduction and the Lyapunov–Schmidt reduction technique, presented in the previous section, has been investigated by a number of authors [222, 236]. The following descriptions are extracted from the excellent sources [72, 84, 324].

In order to introduce the center manifold reduction technique, we assume that the problem under investigation is still defined by Equation (A.1) with the origin being an equilibrium point. We recall from Chapter 3 that the eigenvalues of the Jacobian matrix $f_x(0,0)$ of the linearized system determine the asymptotic stability of the original nonlinear system according to the sign of the real part of the eigenvalue. For each eigenvalue λ, there is an associated eigenspace E_λ, described for the case when λ is real, by

$$E_\lambda = \{v \in R^n | (f_x(0,0) - \lambda I)v = 0\} \tag{A.16}$$

We can divide the eigenspace of the Jacobian matrix to three subsets according to the sign of the real part of the eigenvalue. The stable subspace (E^s) is the eigenspace of the linear system whose base is made by the eigenvectors corresponding to the negative real part of eigenvalues,

$$E^s = Span\{v | v \in E_\lambda \text{ and } Re(\lambda) < 0\} \tag{A.17}$$

Similarly, the unstable subset E^u is the eigenspace associated with the positive real part of the eigenvalues. The eigenspace associated with zero real-part eigenvalues is called center eigenspace E^c. The linearized system can provide an accurate behavior of the original nonlinear system. The theorem of Hartmann-Grossman [143], ensures that the dynamical system is locally topologically equivalent to the linearized one as long as the equilibrium point is hyperbolic, i.e., no eigenvalues on the imaginary axis. In the case of the existence of a nontrivial center eigenspace (i.e., different from the null space), the linearized stability does not apply and the center manifold reduction technique can provide an analytical tool for this degenerate case.

For the original nonlinear system described by Equation (A.1), the stable, unstable, and center manifolds denoted by W^s, W^u, and W^c are generalizations of the linear subspaces E^s, E^u, and E^c. First, we have the following definition for a stable manifold.

Definition 1 For the equilibrium $x = 0$, a stable manifold W^s is an invariant manifold of dimension n_s that contains $x = 0$ and is tangent to E^s at $x = 0$. □

The same definition holds for the unstable W^u and the center W^c manifolds. The center manifold possesses the important property that invariant sets of any type such as equilibria, periodic orbits, and invariant 2-tori will lie in W^c if they are contained in a neighborhood of $x = 0$. For these reasons one may restrict attention to the behavior on W^c when analyzing a local bifurcation.

In the following, we show how to represent dynamics on the center manifold. Suppose that the system of Equation (A.1) can be written for $\lambda = 0$ as

$$\dot{x_1} = A_1 x_1 + g_1(x_1, x_2) \tag{A.18}$$

$$\dot{x_2} = A_2 x_2 + g_2(x_1, x_2) \tag{A.19}$$

where A_1 is a matrix that has all eigenvalues on the imaginary axis and A_2 is a matrix with all eigenvalues off the imaginary axis. $g_1(x_1, x_2)$ and $g_2(x_1, x_2)$ contain nonlinear terms. The main result is that there exists a center manifold described by a function $x_2 = h(x_1)$ such that the following equation

$$\dot{x_1} = A_1 x_1 + g_1(x_1, h(x_1)) \tag{A.20}$$

determines the dynamics of Equation (A.1) near the equilibrium point. The function $h(x)$ obeys the following equation,

$$\frac{dh(x_1)}{dx_1}(A_1 x_1 + g_1(x_1, h(x_1))) \quad = \quad A_2 h(x_1) + g_2(x_1, h(x_1)) \tag{A.21}$$

Generally, there is no simple analytical solution to Equation (A.21), but $h(x)$ can be approximated by the power series, $\phi(x)$ and solved to an arbitrary degree. In this case, let $N(\phi(x))$ be the residual in Equation (A.21)

$$N(\phi(x)) = \frac{d\phi(x_1)}{dx_1}(A_1 x_1 + g_1(x_1, \phi(x_1))) - (A_2\phi(x_1) + g_2(x_1, \phi(x_1))) \tag{A.22}$$

The theory says that if $N(\phi(x)) = O(|x|^q)$ as $x \to 0$ then

$$h(x) = \phi(x) + O(|x|^q) \tag{A.23}$$

In the following we provide a simple illustrating example [72]. Consider the following system

$$\begin{aligned} \dot{x_1} &= a x_1^3 + x_1 x_2 - x_1 x_2^2 \\ \dot{x_2} &= -2x_2 + b x_1^2 + x_1^2 x_2 \end{aligned} \tag{A.24}$$

The Jacobian matrix at the equilibrium point $(0, 0)$ has zero as an eigenvalue. The linearization procedure does not work. Compared with Equations (A.18–A.19), it can be seen that $A_1 = 0$ and $A_2 = -2$. Let $x_2 = h(x_1)$, then Equation (A.21) becomes

$$\frac{dh}{dx_1}(a x_1^3 + x_1 x_2 - x_1 x_2^2) = -2h(x_1) + b x_1^2 + x_1^2 x_2 \tag{A.25}$$

Assume a power series expansion,

$$h(x_1) = p_0 + p_1 x_1 + p_2 x_1^2 + p_3 x_1^3 \tag{A.26}$$

Substituting in Equation (A.25) and equating yields

$$p_0 = 0, p_1 = 0, p_2 = b/2, p_3 = 0 \tag{A.27}$$

Therefore,

$$h(x_1) = \frac{b}{2}x_1^2 + O(x_1^4) \tag{A.28}$$

Substituting $x_2 = \frac{b}{2}x_1^2$, the following equation

$$\dot{u} = (a + \frac{b}{2})u^3 + O(u^5) \tag{A.29}$$

represents an approximation to the invariant center manifold. Therefore, $u = 0$ is an unstable equilibrium when $(a + \frac{b}{2}) > 0$ and stable for $(a + \frac{b}{2}) < 0$. For $(a + \frac{b}{2}) = 0$, high order terms should be included in the approximation.

A.4 Stability of Limit Cycles

Limit cycles such as those studied in Chapters 17 and 18 can lose stability through a number of mechanisms. The stability of limit cycles is determined by the eigenvalues of the monodromy matrix [79, 170, 315]. Consider the following n order system,

$$\dot{x} = f(x, \lambda) \text{ with } x(0) = x_0 \tag{A.30}$$

Let $x(t)$ be a periodic solution of Equation (A.30) with period T. The monodromy matrix is equal to $\Phi(T)$ where $\Phi(t)$ is the solution of the variational equation

$$\dot{\Phi} = f_x(x, \lambda)\Phi, \quad \Phi(0) = I \tag{A.31}$$

The n eigenvalues of $\Phi(T)$ are called Floquet multipliers. The eigenvalue with the largest absolute value is called the principal Floquet multiplier. One of the Floquet multipliers is always constrained to be unity. The remaining $(n - 1)$ multipliers determine the stability of the limit cycle. The periodic orbit is stable if all the eigenvalues lie within the unit circle in the complex plane. When the principal Floquet multiplier crosses the unit circle, the periodic orbit loses its stability resulting in a dynamic bifurcation. Common types of dynamic bifurcation are:

- Saddle-node bifurcation: The bifurcation occurs when a stable limit cycle collides with an unstable one and either the periodic orbit is born or disappears. In this case, the principal Floquet multiplier leaves the unit circle through +1. The bifurcation point is also called a periodic limit point or periodic turning point.

- Period-doubling bifurcation: This is the bifurcation of a periodic branch from another branch. The principal Floquet multiplier crosses the unit circle at -1.
- Neimark or secondary Hopf bifurcation: In an analogy with the Hopf bifurcation of an equilibrium point, complex Floquet multipliers can form a complex conjugate pair whose norm cross +1. This results in a periodic solution bifurcating to a quasi-periodic attractor.

A.5 Poincaré Map

We have seen in Chapter 17, besides continuity diagrams, another tool for the description of bifurcation mechanisms of an autonomous system is obtained when discrete points are taken from the crossing of trajectories onto a fixed hyperplane (Poincaré surface). These discrete points are called return points. The plotting of one of the coordinates of the return points versus the bifurcation parameter is called the Poincaré bifurcation diagram. The plotting of two of the coordinates of the return points for a specific value of the bifurcation parameter is called the two-dimensional Poincaré map [1, 149, 351]. Poincaré maps supplement continuity diagrams and the phase plane (or time trace) plots for the analysis of autonomous systems. The Poincaré bifurcation diagram can for instance help to visualize the transition from periodic regimes to chaos-like regimes. In two-dimensional Poincaré maps, the appearance of a single fixed point on the Poincaré bifurcation diagram corresponds to a period-1 solution while k fixed points correspond to the existence of period-k solutions. Sometimes a two-dimensional Poincaré map becomes a continuous closed curve. The motion in this case could indicate a quasi-periodic or motion on the torus. If a two-dimensional map does not consist of either a finite set of points or a closed curve, and consists instead of an open curve or a fuzzy collection of points then the motion may be chaotic. Other tools are needed to characterize the chaotic nature of the attractors. The maximum Lyapunov exponent (LLE), explained in another section, is one of these tools.

A.6 Routes to Chaos

Theoretical, as well as experimental investigations, have revealed that there is no unique way to chaos. This was also shown in models studied in Chapters 17 and 18. Some of the possible scenarios are [149, 299, 344, 351]:

- Period-doubling route: Period-doubling is considered to be one of the

principal routes to chaotic behavior. This scenario has been backed by strong experimental evidence. In this route, one starts with a system with a periodic motion, then as the bifurcation parameter is varied, the system undergoes a secondary bifurcation to a periodic motion with twice the period of the original motion. The system may bifurcate further to a periodic solution with forth the period of the first motion and so on. Successive period-doubling sequences can therefore take place and lead to chaos. One interesting feature of this route is that the critical value of the bifurcation parameter, e.g., λ, at which successive period-doubling bifurcations occur obey the following rule

$$\lim_{k \to +\infty} \frac{\lambda_k - \lambda_{k-1}}{\lambda_{k+1} - \lambda_k} \to \delta = 4.66920126 \tag{A.32}$$

The number δ is called the Feigenbaum number.

- Torus route: In this route proposed by Newhouse et al. [262], chaos developed through three bifurcations. The system first undergoes a Hopf bifurcation and then a second transition to a two-dimensional torus. Chaotic motions occur when the system undergoes another bifurcation so that the three simultaneous coupled limit cycles are present. This scenario was also justified experimentally.

- Intermittency route: In this third route, one observes a long period of regular motions with interrupted bursts of erratic oscillations of finite durations. As the bifurcation parameter is varied, the chaotic bursts become longer and occur more frequently until the entire motion becomes chaotic. Three types of intermittencies for the onset of chaos were proposed by Pomeau and Manneville [289].

These three scenarios to chaos, that were found in Chapters 17 and 18, are considered as local routes, since the transition is marked by a change in the equilibrium points or limit cycles. Another category of routes are termed global bifurcation since the transition is due to interactions of trajectories with various unstable steady states and limit cycles in the state space. Some examples are the so-called homoclinic and heteroclinic orbits that may appear suddenly as the bifurcation parameter is varied [366].

A.7 Type II and III Hopf Degeneracies

In this part of the appendix, we present the methodology developed by Golubitsky and Langford [131] and modified later by Farr [111] for the study of type II and III Hopf degeneracies, mentioned in Chapter 3.

Consider the system of ordinary differential equations (ODEs)

$$\frac{dx}{dt} + F(x, \theta) = 0 \tag{A.33}$$

Suppose that the singularity under investigation is located at the origin and that the linearization of F at the Hopf point has a pair of eigenvalues $\pm iw$ and no other eigenvalues on the imaginary axis. Applying the Lyapunov–Schmidt reduction technique to the operator L defined by $Lu = \frac{du}{dx} + Au$ where A is the Jacobian matrix of F, Golubitsky and Langford [131] showed that the original bifurcation problem can be reduced to the following single implicitly defined function

$$G(x, \theta) = a(x^2, \theta)x = 0 \tag{A.34}$$

with

$$a(0, 0) = 0 \tag{A.35}$$

where $x = 0$ is for steady-state solution while the solutions of $a = 0$ for $x \neq 0$ represent periodic solutions of the original system. The analysis can be further simplified by defining $z = x^2$. The H2 and H3 Hopf hypotheses are equivalent to

$$a_\theta \neq 0 \tag{A.36}$$

$$a_z \neq 0 \tag{A.37}$$

with $\nu' = a_\theta$ and $a_1 = -\frac{a_z}{a_\theta}$. The singularity theory can be used to study the nontrivial solutions of the single scalar function $a(z, \theta) = 0$.

Denote by a_{ij} the derivatives of a

$$a_{ij} = \frac{\partial^{i+j} a}{\partial z^i \partial \theta^j} \tag{A.38}$$

Next, we present the formulas derived in [111, 131] for the calculations of the coefficients a_{ij}. First, we define the symmetric k-linear form

$$F^k : \qquad \Re^n \times \cdots \times \Re^n \to \Re^n \tag{A.39}$$

$$F_i^k(v^1, \cdots, v^k) = \sum_{m_1=1}^{n} \cdots \sum_{m_k=1}^{n} \frac{\partial^k F_i(0,0)}{\partial v_{m_1} \cdots \partial v_{m_k}} (v^1, \cdots, v^k) \tag{A.40}$$

Similarly,

$$F^{k,l}(v^1, \cdots, v^k) = (d_u^k \frac{\partial^l F}{\partial \theta^l})_{(0,0)}(v^1, \cdots, v^k) \tag{A.41}$$

The bifurcation Equations (A.34) are reduced to the following forms

$$g_1 = p(x^2, \theta, \tau)x = 0 \tag{A.42}$$

$$g_2 = q(x^2, \theta, \tau)x = 0 \tag{A.43}$$

The Taylor series expansion for p and q with $z = x^2$ yields

$$p(z, \theta, \tau) = \sum p_{ijk} z^i \theta^j z^k \tag{A.44}$$

$$q(z, \theta, \tau) = \sum q_{ijk} z^i \theta^j z^k \tag{A.45}$$

Define

$$p_{ijk} = \frac{1}{(2i+1)!j!k!} \frac{\partial^{2i+1+j+k} g_1}{\partial x^{2i+1} \partial \theta^j \partial \tau^k} \tag{A.46}$$

Similarly for q_{ijk} and g_2. The term a can be written as

$$a(z, \theta) = \sum a_{ij} z^i \theta^j \tag{A.47}$$

The formulas for the coefficients a_{ij} are:

$$\begin{aligned}
a_{00} &= 0 && \text{(A.48)}\\
a_{01} &= p_{010} && \text{(A.49)}\\
a_{10} &= p_{100} && \text{(A.50)}\\
a_{02} &= p_{020} && \text{(A.51)}\\
a_{20} &= p_{200} + p_{101} q_{100}/w && \text{(A.52)}\\
a_{11} &= p_{110} + p_{101} q_{010}/w && \text{(A.53)}\\
a_{03} &= p_{030} + p_{021} q_{010}/w && \text{(A.54)}\\
a_{30} &= p_{300} + p_{101}(q_{200}/w + q_{101} q_{100}/w^2) \\
&\quad + p_{201} q_{100}/w + p_{102} q_{100}^2/w^2 && \text{(A.55)}
\end{aligned}$$

Next, we give the formulae for the p_{ijk} coefficients. Computation of these coefficients proceeds in two steps. In a first step, linear algebra problems must be solved to obtain complex-valued vectors that are coefficients in the Fourier series for the function $w(x, \theta, \tau)$. In the second step, these vectors are used to evaluate p and q coefficients [131, 132]. The first set of vectors are found by solving

$$\begin{aligned}
A a_0 &= -0.5 F^2(c, \bar{c}) && \text{(A.56)}\\
(A - 2iwI) a_2 &= -0.25 F^2(c, \bar{c}) && \text{(A.57)}
\end{aligned}$$

where c is the eigenvector of the Jacobian matrix A corresponding to the eigenvalue iw. The first-order coefficients are:

$$\begin{aligned}
a_{01} &= p_{010} = -0.5Re\ \mathrm{F^{11}c} && \text{(A.58)}\\
q_{010} &= 0.5Im\ \mathrm{d^*F^{11}c} && \text{(A.59)}\\
a_{10} &= p_{100} = -0.25Re\ \mathrm{d^*[F^2(c,a_0) + F^2(\bar{c},a_2)} \\
&\quad +0.25F^3(c,c,\bar{c})] && \text{(A.60)}\\
q_{100} &= 0.25Im\ \mathrm{d^*[F^2(c,a_0) + F^2(\bar{c},a_2) + 0.25F^3(c,c,\bar{c})]} && \text{(A.61)}
\end{aligned}$$

where d is the eigenvector of the transpose (A^*) of A corresponding to the eigenvalue $-iw$.
For the second-order a_{ij} $(i+j=2)$, the following linear algebra equations are to be solved:

$$\begin{aligned}
(A-iwI)a_1 &= -1.5[F^2(c,a_0) + F^2(\bar{c},a_2) + 0.25F^3(c,c,\bar{c})] \\
&\quad +0.75d^*[F^2(c,a_0) + F^2(\bar{c},a_2) + 0.25F^3(c,c,\bar{c})] && \text{(A.62)}\\
(A-3iwI)a_3 &= -1.5F^2(c,a_2) - 0.125F^3(c,c,c) && \text{(A.63)}\\
Ab_0 &= -2[F^2(c,\bar{a}_1) + F^2(\bar{c},a_1)] - 3F^2(a_0,a_0) - 6F^2(a_2,\bar{a}_2) \\
&\quad -3F^3(c,\bar{c},a_0) - 1.5F^3(c,c,\bar{a}_2) - 1.5F^3(\bar{c},\bar{c},a_2) \\
&\quad -0.375F^4(c,c,\bar{c},\bar{c}) && \text{(A.64)}\\
(A-2iwI)b_2 &= -2[F^2(c,a_1) + F^2(\bar{c},a_3) + 3F^2(a_0,a-2)] - 3[F^3(c,\bar{c},a_2) \\
&\quad +0.5F^3(c,c,a)] - 0.25F^4(c,c,c,\bar{c}) && \text{(A.65)}\\
(A-iwI)c_1 &= -F^{11}c + 0.5[d^*F^{11}]c && \text{(A.66)}\\
(A-2iwI)c_2 &= 2iwa_2 && \text{(A.67)}\\
Ad_0 &= -0.5[F^2(c,\bar{c}_1) + F^2(\bar{c},c_1) + F^{21}(c,\bar{c})] - F^{11}a_0 && \text{(A.68)}\\
(A-2iwI)d_2 &= -0.5F^2(c,c_1) - 0.25F^{21}(c,c) - F^{11}a_2 && \text{(A.69)}
\end{aligned}$$

The higher order coefficients are now obtained from

$$\begin{aligned}
p_{200} &= (-1/24)Re\ \mathrm{d^*[0.5F^2(c,b_0) + 0.5F^2(\bar{c},b_2)} && \text{(A.70)}\\
&\quad +2F^2(a_0,a_1) + F^2(a_2,\bar{a}_1) + F^2(\bar{a}_2,a_3) && \text{(A.71)}\\
&\quad +0.5F^3(c,c,\bar{a}_1) + F^3(c,\bar{c},a_1) + 0.5F^3(\bar{c},\bar{c},a_3) && \text{(A.72)}\\
&\quad +3[F^3(c,a_2,\bar{a}_2) + F^3(\bar{c},a_0,a_2) + 0.5F^3(c,a_0,a_0)] && \text{(A.73)}\\
&\quad +0.25[F^4(c,c,c,\bar{a}_2) + 3F^4(c,c,\bar{c},a_0) + 3F^4(c,\bar{c},\bar{c},a_2)] && \text{(A.74)}\\
&\quad +(1/16)F^5(c,c,c,\bar{c},\bar{c})] && \text{(A.75)}
\end{aligned}$$

$$p_{110} = -0.25Re\ \mathrm{d}^*[\mathrm{F}^2(\mathrm{c}_1, \mathrm{a}_0) + \mathrm{F}^2(\bar{\mathrm{c}}_1, \mathrm{a}_2) + \mathrm{F}^2(\mathrm{c}, \mathrm{d}_0) \quad \text{(A.76)}$$

$$+F^2(\bar{c}, d_2) + F^{21}(c, a_0) + F^{21}(\bar{c}, a_2) + (2/3)F^{11}a_1 \quad \text{(A.77)}$$

$$+0.25F^3(c, c, \bar{c}) + 0.5F^3(c, \bar{c}, c_1) + 0.25F^{31}(c, c, \bar{c}) \quad \text{(A.78)}$$

$$p_{101} = -0.25Re\ d^*F^2(\bar{c}, c_2) \quad \text{(A.79)}$$

$$p_{020} = -0.5Re\ d^*[F^{11}c_1 + 0.5F^{12}c] \quad \text{(A.80)}$$

$$q_{020} = 0.5Im\ d^*[F^{11}c_1 + 0.5F^{12}c] \quad \text{(A.81)}$$

$$p_{011} = 0 \quad \text{(A.82)}$$

$$q_{002} = 0 \quad \text{(A.83)}$$

Each $q_{i,j,k}$ is obtained from the corresponding $p_{i,j,k}$ by reversing the sign and taking the imaginary part instead of the real part.

A.8 Stroboscopic Technique

Forced systems such as the one discussed in Chapter 18, can be analyzed in a number of ways. One way is to compute stroboscopic maps. The phase portrait of the forced two-dimensional system is three-dimensional spanned by the two state variables and time. When the forcing term is periodic with period T, a Poincaré section is obtained simply by plotting the points (x_1, x_2) in the plane projection whenever t is the multiple of the period T. Any surface transverse to the bundle of trajectories may be used to define a Poincaré section, the intersection of the bundle with the surface. The idea of inspecting the phase projection only at specific times ($t = mT$) is to see a sequence of dots representing the Poincaré mapping. This is also called the stroboscopic technique [351]. Transient motions appear as scattered dots. The emergence of a stable fundamental solution would be seen as the repetition of a single fixed-mapping point. The eventual emergence of stable subharmonics of order n would be seen as jumps between n fixed points. If the Poincaré map does not consist of either a finite set of points or closed curve then the motion may be chaotic. Here the map may consist of an open curve or a fuzzy collection of points. For small forcing amplitudes of the limit cycle, the main important phenomenon is entrainment. In this case, the forcing entrains the system and the response of the system becomes periodic and its period is an integer multiple of the forcing period. At larger amplitudes of forcing, only unique period-1 attractors are found having the same period as the forcing period. The system is called fully entrained because the forcing completely overpowered the natural system. Between small and very large forcing amplitudes, the intermediate region gives rise to dynamics that are dependent on the inherent nonlinearity of each system.

A.9 Computing Period of Limit Cycle

In this section, we describe the numerical procedure for the accurate determination of the natural period of limit cycles of the two-dimensional unforced system studied in Chapter 18. The autonomous system can be written, using a change of variables, in the following dimensionless form

$$\frac{dx}{dt} = Tf(x, \lambda) \tag{A.84}$$

with boundary conditions

$$x^0(t) = x^0(t = 1) \tag{A.85}$$

where T is the unknown period of the limit cycle and x_0 is the vector of initial states. The problem is a two-boundary value problem that can be solved using a shooting method. The integration of Equation (A.84) from $t = 0$ to $t = 1$ yields

$$x_i(1) = f_i(x_1^0, x_2^0, T), \quad (i = 1, 2) \tag{A.86}$$

The solution must satisfy Equation (A.86), which yields

$$f_i(x_1^0, x_2^0, T) - x_i^0(0) = 0, \quad (i = 1, 2) \tag{A.87}$$

Denote by $\phi_i(x_1^0, x_2^0, T), (i = 1, 2)$ the two last equations. Note that the three unknowns are x_1^0, x_2^0, and T. A third equation comes from fixing one of the steady-state components x_{ss1} or x_{ss2} that comes from solving the unforced system. This anchor equation ensures that the fixed-state variable is lying on the limit cycle. The system of two nonlinear equations can be solved by the Newton Method [1]. The Jacobian matrix is

$$J = \begin{pmatrix} \frac{\partial \phi_1}{\partial x_1^0} & \frac{\partial \phi_1}{\partial T} \\ \frac{\partial \phi_2}{\partial x_1^0} & \frac{\partial \phi_2}{\partial T} \end{pmatrix} \tag{A.88}$$

which becomes

$$J = \begin{pmatrix} \frac{\partial f_1}{\partial x_1^0} - 1 & \frac{\partial f_1}{\partial T} \\ \frac{\partial f_2}{\partial x_1^0} & \frac{\partial f_2}{\partial T} \end{pmatrix} \tag{A.89}$$

The different elements of the Jacobian matrix are evaluated by integrating the following variational equation, simultaneously with Equation (A.84).

Let

$$\Psi_{i1} = \frac{\partial x_i}{\partial x_1^0}, \quad (i = 1, 2) \tag{A.90}$$

and

$$\Omega_i = \frac{\partial x_i}{\partial T}, \quad (i = 1, 2) \tag{A.91}$$

Taking the derivative of Equation (A.84) with respect to x_1^0 and T yields the following variational equation

$$\frac{d\Psi_{i1}}{dt} = T \sum_{k=1}^{2} \frac{\partial f_i}{\partial x_k} \Psi_{ki}, \quad (i = 1, 2) \tag{A.92}$$

$$\frac{d\Omega_i}{dt} = f_i + T \sum_{k=1}^{2} \frac{\partial f_i}{\partial x_k} \Omega_k, \quad (i = 1, 2) \tag{A.93}$$

with the following initial conditions

$$\Psi_{i1}(0) = \delta_{i1}, \quad \Omega_i(0) = 0, \quad (i = 1, 2) \tag{A.94}$$

δ_{ij} is the Kronecker symbol. Integrating these variational equations simultaneously with Equation (A.84) to $t = 1$ gives the elements of the Jacobian matrix as follows

$$\frac{\partial f_i}{\partial x_1^0} = \Psi_{i1}, \quad (i = 1, 2) \tag{A.95}$$

$$\frac{\partial f_i}{dT} = \Omega_i, \quad (i = 1, 2) \tag{A.96}$$

A.10 Lyapunov Exponents

Lyapunov exponents are important quantitative measures of the sensitive dependence of trajectories of a dynamical system on initial conditions. It is the average rate of divergence or convergence of two neighboring trajectories in the phase space. The number of Lyapunov exponents is equal to the dimension of the dynamical system. When the largest Lyapunov exponent (LLE) is negative, the system is nonconservative (dissipative) and it attracts to a fixed point or stable limit cycle. If LLE is zero such systems exhibit Lyapunov stability, i.e., they are conservative and in a steady-state mode. When, on the other hand, the LLE is positive, the system is chaotic and unstable. Nearby trajectories diverge irrespective of how close they are. In order to define in simple terms the Lyapunov exponents, consider two orbits, a "reference" orbit and a "test" orbit, separated at initial time by a small phase space distance h_0. If the motion is chaotic, the orbits will, by definition, separate by a phase

space distance $h(t)$ at an exponential rate [251, 315]. The largest LLE is a measure of this rate of separation:

$$LLE = \lim_{t\to\infty} \frac{1}{t} ln \frac{h(t)}{h_0} \tag{A.97}$$

Now consider that the dynamical system is described by the following ODE

$$\dot{x} = f(x,t) \text{ with } x(0) = x_0 \tag{A.98}$$

When the perturbation is small, the system can be described by the linearized system

$$\dot{h} = f_x(x,t)h \tag{A.99}$$

The trajectories $h(t)$ satisfy the following equation

$$h(t) = \Phi(t)h(0) \tag{A.100}$$

where Φ is the fundamental solution matrix satisfying the variational equation

$$\dot{\Phi} = f_x(x,t)\Phi, \quad \Phi(0) = I \tag{A.101}$$

Therefore, using some defined norm $||.||$, the term $\frac{||h(t)||}{||h(0)||} = \frac{||\Phi(t)h(0)||}{||h(0)||}$ is a measure of the expansion in the direction of $h(0)$. The direct integration of Equation (A.101) for a chaotic system is not workable given that at least one Lyapunov exponent is positive, which implies that the solution is unbounded as time approaches infinity. In order to remedy the problem, the techniques to compute the largest Lyapunov exponent rely on a process during which successive integration/normalization procedures are applied to the fundamental matrix. To visualize the procedure, let $h(T)$ be the separation. Define a rescaling parameter

$$\alpha_1 = \frac{h(T)}{h(0)} \tag{A.102}$$

then

$$\lambda(T) = \frac{1}{T} ln(\frac{h(T)}{h(0)}) = \frac{1}{T} ln(\alpha_1) \tag{A.103}$$

The perturbed orbit is then rescaled. Subsequent rescaling yields

$$\lambda(2T) = \frac{1}{2T} ln(\frac{h(2T)\alpha_1}{h(0)}) = \frac{1}{2T} ln(\alpha_1\alpha_2) \tag{A.104}$$

$$\lambda(3T) = \frac{1}{3T} ln(\frac{h(3T)\alpha_2\alpha_1}{h(0)}) = \frac{1}{3T} ln(\alpha_1\alpha_2\alpha_3) \tag{A.105}$$

This procedure of integration/normalization is repeated for K times. When K is large enough

$$LLE = \frac{1}{KT} \sum_{i\,=\,1}^{K} ln(\alpha_i) \tag{A.106}$$

This page intentionally left blank

Bibliography

[1] M.E.E. Abashar. *Bifurcation, Instability and Chaos in Fluidized Bed Catalytic Reactors*. PhD thesis, University of Salford, Salford, UK, 1994.

[2] M.E.E. Abashar and S.S.E.H. Elnashaie. Dynamic and chaotic behavior of periodically forced fermentors for bioethanol production. *Chem. Eng. Sci.*, 65:4894–4905, 2010.

[3] P.A. Abrams and L.R. Ginzburg. The nature of predation: Prey dependent, ratio dependent or neither? *Trends Ecol. Evol.*, 15:337–341, 2000.

[4] E.M. Abulesz and G. Lyberatos. Periodic optimization of continuous microbial growth processes. *Biotechnol. Bioeng.*, 29:1059–1065, 1987.

[5] I.M. Abu-Reesh. Optimal design of chemostats connected in series with microbial growth. *Chem. Biochem. Eng. Q.*, 18:167–175, 2004.

[6] P. Agrawal, G. Koshy, and M. Ramseier. An algorithm for operating a fed-batch fermentor at optimum specific growth rate. *Biotechnol. Bioeng.*, 33:115–125, 1989.

[7] P. Agrawal, C. Lee, H.C. Lim, and D. Ramkrishna. Theoretical investigations of dynamic behavior of isothermal continuous stirred tank biological reactors. *Chem. Eng. Sci.*, 37:453–462, 1982.

[8] P. Agrawal and H.C. Lim. Analyses of various control schemes for continuous bioreactors. In A. Feietcher, editor, *Advances in Biochemical Engineering Biotechnology*, Vol. 30, pages 61–90. Springer-Verlag, 1984.

[9] S. Aiba and J. Koizumi. Effects of temperature on plasmid stability and penicillinase productivity in a transformant *Bacillus stearothermophilus*. *Biotechnol. Bioeng.*, 26:1026–1031, 1984.

[10] S. Aiba and M. Shoda. Reassessment of the product inhibition in alcohol fermentation. *J. Ferment. Technol.*, 47:790–794, 1969.

[11] S. Aiba, M. Shoda, and M. Nagatani. Kinetics of product inhibition in alcohol fermentation. *Biotechnol. Bioeng.*, 10:845–864, 1968.

[12] A. Ajbar. Classification of stability behavior of bioreactors with wall attachment and substrate-inhibited kinetics. *Biotechnol. Bioeng.*, 72:166–176, 2001.

[13] A. Ajbar. Classification of static behavior of a class of unstructured models of continuous processes. *Biotechnol. Prog.*, 17:597–605, 2001.

[14] A. Ajbar. On the existence of oscillatory behavior in unstructured models of bioreactors. *Chem. Eng. Sci.*, 56:1991–1997, 2001.

[15] A. Ajbar. Operability of continuous bioprocesses: Static behavior of a large class of unstructured models. *Eng. Life Sci.*, 1:187–196, 2001.

[16] A. Ajbar. Periodic behaviour of a class of unstructured kinetic models for continuous bioreactors. *Can. J. Chem. Eng.*, 79:791–799, 2001.

[17] A. Ajbar. Stability analysis of the biodegradation of mixed wastes in a continuous bioreactor with cell recycle. *Water Res.*, 35:1201–1208, 2001.

[18] A. Ajbar. Classification of static and dynamic behavior in chemostat for plasmid-bearing, plasmid-free mixed recombinant cultures. *Chem. Eng. Commun.*, 189:1130–1154, 2002.

[19] A. Ajbar. Study of the operability of nonideal continuous bioreactors. *Chem. Eng. Commun.*, 198:385–415, 2011.

[20] A. Ajbar. On the improvement of performance of bioreactors through periodic forcing. *Comput. Chem. Eng.*, 198:385–415, 2011.

[21] A. Ajbar and M. Alahmad and E. Ali. On the dynamics of biodegradation of wastewaters in aerated continuous bioreactors. *Math. Comput. Model.*, (in press).

[22] A. Ajbar and K. Alhumaizi. Biodegradation of substitutable substrates in a continuous bioreactor with cell recycle: A study of static bifurcation. *Math. Comput. Model.*, 31:159–174, 2000.

[23] A. Ajbar and K. Alhumaizi. Microbial competition: Study of global branching phenomena. *AIChEJ*, 46:321–334, 2000.

[24] A. Ajbar and K. Alhumaizi. Gas phase polyethylene reactors: A global study of stability behaviour. *Chem. Eng. Res. Des.*, 79:195–208, 2001.

[25] A. Ajbar, K. Alhumaizi, and S.S.E.H. Elnashaie. Classification of static and dynamic behavior in a fluidized-bed catalytic reactor. *Chem. Eng. J.*, 84:503–516, 2001.

[26] A. Ajbar and G. Ibrahim. Stability and bifurcation of an unstructured model of a bioreactor with cell recycle. *Math. Comput. Model.*, 25:31–48, 1997.

[27] A. Ajbar and G. Ibrahim. Periodic and nonperiodic oscillatory behavior in a model for activated sludge reactors. *Math. Comput. Model.*, 25:9–27, 1997.

[28] H.R. Akçakaya, R. Arditi, and L.R. Ginzburg. Ratio-dependent predation: An abstraction that works. *Ecology*, 76:995–1004, 1995.

[29] A. Al-Rabiah and A. Ajbar. Study of the operability of a continuous bioreactor for the pre-fermentation of cheese. *Eng. Life. Sci.*, 8:157–166, 2008.

[30] K. Alhumaizi and A. Ajbar. Dynamics of predator-prey interactions in continuous cultures. *Eng. Life. Sci.*, 5:139–147, 2005.

[31] K. Alhumaizi, E. Ali, and A. Ajbar. Study of some unique features of ratio-dependent models for predator-prey-substrate interactions in continuous cultures. *Chem. Eng. Commun.*, 193:1164–1184, 2006.

[32] K. Alhumaizi, A. Alwan, and A. Ajbar. Competition of plasmid-bearing and plasmid-free organisms in a chemostat: A study of bifurcation phenomena. *Math. Comput. Model.*, 44:342–367, 2006.

[33] K. Alhumaizi and R. Aris. *Surveying A Dynamical System: A Study of the Gray-Scott Reaction in a Two-Phase Reactor*. Longman, 1995.

[34] K. Alhumaizi. *Dynamics of an Autocatalytic Reaction in a Membrane Reactor*. PhD thesis, University of Minnesota, Minnesota, 1994.

[35] J.F. Andrews. A mathematical model for the continuous culture of microorganisms utilizing inhibitory substrates. *Biotechnol. Bioeng.*, 10:707–723, 1968.

[36] R. Arditi and L.R. Ginzburg. Coupling in predator-prey dynamics: Ratio dependence. *J. Theor. Biol.*, 139:311–326, 1989.

[37] R. Aris and A.E. Humphrey. Dynamics of a chemostat in which two organisms compete for a common substrate. *Biotechnol. Bioeng.*, 19:1375–1386, 1977.

[38] V.I. Arnold. Local normal forms of functions. *Invent. Math.*, 35:87–109, 1976.

[39] V.I. Arnold. *Singularity Theory*. London Mathematical Society Lecture Notes, 53. Cambridge University Press, Cambridge, 1981.

[40] I.C.P. Astudillo and C.A.C. Alzate. Importance of stability study of continuous systems for ethanol production. *J. Biotechnol.*, 151:43–55, 2011.

[41] J.E. Bailey and D. F. Ollis. *Biochemical Engineering Fundamentals*. McGraw-Hill, New York, 2nd edition, 1986.

[42] V. Balakotaiah and D. Luss. Analysis of the multiplicity patterns of a CSTR. *Chem. Eng. Commun.*, 13:111–132, 1981.

[43] V. Balakotaiah and D. Luss. Structure of the steady state solutions of lumped-parameter chemically reacting systems. *Chem. Eng. Sci.*, 37:1611–1623, 1982.

[44] V. Balakotaiah and D. Luss. Multiplicity features of reacting systems: Dependence of the steady states of a CSTR on the residence time. *Chem. Eng. Sci.*, 38:1709–1721, 1983.

[45] V. Balakotaiah and D. Luss. Global analysis of the multiplicity features of multi-reaction lumped-parameter systems. *Chem. Eng. Sci.*, 39:865–881, 1984.

[46] V. Balakotaiah, D. Luss, and B. Keyfitz. Steady state multiplicity analysis of lumped-parameter systems described by a set of algebraic equations. *Chem. Eng. Commun.*, 36:121–147, 1985.

[47] B.C. Baltzis and A.G. Fredrickson. Competition of two microbial populations for a single resource in a chemostat when one of them exhibits wall attachment. *Biotechnol. Bioeng.*, 25:2419–2439, 1983.

[48] B.C. Baltzis and A. G. Fredrickson. Coexistence of two microbial populations competing for a renewable resource in a non-predator-prey system. *Bull. Math. Biol.*, 46:155–174, 1984.

[49] B.C. Baltzis and A.G. Fredrickson. Limitation of growth rate by two complementary nutrients: Some elementary but neglected considerations. *Biotechnol. Bioeng.*, 31:75–86, 1988.

[50] B.C. Baltzis, D.M. Tsangaris, and K.W. Wang. Utilization of substitutable substrates in a bioreactor under cycling: A study on process dynamics and optimization. *Chem. Eng. Sci.*, 51:3801–3811, 1996.

[51] M. Bandyopadhyay and J. Chattopadhyay. Ratio-dependent predator-prey model: Effect of environmental fluctuation and stability. *Nonlinearity*, 18:913–936, 2005.

[52] C.D. Bazua and C.R. Wilke. Ethanol effects on the kinetics of a continuous fermentation with *Saccharomyces cerevisiae*. *Biotechnol. Bioeng. Symp.*, 7:105–118, 1977.

[53] A.D. Bazykin. Nonlinear dynamics of interacting populations. *World Scientific Series on Nonlinear Science*, Vol. 11, Singapore, 1998.

[54] K.-H. Bellgardt. Analysis of synchronous growth of baker's yeast: Part I: Development of a theoretical model for sustained oscillations. *J. Biotechnol.*, 35:19–33, 1994.

[55] J. Beltran-Heredia, J. Torregrosa, J.R. Dominguez, and J. Garcia. Ozonation of black-table-olive industrial wastewaters: effect of an aerobic biological pretreatment. *J. Chem. Technol. Biotechnol.*, 75:561–568, 2000.

[56] F.S. Berezovskaya, G. Karev, and R. Arditi. Parametric analysis of the ratio-dependent predator-prey model. *J. Math. Biol.*, 43:221–246, 2001.

[57] F.S. Berezovskaya and N.B. Medvedeva. A complicated singular point of center-focus type and the Newton diagram. In A.D. Bazykin and Y. Zarkhin, editors, *Mathematics and Modelling*, pages 63–81. Nova Science Publishers, New York, 1993.

[58] F.S. Berezovskaya and N.B. Medvedeva. A complicated singular point of center-focus type and the Newton diagram. *Selecta Mathematica*, 13:1, 1994.

[59] A. Bertucco, P. Volpe, H.E. Klei, T.F. Anderson, and D.W. Sundstrom. The stability of activated sludge reactors with substrate inhibition kinetics and solids recycle. *Water Res.*, 24:169–176, 1990.

[60] S.C. Bhattacharya and P.Q. Khai. Kinetics of anaerobic cowdung digestion. *Energy*, 12:497–500, 1987.

[61] G. Birol, C. Ündey, S. Parulekar, and A. Çinar. A morphologically structured model for penicillin production. *Biotechnol. Bioeng.*, 77:538–552, 2002.

[62] H.W. Blanch and D. S. Clark. *Biochemical Engineering*. Marcel Dekker, New York, 1997.

[63] B.W. Brandt, F. D. Kelpin, I. M. van Leeuwen, and S. A. Kooijman. Modelling microbial adaptation to changing availability of substrates. *Water Res.*, 38:1003–1013, 2004.

[64] B.W. Brandt, I. M. van Leeuwen, and S. A. Kooijman. A general model for multiple substrate biodegradation: Application to co-metabolism of structurally non-analogous compounds. *Water Res.*, 37:4843–4854, 2003.

[65] K.E. Brenan, S.L. Campbell, and L.R. Petzold. *Numerical Solution of Initial-Value Problems in Differential-Algebraic Equations*. North-Holland, New York, 1989.

[66] L.J. Bruce, D.B. Axford, B. Ciszek, and A.J. Daugulis. Extractive fermentation by *Zymomonas mobilis* and the control of oscillatory behavior. *Biotechnol. Lett.*, 13:291–296, 1991.

[67] G.J. Butler and G.S.K. Wolkowicz. A mathematical model of the chemostat with a general class of functions describing nutrient uptake. *SIAM J. Appl. Math.*, 45:138–151, 1985.

[68] J.B. Busby and J.F. Andrews. Dynamic modeling and control strategies for the activated sludge process. *J. Water Pollut. Control Fed.*, 47:1055–1080, 1975.

[69] J.J. Byrd, H.-S. Xu, and R.R. Colwell. Viable but nonculturable bacteria in drinking water. *Appl. Environ. Microbiol.*, 57:875–878, 1991.

[70] A. Cammarota. *Study of the Dynamics of Biochemical Systems for Design and Operation of Continuous Bioreactors.* PhD thesis, Università Degli Studi Di Salerno, Italy, 2008.

[71] R.P. Canale. An analysis of models describing predator-prey interactions. *Biotech. Bioeng.*, 12:353–378, 1970.

[72] J. Carr. *Applications of Centre Manifold Theory.* Springer, New York, 1981.

[73] J.I. Castrillo and U.O. Ugalde. A general model of yeast energy metabolism in aerobic chemostat culture. *Yeast*, 10:185–197, 1994.

[74] L. Cazzador. Analysis of oscillations in yeast continuous cultures by a new simplified model. *Bull. Math. Biol.*, 53:685–700, 1991.

[75] B. Chance, R.W. Estabrook, and A. Ghosh. Damped sinusoidal oscillations of cytoplasmic reduced pyridine nucleotide in yeast cells. *Proc. Natl. Acad. Sci.*, 51:1244–1251, 1964.

[76] Y.K. Chang and H.C. Lim. Static characteristics of a continuous flow bioreactor containing antibiotic-resistant recombinant cells. *Biotechnol. Bioeng.*, 29:950–961, 1987.

[77] C. Cheng, Y.L. Huang, and S.-T. Yang. A novel feeding strategy for enhanced plasmid stability and protein production in recombinant yeast fedbatch fermentation. *Biotechnol. Bioeng.*, 56:23–31, 1997.

[78] C.T. Chi, J.A. Howell, and U. Pawlowsky. The regions of multiple stable steady states of a biological reactor with wall growth, utilising inhibitory substrates. *Chem. Eng. Sci.*, 29:207–211, 1974.

[79] S.-N. Chow and J. K. Hale *Methods of Bifurcation Theory.* Springer, New York, 1982.

[80] G.-S. Chuang, A.-C. Chao, P.-Y. Ho, and H.-Y. Li. Computational multiple steady states in enzymatically catalyzed oxidation of monophenols by tyrosinase in an isothermal CSTR. *Biochem. Eng. J.*, 21:161–170, 2004.

[81] D.E. Contois. Kinetics of bacterial growth: relationship between population density and specific growth rate of continuous cultures. *J. Gen. Microbiol.*, 21:40–50, 1959.

[82] N. S. Cooper, M. E. Brown, and C.A. Cauleott. A mathematical method for analyzing plasmid stability in microorganism. *J. Gen. Microbiol.*, 133:1871–1880, 1987.

[83] G.A. Cordonier, L.D. Schmidt, and R.Aris. Forced oscillations of chemical reactors with multiple steady states. *Chem. Eng. Sci.*, 45:1659–1675, 1990.

[84] J.D. Crawford. Introduction to bifurcation theory. *Rev. Mod. Phys.*, 63:991–1037, 1991.

[85] P.S. Crooke, C.J. Wei, and R.D. Tanner. Effect of the specific growth rate and yield expressions on the existence of oscillatory behavior of a continuous fermentation model. *Chem. Eng. Commun.*, 6:333–347, 1980.

[86] P. D. D'Adamo, A. F. Rozich, and A. F. Gaudy. Analysis of growth data with inhibitory carbon sources. *Biotechnol. Bioeng.*, 26:397–804, 1984.

[87] A.J. Daugulis, P.J. McLellan, and J. Li. Experimental investigation and modeling of oscillatory behavior in the continuous culture of *Zymomonas mobilis*. *Biotechnol. Bioeng.*, 56:99–105, 1997.

[88] B.H. Davison and G. Stephanopoulos. Effect of pH oscillations on a competing mixed culture. *Biotechnol. Bioeng.*, 28:1127–1137, 1986.

[89] S. F. de Azevedo, B. Dahm, and F. R. Oliveira. Hybrid modelling of biochemical processes: A comparison with the conventional approach. *Comput. Chem. Eng.*, 21:S571–S576, 1997.

[90] A. de Raucourt, D. Girard, Y. Prigent, and P. Boyaval. Lactose continuous fermentation with cells recycled by ultrafiltration and lactate separation by electrodialysis: modelling and simulation. *Appl. Microbiol. Biotech.*, 30:521–527, 1989.

[91] D.L. DeAngelis, R.A. Goldstein, and R.V. O'Neill. A model for trophic interaction. *Ecology*, 56:881–892, 1975.

[92] R. W. Dennis and R. L. Irvine. A stoichiometric model of bacterial growth. *Wat. Res.*, 15:1363–1373, 1981.

[93] A. Dhooge, W. Govaerts, and Yu. A. Kuznetsov. MATCONT: A MATLAB package for numerical bifurcation analysis of ODEs. *ACM. TOMS.*, 29:141–146, 2003.

[94] D. DiBiasio, H.C. Lim, and W.A. Weigand. An experimental investigation of stability and multiplicity of steady states in a biological reactor. *AIChEJ*, 27:284–292, 1981.

[95] D. DiBiasio, H.C. Lim, W.A. Weigand, and G.T. Tsao. Phase-plane analysis of feedback control of unstable steady states in a biological reactor. *AIChEJ*, 24:686–693, 1978.

[96] R. Dillon, L. Fauci, A. Fogelson, and D. Gaver. Modeling biofilm processes using the immersed boundary method. *J. Comput. Phys.*, 129:57–73, 1996.

[97] X. Ding and C. Lu. Existence of positive periodic solution for ratio-dependent N-species difference system. *App. Math. Model.*, 33:2748–2756, 2009.

[98] E.J. Doedel and J.P. Kernévez. *AUTO: Software for Continuation and Bifurcation Problems in Ordinary Differential Equations.* Caltech, Pasadena, 1986.

[99] S.N. Dokianakis, M. Kornaros, and G. Lyberatos. Effect of wall growth on the kinetic modeling of nitrite oxidation in a CSTR. *Biotechnol. Bioeng.*, 93:718–726, 2006.

[100] M. M. Domach, S. K. Leung, R. E. Cahn, G. G. Cocks, and M. L. Shuler. Computer model for glucose-limited growth of a single cell of *Escherichia coli* B/r-A. *Biotechnol. Bioeng.*, 26:203–216, 1984.

[101] R.G. Dondo and D. Marques. Optimal control of a batch bioreactor: A study on the use of an imperfect model. *Process Biochem.*, 37:379–385, 2001.

[102] R.M. Donlan. Biofilms: Microbial life on surfaces. *Emerg. Infect. Dis.*, 8:881–890, 2002.

[103] J.F. Drake and M.Tsuchiya. Predation on *Escherichia coli* by *Colpoda steinii. Appl. Environ. Microb.*, 31:870–874, 1976.

[104] S. Dutta, R. Chowdhury, and P. Bhattacharya. Stability and response of bioreactor: An analysis with reference to microbial reduction of SO_2. *Chem. Eng. J.*, 133:343–354, 2007.

[105] H.J. Eberl, C. Picioreanu, J.J. Heijnen, and M.C.M. van Loosdrecht. A three-dimensional numerical study on the correlation of spatial structure, hydrodynamic conditions, and mass transfer and conversion in biofilms. *Chem. Eng. Sci.*, 55:6209–6222, 2000.

[106] I. Edissonov. Bifurcation analysis of biotechnological process regarding the cultural medium viscosity. *Syst. Anal. Model. Sim.*, 24:307–316, 1996.

[107] T. Egli. The ecological and physiological significance of the growth of heterotrophic microorganisms with mixtures of substrates. *Adv. Microb. Ecol.*, 14:305–386, 1995.

[108] S.D. Ehrlich, B. Niaudet, and B. Michel. Use of plasmids from *Staphylococcus aureus* for cloning of DNA in *Bacillus subtilis. Curr. Top. Microbiol. Immunol.*, 96:19–29, 1982.

[109] S.S.E.H. Elnashaie and N.F.Mohamed. Implications of bifurcation/chaos on the design, operation and control of industrial riser-reactor FCC units. *Chem. Eng. Commun.*, 191:813–831, 2004.

[110] A. A. Esener, T. Veerman, J. A. Roels, and N.W.F. Kossen. Modeling of bacterial growth: Formulation and evaluation of a structured model. *Biotechnol. Bioeng.*, 24:1749–1764, 1982.

[111] W.W. Farr. *Mathematical Modelling: Dynamics and Multiplicity.* PhD thesis, University of Minnesota, Minnesota, USA, 1986.

[112] C.J. Franzén, G. Lidén, and C. Niklasson. A new method for studying microaerobic fermentation: II. An experimental investigation of xylose fermentation. *Biotechnol. Bioeng.*, 44:429–435, 1994.

[113] A.G. Fredrickson and G. Stephanopoulos. Microbial competition. *Science*, 213:972–979, 1981.

[114] H.I. Freedman and R.M. Mathsen. Persistence in predator prey systems with ratio dependent predator influence. *Bull. Math. Biol.*, 55:817–827, 1993.

[115] R. Freter, H. Brickner, J. Fekete, M. Vickerman, and K. Carey. Survival and implantation of *Escherichia coli* in the intestinal tract. *Infect. Immunol.*, 39:686–703, 1983.

[116] H. Funahashi, J.H. Lee, S. Ensari, and H.C Lim. Experimental studies of cheese prefermentation; a mathematical model reflecting the pH effect. *Milchwissenschaft*, 55:75–78, 2000.

[117] H. Funahashi and Y. Nakamura. Model of the continuous prefermentation process in cheese manufacture and stability analysis of steady state. *J. Food. Process. Eng.*, 30:522–537, 2007.

[118] A. Gaki, A. Theodorou, D. V. Vayenas, and S. Pavlou. Complex dynamics of microbial competition in the gradostat. *J. Biotechnol.*, 139:38–46, 2009.

[119] A. Gambhir, A.F. Europa, and W.S. Hu. Alteration of cellular metabolism by consecutive fed-batch cultures of mammalian cells. *J. Biosci. Bioeng.*, 87:805–810, 1999.

[120] A.E. Gamboa-Torres and A. Flores-Tlacuahuac. Effect of process modeling on the nonlinear behaviour of a CSTR reactions. A $\rightarrow$ B $\rightarrow$ C. *Chem. Eng. J.*, 77:153–164, 2000.

[121] P. Garhyan and S. S. E. H. Elnashaie. Bifurcation analysis of two continuous membrane fermentor configurations for producing ethanol. *Chem. Eng. Sci.*, 59:3235–3268, 2004.

[122] P. Garhyan and S. S. E. H. Elnashaie. Utilization of mathematical models to investigate the bifurcation and chaotic behavior of ethanol fermentors. *Math. Comput. Model.*, 39:381–427, 2004.

[123] P. Garhyan, S. S. E. H. Elnashaie, S. M. Al-Haddad, G. Ibrahim, and S. S. Elshishini. Exploration and exploitation of bifurcation/chaotic behavior of a continuous fermentor for the production of ethanol. *Chem. Eng. Sci.*, 58:1479–1496, 2003.

[124] G.F. Gause. *The Struggle for Existence*. Dover, New York, 2003.

[125] A.E. Ghaly, S.S. Sadaka, and A. Hazza'a. Kinetics of an intermittent-flow, continuous-mix anaerobic reactor. *Energ. Source*, 22:525–542, 2000.

[126] T.K. Ghose and R.D. Tyagi. Rapid ethanol fermentation of cellulose hydrolysate. II. Product and substrate inhibition and optimization of fermenter design. *Biotechnol. Bioeng.*, 21:1401–1420, 1979.

[127] R. Giudici, C.R. Pamboukian, and M.C. Facciotti. Morphologically structured model for antitumoral retamycin production during batch and fed-batch cultivations of *Streptomyces olindensis*. *Biotechnol. Bioeng.*, 86:414–424, 2004.

[128] A. N. Godrej and J. H. Sherrard. Kinetics and stoichiometry of activated sludge treatment of a toxic organic wastewater. *J. Water Pollut. Control. Fed.*, 60:221–226, 1988.

[129] A. Goldberter. *Biochemical Oscillations and Cellular Rhythms: The Molecular Bases of Periodic and Chaotic Behaviour*. Cambridge University Press, Cambridge, 1997.

[130] M. Golubitsky and B.L. Keyfitz. A qualitative study of the steady-state solutions for a continuous flow stirred tank chemical reactor. *SIAM J. Math. Anal.*, 11:316–339, 1980.

[131] M. Golubitsky and W.F. Langford. Classification and unfoldings of degenerate Hopf bifurcations. *J. Differ. Equations.*, 41:375–415, 1981.

[132] M. Golubitsky and D.G. Schaeffer. *Singularities and Groups in Bifurcation Theory*, Vol. I. Springer-Verlag, New York, 1985.

[133] M. Golubitsky, I. Stewart, and D.G. Schaeffer. *Singularities and Groups in Bifurcation Theory*, Vol. II. Springer, New York, 1988.

[134] W. J. F. Govaerts. *Numerical Methods for Bifurcations of Dynamical Equilibria*. SIAM, Philadelphia, 2000.

[135] M.J. Guardia, A. Gambhir, A.F. Europa, D. Ramkrishna, and W.S. Hu. Cybernetic modeling and regulation of metabolic pathways in multiple steady states of hybridoma cells. *Biotechnol. Prog.*, 16:847–853, 2000.

[136] J. Guckenheimer and P. Holmes. *Nonlinear Oscillations, Dynamical Systems, and Bifurcations of Vector Fields*. Springer, New York, 1983.

[137] M. Häfele, A. Kienle, E. Klein, A. Kremling, C. Majer, M. Mangold, A. Spieker, E. Stein, R. Waschler, and K. P. Zeyer. *User Manual DIVA 3.9.* Universität Stuttgart, 2003.

[138] D. Hagopian and J. Riley. A closer look at the bacteriology of nitrification. *Aquacult. Eng*, 18:223–244, 1998.

[139] J.K. Hale and A. S. Somolinos. Competition for fluctuating nutrient. *J. Math. Biol.*, 18:255–280, 1983.

[140] S.R. Hansen and S. P. Hubbell. Single-nutrient microbial competition: Qualitative agreement between experimental and theoretically forecast outcomes. *Science*, 207:1491–1493, 1980.

[141] A. Harder and J.A. Roels. Application of simple structured models in bioengineering. *Adv. Biochem. Eng. Biot.*, 21:55–107, 1982.

[142] G. Hardin. The competitive exclusion principle. *Science*, 131:1292–1297, 1960.

[143] P. Hartman. *Ordinary Differential Equations.* SIAM, Philadelphia, 2002.

[144] E. Hegewald and W.A. Knorre. Kinetics of growth and substrate consumption of *Escherichia coli* ML 30 on two carbon sources. *Z. Allg. Mikrobiol*, 18:415–426, 1978.

[145] B. Hendricks, R.A. Korus, and R.C. Heimsch. Propionic acid production by bacterial fermentation. *Biotechnol. Bioeng. Symp.*, 15:241–245, 1985.

[146] M. A. Henson. Dynamic modeling of microbial cell populations. *Curr. Opin. Biotech.*, 14:460–467, 2003.

[147] M. Henze, W. Gujer, T. Mino, and M.C.M. van Loosdrecht. *Activated Sludge Models ASM1, ASM2, ASM2d and ASM3.* IWA Scientific and Technical Report. IWA, London, 2000.

[148] M. Henze, C.P.L. Grady Jr, W. Gujer, G.V.R. Marais, and T. Matsuo. A general model for single-sludge wastewater treatment systems. *Wat. Res.*, 21:505–515, 1987.

[149] R. Hillborn. *Chaos and Nonlinear Dynamics: An Introduction for Scientists and Engineers.* Oxford University Press, 2001.

[150] M.A. Hjortso and J.E. Bailey. Plasmid stability in budding yeast populations: Dynamics following a shift to nonselective medium. *Biotechnol. Bioeng.*, 26:814–819, 1984.

[151] M.A. Hjortso and J. Nielsen. A conceptual model of autonomous oscillations in microbial cultures. *Chem. Eng. Sci.*, 49:1083–1095, 1994.

[152] P.-Y. Ho, G.-S. Chuang, A.-C. Chao, and H.-Y. Li. Computational multiple steady states for enzymatic esterification of ethanol and oleic acid in an isothermal CSTR. *Biosystems*, 80:133–143, 2005.

[153] P.-Y. Ho, G.S. Chuang, and H.Y. Li. Computational multiple steady states for enzymic production of L-DOPA in an isothermal CSTR. *Process Biochem.*, 40:469–478, 2005.

[154] P.-Y. Ho and H.-Y. Li. Determination of multiple steady states in an enzyme kinetics involving two substrates in a CSTR. *Bioproc. Biosyst. Eng.*, 22:557–561, 2000.

[155] H. Honda, T. Mano, M. Taya, K. Shimizu, M. Matsubara, and T. Kobayash. A general framework for the assessment of extractive fermentations. *Chem. Eng. Sci.*, 42:493–498, 1987.

[156] S.-B. Hsu and P. Waltman. Competition between plasmid-bearing and plasmid-free organisms in selective media. *Chem. Eng. Sci.*, 23:35, 1997.

[157] S.-B. Hsu, T.-W. Hwang, and Y. Kuang. Global analysis of the Michaelis-Menten-type ratio-dependence predator-prey system. *J. Math. Biol.*, 42:489–506, 2001.

[158] S.-B. Hsu, P. Waltman, and G.S.K. Wolkowicz. Global analysis of a model of plasmid-bearing, plasmid-free competition in a chemostat. *J. Math. Biol.*, 32:731–742, 1994.

[159] S.B. Hsu. Limiting behaviour for competing species. *SIAM J. Appl. Math.*, 34:760–763, 1978.

[160] S.B. Hsu. A competition model for a seasonally fluctuating nutrient. *J. Math. Biol.*, 9:115–132, 1980.

[161] W.C. Hu, K. Thayanithy, and C.F. Forster. A kinetic study of the anaerobic digestion of ice-cream wastewater. *Process. Biochem.*, 37:965–971, 2002.

[162] G.E. Hutchinson. The paradox of the plankton. *Am. Nat.*, 95:137–145, 1961.

[163] V. Ibarra-Junquera and H.C. Rosu. PI-controlled bioreactor as a generalized Liénard system. *Comput. Chem. Eng.*, 31:136–141, 2007.

[164] G. Ibrahim and A. E. Abasaeed. Modelling of sequencing batch reactors. *Water Res.*, 29:1761–1766, 1995.

[165] G. Ibrahim, H. Habib, and O. Saleh. Periodic and chaotic solutions for a model of a bioreactor with cell recycle. *Biochem. Eng. J.*, 38:124–137, 2008.

[166] G. Ibrahim, M.A. Ramadan, S. A. A. El-Marouf, and A. M. Al-Mahdi. Periodic and non periodic (complex) behavior of a model of bioreactor with cell recycling. *J. Math. Stat.*, 3:1–11, 2007.

[167] T. Imanaka and S. Aiba. A perspective on the application of genetic engineering: Stability of recombinant plasmid. *Ann. N.Y. Acad. Sci.*, 369:1–14, 1981.

[168] IMSL. *(International Mathematics and Statistics Library).* Visual Numerics, Inc., Boulder, Co., 2000.

[169] S.R. Inamdar and I.A. Karimi. Application of reductive perturbation method to branching of stationary solutions. *Chem. Eng. Sci.*, 56:3915–3922, 2001.

[170] G. Iooss and D. D. Joseph *Elementary Stability and Bifurcation Theory.* Springer-Verlag, New York, 1980.

[171] M. Işik and D.T. Sponza. Substrate removal kinetics in an upflow anaerobic sludge blanket reactor decolorising simulated textile wastewater. *Process. Biochem.*, 40:1189–1198, 2005.

[172] J.G. Ivanitskaya, S.B. Petrikevich, and A.D. Bazykin. Oscillations in continuous cultures of microorganisms: Criteria of utility of mathematical models. *Biotechnol. Bioeng.*, 33:1162–1166, 1989.

[173] J. W. Jeong, J. Snay, and M. M. Ataai. A mathematical model for examining growth and sporulation processes of *Bacillus subtilis*. *Biotechnol. Bioeng.*, 35:160–184, 1990.

[174] I.M.L Jöbses, G.T.C. Egberts, A. van Baalen, and J.A. Roels. Mathematical modeling of growth and substrate conversion of *Zymomonas mobilis* at 30 and 35^{o}C. *Biotechnol. Bioeng.*, 27:984–995, 1985.

[175] I.M.L. Jöbses, G.T.C. Egberts, K.C.A.M Luyben, and J.A Roels. Fermentation kinetics of *Zymomonas mobilis* at high ethanol concentration: oscillations in continuous cultures. *Biotechnol. Bioeng.*, 28:868–877, 1986.

[176] D. Jones, H.V. Kojouharov, D. Le, and H. Smith. The Freter model: A simple model of biofilm formation. *J. Math. Biol.*, 47:137–152, 2003.

[177] K.D. Jones and D.S Kompala. Cybernetic model of the growth dynamics of *Saccharomyces cerevisiae* in batch and continuous cultures. *J. Biotechnol.*, 71:105–131, 1999.

[178] M.H. Jørgensen and K. Nikolajsen. Mathematic model for lactic acid formation with *Streptococcus cremoris* from glucose. *Appl. Microbiol. Biotech.*, 25:313–316, 1987.

[179] C. Jost, O. Arino, and R. Arditi. About deterministic extinction in ratio-dependent predator-prey models. *Bull. Math. Biol.*, 61:19–32, 1999.

[180] J.L. Jost, J.F. Drake, A.G. Fredrickson, and H.M. Tsuchiya. Interactions of *Tetrahymena pyriformis*, *Escherichia coli*, *Azotobacter vinelandii* and glucose in a minimal medium. *J. Bacteriol.*, 113:834–840, 1973.

[181] J.P. Keener. Secondary bifurcation and multiple eigenvalues. *SIAM J. Appl. Math.*, 37:330–349, 1979.

[182] I.G. Kevrekidis, L.D. Schmidt, and R. Aris. Some common features of periodically forced reacting systems. *Chem. Eng. Sci.*, 41:1263–1276, 1986.

[183] A.I. Khibnik, Y.A. Kuznetsov, V.V. Levitin, and E.V. Nikolaev. *LocBif, version 2: Interactive LOCal BIFurcation Analyzer*. CAN Expertise Centre, Amsterdam, 1993.

[184] S.H. Kim and D.D.Y Ryu. Instability kinetics of *trp* operon plasmid colEl-*trp* in recombinant *Escherichia coli* MV12[pvH5] and MV12*trpR*[pvH5]. *Biotechnol. Bioeng.*, 26:497–502, 1984.

[185] K. Kiss and S. Kovàcs. Qualitative behavior of n-dimensional ratio-dependent predator-prey systems. *Appl. Math. Comput.*, 199:535–546, 2008.

[186] D.S. Kompala, D. Ramkrishna, N.B. Jansen, and G.T. Tsao. Investigation of bacterial growth on mixed substrates: Experimental evaluation of cybernetic models. *Biotechnol. Bioeng.*, 28:1044–1055, 1986.

[187] S. Kovàcs, K. Kiss, and M. Farkas. Qualitative behaviour of a ratio-dependent predator-prey system. *Nonlinear Anal-Real.*, 10:1627–1642, 2009.

[188] S. G. Krantz and H. R. Parks. *The Implicit Function Theorem: History, Theory and Applications*. Birkhaüser, Boston, 2002.

[189] M. Krasnyk. *Numerical Nonlinear Analysis in DIANA*. Universität Stuttgart, 2009.

[190] L. Krzystek, S. Ledakowicz, H.-J. Kahle, and K. Kaczorek. Degradation of household biowaste in reactors. *J. Biotechnol.*, 92:103–112, 2001.

[191] Y. Kuang and E. Beretta. Global qualitative analysis of a ratio-dependent predator-prey system. *J. Math. Biol.*, 36:389–406, 1998.

[192] M. Kubicek and M. Marek. *Computational Methods in Bifurcation Theory and Dissipative Structures*. Springer, New York, 1983.

[193] L.D. Kudryavtsev. Implicit function. In M. Hazewinkel, editor, *Encyclopedia of Mathematics*. Kluwer, 1990.

[194] G.P. Kumar, I.V.K. Subrahmanya, and M. Chidambaram. Periodic operation of a bioreactor with input multiplicities. *Can. J. Chem. Eng.*, 71:766–770, 1993.

[195] P.K.R. Kumar, H.-E. Maschke, K. Friehs, and K. Schügerl. Strategies for improving plasmid stability in genetically modified bacteria in bioreactors. *Trends Biotechnol.*, 9:279–284, 1991.

[196] C.-M. Kung and B.C. Baltzis. Operating parameters effects on the outcome of pure and simple competition between two populations in configurations of two interconnected chemostats. *Biotechnol. Bioeng.*, 30:1006–1018, 1987.

[197] Z. Kurtanjek. Steady state multiplicity and stability of the temperature regulated continuous biochemical reactor. *Chem. Biochem. Eng. Q.*, 1:31–37, 1987.

[198] Yu. Kuznetsov. *Elements of Applied Bifurcation Theory.* Springer, 2001.

[199] Y.A. Kuznetsov and V.V. Levitin. *CONTENT: A Multiplatform Environment for Continuation and Bifurcation Analysis of Dynamical Systems.* Centrum voor Wiskunde en Informatica, Amsterdam, 1997.

[200] W.F. Langford. A review of interactions of Hopf and steady-state bifurcations. *J. Appl. Math*, 37:22-48, 1979.

[201] W.F. Langford. A review of interactions of Hopf and steady-state bifurcations. In: G.I. Barenblatt, G. Iooss and D.D. Joseph, editors, *Nonlinear Dynamics and Turbulence*, pages 215-237, Pitnam, Boston, 1983.

[202] G.I. Lapshenkov and L.Yu. Kharitonova. Biotechnological process dynamics under the conditions of multiplicity of steady states. *Theor. Found. Chem. Eng.*, 38:173–178, 2004.

[203] C.S. Laspidou, A. Kungolos, and P. Samaras. Cellular-automata and individual-based approaches for the modeling of biofilm structures: Pros and cons? *Desalination*, 250:390–394, 2010.

[204] J. Lee and S. J. Parulekar. Periodic operation of continuous recombinant cultures improves antibiotic selection. *Chem. Eng. Sci.*, 51:217–231, 1996.

[205] J.H. Lee and H.C. Lim. Multiplicity and stability analysis of continuous pre-fermentation of cheese culture. *Process Biochem.*, 34:467–475, 1999.

[206] J.M. Lee, J.F. Pollard, and G.A. Coulman. Ethanol fermentation with cell recycling: Computer simulation. *Biotechnol. Bioeng.*, 25:497–511, 1983.

[207] K.J. Lee, D.E. Tribe, and P.L. Rogers. Ethanol production by *Zymomonas mobilis* in continuous culture at high glucose concentrations. *Biotechnol. Lett.*, 1:421–426, 1979.

[208] S.B. Lee and J.E. Bailey. Analysis of growth rate effects on productivity of recombinant *Escherichia coli* populations using molecular mechanism models. *Biotechnol. Bioeng.*, 26:66–73, 1984.

[209] S.B. Lee and J.E. Bailey. A mathematical model for λdv plasmid replication: Analysis of copy numbers mutants. *Plasmid*, 11:166–177, 1984.

[210] P. Lenas, B.C. Baltzis, G.A. Lewandowski, and Y.-F. Ko. Biodegradation of wastes in a cyclically operated reactor: Theory, experimental verification and optimization studies. *Chem. Eng. Sci.*, 49:4547, 1994.

[211] P. Lenas and S. Pavlou. Chaotic response of a periodically forced system of two competing microbial species. In: T. Bountis, editor, *Chaotic Dynamics: Theory and Practice*, pages 283, Springer, New York, 1992.

[212] P. Lenas and S. Pavlou. Periodic, quasi-periodic and chaotic coexistence of two competing microbial populations in a periodically operated chemostat. *Math. Biosci.*, 121:61–110, 1994.

[213] P. Lenas, N.A. Thomopoulos, D.V. Vayenas, and S. Pavlou. Oscillations of two competing microbial populations in configurations of two interconnected chemostats. *Math. Biosci.*, 148:43–63, 1998.

[214] Y. Lenbury, B. Novaprateep, and B. Wiwatpataphee. Dynamic behavior classification of a model for a continuous bio-reactor subject to product inhibition. *Math. Comput. Model.*, 19:107–117, 1994.

[215] Y. Lenbury, B. Sukprasong, and B. Novaprateep. Bifurcation and chaos in a membrane permeability sensitive model for a continuous bioreactor. *Math. Comput. Model.*, 24:37–48, 1996.

[216] U. Lendenmann and T. Egli. Is *Escherichia coli* growing in glucose-limited chemostat cultures able to utilize other sugars without lag? *Microbiology*, 141:71–78, 1995.

[217] U. Lendenmann and T. Egli. Kinetic models for the growth of *Escherichia coli* with mixtures of sugars under carbon-limited conditions. *Biotechnol. Bioeng.*, 59:99–107, 1998.

[218] U. Lendenmann, M. Snozzi, and T. Egli. Kinetics of the simultaneous utilization of sugar mixtures by *Escherichia coli* in continuous culture. *Appl. Environ. Microbiol.*, 62:1493–1499, 1996.

[219] O. Levenspiel. The Monod equation: A revisit and a generalization to product inhibition situations. *Biotechnol. Bioeng.*, 22:1671–1687, 1980.

[220] B.R. Levin and F.M. Stewart. The population biology of bacterial plasmids: A priori conditions for the existence of mobilizable nonconjugative factors. *Genetics*, 94:425–443, 1980.

[221] B. Li. Global asymptotic behavior of the chemostat: General response functions and different removal rates. *SIAM J. Appl. Math.*, 59:411–422, 1998.

[222] Y. Lijun. On the generalized Lyapunov-Schmidt reduction. *ZAMM Z. Angew. Math. Mech.*, 84:528–537, 2004.

[223] C.-S Lin and H. C. Lim. A kinetic model and steady-state analysis for polysaccharide production by *Methylomonas mucosa*. *J. Biotechnol.*, 16:137–151, 1990.

[224] C-.T. Liou and Y-.S. Chien. Effect of micromixing on steady-state multiplicity for autocatalytic reactions in a nonideal mixing of CSTR. *Chem. Eng. Sci.*, 50:3637–3644, 1995.

[225] S.N. Lo and A. Cholette. Multiplicity of a conversion in cascade in imperfectly stirred tank reactors. *Chem. Eng. Sci.*, 38:367–372, 1983.

[226] R.W. Lovitt and J.W.T. Wimpenny. The gradostat: A bidirectional compound chemostat and its application in microbiological research. *J. Gen. Microbiol.*, 127:261–268, 1981.

[227] Y-.C. Lu. *Singularity Theory and an Introduction to Catastrophe Theory*. Springer, New York, 1980.

[228] T-.K Luo and S-.B Hsu. Global analysis of a model of plasmid-bearing, plasmid-free competition in a chemostat with inhibitions. *J. Math. Biol.*, 34:41–76, 1995.

[229] G. Lyberatos, B. Kuszta, and J.E. Bailey. Steady-state multiplicity and bifurcation analysis via the Newton polyhedron approach. *Chem. Eng. Sci.*, 39:947–960, 1984.

[230] G. Lyberatos, B. Kuszta, and J.E. Bailey. Versal matrix families, normal forms and higher order bifurcations in dynamics chemical systems. *Chem. Eng. Sci.*, 40:1177–1189, 1985.

[231] T. Ma and S. Wang. *Bifurcation Theory and Applications*. World Scientific, New Jersey, 2005.

[232] C.A. Macken, S.A. Levin, and R. Waldstätter. The dynamics of bacteria-plasmid systems. *J. Math. Biol.*, 32:123–145, 1994.

[233] A. Mahecha-Botero, P. Garhyan, and S.S.E.H. Elnashaie. Non-linear characteristics of a membrane fermentor for ethanol production and their implications. *Nonlinear Anal-Real.*, 7:432–457, 2006.

[234] N.I. Marcos, M. Guay, and D. Dochain. Output feedback adaptive extremum seeking control of a continuous stirred tank bioreactor with Monod's kinetics. *J. Process Contr.*, 14:807–818, 2004.

[235] W. Marquardt. Towards a process modeling methodology. In R. Berber, editor *Methods of Model Based Process Control*, pages 3–40. Springer, 1995.

[236] J. E. Marsden. On the geometry of the Liapunov-Schmidt procedure. In M. Grmela and J.E. Marsden, editors, *Encyclopedia of Mathematics*, pages 77–82. Springer, 179.

[237] J.E. Marsden and M. McCracken. *The Hopf Bifurcation and its Applications*. Springer, New York, 1976.

[238] Mathematica. Wolfram Research, Champaign, IL., 1990.

[239] J.H. Mather. Stability of C^∞ mappings, III. Finitely determined map germs. *Publ. Math. I.H.E.S.*, 35:127–156, 1968.

[240] J.H. Mather. Stability of C^∞ mappings, II. Infinitesimal stability implies stability. *Ann. Math.*, 89:254–291, 1969.

[241] R.M. May. *Stability and Complexity in Model Ecosystems*. Princeton University Press, 1972.

[242] M.A. McKarnin, L.D. Schmidt, and R. Aris. Response of non-linear oscillations to forced oscillation: Three chemical reaction systems. *Chem. Eng. Sci.*, 43:2833–2844, 1988.

[243] P.J. McLellan, A.J. Daugulis, and J. Li. The incidence of oscillatory behavior in the continuous fermentation of *Zymomonas mobilis*. *Biotechnol. Prog.*, 15:667–680, 1999.

[244] J.L. Meers. Effect of dilution rate on the outcome of chemostat mixed culture experiments. *J. Gen. Microbiol.*, 67:359–361, 1971.

[245] R.D. Megee III, J.F. Drake, A.G. Fredrickson, and H.M. Tsuchiya. Studies in intermicrobial symbiosis, *Saccharomyces cerevisiae* and *Lactobacillus casei*. *Can. J. Microbiol.*, 18:1733–1742, 1972.

[246] K. Menzel, A.-P. Zeng, H. Biebl, and W.-D. Deckwer. Kinetic, dynamic and pathway studies of gluycerol metabolism by *Klebsiella pneuomiae* in anaerobic continuous cultures. I. The phenomena and characterization of oscillation and hysteresis. *Biotechnol. Bioeng.*, 52:549–560, 1996.

[247] R. Mihail and S. Straja. An analysis of the steady states of a chemostat with applications to its design. *Biotechnol. Bioeng.*, 31:87–90, 1988.

[248] H.G. Monbouquette, G.D. Sayles, and D.F. Ollis. Immobilized cell biocatalyst activation and pseudo-steady-state behavior: Model and experiment. *Biotechnol. Bioeng.*, 35:609–629, 1990.

[249] J. Monod. The growth of bacterial cultures. *Annu. Rev. Microbiol.*, 3:371–394, 1949.

[250] R.J. Munson. Turbidostats. In J.R. Norris and D.W. Ribbons, editors, *Methods in Microbiology*, pages 349–376, New York, 1970. Academic Press.

[251] M.A. Murison. On the applicability of the Lyapunov exponent relation. *Bulletin of the American Astronomical Society*, 28:1181–183, 1996.

[252] D.B. Murray, R.R. Klevecz, and D. Lloyd. Generation and maintenance of synchrony in *Saccharomyces cerevisiae*. *Exp. Cell Res.*, 287:10–15, 2003.

[253] A. Namjoshi and D. Ramkrishna. Multiplicity and stability of steady states in continuous bioreactors: dissection of cybernetic models. *Chem. Eng. Sci.*, 56:5593–5607, 2001.

[254] A. Namjoshi, A. Kienle, and D. Ramkrishna. Steady-state multiplicity in bioreactors: Bifurcation analysis of cybernetic models. *Chem. Eng. Sci.*, 58:793–800, 2003.

[255] A. Narang. The steady states of microbial growth on mixture of substitutable substrates. *J. Theor. Biol.*, 190:241–261, 1998.

[256] A. Narang. Comparative analysis of some models of gene regulation in mixed-substrate microbial growth. *J. Theor. Biol.*, 242:489–501, 2006.

[257] A. Narang, A. Konopka, and D. Ramkrishna. The dynamics of microbial growth on mixtures of substrates in batch reactors. *J. Theor. Biol.*, 184:310–317, 1997.

[258] A.H. Nayfeh. *Method of Normal Forms*. Wiley, New York, 1993.

[259] M.I. Nelson, E. Balakrishnan, H.S. Sidhu, and X.D. Chen. A fundamental analysis of continuous flow bioreactor and membrane reactor models to process industrial wastewaters. *Chem. Eng. J.*, 140:521–528, 2008.

[260] M.I. Nelson and H.S. Sidhu. Reducing the emission of pollutants in food processing wastewaters. *Chem. Eng. Process.*, 46:429–436, 2007.

[261] M.I. Nelson and H.S. Sidhu. Analysis of the activated sludge model (number 1). *Appl. Math. Lett.*, 22:629–635, 2009.

[262] S. Newhouse, D. Ruelle, and F. Takens. Occurrence of strange axiom A attractors near quasiperiodic flows on T^m, $m \geq 3$. *Comm. Math. Phys.*, 64:35–40, 1978.

[263] J. Nielsen, K. Nikolajsen, and J. Villadsen. Structured modeling of a microbial system: I. A theoretical study of lactic acid fermentation. *Biotechnol. Bioeng.*, 38:1–10, 1991.

[264] J. Nielsen, K. Nikolajsen, and J. Villadsen. Structured modeling of a microbial system: II. Experimental verification of a structured lactic acid fermentation model. *Biotechnol. Bioeng.*, 38:11–23, 1991.

[265] J. Nielsen, J. Villadsen, and J.Lidén. *Bioreaction Engineering Principles*. Springer, New York, 2002.

[266] D.R. Noguera, S. Okabe, and C. Picioreanu. Biofilm modeling: Present status and future directions. *Water Sci. Technol.*, 39:273–278, 1999.

[267] H. Ohara, K. Hiyama, and T. Yoshida. Kinetics of growth and lactic acid production in continuous and batch culture. *Appl. Microbiol. Biotech.*, 37:544–548, 1992.

[268] D.F. Ollis and H. Chang. Industrial fermentations with (unstable) recombinant cultures. *Phil. Trans. R. Soc. Lond.*, B297:617–629, 1982.

[269] J. Palmer, S. Flint, and J. Brooks. Bacterial cell attachment, the beginning of a biofilm. *J. Ind. Microbiol. Biotechnol.*, 34:557–588, 2007.

[270] M. Papagianni, Y. Boonpooh, M. Mattey, and B. B. Kristiansen. Substrate inhibition kinetics of *Saccharomyces cerevisiae* in fed-batch cultures operated at constant glucose and maltose concentration levels. *J. Ind. Microbiol. Biotechnol.*, 34:301–309, 2007.

[271] R. S. Parker and F. J. Doyle III. Optimal control of a continuous bioreactor using an empirical non-linear model. *Ind. Eng. Chem. Res.*, 40:1939-1951, 2001.

[272] S. Parulekar. Analysis of forced periodic operations of continuous bioprocesses-single input variations. *Chem. Eng. Sci.*, 53:2481–2502, 1998.

[273] S. Parulekar. Analysis of forced periodic operations of continuous bioprocesses: Multiple input variations. *Chem. Eng. Sci.*, 55:513–533, 2000.

[274] S. Parulekar, G.B. Semones, M.J. Rolf, J.C. Lievense, and H.C. Lim. Induction and elimination of oscillations in continuous cultures of *Saccharomyces cerevisiae*. *Biotechnol. Bioeng.*, 28:700–710, 1986.

[275] S. J. Parulekar and H. C. Lim. Dynamics of continuous commensalistic cultures-I. Multiplicity and local stability of steady states and bifurcation analysis. *Chem. Eng. Sci.*, 41:2605–2616, 1986.

[276] P.R. Patnaik. Effect of feed cycling on plasmid stabilization during continuous fermentation: the case of variable plasmid loss probability. *Can. J. Chem. Eng.*, 72:929–934, 1994.

[277] P.R. Patnaik. Bistability of stationary states during competition between plasmid-bearing and plasmid-free cells under selection pressure. *Food Bioprod, Process.*, 77:243–247, 1999.

[278] S. Pavlou. Computing operating diagrams of bioreactors. *J. Biotechnol.*, 71:7–16, 1999.

[279] S. Pavlou. Microbial competition in bioreactors. *Chem. Ind. Chem. Eng. Q.*, 12:71–81, 2006.

[280] S. Pavlou and I.G. Kevrekidis. Microbial predation in a periodically operated chemostat: A global study of the interaction between natural and externally imposed frequencies. *Math. Biosci.*, 108:1–55, 1992.

[281] S. Pavlou, I.G. Kevrekidis, and G. Lyberatos. On the coexistence of competing microbial species in a chemostat under cycling. *Biotechnol. Bioeng.*, 35:224–232, 1990.

[282] U. Pawlowsky, J.A. Howell, and C.T. Chi. Mixed culture bioxidation of phenol. III. Existence of multiple steady states in continuous cultures with wall growth. *Biotechnol. Bioeng.*, 15:905–916, 1973.

[283] L. Pellegrini and C.T. Possio. A non-ideal CSTR: A high codimension bifurcation analysis. *Chem. Eng. Sci.*, 51:3151–3156, 1996.

[284] C. Picioreanu, M.C.M. van Loosdrecht, and J. Heijnen. Mathematical modeling of biofilm structure with a hybrid differential-discrete cellular automaton approach. *Biotechnol. Bioeng.*, 58:101–116, 1998.

[285] S.S. Pilyugin and P. Waltman. The simple chemostat with wall growth. *SIAM. J. Appl. Math.*, 59:1552–1572, 1999.

[286] S.S. Pilyugin and P. Waltman. Multiple limit cycles in the chemostat with variable yield. *Math. Biosci.*, 182:151–166, 2003.

[287] I.O. Pinheiro, M.B. De Souza Jr., and C.E. Lopes. The dynamic behaviour of aerated continuous flow stirred tank bioreactor. *Math. Comput. Model.*, 39:541–566, 2004.

[288] L.M. Pismen. Dynamics of lumped chemically reacting systems near singular bifurcation points. II. Almost Hamiltonian dynamics. *Chem. Eng. Sci.*, 40:905–916, 1985.

[289] Y. Pomeau and P. Manneville. Intermittent transition to turbulence in dissipative dynamical systems. *Commun. Math. Phys.*, 74:189–197, 1980.

[290] D. Porro, E. Martegani, B.M. Ranzi, and L. Alberghina. Oscillations in continuous cultures of budding yeast: A segregated parameter analysis. *Biotechnol. Bioeng.*, 32:411–417, 1988.

[291] G.E. Powell. Structural instability of the theory of simple competition. *J. Theor. Biol.*, 132:421–435, 1988.

[292] T.K. Radhakrishnan, S. Sundaram, and M. Chidambaram. Non-linear control of continuous bioreactors. *Bioproc. Biosyst. Eng.*, 20:173–178, 1999.

[293] R. Ramakrishna, D. Ramkrishna, and A.E. Konopka. Cybernetic modeling of growth in mixed, substitutable substrate environments: Preferential and simultaneous utilization. *Biotechnol. Bioeng.*, 52:141–151, 1996.

[294] R. Ramakrishna, D. Ramkrishna, and A.E. Konopka. Microbial growth on substitutable substrates: Characterizing the consumer resource relationship. *Biotechnol. Bioeng.*, 54:77–90, 1997.

[295] S. Ramaswamy, T.J. Cutright, and H.K. Qammar. Control of a continuous bioreactor using model predictive control. *Process Biochem.*, 40:2763–2770, 2005.

[296] D. Ramkrishna. A cybernetic perspective of microbial growth. In E. Papoutsakis, G.N. Stephanopoulos, and H.W. Blanch, editors, *Foundations of Biochemical Engineering: Kinetics and Thermodynamics in Biological Systems*, pages 161–178. Am. Chem. Soc., Washington DC, 1982.

[297] D. Ramkrishna, D.S. Kompala, and G.T. Tsao. Are microbes optimal strategists? *Biotechnol. Prog.*, 3:121–126, 1987.

[298] A.D. Ratnam, S. Pavlou, and A. G. Fredrickson. Effects of attachment of bacteria to chemostat walls in a microbial predator-prey relationship. *Biotechnol. Bioeng.*, 24:2675–2694, 1982.

[299] S.N. Rasband. *Chaotic Dynamics of Nonlinear Systems.* Wiley, New York, 1990.

[300] G. T. Reeves, A. Narang, and S. S. Pilyugin. Growth of mixed cultures on mixtures of substitutable substrates: The operating diagram for a structured model. *J. Theor. Biol.*, 226:143–157, 2004.

[301] P. Richard, J.A. Diderich, B.M. Bakker, B. Teusink, K. van Dam, and H.V. Westerhoff. Yeast cells with a specific cellular make-up and an environment that removes acetaldehyde are prone to sustained glycolytic oscillations. *FEBS Lett.*, 341:223–226, 1994.

[302] B. E. Rittman, W. Bae, E. Namkung, and C. J. Lu. A critical evaluation of microbial product formation in biological processes. *Wat. Sci. Tech.*, 19:517–528, 1987.

[303] C. Robinson. *Dynamical Systems: Stability, Symbolic Dynamics, and Chaos.* CRC Press, New York 1998.

[304] A.F. Rozich and A.F. Gaudy. Critical points analysis for toxic waste treatment. *J. Envir. Engng Dib. Am. Soc. Civ. Engrs.*, 110:562–572, 1984.

[305] A.F. Rozich and A.F. Gaudy. Response of phenol-acclimated activated sludge process to quantitative shock loading. *J. Water Pollut. Control. Fed.*, 57:795–804, 1985.

[306] L. Ruan and X.D. Chen. Comparison of several periodic operations of a continuous fermentation process. *Biotechnol. Prog.*, 12:286–288, 1996.

[307] L.P. Russo and B.W. Bequette. Impact of process design on the multiplicity behavior of a jacketed exothermic CSTR. *AIChEJ*, 41:135–147, 1995.

[308] L.P. Russo and B.W. Bequette. Effect of process design on the open-loop behavior of a jacketed exothermic CSTR. *Comput. Chem. Eng.*, 20:417–426, 1996.

[309] L.P. Russo and B.W. Bequette. Process design for operability: A styrene polymerization application. *Comput. Chem. Eng.*, 21:S571–S576, 1997.

[310] M.E. Russo, P.L. Maffettone, A. Marzocchella, and P. Salatino. Bifurcational and dynamical analysis of a continuous biofilm reactor. *J. Biotechnol.*, 135:295–303, 2008.

[311] D.F. Ryder and D. DiBiasio. An operational strategy for unstable recombinant DNA cultures. *Biotechnol. Bioeng.*, 26:942–947, 1984.

[312] A. Sambanis and A.G. Fredrickson. Effect of addition of wall growth to a model of cilicate-bacterial interactions. *Biotechnol. Bioeng.*, 34:875–881, 1989.

[313] C. A. Sardonini and D. DiBiasio. A model for growth of *Saccharomyces cerevisiae* containing a recombinant plasmid in selective media. *Biotechnol. Bioeng.*, 29:469–475, 1987.

[314] K. Schügerl and K-H. Bellgardt. *Bioreaction Engineering Modeling and Control*. Springer, 2000.

[315] R. Seydel. *From Equilibrium to Chaos: Practical Bifurcation and Stability Analysis*. Elsevier, New York, 1988.

[316] M.S. Sheffer, M. Hiraoka, and K. Tsumura. Flexible modelling of the activated sludge system—Theoretical and practical aspects. *Wat. Sci. Tech.*, 17:247–258, 1985.

[317] M. Sheintuch. Dynamics of commensalistic systems with self and cross-inhibition. *Biotechnol. Bioeng.*, 22:2557–2577, 1980.

[318] M. Sheintuch. Multiplicity patterns of activated-sludge with substrate-inhibition kinetics. *Water Res.*, 27:929–938, 1993.

[319] M. Sheintuch, B. Tartakovsky, N. Narkis, and M. Rebhun. Substrate inhibition and multiple states in a continuous nitrification process. *Water Res.*, 29:953–963, 1995.

[320] K. Shimizu and M. Matsubara. A solvent screening criterion for multicomponent extractive fermentation. *Chem. Eng. Sci.*, 42:499–504, 1987.

[321] M.L. Shuler and F. Kargi. *Bioprocess Engineering: Basic Concepts*. Prentice-Hall, New Jersey, 1992.

[322] H.S. Sidhu, S. D. Watt, and M.I. Nelson. Performance comparison between a two-reactor cascade and a single tank in an activated sludge wastewater treatment process. *IJEWM*, 3:214–225, 2009.

[323] N. Sidorov, B. Loginov, A.V. Sinitsyn, and M.V. Falaleev. *Lyapunov-Schmidt Methods in Nonlinear Analysis and Applications*. Springer, 2002.

[324] J. Sijbrand. Properties of center manifolds. *T. Am. Math. Soc.*, 289:431–469, 1985.

[325] A. Silva-Beard and A. Flores-Tlacuahuac. Effect of process design/operation on the steady-state operability of a methyl methacrylate polymerization reactor. *Ind. Eng. Chem. Res.*, 38:4790–4804, 1999.

[326] P.L. Silveston, H. Budman, and E. Jervis. Forced modulation of biological processes: A review. *Chem. Eng. Sci.*, 63:5089–5105, 2008.

[327] D. Sinčić and J.E. Bailey. Analytical optimization and sensitivity analysis of forced periodic chemical processes. *Chem. Eng. Sci.*, 35:1153–1161, 1980.

[328] H. Smith and B. Tang. Competition in the gradostat: The role of the communication rate. *J. Math. Biol.*, 27:139–165, 1989.

[329] H. Smith and P. Waltman. *The Theory of the Chemostat: Dynamics of Microbial Competition*. Cambridge University Press, Cambridge, 1995.

[330] H.-X. Song, Y.-Y. Peng, and Z.-F. Zhu. Competition between plasmid-bearing and plasmid-free organisms in the host: Population dynamics and antibiotic resistance. *Med. Princ. Pract.*, 15:436–442, 2006.

[331] A. Soni. *A Multi-Scale Approach to Fed-batch Bioreactor Control*. Master's thesis, University of Pittsburgh, 2002.

[332] R. Sousa Jr., G.P. Lopes, G.A. Pinto, P.I.F. Almeida, and R.C. Giordano. GMC-fuzzy control of pH during enzymatic hydrolysis of cheese whey proteins. *Comput. Chem. Eng.*, 28:1661–1672, 2004.

[333] M. Staniszewski and S. Koter. Theoretical analysis of steady states for ester hydrolysis in an enzymatic membrane reactor with product retention. *Desalination*, 246:545–555, 2009.

[334] G. Stephanopoulos, R. Aris, and A. G. Fredrickson. A stochastic analysis of the growth of competing microbial populations in a continuous biochemical reactor. *Math. Biosci.*, 45:99–135, 1979.

[335] G. Stephanopoulos and A.G. Fredrickson. Effect of spatial inhomogeneities on the coexistence of competing microbial populations. *Biotechnol. Bioeng.*, 21:1491–1498, 1979.

[336] G. Stephanopoulos, A.G. Fredrickson, and R. Aris. The growth of competing microbial populations in a CSTR with periodically varying inputs. *AIChEJ*, 25:863–872, 1979.

[337] G. Stephanopoulos and G. R. Lapidus. Chemostat dynamics of plasmid-bearing, plasmid-free mixed recombinant cultures. *Chem. Eng. Sci.*, 43:49–57, 1988.

[338] M. L. Stephens and G. Lyberatos. Effect of cycling on the stability of plasmid-bearing microorganisms in continuous culture. *Biotechnol. Bioeng,*, 31:464–469, 1988.

[339] M.L. Stephens, C. Christensen, and G. Lyberatos. Plasmid stabilization of an *Escherichia coli* culture through cycling. *Biotechnol. Prog.*, 8:1–4, 1992.

[340] L.E. Sterman and B.E. Ydstie. Periodic forcing of the CSTR: An application of the generalized π-criterion. *AIChEJ*, 37:986–996, 1991.

[341] R.W. Stieber and P. Gerhardt. Dialysis continuous process for ammonium lactate fermentation: Simulated and experimental dialysate-feed, immobilized-cell systems. *Biotechnol. Bioeng.*, 23:535–549, 1981.

[342] J.V. Straight and D. Ramkrishna. Cybernetic modeling and regulation of metabolic pathways. growth on complementary nutrients. *Biotechnol. Progr.*, 10:574–587, 1994.

[343] C. Strässle, B. Sonnleitner, and A. Fiechter. A predictive model for the spontaneous synchronization of *Saccharomyces cerevisiae* grown in continuous culture. II. Experimental verification. *J. Biotechnol.*, 9:191–208, 1989.

[344] S. H. Strogatz. *Nonlinear Dynamics and Chaos: With Applications to Physics, Biology, Chemistry, and Engineering*. Westview Press, 2001.

[345] K. Syamsu, P. F. Greenfield, and D. A. Mitchell. The use of dilution rate cycling to stabilise recombinant plasmids in continuous culture of recombinant *Saccharomyces cerevisiae*. *J. Biotechnol.*, 45:205–210, 1996.

[346] K. Takeya, A. Kuwata, M. Yoshida, and T. Miyazaki. Effect of dilution rate on competitive interactions between the cyanobacterium *Microcystis novacekii* and the green alga *Scenedesmus quadricauda* in mixed chemostat cultures. *J. Plankton Res.*, 26:29–35, 2004.

[347] B. Tang and G.S. Wolkowicz. Mathematical models of microbial growth and competition in the chemostat regulated by cell-bound extracellular enzymes. *J. Math. Biol.*, 31:1–23, 1992.

[348] H.R. Thieme. Convergence results and a Poincaré-Bendixson trichotomy for asymptotically autonomous differential equations. *J. Math. Biol.*, 30:755–763, 1992.

[349] K. Toda and I. Yabe. Mathematical model of cell growth and phosphatase biosynthesis in *Saccharomyces carlsbergensis* under phosphate limitation. *Biotechnol. Bioeng.*, 21:487–502, 1979.

[350] R. Thom. Une lemme sur les applications differentiables. *Bol. Soc. Math.*, 59:322, 1956.

[351] J.M.T. Thompson and H.B. Stewart. *Nonlinear Dynamics and Chaos*. Wiley, New York, 2002.

[352] H.H. Topiwala and G. Hamer. Effect of wall growth in steady state continuous culture. *Biotechnol. Bioeng.*, 13:919–922, 1971.

[353] M. Trenogin and V. Vainberg. The Liapunov and Schmidt methods in the theory of non-linear equations and their subsequent development. *Russian Mathematical Surveys*, 17:1–60, 1962.

[354] H. Troger and A. Steindl. *Nonlinear Stability and Bifurcation Theory: An Introduction for Engineers and Applied Scientists*. Springer, New York, 1991.

[355] C.A. Tsiligiannis and G. Lyberatos. A linear algebraic approach to steady-state bifurcation of chemical reaction systems. *Chem. Eng. Sci.*, 42:535–541, 1987.

[356] H.M. Tsuchiya, J.F. Drake, J.L. Jost, and A.G. Fredrickson. Predator-prey interactions of *Dictyostelium discoideum* and *Escherichia coli* in continuous culture. *J. Bacteriol.*, 110:1147–1153, 1972.

[357] R.D. Tyagi and T.K. Ghose. Batch and multistage continuous ethanol fermentation of cellulose hydrolysate and optimum design of fermenter by graphical analysis. *Biotechnol. Bioeng.*, 22:1907–1928, 1980.

[358] A. Varma and M. Morbidelli. *Mathematical Methods in Chemical Engineering*. Oxford University Press, Oxford, 1997.

[359] J. Vásquez-Bahena, M.C. Montes-Horcasitas, J. Ortega-López, I. Magaña-Plaza, and L.B. Flores-Cotera. Multiple steady states in a continuous stirred tank reactor: An experimental case study for hydrolysis of sucrose by invertase. *Process Biochem.*, 39:2179–2182, 2004.

[360] A. Vicente, J. I. Castrillo, J.A. Teixeira, and U. Ugalde. On-line estimation of biomass through pH control analysis in aerobic yeast fermentation systems. *Biotechnol. Bioeng.*, 58:445–450, 1998.

[361] J. Villadsen. On the optimal design and control of a biodegradation process with substrate inhibition kinetics. *Ind. Eng. Chem. Res.*, 38:660–666, 1999.

[362] H.K. von Meyenburg. Stable synchrony oscillations in continuous culture of *Saccharomyces cerevisiae* under glucose limitation. In B. Chance, E.K. Pye, A.K. Shosh, and B. Hess, editors, *Biological and Biochemical Oscillators*, pages 441–417. Academic Press, 1973.

[363] J.-H. Wang, B.C. Baltzis, and G.A. Lewandowski. Reduction of nitrate and nitrite in a cyclically operated continuous biological reactor. *Biotechnol. Bioeng.*, 46:159–171, 1995.

[364] K.-W. Wang, D.M. Tsangaris, B.C. Baltzis, and G.A. Lewandowski. Biodegradation of mixed wastes in continuously operated cyclic reactors. *Appl. Biochem. Biotech.*, 57/58:803–815, 1996.

[365] N. Watanabe, S. Ohbayashi, and H. Kurimoto. Application of the infinite-frequency pi criterion to a periodically operated isothermal CSTR. *Chem. Eng. Sci.*, 45:2984–2986, 1990.

[366] S. Wiggins. *Introduction to Applied Nonlinear Dynamical Systems and Chaos*. Springer, 2003.

[367] J.W.T. Wimpenny and R. Colasanti. A unifying hypothesis for the structure of microbial biofilms based on cellular automaton models. *FEMS. Microb. Ecol.*, 22:1–16, 1997.

[368] P. A. Wisnewski, F. J. Doyle III, and F. Kayihan. Fundamental continuous-pulp-digester model for simulation and control. *AIChEJ*, 43:3175–3192, 1997.

[369] A. Wolf, J.B. Swift, H.L. Swinney, and J.A. Vastano. Determining lyapunov exponents from a time series. *Physica.*, 16D:285–317, 1985.

[370] G.S.K. Wolkowicz and Z. Lu. Global dynamics of a mathematical model of competition in the chemostat: General response functions and differential death rates. *SIAM J. Appl. Math.*, 52:222–233, 1992.

[371] Y. Xia and M. Han. Multiple periodic solutions of a ratio-dependent predator-prey model. *Chaos Soliton. Fract.*, 39:1100–1108, 2009.

[372] Z. Xiang and X. Song. A model of competition between plasmid-bearing and plasmid-free organisms in a chemostat with periodic input. *Chaos Soliton. Fract.*, 32:1419–1428, 2007.

[373] D. Xiao and S. Ruan. Global dynamics of a ratio-dependent predator-prey system. *J. Math. Biol.*, 43:268–290, 2001.

[374] Z.-L. Xiu, A.-P. Zeng, and W.-D. Deckwer Multiplicity and stability analysis of microorganisms in continuous culture: Effects of metabolic overflow and growth inhibition. *Biotechnol. Bieng.*, 57:251–261, 1998.

[375] S.-T. Yang and J.-J. Zhong. Bioreactor engineering. In S.-T. Yang, editor, *Bioprocessing for Value-Added Products from Renewable Resources*, pages 131–161. Elsevier, 2007.

[376] P.L.-H. Yeh, R.K. Bajpai, and E.L. Iannotti. An improved kinetic model for lactic acid fermentation. *J. Ferm. Bioeng.*, 71:75–77, 1991.

[377] H.R. Zeike, C.L. Zeike, and P.T. Ozand. Glutamine: A major energy source for cultured mammalian cells. *Fed. Proc.*, 43:121–125, 1984.

[378] Y. Zhang and M. A. Henson. Bifurcation analysis of continuous biochemical reactor models. *Biotechnol. Prog.*, 17:647–660, 2001.

[379] W.C. Zhou, J. Rehm, A. Europa, and W.-S. Hu. Alteration of mammalian cell metabolism by dynamic nutrient feeding. *Cytotechnology*, 24:99–108, 1997.

[380] G.-Y. Zhu, A. Zamamiri, M.A. Henson, and M. Hjortsø. Model predictive control of continuous yeast bioreactors using cell population balance models. *Chem. Eng. Sci.*, 55:6155–6167, 2000.

[381] M. Zinn, B. Witholt, and T. Egli. Dual nutrient limited growth: Models, experimental observations and applications. *J. Biotechnol.*, 113:263–279, 2004.

Based on the authors' extensive work in this field, **Dynamics of the Chemostat: A Bifurcation Theory Approach** explores the use of bifurcation theory to analyze the static and dynamic behavior of the chemostat.

The authors first survey the major work that has been carried out on the stability of continuous bioreactors. They next present the modeling approaches used for bioreactive systems, the different kinetic expressions for growth rates, and tools, such as multiplicity, bifurcation, and singularity theory, for analyzing nonlinear systems.

The text moves on to the static and dynamic behavior of the basic unstructured model of the chemostat for constant and variable yield coefficients as well as in the presence of wall attachment. It then covers the dynamics of interacting species, including pure and simple microbial competition, biodegradation of mixed substrates, dynamics of plasmid-bearing and plasmid-free recombinant cultures, and dynamics of predator–prey interactions. The authors also examine dynamics of the chemostat with product formation for various growth models, provide examples of bifurcation theory for studying the operability and dynamics of continuous bioreactor models, and apply elementary concepts of bifurcation theory to analyze the dynamics of a periodically forced bioreactor.

Using singularity theory and bifurcation techniques, this book presents a cohesive mathematical framework for analyzing and modeling the macro- and microscopic interactions occurring in chemostats. The text includes models that describe the intracellular and operating elements of the bioreactive system. It also explains the mathematical theory behind the models.

CRC Press
Taylor & Francis Group
an **informa** business
www.crcpress.com

6000 Broken Sound Parkway, NW
Suite 300, Boca Raton, FL 33487
711 Third Avenue
New York, NY 10017
2 Park Square, Milton Park
Abingdon, Oxon OX14 4RN, UK

K13016

ISBN: 978-1-4398-6714-3
90000
9 781439 867143